Spectrum-sliced Split-step Fourier Method for Precise Simulation of Supercontinuum Generation in Dispersion-Engineered Photonic Crystal Fibers

Di Yang[1, 2], **Ming Tang**[1, 2], **Songnian Fu**[1, 2], **and P. Shum**[1, 2]

[1]National Engineering Laboratory for Next Generation Internet Access System (NGIA)
Huazhong University of Science and Technology (HUST), Wuhan 430074, China
[2]Wuhan National Laboratory for Optoelectronics (WNLO), Wuhan 430074, China

Abstract— Supercontinuum (SC) generation in the nonlinear optical fiber is an attractive solution to produce significantly broadened intense spectrum (several hundreds of nm or even more) using laser pulse with moderate peak power. Traditionally, split-step Fourier (SSF) method and its variations have been developed and utilized to simulate complicated nonlinear dynamics associated with the continuum process successfully. However, the dispersion engineering of photonic crystal fibers (PCFs) raise difficulties of numerical simulations because only the dispersion coefficient at the central frequency of the injected pump pulse is used to present dispersion value of the entire spectrum window in normal SSF algorithm. In this paper, we propose a modified SSF algorithm to accurately simulate SC process in optical fibers with arbitrary dispersion profiles and no additional computational efforts are needed for the modified generalized nonlinear Schrödinger equation (GNLSE) simulation.

1. INTRODUCTION

Since its first observation by Ranka et al. in 2000 [1], SC generation in PCF [2] significantly attracts extensive research since its wide applications. Nonlinearity and dispersion are two key players in the formation of SC and the numerical operation about them determines the validity and accuracy of SSF algorithm. While the nonlinearity shows less wavelength dependence, the dispersion map of the nonlinear optical fiber exhibits strong spectrum related features. Since the dispersion property is essential to control the ultra-short pulse evolution along the fiber length, PCFs are employed to tailor the dispersion profile precisely in favor of the applied pump wavelength. Due to the air-hole cladding structure surrounding the central silica core, PCF has the flexibility to create non-traditional dispersion map (parabolic profile for instance) to optimize the spectral and temporal properties of SC pulses. Nevertheless, the dispersion engineering of PCFs raises difficulties of numerical simulations. Since the simulation covers an extremely broad bandwidth and generally a broadband optical pulse is used as the seeding pump, SSF simulation using single point dispersion value fails to produce accurate results even considering higher order dispersion coefficients.

In this paper, we formulate the dispersion curve into multiple sections at different wavelengths and put them into the GNLSE. The reconstructed GNLSE system takes into account dispersion properties at different wavelength separately and the section number of the sliced dispersion curve is decided by the sampling points set in the entire time-window we observe in the simulation and therefore no additional computational efforts are needed for the modified GNLSE simulation.

2. NUMERICAL MODEL

In this paper, all fibers fulfill the condition for endlessly single-mode propagation [3] and our numerical model is based on GNLSE [4]. According to traditional SSF method, differential operator $\hat{D}$ models linear loss and higher order dispersion effects with dispersion coefficients associated with the Taylor series expansion of the propagation constant around the center frequency ω_0. In our modified SSF algorithm, $\hat{D}$ is calculated as the following model:

$$\begin{cases} \hat{D}(\omega_1) = -\frac{\alpha}{2} + \sum\limits_{m\geq 2} \frac{i^{m+1}\beta_m(\omega_1)}{m!} \frac{\partial^m A_1}{\partial T^m} \\ \hat{D}(\omega_2) = -\frac{\alpha}{2} + \sum\limits_{m\geq 2} \frac{i^{m+1}\beta_m(\omega_2)}{m!} \frac{\partial^m A_2}{\partial T^m} \\ \vdots \\ \hat{D}(\omega_k) = -\frac{\alpha}{2} + \sum\limits_{m\geq 2} \frac{i^{m+1}\beta_m(\omega_k)}{m!} \frac{\partial^m A_k}{\partial T^m} \end{cases}, \tag{1}$$

where the electric field with amplitude A propagates along the fiber with longitudinal coordinate z and time in a reference frame traveling with the pump light is represented by T. $\beta_m(\omega_i)\,(i = 1, 2, \ldots, k)$ is the mth order dispersion coefficients at different frequency ω_i, α is the fiber loss. Then put $\hat{D}(\omega_i)$ into GNLSE separately, and we can get the following matrix equation in frequency domain after Fourier transform:

$$\frac{\partial\left[\tilde{A}_1(\omega_1), \tilde{A}_2(\omega_2), \ldots \tilde{A}_k(\omega_k)\right]^T}{\partial z} + \left[\sum_{m\geq 2}\frac{i^{m+1}\beta_m(\omega_1)}{m!}(i\omega_1)^m\tilde{A}_1, \sum_{m\geq 2}\frac{i^{m+1}\beta_m(\omega_2)}{m!}(i\omega_2)^m\tilde{A}_2,\right.$$
$$\left.\ldots\sum_{m\geq 2}\frac{i^{m+1}\beta_m(\omega_k)}{m!}(i\omega_k)^m\tilde{A}_k\right]^T + \frac{\alpha}{2}\left[\tilde{A}_1(\omega_1), \tilde{A}_2(\omega_2), \ldots \tilde{A}_k(\omega_k)\right]^T = 0 \quad (2)$$

The section number of the sliced dispersion curve is decided by the sampling points set in the entire time-window we observe in the simulation and they have the following relation:

$$\lambda_i = \lambda_0 + n_i/L/f_0 * \lambda_0 \quad (3)$$

where $f_0 = c/\lambda_0$ (λ_0 is the center wavelength, c equals the light transmission speed in vacuum) and L represents the width of time window in our simulation which is proportional to initial pulse bandwidth. n_i is one point among $[-N/2 : 1 : N/2]$ while N is the sampling point and λ_i is the wavelength to the homologous ω_i. Through (3), the values of sampling point n_i at different λ_i could be calculated. Then, we compute a string of $\beta_m(\omega_i)$ which is corresponding to n_i at different wavelength and the number of the sliced dispersion curve k is the same with the sampling points set in the entire time-window. After that, put the variable $\beta_m(\omega_i)$ into the reconstructed GNLSE system (2) separately.

3. NUMERICAL RESULTS

Two types of dispersion profiles in PCF are considered for numerical simulation. One is the conventional dispersion curve with one zero dispersion wavelength (ZDW), namely type I; another is a parabolic dispersion curve with two ZDWs, namely type II. The initial pulse is Gaussian and the initial pulse width $T_0 = 100\,\text{fs}$. To type I, we choose NL-PM-750 made by NKT as the delegate and the detailed parameters can be searched in [5] and in the simulation of type II, a parabolic

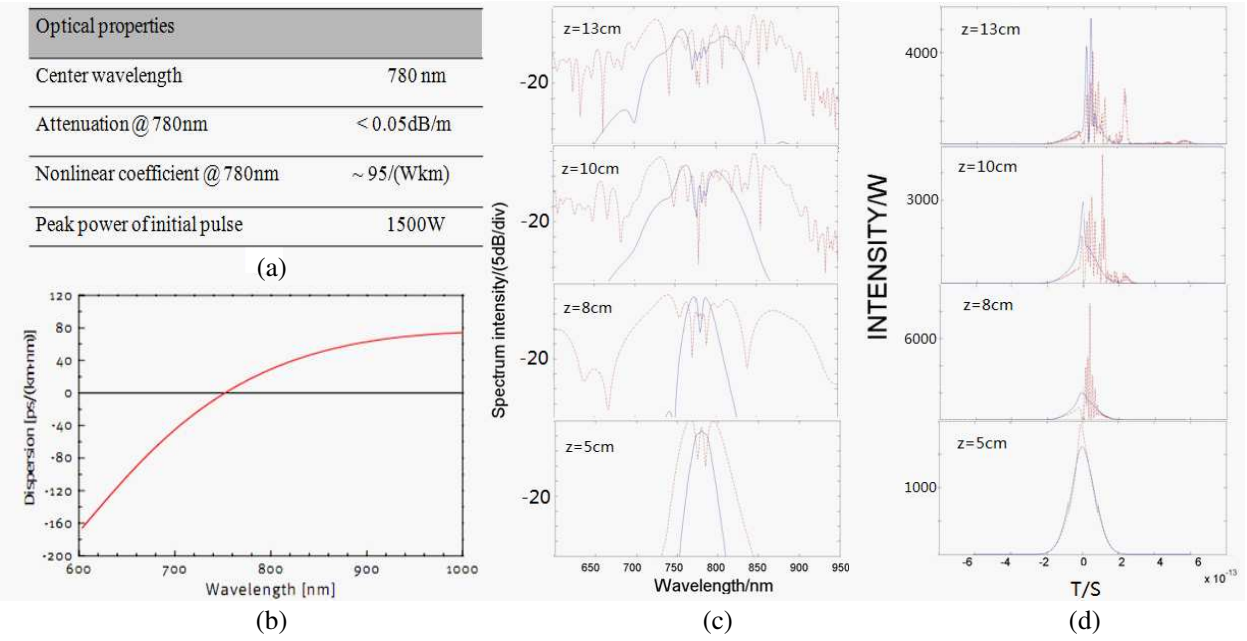

Figure 1: (a) Optical properties of PCF in type I. (b) The dispersion curve. (c) Temporal and (d) spectral evolution of an optical pulse. The red dashed line is simulation in traditional SSF while the blue solid line is in modified SSF.

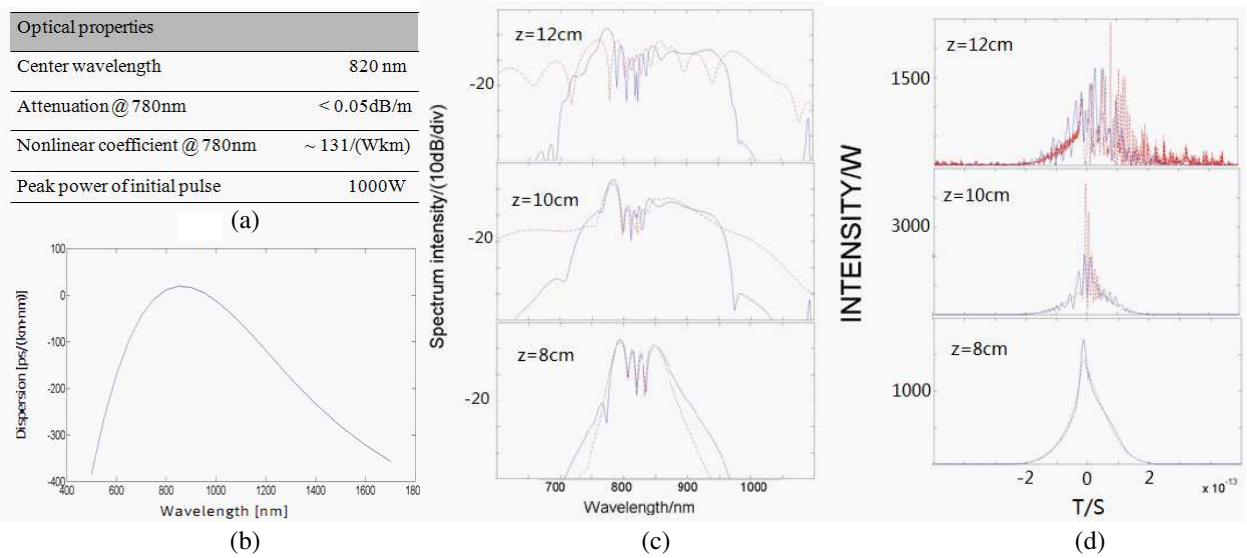

Figure 2: (a) Optical properties of PCF in type II. (b) The dispersion curve. (c) Temporal and (d) spectral evolution of an optical pulse. The red dashed line is simulation in traditional SSF while the blue solid line in modified SSF.

dispersion curve reported in [6] is selected to do research. Figures 1 and 2 are the results of type I and type II respectively.

From the results, we can see the speed of pulse evolution in modified SSF is not as fast as that getting from traditional SSF. This phenomenon is caused by the following reasons: the center wavelength is in anomalous dispersion regime, so the lower frequency means the slower transmission speed and the red-shifted part will accelerate the speed of pulse broadening. However, when spectrum is significantly broadened, it will arrive into normal dispersion regime whose features are different from that at the center wavelength. Therefore, conventional SSF simulation using single point dispersion value will increase the red-shifted part and speed up the evolution. SSF simulation using single point dispersion value fails to produce accurate results even considering higher order dispersion coefficients especially to type II.

4. CONCLUSION

We conduct intensive numerical experiments to investigate our proposed algorithm and compare results with the conventional SSF method. The results show that the accuracy of SC simulation with modified GNLSE is improved and to type II, the distance between two ZDWs is closer, the deviation is greater in traditional SSF. This method is effective to correct the changed dispersion coefficients, reduce the deviation of SC generation in dispersion-engineered PCF and moreover, no additional computational efforts are needed for the modified GNLSE simulation.

REFERENCES

1. Ranka, J. K., R. S. Windeler, and A. J. Stentz, "Visible continuum generation in air-silica microstructure optical fibers with anomalous dispersion at 800 nm," *Opt. Lett.*, Vol. 25, 25–27, 2000.
2. Dudley, J. M., G. Genty, and S. Coen, "Supercontinuum generation in photonics crystal fiber," *Rev. Mod. Phys.*, Vol. 78, No. 4, 1135–1184, 2006.
3. Koshiba, M. and K. Saitoh, "Applicability of classical opticalfiber theories to holey fibers," *Opt. Lett.*, Vol. 29, 1739–1741, 2004.
4. Dudley, J. M., G. Genty, and S. Coen, "Supercontinuum generation in photonic crystal fiber," *Rev. Mod. Phys.*, Vol. 78, No. 4, 1135–1184, 2006.
5. http://www.nktphotonics.com/files/files/NL-PM-750-090612.pdf.
6. Zhang, H., S. Yu, J. Zhang, et al., "Effect of frequency chirp on supercontinuum generation in photonic crystal fibers with two zero-dispersion wavelengths," *Opt. Express*, Vol. 15, No. 3, 1147–1154, 2007.

Influence of Geometric Parameters on the SOI Racetrack Resonator Properties

P. Matavulj[1] **and T. Kečа**[2]

[1]Faculty of Electrical Engineering, University of Belgrade, Serbia
[2]ICT College of Vocational Studies, Belgrade, Serbia

Abstract— In this paper, we investigate the influence of SOI racetrack resonator's geometric parameters on its transfer function. Several different geometric parameters divided into two groups were considered. All obtained functions, as well as their differences for input TE and TM mode, give the opportunity for detailed analysis of resonator's features. Furthermore, this procedure opens up the possibility to estimate the FSR and resonant wavelength for different geometric parameters and consequently to predict resonator functionality.

1. INTRODUCTION

The silicone rib racetrack resonators have several geometric parameters with significant influence on the propagation of light. We separated them into two groups (Figure 1), mostly by their size. The first group includes ring-shape parameters, coupling length (L_c) and ring circumference (ρ). Those parameters are usually several hundreds micrometers long. The second group includes much smaller cross-section parameters: waveguide width (w), oxide layer thickness (t) and slope angle (α). Waveguide width and oxide layer thickness are usually less than one micrometer in size. Possible values for sidewall inclination are in interval 80°–90°. The influence of ring-shape parameters has already been studied [1]. In this paper, we also analyze the influence of cross-section parameters on propagation of light.

To investigate geometric parameters influence, the transfer function (output-input light intensity ratio) is calculated using Coupled Mode Theory (CMT). When polarized input light enters a waveguide, coupling occurs in a coupling region where two waveguides are near and parallel to each other. The part of input light which enters the racetrack changes its polarization state in circular segments. Then, another coupling occurs, this time in the opposite direction: from racetrack to rectilinear waveguide. Both processes are described with corresponding transfer matrices [2–4]. By combining transfer matrices transfer functions can be derived. Those transfer functions describe parts of incident light that remain in the same polarization state (TE → TE and TM → TM), as well as the parts that change the polarization state (TE → TM and TM → TE).

The whole ring resonator acts like a kind of resonant cavity, and at least two resonant minima can be seen in the transfer function for wavelength interval of our interest (1550 ± 0.5 nm). Free Spectral Range (FSR) and first resonant wavelength are two main parameters by which transfer

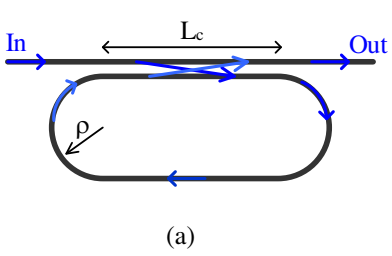

Figure 1: Ring resonator's geometric parameters: (a) ring-shape and (b) cross-section.

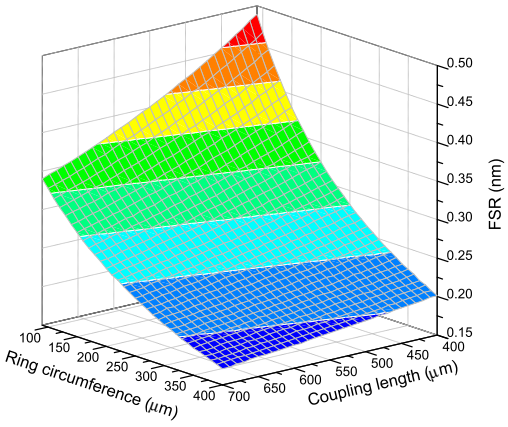

Figure 2: FSR as a function of coupling length and ring circumference for incident TM mode. Cross-section parameters: $w = 1\,\mu$m, $\alpha = 90°$ and $t = 0.3\,\mu$m.

functions are distinguished for different geometric values. So, we calculated transfer functions of ring resonators for different geometric parameters and extracted FSR and first resonant wavelength dependencies for each of them.

2. INFLUENCE OF RING-SHAPE PARAMETERS

FSR and first resonant wavelength dependencies of coupling length and ring circumference have already been presented, but some of the main results will be given again, so as to make a comparison and draw a conclusion. FSR shows reciprocal dependence on both ring-shape parameters. These relations are slightly weaker for coupling length compared to ring circumference. Both of them are shown together in Figure 2.

This FSR dependence is easy to fit in an adequate mathematical function. The one with the smallest standard deviation is the form of reciprocal function:

$$FSR = \frac{f_0}{1 + aL_c + b\rho + c\rho L_c}, \tag{1}$$

where f_0, a, b and c are constants which should be determined for individual case, depending on whether the incident is TE or TM mode, as well as on the width of the waveguide. In the example given in Figure 2 the above mentioned constants for input TM mode are: $f_0 = 232.76\,\text{nm}$, $a = 0.695\,\mu\text{m}^{-1}$, $b = 2.185\,\mu\text{m}^{-1}$ and $c = 10.435\,\text{mm}^{-2}$. For TE mode and same cross-section geometric parameters, those constants would be: $f_0 = 248.32\,\text{nm}$, $a = 0.734\,\mu\text{m}^{-1}$, $b = 2.274\,\mu\text{m}^{-1}$ and $c = 14.854\,\text{mm}^{-2}$.

First resonant wavelength strongly depends on both ring-shape parameters, Figure 3. Dependencies have a periodic property, due to the transfer function itself and its FSR. In other words, the increase of one resonant wavelength towards upper values causes the subsequent resonant wavelength to become the first. Spatial periods of these periodic functions are small, especially for the ring circumference dependence.

In one spatial period both functions are linear. Both of these functions can be fitted with similar Fourier's series:

$$\lambda_{res} = A_0 + \sum_n B_n \sin\left(2n\pi\left(x - x_0\right)\right), \tag{2}$$

where x represents either coupling length (L_c) or ring circumference (ρ) and x_0 is any beginning of their spatial periods (any coupling length or ring circumference for which minimal resonant wavelength occurs). Spatial periods Δx (ΔL or $\Delta\rho$) of these dependencies are approximately $\Delta L = 230\,\text{nm}$ for coupling length, and $\Delta\rho = 72\,\text{nm}$ for ring circumference. Fourier's parameters for this type of functions are $A_0 = k(2x_0 + \Delta x) + 2l$ and $B_n = k\Delta x/n\pi$, where parameters k and l need to be extracted from the function itself.

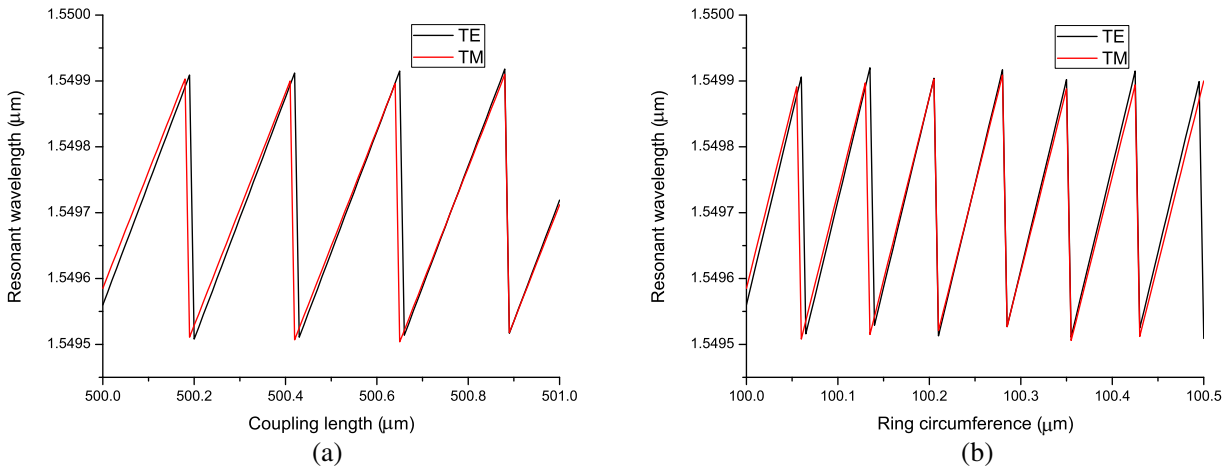

Figure 3: First resonant wavelength as a function of (a) coupling length and (b) ring circumference, for both TE and TM mode. Cross-section parameters: $w = 1\,\mu\text{m}$, $\alpha = 90°$, $t = 0.3\,\mu\text{m}$.

3. INFLUENCE OF CROSS-SECTION PARAMETERS

In case of cross-section geometric parameters, FSR does not depend at all on oxide layer thickness or slope angle. Considering waveguide width, FSR shows no dependence for input TE mode and very weak one for TM mode, as shown in Figure 4.

Unlike the FSR, first resonant wavelength strongly depends on cross-section geometric parameters and, generally, changes very rapidly. First resonant wavelength as a function of waveguide width is shown in Figures 5, 6, and 7 for different ring circumferences and for both input modes. These relations show some periodicity for input TE mode (black line, square marks) and no regularity for TM mode (red line, circle marks).

Slope angle dependence has similar behavior as shown in Figures 8, 10, and 12, again for different ring circumferences and both input modes. They are also approximately periodic for TE, but not for TM mode. Spatial periods of these approximately periodic functions are very small: less than 10 nm for waveguide width and parts of degree for slope angle. On the other side, oxide thickness dependence, as depicted in Figures 9, 11, and 13 (for three values of ring circumferences and both input modes), show no periodicity for any input mode, TE or TM.

All of these functions have the same role: to find the correlations between responses for two input modes. In experimentally obtained transfer functions, adjacent resonant TE and TM minima can be seen, and their first resonant wavelength difference is naturally less than FSR. Our investigation

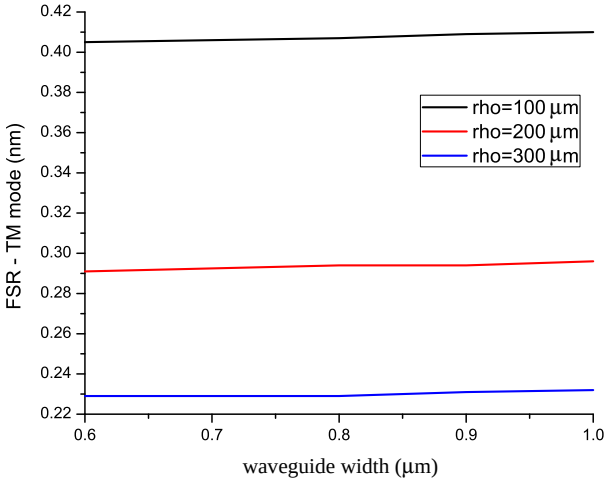

Figure 4: FSR (TM mode) as a function of waveguide width for three ring circumference values: 100, 200 and 300 μm ($\alpha = 80°$, $t = 0.3$ μm).

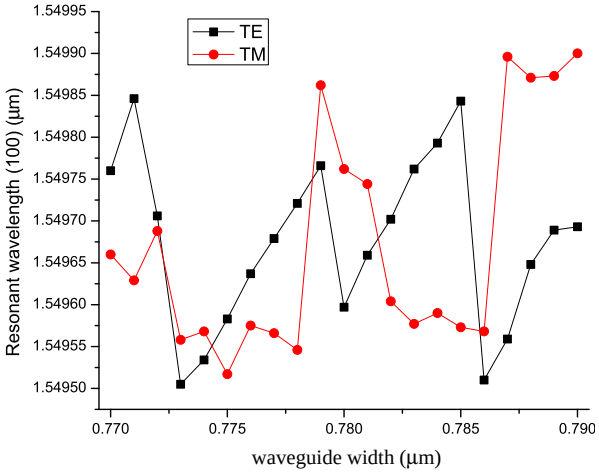

Figure 5: First resonant wavelength (TE/TM mode) as a function of waveguide width ($\rho = 100$ μm, $\alpha = 90°$, $t = 0$ μm).

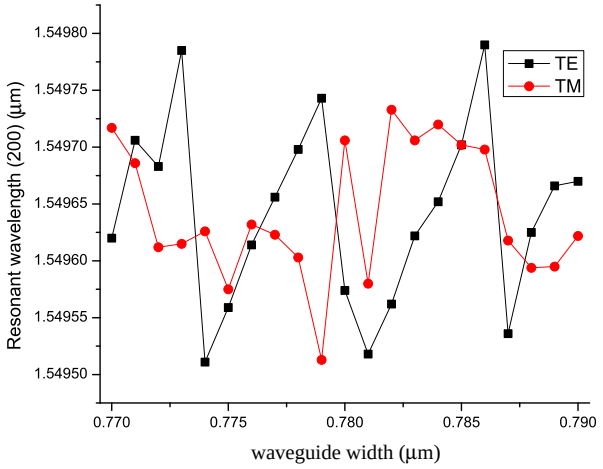

Figure 6: First resonant wavelength (TE/TM mode) as a function of waveguide width ($\rho = 200$ μm, $\alpha = 90°$, $t = 0$ μm).

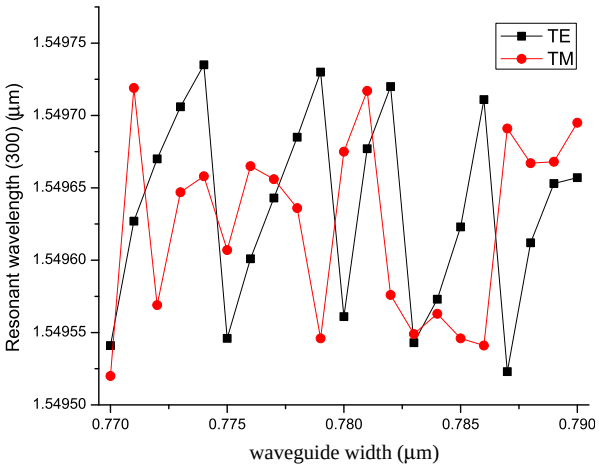

Figure 7: First resonant wavelength (TE/TM mode) as a function of waveguide width ($\rho = 300$ μm, $\alpha = 90°$, $t = 0$ μm).

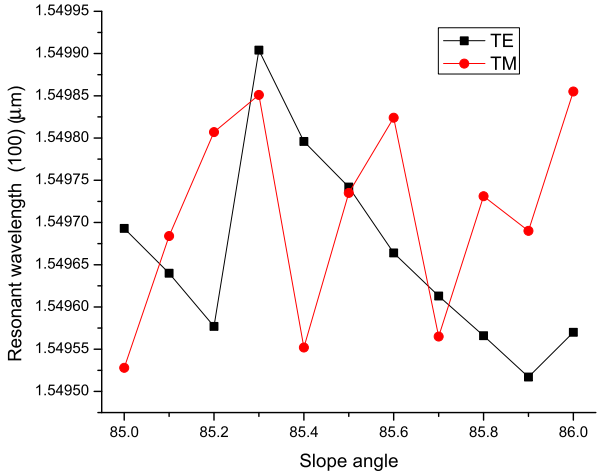

Figure 8: First resonant wavelength (TE/TM mode) as a function of slope angle ($\rho = 100\,\mu\text{m}$, $w = 0.7\,\mu\text{m}$, $t = 0\,\mu\text{m}$).

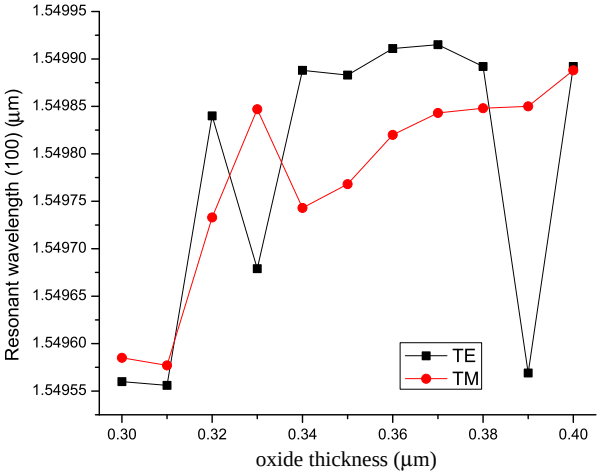

Figure 9: First resonant wavelength (TE/TM mode) as a function of oxide thickness ($\rho = 100\,\mu\text{m}$, $w = 0.9\,\mu\text{m}$, $\alpha = 90°$).

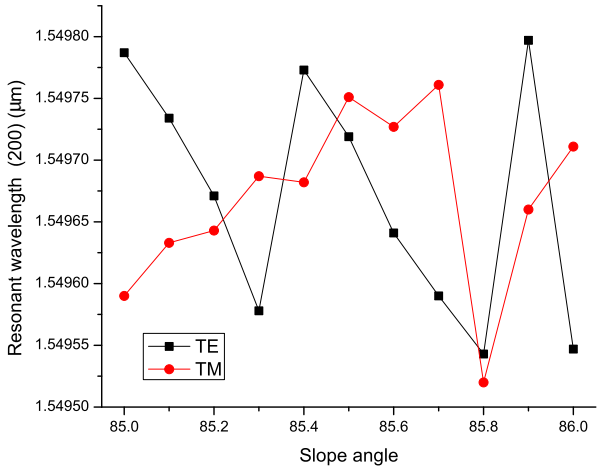

Figure 10: First resonant wavelength (TE/TM mode) as a function of slope angle ($\rho = 200\,\mu\text{m}$, $w = 0.7\,\mu\text{m}$, $t = 0\,\mu\text{m}$).

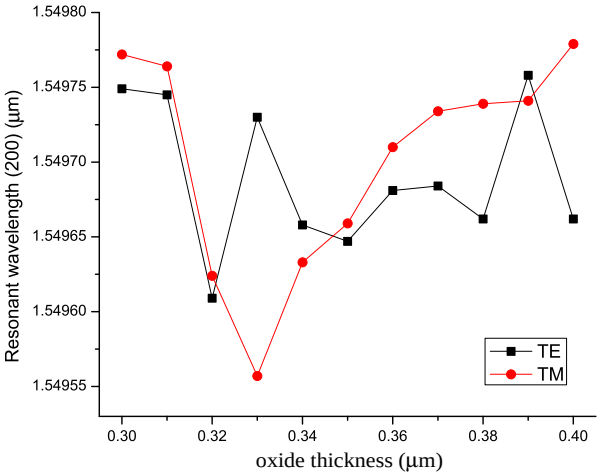

Figure 11: First resonant wavelength (TE/TM mode) as a function of oxide thickness ($\rho = 200\,\mu\text{m}$, $w = 0.9\,\mu\text{m}$, $\alpha = 90°$).

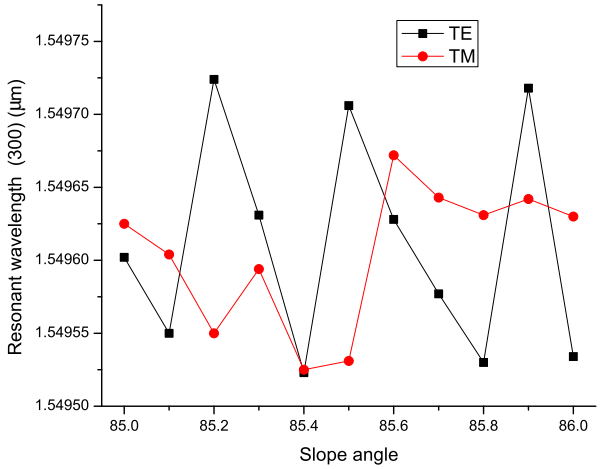

Figure 12: First resonant wavelength (TE/TM mode) as a function of slope angle ($\rho = 300\,\mu\text{m}$, $w = 0.7\,\mu\text{m}$, $t = 0\,\mu\text{m}$).

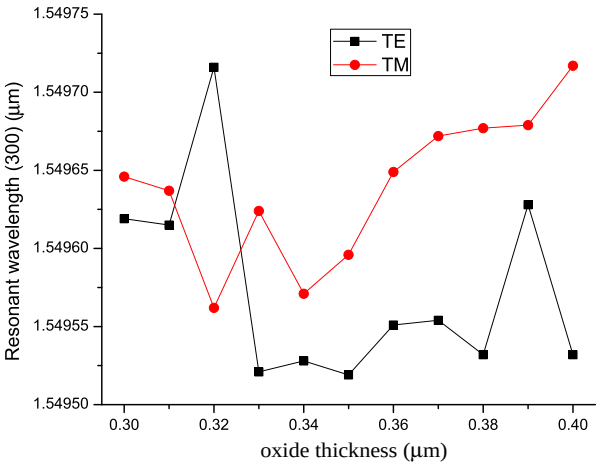

Figure 13: First resonant wavelength (TE/TM mode) as a function of oxide thickness ($\rho = 300\,\mu\text{m}$, $w = 0.9\,\mu\text{m}$, $\alpha = 90°$).

shows that there are combinations of geometric parameters for which resonant minima coincide for both modes (cross-sections of lines in Figures 5–13). The easiest way to extract these cross-section parameters is from the graph itself. We withdraw to fit those functions considering that the size of cross-section geometric parameters is less than one micrometer. Establishing the exact functions dependencies is feasible, but questionable. These functions are important in our further work because they give possibilities for fine adjustment of transfer functions.

4. CONCLUSIONS

Geometric parameters of silicon rib racetrack resonator are divided into two groups and influence of both of them is analyzed. Transfer functions were calculated using CMT for variety of different resonator's geometric parameters. FSR and first resonant wavelength were extracted from those transfer functions and their geometric parameters dependencies were obtained.

The study of geometric parameters influence on ring resonator properties is necessary for the comparison of theoretically obtained transfer functions and real, experimental results [5, 6]. By analyzing the influence of geometric parameters on ring resonator, its functionality can be predicted and projected, despite small variations of these parameters in manufacturing process, which are inevitable and unpredictable.

REFERENCES

1. Keča, T., P. Matavulj, W. Headley, and G. Mashanovich, "Free spectral range adjustment of a silicon rib racetrack resonator," *Physica Scripta*, Vol. T149, 014031-4, 2012.
2. Lui, W., T. Hirono, K. Yokoyama, and W. P. Huang, "Polarisation rotation in semiconductor bending waveguides: A coupled-mode theory formulation," *J. Lightwave Technol.*, Vol. 16, 929–936, 1998.
3. Cusmai, G., F. Morichetti, P. Rosotti, R. Costa, and A. Melloni, "Circuit-oriented modelling of ring-resonators," *Opt. Quantum. Electron.*, Vol. 37, 343–258, 2005.
4. Morichetti, F., A. Melloni, and M. Martinelli, "Effect of polarisation rotation in optical ring-resonator- based devices," *J. Lightwave Technol.*, Vol. 24, 573–585, 2006.
5. Headly, W., G. Reed, and S. Howe, "Polarization-independent optical racetrack resonators using rib waveguides on silicon-on-insulator," *Appl. Phy. Lett.*, Vol. 85, 23, 2004.
6. Miloševic, M., P. Matavulj, B. Timotijevic, G. Reed, and G. Mashanovich, "Design rules for single-mode and polarization-independent silicon-on-insulator rib waveguides using stress engineering," *J. Lightwave Technol.*, Vol. 26 1840–1846, 2008.

Formation Mechanism and Applications of Laser Induced Elemental Distribution in Glasses

K. Miura[1], **M. Shimizu**[1], **M. Sakakura**[2], **T. Kurita**[1], **Y. Shimotsuma**[1], **and K. Hirao**[1]

[1]Department of Material Chemistry, Kyoto University, Nishikyo-ku, Kyoto 615-8510, Japan
[2]International Innovation Center, Kyoto University, Nishikyo-ku, Kyoto 615-8510, Japan

Abstract—In this paper, we present the behavior of elemental distribution for various types of glass. We also discuss the effect of the temperature distribution formed by the heat accumulation with irradiation of femtosecond laser at a high repetition rate. It was found that the tendency in the elemental distribution depended on the strength of the bond between cations and oxygen ions. Strongly bonded ions like Si-O migrated to the center of the irradiated spot, whereas weakly bonded ions such as Na-O or Ca-O migrated to the outside. Si ions in the glass tended to stay in the center of the laser irradiation area. We also confirmed that various shapes of the element distribution can be produced by making multiple irradiated points with a LCOS-SLM and adjusting the temperature distribution.

1. INTRODUCTION

When a transparent material like glass is irradiated by a tightly focused femtosecond laser, photo-induced reactions should occur only near the focused part of the laser beam due to nonlinear optical phenomena such as multiphoton absorption. Thus, a femtosecond laser can be used to modify transparent materials like glass microscopically and three-dimensionally [1–4]. We investigated the irradiation effects of a femtosecond laser pulse inside the glass using the transient lens method with a sub-picosecond time resolution. It was evident that a shock wave forms at the focal point inside the glass of the beam created by the femtosecond laser and propagates to the surrounding area. By irradiating a single pulse of 0.1 μJ, it was also confirmed that the temperature at the center of the laser beam reaches 3000°C or more within 1 ps [5], and that the temperature then decreases from $\sim$ 3000°C to $\sim$ 300°C within 10 μs [6]. This result suggests that the heat accumulation becomes critical when the repetition rate of the irradiation is higher than 100 kHz. When a lot of laser pulses are focused at a high repetition rate (more than several hundred kHz), the released heat is accumulated around the photoexcited region and the surrounding glass is modified due to the high temperature increase. If the heat accumulation, also known as thermo-migration, occurs inside glass during laser irradiation, the constituent elements of the glass may spread or migrate in a specific direction because of the formation of thermal gradient in a small area. To clarify this assumption, we investigated the temperature distribution due to heat accumulation in a modification area inside a glass. Results showed that the elemental distribution of a ring shaped pattern can be formed in a area where a steep temperature gradient was formed in a glass.

In this article, we report the distribution behavior of each element for various types of multi-component glass. We also discuss the effect of the temperature distribution formed by the heat accumulation with the irradiation of the femtosecond laser at a high repetition rate. The objective of the present investigation is the development of a new technique for controlling optical properties in a local area using ion migration.

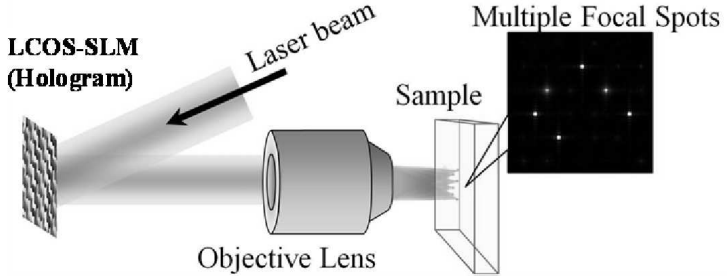

Figure 1: Simplified illustration of parallel laser processing with an SLM.

2. EXPERIMENTAL PROCEDURE

Investigations were carried out on various types of glass possessing different types of glass formers and modifiers. We accurately focused femtosecond laser pulses inside a glass sample to create elemental distribution by ion migration. The irradiation source was a regeneratively amplified 800-nm Ti:sapphire laser that emitted 1 kHz and 250-kHz mode-locked pulses with a pulse duration of 80–120 fs (FWHM). Glass samples of ∼3 mm thickness were placed on an XYZ stage under the optical microscope. The infrared laser radiation reflected by a dichroic mirror inside the microscope was focused via an objective onto the sample. The irradiated area was imaged in the visible spectral range via the microscope by simultaneously using a color CCD camera. After laser irradiation, to obtain information on the distribution of each element, the glass samples were polished to the depth of the beam waist location, and then analyzed by electron probe micro-analysis (EPMA). For several glasses, with the help of an XYZ stage controlled via computer, the elemental distribution was formed like a line by translating the sample parallel to the axis of the laser beam at a rate of 20 µm/s. For these samples, the distributions of refractive index were estimated from the results of the reflectance obtained using a confocal laser scanning microscope. On the sample with the refractive index increasing in a central region, we observed the near-field patterns from elemental distribution lines at 633 nm. The light for observation focused via a 20X microscope objective lens was coupled on one end of the core and the intensity distributions for the translated light were measured with a beam profiler. Furthermore, to control the shape of the elemental distribution, 1-kHz and 250-kHs fs laser pulses were focused simultaneously at multiple positions inside a glass by a parallel laser processing system with a Liquid Crystal on Silicon-Spatial Light Modulator (LCOS-SLM, X10468-02, Hamamatsu Photonics K. K.). The simplified illustration of the parallel laser processing with an SLM is shown in Fig. 1. The spatial phase distribution of the laser beam is modulated by an SLM, and the laser beam is then focused by a lens. After the focusing, the focal spots are generated at multiple positions, depending on the phase distribution by the SLM.

3. RESULTS AND DISCUSSION

A microphotograph in Fig. 2(a) was taken near the focal point in glass sample after irradiation with pulse energy of 3.0 µJ and focused with a 20X objective lens with a numerical aperture of 0.40 on a spot for 1 s at a repetition rate of 250 kHz. Fig. 1(b) shows the temperature distribution during laser irradiation on the same area in (a). The composition of the glass sample was Na_2O (9.25 wt.%), SiO_2 (67.3 wt.%), CaO (7.21 wt.%), K_2O (8.97 wt.%), and ZnO (4.14 wt.%). It was

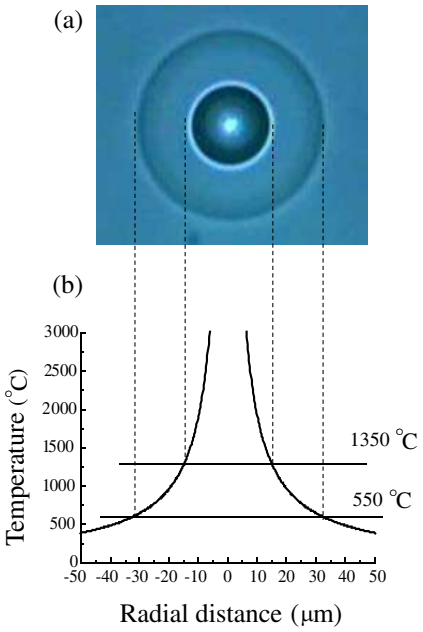

Figure 2: (a) A microphotograph and (b) temperature distribution immediately after the 100,000-pulses irradiation with 250 kHz.

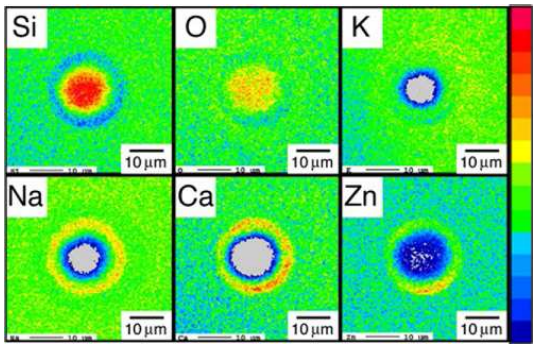

Figure 3: Profile of the elemental concentration around the focal point in a silicate glass after laser irradiation, as analyzed by EPMA.

conformed that the modification in a glass due to heat accumulation has two boundary structures. The inner structure should be attributed to the photoexcitation and modification due to shock wave generation and high temperature elevation [7]. Because the temperature of an inside boundary is 1350°C, the inner area is melting glass which has a steep temperature gradient. The temperature of an outside boundary is 550°C, and this temperature corresponds to the glass transition temperature. Fig. 3 shows a profile of the elemental distribution around the focal point after laser irradiation, as analyzed by EPMA. The relative concentration of Si and O ions increase and those of K, Na, Ca, and Zn decrease at the focal point. An opposite trend is observed in the area around the focal point by the ion exchanges. The elemental distribution of a ring shaped pattern could be observed in only the inner area shown in Fig. 2. We conducted the same measurements for the other types of glass and found that the ion migration occurred at a high temperature area above the melting temperature. That is, the formation of elemental distribution is expected to have an effect at a high repetition rate.

Figures 4(a) and (b) show the results of back scattered electron images (BEI) and EPMA spectra mappings on the polished SiO_2-Al_2O_3-CaO glass surface after irradiation with repetition rates of 1 kHz and 250 kHz, respectively. In the case of the 250-kHz repetition rate, heat caused by laser energy absorption was diffused over only $\sim$ 2 µm during the interval between successive pulses (4 µs). In the case of the 1-kHz rate (interval of pulses: 1 ms), in contrast, the heat could diffuse away out of the focal volume to $\sim$ 30 µm during the interval of successive pulses [8]. Therefore, the formation of elemental distribution is expected to have an effect at a repetition rate of 250 kHz. Figs. 5(a) and (b) show the results of EPMA spectra mappings on the polished SiO_2-B_2O_3-Al_2O_3-CaO glass surface after irradiation with pulse energy of 2.0 µJ and 3.5 µJ, respectively. In both cases, the concentrations of silicon and aluminum elements are denser in the center of the irradiated

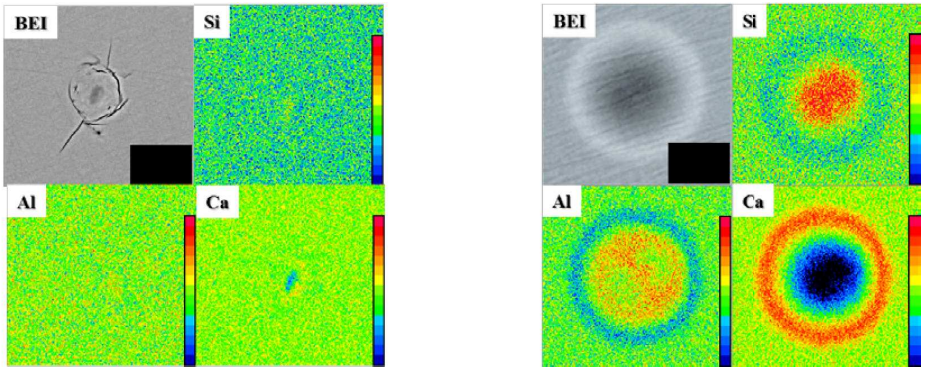

(a) (b)

Figure 4: Back scattered electron images (BEI) and EPMA spectra mappings on the polished SiO_2-Al_2O_3-CaO glass surface after irradiation with repetition rates of (a) 1 kHz and (b) 250 kHz.

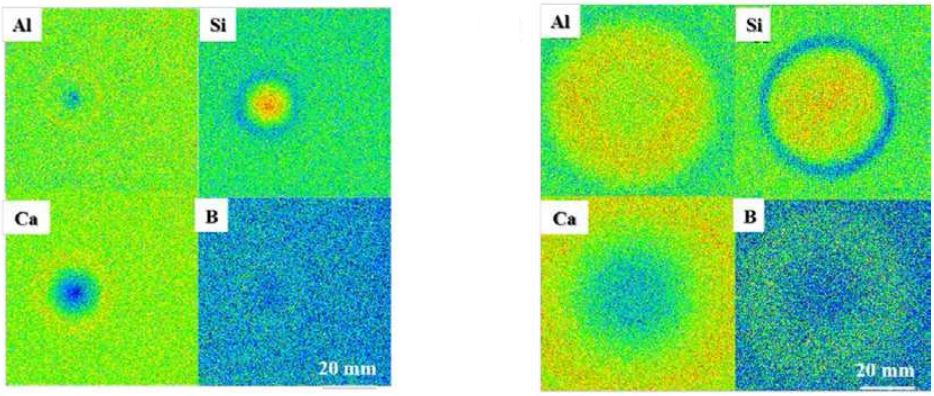

(a) (b)

Figure 5: EPMA spectra mappings on the polished SiO_2-B_2O_3-Al_2O_3-CaO glass surface after irradiation with pulse energy of (a) 2.0 µJ and (b) 3.5 µJ.

area and more diffuse toward the edges. In contrast, calcium and boron migrate to the outside from the center.

The calculated temperature distributions during laser irradiation with different pulse energies are shown in Fig. 6. The method we used to calculat the temperature distributions was similar to a previously reported method [7]. The distributions in the central region are not shown in this figure, because the temperature change in this region is dramatic due to repeated laser irradiation. From these results, it was found that an increase in the pulse energy caused dramatic increases in the central temperature and the size of the liquid phase (melting glass) area. The temperature gradient was over several tens °C/µm in the ion migration area during laser irradiation. As a result, the area of elemental distribution tended to significantly broaden with increasing incident pulse energy. From the results of the ion migration for various types of silicate glass, it was confirmed that elemental distributions in silicate glass tend to become visible in Fig. 7. Based on experimental results obtained for various types of glass, it was found that the tendency in the elemental distribution depended on the strength of the bond between cations and oxygen ions. Strongly bonded ions like Si-O migrated to the center of the irradiated spot, whereas weakly bonded ions such as Na-O or Ca-O migrated to the outside. Si ions in the glass tended to stay in the center of the laser irradiation area. As the temperature of a glass local increased, additional elemental distribution in a glass appear, the sequence being first glass network formers, then intermediate oxides and finally network modifiers from the center of an irradiated spot. These results accords with other reports [9, 10] and demonstrate that elements strongly bonded with oxygen have a tendency to migrate to hot regions. Therefore, the temperature gradient should be responsible for element migration, i.e., this phenomenon should be interpreted as thermomigration.

The increase of Si ions means a decrease in the refractive index in most glass. In the case of the

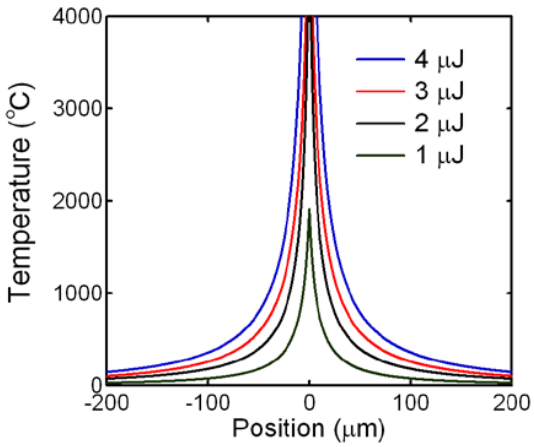

Figure 6: Calculated temperature distributions during laser irradiation with different pulse energies.

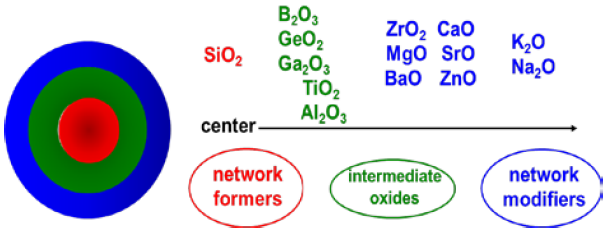

Figure 7: Tendency in the elemental distribution depended on the strength of the bond between cations and oxygen ions.

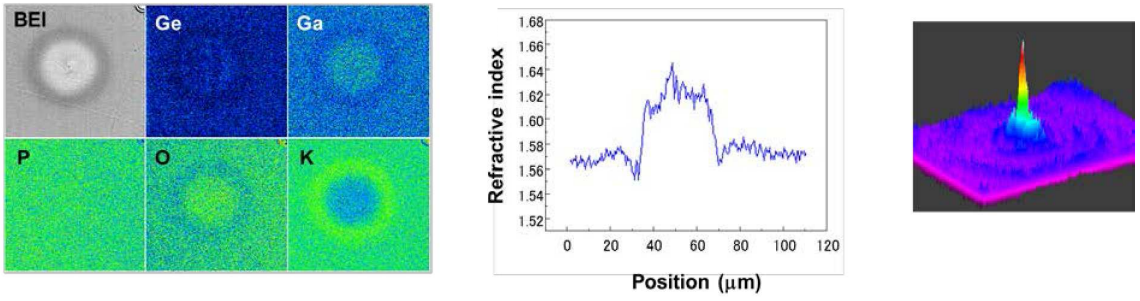

(a) (b) (c)

Figure 8: (a) EPMA spectra mappings, (b) refractive index distribution in same area and (c) near-field patterns from a waveguide formed by using elemental distribution for a P_2O_5-GeO_2-Ga_2O_3-K_2O glass.

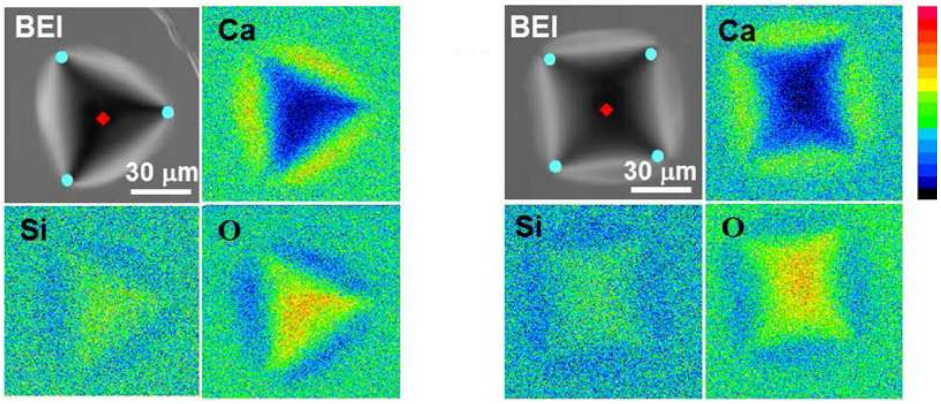

(a) (b)

Figure 9: Element distributions in CaO-SiO_2 glass after simultaneous fs laser irradiations at multiple positions with a LCOS-SLM. (a) Triangle and (b) square elemental distribution induced by irradiation at four and five points. Red (250 kHz) and blue (1 kHz) points depict the photoexcited points.

phosphate (P_2O_5-GeO_2-Ga_2O_3-K_2O) glass, it was also confirmed that Ge and Ga were moved to the center in the laser irradiated area, as shown in Fig. 8(a). An increase of Ge and Ga contributes to an increase in the refractive index (see Fig. 8(b)). By using this phenomenon, we were able to successfully write optical waveguides, where the elemental distributions were continuously induced along a scanning path of the focal point (see Fig. 8(c)). The spatial distribution of glass components is very important for controlling the property of glass, because the composition of a glass affects its chemical, mechanical and optical properties. However, there is a limitation of the spatial control, because thermal energy diffuses isotropically away from the photoexcited region inside glasses. Therefore, the distributions of glass elements are always ring-shaped or circular, which is due to the circular symmetric temperature distribution. This limitation can be overcome by adjusting the temperature distribution by the simultaneous irradiation of 1-kHz and 250-kHz lasers varying in a heat accumulation effect. Fig. 9 shows shaped-element distributions in a CaO-SiO_2 glass by making multiple irradiated points with a LCOS-SLM. The sharp vertex in the triangle can be made by choosing the optimal repetition rate of the excitation laser pulses (see Fig. 9(a)). In a similar way, squared heat-modification and distributions of each element can be obtained (see Fig. 9(b)). These results clearly show that parallel laser processing can be applied to the spatial control of material properties.

4. CONCLUSIONS

We investigated the distribution behavior of each element for various types of multicomponent glass. Experimental showed that the tendency in the elemental distribution depended on the strength of the bond between cations and oxygen ions. As the temperature of a glass local increases, additional elemental distribution in a glass appear, the sequence being first glass network formers, then intermediate oxides and finally network modifiers from the center of an irradiated spot. The elements strongly bonded with oxygen have tendency to migrate to the hot region. Therefore, the temperature gradient should be responsible for element migration, i.e., this phenomenon should be interpreted as thermomigration. We also confirmed that various shapes of element distribution can be produced by adjusting the temperature distribution by making multiple irradiated points with a LCOS-SLM. The spatial distribution of glass components is very important for controlling the property of glass, because the composition of a glass affects its chemical, mechanical and optical properties.

ACKNOWLEDGMENT

This work was supported by MEXT/JSPS Grant-in-Aid for Scientific Research (A) 23246121, the Kyoto Environmental Nanotechnology Cluster from MEXT and Next Generation Laser Processing Technology Research Association.

REFERENCES

1. Davis, K. M., K. Miura, N. Sugimoto, and K. Hirao, "Writing waveguides in glass with a femtosecond laser," *Opt. Lett.*, Vol. 21, 1729–1731, 1996.
2. Glezer, E. N., M. Milosavljevic, L. Huang, R. J. Finlay, T.-H. Her, J. P. Callan, and E. Mazur, "Three dimensional optical storage inside transparent materials," *Opt. Lett.*, Vol. 21, 2023–2025, 1996.
3. Miura, K., J. Qiu, H. Inouye, T. Mitsuyu, and K. Hirao, "Photowritten optical waveguides in various glasses with ultrashort pulse laser," *Applied Physics Letters*, Vol. 71, 3329–3331, 1997.
4. Shimotsuma, Y., M. Sakakura, K. Miura, J. Qiu, P. G. Kazansky, K. Fujita, and K. Hirao, "Application of femtosecond-laser induced nanostructures in optical memory," *Journal of Nanoscience and Nanotechnology*, Vol. 7, 94–104, 2007.
5. Sakakura, M., M. Terazima, Y. Shimotsuma, K. Miura, and K. Hirao, "Observation of pressure wave generated by focusing a femtosecond laser pulse inside a glass," *Optics Express*, Vol. 15, No. 9, 5674–5686, 2007.
6. Sakakura, M., M. Terazima, Y. Shimotsuma, K. Miura, and K. Hirao, "Heating and rapid cooling of bulk glass after photoexcitation by a focused femtosecond laser pulse," *Optics Express*, Vol. 15, No. 25, 16800–16807, 2007.
7. Shimizu, M., M. Sakakura, M. Ohnishi, Y. Shimotsuma, T. Nakaya, K. Miura, and K. Hirao, "Mechanism of heat-modification inside a glass after irradiation with high-repetition rate femtosecond laser pulses," *J. Appl. Phys.*, Vol. 108, 073533, 2010.
8. Sakakura, M., M. Shimizu, Y. Shimotsuma, K. Miura, and K. Hirao, "Temperature distribution and modification mechanism inside glass with heat accumulation during 250 kHz irradiation of femtosecond laser pulse," *Applied Physics Letters*, Vol. 93, 231112, 2008.
9. Kanehira, S., K. Miura, and K. Hirao, "Ion exchange in glass using femtosecond laser irradiation," *Applied Physics Letters*, Vol. 93, No. 2, 023112, 2008.
10. Shimizu, M., M. Sakakura, S. Kanehira, M. Nishi, Y. Shimotsuma, K Hirao, and K. Miura, "Formation mechanism of element distribution in glass under femtosecond laser irradiation," *Opt. Lett.*, Vol. 36, 2161–2163, 2011.

Effect of Gap Shape on the Spectral Response and Field Enhancement of Dimer-based Biosensor

Sameh Kessentini and Dominique Barchiesi
Project Group for Automatic Mesh Generation and Advanced Methods
Gamma 3 Project (UTT-INRIA), University of Technology of Troyes, France

Abstract— The sensitivity of the metallic nanoparticles strongly depends on the geometrical features (size and shape). Within this perspective, the objective of this study is to depict the impact of some geometrical features on the optical properties of a specific biosensor in the visible range to ensure high signal enhancement. The considered biosensor consists of a coupled array of dimer antenna that exhibits great potential as reported in many previous studies. The shape of antenna was investigated by Fischer and Martin [1]. However, the shape of the gap separating the dimer was never been investigated. We consider different configurations of the gap shape (straight, slanted, rounded, tie) and find important shifts of the extinction peak wavelength exceeding 100 nm. It follows that the gap shape can be used to tune the plasmon resonance of the biosensor. Furthermore, the near field analysis (zero to few nanometers from the surface of the biosensor) shows a potential doubled resonance that can be investigated to get important SERS enhancement.

1. INTRODUCTION

Metallic nanoparticles have interesting optical properties resulting in several physical processes such as resonance with incident electromagnetic field at a given wavelength yielding a strongly enhanced field. The field enhancement can be exploited in vibrational spectroscopy. For instance, Raman signal enhancement factor can reach several orders of magnitude [2–4] which enables the observation of a very low amount of molecules or even the single-molecule sensitivity in SERS (Surface Enhanced Raman Spectroscopy) [5, 6].

The efficiency of the metallic nanoparticles strongly depends on the geometrical features (size and shape). Then, the objective of this study is to depict the impact of some geometrical features on the optical properties of a specific biosensor in the visible range to ensure important field enhancement. The considered biosensor (see Figure 1) consists of an array of dimer antenna that exhibits great potential as reported in many previous studies. For instance, Fischer and Martin [1] compared the dimer bowtie to the dimer antenna and found that the dimer antenna produces a stronger field enhancement than the bowtie antenna for all investigated dimers (different shapes and dimensions). An additional geometrical parameter would be of great interest on dimer antenna efficiency: the gap shape which is investigated in this study.

The effect of gap shape on the optical properties of dimers-based biosensor is investigated in this study. The discrete dipole approximation (DDA) is used to model the biosensor with different shapes of the gap separating the dimer. The considered shapes are circular, straight, slanted and tie gap (triangular edges in the gap) as shown by Figure 2). Assuming constant length L, width w

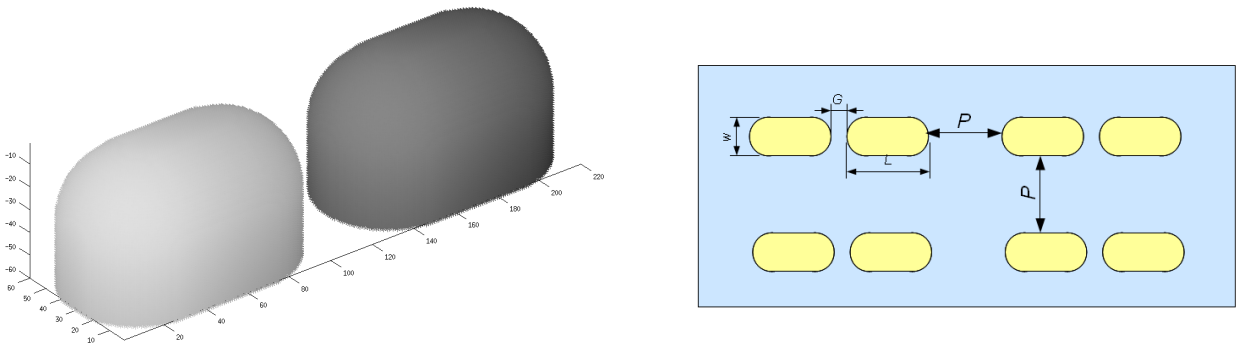

(a) 3D view (b) Upper view

Figure 1: Periodic dimer-antenna based biosensor (P interparticle distance in both directions, G the gap size, L length and w width of single antenna).

and height h of the antenna, as well as a constant gap size G, the effect of the gap shape on both the near field and the far field are investigated.

The reminder of the paper is organized as follows. The second section provides an overview of the numerical method and model used for the simulations. The third section is devoted to the far field and the near field simulation results and their discussion. Finally, concluding remarks are summarized in the fourth section.

2. NUMERICAL MODEL

The electromagnetic scattering problem is governed by a set of equations [13]. The analytical solutions of these equations are known for few target shapes, therefore adequate numerical methods should were defined to deal with arbitrary target shape. We use the discrete dipole approximation (DDA), which is a volume-integral equation method. The DDA, introduced by DeVoe [7, 8] and Purcell and Pennypacker [9], has the advantage of dealing with any arbitrary target shape within reasonable computation time for small target (few hundreds of nanometres).

The main idea of DDA is to discretize a target shape into a set of N polarizable elements (Figure 3). These elements get dipole moments and interact each with others when an electric field is applied and hence are called dipoles. Many development of the method were done [10–12] to deal with periodic structures. These latest contributions make the DDA method able to compute the far and near field of biosensors based on reproducing periodically a shape as the dimer antenna-based biosensor considered in this study (Figure 1).

The extinction efficiencies as well as electromagnetic field could be computed using DDSCAT 7.1, which is a Fortran code based on the DDA [14, 15]. We edit the code to define the target dimer biosensor (Figure 1(a)) taking account also of the adhesion layer. Then the inter-dipole distance d should be chosen. For this, in a previous study [16], we compared the DDA results to those of Mie theory for a sphere of radius 40 nm (different value of d were considered). The results showed that an inter-dipole distance of 1 nm is sufficient to achieve reasonable accuracy for targets in this size range.

3. RESULTS AND DISCUSSION

In this section, we report the results of simulations carried for the different shapes of gap reported in Figure 2 with equal gap distance G.

3.1. Size Parameters

For simulations, we consider the gold dimer antenna (Figure 1) with the following size parameters: length $L = 100$ nm for each antenna, equal width and hight $w = h = 60$ nm, an adhesion layer of Titanium of 5 nm and a gap separating the two antennas $G = 20$ nm. The dimer is deposited on CaF2 substrate with inter-dimer distance $P = 200$ nm. As shown in many topographic images, the antennas have rounded edges. For this, we consider semi-spherical edges of the antennas (Figure 1(a)). Then, with the same gap distance, other shapes of gap are considered: the straight gap, the slanted gap with a slop of 45°, the tie gap with equilateral right-angled triangle edges.

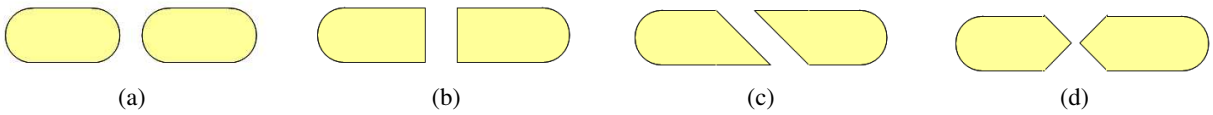

Figure 2: Upper view of dimers with different shape of gap: (a) rounded gap, (b) straight gap, (c) slanted gap and (d) tie gap.

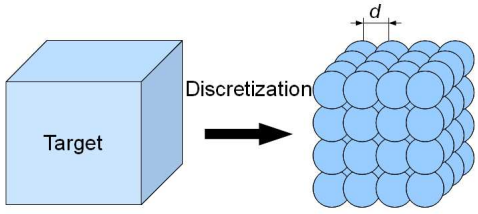

Figure 3: The basic idea of DDA: discretizing the target in a set of dipoles (d inter-dipole distance).

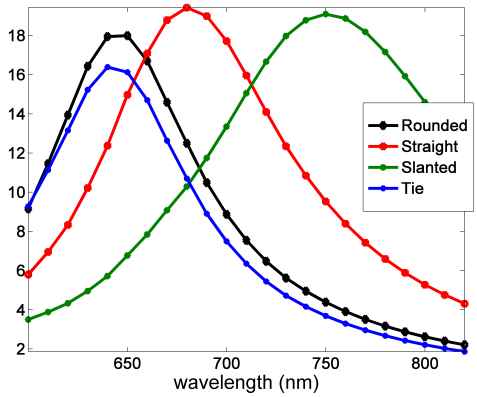

Figure 4: Extinction efficiency spectra (Q_{ext}) for the different gap shapes shown in Figure 2.

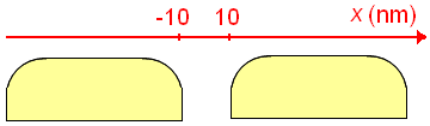

Figure 5: Computing the electric field above the surface (the gap is between $x = -10$ and 10 nm).

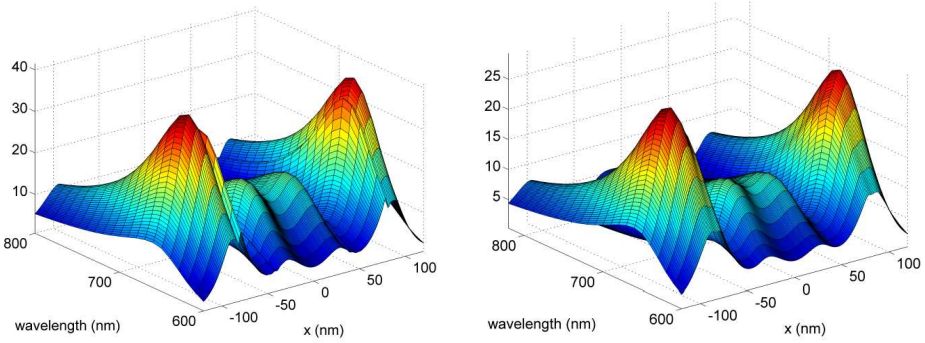

(a) at the surface (b) at 3 nm above the surface

Figure 6: Relative field intensity $|E|^2/|E_0|^2$ above the dimer with rounded gap.

3.2. Far Field

The LSPR (extinction peak wavelength) are shifted when the gap shape changes, whereas the extinction peak amplitude is almost the same. The shift can exceed 100 nm (Figure 4). It follows that the gap shape can be used to tune the plasmon resonance of the biosensor. For instance, different slope of the slanted gap (45° is used here for the considered slanted gap and 90° for straight gap) can be used to tune the plasmon resonance.

3.3. Near Field

For SERS application, it is more interesting to characterize the biosensor ability to excite biological molecules fixed just on the surface of the biosensor or trapped on a functionalization layer at few nanometers from its surface. Therefore to depict the potential SERS enhancement, we compute the electric field intensity in the symmetry plane along the dimer at two levels: at its upper surface and at 3 nm above the upper surface (Figure 5) for different wavelengths (600 to 800 nm).

The results are reported in Figures 6–9. The comparison between the relative field intensity just above the surface and at 3 nm above the surface, show that the field enhancement is rapidly damped with the distance (for the different gap shapes). Therefore, when a functionalization layer is needed, the layer should be as thin as possible to get more SERS enhancement.

Regarding the impact of the gap shape, results show different topologies of the near field. The first topologic difference is the presence of two peaks for two different wavelengths (e.g., at 670 nm and 760 nm at the surface) in the near field for the slanted gap (Figure 8) whereas the

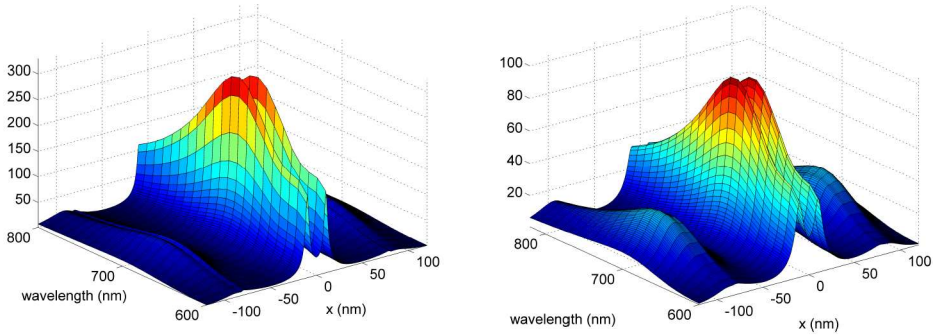

(a) at the surface (b) at 3 nm above the surface

Figure 7: Relative field intensity $|E|^2/|E_0|^2$ above the dimer with straight gap.

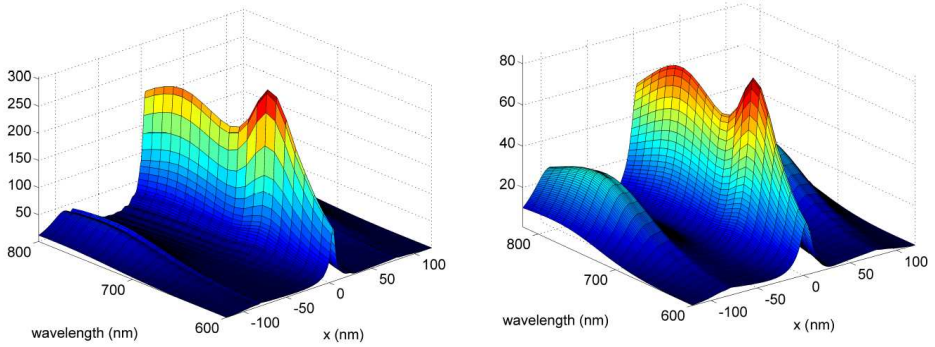

(a) at the surface (b) at 3 nm above the surface

Figure 8: Relative field intensity $|E|^2/|E_0|^2$ above the dimer with slanted gap.

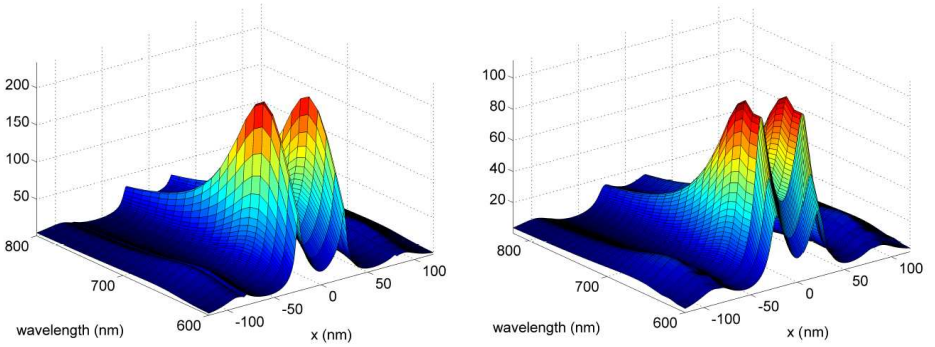

(a) at the surface (b) at 3 nm above the surface

Figure 9: Relative field intensity $|E|^2/|E_0|^2$ above the dimer with tie gap.

other gap shapes exhibit a single mode in the considered spectral range. The presence of the doubled resonances may be explained by the confinement of charges in the gap as the effective distance in the gap is just $20 \times \cos(45°) \approx 14\,\text{nm}$ (similar effect is observed with straight gap $G = 10\,\text{nm}$). The doubled resonance can be investigated to improve the SERS gain. In fact, the SERS is $\alpha f(\lambda_{exc}) \cdot f(\lambda_{Raman})$, i.e., depends on field enhancement at two different wavelengths: the excitation wavelength and the Raman wavelength. Tuning the doubled resonance (different slopes and gap sizes) can be used to get much important SERS enhancement for different target molecules (λ_{Raman}) and using different excitation wavelengths (λ_{exc}).

Finally, the relative electric field distribution differs between the rounded gap and the other shapes. The peaks are obtained around the tips of the dimer with rounded gap, whereas they are around the gap for the other shapes. Moreover, the maximum level of the relative electric field has the lowest value for rounded gap (41 for circular gap v.s. 329 for straight gap, 304 for slanted gap, 234 for tie gap, at the surface). At the surface of the dimer, the relative electric field at the LSPR wavelength (Figure 2) has mean value of 20, 32, 41 and 45 for rounded gap, slanted gap, tie gap

and straight gap, respectively. This further show that the relative electric field is more enhanced with non-rounded gap edges.

4. CONCLUSIONS

In this study, we modeled and investigated the effect of gap shape on the optical properties of a dimer-based biosensor. The dimer consists of a pair of antennas (rods) with different gap shapes: rounded, straight, slanted and tie gap. Simulations show that the LSPR can be shifted using the different shape of the gap (with almost same level of extinction), mainly considering a slanted gap. The near field analysis shows different behavior with different level of near field enhancement and topology. The main issue is that rounded gap does not guarantee the best near field enhancement. On the other hand, results show that using a slanted gap, the near field may present a doubled resonance that can be investigated to much more SERS gain (function of the excitation and emission wavelengths).

ACKNOWLEDGMENT

This work was supported by the regional council of Champagne Ardenne and the European project Nanoantenna (FP7 Health-F5-2009-241818).

REFERENCES

1. Fischer, H. and O. J. F. Martin, "Engineering the optical response of plasmonic nanoantennas," *Optics Express*, Vol. 16, No. 12, 9144–9154, 2008.
2. Kottmann, J. P. and O. J. F. Martin, "Plasmon resonant coupling in metallic nanowires," *Optics Express*, Vol. 8, 655–663, 2001.
3. Hao, E. and G. C. Schatz, "Electromagnetic fields around silver nanoparticles and dimers," *J. Chem. Phys.*, Vol. 120, 357–346, 2004.
4. Zou, S. and G. C. Schatz, "Silver nanoparticle array structures that produce giant enhancements in electromagnetic fields," *Chem. Phys. Lett.*, Vol. 403, 62–67, 2005.
5. Nie, S. and S. R. Emory, "Probing single molecules and single nanoparticles by surface-enhanced raman scattering," *Science*, Vol. 275, No. 5303, 1102–1106, 1997.
6. Kneipp, K., Y. Wang, H. Kneipp, L. T. Perelman, I. Itzkan, R. R. Dasari, and M. S. Feld, "Single molecule detection using surface-enhanced Raman scattering," *Phys. Rev. Lett.*, Vol. 78, 1667–1670, 1997.
7. Devoe, H., "Optical properties of molecular aggregates. I. Classical model of electronic absorption and refraction," *J. Chem. Phys.*, Vol. 41, 393–400, 1964.
8. Devoe, H., "Optical properties of molecular aggregates. II. Classical theory of the refraction, absorption, and optical activity of solutions and crystals," *J. Chem. Phys.*, Vol. 43, 3199–3208, 1965.
9. Purcell, E. M. and C. R. Pennypacker, "Scattering and absorption of light by nanspherical dielectric grains," *Astrophysical Journal*, Vol. 186, 705–714, 1973.
10. Markel, V. A., "Coupled-dipole approach to scattering of light from a one-dimensional periodic dipole structure," *Journal of Modern Optics*, Vol. 40, No. 11, 2281–2291, 1993.
11. Chaumet, P. C., A. Rahmani, and G. W. Bryant, "Generalization of the coupled dipole method to periodic structures," *Phys. Rev. B*, Vol. 67, No. 16, 165404-1–5, 2003.
12. Draine, B. T. and P. J. Flatau, "Discrete-dipole approximation for periodic targets: Theory and tests," *J. Opt. Soc. Am. A*, Vol. 25, 2693–2703, 2008.
13. Kahnert, F. M., "Numerical method in electromagnetic scattering theory," *Journal of Quantitive Spectroscopy & Radiative Transfer*, 79–89, 775–824, 2003.
14. Draine, B. T. and P. J. Flatau, User Guide to the Discrete Dipole Approximation Code DDSCAT 7.1, 2010, http://arXiv.org/abs/1002.1505v1.
15. Draine, B. T. and P. J. Flatau, "Discrete-dipole approximation for scattering calculations," *J. Opt. Soc. Am. A*, Vol. 11, 1491–1499, 1994.
16. Kessentini, S. and D. Barchiesi, "Quantitative comparison of optimized nanorods, nanoshells and hollow nanospheres for photothermal therapy," *Biomedical Optics Express*, Vol. 3, 590–604, 2012.

Artificial Neural Network Model for MNG-Metamaterial Spiral Resonator

R. Pandeeswari[1], **S. Raghavan**[1], **Amrit Krishnan**[2], **and Priyank Jain**[2]

[1]Electronics and Communication Department, National Institute of Technology, Trichy, India
[2]National Institute of Technology, Trichy, India

Abstract— In this paper, an ANN model for Spiral Resonators with miniaturized resonant inclusions is presented which approximates the design using four different training algorithms. The design model used to train the neural network is suitable to be employed in the practical realization of magnetic metamaterials, such as μ-negative (MNG) materials and artificial magneto dielectrics. The paper compares the performance and the capability of the four algorithms. The algorithms are Levenberg-Marquardt, Scaled Conjugate Gradient, BFGS quasi-Newton backpropagation algorithms and Radial Basis Approximation. The approximation involves the determination of three parameters which are side length, strip width and dielectric spacing of the resonators for a given resonant frequency. The results highlight the exceptional capability of neural networks in solving approximation and curve fitting problems and the ease with which we obtain the solution without tedious calculations.

1. INTRODUCTION

Metamaterials are a special class of artificially engineered substances which exhibit anomalous properties that can be used in variety of applications. Materials with negative refractive index (μ-negative) are of particular interest in the design of miniaturized antenna systems. These antennas with improved efficiency are created using these materials which are obtained at microwave frequencies by creating metallic resonating inclusions on supporting dielectric boards. When these are boards are stacked, they form the desired medium. Antenna designs incorporating metamaterials step-up the radiated power of an antenna by storing energy and re-radiating it [17]. Electrically small samples of artificial magnetic materials squeezed in these radiating microwave components pave way for miniaturization of antennas. Circuit designs which have a broader range of material parameters resulting in negative refractive index have resulted in antennas that are innovative. Commonly used configurations for the resonators that form the main component of the antennas are Split-Ring, Spiral and Labyrinth Resonators. Split-Ring Resonators exhibit a physical dimension of the order of $\lambda/20$ which is a significant design limitation. Thus, the Spiral configuration is a better choice for the design and development of resonator structures.

In our paper, we have considered the equivalent circuit model of spiral resonators initially without a dielectric substrate in the gap between the inclusions and later a modified model with a dielectric medium. During the design of the miniaturized spiral resonators, these models give the desired geometrical parameters such as side length of the external ring, width of the strips and separation between two adjacent strips when a particular resonant frequency is specified. The multi-layer ANN algorithms are used to train networks to perform a curve-fitting operation and thus obtain the design parameters when a given specification such as resonant frequency is given. Such ANN can be easily adopted for similar design projects that involve such computation.

2. MODEL FORMULATION AND RELEVANT EQUATIONS

A sketch of the spiral resonator considered along with its static equivalent circuit model for the two cases of with and without substrate is shown in Figure 1.

The equations for the equivalent circuit model of Fig. 1(b) for the spiral resonator without a dielectric substrate [1] are given as follows. The total capacitance C_{sr} including the empirical correction factor is given by

$$C_{sr} = Co\frac{l}{4(w+s)}\frac{N^2}{N^2+1}\sum_{n=1}^{N-1}\left[l-\left(n+\frac{1}{2}\right)(w+s)\right] \tag{1}$$

The expression for L_{sr} is

$$L_{sr} = \frac{\mu_0}{2\pi}l_{avg}^{sr}\left[\frac{1}{2}+\ln\left(\frac{l_{avg}^{sr}}{2w}\right)\right] \tag{2}$$

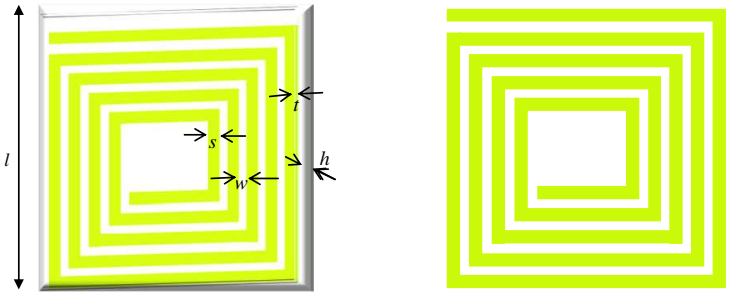

Figure 1: (a) Sketch and geometrical dimensions of a spiral resonator. (b) An example of SR with $N = 5$, parameters are 3–12 mm for 'l' (side length) and 0.1–1 mm for 's' and 'w' (thickness and width).

where N is the total number of turns in the resonator. Thus the resonant frequency is obtained by

$$f = \frac{1}{2\pi\sqrt{L_{sr} * C_{sr}}} \tag{3}$$

The equations for the equivalent circuit model of Fig. 1(a) for the spiral resonator with a dielectric substrate (RO 4003) [2] are given as follows

$$L_{sr} = \frac{\mu_0}{2\pi} l_{avg}^{sr} \left[\frac{1}{2} + \ln\left(\frac{l_{avg}^{sr}}{2w}\right)\right] \tag{4}$$

$$C_{sr} = C_o \frac{l}{4(w+s)} \frac{N^2}{N^2+1} * \left[l(N-1) - \frac{N^2-1}{2}(w+s)\right] \tag{5}$$

The shunt resistance which takes into account the dissipation in the lossy dielectric is given as

$$R_{sr}^{d} = \frac{1}{\sigma_d} \frac{s}{4h[l-(2w+s)]} \frac{l_{avg}^{sr}}{41} \tag{6}$$

The equivalent circuit is modified and the resonant frequency is given as

$$f_r = \sqrt{\frac{1}{L_{sr}C_{sr}} - \frac{1}{\left(R_d^{sr}C_{sr}\right)^2}} \tag{7}$$

The number of turns in the SR considered for the modeling has been taken to be $N = 12$.

3. ARTIFICIAL NEURAL NETWORKS (ANN)

Neural Networks have emerged as a powerful computational tool for modelling any complex non-linear function. The computational advantages come as a result of the weight updating of neurons in multiple layers similar to the topology in the human brain. The weighted sum of inputs to a particular neuron enables its activation [6, 13]. The range of the target values of the parameters are 3–12 mm for 'l' (side length) and 0.1–1 mm for 's' and 'w' (thickness and width). There are numerous training algorithms that can be employed to train ANNs; however their performance varies according to the type of input and target values supplied. Thus, a comparison of these training functions for the curve-fitting operation is done and the performance analysis is facilitated.

3.1. Levenberg-Marquardt (LM) Algorithm

This is a popular algorithm known for its fast convergence and is based on least-square estimation [14]. The Levenberg-Marquardt, method uses a search direction that is a solution of the linear set of equations:

$$(J(x_k)^T J(x_k) + \lambda_k I)d_k = -J(x_k)^T F(x_k) \tag{8}$$

where the scalar λ_k controls both the magnitude and direction of d_k. The Levenberg-Marquardt method uses a search direction that is a cross between the Gauss-Newton direction and the steepest descent direction.

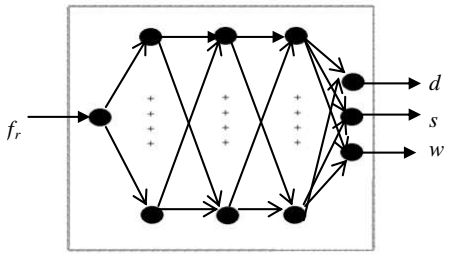

Figure 2: General ANN model used in the feed-forward back-propagation networks.

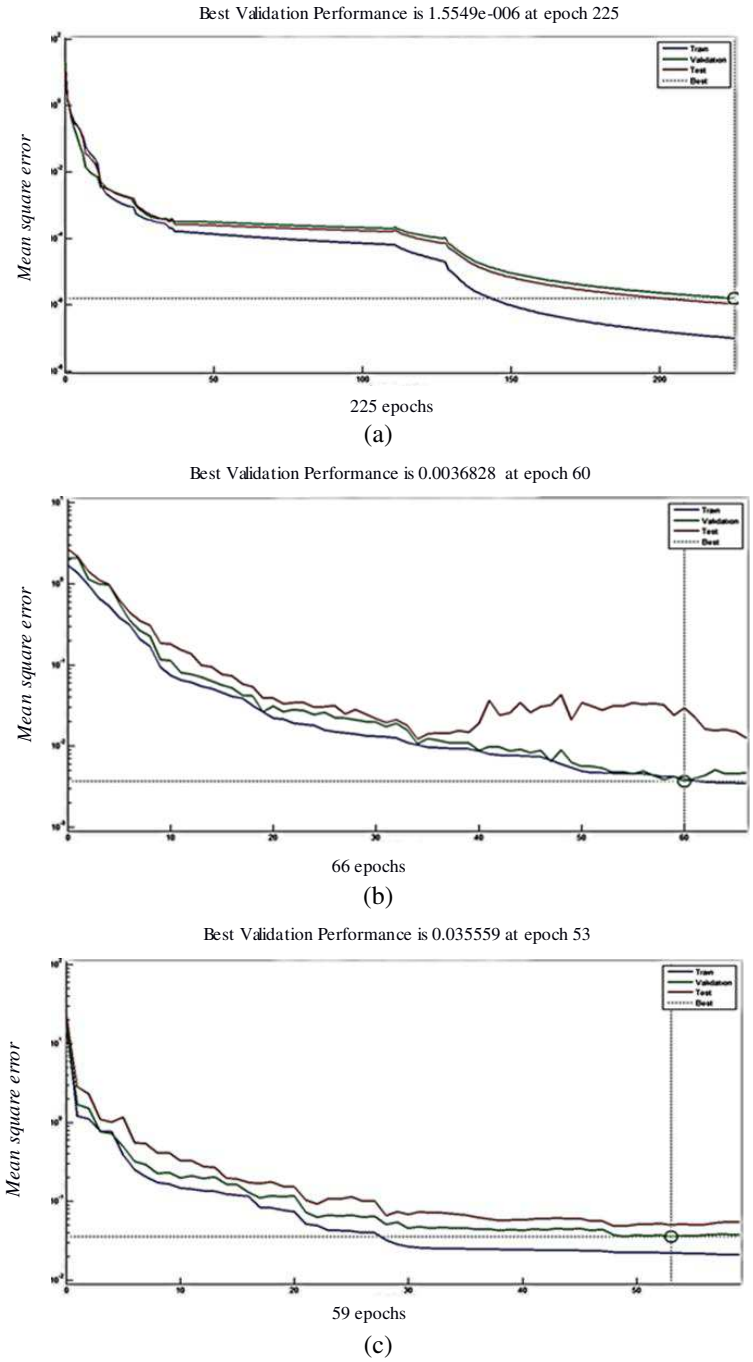

Figure 3: (a) MATLAB simulated Training performance using LM algorithm. (b) MATLAB simulated training performance using BFGS quasi-Newton Back-propagation algorithm. (c) MATLAB simulated Training performance using Scaled Conjugate Gradient (SCG) Algorithm.

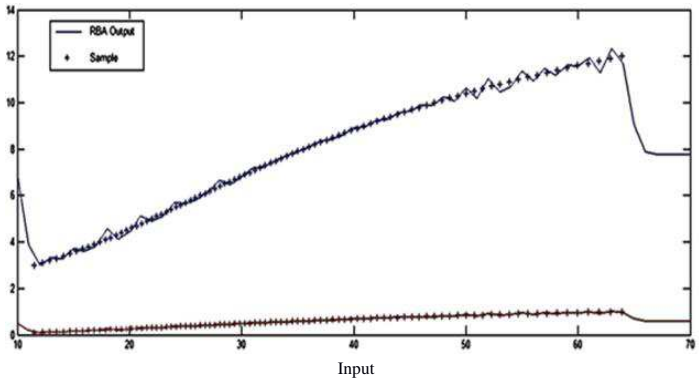

Figure 4: Comparison of the actual function and the corresponding RBA approximation.

Table 1: Training and validation mean squared errors (MSE) of the neural model.

Learning Algorithms	MSE in training and Validation	No. of epochs	No. of epochs (after model is modified with substrate)
LM	1.5549e-006	225	41
BFGS Quasi-Newton	3.6828e-003	60	32
SCG	3.5559e-002	59	26
RBA	1.04181e-002	31	14

3.2. BFGS Quasi-Newton Back-propagation Algorithm

The Broyden-Fletcher-Goldfarb-Shanno (BFGS) method is an approximation of Newton's method [5], a class of hill-climbing optimization techniques that searches a stationary point of a function [9]. These methods use the first and second derivatives. In quasi-Newton methods, the Hessian matrix of second derivatives need not be evaluated directly [11]. The weight update for the general Newton method is $w_{k+1} = w_k - g_k/A_k$, A_k is the corresponding Hessian matrix of the performance index at the current value of the weights and biases.

3.3. Scaled Conjugate Gradient (SCG) Algorithm

SCG is a conjugate gradient method which is fully-automated, includes no critical user-dependent parameters, and avoids a time consuming line search, which CGL (Conjugate Gradient Algorithm with line search) and BFGS use in each iteration in order to determine an appropriate step size [15]. The neural network learning in this algorithm is a mirror of the minimization of a global error function [7, 10].

3.4. Radial Basis Approximation Algorithm

A radial basis network is a network with two layers. It consists of a hidden layer of radial basis neurons and an output layer of linear neurons. Here the radial basis transfer function is used by the hidden layer. The weights and biases of each neuron in the hidden layer define the position and width of a radial basis function. Each linear output neuron forms a weighted sum of these radial basis functions. With the correct weight and bias values for each layer, and enough hidden neurons, a radial basis network can fit any function with any desired accuracy [8]. The sum-squared error goal is set to 0.02 and the spread constant value is 1.

4. THE ANN NETWORK CONFIGURATION FOR THE RESONATOR MODEL

The ANN model consists of an input, output and three hidden layers in accordance to the universal approximation theorem that a three hidden layer network can approximate any parameter to any accuracy [12]. After numerous trials, the number of neurons in each hidden layer was set to five, which provided maximum accuracy. The neurons in the hidden layers are characterized by a log-sigmoid activation function and those in the output layer have a pure linear activation function. Thus the configuration of the ANN is $1 \times 5 \times 5 \times 5 \times 3$ [16].

5. CONCLUSIONS

The ANN model was designed and trained using four different algorithms to check for suitability, faster convergence, and better performance. Certain constraints prevent the use of some algorithms

and thus suitability is an important criterion that must be checked before training the neural net. The MSE values obtained from the neural models during training for the parameters of the spiral resonators are given in Table 1. The training performance analysis is given in Figures 3(a), (b) and (c). The results show that LM algorithm is very accurate and approaches a close approximation after more epochs. The other algorithms are less accurate but have a faster convergence. The plots in Figures 3(a), (b) and (c) also indicate the fluctuations in the errors which indirectly imply the fluctuation in weights and biases. The number of epochs taken to approximate the modified model is also important as it directly shows the ability of the net to adapt. The Radial Basis Approximation technique is very easily implemented and has its own unique advantages over the other algorithms. It can fit a function to any desired accuracy and thus is recommended. The Figure 4 shows that the RBA after training and the functions values are in good agreement. The neural model presented in this paper achieves the determination of the geometrical parameters of a spiral resonator for a given input resonant frequency. The neural network is seen to be an adaptive tool that can be used to fit functions that change over time. The procedure also bypasses the tedious mathematical calculations required during the computation and updating process.

REFERENCES

1. Bilotti, F., A. Toscano, and L. Vegni, "Design of spiral and multiple split-ring resonators for the realization of miniaturized metamaterial samples," *IEEE Trans. Antennas Propagation*, Vol. 55, No. 8, August 2007.
2. Bilotti, F., A. Toscano, L. Vegni, K. Aydin, K. B. Alici, and E. Ozbay, "Equivalent-circuit models for the design of metamaterials based on artificial magnetic inclusions," *IEEE Trans. on Microwave Theory and Techniques*, Vol. 55, No. 12, December 2007.
3. Buell, K., H. Mosallaei, and K. Sarabandi, "A substrate for small patch antennas providing tuneable miniaturization factors," *IEEE Trans. on Microwave Theory and Techniques*, Vol. 54, No. 1, 135–146, January 2006.
4. Baena, J. D., R. Marques, F. Medina, and J. Martel, "Artificial magnetic metamaterial design by using spiral resonators," *Phys. Rev. B: Condens. Matter*, Vol. 69, No. 1, 014402-1–5, 2004.
5. Battiti, R., "First and second order methods for learning: Between steepest descent and Newton's method," *Neural Computation*, Vol. 4, No. 2, 141–166, 1992.
6. Caudill, M. and C. Butler, *Understanding Neural Networks: Computer Explorations*, Vols. 1–2, The MIT Press, Cambridge, MA, 1992.
7. Charalambous, C., "Conjugate gradient algorithm for efficient training of artificial neural networks," *IEEE Proceedings*, Vol. 139, No. 3, 301–310, 1992.
8. Chen, S., C. F. N. Cowan, and P. M. Grant, "Orthogonal least squares learning algorithm for radial basis function networks," *IEEE Transactions on Neural Networks*, Vol. 2, No. 2, 302–309, 1991.
9. Dennis, J. E. and R. B. Schnabel, *Numerical Methods for Unconstrained Optimization and Nonlinear Equations*, Prentice-Hall, Englewood Cliffs, NJ, 1983.
10. Fletcher, R. and C. M. Reeves, "Function minimization by conjugate gradients," *Computer Journal*, Vol. 7, 149–154, 1964.
11. Gill, P. E., W. Murray, and M. H. Wright, *Practical Optimization*, Academic Press, New York, 1981.
12. Hagan, M. T., H. B. Demuth, and M. H. Beale, *Neural Network Design*, PWS Publishing, Boston, MA, 1996.
13. Haykin, S., *Neural Networks: A Comprehensive Foundation*, Macmillan College Publishing Company, 1994.
14. Levenberg, K., "A method for the solution of certain nonlinear problems in least squares," *Quarterly of Applied Mathematics*, Vol. 11, 431–441, 1963.
15. Moller, M. F., "A scaled conjugate gradient algorithm for fast supervised learning," *Neural Networks*, Vol. 6, 525–533, 1993.
16. Thiruvalar Selvan, P. and S. Raghavan, "Neural model for circular-shaped micro shield and conductor-backed coplanar waveguide," *Progress In Electromagnetics Research M*, Vol. 8, 119–129, 2009.
17. Ziolkowski, R. W. and A. D. Kipple, "Application of double negative materials to increase the power radiated by electrically small antennas," *IEEE Trans. Antennas Propagation*, Vol. 51, No. 10, 2626–2640, Oct. 2000.

Guiding Behavior of a Periodic Subwavelength Metallic Domino Array

Y. H. Kao[1], **D. J. Hou**[2], **T. J. Yang**[3], **and J. J. Wu**[2]

[1]Department of Communication Engineering, Chung Hua University, Hsinchu 30012, Taiwan, R.O.C.
[2]Department of Electrical Engineering, Chung Hua University, Hsinchu 30012, Taiwan, R.O.C.
[3]College of Engineering, Chung Hua University, Hsinchu 30012, Taiwan, R.O.C.

Abstract— Based on the mechanism of spoof surface plasmon polaritions (spoof SPPs), we present a kind of microwave band pass filter in both theory and experiment, which is realized by periodic subwavelength metallic Domino array. The transmission bandwidth of spoof SPPs is controllable by designing the geometric parameters of the periodic structure. Simulation and experimental results of the spoof SPPs agree well with each other and verify the feasibility in band pass filter application.

1. INTRODUCTION

Periodic structure has been utilized in microwave and optical components applications in the past [1], such as reflection mirror, DFB laser, light beam coupler in optical regime, and band stop filter, leaky wave antenna in microwave frequency [2]. In 2004, Pendry put forward a concept of spoof surface plasmon polaritons (SPPs) in low frequency band using subwavelength periodic hole on the surface of metal to increase the penetration depth [3], and the working frequency is controllable by the geometric parameters of the structure. The spoof SPPs in microwave regime has been verified theoretically and experimentally in [4] and [5], and the mechanism of electromagnetic field confinement of the spoof SPPs is studied in [6].

In this paper, we put forward a new kind of band pass filter in X-band based on the principle of spoof SPPs constructed by periodic subwavelength Domino structure. The modal field of guided mode in the Domino structure is almost constraint inside the structure. By adjusting the lattice constant and height of Domino, we can control the transmission bandwidth and transmission efficiency. Such structure can be applied in the high power filter component.

2. NUMERICAL ANALYSIS

The proposed spoof SPPs structure is composed of subwavelength periodic rectangular Domino structure on metallic surface, as shown in Figure 1(a), with the height h, the lattice constant d, the spacing a and the width L simplicity, the metal is assumed to the perfect electric conductor (PEC)

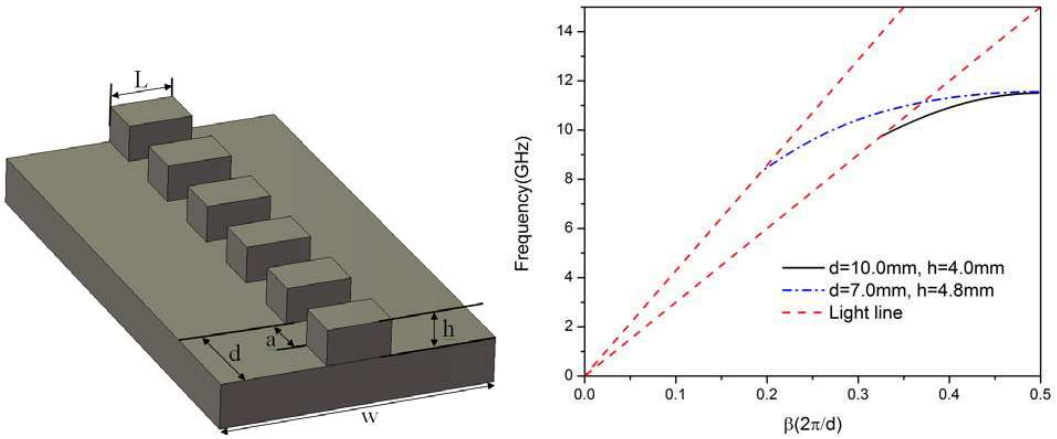

(a) (b)

Figure 1: (a) Subwavelength periodic Domino strucuture supporting spoof surface plasmon polaritons. (b) Dispersion lines for the Domino structure with $d = 10.0\,\text{mm}$, $h = 4.0\,\text{mm}$ and $d = 7.0\,\text{mm}$, $h = 4.8\,\text{mm}$ respectively.

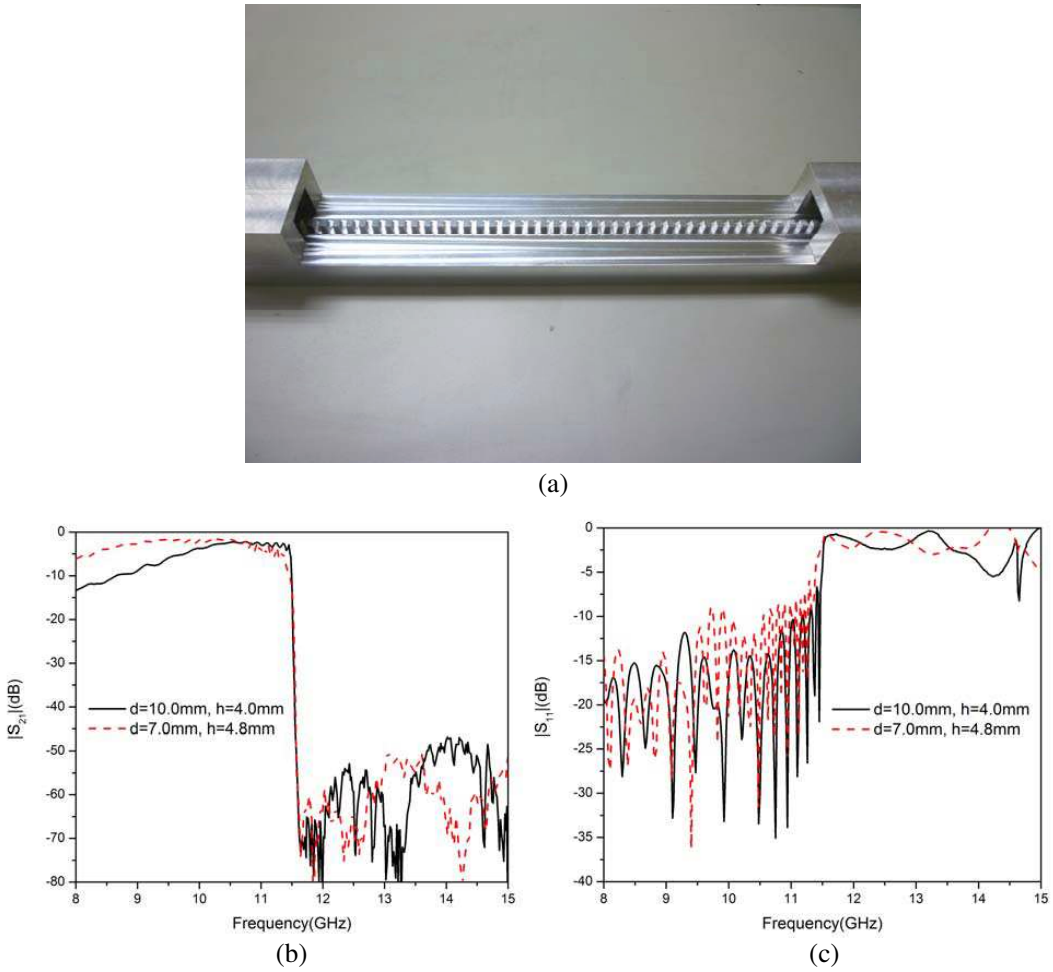

Figure 2: (a) Spoof SPPs waveguide with subwavelength periodic Domino structure with the spacing $a = 0.5d$ and the width $L = 5\,\text{mm}$ in experiment. (b) S_{21} and (c) S_{11} parameters for the spoof SPPs waveguide. The solid line represents the case $d = 10\,\text{mm}$, $h = 4\,\text{mm}$, and the dashed red line represents the case $d = 7.0\,\text{mm}$, $h = 4.8\,\text{mm}$.

in simulation, which is reasonable in microwave regime. Figure 1(b) shows the dispersion relation between propagation constant β and working frequency for such plasmonic waveguide structure obtained from finite element method (FEM). The propagation constant β is confined in the first Brillouin uin zone, i.e., $\beta \leq \pi/d$. The geometric parameters for the solid black line in Figure 1(b) are: $d = 10.0\,\text{mm}$, $a = 0.5d$, $L = 5\,\text{mm}$, $w = 75\,\text{mm}$ and $h = 4.0\,\text{mm}$. Our numerical analysis focuses on the fundamental mode of the plasmonic waveguide, as it has the strongest field confinement. Such structure has a bandwidth of 1.785 GHz with the asymptotic frequency 11.505 GHz and the cutoff frequency 9.72 GHz. The dotted blue line represents the dispersion line for the structure of $d = 7.0\,\text{mm}$, $h = 4.8\,\text{mm}$ and $a = 3.5\,\text{mm}$, with the asymptotic frequency 11.5608 GHz, the cutoff frequency 8.322 GHz and the bandwidth 3.238 GHz. Compared with the previous case, the bandwidth is widen by controlling the two parameters d and h.

3. EXPERIMENTAL RESULTS

To utilize such plasmonic waveguide in the application of band pass filter, we measure the filter properties of this periodic structure in experiment. The plasmonic waveguide in experiment is shown in Figure 2(a). To feed the energy into the plasmonic waveguide effectively from the rectangular waveguide, we introduce a transition region of 50 mm length, which increases the matching condition between the input port and the plasmonic waveguide. The S parameters are measured by vector network analyzer (VNA) for the case $h = 4.0\,\text{mm}$, $d = 10.0\,\text{mm}$, and $h = 4.8\,\text{mm}$, $d = 7.0\,\text{mm}$ respectively, with the total length $t = 375\,\text{mm}$. Figures 2(b) and 2(c) display the S parameters of the plasmonic waveguide. For the case $h = 4.0\,\text{mm}$, $d = 10.0\,\text{mm}$, the S_{21} increase from $-13.4\,\text{dB}$ at 8 GHz to $-2.248\,\text{dB}$ at 10.56 GHz, and drops to $-5.58\,\text{dB}$ at 11.48 GHz, then it is stop band in

higher frequency and the value decreases to $-74.4\,\mathrm{dB}$ at $11.73\,\mathrm{GHz}$. It is noticed that the S_{21} is above $-5\,\mathrm{dB}$ between the cutoff frequency $9.75\,\mathrm{GHz}$ and the asymptotic frequency $11.47\,\mathrm{GHz}$, and can be as high as $-2.248\,\mathrm{dB}$ near the frequency $10.56\,\mathrm{GHz}$. For the case $h = 4.8\,\mathrm{mm}$, $d = 7.0\,\mathrm{mm}$, S_{21} is increase from $-4.5\,\mathrm{dB}$ at the cutoff frequency $8.32\,\mathrm{GHz}$ to $-1.48\,\mathrm{dB}$ at $10.31\,\mathrm{GHz}$, and drops to $-4.87\,\mathrm{dB}$ at $11.36\,\mathrm{GHz}$. The S_{11} is between $-15\,\mathrm{dB}$ and $-8\,\mathrm{dB}$ blow the asymptotic frequency for both cases, as shown in Figure 2(c). The asymptotic frequency has a little difference between the theory and experiment, due to the fabrication error.

4. CONCLUSIONS

In conclusion, we have proposed a kind of plasmonic waveguide, which is composed of subwavelength periodic Domino structure array. Spoof SPPs can be exited in such subwavelength periodic structure. The bandwidth of this waveguide is controllable by adjusting the lattice constant and the height of the Domino structure. Such waveguide can be utilized in band pass filter application. Experimental results match well with the numerical analysis.

ACKNOWLEDGMENT

The financial supports by the National Science Council of ROC under Grant Nos. NSC 100-2112-M-216-002, NSC 100-2221-E-216-015 and the National Natural Science Foundation of China under Grant No. 60971062 are gratefully acknowledged.

REFERENCES

1. Tamir, T., Ed., *Guided-wave Optoelectronics*, Springer Verlag, 1990.
2. Schwering, F. K. and S. T. Peng, "Design of dielectric grating antennas for millimeter-wave applications," *IEEE Trans. Microwave Theory Tech.*, Vol. 31, 199–209, 1983.
3. Pendry, J. B., L. Martin-Moreno, and F. J. Garcia-Vidal, "Mimicking surface plasmons with structured surfaces," *Science*, Vol. 305, 847–848, 2004.
4. Wu, J.-J., T.-J. Yang, and L. F. Shen, "Subwavelength microwave guiding by a periodically corrugated metal wire," *Journal of Electromagnetic Waves and Applications*, Vol. 23, No. 1, 11–19, 2009.
5. Hibbins, P., B. R. Evans, and J. R. Sambles, "Experimental verification of designer surface plasmons," *Science*, Vol. 308, 670–672, 2005.
6. Garcia de Abajo, F. J. and J. J. Saenz, "Electromagnetic surface modes in structured perfect-conductor surfaces," *Phys. Rev. Lett.*, Vol. 95, 233901, 2005.

A Compact Split Ring Resonator Loaded Antenna

R. Pandeeswari[1], **Singaravelu Raghavan**[1], **and Keloth Ramesh**[2]

[1]Electronics and Communication Department, National Institute of Technology, Trichy, India
[2]National Institute of Technology, Trichy, India

Abstract— In recent years, there has been a growing interest for the use of metamaterials in the antenna design. Antenna researchers tried to utilize the metamaterial properties to the maximum extend. It has been proved that metamaterials are a good candidate for the enhancement of antenna performance over the past years. Metamaterial properties are particularly used for miniaturization of the antenna. In this paper, a compact split ring resonator loaded antenna is presented. The proposed structure is designed on an FR4 substrate with dielectric constant 2.4 with thickness 1.6 mm and consists of small patch and circular SRR. The antenna resonates at 15.5 GHz without SRR. After loading by SRR resonant frequency is reduced to 10.35 GHz. The reduction in resonant frequency is 33.22%. The distance between the patch and SRR is very important in determining the resonant frequency. Coaxial feeding is used for the excitation of the antenna. Simulation tool based on the method of moment (MOM)-Zeland IE3d 12.0 has been used to analyze and optimize the antenna. The fundamental parameters of the antenna such as return loss, VSWR, gain, radiation pattern are obtained and all meets the acceptable antenna standard.

1. INTRODUCTION

Metamaterials are artificial materials were introduced by Russian scientist Vesalago in the year 1960 [1]. In contrast to conventional material, left handed metamaterial is designed to exhibit negative permeability and negative permittivity in the microwave frequency range of interest. SRR was proposed by Pendry et al., is designed to exhibit negative permeability [2] and thin wire structure is used to exhibit negative permittivity. Smith et al. combined SRR and thin wire structure to form a double negative metamaterial [3]. In DNG material, the wave vector, electric field intensity and magnetic field intensity form a left handed triad [4]. Reversal of snell's law, Doppler effect, Cheronkov radiation due to anomalous properties of metamaterial [5]. There are variety of SRR structures have been reported in literature like square, circular, triangular, omega, labyrinth resonator. Metamaterials are used for optical and microwave applications such as filters, couplers, lenses, and switches etc.. Artificial metamaterial structures are also used in the antenna design to enhance the antenna performance. DNG material was used to improve the power radiated by antenna [6]. It was observed that gain of the antenna was improved by placing metamaterial slab (superstrate) above the patch. Metamaterial as superstrate was used for gain improvement [7] and as substrate was used for antenna miniaturization [8]. This was also proved that metamaterial structure itself act as a radiating element. Thin sub wavelength cavity resonator was formed by combining DPS (Double positive) material with DNG material (Double Negative) material, in which phase compensation property of DNG material was used [9]. Sub wavelength Rectangular and circular patch antenna was proposed by Andrea Alu et al., in which part of the substrate was filled with metamaterial and remaining part was filled with DPS material [10]. Miniaturized annular patch resonator was developed by partial loading of metamaterial [11]. In this paper, SRR is placed nearby patch and characteristics have been studied with SRR and without SRR.

2. ANTENNA STRUCTURE

The proposed antenna was designed on low cost FR4 substrate with relative permittivity 4.4 and with thickness 1.6 mm. Antenna structure consists of rectangular patch and SRR . Antenna performance is observed without SRR and with SRR. The length and width of the rectangular patch is 0.5 mm and 5 mm. Coaxial feed is used for the excitation of the antenna. Coaxial feed is given at $x = .25$ mm and $y = 4.2$ mm. Antenna resonates at the frequency of 15.5 GHz without SRR. The antenna structure without SRR and its return loss is shown in Fig. 1 & Fig. 2 respectively.

3. PERFORMANCE OF THE ANTENNA WITH SRR

Then SRR is placed nearby the patch. SRR is excited by the rectangular patch. SRR resonant frequency must be less than the patch resonant frequency. The antenna structure with SRR and

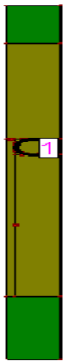

Figure 1: Antenna structure from IE3d tool.

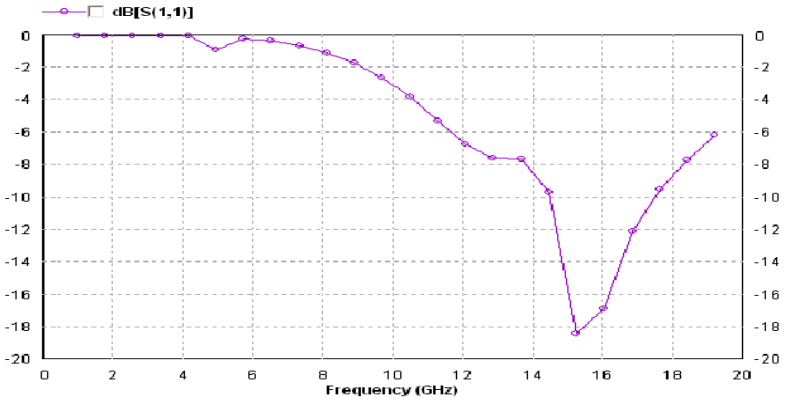

Figure 2: Return loss characteristics of antenna without SRR.

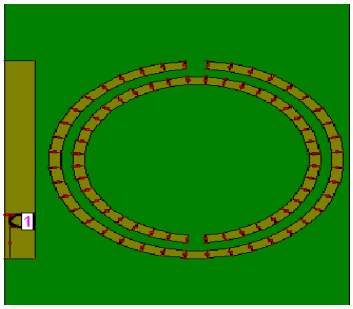

Figure 3: Antenna structure with SRR IE3d tool.

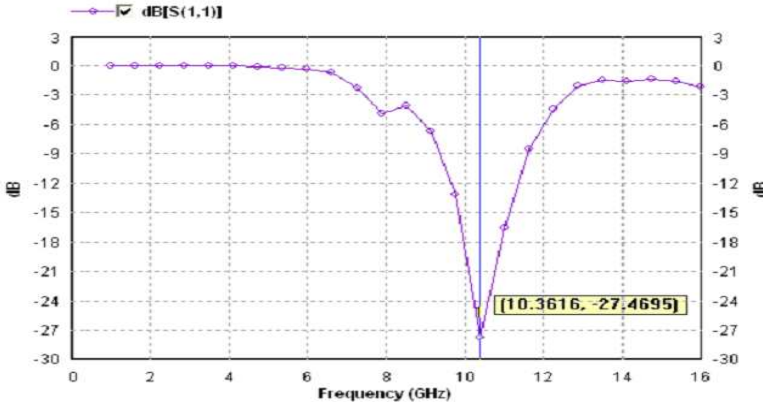

Figure 4: Return loss of antenna with SRR.

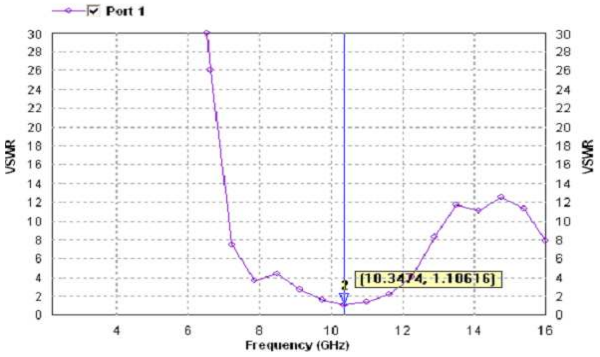

Figure 5: VSWR curve of the antenna.

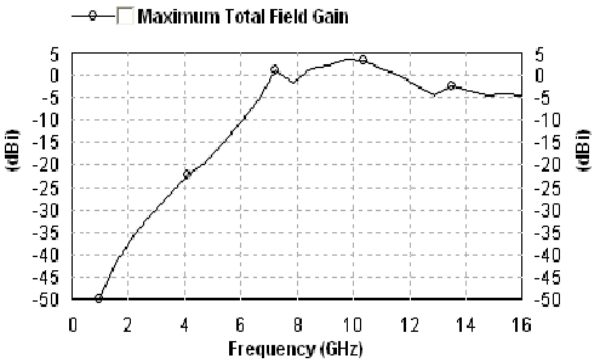

Figure 6: Gain curve of the antenna.

its return loss curve is shown in Fig. 3 and Fig. 4 respectively. The gap between patch and SRR is 0.25 mm. The length and width of the ground plane is $L = 5.85$ mm and $W = 7$ mm.

Coaxial feed was given at $x = 0.25$ mm and $y = 2.2$ mm for the composite structure. The antenna structure with SRR and return loss curve is shown in Fig. 3 and Fig. 4 respectively. The composite structure resonates at the frequency of 10.35 GHz and return loss at the resonant frequency is -27 dB. VSWR is less than 2 over the entire bandwidth and is shown in Fig. 5. The gain of the antenna is 3 dBi at the resonant frequency and is shown in Fig. 6. Simulated radiation patterns of antenna in E-plane and H-plane are shown in Fig. 7 and Fig. 8 respectively. E-field pattern and Azimuthal pattern is observed at 10.375 GHz and is shown in Fig. 7 & Fig. 8 respectively.

The gap between patch and SRR is very important. By changing gap resonant frequency of the antenna can be varied. The antenna resonates at 15.5 GHz without SRR and 10.35 GHz with SRR.

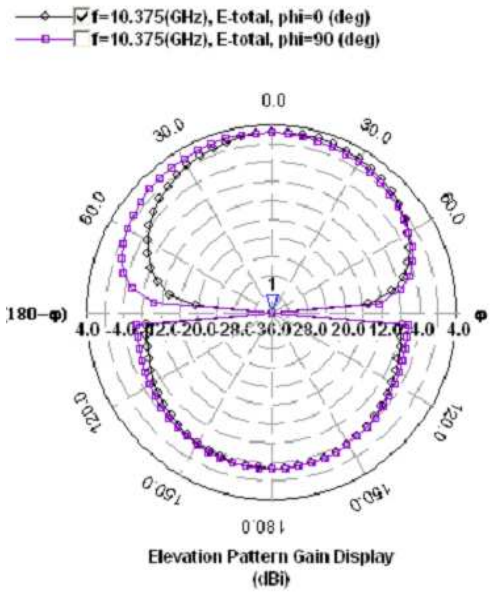

Figure 7: Radiation pattern in the E-plane at 10.375 GHz.

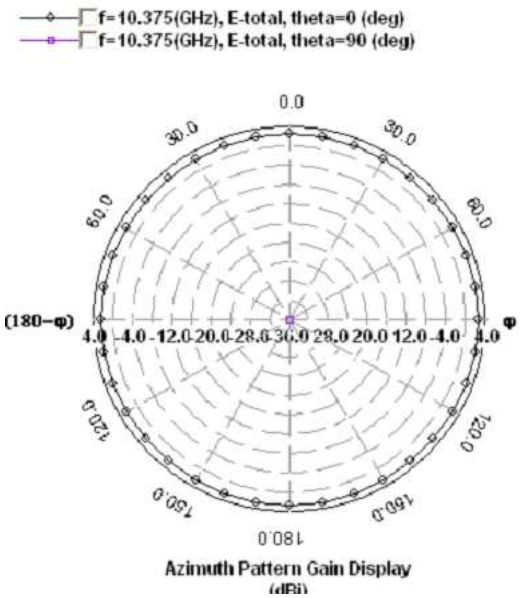

Figure 8: Radiation pattern in the H-plane at 10.375 GHz.

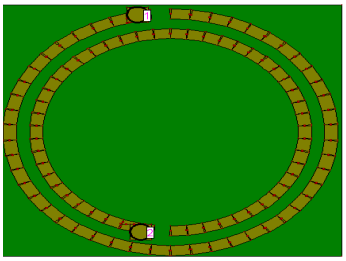

Figure 9: SRR structure from IE3d simulation tool.

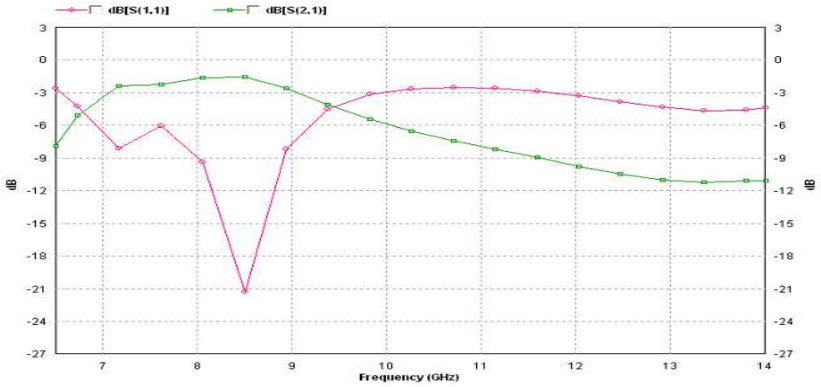

Figure 10: Transmission and reflection coefficient of SRR.

The reduction in resonant frequency is calculated by using the following.

$$\text{reduction in resonant frequency } \%s = \frac{\text{Resonant frequency without SRR} - \text{Resonant frequency with SRR}}{\text{Resonant frequency without SRR}} \times 100$$

The reduction in resonant frequency is 33.33%.

4. SRR CHARACTERISTICS

SRR is designed on an FR4 substrate. SRR structure is used to exhibit negative permeability. Coaxial feed is given to both inner and outer rings of SRR. Metamaterial characteristics have been verified by transmission and reflection coefficient of SRR. SRR structure also satisfies homogeneous condition. Average cell size p of SRR must be less than $\lambda_g/4$. SRR structure resonates at the frequency of 8.6 GHz. The radius of the inner ring is 2.1 mm and outerring is 2.5 mm. The gap between the inner ring and outer ring is 0.2 mm. Coaxial feed is given at $x = 3.425$ mm, $y = 6.15$ mm for the outer ring and at $x = 3.25$, $y = 1.75$ for the inner ring.

5. CONCLUSIONS

A compact SRR loaded antenna is presented and resonates at 15.5 GHz without SRR and at 10.35 GHz with SRR. Resonant frequency of the antenna can be designed to desired frequency by changing the gap between patch and SRR and by changing the no. of rings of SRR.

REFERENCES

1. Vesalago, V., "The electrodynamics of substance with simultaneously negative values of ϵ and μ," *Soviet Physics Uspekhi*, Vol. 10, No. 4, 509–514, Jan.–Feb. 1968.
2. Pendry, J. B., A. J. Holden, D. J. Robbins, and W. J. Stewart, "Magnetism from conductors and enhanced nonlinear phenomena," *IEEE Trans. Micr. Theory. Tech.*, Vol. 47, No. 11, 1084–2075, Nov. 1999.
3. Caloz, C. and T. Itoh, *Electromagnetic Metamaterials: Transmission Line Theory and Microwave Applications*, 1st Edition, The Engineering Approach, A John Wiley Sons Inc., 2005.
4. Ziolkowski, R. W. and A. D. Kipple, "Application of double negative materials to increase the power radiated by electrically small antennas," *IEEE Transactions on Antennas and Propagation*, Vol. 51, No. 10, Oct. 2003.
5. Si, L.-M., H.-J. Sun, Y. Yuan, and X. Lv, "CPW-fed compact planar UWB antenna with circular disc and spiral split ring resonators," *PIERS Proceedings*, 502–505, Beijing, China, Mar. 23–27, 2009.
6. Joshi, J. G., S. S. Patnaik, S. Devi, M. R. Lohokare, and C. Vidyasagar, "Offset fed diamond shaped split ring (DSRR) planar metamaterial antenna," *IEEE Proceedings*, 1–4, 2009.
7. Attia, H., L. Yousefi, M. M. Bait-Suwailam, M. S. Boybay, and O. M. Ramahi, "Enhanced-gain microstrip antenna using engineered magnetic superstrates," *IEEE Antennas and Wireless Propagation Letters*, Vol. 8, 2009.
8. Buell, K., H. Mosallaei, and K. Sarabandhi, "A substrate for small patch antennas providing tunable miniaturization factors," *IEEE Transactions on Microwave Theory and Techniques*, Vol. 54, No. 1, Jan. 2006.
9. Engheta, N., "An idea for thin subwavelength cavity resonators using metamaterials with negative permittivity and permeability," *IEEE Antennas and Wireless Propagation Letters*, Vol. 1, 2002.
10. Alu, A., F. Bilotti, N. Engheta, and L. Vegni, "Subwavelength, compact, resonant patch antennas loaded with metamaterials," *IEEE Transactions on Antennas and Propagation*, Vol. 55, No. 1, Jan. 2007.
11. Mahmoud, S. F., "A new miniaturized annular ring patch resonator partially loaded by a metamaterial ring with negative permeability and permittivity," *IEEE Antennas and Wireless Propagation Letters*, Vol. 3, 2004.

WA-systems of Functions in Reconstruction and Visualization of 2D and 3D Images

V. F. Kravchenko[1], **D. V. Churikov**[1], **V. I. Ponomaryov**[2], **and H. M. Perez-Meana**[2]

[1]Kotel'nikov Institute of Radio Engineering and Electronics
Russian Academy of Sciences, Moscow, Russia
[2]National Polytechnic Institute of Mexico, Mexico-city, Mexico

Abstract— This invited report presents short review of novel class of functions: *Atomic Functions* (AF) and following from them novel families of wavelets: *Wavelet Atomic Function* (WAF). In this paper presented several examples of successful applications of WAF in different problems explained below.

1. 3D VIDEO VISUALIZATION EMPLOYING WAVELET MULTILEVEL DECOMPOSITION

Novel approach based on WAF has been efficiently employed in 3D video sequence visualization. The procedure consists of multilevel decomposition and 3D visualization applying color anaglyphs synthesis. Simulations on synthetic images and video sequences, also on real-life video sequences have confirmed sufficiently better proposal performance in depth and spatial perception in comparison with existing methods.

The proposed framework consists of the following stages: 2D color video sequence decomposition, RGB component separation, *DM* computation using wavelets at multiple decomposition levels (M-W), in particular *wavelet atomic functions* (M-WAF) [1–5], disparity map improvement via dynamic range compression, anaglyph synthesis employing *the nearest neighbor interpolation (NNI)*, and 3D video sequence reconstruction and visualization. Below, we explain in detail the principal 3D reconstruction stages.

Disparity map computation. Stereo correspondence estimation based on the M-W (M-WAF) technique is proposed to obtain the disparity map. The stereo correspondence procedure consists of two stages: the *WAF* implementation and the *WTM* computation. Here, we will present a novel type of wavelets known as *WAFs*, first introducing basic atomic functions (*up, fup*$_n$, π_n) used as the mother functions in wavelet construction. The definition of AFs is connected with a mathematical problem: the isolation of a function that has derivatives with a maximum and minimum similar to those of the initial function. To solve this problem requires an infinitely differentiable solution to the differential equations with a shifted argument [3–5]. It has been shown that *AFs* fall within an intermediate category between splines and classical polynomials: like B-splines, *AFs* are compactly supported, and like polynomials, they are universal in terms of their approximation properties.

The simplest and most important AF is generated by infinity-to-one convolutions of rectangular impulses that are easy to analyse via the Fourier transform. The detailed definitions and properties of these functions can be found in [1–5]. The Wavelet technique, which the developed method uses, is based on the *discrete wavelet transform* (DWT) [3–6]. The wavelet decomposition procedures employ several decomposition levels to enhance the quality of the depth maps. The DWT and inverse DWT are usually implemented using the filter bank techniques for a scheme with only two filters: low pass (LP) $H(z)$ (decomposition) and $\tilde{H}(z)$ (reconstruction), and high pass (HP) $G(z)$ (decomposition) and $\tilde{G}(z)$ (reconstruction), where $G(z) = zH(-z)$ and $\tilde{G}(z) = z^{-1}H(-z)$. A block diagram of the proposed *M-WAF* framework is presented in Figure 1(b).

Simulation results. In the simulation experiments, various synthetic images in the *PNG* format are used to obtain the quantitative measurements. The synthetic images were obtained from *http://vision.middlebury.edu/stereo/data*. *Aloe*, *Venus*, *Lampshade1*, *Wood1*, *Bowling1* and *Reindeer* were the synthetic images used, all in *PNG* format (480×720 pixels). We also used the following test color video sequences in the *AVI* format: *Coastguard, Flowers and Foreman* (300 frames, 480 × 720 pixels each one). The test video sequences were obtained from *http://trace.eas.asu.edu/yuv/index.html*. Additionally, the real life video sequences named *Video Test1* (200 frames, 480×720 pixels) and Video Test2 (200 frames, 480 × 720 pixels) were recorded to apply the proposed algorithm in a common scenario. *Video Test1* shows a truck moving in the scenery and *Video Test2* shows three people walking toward the camera. Two quality objective criteria, *Quantity of Bad Disparities*

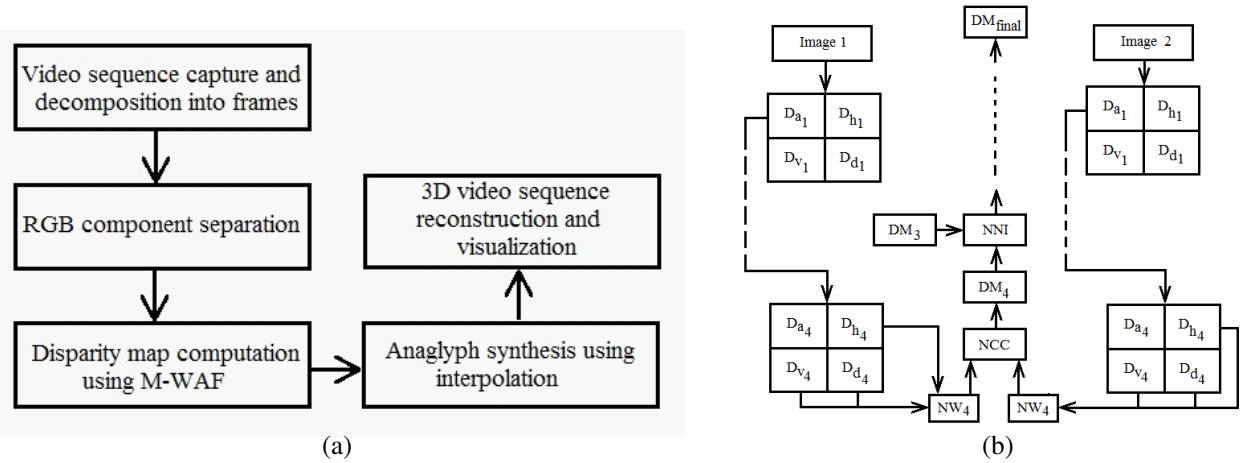

Figure 1: (a) The proposed framework, (b) the proposed *M-WAF* algorithm with four levels of decomposition.

(QBD) [7] *and Similarity Structure Image Measurement (SSIM)* [8], were chosen as the quantitative metrics to justify the selection of the best disparity map algorithm in the 3D video sequence reconstruction. Table 2 presents the values of *QBD* and *SSIM* for the proposed framework based on *M-WAFs* and the other techniques applied to different synthetic images. The simulation results indicate that the best overall performance of disparity map reconstruction is produced by the *M-WAF* framework. The minimum value of *QBP* and the maximum value of *SSIM* are obtained when the M-WAF π_6 is used, followed by WAF π_6. At the final stage, when the anaglyphs were synthesized, the *NCC* was calculated in a sliding window with 5×5 pixels. The *SSD* algorithm was implemented in a window of size 9×9 pixels. The *L&K* algorithm was performed according to [9]. This study analyzed the performance of various 3D reconstruction methods. The proposed framework based on *M-WAFs* is the most effective method to reconstruct the disparity map for 3D video sequences with different types of movements. Such framework produces the best depth and the best spatial perception in synthesized 3D video sequences against other analyzed algorithms that is confirmed by numerous simulations for different initial 2D color video sequences. The *M-WAF* algorithm can be applied to any type of color video sequence without additional information. The performance of the DSP implementation shows that the proposed algorithm can practically visualize the final 3D color video sequence in real time mode. In future, we suppose to optimize the proposed algorithm in order to increase the processing speed up to the film velocity.

2. SUPER-RESOLUTION APPLYING CLASSIC WAVELETS AND WAF

Novel method in high-resolution uses WAF [1–3] in the reconstruction of colour and greyscale video sequences of different types. The approach is theoretically justified by analysis based on key wavelet properties (*cosine projection*, *Reisz values*, etc.). Statistical simulation results have shown that method based on WAFs performs better at improving resolution than do existing frameworks. Implementations on DSP have demonstrated the possibility of real-time processing in super-resolution.

Performance and simulation issues. This section reports the results of the statistical simulation and the performance evaluation conducted via objective metrics (*PSNR, MAE*). The simulation experiments were run using several popular video sequences: *Toy* (256×256 pixels, 8 bits), *Stephan* and *Flowers* (352×240 pixels, 8 bits). Both the proposed SR procedures and several other existing procedures were used. The *Flowers* sequence was reconstructed in gray and colour formats. The *Toy* video sequence depicts moving toys; the images have defined borders and a plain background. The *Stephan* sequences show the movements of a tennis player and include many fine details. The *Flowers* sequence presents a tree with edges and the field of numerous flowers that contains many fine details. In all cases, the initial LR images were obtained by reducing the size of the original image HR by four times, summing and averaging the values of every four pixels.

The resolution reconstruction process conducted using the SR technique was used to restore the images to their initial sizes. Then, the original HR and the reconstructed SR images were compared based on the quality criteria mentioned above. We also employed subjective visual comparison, forming an error image to compare the noise suppression, artefact limitation and

preservation of detail achieved using the different algorithms. Numerous simulation experiments were run using different methods of SR reconstruction, but for each video sequence, we now only present the results of the better procedures included in the tables (2 thru 4) and figures (2 thru 4) that follow. These are the reconstruction results obtained using the following [3–5] techniques: *Bi-cubic, Nearest neighbour, Warp, DCT, FFT, Sinc, Fuzzy-ELA*, *Recursive logic*, and *Wavelets* (these are associated with the *Biorthogonal* family and the *Daubechies, Symlets, and Coiflets.*) The proposed *WAF* approach is shown to have performed best in terms of PSNR and MAE for different WAFs: Ξ_n, fup_n, π_n, g_n, and up_n. The better algorithms were also implemented on the DSP platform to demonstrate real-time processing.

The simulation results for the *Toy* video sequence are presented in Table 1; they allow us to comparing the original HR and LR zoom images, determining their performance in terms of the objective criteria PSNR and MAE and based on subjective perceptions calculated using WAF fup_1 and the DCT algorithm. The results indicate that better subjective perception is associated with WAF fup_1 than with the DCT technique.

This study analysed the performance of different SR methods. Some of these methods are used only for specific types of images, while others require additional prior information about images or require that a training stage be conducted before processing to perform HR image reconstruction. The analysed approach, which uses WAFs in the resolution enhancement process, can be used with any kind of image or video sequence and without any additional information. Numerous simulations and DSP and MatLab processing results show that the WAF framework is effective in performing SR for different video sequences; this procedure has demonstrated more robust performance in frames of different types with varying textures and other characteristics (edges, fine details, movement, etc.). The real-time implementation of the proposed framework on MatLab and DSP platforms confirms that the procedure features a processing velocity of roughly 25 frames per second for different video sequences.

3. MAMMOGRAPHY FEATURES CLASSIFICATION IN WAVELET TRANSFORM SPACE

The principal mammography [10] (MG) signs of breast cancer are clustered in the micro calcifications (MCs) and masses. Novel method for masses and MCs classification in the MG employs Wavelet Transform (WT) based on classical and WAF [3–5], decomposing MG for reducing data volume in the classification stage that is performed via multilayer artificial neural network (ANN) type classifier. The best results applying WT were obtained for *db4, db8, db16, sym1, sym2*, and

Table 1: Criteria values for video sequence *Toy*.

Algorithm	fup_3			fup_1			**DCT**			**Daubechies 2**		
No. of frame	1	2	3	1	2	3	1	2	3	1	2	3
MAE	*12.36*	*12.67*	*12.78*	**11.38**	**11.35**	**11.51**	*12.09*	*12.45*	*12.43*	13.20	13.44	13.55
PSNR	*34.76*	*34.65*	*34.56*	**34.91**	**34.90**	**34.90**	*34.90*	*34.59*	*34.61*	34.50	34.37	34.34

Table 2: Performance of the MLP classifiers for number of features (training percentage and test percentage).

No. Feature	**% Training**	**% Test**
2	75.2	74.0
3	77.0	76.2
4	78.6	76.0
5	82.0	80.0
6	85.4	82.5
7	88.0	85.0
8	92.0	90.0
9	95.2	93.5
10	95.0	94.0
11	100	95.0

Table 3: Performance of the MLP classifiers (training percentage, test percentage, and computational iterations).

Architecture	% Training	% Test	Iterations
400 : 10 : 2	95.2	91.2	13000
400 : 20 : 2	96.4	92.4	10000
400 : 30 : 2	97.3	93.5	8000
400 : 40 : 2	98.6	94.0	8200
400 : 50 : 2	99.0	95.5	7900
400 : 60 : 2	99.5	97.0	7500
400 : 70 : 2	99.5	96.8	7100
400 : 80 : 2	100	97.2	7100
400 : 90 : 2	100	98.0	7000
400 : 100 : 2	100	97.5	7000
400 : 500 : 2	100	97.8	5700

sym4 functions. The proposed algorithm for segmentation of MG images has been proven employing 30 images, where separation of the region of interest was obtained with accuracy inside the area breast. For the classification of MCs, there were considered its segmented patterns. Each a segmented pattern of MC indicates the presence of a malignant tumor in the MG images. It has been considered two test types, the first one, considering the features of the MC patterns and the second one, the MC patterns that are used only for classification. In Table 2, there are presented the training and test percentages considered from two features to eleven.

The architectures are presented among brackets with three numbers separated by two points. Here, the first number corresponds to size of the pattern of MC, the second one is a number of the hidden nodes in the structure ANN, and third one is a number of identified classes. Table 3 presenting the MLP type classifiers exposes that the best results were obtained for [400 : 60 : 2] and [400 : 90 : 2] architectures. The efficient performance obtained for a MLP classifier was 100% and 98% for training and testing, respectively. So, the proposed and implemented method is based on WT, segmentation, and MLP classifiers for MG medical image. It permits to reduce the iterations number during the training of the neural network MLP applying WT. The Wavelet functions: *Daubechies, Symlet, Coiflet* and *biorthogonal* have been employed in MLP network for microcalcifications classification in the MG images. The experimental results have shown good performance of the implemented algorithms [11, 12]. Other examples of sufficiently effective AF and WAF employment are exposed in this lecture, among them: *pulse compression in radars, medical image compression*, and *image segmentation*.

REFERENCES

1. Kravchenko, V. F., *Lectures on the Theory of Atomic Functions and Their Some Applications*, Radiotechnika, Moscow, 2003.
2. Kravchenko, V. F. and V. L. Rvachev, *Boolean Algebra, Atomic Functions, and Wavelets in Physical Applications*, Fizmatlit, Moscow, 2006.
3. Kravchenko, V. F., H. M. Perez-Meana, and V. I. Ponomaryov, *Adaptive Digital Processing of Multidimensional Signals with Applications*, Fizmatlit Edit., Moscow, 2009. http://www.posgrados.esimecu.ipn.mx/docs/Kravchenko_Perez_Ponomaryov_Book.pdf).
4. *Digital Signal and Image Processing in Radio Physical Applications*, Edited by V. F. Kravchenko, Moscow, Fizmatlit, 2007.
5. Kravchenko, V. F., O. S. Labun'ko, A. M. Lerer, and G. P. Sinyavsky, *Computing Methods in the Modern Radio Physics*, Edited by V. F. Kravchenko, Moscow, Fizmatlit, 2009.
6. Meyer, Y., *Ondelettes*, Ed., Hermann, 1991.
7. Bhatti, A. and S. Nahavandi, *Stereo Vision*, Chapter 6, 27–48, Edit, I-Tech, Vienna, 2008.
8. Malpica, W. S. and A. C. Bovik, "Range image quality assessment by structural similarity," *ICASSP 2009 IEEE International Conference on Acoustics, Speech and Signal Processing*, 1149–1152, 2009.

9. Beauchemin, S. S. and J. L. Barron, "The computation of optical flow," *ACM Computing Surveys*, Vol. 27, No. 3, 433–465, 1995.
10. Chan, H. P., K. Doi, and C. J. Vyborny, "Improvement in radiologists detection of clustered microcalcifications on mammograms: The potential of computer-aided diagnosis," *Acad. Radiol.*, Vol. 25, 1102, 1990.
11. Qian, W. and L. P. Carke, "Tree-structured nonlinear filter and wavelet transform for microcalcification segmentation in mammography," *Proc. SPIE Medical Imaging*, Vol. 1905, 716, 1993.
12. Zhang, W., K. Doi, and M. L. Giger, "Computerized detection of clustered microcalcifications in digital mammograms using a shift-invariant artificial neural network," *Medical Physics*, Vol. 21, 517, 1994.

Nonparametric Estimations of Probability Density Functions Based on the Family of Atomic Functions $ch_{a,n}(x)$ in Problems of Digital Signal Processing

Victor Filippovich Kravchenko[1], **Yaroslav Yu. Konovalov**[2], **and Dmitry Victorovich Churikov**[1]

[1]Kotel'nikov Institute of Radio Engineering and Electronics
Russian Academy of Sciences, Moscow, Russia
[2]Bauman Moscow State Technical University, Moscow, Russia

Abstract— On the basis of atomic functions (AF) the new constructions of weight functions (WF) with the compact support are offered and proved. On their basis integrated nonparametric estimations of probability density, and also its derivatives of the 1st and 2nd orders are constructed. As has shown numerical experiment using of the integrated approach allows receiving more smooth estimations. The physical analysis of nonparametric estimations of probability density function by means of new WF constructed on the basis of the AF family confirm their efficiency.

1. INTRODUCTION

Atomic functions (AF) [1–8] have found wide application at the decision of applied problems of physics and technics. The most known and studied AF is function $\mathrm{up}(x)$. Its natural generalisation is family of AF $h_a(x)$. The convolutions of these functions $\Xi_n(x) = \underbrace{h_{n+1} * \ldots * h_{n+1}}_{n}$ and $\mathrm{cup}(x) = \mathrm{up}(x) * \mathrm{up}(x)$ which also are AFs have practical importance. In the report the family of AFs $ch_{a,n}(x) = \underbrace{h_a * \ldots * h_a}_{n}$ which is generalisation of listed families of functions is considered. Using of new family of AFs $ch_{a,n}(x)$ as weight functions (WF) offers the following advantages:

- Allows to investigate properties of known AFs $\mathrm{up}(x)$, $h_a(x)$, $\mathrm{cup}(x)$ and $\Xi_n(x)$ from uniform positions.
- Presence of two parametres allows applying the AFs $ch_{a,n}(x)$ more flexibly for a wide range of problems of digital signal processing (DSP) and the mathematical physics, choosing for each of them the most suitable functions from this family.
- As the AFs $ch_{a,n}(x)$ are generalisation of known AFs then their application is possible in any problems to which decision the AFs $\mathrm{up}(x)$, $h_a(x)$, $\mathrm{cup}(x)$ and $\Xi_n(x)$ are applied.

2. FAMILY OF ATOMIC FUNCTIONS $ch_{a,n}(x)$

In this section the definition of family of AF $ch_{a,n}(x)$ and also the proof of their existence is made. Methods of their calculation are offered.

Definition. AF $ch_{a,n}(x)$ is finite decisions of the functional-differential equation

$$y^{(n)} = a^{n+1}2^{-n}\sum_{k=0}^{n} C_n^k(-1)^k y(ax+n-2k), \quad a>1, \quad n=1,2,3,\ldots, \tag{1}$$

with the support $[-\frac{n}{a-1};\frac{n}{a-1}]$ and satisfying to a condition $\int\limits_{-\infty}^{\infty} y(x)dx = 1$.

Theorem. At everyone and $n=1,2,3,\ldots, a>1$ the is functional-differential equation

$$y^{(n)} = l\sum_{k=0}^{n} C_n^k(-1)^k y(ax+n-2k)$$

has the only one infinitely differentiated decision with finite support $[-n/(a-1); n/(a-1)]$ satisfying to a condition $\int\limits_{-\infty}^{\infty} y(x)dx = 1$. Thus, for decision existence it is necessary that $l = a^{n+1}2^{-n}$.

Proof. We will search for the equation decision in space L_1 of functions summarized on all axis. We will apply to the equation of Fourier transform:

$$(it)^n F(t) = l\sum_{k=0}^{n} C_n^k (-1)^k \frac{1}{a} F\left(\frac{t}{a}\right) \exp\left(\frac{it}{a}(n-2k)\right). \tag{2}$$

For simplification of the received expression we will use the identity following from a binomial of Newton:

$$\sum_{k=0}^{n} C_n^k (-1)^k \exp\left(\frac{it}{a}(n-2k)\right) = \left(\exp\left(\frac{it}{a}\right) - \exp\left(-\frac{it}{a}\right)\right)^n = 2^n i^n \sin^n\left(\frac{t}{a}\right). \tag{3}$$

Substituting expression (3) in (2), we will receive $F(t) = l\frac{2^n}{a}F(\frac{t}{a})\frac{\sin^n(\frac{t}{a})}{t^n} = l\frac{2^n}{a^{n+1}}F(\frac{t}{a})\mathrm{sinc}^n(\frac{t}{a})$. Then $F(t)$ can be found as $F(t) = \prod\limits_{k=1}^{\infty} l\frac{2^n}{a^{n+1}}\mathrm{sinc}^n(\frac{t}{a^k})$. For convergence of infinite product it is necessary, that $l = 2^{-n}a^{n+1}$. Then

$$F(t) = \prod_{k=1}^{\infty} \mathrm{sinc}^n\left(\frac{t}{a^k}\right). \tag{4}$$

According to the Paley-Wiener theorem the function $y(x)$ exists and can be found in a kind $y(x) = \frac{1}{2\pi}\int\limits_{-\infty}^{\infty} \exp(itx)F(t)dt$. It equals to zero out of interval $[-\frac{n}{a-1}; \frac{n}{a-1}]$. According to (4) $\int\limits_{-\infty}^{\infty} y(x)dx = 1$.

The theorem is proved. The received function we will designate $ch_{a,n}(x) = y(x)$. As $F(t) = \prod\limits_{k=1}^{\infty}\mathrm{sinc}^n(\frac{t}{a^k}) = (\prod\limits_{k=1}^{\infty}\mathrm{sinc}(\frac{t}{a^k}))^n = (\hat{h}_a(t))^n$ then function $ch_{a,n}(x)$ represents convolution of n copies of $h_a(x)$. Owing to it AF $\mathrm{up}(x)$, $h_a(x)$, $\mathrm{cup}(x)$ and also $\Xi_n(x)$ are special cases of AF $ch_{a,n}(x)$. Namely $ch_{2,1}(x) = \mathrm{up}(x)$, $ch_{2,2}(x) = \mathrm{cup}(x)$, $ch_{a,1}(x) = h_a(x)$, $ch_{n+1,n}(x) = \Xi_n(x)$. Thus, the Equation (1) coincides with the equation corresponding AF. Besides $ch_{a,n}(x)$ can possible to consider as infinite convolution of Schonberg B-splines of $(n-1)$-degree. Let's result the following main properties AF $ch_{a,n}(x)$:

1) $ch_{a,n}(x) \geq 0$ As is convolution of non-negative functions $h_a(x)$, 2) $\int\limits_{-\infty}^{\infty} ch_{a,n}(x)dx = 1$ according to theorem conditions, 3) $ch_{a,n}(x)$ Is even as convolution of even functions, 4) derivatives $ch_{a,n}^{(2n)}$, $ch_{a,n}^{(3n)}$ etc. calculated by consecutive substitution to expression (1), 5) the symmetric even moments $ch_{a,n}(x)$ are rational numbers and can be found under recurrent formulas by expression of the moments of higher order through the moments of lower. The kind of these parities is defined by value of parameter n. We will result formulas for and $n = 2$, 3.

$$\int\limits_{-2/(a-1)}^{2/(a-1)} x^{2m} ch_{a,2} = (-1)^m (2m)! c_{2m} \quad \text{where} \quad c_{2m} = \frac{1}{a^{2m}-1}\sum_{k=0}^{m-1}\frac{(-1)^{m-k}2^{2m-2k+1}c_{2k}}{(2m-2k+2)!}.$$

$$\int\limits_{-3/(a-1)}^{3/(a-1)} x^{2m} ch_{a,3} = (-1)^m (2m)! c_{2m} \quad \text{where} \quad c_{2m} = \frac{1}{a^{2m}-1}\sum_{k=0}^{m-1}\frac{(-1)^{m-k}\left(3^{2m-2k+1}-1\right)\cdot 3c_{2k}}{4\cdot(2m-2k+2)!}.$$

At corresponding values of parameters of the formula coincide with known parities for moments AF $\mathrm{up}(x)$, $h_a(x)$ and $\Xi_n(x)$. Calculation $ch_{a,n}(x)$ can be made by the following approaches:

- At periodic continuation of AF $ch_{a,n}(x)$ it is represented by the following Fourier transform (FT):

$$ch_{a,n}(x) = \frac{a-1}{n}\left(\frac{1}{2} + \sum_{k=1}^{\infty} F\left(\frac{a-1}{n}\pi k\right)\cos\left(\frac{a-1}{n}\pi k x\right)\right) \quad \text{where} \quad F(t) = \prod_{k=1}^{\infty}\mathrm{sinc}^n\left(\frac{t}{a^k}\right).$$

- We will consider the operator

$$A(y) = a^{n+1}2^{-n}I^n\left(\sum_{k=0}^{n} C_n^k(-1)^k y(ax+n-2k)\right) \quad \text{where} \quad I(y(x)) = \int\limits_{-n/(a-1)}^{x} y(t)dt.$$

Being the decision of the Equation (1), $ch_{a,n}(x)$ will be a motionless point of this operator. Then $ch_{a,n}(x)$is a limit of in regular intervals converging sequence $\{f_k(x)\}$. $f_0(x) = (a-1)/2nf_k(x) = A(f_{k-1}(x))$. By analogy with [8] $f_k(x)$ we name perfect splines AF $ch_{a,n}(x)$. At $a = 2$, $n = 1f_k(x)$ coincide with defined in [8] perfect splines for AF $up(x)$. Besides perfect splines we will consider construction consecutive approximations in $f_k(x)$ space of step functions. Then $f_k(x)$ it is represented sequence of length l_k. The operator $A(y)$ is a composition of two operations: additions of the shifted copies of initial function and n-fold integration. The first operation is represented drawing up of new sequence of length of the $l_{k+1} = [al_k]$ displaced pieces of initial sequence ($f_k(x)$ operation of continuation of sequence). The second is summation of the received sequence. As the algorithm kind depends on structure of the right member of Equation (1), we will consider it more in detail. The right part of (1) consists from $n+1$ composed, representing the function compressed in a time. Each composed is shifted concerning previous for $(a-1)/n$ the lengths. Two essentially various situations thus take a place. If $(a-1)/n > 1$, supports of the composed are not crossed. In this case in intervals between supports composed also $ch_{a,n}^{(n)} = 0$ and $ch_{a,n}(x)$ coincides with a multinomial $(n-1)$-degree. It is possible to show that in this case function coincides with degree polynomials on $kn-1$ sets similar to set of Cantor. If $(a-1)/n < 1$, supports of the composed are crossed. On border between these two cases there are functions $\Xi_n(x)$ at which the end of the previous composed coincides with the following beginning. The structure of supports of AF $ch_{a,n}(x)$ for some a is presented in Table 1.

It is the most convenient to build algorithm at the rational a. In this case we will choose as initial the sequence which length shares on a rational number denominator $(a-1)/n$. Then continuation operation consists in addition to initial sequence of its n copies shifted on $l_k(a-1)/n$ samples. At $(a-1)/n > 1$ it is filled empty intervals by zero samples. If a is irrational, it is possible to use rational approximating to a, carrying out each following operation of continuation of sequence with more and more exact approximating.

Let's give an example calculations of AF $ch_{3,3}(x)$. As $(a-1)/n = 2/3$, the length of initial sequence l_0 should be multiple 3. We will choose $l_0 = 3$. We will set initial sequence and the operator is applicable to it A. Operation of continuation of sequence consists in addition to its initial sequence increased, accordingly, on -3, 3 and 1. Composed are displaced from each other on 2 samples. We will receive sequence of three times more lengths. We summarise its three times. To the received sequence the operator etc. Examples of construction of algorithms for calculation of AF up(x), $h_a(x)$, and $\Xi_n(x)$ are considered in [8].

The technique offered in the report is illustrated on concrete physical models.

3. NONPARAMETRIC PROBABILITY DENSITY FUNCTION ESTIMATION

Here, on basis of the new WFs the nonparametric estimations of probability density function and its derivatives are considered. The technique offered in the report is illustrated on concrete physical models.

Table 1: Supports of the right member of Equation (1) for $n = 1, 2, 3$; $a = 2, \ldots, 5$.

n	$a=2$	$a=3$	$a=4$	$a=5$
1	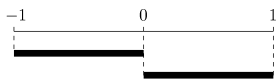		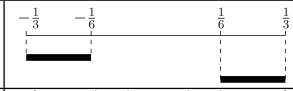	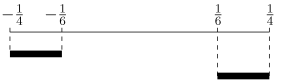
2		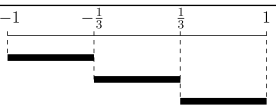	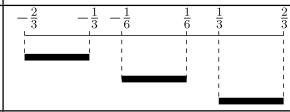	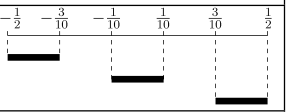
3	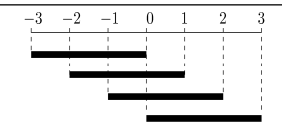	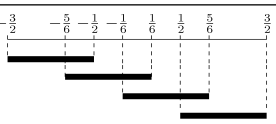	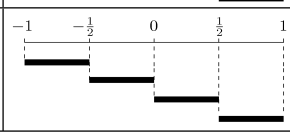	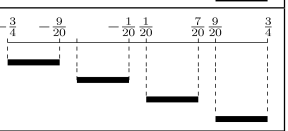

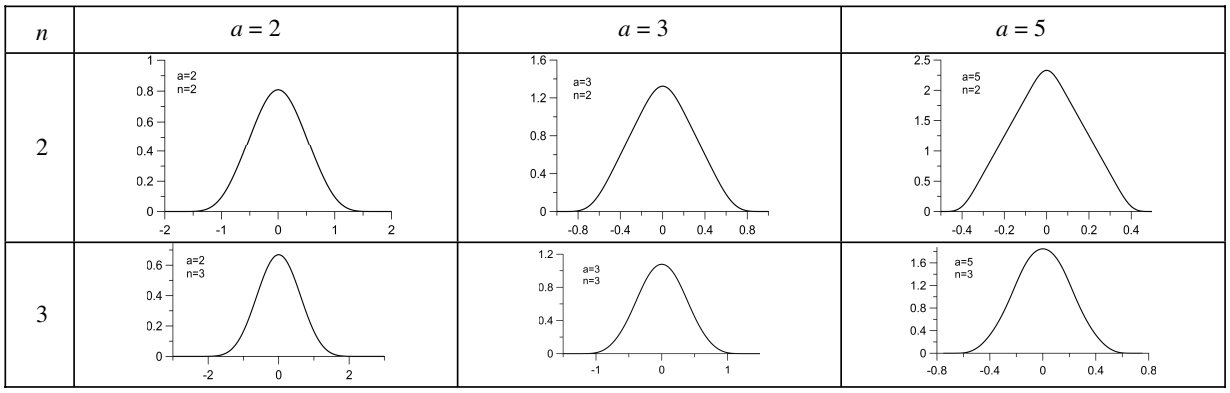

Figure 1: Behaviour of AF $ch_{a,n}(x)$ for $n = 2, 3$; $a = 2, 3, 5$.

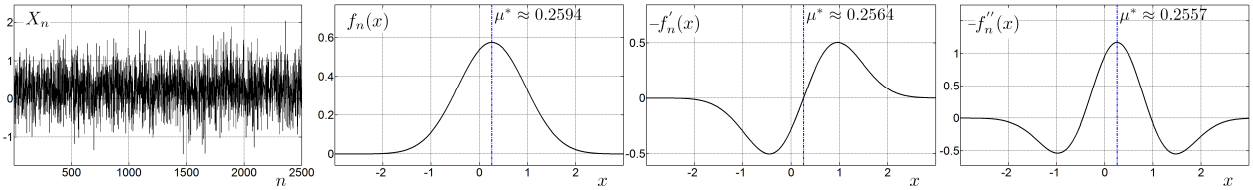

Figure 2: (a) Sequence of random variables X_n, $n = 2500$ and (b), (c), (d) estimation of $f_n(x)$, $Df_n(x)$, $D^2 f_n(x)$ for $a = 2$, $r = 2$.

Definition. The nonparametric problem of estimation of unknown distributions is a problem of a finding of procedure with which help it is possible to estimate nonparametric distributions from some class of distributions. The nonparametric probability density estimation of n independent observation $X_1, X_2, \ldots, X_n$ is defined so $f_n(x) = \frac{1}{nh} \sum\limits_{j=1}^{n} K(\frac{X_j - x}{h})$ where $h = h(n)$ is some sequence of positive numbers $\lim\limits_{n\to\infty} h(n) = 0$, the $K(x)$ is even function, $\int\limits_{-\infty}^{\infty} K(x)dx = 1$, and $K(x) \in L_2$. The WF $K(x) \equiv ch_{a,n}(x)$. Estimation of $f'(x)$ and $f''(x)$ will write down in the following form: $Df_n(x) = \frac{1}{nh^2} \sum\limits_{j=1}^{n} N(\frac{X_j - x}{h})$, $D^2 f_n(x) = \frac{1}{nh^3} \sum\limits_{j=1}^{n} M(\frac{X_j - x}{h})$. Here, $h = h(n)$ is decreasing sequence of positive numbers $\int\limits_{-\infty}^{\infty} N(x)dx = 1$, $N(x) \in L_2$, $\int\limits_{-\infty}^{\infty} M(x)dx = 1$, $M(x) \in L_2$ where $N_r(x) = K'_{r-1}(x)$, $r = 3, 5, \ldots$. $M_r(x) = K''_{r-2}(x)$, $r = 4, 6, \ldots$. To improve approximating properties of nonparametric estimations probably, spending optimisation both on factor h and on kernel function $K(x)$ for each concrete probabilistic process.

Physical characteristics of weight functions. For research of spectral kernels we will use the modified physical characteristics: width of spectral density function on level -3 dB (γ_3), relative width of spectral density function on level -6 dB (γ_4/γ_3), maximum level of side lobes (in dB) γ_9, L_2-norm (P), uncertainty constant (Δ), the support (supp) and the effective support $\text{supp}_E = \{x \,|\, \|f(x)\|_{L_2} = 0.999P\}$.

4. NUMERICAL EXPERIMENT

Let's consider an example of an estimation of function of density of probability of sequence of random variables with the X_n normal law of distribution $f(x) = \frac{1}{\sqrt{2\pi\sigma^2}} \exp(-\frac{(x-\mu)^2}{2\sigma^2})$ where expected value $\mu = 0.25$, standard deviation $\sigma = 0.5$. Let's spend comparison of characteristics of the distribution calculated on sequence, and also from estimations [6, 7].

For the analysis of the received estimations we will calculate the moments of function of density of distribution $m_k = \int\limits_{-\infty}^{\infty} (x - \mu^*)^k f_n(x)dx$, asymmetry $A = \frac{m_3}{\sigma^3}$, and also an excess $E = \frac{m_4}{\sigma^4} - 3$ (see Table 2).

Table 2: Characteristics of $f_n(x)$ ($n = 2500$).

n	a	$2\mu^*$	$2\sigma^*$	$m_1 \times 10^3$	m_2	$m_3 \times 10^3$	m_4	$A \times 10^3$	$E \times 10^3$
2	2	0.524	1.103	−4.78	1.218	−32.41	4.437	−24.13	−6.68
	3	0.524	1.039	−5.49	1.079	−32.72	3.495	−29.20	3.94
	4	0.525	1.020	−5.77	1.040	−32.93	3.250	−31.06	6.24
	5	0.525	1.011	−5.96	1.023	−33.23	3.148	−32.11	7.18
6	2	0.525	0.998	−5.95	0.995	−32.71	2.980	−32.94	8.01
	3	0.525	0.999	−5.99	0.995	−32.83	2.980	−32.94	−6.56
	4	0.525	0.999	−6.24	0.995	−33.57	2.980	−33.69	−6.15
	5	0.525	0.999	−6.47	0.995	−34.24	2.980	−34.37	−5.11

5. CONCLUSIONS

On the basis of atomic functions new designs of weight functions with the compact support are offered and proved. On their basis integrated nonparametric estimations of density of probability, and also its derivative 1st and 2nd orders are constructed. The physical analysis of nonparametric estimations of function of density of probability by means of new weight functions, constructed on the basis of family atomic functions, confirm their efficiency.

REFERENCES

1. Kravchenko, V. F., *Lectures on the Theory of Atomic Functions and Their Some Applications*, Radiotechnika, Moscow, 2003.
2. *Digital Signal and Image Processing in Radio Physical Applications*, edited by V. F. Kravchenko, Moscow, Fizmatlit, 2007.
3. Kravchenko, V. F., O. S. Labun'ko, A. M. Lerer, and G. P. Sinyavsky, *Computing Methods in the Modern Radio Physics*, edited by V. F. Kravchenko, Moscow, Fizmatlit, 2009.
4. Kravchenko, V. F., "New synthesized windows," *Dokl. Akad. Nauk*, Vol. 382, No. 2, 190–198, 2002.
5. Kravchenko, V. F., V. L. Rvachev, and V. A. Rvachev, "Mathematical methods for signal processing based on atomic functions," *Journal of Communications Technology and Electronics*, Vol. 40, No. 12, 118–137, 1995.
6. Kravchenko, V. F., V. I. Pustovoit, and D. V. Churikov, "Atomic functions and the probability density function estimations," *Doklady Physics*, Vol. 56, No. 9, 474–478, 2011.
7. Kravchenko, V. F. and D. V. Churikov, "Atomic functions in nonparametric estimations of probability density functions and their derivatives," *Proceedings. Int. Conference "Days on Diffraction"*, 103–105, St. Petersburg, Russia, May 30–Jun. 3, 2011.
8. Konovalov, Ya. Yu., "Iterative algorithms for numerical solution of differential equations with linearly transformed argument," *An International Journal Electromagnetic Waves and Electronic Systems*, Vol 16, No. 9, 49–57, 2011.

Statistical Synthesis of Optimal and Quasi-optimal Chopper Radiometers

Victor F. Kravchenko[1], **Valery K. Volosyuk**[2], **and Vladimir V. Pavlikov**[2]

[1]Kotel'nikov Institute of Radio Engineering and Electronics
Russian Academy of Sciences, Moscow, Russia
[2]N. Ye. Zhukovsky National Aerospace University ("Kharkov Aviation Institute")
Kharkov, Ukraine

Abstract— Optimal and quasi-optimal algorithms for ultra wideband signal processing in chopper radiometers are synthesized. Their theoretical potential accuracy and potential radiometric sensitivity are derived. Corresponding block diagrams of radiometers are provided.

1. INTRODUCTION

It is known that radiometric devices have found applications for antenna parameter measurement [1] in remote sensing [2], radio astronomy [3], medical problems, etc. One particular class of such devices is radiometers with modulation of a useful signal: Dicke radiometer [4], null balancing radiometer [2] and their modifications. All of them have been developed based on engineering experience that cannot reflect refinements provided by optimal radiometric signal processing and its potential characteristics. In active location, better accuracy can be achieved by choosing a proper sounding signal, signal-to-noise ratio and other system characteristics. In contrast, in passive location it is stochastic signals that are processed, limiting possibilities during radiometric devices design. That is why widespread methods to control system characteristic are based on partly defining structure of a radiometer predetection section. In particular, for chopper radiometers design the predetection section of radiometer placed after the antenna before receiver non-linear elements can be fixed. The predetection section comprises a modulator and an oscillator with known parameters.

The contribution of this paper is statistical synthesis of optimal and quasi-optimal single-antenna chopper radiometers and analysis of their potential characteristics.

Authors obtained new and generalized published earlier results [5–7] that has allowed developing optimal chopper radiometer. Its relation to some existing radiometers used in practice is shown under different assumptions.

2. FORMULATION OF OPTIMIZATION PROBLEMS. THE OBSERVATION EQUATION. ASSUMPTIONS ON STATISTICAL SIGNAL AND NOISE CHARACTERISTICS'

2.1. The General Formulation of the Optimization Problem. The Observation Equation

Optimization is performed for a partly preselected structure of the radiometer (Fig. 1), that contains antenna (A) and predetection section, characterized by unstable in time amplitude-frequency characteristic $\dot{K}(j2\pi f, t)$. It is assumed that the signal $s(t, \lambda)$ is modulated before the receiver, and only then is mixed with the internal noise of the receiver $n(t)$. Unstable function of radiometer $\xi(t)$ is a slowly varying (compared to the modulation period T_m) unknown but nonrandom function of time. The optimization problem formulates as follows. On the observation interval $[0, T]$ estimates of the unknown parameters λ of the signal $s_{\dot{K}}(t, \lambda)$ (that is observes on the background of internal radiometer noise $n_{\dot{K}}(t)$) are to be found. Here the following notations are used: $s_{\dot{K}}(t, \lambda)$ and $n_{\dot{K}}(t)$ are useful process and internal noise at the output of the radiometer receiver predetection section.

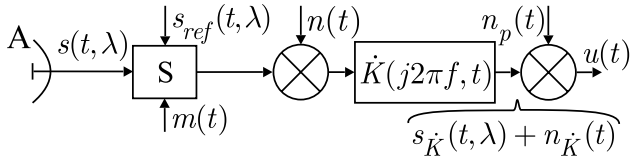

Figure 1: Diagram which corresponds to the Equation (1).

In the partly predefined structure of the input channel (Fig. 1), a reference signal $s_{ref}(t,\lambda)$ is introduced as well as additive regularizing noise $n_p(t)$. The latter is white Gaussian noise with zero mean and a low spectral power density N_p. This addition eliminates singularities of integral equations solution.

The following observation equation corresponds to the diagram shown in Fig. 1:

$$u(t) = s_{\dot{K}}(t,\lambda) + n_{\dot{K}}(t) + n_p(t) \tag{1}$$

where

$$s_{\dot{K}}(t,\lambda) = \int_{-\infty}^{\infty} [s(\tau,\lambda)\, m(\tau) + s_{ref}(\tau,\lambda)\,(1-m(\tau))] h(t-\tau)\,[1+\xi(t-\tau)]\, d\tau, \tag{2}$$

$$n_{\dot{K}}(t) = \int_{-\infty}^{\infty} n(\tau)\;\; h(t-\tau)\,[1+\xi(t-\tau)]\, d\tau. \tag{3}$$

Here, $h(t)$ is an impulse response of the radiometer input channel; $\tau \in [0,T]$ is observation period; $m(t)$ is modulating function (square wave).

2.2. Particular Formulation the Optimization Problem

Let us introduce the following additional simplifications to the general problem:

- transfer characteristic is stable within the observation period ($\dot{K}(j2\pi f,t) = \dot{K}(j2\pi f)$, $\xi(t) = 0$). This assumption is valid in practice for short periods of measurement;
- reference source is controllable;
- modulation and the reference channel are not available ($m(t) = 1$).

2.3. Assumptions and Statistical Characteristics of Signals and Noise

1) $s(t,\lambda)$, $s_{ref}(t,\lambda)$, $n(t)$ and $n_p(t)$ are statistically independent Gaussian random processes with zero mean and autocorrelation functions given by

$$R_s(t_1,t_2,\lambda) = \langle s(t_1,\lambda)s(t_2,\lambda)\rangle = B_{BrA}(f_0,\vartheta_0,\lambda)\delta(t_1-t_2)/2, \tag{4}$$

$$R_{ref}(t_1-t_2,\lambda) = \langle s_{ref}(t_1,\lambda)s_{ref}(t_2,\lambda)\rangle = S_{ref}(\lambda)\delta(t_1-t_2)/2,$$

$$R_n(t_1-t_2) = \langle n(t_1)n(t_2)\rangle = N_0\delta(t_1-t_2)/2, \tag{5}$$

$$R_p(t_1-t_2) = \langle n_p(t_1)\, n_p(t_2)\rangle = N_p\delta(t_1-t_2)/2;$$

2) spectral power densities $B_{BrA}(f,\vartheta_0,\lambda) = B_{BrA}(f_0,\vartheta_0,\lambda)$, $S_{ref}(\lambda)$, N_0, N_p are constant within the radiometer frequency band;

3) the gain $\dot{K}(j2\pi f,t)$ varies with time in an nonrandom but unknown way. This is taken into account by introducing a function $\xi(t)$. This function varies slowly and within one modulation period T_m we can treat it as constant;

4) square wave modulation function $m(t)$ has been chosen that takes values 0 and 1.

The assumption 1) is satisfied in practice and describes physical properties of real radiometric signals and noise. The assumption 2) is not so determinant as it is possible to use the mean value theorem considering monotony of introduced functions in a band of working frequencies of radiometer. Assumption 3) is fulfilled by a proper choice of modulation frequency. Assumption 4) greatly simplifies the hardware implementation of the receiver.

In Equations (4) and (5), $B_{BrA}(f_0,\vartheta_0,\lambda)/2$, $S_{ref}(\lambda)/2$, $N_0/2$, $N_p/2$ are two-sided (w.r.t. frequency) power spectral densities of the corresponding processes and noises. The spectral density and equivalent temperature are linked through the Boltzmann constant k

$$B_{BrA}(f_0,\vartheta_0,\lambda) = k\,T_A^\circ, \quad S_{ref}(\lambda) = k\,T_{ref}^\circ, \quad N_0 = k\,T_n^\circ, \tag{6}$$

where, T_A°, T_{ref}°, T_n° are effective temperatures of antenna, reference source and inner noise, respectively.

The correlation function of observation has the following form:

$$R(t_1,t_2,\lambda) = 0.5\{(B_{BrA}(f_0,\vartheta_0,\lambda)m^2(t_1)+S_{ref}(\lambda)[1-m(t_1)]^2+N_{0n})R_h(\Delta t)[1+\xi(t_1)]^{\,2}+N_p\delta(\Delta t)\}, \tag{7}$$

where, $t_1-t_2=\Delta t$, $R_h(\Delta t) = \int_{-\infty}^{\infty} h(t_1-\tau)\,h(t_2-\tau)\,d\tau$. In (7) it is taken into account that, first, the inner path of radiometer is ultra wideband. Second, within the main lobe of the narrow function $h(t)$, that describes the impulse characteristic of the system, functions $m^2(\tau)$, and $[1+\xi(\tau)]^{\,2}$ are constant.

3. SOLUTION OF GENERAL OPTIMIZATION PROBLEM

From assumption 4) it follows that one can solve the problem using the maximum likelihood approach.

3.1. Synthesis of the Optimal Algorithm

Likelihood functional for Gaussian stochastic processes can be written as

$$P\left[u\left(t\right)|\lambda\right] = k\left(\lambda\right)\exp\left\{-0.5\int_0^T\int_0^T u\left(t_1\right)W\left(t_1,t_2,\lambda\right)u\left(t_2\right)\ dt_1\,dt_2\right\} = \max \tag{8}$$

where $W(t_1,t_2,\lambda)$ is the inverse of the correlation function found from the following integral equation: $\int_{-\infty}^{\infty} R\left(t_1,t_2,\lambda\right)W\left(t_2,t_3,\lambda\right)dt_2 = \delta\left(t_1-t_3\right)$; $k\left(\lambda\right)$ is a parameter that depends on λ. It was shown in [5, 6] that the solution of the functional (8) is equivalent to the following system of equations:

$$\begin{cases} 0.25(B_{BrA}\left(f_0,\vartheta_0,\lambda\right)+N_0)T_m\sum\limits_{n=0}^{N-1}\Delta F_n = \int_{-\infty}^{\infty} m\left(t\right)u_d^2\left(t\right)dt + 0.25\,N_pT_m\sum_{n=0}^{N-1}\Delta f_n\ , \\ 0.25(S_{ref}\left(\lambda\right)+N_{0n})T_m\sum\limits_{n=0}^{N-1}\Delta F_n = \int_{-\infty}^{\infty}\left[1-m\left(t\right)\right]u_d^2\left(t\right)dt + 0.25\,N_pT_m\sum_{n=0}^{N-1}\Delta f_n \end{cases} \tag{9}$$

where $\Delta F_n = \int_{-\infty}^{\infty}\left|\dot{K}\left(j2\pi f\right)\right|^4\left[1+\xi_n\right]^4 G_R^{-2}\left(j2\pi f,n,\lambda\right)df$ is the bandwidth of the predetection section of the radiometer after decorrelation filter; $\Delta f_n = \int_{-\infty}^{\infty}|\dot{K}(j2\pi f)|^2[1+\xi_n]^2G_R^{-2}(j2\pi f,n,\lambda)df$ is the bandwidth of the decorrelation filter. Given (6), the system (9) can be solved via the following optimal algorithm

$$\Delta T^{\circ} = \left(T_{cd}^{\circ}+T_n^{\circ}\right)\left\{\int_{-\infty}^{\infty} m(t)u_d^2(t)dt \Big/ \int_{-\infty}^{\infty}\left[1-m(t)\right]u_d^2(t)dt - 1\right\} \tag{10}$$

where $u_d^2(t)$ is squared observation after decorrelation filter.

Given modulation radiometer with gain of the input path fluctuating in time, two operations of the optimal treatment follow from (10): whitening and quadratic detection $u_d^2\left(t\right)$, synchronous detection (multiple of modulating function and integration) and division measured at adjacent intervals intensities of the input and reference signals followed by subtraction of unity and amplification.

3.2. The Potential Accuracy of Estimation

The potential accuracy of the estimates is obtained by inverting of Fisher Information Matrix:

$$\Phi_{\mu\nu} = -\left\langle\partial^2\ln P[u(t)|\lambda]/\partial\lambda_\mu\partial\lambda_\nu\right\rangle. \tag{11}$$

The variance of parameter λ estimation is given by

$$\sigma_\lambda^2 = 4(T_A^{\circ}(\lambda)+T_n^{\circ})^2N/T\sum_{n=0}^{N-1}\Delta F_n \tag{12}$$

where $N^{-1}\sum_{n=0}^{N-1}\Delta F_n$ is the mean frequency band corresponding to some mean value of function ξ over an observation interval. Here we use that $T_m = T/N$.

3.3. Potential Radiometric Sensitivity

Using the generalized definition of potential fluctuation sensitivity [5], we obtain potentially detectable signal increase:

$$\Delta T_{\min}^{\circ} = 2\sqrt{2}\left(T_A^{\circ}(\lambda)+T_n^{\circ}\right)\Big/\left[T_m\sum_{n=0}^{N-1}\Delta F_n\right]^{-0.5}. \tag{13}$$

3.4. Block Diagram Synthesis

The block diagram corresponding to (10) is shown in Fig. 2. Note that the block diagram that corresponds to the observation equation contains two summators entering noise (internal and regularizing) into the observation equation. This allows to present mathematical model of the observation equation in a form convenient for analytical calculations. In practice, this model corresponds to the process of signal propagation through the predetection section of the receiver (enclosed by the dash-dot line).

Let us next describe the block diagram operation principle. The modulating voltage generator controls the CS switcher, that sequentially connects signals from the antenna output and from the reference source to the radiometer input. Control signals from the modulating voltage generator connect corresponding decorrelation filters DF1 and DF2 synchronously with CS. Amplitude-frequency characteristics of decorrelation filters DF1 and DF2 have the following form [7]:

$$2\,|\dot{K}(j2\pi f)|\left[(B_{BrA}(f_0,\vartheta_0,\lambda)\;+N_0)\,|\dot{K}(j2\pi f)\,|^2\;[1+\xi(t)]\;^2+N_p\right]^{-1}, \tag{14}$$

$$2\,|\dot{K}(j2\pi f)|\left[(S_{cd}(\lambda)\;+N_0)\,|\dot{K}(j2\pi f)\,|^2\;[1+\xi(t)]\;^2+N_p\right]^{-1}. \tag{15}$$

Further, mixtures of the signal and noise arrive to quadratic detectors (multipliers in Fig. 2) and to synchronous detectors. Modulating functions $m(t)$ and $1-m(t)$ are provided to second inputs of these detectors. This is followed by calculation of the ratio between the measured intensity of useful and basic signals. From this ratio unity is subtracted. On the block-diagram output, an estimation of ratio between temperature increase of the useful signal and equivalent noise temperatures of the base channel and internal radiometer noise is obtained.

4. THE ASSUMPTION 1. GAIN OF PREDETECTION SECTION IS STABLE

Letting the gain of radiometer predetection section to be stable ($\dot{K}\,(j2\pi f,t)\;=\;\dot{K}\,(j2\pi f)$), the solution of (9) is given by

$$\sigma^2_{s-ref}=0.5T^{-1}\left\{\int_0^T m(t)u_d^2(t)dt-\int_0^T\left[1-m(t)\right]u_d^2(t)dt\right\} \tag{16}$$

where σ^2_{s-ref} is difference between the useful signal and reference source signal powers on the radiometer output. Equation (16) describes Dicke radiometer.

Lower bound on estimation variance and potential radiometric sensitivity stems from (12) and (13), taking into account that the width of frequency band is constant within measurement time ($N^{-1}\sum_{n=0}^{N-1}\Delta F_n=\Delta F$)

$$\sigma^2_\lambda \;=\; 4(T^\circ_A(\lambda)+T^\circ_n)^2/T\Delta F, \tag{17}$$

$$\Delta T^\circ_{\min} \;=\; 2\sqrt{2}T^\circ_A(\lambda)+T^\circ_n/\sqrt{T\Delta F}. \tag{18}$$

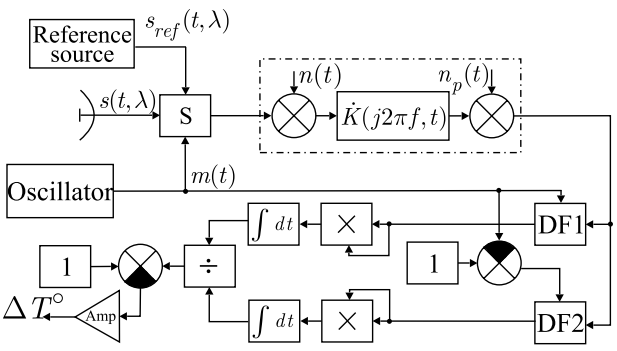

Figure 2: Block-diagram of optimal radiometer.

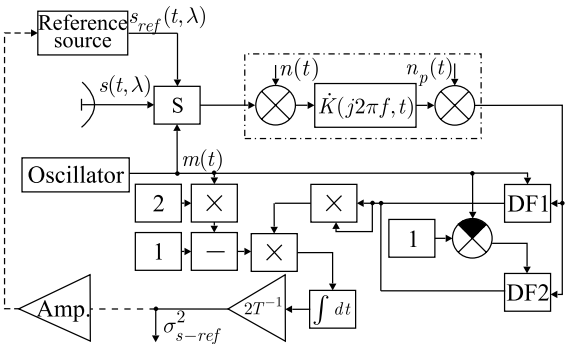

Figure 3: Block-diagrams of quasi-optimal radiometers.

5. THE ASSUMPTION 2. A SOURCE OF THE BASIC CHANNEL IS REGULATED

Assuming that the radiometer predetection section gain is stationary ($\dot{K}(j2\pi f,t)=\dot{K}(j2\pi f)$) and the source of reference signal is controllable, (9) is solved as follows:

$$2\left\{\int_{-\infty}^{\infty} m\left(t\right)u_d^2\left(t\right)dt-\int_{-\infty}^{\infty}\left[1-m\left(t\right)\right]u_d^2\left(t\right)dt\right\}/Tk\Delta F=0. \tag{19}$$

Potential characteristics of this radiometer are described by (17) and (18).

Algorithm (19) is close to the scheme of null-balancing radiometer [2] (the dashed line between output of the diagram in Fig. 3 and input of the reference signal block). The feedback provides constant control of reference signal source in such manner that the difference signal equals zero on the output.

The operation principle of the block-diagram in Fig. 3 corresponds to the block-diagram shown in Fig. 2. Here, decorrelation filters DF1 and DF2 have amplitude-frequency characteristic (14), (15), and $\xi(t)=0$.

6. THE ASSUMPTION 3. THE REFERENCE CHANNEL AND MODULATION OF THE USEFUL SIGNAL ARE ABSENT

In addition, let us consider one more special case when the gain factor is stable, modulation and the basic channels are absent. In this case, it is possible to present the solution of the system (10) as follows:

$$\sigma_s^2=T^{-1}\int_{-\infty}^{\infty}u_d^2\left(t\right)dt-\sigma_n^2 \tag{20}$$

where $\sigma_s^2=kT_A^{\circ}\Delta F$ and $\sigma_n^2=N_{0n}\Delta F=kT_n^{\circ}\Delta F$ are estimates of the useful signal and the radiometer noise powers.

Algorithm (20) corresponds to the total-power radiometer [3].

The estimation variance and potential radiometric sensitivity of this radiometer are given by

$$\sigma_\lambda^2=2(B_{BrA}(\lambda)+N_0)^2/T\Delta F,\quad \Delta T_{\min}^{\circ}=\sqrt{2}\left(T_A^{\circ}(\lambda)+T_n^{\circ}\right)/\sqrt{T\Delta F}. \tag{21}$$

7. CONCLUSIONS

In this paper, optimal (expression (10)) and quasi-optimal (expressions (16), (19)) algorithms of ultra wideband signals processing in chopper radiometer and total-power radiometer (expression (20)) are obtained from a uniform position of statistical synthesis. Their potential accuracy and potential radiometric sensitivity are derived. Potential radiometric sensitivity is obtained based on Fisher information matrix. This is in contrast to the classical approach based on analysis of signal propagation through radiometer typical blocks. The corresponding block diagrams of radiometers are provided and discussed.

REFERENCES

1. Wait, D. F., "Precision measurement of antenna system noise using radio stars," *IEEE Transactions on Instrumentation and Measurement*, Vol. 32, No. 1, 110–116, 1983.
2. Sharkov, E. A., *Passive Microwave Remote Sensing of the Earth: Physical Foundations*, Praxis Publishing Ltd, Chishester, UK, 2003.
3. Bhattacharya, A. B., S. Jaoardar, and R. Bhattacharya, *Astronomy and Astrophysics*, Infinity Science Press LLC, Hingham, Massachusetts, New Delhi, India, 2008.
4. Dicke, R. H., "The measurement of thermal radiation at microwave frequencies," *Review of Scientific Instruments*, Vol. 17, 268–275, 1946.
5. Volosyuk, V. K. and V. V. Pavlikov, "Statistical synthesis of one-antenna chopper radiometric receivers," *Applied Radio Electronics: Sci. Mag.*, Vol. 10, No. 3, 285–294, 2011 (in Russian).
6. Volosyuk, V. K., V. V. Pavlikov, and S. S. Zhyla, "Parameter estimation for UWB signals in the radiometric systems of modulation type with fluctuating gain input path," *Proceedings of International Conference*, 237–240, Kharkiv, Ukraine, October 2011.
7. Volosyuk, V. K. and V. F. Kravchenko, *Statistical Theory of Radiotechnikal Systems of Remote Sensing and Radar*, V. F. Kravchenko, Eds, Fizmatlit, Moscow, 2008 (in Russian).

Maximum Permissible Values of Biometric Code Bits Correlation

V. Bezyaev[1], **I. Serikov**[1], **A. Kruchinin**[1], **N. Ivanushchak**[1], **and M. Sekretov**[2]

[1]Public Corporation "Research and Production Enterprise 'Rubin'", Russia
[2]Public Corporation "Penza Research Electrical Engineering Institute", Russia

Abstract— The article considers a problem of modeling long output codes of the neural network "biometrics-code" transformer.

The work shows that it is complicated to investigate statistical features of the 256-bit "Foe" code with its entropy of around 60 bits by common techniques.

In order to simplify the problem under investigation the authors suggest a conversion into Hamming distances dimension between "Friend" and "Foe" codes. The conversion from investigating statistics of normal codes emergence to investigating statistics of distribution of Hamming distances emergence probabilities theoretically allows to decrease problem's complexity from exponential to nearly linear complexity. The cause of such cardinal simplification of the problem is the fact that the Hamming distances distribution for long biometric codes is well-described by the normal law of values distribution.

The researchers have built a nomogram of the Hamming distance distribution for 256-bit codes and various correlation values between biometric code bits. The nomogram shows that provided low values of code bits correlation coefficient the distribution of Hamming distance values is close to the normal distribution law. However, as the controlled parameter — r increases, the normal law of distribution gradually transforms into the uniform law of values distribution. As the code bits correlation changes from 0.0 to 0.35, the hypothesis of normality of the Hamming code distribution remains operable.

The authors emphasize that, according to the nomogram, for the codes of any length with bits correlation of 0.5 the Hamming distance distribution remains uniform. This means that $r = 0.5$ is the maximum permissible point. In case the code bits correlation is higher, the neural network "biometrics-code" transformer is absolutely unable to protect user's biometrics data, marked during the instruction in its artificial neuronet parameters.

When the code bits correlation decreases, the "biometrics-code" transformer exponentially recovers its protective capability. If the biometric code bits correlation tends to 0.0, the level of biometric data security is comparable to the cryptographic algorithm security level.

1. INTRODUCTION

The ideal "biometrics-code" transformer should unequivocally convert a vector of N continuous biometric parameters of "Friend" image — $\bar{\nu}_i$ into an output code vector — $\bar{c}$, consisting of n binary bits. In case the input of "biometrics-code" transformer receives a vector of N continuous biometric parameters — $\bar{\xi}_i$ of "Foe" image sample, in the output there should emerge a random code — $\bar{z}_i$, consisting of n binary bits.

At the same time the entropy of "Friend" codes, obtained in production of different "Friend" image samples, should have a value close to zero from 0.01 to 0.05 bits. The entropy of "Foe" codes should on the contrary have a greater value from 20 to 60 bits.

2. TRANSITION FROM INVESTIGATING STATISTICS OF NORMAL CODES' EMERGENCE TO INVESTIGATING STATISTICS OF HAMMING DISTANCES

Investigation of statistical features of 256-bit "Foe" codes with intrinsic entropy of approximately 60 bits by means of common methods is complicated. To simplify the problem one should shift to Hamming distances dimension between "Friend" and "Foe" codes:

$$h_i = \sum_{m=1}^{n} c_m \oplus z_{m,i}, \tag{1}$$

where i — number of the code in the string under investigation; m — number of the bit in $\bar{z}_i$ codes under investigation; h — Hamming distance; $\oplus$ — modulo two addition of compared bits.

The shift from investigating statistics of common codes' emergence to investigating statistics of distribution of various Hamming distances emergence probabilities (1) allows to decrease complexity

of the problem under consideration from exponential to nearly linear complexity [1–3]. The cause of such cardinal simplification of the problem is the fact that for long biometric codes the distribution of Hamming distances is well-described by the normal law of values distribution. That is, the probability of "Friend" code emergence in the selection of biometric codes under investigation is well-described by the following correlation:

$$P_2 = \frac{1}{\sqrt{2\pi}\sigma(h)} \int_0^1 \exp\left(\frac{-(E(h)-u)^2}{2\sigma^2(h)}\right) \cdot du \tag{2}$$

where P_2 — probability of incorrect identification of "Foe" as "Friend" for the "biometrics-code" transformer under investigation; $\sigma(h)$ — root-mean-square deviation of Hamming codes' deviation; $E(h)$ — mathematical expectation of Hamming codes.

3. MODELING OF BIOMETRIC CODE STRINGS

Modeling of independent code strings is not a complicated problem. For example, in order to model a single 256-bit code it is sufficient to execute a 256-fold reference to the software or hardware random-number generator. However the emergence of biometric codes with absolutely dependent bits is typical only for ideal "biometrics-code" transformers. Real "biometrics-code" transformers deliver the strings of dependent codes. The article [1] describes in detail the reproduction of code strings with controlled value of correlation coefficients coinciding with each other, calculated for any pairs of code bits. If the value of pair correlation coefficients, fixed during modeling, is changed gradually, one will obtain a nomogram of Hamming distances distribution, shown in Fig. 1.

According to Fig. 1, if the values of code bits correlation coefficients are low, the distribution of Hamming distance values is close the normal law of value distribution. However, the increase of converted parameter — r results in gradual transformation of the normal law of value distribution into a uniform law of value distribution. As the code bits correlation changes from 0.0 to 0.35, the hypothesis of normality of the Hamming code distribution remains operable, and it is admissible to apply the correlation (2) for evaluation of errors of second type. Within the range of code bit correlation between 0.35 and 0.5 the correlation (2) produces a significant error.

4. STATISTICAL DESCRIPTION OF LONG BIOMETRIC CODES WITH STRONGLY CORRELATED BITS

In connection with $r = 0.5$ and the distribution of Hamming distances becomes uniform:

$$p(h) = \text{const}, \tag{3}$$

the density of Hamming distance values distribution should be described by the combination of normal and uniform laws of value distribution [4].

Particularly for 256-bit codes in the range of code bit correlation between 0.35 and 0.5 the

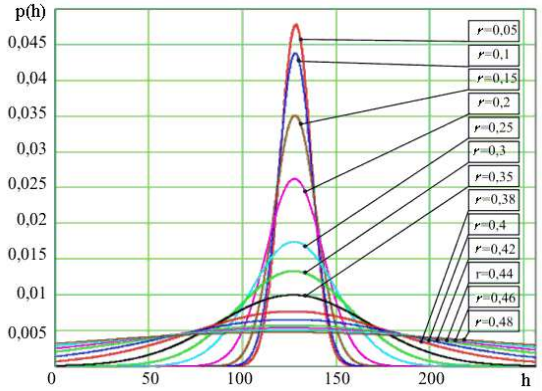

Figure 1: A nomogram of hamming distance distribution for 256-bit codes and various values of correlations between biometric code bits.

distribution of Hamming distances is well-described by the following approximation:

$$p(h) \approx a(r) \cdot \frac{1}{257} + \frac{(1 - a(r)) \cdot \exp\left(\frac{-(128-h)^2}{2\sigma^2(h)\cdot(1-a^2(r))}\right)}{\sqrt{2\pi} \cdot \sigma(h) \cdot (1 - a(r))}, \tag{4}$$

where

$$a(r) = \frac{r - 0.35}{0.15}. \tag{5}$$

It is evident that for other lengths of biometric codes $n \neq 256$ the hypothesis of Hamming distances distribution normality would be operable in another range of bit correlation values. Nevertheless, it is possible to build a system of Hamming distances distribution for biometric codes of any length, and restore the linear function $a(r)$ on the basis of those distances. That is, the problem of statistical description of Hamming distances distribution is independent of code length in the output of "biometrics-code" transformer.

5. CONCLUSIONS

The fact that for codes of any length with bit correlation being equal to 0.5 the distribution of Hamming distances always becomes uniform is of essential importance. This means that the point $r = 0.5$ is ultimate. In case of higher code bit correlation the neural network "biometrics-code" transformer becomes absolutely incapable of protecting user's biometric data, marked during the instruction in parameters of its artificial neural network. When the code bit correlatedness decreases the "biometrics-code" transformer rapidly (exponentially) restores its protective capability. If the biometric code bits correlation tends to 0.0, the level of biometric data security is comparable to the cryptographic algorithm security level.

ACKNOWLEDGMENT

The article has been prepared in the framework of a complex project "Development and preproduction of telecommunication equipment, development of software, network, applied and special provision to build a digital communication network with personal access" in accordance with the Russian Federation Government Regulation No. 218 from 09.04.2010 (Contract with the Ministry of education and research No. 13.G25.31.0039 from 07.09.2010).

REFERENCES

1. Malygin, A. Y., V. I. Volchikhin, A. I. Ivanov, and V. A. Funtikov, *Fast Testing Algorithms for Neural Network Mechanisms of Biometric-cryptographic Data Protection*, 161, Penza State University Publishing, Penza, 2006.
2. Shannon, K., *Works on Theory of Information and Cybernetics*, Foreign Literature Publishing, Moscow, 2002.
3. Standard ГОСТ Р 52633.0-2006, "Information security. Information security technique. Requirements for means of high-reliability biometric authentication," 2006.
4. Malygin, A. Y., D. N. Nadeev, and A. I. Ivanov, "Two causes of nonidealness of 'Foe' output random code states in neural network 'biometrics-code' transformers," *Problems of Data Protection*, No. 2, 19–21, 2008.

On the Issue of Modeling Long Biometric Codes with Dependent Bit States

V. Bezyaev[1], **I. Serikov**[1], **A. Ivanov**[2], **I. Urnev**[3], **A. Kruchinin**[1], **and N. Ivanushchak**[1]

[1]Public Corporation "Research and Production Enterprise 'Rubin'", Russia
[2]Public Corporation "Penza Research Electrical Engineering Institute", Russia
[3]Penza State University, Russia

Abstract— The article considers a problem of modeling long output codes for the neural network transformer of analogue (continuous) biometric data into the output digital code. Modeling of independent code strings is not a complicated problem. For example, in order to model a single 256-bit code it is sufficient to execute a 256-fold reference to the software or hardware random-number generator. After that, one may find a matrix of biometric code bits correlations and build a proper matrix of transformation for it. It is technically feasible to calculate the correlation matrix and the corresponding matrix transformation for codes of 2–16 bits length. However, this method works out only for the codes of short length. Beyond this limit the problem becomes incorrect.

Thereby, it is necessary to synthesize the matrix binding independent data by means of another non-classical algorithm. The new concept of binding independent pseudorandom data is based on the necessity to synthesize a certain data-binding matrix which would save only statistics of correlations. If the precise transformation is impossible to create, the transformation providing the required pair correlation coefficient distribution is real.

As a result of statistical investigation the authors have built a nomogram of connection between the controlled modeling parameters and the mathematical expectation of the module of pair correlation coefficients with the length of parameters' vector $n = 2$, 4, 8, 16, 32, 64, 128. Nomogram results show that the increase of problem's dimensionality causes the values of pair correlation coefficients $r(a)$ to tend closer and closer to the coordinate axes. In general, evaluation of $r(a)$ function is quite a simple problem not requiring any considerable computing resources. The controlled parameter "a" is conveniently located in the range from 0.0 to 1.0, as well as the module of pair correlation coefficients.

Thus, one may obtain the distribution of biometric data (biometric codes) generator with the possibility to control the mathematical expectation and the root-mean-square deviation of distribution of pair correlation coefficients of biometric data and biometric codes.

1. INTRODUCTION

Modeling of independent code strings is not a complicated problem. For example, in order to model a single 256-bit code it is sufficient to execute a 256-fold reference to the appropriate software or hardware random-number generator. After that, one may find a matrix of biometric code bits correlations and build a proper matrix of transformation for it [1]. Unfortunately, this method works out only for the codes of short length. It is technically feasible to calculate the correlation matrix and the corresponding matrix transformation for codes of 2–16 bits length. After that the problems becomes incorrect. In this connection, it is necessary to synthesize the matrix binding independent data by means of another non-classical algorithm.

The new concept of binding independent pseudorandom data is based on the necessity to synthesize a certain data-binding matrix which would save only statistics of correlations. If the precise transformation is impossible to create, the transformation providing the required pair correlation coefficient distribution is real.

2. SYNTHESIS OF EQUALLY CORRELATED RANDOM DATA

The authors proceed from the assumption that the data of a certain vector of biometric parameters (biometric codes) remain independent, if the binding matrix is a unit one:

$$\begin{bmatrix} 1 & 0 & \cdots\cdots & 0 \\ 0 & 1 & \cdots\cdots & 0 \\ \cdots & \cdots & \cdots\cdots & \cdots \\ 0 & 0 & \cdots\cdots & 1 \end{bmatrix} \times \begin{bmatrix} x_{1,i} \\ x_{2.i} \\ \cdots\cdots \\ x_{n,i} \end{bmatrix} = \begin{bmatrix} x_{1,i} \\ x_{2.i} \\ \cdots \\ x_{n,i} \end{bmatrix} \quad \Rightarrow \quad R = \begin{bmatrix} 1 & 0 & \cdots\cdots & 0 \\ 0 & 1 & \cdots\cdots & 0 \\ \cdots & \cdots & \cdots\cdots & \cdots \\ 0 & 0 & \cdots\cdots & 1 \end{bmatrix} \tag{1}$$

If it is required to create data with identical pair correlation coefficients, it is necessary to use the binding matrix with identical elements remaining outside the unit diagonal of the data binding matrix [2]:

$$\begin{bmatrix} 1 & a & \cdots\cdots & a \\ a & 1 & \cdots\cdots & a \\ \cdots & \cdots & \cdots\cdots & \cdots \\ a & a & \cdots\cdots & 1 \end{bmatrix} \times \begin{bmatrix} x_{1,i} \\ x_{2.i} \\ \cdots\cdots \\ x_{n,i} \end{bmatrix} = \begin{bmatrix} y_{1,i} \\ y_{2.i} \\ \cdots\cdots \\ y_{n,i} \end{bmatrix} \quad \Rightarrow \quad R = \begin{bmatrix} 1 & r & \cdots\cdots & r \\ r & 1 & \cdots\cdots & r \\ \cdots & \cdots & \cdots\cdots & \cdots \\ r & r & \cdots\cdots & 1 \end{bmatrix} \tag{2}$$

The elements of the binding matrix remaining outside the diagonal unequivocally determine the values of pair correlations; a nomogram of this two-dimensional relation $r(a, n)$ for different length of synthesized vectors of biometric data (codes after data digitization for $n = 2$, 4, 8, 16, 32, 64, 128) is shown in Figure 1.

Figure 1 shows that the increase of problem's dimensionality causes the values of pair correlation coefficients $r(a)$ to tend closer and closer to the coordinate axes. In general, evaluation of $r(a)$ function is quite a simple problem not requiring any considerable computing resources. The controlled parameter "a" is conveniently located in the range from 0.0 to 1.0, as well as the module of pair correlation coefficients.

3. MODELING OF DATA WITH RANDOM ALTERNATING COEFFICIENTS OF CORRELATION

In practice, random arrangement of signs ± with nondiagonal elements of the binding matrix (2) results in appropriate imitation of alternating correlations typical for natural biometric data. In order to additionally model module value variations of pair correlation alternating coefficients, it is sufficient to make nondiagonal elements of the binding matrix random [2]. An example of such random distribution of values for positive and negative elements is shown in Figure 2. By-turn

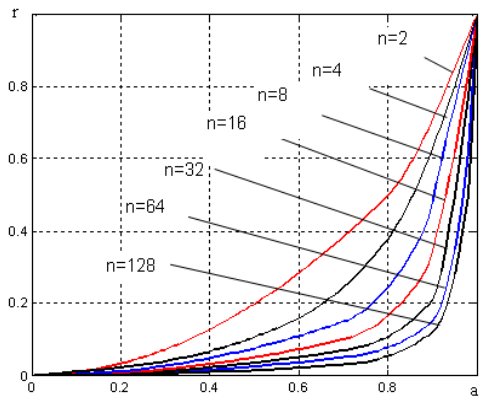

Figure 1: A nomogram of relation between the values of the binding matrix "a" elements and the values of pair correlation coefficients r of modeled data with parameter vector length $n = 2$, 4, 8, 16, 32, 64, 128.

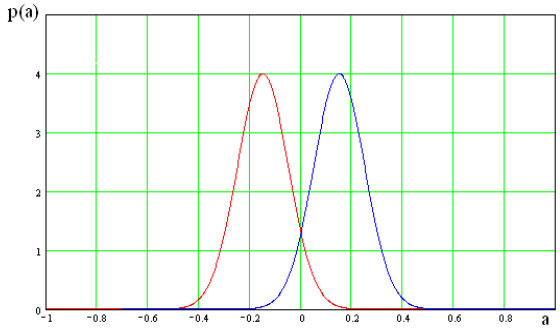

Figure 2: An example of splattering of outside-diagonal elements "$\pm a$" of the binding matrix according to the normal law.

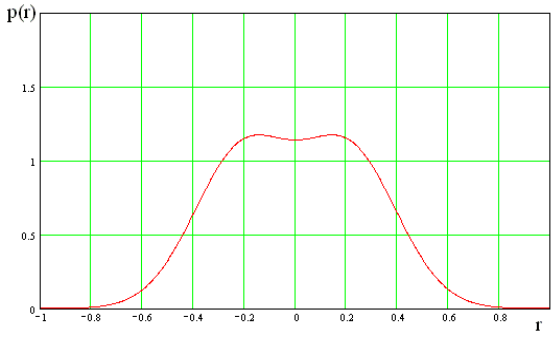

Figure 3: Distribution of pair correlation coefficient values, obtained using the two given symmetric generators of "a" parameters of the binding matrix.

the random distribution of binding matrix's elements leads to the complicated distribution of pair correlation coefficients values of the modeled biometric codes. The distribution of pair correlation values, typical for random data in Figure 2, is shown in Figure 3.

As the final result, the modeling of biometric data correlations is convenient to implement in reverse order. Doing so, it is primarily necessary to calculate the mathematical expectation of correlation coefficient modules — $E(|r|)$. Then, according to the value of this module it is easy to determine parameter "a" of the binding matrix using nomogram in Figure 1 or using corresponding tables prepared beforehand. Next, the researchers implement splattering of positive and negative values of outside-diagonal elements of the binding matrix. As a result, the authors receive output data with a certain density of pair correlation coefficient values distribution. An example of such distribution is shown in Figure 3.

4. REGULATION OF ROOT-MEAN-SQUARE DEVIATION OF THE FINAL DISTRIBUTION OF PAIR CORRELATION COEFFICIENTS

As a rule, splattering of positive and negative nondiagonal elements of the binding matrix is implemented by means of the normal law (see Figure 2), however for this purpose it is possible to use any other random-number generator. Splattering shall be implemented, gradually increasing root-mean-square deviation of the normal laws of distribution with mathematical expectation $\pm a$ set beforehand. Doing so, it is necessary to control splattering of pair correlation coefficients of the modeled biometric data. There is unequivocal monotonic relation between the dispersions of two laws of value distribution of the binding matrix parameters "a" and "$-a$" and the root-mean-square deviation of pair correlation coefficient modules $\sigma(|r|)$.

If positive and negative binding parameters "a" have identical (symmetric with respect to the point $r = 0.0$) distributions, then the density of distribution $p(r)$, will also be symmetric with respect to the point $r = 0.0$. In this case the root-mean-square deviation $\sigma(r)$ of distribution $p(r)$ is a three-dimensional function:

$$\sigma(r) = f(a, \sigma(a), n). \tag{3}$$

Partial derivatives of the three-dimensional function for each of its parameters are analytical and have a single sign. These facts significantly simplify the regulation of the root-mean-square deviation of pair correlation coefficients distribution. As the final result, the modeling is reduced to successive reference to several nomograms similar to the nomogram in Figure 1 and to multiple launch of n generators of pseudorandom independent data with the normal law of value distribution.

5. CONCLUSIONS

The present method allows to reliably reproduce averaged characteristics of biometric data and biometric codes subject to these data are digitized. It is impossible to achieve the correlation matrix of modeled data in advance by means of the present method, however, according to the distributions of controlled statistical parameters (e.g., according to the distributions of correlation coefficient values or correlation coefficient modules) the data is well-matched. As the final result the authors achieve the distribution of the biometric data (biometric codes) generator with capacity to control mathematical expectation and root-mean-square distribution of pair correlation coefficient values of biometric data and biometric codes.

ACKNOWLEDGMENT

The article has been prepared in the framework of a complex project "Development and preproduction of telecommunication equipment, development of software, network, applied and special provision to build a digital communication network with personal access" in accordance with the Russian Federation Government Regulation No. 218 from 09.04.2010 (Contract with the Ministry of education and research No. 13.G25.31.0039 from 07.09.2010).

REFERENCES

1. Shalygin, A. S. and Y. I. Palagin, "Applied methods of statistical modeling," *Mechanical Engineering*, 320, Leningrad, 1986.
2. Malygin, A. Y., V. I. Volchikhin, A. I. Ivanov, and V. A. Funtikov, *Fast Testing Algorithms for Neural Network Mechanisms of Biometric-cryptographic Data Protection*, 161, Penza State University Publishing, Penza, 2006.

Statistical Description of Output States of the Neural Network "Biometrics-code" Transformers

A. Ivanov[1], **B. Akhmetov**[2], **V. Funtikov**[1],
A. Malygin[3], **and I. Urnev**[3]

[1]Public Corporation "Penza Research Electrical Engineering Institute", Russia
[2]Institute of Information and Telecommunication Technologies, Republic of Kazakhstan
[3]Penza State University, Russia

Abstract— The article considers a problem of statistical description of the neural network "biometrics- code" transformer. It is shown that the classic binominal law of distribution is applicable only for ideal "biometrics-code" transformers. According to the standard ГОСТ Р 52633.0-2006 stipulating general requirements for output codes, the ideal "biometrics-code" transformers should provide absolute dual independence of output code bits.

For real "biometrics-code" transformers it is necessary to modify the binary law of distribution to take into consideration the misbalance of probabilities of biometric code bits' states and the correlation of the bits. Any misbalance of "0" and "1" states of emergence probability will inevitably result in quality decrease of "biometrics-code" transformers (decrease in output codes entropy).

The article also considers registration of existing correlations between biometric code bits. During statistical analysis the authors have imitated the operation of a "biometrics-code" transformer with 256 outputs. The identical value of dual coefficients of correlation between output code bits has been taken as the only controlled parameter — "r". The article adduces the distribution of Hamming distance values' emergence probabilities with different values of the controlled parameter $r = 0.05, 0.10, \ldots, 0.48$.

Another peculiarity of real "biometrics-code" transformer is that the values of dual coefficients of correlation between code bits have a symmetric distribution relative to the point $r = 0.0$. The article gives an example of correlation coefficients distribution in the 256-bit "biometrics-code" transformer. The most probable value of correlation coefficients is zero; all the obtained values of correlation coefficients remain in the range ± 0.5. Simple averaging of correlation coefficients is inadmissible. According to the experience, the best approach to obtain a good match of imitation results with reality is to use mathematical expectation of modules of dual correlation coefficients as the controlled parameter — r.

In case of averaged parameters application the dimensionality of statistical description of output code states may significantly decrease. If the key length is $n = 256$, the statistical description in the Hamming distances dimension is displayed in the form of corresponding tables with convertible parameters r (pitch 0.01, interval from 0.00 to 0.99) and P ("0") (pitch 0.01, interval from 0.01 to 0.5).

1. INTRODUCTION

"Biometrics-code" transformer (BCT) should unequivocally convert a vector of N continuous biometric parameters of "Friend" image — $\bar{\nu}_i$ into an output code vector — $\bar{c}$, consisting of n binary bits. In case the input of "biometrics-code" transformer receives a vector of N continuous biometric parameters — $\bar{\xi}_i$ of "Foe" image sample, in the output there should emerge a random code — $\bar{z}_i$, consisting of n binary bits. It means that the "biometrics-code" transformer for "Friend" and "Foe" input data should be described by two different vector-functional equations of discretization:

$$\begin{bmatrix} \text{BCT} \\ N \times n \end{bmatrix} \cdot \bar{\nu}_i = \bar{c}, \tag{1}$$

$$\begin{bmatrix} \text{BCT} \\ N \times n \end{bmatrix} \cdot \bar{\xi}_i = \bar{z}_i, \tag{2}$$

where $\begin{bmatrix} \text{BCT} \\ N \times n \end{bmatrix}$-matrix of nonlinear indistinct (neural network) functionals, executing input data enrichment and discretization (transforming the vector of input continuous biometric data of low quality into the output code).

Equation (1) is trivial in comparison with Equation (2), as it describes a sole state of the output code — $\bar{c}$. Statistically, Equation (2) is a lot more complicated as it describes BCT under the influence of random vectors of biometric parameters — $\bar{\xi}_i$, which give random output codes $\bar{z}_i$.

2. STATISTICAL DESCRIPTION OF THE IDEAL "BIOMETRICS-CODE" TRANSFORMER

Standard ГОСТ Р 52633.0-2006 [1] formulates general requirements for output codes $\bar{z}_i$, particularly, the ideal "biometrics-code" transformer should provide absolute pair independence of output code bits:

$$r_{m,j} \equiv 0.0, \tag{3}$$

where m, j — numbers of output codes stream bits —$\bar{z}_i$ of "Foe" images, $r_{m,j}$ — correlation coefficients between output biometric codes stream bits under investigation.

Moreover, standard ГОСТ Р 52633.0-2006 requires provision of equiprobable states "0" and "1" in every "Foe" code bits:

$$P_i(\text{“0”}) = P_i(\text{“1”}) = 0.5. \tag{4}$$

The conducted research shows that it is technically impossible to comply with conditions (3) and (4) for real "biometrics-code" transformers, even with one at a time. For real "biometrics-code" transformers the conditions (3) and (4) are accomplished approximately, and it is required to take account of real values of errors in complying with conditions (3), (4).

If the conditions (3) and (4) are accomplished for all biometric code bits, the "biometrics-code" transformer shall be considered as ideal. The easiest way to describe ideal "biometrics-code" transformers is to shift from probabilities of one or another code state emergence to probabilities of Hamming distances emergence from code $\bar{c}$ to code $\bar{z}_i$:

$$h_i = \sum_{m=1}^{n} c_m \oplus z_{m,i}, \tag{5}$$

where i — number of the code of the string under investigation;

m — number of the bit of $\bar{z}_i$ codes under investigation;

h — Hamming distance;

$\oplus$ — modulo two addition of compared bits.

The probability of "Friend/Foe" Hamming distances emergence for output biometric codes of the ideal transformer (compliance with conditions (3), (4)) can be described by the classic binominal law:

$$P(h) = \frac{n!}{h!(n-h)!} \cdot \{P(\text{“0”})\}^h \cdot \{1 - (P(\text{“0”}))\}^{n-h}, \tag{6}$$

where $h = 0, 1, 2, 3, \ldots, n$ — probable values of Hamming distances.

It should be noted that in formula (6) value $P(\langle\langle 0\rangle\rangle)$ is the probability of $\langle\langle 0\rangle\rangle$ state occurrence for the same tossed "coin" in the course of numerical experiment based on Bernoulli scheme. In this respect for ideal "biometrics-code" transformer there shall be used a substitution $P(\langle\langle 0\rangle\rangle) = 0.5$.

In case the "biometrics-code" transformer is not ideal according to "0" and "1" states balance in every output bit, but all that nonidealness is equal for all bits:

$$P_1(\langle\langle 0\rangle\rangle) = P_2(\langle\langle 0\rangle\rangle) = P_3(\langle\langle 0\rangle\rangle) =, \quad , P_m(\langle\langle 0\rangle\rangle), \ldots, = P_n(\langle\langle 0\rangle\rangle) \neq 0.5, \tag{7}$$

the classic formula (6) remains operable. It is caused by the fact that it is still the matter of realization of Bernoulli scheme of tossing a single "coin" with quite definite asymmetry. To perform calculations it is enough to find the required value of asymmetry $P(\langle\langle 0\rangle\rangle) \neq 0.5$ and enter it into formula (6).

3. REGISTRATION OF INDIVIDUAL MISBALANCES OF "0" AND "1" STATES IN EVERY BIOMETRIC CODE BIT

According to practice, every biometric code bit has its misbalance of states:

$$P_1(\langle\langle 0\rangle\rangle) = 0.45; \quad P_2(\langle\langle 0\rangle\rangle) = 0.56; \quad P_m(\langle\langle 0\rangle\rangle) = 0.3, \ldots, = P_{256}(\langle\langle 0\rangle\rangle) = 0.5. \tag{8}$$

To register the misbalance it is necessary to find the average geometric deviation of modules from $P(\langle\langle 0\rangle\rangle) = 0.5$ state:

$$\tilde{P}(\text{“0”}) = \sqrt[n]{\prod_{m=1}^{n} \{0.5 + |0.5 - P_m(\text{“0”})|\}}. \tag{9}$$

Special attention should be paid to the fact that the geometric average of deviations from $P(\langle\langle 0\rangle\rangle) = 0.5$ state to maximum or minimum, e.g., $P_1(\langle\langle 0\rangle\rangle) = 0.45$ and $P_2(\langle\langle 0\rangle\rangle) = 0.55$, do not compensate each other in calculation of the geometric average. That is, any misbalance of "0" and "1" states emergence probabilities unequivocally leads to decrease in quality of the "biometrics-code" transformer (decrease in output codes' entropy).

It is notable that Equation (9) can be also obtained in case of refusal to operate the classic Bernoulli scheme and application of its modification, taking account of using n various coins with different asymmetry values. In doing so the coins should be numbered. In numerical experiment the sequence of coin toss exactly matches their numbers. The tossing is executed from the same position, however every toss is realized from various height and with random value of coin twist (if the number of tosses is large the probabilities $P_m(\langle\langle 0\rangle\rangle)$ and $P_m(\langle\langle 1\rangle\rangle)$ supplement each other $P_m(\langle\langle 0\rangle\rangle) + P_m(\langle\langle 1\rangle\rangle) = 1.0$)).

4. REGISTRATION OF INFLUENCE OF EQUAL CORRELATIONS BETWEEN BIOMETRIC CODE BITS

Another problem is registration of correlations between biometric code bits. In the simplest case one shall consider the values of equal correlatedness between all pairs of code bits. The easiest way to model this situation is by means of programs [2, 3]. In research the authors have modeled the "biometrics-code" transformer with 256 outputs (according to the standard ГОСТ Р 34.10-94 a personal key forming digital signature has a length of 256 bits); the identical value of pair correlation coefficients between output code bits has been take as the only controlled parameter — $\langle\langle r\rangle\rangle$. Figure 1 represents the distribution of probabilities of Hamming distance values emergence with different values of controlled parameter $r = 0.05, 0.10, \ldots, 0.48$.

At the present time there is no precise analytical description of two-dimensional function $P\,(h,\, r)$, however it might be supposed that it is possible to create such analytical description by means of introduction of three different function parameters — r into the classic binomial law (6):

$$P(h, r) = \frac{a_1(r) \cdot n!}{h!(n-h)!} \cdot \{P(\text{“0“})\}^{a_2(r)\cdot h} \cdot \{1 - (P(\text{“0”}))\}^{a_3(r)\cdot(n-h)}. \tag{10}$$

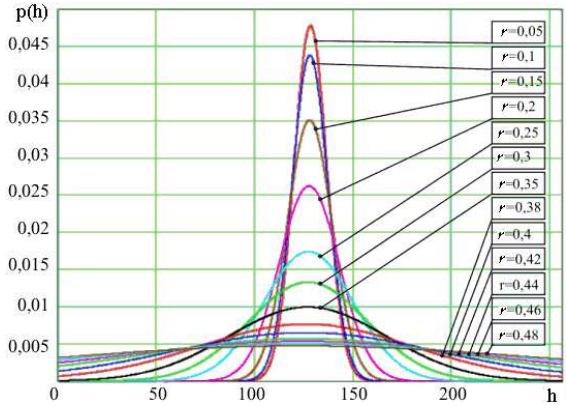

Figure 1: Nomogram of Hamming distance distribution for 256-bit codes and different values of correlation between biometric code bits.

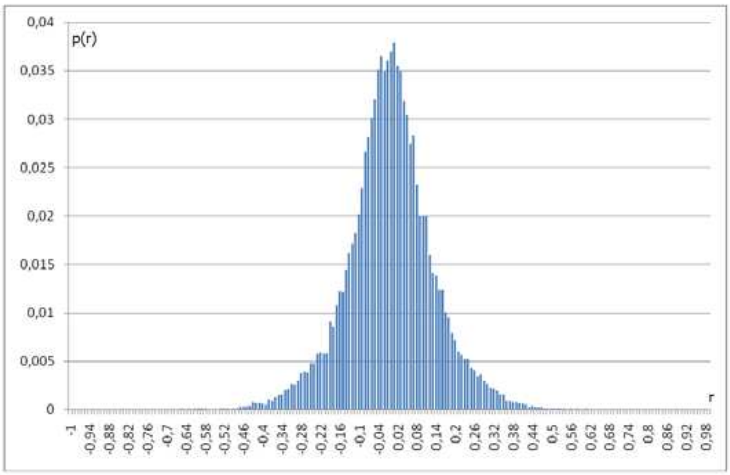

Figure 2: An example of distribution of pair correlation coefficients of randomly selected bits of the 256-bit output code.

Supposedly functions $a_1(r)$, $a_2(r)$, $a_3(r)$ are analytical at least for appropriately investigated code length point $n = 256$.

It is notable that for the scheme of acquisition of codes with equally correlated bits it is possible to designate the corresponding modification of Bernoulli scheme. The scheme is reduced to placement of all coins on a pan in a certain order and in give positions "0" or "1", and to further uplift of a sheet to a random height above the surface of coin drop. The tossing of all coins is executed simultaneously (dependently) by a stroke to the bottom of the sheet. The motion paths of multiple coins are close and therefore their final states are interrelated. The only random values are the height, stroke power and impact point on the pan.

5. REGISTRATION OF PAIR CORRELATION COEFFICIENT VARIATIONS BETWEEN RANDOMLY SELECTED BIOMETRIC CODE BITS

Another peculiarity of real "biometrics-code" transformers is the fact that the values of pair correlation coefficients between code bits are symmetrically distributed with respect to the point $r = 0.0$. However the law of distribution of pair correlation coefficient values itself is significantly abnormal (distribution has "heavy tails"). Figure 2 shows an example of correlation coefficients distribution of the real "biometrics-code" transformer of 256 bits.

As we can see in Figure 2, the most probable value of correlation coefficients is zero, all discovered values of correlation coefficients remain in the range ± 0.5. Simple averaging of correlation coefficients is inadmissible. According to the experience, the best match of modeling results with reality can be obtained by using as the controlled parameter — r:

$$r = E(|r_{m,j}|), \tag{11}$$

where $m \neq j$, and their values are selected randomly in the range from 1 to 256, $E(|r_{m,j}|)$-calculation of mathematical expectation of modules of pair correlation coefficients.

6. CONCLUSIONS

Thus, the correct statistical description of biometric codes is quite possible. To accomplish the description it is necessary at least to calculate the average geometric deviation of "0" and "1" states probability misbalances in every bit and the average value of modules of bit pair correlation coefficients in code string under investigation. The use of these averaged parameters results in significant decrease of dimensionality of statistical description of output codes' states. And if the key length is $n = 256$, the statistical description in the Hamming distances dimension has been already obtained in the form of corresponding tables with convertible parameters r (pitch 0.01, interval from 0.00 to 0.99) and P ("0") (pitch 0.01, interval from 0.01 to 0.5).

ACKNOWLEDGMENT

The article has been prepared in the framework of a complex project "Development and preproduction of telecommunication equipment, development of software, network, applied and special provision to build a digital communication network with personal access" in accordance with the Russian Federation Government Regulation No. 218 from 09.04.2010 (Contract with the Ministry of education and research No. 13.G25.31.0039 from 07.09.2010).

REFERENCES

1. Standard ГОСТ Р 52633.0-2006, "Information security. Information security technique. Requirements for means of high-reliability biometric authentication," 2006.
2. Malygin, A. Y., V. I. Volchikhin, A. I. Ivanov, and V. A. Funtikov, "Fast testing algorithms for neural network mechanisms of biometric-cryptographic data protection," 161, Penza State University Publishing, Penza, 2006
3. Zakharov, O. S. and A. I. Ivanov, "Registration of biometric data correlations through fractional exponent of freedom degrees of the chi-square value distribution law," *Infocommunication Technologies*, Vol. 6, No. 1, 12–15, 2008.

Evaluation of Multidimensional Entropy on Short Strings of Biometric Codes with Dependent Bits

V. Funtikov[1], **B. Akhmetov**[2], **A. Ivanov**[1], **and I. Urnev**[3]

[1]Public Corporation "Penza Research Electrical Engineering Institute", Russia
[2]Institute of Information and Telecommunication Technologies, Republic of Kazakhstan
[3]Penza State University, Russia

Abstract— The article considers a problem of evaluating output codes entropy at the neural network "biometrics-code" transformer of the analogue (continuous) biometric data into output digital code.

For the codes with independent bits (white noise) the entropy matches the length of the binary code. The problem becomes sophisticated if the code bits of the string under investigation turn out to be dependent (correlated). Evaluation of the dependent bit codes' entropy is carried out during the analysis of languages (artificial and natural), as well as during the testing of biometric codes, obtained in the output of neural network "biometrics-code" transformers. Investigating the entropy of emergence of 8-bit codes of single letters in the texts of Russian and Kazakh languages, the researchers have encountered the bit dependence in the 8-bit code string. The same dependence emerges during the investigation of 16-bit codes of letter pairs, 32-bit codes of letter quadruples, ..., 256-bit codes of 32-letter groups of text in Russian and Kazakh languages. Attempts to determine the code entropy of the natural language by means of the classic technique (through estimating the probability of either code emergence) appear to be a problem of exponentially increasing complexity. The importance of the given problem emphasizes even more when testing the neural network human biometry transformers of personal keys into 256-bit codes.

The objective of the article is to evaluate the entropy of various length codes with dependent bits. The authors consider the dependence (correlation) of the states of the code within its length, as well as the correlation (dependence) of the states of the same bits of different codes in the string under investigation. The article shows that the output multidimensional entropy significantly depends on the dual correlations of output code bits.

In the course of statistical analysis the researchers has built a nomogram of correlation values of the entropy of different dimensions with an averaged value of dual correlations module. The given nomograms display that data independence (noncorrelatedness) requirements considerably vary with an increase of problem dimensionality. With low amount of outputs up to 16, the independence (noncorrelatedness) requirements remain low. They are negligible.

For "biometrics-code" transformers with high number of outputs $n = 128$; 256; 512; 1024 it is necessary to make severe demands to the independence (noncorrelatedness) of output code bits (average value of correlation coefficient modules should be no less than 0.15, which corresponds to the standard ГСТР 52633.0-2006).

1. INTRODUCTION

In cases when codes in certain strings appear to be independent, the evaluation of their entropy becomes trivial. For codes with independent bits (for white noise) the entropy exactly matches the binary code length. The problem turns complicated if the code bits of the string under investigation appear to be dependent (correlated).

The research pursues the objective of evaluation of various length entropy codes with dependent bits. That purports both the dependence (correlatedness) of code states within its length and the correlatedness (dependence) of the same bits' states of various codes in the string under investigation.

The objective of evaluation of dependent bit codes entropy emerges during the investigation of languages (artificial and natural [1]) and during the testing of biometric codes in the output of neural network "biometrics-code" transformers [2–4]. Thus, investigating the entropy of emergence of 8-bit codes of single letters in the texts of Russian and Kazakh languages, the researchers have encountered the bit dependence in the 8-bit code string.

The same dependence emerges during the investigation of 16-bit codes of letter pairs, 32-bit codes of letter quadruples, ..., 256-bit codes of 32-letter groups of text in Russian and Kazakh languages.

It is notable that attempts to determine the code entropy of the natural language by means of the classic technique (through estimating the probability of either code emergence) appear to be a problem of exponentially increasing complexity. Thus, the text containing 500 letters is enough to evaluate the entropy of single letters' codes. The text containing approximately 50 000 letters is required to evaluate the entropy of letter pairs' codes. In order to evaluate the codes entropy of the string containing 32 letters it is required to have a text of enormous length -10^{42} letters. Neither Russian, nor Kazakh national libraries keep such considerable volumes of digitized text. In this connection, there is an emerging problem to find a bypass method of entropy calculation for dependent strings of long codes in the code strings of appropriate size. The importance of the given problem emphasizes even more when testing the neural network human biometry transformers of personal keys into 256-bit codes.

2. THE RATE OF AVERAGED BIT DEPENDENCE (CORRELATEDNESS) OF THE CODE STRING UNDER INVESTIGATION

Demonstrably, the data for digitized "white noise", corresponding to a single specific bit of the code string and as well to two different bits of the code string, appear to be independent (noncorrelated), i.e.:

$$r(x_{i,k}, x_{i,k+j}) \equiv 0.0 \quad \text{for every } i, j, k, \tag{1a}$$

$$\text{as well as} \quad r(_{ik}, x_{jk}) \equiv 0.0 \quad \text{when } i \neq j, \tag{1b}$$

where k — number of a code in the string under analysis; i, j — numbers of bits of codes under investigation; $x_{i,k}$ — state of "i" bit of "k" code of the string under analysis.

It is notable that the location changes sharply when the code bits are dependent. In this case an overwhelming majority of pair correlation coefficients is dependent:

$$r(x_{i,k}, x_{i,k+j}) \neq 0.0 \quad \text{for every } i, j, k, \tag{2a}$$

$$\text{as well as} \quad r(x_{ik}, x_{jk}) \neq 0.0 \quad \text{when } i \neq j. \tag{2b}$$

As a rule, the distribution of pair correlation coefficients for biometric codes is symmetric to the value $r(x_i, x_j) = 0.0$ and close to normal. For letter group codes of one or another natural language it cannot be executed, but it is possible to center the corresponding distribution of pair coefficient values of the correlation.

For biometric output codes of the properly instructed neural network transformer the condition of symmetric distribution of pair correlation coefficient values is always fulfilled:

$$E(r(x_i, x_j)) = 0.0, \tag{3}$$

where $E(.)$ — calculation of mathematical expectation.

The expression (3) cannot be considered as a factor indicating the operational pair correlation coefficient value in one or another code selection. If one executes simple averaging of pair correlation coefficient values (3), it will be impossible to evaluate the "averaged" degree of data dependence. Due to this fact, the standard ГОСТ Р 52633.0-2006 requires to control the average value of pair correlation coefficient modules. The averaged module of pair correlation coefficients for the digitized "white noise" appears to be zero:

$$E(|r(x_i, x_j)|) = 0.0 \tag{4}$$

and significantly above zero for codes with dependent bits:

$$E(|r(x_i, x_j)|) > 0.0. \tag{5}$$

Moreover, ГОСТ Р 52633.0-2006 standard forbids the "biometrics-code" transformers to have the average value of correlation modules higher than 0.15. This means that the rate of the averaged module of code bits correlation pair coefficients will be quite suitable to act as a certain indicator of the averaged (operational) value of pair correlation coefficients.

3. CONNECTION BETWEEN THE AVERAGE MODULE OF PAIR CORRELATION COEFFICIENTS AND THE HIGH-DIMENSIONAL ENTROPY OF CODES

As it has been stated previously, it is quite simple to calculate the entropy of short codes string, unlike the entropy of long codes. The calculation of the average value of pair correlation coefficients

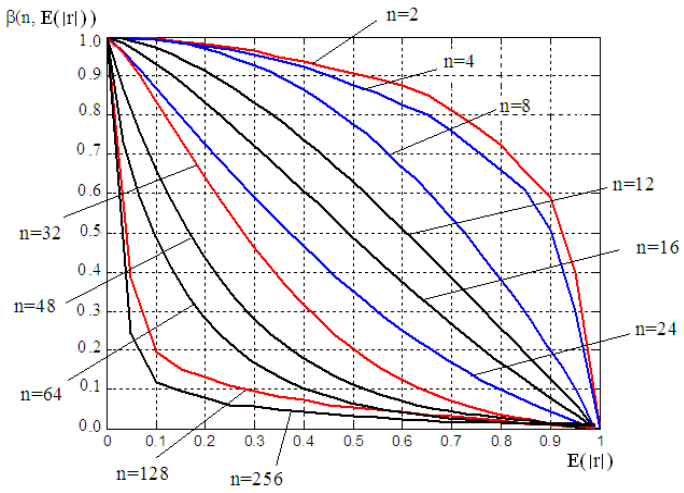

Figure 1: Nomogram of two-dimensional near multiplicative function reflecting the connection between a single bit and n bits of a code and the averaged module of pair correlation coefficients.

is somewhat different. As practice has shown, the complexity of calculating this parameter is independent of code's length. In order to reliably evaluate this parameter for 256-bit codes it is sufficient to use 10 000 codes, allowing to evaluate 10 000 modules of coefficient correlations (in calculation of correlation coefficients the pair bits are selected randomly).

It is intuitively clear that absolute lack of correlation $E(|r|) \equiv 0.0$ (digitization of "white noise") results in codes with limit value of entropy. In case of limit value of pair correlation coefficients $E(|r|) \equiv 1.0$ the entropy of random codes of any length equals 1 bit. There is an apparent randomness of codes, but all their bits are dependent. Notably it is possible to build a nomogram binding the entropy of codes with output dimensions $n = 1, 2, 3, 4, \ldots, 256$ with similar values of code bits correlation coefficients [2] by means of imitation modeling [2]. That is, in order to evaluate long codes' entropy it is sufficient to calculate the entropy of a single bit — $H(x_1)$ and determine $E(|r|)$. Then, the multidimensional entropy can be evaluated as follows:

$$H(x_1, x_2, \ldots, x_n) = (\beta(n, E(|r|) + 1) \cdot H(x_1). \tag{6}$$

The expression (6) includes a bivariant function $\beta(n, E(|r|)$, for which there is a nomogram shown in Figure 1.

4. CONCLUSIONS

Thus, the entropy of long codes is possible to calculate by figuring out the average module of pair correlation coefficients. To do so the selection out of 10^4 codes of 256-bits is sufficient. The classic method of entropy calculation [3] through evaluation long codes emergence probabilities would require a selection out of 10^{42} codes, which is almost impossible to obtain and process. The application of a nomogram, shown in Figure 1, in the process of 256-bit codes' entropy evaluation allows to decrease the size of selection by 38 degrees and simplify the calculations. "Penza State University" and "Kazakh National Technical University" set a goal to develop running modules with open codes, executing calculation of type (6) multidimensional conversions.

According to the nomogram in Figure 1 it is evident that the data independence (noncorrelatedness) requirements significantly change with increase of problem's complexity. If the output's number is low not more than 16, the independence (noncorrelatedness) requirements are low. The increase of "biometrics-code" transformer's outputs changes the situation. For "biometrics-code" transformers with large number of outputs $n = 128, 256, 512, 1024$ it is necessary to produce strict requirements for output code bits' independence (noncorrelatedness). Due to this cause ГОСТ Р 52633.0-2006 standard requires to achieve the average value of correlation coefficient modules to be below 0.15.

ACKNOWLEDGMENT

The article has been prepared in the framework of a complex project "Development and preproduction of telecommunication equipment, development of software, network, applied and special

provision to build a digital communication network with personal access" in accordance with the Russian Federation Government Regulation No. 218 from 09.04.2010 (Contract with the Ministry of education and research No. 13.G25.31.0039 from 07.09.2010).

REFERENCES

1. Ivanov, A. I., V. A. Funtikov, A. V. Mayorov, and D. N. Nadeev, "Modeling of code string with entropy of natural and artificial languages," *Infocommunication Technologies*, Vol. 4, 75–79, 2010, http://ikt.psuti.ru.
2. Malygin, A. Y., V. I. Volchikhin, A. I. Ivanov, and V. A. Funtikov, *Fast Testing Algorithms for Neural Network Mechanisms of Biometric-cryptographic Data Protection*, 161, Penza State University Publishing, Penza, 2006.
3. Yaglom, A. M. and I. M. Yaglom, *Probability and Information*, 512, Book House Publishing, Moscow, 2007.
4. Standard ГОСТ Р 52633.0-2006, "Information security. Information security technique. Requirements for means of high-reliability biometric authentication," 2006.

Information-telecommunication System with Multibiometric Protection of User's Personal Data

Vladimir Volchikhin[1], **Alexander Ivanov**[2], **Ivan Urnev**[1], **and Alexander Malygin**[1]

[1]Penza State University, 40 Krasnaya Str., Penza 440026, Russia
[2]Penza Research Electrical Engineering Institute, 9 Sovetskaya Str., Penza 440000, Russia

Abstract— The development of digital information technologies has faced a problem of access and protection of information resources from unauthorized access.

Penza State University (PSU) together with "Rubin" plc. and "Penza Research Electrical Engineering Institute" plc. is on the final stage of development and preproduction of telecommunication equipment, as well as development of network, applied and special software to build a digital communication network with personal access, maintaining high-level protection of personal data on the basis of biometric methods.

The system provides transformation of personal biometric data into the access code and safe storage in a neural network container in accordance with the standard ГОСТ Р526333.0-2006.

The authors have used the following image processing methods as personal biometric parameters:

- processing of papillary finger print;
- processing of handwritten password;
- processing of 3D face image.

Research and technical solutions offered in the given project are based on the concept of a neural network biometric depersonalized container, which can be created by instructing a neuronet. It is a person with his/her fingers, handwriting and face who is the access key into the information-telecommunication system. He/she doesn't have to wright down and memorize a pin-code or any other key information vulnerable to external threats and attacks.

The developed means of highly reliable multibiometric authentication have to provide the personal authentication index on the level 10^{-12} in accordance with the standard ГОСТ Р 52633.0 ÷ 52633.5. American Bio IP systems of standards provide this index on the level 10^{-5}.

At the present time PSU in cooperation with its contractors is completing the development of construction and technological documents on component elements of the information-telecommunication system, intended to be applied by corporative structures (schools, universities, organizations, business), as well as by government bodies.

Testing samples of components and software have already passed the preliminary testing and are ready for operation testing.

1. INTRODUCTION

The life in modern society appears to be insufficient without computers, internet, mobile means of communication. However, the processes of comprehensive informatization of the society lead to positive changes, as well as produce a variety of problems. Among these problems are the following: reliable identification and authentication of an individual, demarcation of access to data and services and protection user's personal data. In this connection, research in the present field is contemporary and urgent. The article is dedicated to development of information-communication systems with personal data protection through application of biometric methods for mass user [1].

2. SIZE AND STRUCTURE OF BIOMETRIC TECHNOLOGY MARKET

Biometric attributes are unalienable attributes of an individual. Passports, various certificates, pin-codes, logins and passwords providing individual's identification and authentication reflect only secondary identity information and lack firm connection with an individual. Modern information technologies offer a wide range of various papillary finger image sensors, signature pads, digital photo cameras, sound converters etc., that enable to develop diverse systems for access, identification and authentication.

However, all known commercial products, which apply biometric attributes, have significant disadvantages. Firstly, they storage biometric templates, which are as well as biometric data subject to protection and which might be stolen by perpetrators from servers and personal computers and

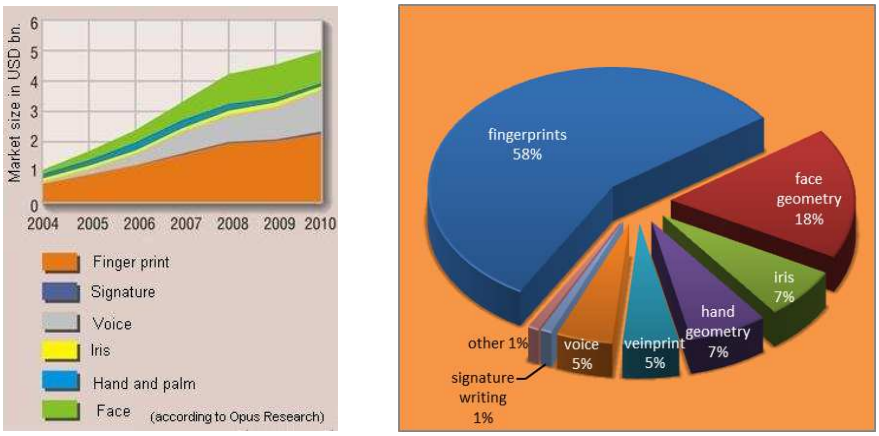

Figure 1: Size and structure of biometric technology market.

employed criminally. Secondly, biometric attributes are distinguished by instability leading to errors of the first and the second type (failure to identify "Friend" and admission of "Foe"). To resolve this situation American standards BioAPI apply fuzzy logic enabling to reach first type error level of 10^{-5}, which is unsatisfactory for many information services users. Complexity of algorithms for biometric attributes processing can be also considered as a disadvantage due to high demands to computer productivity.

The suggested system provides personal data protection based on the following biometric techniques:

- processing of papillary finger print;
- processing of handwritten password;
- processing of 3D face image.

The structure and size of world market of biometric technologies is shown on Figure 1.

The present figure displays that finger print and face geometry technologies take the leading positions. However, it should be noted that the given statistics reflects the application of biometric technologies by police service. There is no exact information on application of finger print, face geometry and handwritten text identification in general purpose information systems.

It is known that the first European to use finger prints for criminals' identification was William Gershel (1833–1917) — a police official. The decisive contribution in foundation of dactylography was made by the famous English anthropologist Francis Galton (1822–1911). It was he who developed three general conclusions:

- papillary pattern remains unchanged for the whole period of human life;
- papillary pattern is unique and individual;
- despite its' individuality, papillary patterns can be classified.

In 1892 he published a book "Finger prints" and in 1895 he managed to achieve the introduction of dactylographic method of criminal registration in England. In Russia this method has been implemented since 1906.

However, those methods of dactylography used for criminal identification for quite a long period of time are absolutely impossible to implement in securing personal data in digital systems of personal data storage and processing.

3. SYSTEM CONFIGURATION AND HASHING TECHNOLOGIES

The authors suggest scientific and engineering solutions based on implementation of a neural network biometric depersonalized container, which is created by means of neural network instruction. It is a person with his/her fingers, handwriting and face who is the access key into the information telecommunication system. He/she doesn't have to wright down and memorize a pin-code (login and password) or any other key information vulnerable to external threats and attacks. The most widespread technology of 4-bit digital pin-codes used in ATMs has a low safety level of 10^{-4}.

The developed means of highly reliable multibiometric authentication have to provide the personal authentication index on the level 10^{-12} in accordance with the standard ГОСТ Р 52633.0 ÷ 52633.5. American Bio IP systems of standards provide this index on the level 10^{-5}, i.e., the difference is by 10^7 times. The Figure 2 presents the biometric technology standardization in USA and Russia.

The configuration of the system under development and the technology providing confidentiality, anonymity and depersonalization of personal biometric data are shown in the Figures 3 and 4.

At the present time PSU in cooperation with its contractors is completing the development of construction and technological documents on component elements of the information-telecommunication system, intended for application by corporative structures (schools, universities, organizations, business), as well as by government bodies [5].

Testing samples of the device and software have been adjusted in terms of scalability and capacity of operation by the application method, i.e., the technology can be integrated into running information-telecommunication systems through hardware and software upgrade.

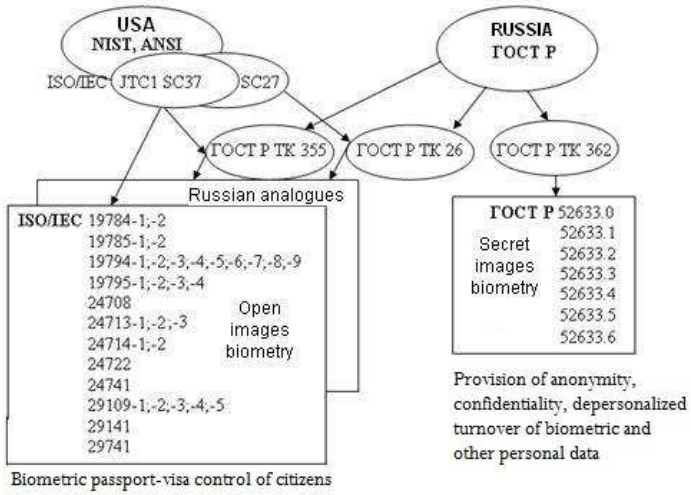

Figure 2: Standardization of biometric technologies.

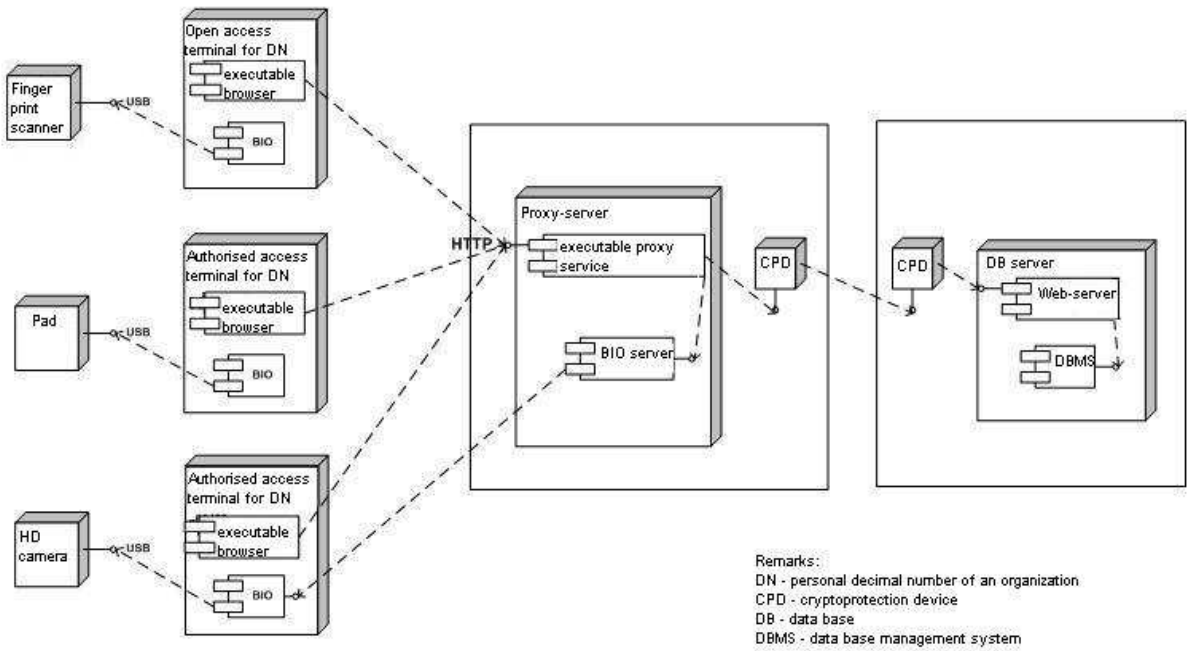

Figure 3: System configuration.

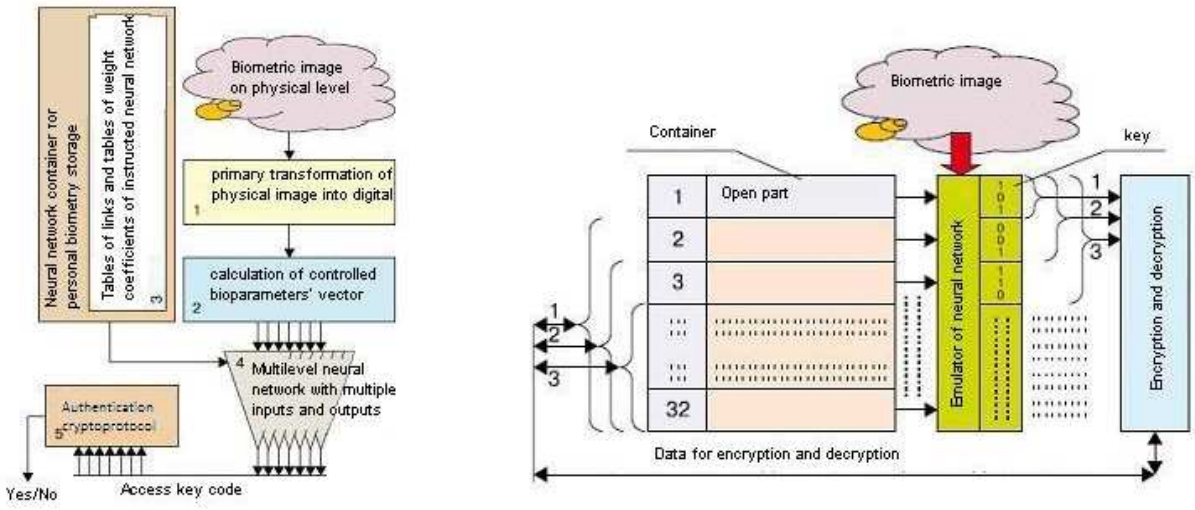

Figure 4: Technology providing confidentiality, anonymity and depersonalization of human personal biometric data. (a) Flowchart of biometric authentication procedures. (b) Flowchart of neural network container automatic encryption.

4. CONCLUSIONS

The present development of information-telecommunication system with personal data protection through biometric methods is based on implementation of the neural network biometric container that contains tables of weights and relations, which provide depersonalization of biometric images. In the output of the "biometrics-code" transformer there is a 256-bit code that is applied as a hash-function for access to personal data.

ACKNOWLEDGMENT

The article has been prepared in the framework of a complex project "Development and preproduction of telecommunication equipment, development of software, network, applied and special provision to build a digital communication network with personal access" in accordance with the Russian Federation Government Regulation No. 218 from 09.04.2010 (Treaty with the Ministry of education and research No. 13.G25.31.0039 from 07.09.2010).

REFERENCES

1. Yazov, Y. K., I. G. Nazarov, A. I. Ivanov, and O. V. Efimov, "Neural network technologies for personal biometric data protection," *Neurocomputer: Development and Implementation*, No. 6, 5–10, Radio Engineering, Moscow, 2009.
2. Funtikov, D. I., "Human identification by finger print pattern with further placement of biometric data into neural network container," *Neurocomputer: Development and Implementation*, No. 6, 5–10, Radio Engineering, Moscow, 2009.
3. Ivanov, A. I., "Orthogonalization of algorithms for rapid instruction of artificial neural networks of large and super large dimensionality," *Neurocomputer: Development and Implementation*, No. 6, 5–10, Radio Engineering, Moscow, 2009.
4. Funtikov, V. A., O. V. Efimov, and A. I. Ivanov, "Biometric neural network control of cryptographic data protection mechanisms," *Neural Network Transformers of Human Biometric Images into a Code of His/her Personal Cryptographic Key*, Vol. 29, 88, Radio Engineering, Moscow, 2008.
5. Malygin, A. Y., V. I. Volchikhin, A. I. Ivanov, and V. A. Funtikov, *Fast Algorithms for Testing of Mechanisms of Biometric-cryptographic Data Protection*, 161, Penza State University Publishing, Penza, 2006.
6. Standard ГОСТ Р 52633.0-2006, "Information security. Information security technique. Requirements for means of high-reliability biometric authentication," 2006.

Optimum Algorithm of Formation of Radar-tracking Images in CW SAR

A. A. Prilutskiy, **A. N. Detkov**, **and D. A. Nitsak**
JSC Distant Radiocommunication Scientific Research Institute
d.12/11, 1-ya vul. Buhvostova, Moscow 107258, Russia

Abstract—From positions of the Markov's theory of an estimation the structure of system of processing CW SAR is offered, allowing by criterion of a minimum of an average square of an error to restore a radar-tracking lay of land which is probed by continuous signals with linearly frequency modulation.

1. INTRODUCTION

The problem of formation of radar-tracking images (SAR images), the earth's surface in quasireal time is one of the actual radio vision in solving problems [1].

The main purpose of the formation of radar images — to achieve the highest accuracy of restoration of radar terrain at a given quality criteria in a real limitation. Such limitations are, first of all by the departure of the parameters of the received trajectory signal at an interval of synthesis, exposure to a wide range of noise and clutter (both external and internal), abnormalities in the formation of a given diagram to the antenna directivity (DAD) and the characteristics of the transmitter-receiver devices.

Solving the problem of formation of high-quality radar images of these conditions involves the use of optimal algorithms for digital processing of the trajectory signals and SAR images.

However, a large number of publications in this area, reflecting a range of new methods and algorithms for trajectory signals in order to improve image quality, devoted mainly to a pulsed SAR [1, 2]. It should be noted that in recent years both in this country and abroad, more and more attention is paid to small-sized CW SAR, for example [3–5].

Therefore, the actual problem is that the synthesis of optimal algorithms in order to create high-quality radar images of CW SAR data. In order to achieve resolution of less than 1 m in a pulsed SAR methods have been successfully used Markov estimation theory [6]. These methods are well developed and already tested in the synthesis of optimal navigation CW devices [7], in particular, in signal processing of Doppler velocity meters, with a similar structure with CW SAR.

However, the use of the CW SAR itself or for the formation of high-quality radar images than pulsed SAR has several significant features.

2. FORMULATION OF THE PROBLEM

The signal reflected from the target point with coordinates (x, y) at the output of the balanced mixer is of the form

$$s(r, t) = s_R(r, t)s_T(t) = UG(x, y) \exp\left\{j2\pi\mu\frac{2r(x, y, t)}{c}t\right\} \exp\left\{j\frac{4\pi}{\lambda}r(x, y) + j\varphi_0\right\}, \quad (1)$$

where $U = Aa_0$ — the complex amplitude of the signal at the output of the mixer.

Equation (1) essentially describes the process of compression of the signal range, which consists of multiplying the received signal at the reference probe signal. The first phase factor in Equation (1) determine the frequency of the signal at the output of the mixer, which is proportional to the signal propagation time to the target and back. The second phase factor describes the change in phase of the signal when the distance to the target in the process of synthesis.

On the other side of the useful signal $s(t)$ depends on the function of radar elevation $\dot{e}(x, y)$. This dependence is determined by the operator of radar remote sensing [3]

$$s(r, t) = L_z\{\dot{e}(x, y)\} = \iint\limits_{S_\Sigma} \dot{e}(x, y)g(x, y, r, t)dxdy, \quad (2)$$

where $g(x, y, r, t)$ — the impulse response of the target point with coordinates (x, y), S_Σ — span the earth's surface during the observation period (analysis) $t \in T_H$.

As a result of the Fourier transform accumulated during T_H the beat signals generated from the N_d channels a range of channels with a given resolution range δ_r, eat within a given area of the capture range. However, the useful signal (1) inevitably distorted by noise, especially the internal noise of the SAR. Therefore, direct observation, access to an additive mixture of useful signal $s(t)$ and the complex white Gaussian noise $n(t)$ with the spectral density N_o:

$$\xi(r,\, t) = s(r,\, t) + n(t). \tag{3}$$

Further processing of observations (6) reduces to a sampling time of the process $\xi(r,\, t)$ at regular intervals $\Delta = t_k - t_{k-1}$ and level quantization using two-channel ADC for the implementation of the algorithm of digital spectrum analyzer based on Fourier transform:

$$\xi_k^{(\omega_y)} = F_y\{\xi(r,\, t_k)\} = \sum_{m=0}^{N_d-1} \xi(m\delta r,\, t_k) \exp\{-j\omega_{yx}\Delta y m\}, \tag{4}$$

where ω_{yk} — the counting of the spatial frequency ω_y, Δy — sampling step of coordination y. Given the fact that the number of ADC bits is 8–12 can be neglected noise amplitude quantization levels and consider the process at the ADC output is discrete. Sampling interval $\Delta = t_k - t_{k-1}$ is chosen based on the top of the beat frequency signals (1) and the environment in which the sampling theorem.

In general, the output of the digital spectrum analyzer at each discrete point in time $t_k \in [0,\, T_C)$ the vector formed by the size $N_d \times 1$ of the observed processes $\Xi_k^{(\omega_y)} = \lfloor \xi_{p,\,k}^{(\omega_y)} \rfloor$:

$$\Xi_k^{(\omega_y)} = \mathbf{H}_k^{(\omega_y)} \mathbf{e}_k^{(\omega_y)} + \mathbf{n}_k^{(\omega_y)}, \tag{5}$$

where $\mathbf{H}_k^{(\omega_y)} = \lfloor g_{p,m}^{(\omega_y)} \rfloor$ — a complex matrix of the size $N_d \times M$ of the reference signals, corepresentation of the elements (9), $\mathbf{n}_k^{(\omega_y)} = \lfloor n_{p,\,k}^{(\omega_y)} \rfloor$ — the size $N_d \times 1$ of the complex vector observation noise in the frequency domain with respect to the coordinate with the known statistical characteristics: $\mathbf{M}\{\mathbf{n}_k^{(\omega_y)}\} = \mathbf{0}$, $\mathbf{M}\{\mathbf{n}_k^{(\omega_y)} \mathbf{n}_k^{(\omega_y)T}\} = \mathbf{I} D_n$, $D_n = \frac{N_o}{2\Delta}$.

The problem is that for notifiable data (observations)

$$\Xi_{1,\,N}^{(\omega_y)} = \{\Xi_1^{(\omega_y)} \quad \Xi_2^{(\omega_y)} \quad \cdots \quad \Xi_k^{(\omega_y)} \quad \cdots \quad \Xi_N^{(\omega_y)}\},\ t_k \in [0,\, Tc),$$

formed at the output of the digital spectrum analyzer CW SAR, play in the analysis $\rho \in S_\Sigma$ of a given quality criterion for the desired FRE $\dot{e}(x,\, y)$, which is commonly used as a radar image: $|\dot{e}(x,\, y)|$ either $|\dot{e}(x,\, y)|^2$. It is assumed that the motion parameters that determine the trajectory of SAR on the observation interval T_c are known with an accuracy sufficient for synthesizing a period of time $T_c(\tilde{g}(t_k) \equiv 0)$.

3. QUASI-OPTIMAL FILTERING ALGORITHM FOR THE DISCRETE STATE VECTOR OF THE FRE

The peculiarity of the problem lies in the fact that, in general, FRE $\dot{e}(x,\, y)$ is a random field (Fig. 1), and the processing of trajectory signals produced in the frequency domain to the coordinate y. This approach allows the azimuth compression process is represented as a sequence of one-dimensional convolution [1]. To do this, the estimated vector of the FRE should also be represented in the frequency domain to the coordinate y in the form of the Fourier transform of the random field $\dot{e}(x,\, y)$:

$$\mathbf{e}_k^{(\omega_y)}(x) = F_y\{\mathbf{e}(x,\, y),\, t_k\} = \sum_{l=0}^{N_d-1} e(l \cdot \delta r,\, t_k) \exp\{-j\omega_{ym}\Delta y \cdot l\}. \tag{6}$$

Independence of samples FRE that are meaningful reflections of random complex coefficients (effective height), the equivalent of point reflectors distributed in a Gaussian law with zero, and the mathematical expectation and, in general, unequal variance, gives reason to write the a priori probability density (PD) of the vector FRE in the form [5]

$$f_{pr}(\mathbf{e}^{(\omega_y)}(x)) = \frac{1}{\sqrt{2\pi|\mathbf{D}_e^{(\omega_y)}|}} \exp\left\{-\frac{1}{2}\mathbf{e}^{(\omega_y)} + (x)(\mathbf{D}_e^{(\omega_y)})^{-1}\mathbf{e}^{(\omega_y)}(x)\right\}, \tag{7}$$

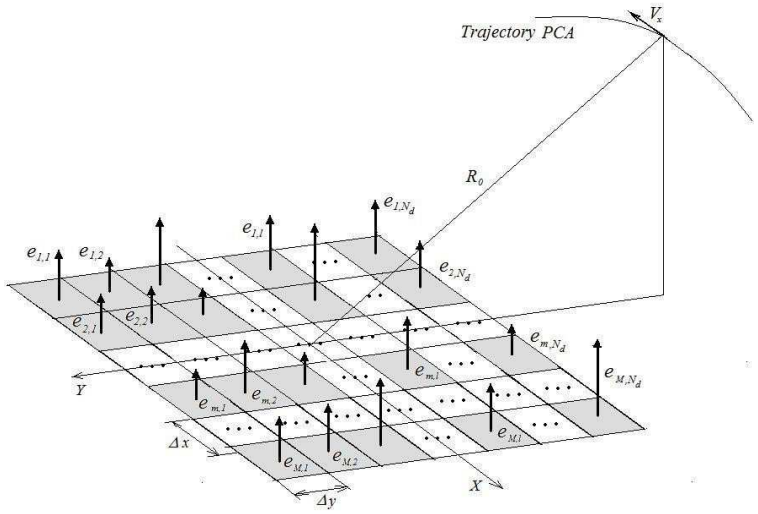

Figure 1: The geometry of surveying SAR.

where $\mathbf{D}_e^{(\omega_y)}$ is a diagonal matrix of variances, the components of which are associated with the spectral density $N_e(x,\, y)$ of the continuous model ratio FRE

$$D_e^{(\omega_y)}(i,\, i) = \frac{N_e^{(\omega_y)}(x_i)}{\Delta x}.$$

In this case, FRE described by the stochastic difference equation [5]

$$\mathbf{e}_k^{(\omega_y)}(x) = \mathbf{F}_e \mathbf{e}_{k-1}^{(\omega_y)}(x) + \mathbf{G}_e \mathbf{n}_e(t_{k-1}), \tag{8}$$

where $\mathbf{F}_e$, $\mathbf{G}_e$ — known matrices of appropriate dimensions, $\mathbf{n}_e(t_{k-1})$ — mutually independent N_d — dimensional vectors of the form of white Gaussian noise (WGN) with zero expectations and unit matrices of the intensities of the corresponding dimension.

In solving the problems of mapping the naturally present requirement that the FRE score was as close as possible to its true value and the degree of undesirability of errors should increase as the value of this error. In this case, the so-called quadratic loss function [8]

$$c[\hat{\mathbf{e}}^{(\omega_y)},\, \mathbf{e}^{(\omega_y)}] = Sp\left(\left(\mathbf{e}^{(\omega_y)} - \hat{\mathbf{e}}^{(\omega_y)}\right)\left(\mathbf{e}^{(\omega_y)} - \hat{\mathbf{e}}^{(\omega_y)}\right)^T\right),$$

where Sp — the trace of the matrix, the optimal Bayesian estimate $\hat{\mathbf{e}}^{(\omega_y)}$ coincides with the a posteriori expectation.

To determine the vector of estimated parameters $\mathbf{e}_k^{(\omega_y)}$ can be used quasi-optimal filtering algorithm for the discrete components of the state vector of FRE, which is described by a system of recurrence equations, and obtained by taking into account the Gaussian approximation of conditional DP $\tilde{f}(\mathbf{e}_k^{(\omega_y)})$ [9]:

$$\tilde{\mathbf{e}}_{k,\,k-1}^{(\omega_y)}(x) = \mathbf{F}_e \hat{\mathbf{e}}_{k-1}^{(\omega_y)}(x), \tag{9}$$

$$\tilde{\mathbf{R}}_k^{(\omega_y)} = \mathbf{F}_e \hat{\mathbf{e}}_{k-1}^{(\omega_y)}(x)\mathbf{F}_e^T + \mathbf{D}_e, \quad \mathbf{Y}_k^{(\omega_y)} = \mathbf{H}_k^{(\omega_y)} \mathbf{F}_e \hat{\mathbf{e}}_{k-1}^{(\omega_y)}(x)\mathbf{F}_e^T \mathbf{H}_k^{(\omega_y)T} + \mathbf{D}_n, \tag{10}$$

$$\mathbf{K}_k = \tilde{\mathbf{R}}_k^{(\omega_y)} \left(\mathbf{Y}_k^{(\omega_y)}\right)^{-1}, \quad \hat{\mathbf{e}}_k^{(\omega_y)}(x) = \tilde{\mathbf{e}}_{k,\,k-1}^{(\omega_y)}(x) + \mathbf{K}_k \left(\Xi_k - \mathbf{H}_k^{(\omega_y)} \mathbf{F}_e \hat{\mathbf{e}}_{k-1}^{(\omega_y)}(x)\right), \tag{11}$$

$$\hat{\mathbf{R}}_k^{(\omega_y)} = \tilde{\mathbf{R}}_k^{(\omega_y)} + \tilde{\mathbf{R}}_k^{(\omega_y)} \tilde{\mathbf{H}}_k^{(\omega_y)} \left(\mathbf{Y}_k^{(\omega_y)}\right)^{-1} \tilde{\mathbf{H}}_k^{(\omega_y)T} \tilde{\mathbf{R}}_k^{(\omega_y)^T}. \tag{12}$$

Quasi-optimal DF that implements the algorithm (9)–(12), is a multi-channel with the number of channels M. Each channel has a power estimation, power prediction and delay elements in a single cycle. The final assessment of the state vector FRE performed in discrete time for which

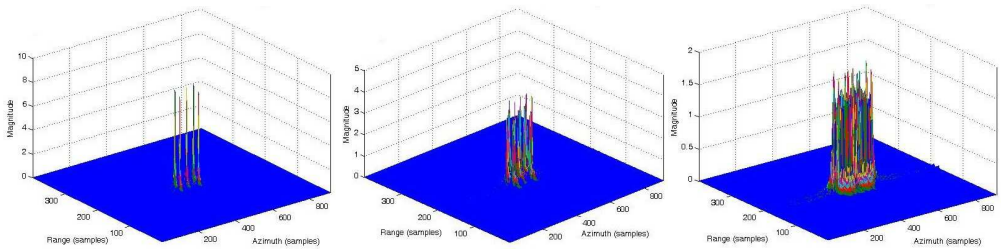

Figure 2: Evaluation of the test FRE with 5 point targets (a), (c) — FRE score at the output of the matched filter [1], (a), (b) — FRE score at the output of quasi-optimal filter ??? ((a) — SNR= 25 dB, (b), (c) — SNR= 10 dB).

the evaluation of $\hat{\mathbf{e}}^{(\omega_y)}$ undergoes the reverse Fourier transform, and the operation of taking the module to form a line of radar images.

In general, the recursive estimation method (9)–(12) is a variant of the linear Kalman filter, adjusted for SAR signal processing. One of the advantages of this method is that unlike all other signal processing algorithm is recursive, estimation FRE begin at the start probing with a delay time of signal accumulation T_H, to the end of the synthesis process of the formation interval of the radar image to an end.

An important advantage of this method is that it is possible to obtain high resolution in azimuth, by implementing the principles of super-resolution (resolution higher than the output of the matched filter). The synthesized filter is the basis for subsequent operations automated or automatic focusing of the radar image.

4. THE RESULTS OF THE SIMULATION

To test the efficiency of algorithms of digital processing of the trajectory signal is simulated and compared two methods of treatment: matched filtering performed by means of harmonic analysis [1], and quasi-optimal recursive filtering (9)–(12).

In Fig. 3 shows the normalized estimate FRE obtained at the output of the matched filter (Figs. 3(a) and (c)) and output the quasi-optimal recursive filter (Figs. 3(a) and (b)) with the following values of the a priori parameters: the number of channels range — 400, the distance between the azimuth readings — 0.25 m, the maximum tilt distance — 3000 m, the interval of synthesis — 1 s, the frequency deviation of 300 MHz, the wavelength of 4 cm. Simulation was carried out at different signal-to-noise ratio (SNR).

From Fig. 3 shows that the agreed process is greatly inferior to the implementation of quasi potential resolution in azimuth at small values of SNR.

5. CONCLUSION

Synthesized quasi-optimal filtering algorithm for the discrete state vector FRE allows us to construct almost realized DF-based high-performance computing.

However, in real terms a priori information about the nature of the probed area sometimes absent. Therefore, the synthesis algorithms of Bayesian estimation FRE applied to the task will be carried out in conditions of a priori uncertainty about the FRE. To solve the problem of optimal estimation of FRE in substantial prior uncertainty allows an adaptive Bayesian approach proposed R. L. Stratonovich [10] and developed in recent years.

REFERENCES

1. Goryainov, V. T., ed., "Radar stations with digital synthetic aperture," *Radio and Swyaz'*, Moskow, 1988 (in Russian).
2. Kondratenkov, G. S. and A. U. Frolov, "Radio-wave imaging. Radar remote sensing of the Earth," *Radiotechnika*, G. S. Kondratenkov, ed., Moskow, 2005 (in Russian).
3. Jankiraman, M., *Design of Multi-Frequency CW-Radars*, SciTech Publishing, 2007.
4. Antipov, V. N., E. E. Koltyshev, V. V. Muhin, et al., "The radar system of UAV," *Radiotechnika*, No. 7, 14–20, 2006 (in Russian).
5. Detkov, A. N., "An optimal algorithm for processing CW SAR," *The Successes of Modern Electronics*, No. 4, 46–52, 2011 (in Russian).

6. Yarlykov, M. S., "Markov estimation theory in radio engineering," *Radiotechnika*, Moskow, 2004 (in Russian).
7. Yarlykov, M. S., "Statistical theory of radionavigation," *Radio and Swyaz'*, Moskow, 1985 (in Russian).
8. Tihonov, V. I. and V. N. Harisov, "Statistical analysis and synthesis of wireless devices and systems," *Radio and Swyaz'*, Moskow, 1991 (in Russian).
9. Detkov, A. N., "Optimal filtering of continuous vector random process digital signals from the observed," *Radiotechnology and Electronics*, Vol. 42, No. 1, 141–149, 1995 (in Russian).
10. Stratonovich, R. L., "The principles of adaptive reception," *Soviet Radio*, Moskow, 1973 (in Russian).

Design and Manufacturing of a Dual-band, Dual-polarized and Dual Fed Perforated Array Patch Antenna Pair

T. D. Sudikila and T. E. Gilles
Department of Communication, Information, Systems and Signals
Royal Military Academy, Brussels, Belgium

Abstract—The low weight and low manufacturing cost of patch antennas make them excellent candidates for space applications. To overcome their low gain, one may easily combine them into arrays. In multi-frequency operation, several patch arrays can be arranged side by side on a single substrate. Overall size and weight reduction can be obtained if such arrays can be colocated through perforation of each lower frequency patch by several higher frequency ones. The design and realized performances of such a highly coupled configuration is investigated in a dual band and dual polarisation case.

1. INTRODUCTION

The light weight of patch antennas make them suitable for space applications. To increase their moderate gain, a patch array is nowadays easy to design and build. In the specific context of spaceborne radar applications, dual polarization operation increases the probability of detection or provides more information on the scattering objects, as their response to electromagnetic waves depends on the incident polarization. The reflection characteristics of an object or a scene are also frequency dependant. Multiple frequency operation provides therefore more information than single frequency operation.

The planar structure of patch antennas easily allows to arrange multiple arrays on a single substrate, as shown in Figure 1. The size and weight of a dual array can be reduced by perforating the high frequency array into the low frequency one, as shown in Figure 1.

There are many ways to feed patch antennas and arrays. In the case of a perforated dual array, the high frequency elements can only be fed from the backplane and not with strip lines on the top plane, that would destroy the integrity of the edges of the low frequency patches. In this paper we present the design and realization of a dual band, dual polarization and dual fed (respectively strip line fed and pin fed) patches arrangement shown in Figure 2, consisting of a single L-band element perforated by a 4×2 C-band array.

Figure 1: Dual array without (a) and with (b) perforation.

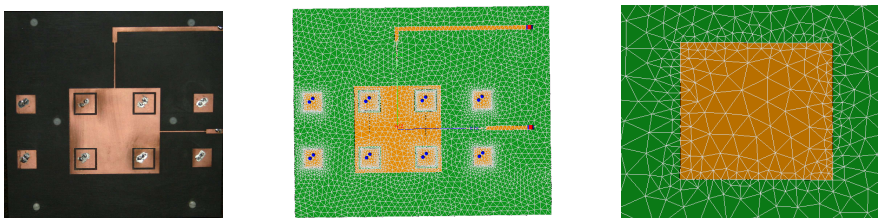

Figure 2: Manufactured antenna pair, its numerical model and a zoom on one C-band meshed element.

Table 1: Dimensions of the patch elements and characteristics of the patch substrate.

Band	f_0 [GHz]	L [mm]	L_{eff} [mm]	h [mm]	ϵ_r	$\tan\gamma$
L	1.15	85	86.6	1.57	2.33	0.0014
C	5.3	18	19.6	1.57	2.33	0.0014

2. INITIAL DESIGN

To realize a double polarization, one must choose a patch of symmetrical shape [1]. Otherwise the double polarization would be realized at different frequencies. The proposed initial design consists in determining the dimensions of a single L- or C-band patch on an infinite substrate. The effective length L_{eff} of an isolated square patch is given [2] by Eq. (1):

$$L_{eff} = \frac{c}{2f_0\sqrt{\epsilon_e}} = \frac{\lambda_0}{2\sqrt{\epsilon_e}} \tag{1}$$

with:

- ϵ_e effective dielectric constant of the substrate
- f_0 resonant frequency of the patch (L-band: 1.15 GHz and C-band: 5.3 GHz)
- $\lambda_0 = \frac{c}{f_0}$ free space wavelength, with c the speed of light

The concept of effective dielectric constant accounts for the fact that fringing fields extend both in the air and in the substrate [2]:

$$\epsilon_e = \frac{\epsilon_r + 1}{2} + \frac{\epsilon_r - 1}{2}[1 + 10h/W]^{-1/2} \tag{2}$$

with:

- h the height of the dielectric substrate
- W the physical width of the patch, equal to its physical length L for a square patch

Because of the fringing effect, the effective length of the patch is larger than the physical one. The extension length can be approximated by Eq. (3):

$$2\Delta L = \frac{2h}{\sqrt{\epsilon_e}} = L_{eff} - L \tag{3}$$

Every C-band patch element is fed by two pins, one for each polarisation. To ensure the impedance matching between the 50 Ω coaxial cable and the patch, Eq. (4) must be solved to determine x, the distance along the polarisation direction from the center of the patch where the pin must be attached [2].

$$50 = R_{e,C}\sin\left(\frac{\pi x}{L}\right) \tag{4}$$

The value of $R_{e,C}$, the impedance on the feeding edge of the C-band patch, results from lengthy calculations [2], not detailed here. For our C band elements, $R_{e,C} = 183.4\,\Omega$, giving $x = 3.4$ mm.

The two feeding networks at the back of our C-band patch array, one for each polarization, consist of RG 402 flexible cables of equal length directly soldered to the antenna backplane followed by a cascade of divider-combiners. These networks ensure equi-amplitude and equi-phase feeding of all eight C-band patches. The L-band patch element is fed by two 50 Ω strip lines, whose width $w(= 4.1\,\text{mm})$ can be determined with Eq. (5) [3], where $R_{stripline} = 50$:

$$R_{stripline} = \frac{120\pi}{\sqrt{\epsilon_e}(\frac{w}{h} + 1.393 + 0.667\ln(\frac{w}{h} + 1.44))}. \tag{5}$$

The impedance $R_{e,L}$ of the feeding edge of the L-band patch (241 Ω) can be obtained with the same formulas used to obtain $R_{e,C}$ [2]. To ensure impedance matching with the patch, a quarter wave transformer ($\lambda/4 = 44$ mm) can be used, having an impedance equal to $\sqrt{50R_{e,L}} = 110\,\Omega$ and whose width $w(= 0.8\,\text{mm})$ can be determined by using again Eq. (5) with $R_{stripline} = 110$.

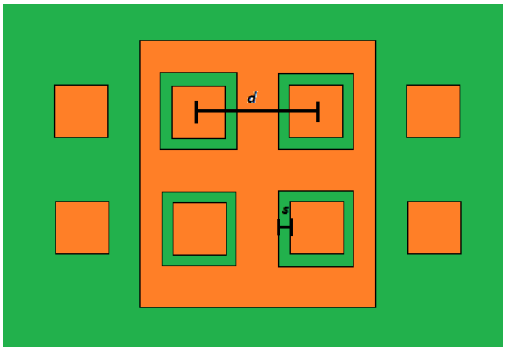

Figure 3: Optimized parameters d and s.

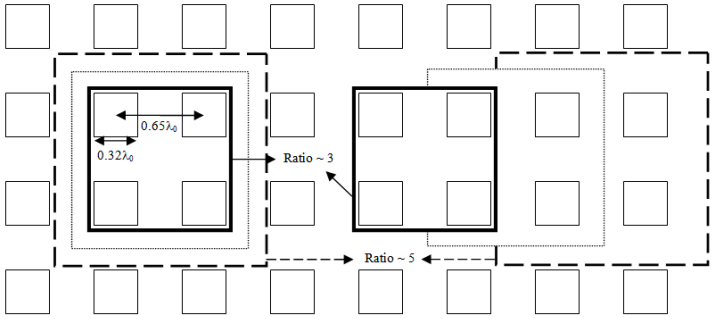

Figure 4: High to low ratio limits in the case $n = 2$.

3. FINAL DESIGN NUMERICAL MODEL AND OPTIMIZATION

After the initial design based on isolated patches, the final design of the L-band patch perforated by the C-band array was performed with the commercial software $FEKO^{TM}$, based on frequency domain numerical techniques (Method of Moments). Figure 2 shows the manufactured antenna pair and the numerical model. A global mesh with size λ_0, $C/8$ is applied to the whole structure except close to the patch edges, where it is refined to λ_0, $C/40$. The finite substrate extends $\lambda_C/4$ beyond the patches for a good accuracy.

The $FEKO^{TM}$ built-in optimizer has been used to search optimum values for the two parameters d and s depicted in Figure 3, without modifying the physical dimensions of the patches and the strip lines as well as the location of the feeding pins determined by the initial design and reported in paragraph 2.

It must be noted here that the perforation technique can only be applied when an entire number n of high frequency patches fit into a low frequency one. To maximize the gain of the high frequency array while avoiding grating lobes the distance separating the centres of adjacent patches is approximately twice the patch length ($\sim 0.32\lambda_0$ for the substrate described in Table 1). Straightforward generalization of Figure 4 shows that the ratio high to low frequency must be comprised between somewhat more than $2n - 1$ and somewhat less than $2n + 1$, considering that the high frequency patches should not come too close to the edges of the low frequency patches.

An optimum was thus searched for d and s between minimum and maximum values that must ensure a return loss below -10 dB at the design resonance frequencies while maximizing the gains in L- and C-band. The groove width s proved to be very critical to obtain or not an acceptable bandwidth for the L-band patch. As avoiding grating lobes was not a concern in our experimental design, the parameter d could reach the unusual value of $0.97\lambda_0$.

4. SIMULATION AND MEASUREMENT RESULTS

Figure 5 shows the measured -10 dB return loss bandwidths of the manufactured antenna pair, and also the simulation results, in L-band. As we work in two polarizations the least common bandwidth obtained in both polarizations individually must be considered as the dual polarisation antenna bandwidth.

Table 2: Optimized parameters.

Parameters	Minimum	Maximum	Optimum
d	$0.5\lambda_0$	λ_0	$0.97\lambda_0$
s	1 mm	4 mm	2 mm

Table 3: Performances of the antenna pair (H port).

Band	State	Model	f_0 [GHz]	BW [%]	H/V isolation [dB]	Gain [dB]	η [%]
L	Isolated antenna	Analytic	1.150	0.76	Not calculated		
L	Isolated antenna	Simulations	1.124	0.63	−26	6.3	82
L	Perforated antenna	Simulations	1.133	$\lvert S_{11}\rvert > -10$ dB	−29	-	65
L	Integrated antenna	Simulations	1.134	$\lvert S_{11}\rvert > -10$ dB	−29	5.0	55
L	Integrated antenna	Measurements	1.16	0.8	−28	6.4	78.5
C	Isolated antenna	Analytic	5.3	3.6	Not calculated		
C	Isolated antenna	Simulations	5.08	3.1	−39	7.2	95
C	4×2 array	Simulations	5.03	2.6	−37	16.8	95
C	Integrated array	Simulations	5.05	2.8	−42	16.2	87.3
C	Integrated array	Measurements	5.05	5.1	−27	17.4	81.5

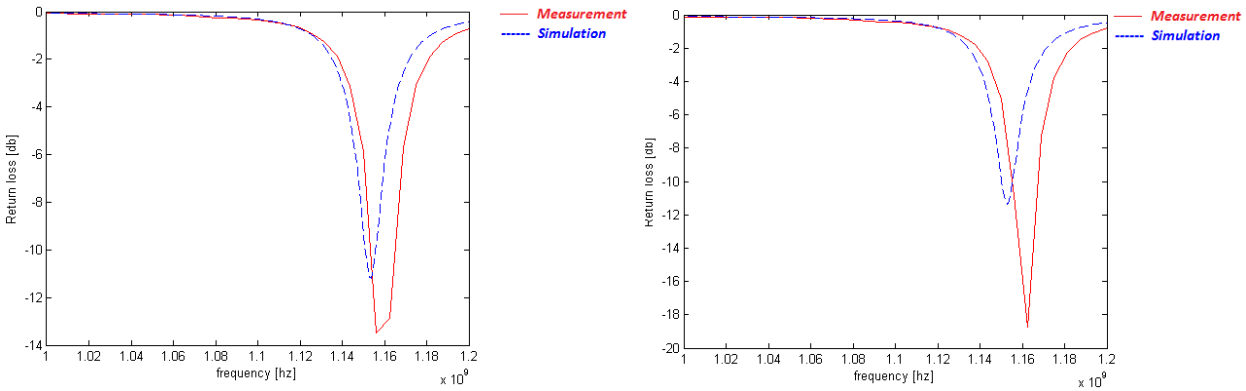

(a) H port (b) V port

Figure 5: Bandwidth simulations and measurements in L-band.

In spaceborne radar applications the isolation between the V and H ports is often required to exceed −30 dB. As shown in Table 3, our antenna pair is close to meet this stringent requirement. Antenna efficiency is defined as the total radiated power divided by the total input power, when the antenna is assumed to be impedance matched [4].

It has been measured with an estimated 10% accuracy, but also simulated, considering the

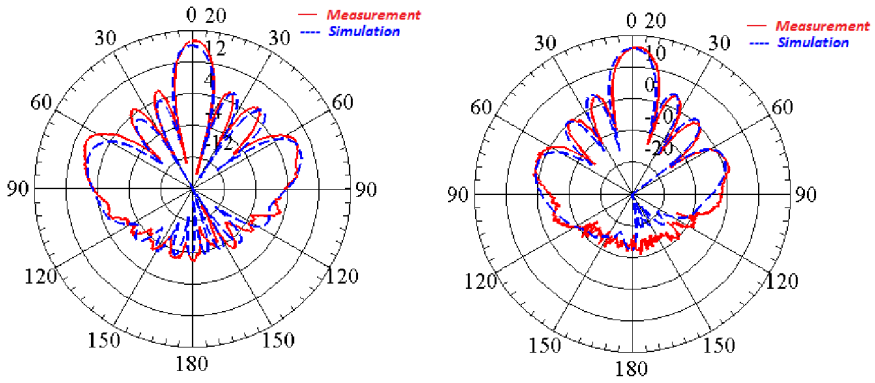

(a) H port (b) V port

Figure 6: C-band Radiation pattern in Azimuth.

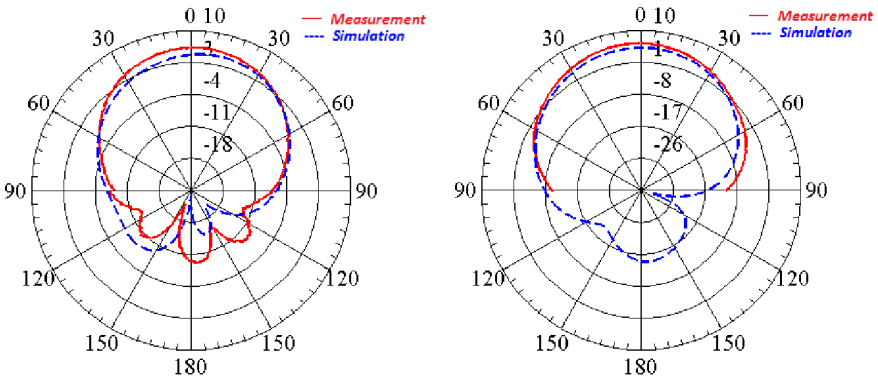

(a) H port (b) V port

Figure 7: L-band Radiation pattern in Azimuth.

factory parameters of the substrate reported in Table 1. The results are summarised in Table 3.

Finally we show in Figure 6 and Figure 7 the very good agreement between simulated and measured radiation azimuth patterns in both bands and for both polarizations. The absolute value of the simulated gains are also reported in Table 3, showing that the perforated configuration induces a gain reduction of 1.3 dB gain reduction in the L-band and 0.6 dB in the C-band.

5. CONCLUSION

The perforation of a patch antenna by a higher frequency patch array has been analyzed, designed in a simple two steps procedure and then realized. The measurements show very good agreement with the selected optimum design obtained with a numerical method. A critical parameter for the perforated configuration proved to be the groove width: if properly adjusted, the bandwidth and gain reduction that unavoidably result from the high coupling induced by the perforation could be limited to acceptable values.

REFERENCES

1. Zurcher, J. F. and F. E. Gardiol, *Broadband Patch Antennas*, Artech House, Boston, London, 1995.
2. Kumar, G. and K. P. Ray, *Broadband Microstrip Antennas*, Artech House, Boston, London, 2003.
3. Huang, Y. and K. Boyle, *Antennas: From Theory to Practice*, Wiley, 2008.
4. Tsigros, C., M. Piette, G. A. E. Vandenbosch, and D. Van Troyen, "Antenna efficency determination in a reverberation chamber: From the relative to the E-field method," *EMC Europe 2011*, 164–169, York, UK, September 2011.

Dual-frequency, Two Shorting Pin-loaded Equilateral Triangular Patch Antennas

Sultan Can, K. Yavuz Kapusuz, and Elif Aydın
Department of Electrical & Electronics Engineering, Atilim University, Ankara, Turkey

Abstract— This study presents the resonant frequencies of several antennas, which are dual-frequency antennas. These antennas possess two shorting pins to form dual frequency. Among several methods to provide dual operation, two shorting pins are used to form dual frequency equilateral triangular antennas since there are limited studies on this issue and higher frequency ratios are achievable. The present study has been done with this in mind in order to contribute to related literature on such antennas. Here, the parameters that affect the resonant frequencies of the antenna are also evaluated. The thickness, side length, and shorting pin positions are changed numerous times, and the resonant frequencies are examined according to the change of these parameters. Finally, the frequency ratios are determined for each variation, and the results are compared. The proposed antennas in present study achieved a frequency ratio around 5.7, which is significantly higher from the ones presented in the literature.

1. INTRODUCTION

Patch antennas are the most widely used antennas in today's wireless communication systems. Although triangular patch antennas have narrow-band properties, they are one of the most preferred types because of its small size and low cost [1]. Since these antennas have a narrow bandwidth, calculating the resonant frequency becomes getting more important. The studies presented in the literature indicates that calculating the resonant frequency of patch antennas generally depends on the curve fitting formulations [1, 2, 5, 8, 9] and in order to obtain better curve fitting for the calculation, the more antenna is examined the more accuracy is obtained. Dual-frequency operations are widely used in wireless systems and there are various ways to make a dual frequency antenna. Slit-loaded, slot-loaded, shorting pin and circuitry-loaded patch antennas are some of the methods to form a dual frequency operation [5–7]. Among these methods, inserting shorting pin is the most popular since it provides better upper to lower frequency ratios. It is also known that inserting shorting pin to an antenna significantly reduces the size of the antenna [4, 6–8, 10]. As far as the authors of this paper are concerned, there is only one study presenting two shorting pin-loaded equilateral triangular patch antenna [11], which proposes four different antennas with frequency ratios in between 1.46 and 1.68.

In this study, higher frequency ratios will be presented for various antennas and the effects of a number of — parameters such as the side length, thickness, and shorting pins position to the resonant frequencies — are determined. It is worth nothing that, since accurate calculation of the resonant frequency and input impedance depends on curve fitting equations, one study obviously is not enough to determine the best formulation. Therefore, the present research is carried out in order to present several dual frequency antennas and to expand the available literature on this issue. The frequency ratios will be determined for different shorting pin positions and the relation of the side length and thickness to the operating frequencies will also be addressed. Later, comparison will be made as to measured frequencies presented in the literature [11] and the simulation results obtained here. The upper and the lower resonant frequencies of the proposed antennas will be provided as well as the frequency ratios.

2. PROPOSED ANTENNA GEOMETRY

The proposed antennas with two shorting pins are given as Figure 1. These antennas are fed by coax, and the side lengths are defined as S. The thickness is denoted as h and the distance between the second shorting pin and the tip of triangle is determined as d. The distances of the coax, first and second shorting pin is determined as p_f, p_{s1}, and p_{s2}, respectively.

A frequency ratio r is defined between the upper and lower resonant frequency, and a equation is formulated as in Eq. (1);

$$r = \frac{f_{upper}}{f_{lower}} \tag{1}$$

The variation of r will be presented in the following sections where the effects of all antenna parameters, such as side length, thickness, and pin position values, will also be highlighted.

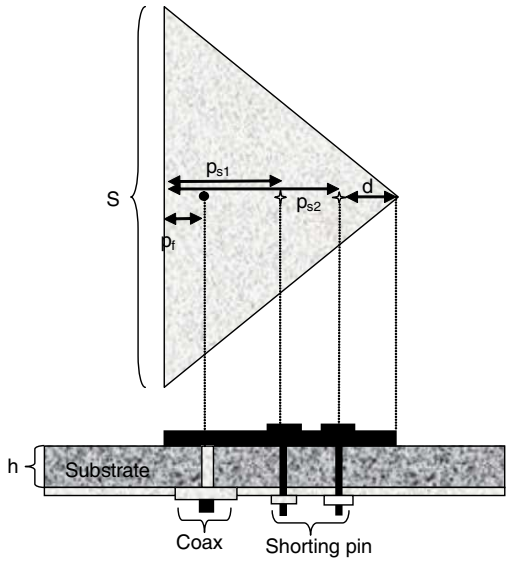

Figure 1: Geometry of two shorting pin loaded equilateral triangular patch.

Table 1: Geometry of two shorting pin loaded equilateral triangular patch.

Antenna	**S** (mm)	$\mathbf{p}_{s1}$ (mm)	$\mathbf{p}_{s2}$–$\mathbf{p}_{s1}$ (mm)	$\mathbf{f}_{lower}$ [11] (MHz)	$\mathbf{f}_{upper}$ [11] (MHz)	**r** [11]	$\mathbf{f}_{lowersim.}$	$\mathbf{f}_{uppersim.}$	$\mathbf{r}_{proposed}$
A	45	10	3.7	1470	2150	1.46	1352.2	2042.5	1.51
B	60	13	4	1020	1600	1.56	974.9	1576.9	1.61
C	100	15	3	-	-	-	493.3	2106.7	4.27

3. RESULTS

Three antennas with different side lengths are examined as seen in Table 1. The antennas A, B, and C have side length of 45 mm, 60 mm, and 100 mm, respectively. FR4 is used as a substrate, which has a permittivity value of 4.4 in all three antennas. The proposed antennas and the antennas in [11] with a side length of 45 mm has an upper frequency of 2150 MHz and a lower frequency of 1470 MHz. For the antennas proposed in [11] the upper and lower frequencies are compared and the average error for the lower frequency is 8.01% and 5% for the upper frequency. The proposed antenna in this study with a side length of 100 mm has an upper frequency of 2106.7 MHz and a lower frequency of 493.3 MHz.

The frequency ratio of the upper and the lower resonant frequencies, obtained from the previous studies in the literature was in between 1.51 and 1.61. As mentioned earlier, this ratio is a critical parameter for various applications. Consequently, achieving a higher frequency ratio is an advantage in dual-frequency antenna designs. For this purpose, an antenna with a side length of 100 mm can achieved with a frequency ratio 4.27, which is a satisfactory result for obtaining the requirements of high frequency ratio needed applications in wireless systems. The effects of the shorting pin position and thickness are also examined, and the results are presented in Figure 2. The thickness is varied in between 1 mm to 10 mm, and the variation of the frequency ratio according to the thickness is examined.

As it is seen in Figure 2 with the lower thickness, the higher frequency ratios are obtained for every distance value. The frequency ratio for a thickness of 1 mm is in between 1.35 and 1.76 while it yields in between 1.72 and 2.03 for a thickness value of 10 mm. The position difference is another parameter that affects the frequency ratio. As presented in Figure 2 the increment in the distance d causes an increment in the frequency ratio.

Frequency ratio of an antenna with a side length of 10 mm is examined for different thickness and distance (d) values. The results are presented in Figure 3. The frequency ratio is 3.9 when the thickness is 1 mm and 4.45 for a thickness value of 10 mm. The ratio reaches to 5.78 for a thickness of 1 mm at a distance value of $d = 6.86$ while it is 4.45 at a distance $d = 5.5$. The maximum frequency ratio is 4.59 for 1 mm thickness at a distance of $d = 6.86$.

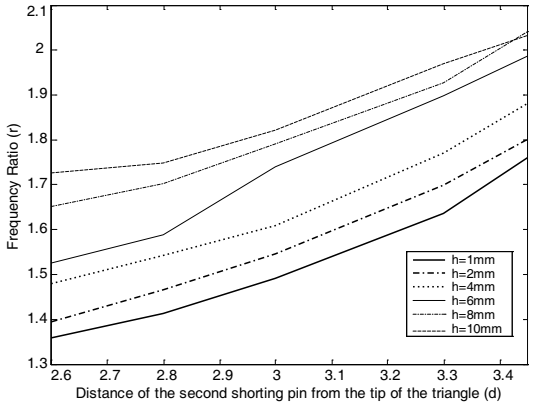

Figure 2: The frequency ratio variation with respect to thickness and shorting pin position for an antenna with a side length = 50 mm substrate and permittivity of 4.4.

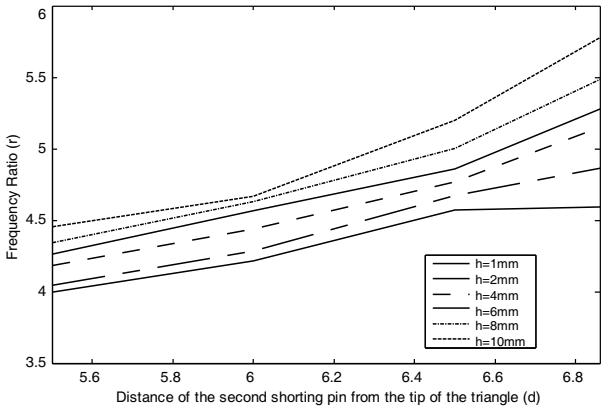

Figure 3: The frequency ratio variation of an antenna with a side length of 100 mm with respect to distance d and thickness values.

4. CONCLUSION

In this paper, several antennas are proposed to analyze two shorting pin-loaded equilateral antennas and the effects of several parameters to the resonant frequencies of these antennas. Resonant frequencies of these antennas are examined for various antenna parameters such as side length, thickness of the substrate and shorting pin positions. It is concluded that the thickness parameter has an effect on both upper and lower frequency of the antenna. The frequency ratio r increases with the thickness. A relation between the distance d and the frequency ratio is also observed. An increment in distance d causes an increment in frequency ratios. The side length is also varied in between 45 mm to 100 mm. It is observed that if the side length increases the frequency ratio increases. In this study, the importance of higher frequency and the accurate calculation of resonant frequency underlined. The various results of resonant frequencies of dual frequency two shorting pin-loaded antenna are proposed which is a background for computation of resonant frequencies in an accurate way by using curve fitting. Also higher frequency ratio values are obtained with the proposed antennas, which varies in between 3.99 and 5.78 for different thickness and for different pin position while validating the effects of side length.

REFERENCES

1. Aydın, E. and S. Can, "Modified resonant frequency computation for tunable equilateral triangular microstrip patch," *IEICE Electronics Express*, Vol. 7, No. 7, 500–505, 2010.
2. Can, S., "Computation of resonant frequency of dual band triangular patch antenna," *Master's Thesis in Electrical & Electronics Engineering*, Atılım University, Turkey, Jul. 2011.
3. Pant, R., P. Kala, R. C. Saraswat, and S. S. Pattnaik, "Analysis of dual frequency equilateral triangular microstrip patch antenna with shorting pin," *Microwave and Optical Technology Letters*, Vol. 3, No. 2, 63–68, 2008.
4. Wong, K. L. and S. C. Pan, "Compact triangular microstrip antenna," *Electronics Letters*, Vol. 33, No. 6, 433–434, Mar. 1997.
5. Aydın, E., "Computation of a tunable-slot loaded equilateral triangular microstrip antenna," *Journal of Electromagnetic Waves and Applications*, Vol. 23, Nos. 14–15, 2001–2009, 2009.
6. Pan, S. C. and K. L. Wong, "Design of dual-frequency microstrip antennas with a shorting pin loading," *Antennas and Propagation Society International Symposium*, Vol. 1, 312–315, 1998.
7. Wong, K. L. and S. C. Pan, "Compact triangular microstrip antenna," *Electronics Letters*, Vol. 33, No. 6, 433–434, 1997.
8. Aydın, E. and S. Can, "Operating frequency calculation of a shorting pin-loaded ETMA," *Microwave and Optical Technology Letters*, Vol. 54, No. 6, 1432–1435, Jun. 2012.
9. Liu, Q. and W. C. Chew, "Curve-fitting formulas for fast determination of accurate resonant frequency of circular microstrip patches," *IEE Proceedings*, Vol. 135, Part H, No. 5, Oct. 1988.
10. Wong, K. L., S. T. Fang, and J. H. Lu, "Dual frequency equilateral triangular microstrip antenna with a slit," *Microwave and Optical Technology Letters*, Vol. 19, No. 5, 348–350, Dec. 1998.
11. Row, J.-S. and K.-W. Lin, "Low-profile design of dual frequency and dual polarized triangular microstrip antennas," *Electronics Letters,* Vol. 40, No. 3, 156–157, Feb. 5, 2004.

Design of Monopole Antenna Using Coupling Characteristic of Spiral Parasitic Patch

Kwangyeol Yoon, Seungwoo Lee, and Nam Kim
Chungbuk National University, Korea

Abstract— This paper presents a monopole antenna that uses parasitic patch coupling characteristics. The proposed antenna structure consists of a rectangular shape patch, a spiral-shaped parasitic patch, and two L-shaped resonators. When using only the rectangular patch, the resonant bandwidth is 3.50–6.17 GHz. We obtain resonance frequency properties by adding the spiral-shaped parasitic patch in the ground plane coupled to the rectangular patch. To achieve frequency notched characteristics at the 4.5 GHz band, two short-circuited quarter wavelength L-shaped resonators connected to the ground plane are inserted beside the feed line. The proposed antenna dimension is $60 \times 40 \times 1\,\text{mm}^3$, and is designed on the FR-4 substrate having a relative dielectric constant of 4.4. The designed antenna shows that the resonant frequency bands are 1.75–2.55 GHz, 3.18–3.88 GHz, and 4.82–6.30 GHz below the return loss of −10 dB. Also, the radiation pattern is omnidirectional.

1. INTRODUCTION

With the rapid development of wireless communication technology, various service bands have appeared and various antenna designs are being studied to meet applications. Almost all of the initial antenna shapes for mobile communication devices were external, but over time they have changed to be internal for reasons of convenience. There were some problems with interior space when installing these antennas, however, depending on the miniaturization of the wireless devices. The initial kinds of antennas were Planar Inverted F Antenna (PIPA), Small Loop Antenna, Chip Antenna, and Surface Mounted (SMD) antenna.

In addition, as GPS, WiFi, and Bluetooth services were developed and used, the need for broadband and multi-band antennas to cover these services has emerged. To meet the increased needs of mobile devices, fractal antennas, bow-tie antennas, spiral antennas, and LP antennas have been created for different characteristics. These antennas are bulky and have very complicated structures, so the search for a simple, effective planar monopole antenna is always in progress. A planar monopole antenna's length is one quarter of the wavelength of the resonance frequency. Also, its impedance bandwidth is narrow. These are problems that have been partially solved with the introduction of different types of radiation patches.

In this paper, we suggested a monopole antenna which is composed of a square-shaped emitter and a parasitic element connected to a ground plane. The single resonance generated from the front rectangular patch and multiple resonances generated from a parasitic element get together and show broadband characteristics. We designed and fabricated a planar monopole antenna by inserting the L-shaped resonators at both sides of the feed line. The proposed antenna can cover the service bands of PCS, WCDMA, WLAN and WiMAX.

2. ANTENNA DESIGN AND RESULT

Figure 1(a) shows the structure of the proposed antenna. Its entire size is $40 \times 60 \times 1\,\text{mm}^3$ and it is made of an FR-4 substrate with a permittivity of 4.4. The detailed design parameters of the antenna are written in Table 1. We determined the resonance frequency and bandwidth of a rectangular patch antenna to cover a WLAN application. To improve the restricted bandwidth that we get when we use a square patch, we inserted a parasite element connected to the ground plane. We used a spiral-shaped parasitic element to minimize the area of the antenna and to get multi-band characteristics, and maximized the coupling effect by adjusting the gap between the square patch and the parasite element. For low-frequency PCS and WCDMA applications, we decided to match up the resonance frequency with the total length of the spiral structure and optimized the length of each side of the gap. By optimizing the distance between patches, impedance matching and low frequency bandwidth is improved. Also, we eliminated unnecessary frequency bands by inserting an L-shaped resonator at both sides of the feed line. Figure 1(b) shows a typical configuration for TEM or quasi-TEM narrowband band-stop filters with shunt-connected L-resonators. The main transmission line is electromagnetically coupled to the open-circuited half wavelength resonator or

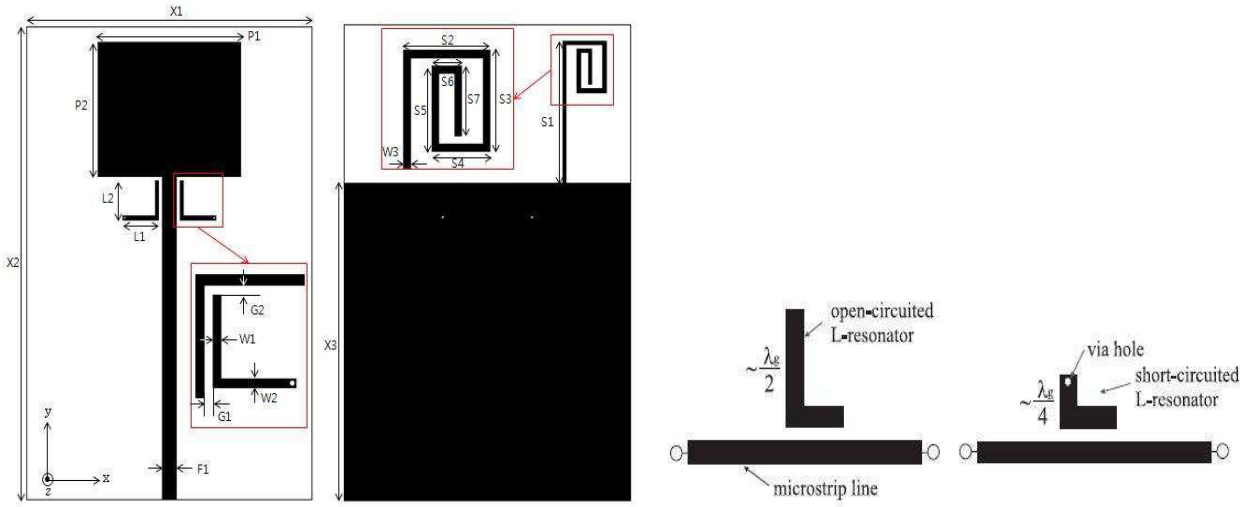

(a) Geometry of the proposed antenna (b) Geometry of the L-resonator

Figure 1: Geometry of the proposed antenna and L-resonator.

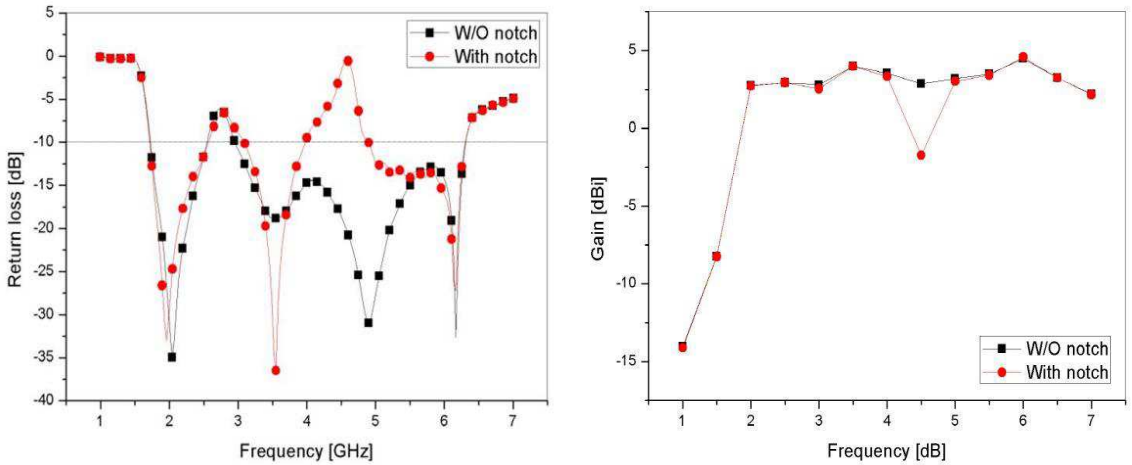

(a) Simulated result of return loss (b) Simulated result of gain

Figure 2: Comparison of the simulated return loss and gain according to the existence of the L-resonator.

Table 1: Optimized parameter of the proposed antenna.

Parameter	X_1	X_2	X_3	P_1	P_2	F_1	L_1	L_2	G_1	G_2
Value (mm)	40	30	40	20	17	2	5	4.5	0.5	1
Parameter	W_1	W_2	W_3	S_1	S_2	S_3	S_4	S_5	S_6	S_7
Value (mm)	0.5	0.5	0.5	18	6.1	6.5	4.1	5.5	2.1	4.5

the short-circuited quarter wavelength resonator. To minimize the space taken up by the resonator, we inserted a via-hole with a diameter of 0.3 mm and connected it to the ground plane like the right picture. Similar to the case of the parasitic element, we optimized the resonator's location, because it effected band rejection characteristics and impedance matching.

Figure 2(a) is return loss result according to the existence of an L-resonator, and Figure 2(b) is the rate of change without gain. We identified that the band-notched characteristic appeared at 4.5 GHz band by inserting an L-resonator during the simulation, and the gain was seen to decrease dramatically. In the current distribution analysis, there is also strong current flow to the L-resonator. Finally, simulated return loss is about 1.71–2.56 GHz, 3.08–3.97 GHz, and 4.9–6.3 GHz on the basis of the standard -10 dB.

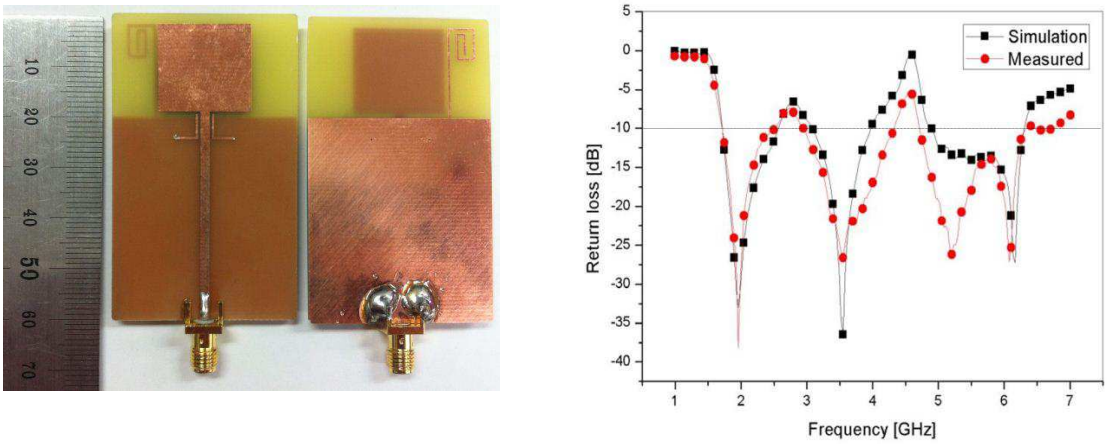

(a) (b)

Figure 3: Photograph of the fabricated proposed antenna and its return loss. (a) Photograph of the fabricated antenna. (b) Comparison of the simulated and measured return loss of the optimized antenna.

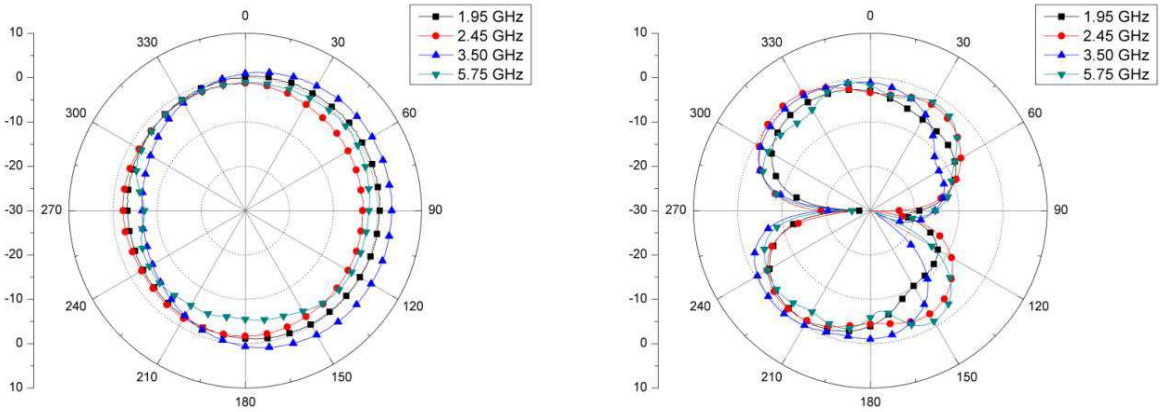

(a) *H*-plane (*xy* plane) (b) *E*-plane (*yz* plane)

Figure 4: Measured radiation pattern.

Figure 3(a) presents a photograph of the fabricated antenna, and the simulated and measured reflection coefficients (S_{11}) of the proposed antenna are illustrated in Figure 3(b). As observed, the fabricated antenna achieves three resonant frequency bands of 1.72–2.53 GHz, 2.98–4.30 GHz, and 4.72–6.31 GHz below the return loss of −10 dB. Simulated and measured results show a similar pattern.

Figure 4 shows measured radiation patterns of the proposed antenna at 1.95 GHz, 2.45 GHz, 3.50 GHz, and 5.75 GHz. From the overall view, the antenna behaves nearly omnidirectional performance with some deterioration at highest resonant mode.

3. CONCLUSIONS

In this paper, a monopole antenna for broadband using a coupling effect between a rectangular patch and a spiral-shaped parasitic patch with a connected ground plane was proposed. The distance of each patch was optimized to maximize the induced current, and we obtained the proper resonance frequency band through the parameter change of the spiral structure. In addition, we achieved the band reject characteristic using two short-circuited quarter wavelength L-shaped resonators next to the feed-line. The proposed antenna achieves three resonant frequency bands of 1.75–2.55 GHz, 3.18–3.88 GHz, and 4.82–6.30 GHz below a return loss of −10 dB, and it also covers the service band of PCS (1850–1990 MHz), WCDMA (1920–2170 MHz), WLAN (2400–2483 MHz, 5750–5825 MHz), and WiMAX (3300–3700 MHz).

REFERENCES

1. Song, C. T. P., P. S. Hall, H. Ghafouri, and I. Henning, "Fractal antenna research at University of Bir-mingham," *11th Int. Conf. on Antennas and Propagation*, Vol. 2, 724–727, 2001.
2. Shlarger, K. L., G. S. Smith, and J. G. Maloney, "Optimization of bow-tie antennas for pulse radiation," *IEEE Trans. Antennas and Propag.*, Vol. 42, No. 7, 975–982, Jul. 1994.
3. Daniels, D. J., "Surface-penetrating radar," *Electronics & Communication Engineering Journal*, Vol. 8, No. 4, 165–182, 1996.
4. Lim, H., J. H. Lee, S. H. Lim, D. H. Shin, and N. H. Myung, "A novel compact microstrip bandstop filter based on spiral resonators," *Asia Pacific Microwave Conference (APMC2007)*, 2221–2224, Bangkok, Thailand, Dec. 2007.
5. Kim, Y.-H., W.-G. Lin, W.-S. Lee, and J.-W. Yu, "Integrated printed wideband antenna with L-resonator band-stop filters," *European Conference on Antennas and Propagation: EuCAP 2006 (ESA SP-626)*, 831.1, Published on CDROM, Nov. 6–10, 2006.
6. Greenhouse, H. M., "Design of planar rectangular microelectronic inductors," *IEEE Transactions on Parts, Hybrids, and Pacaging*, Vol. 10, No. 2, 101–109, Jun. 1974.
7. Park, S. M., J. M. Kim, and N. Kim, "The design and SAR analysis of the spiral planar monopole antenna for dual-band," *The Journal of Korea Electromagnetic Engineering Society*, Vol. 18, No. 12, 1370–1382, 2007.
8. Shin, C. S., H. S. Shin, N. Kim, J. I. Choi, and J. D. Park, "Internal monopole antenna design for multiband operation and SAR analysis," *The Journal of Korea Electromagnetic Engineering Society*, Vol. 15, No. 12, 1190–1198, 2004.
9. Choi, D. G., H. S. Shin, N. Kim, and Y. K. Kim, "Design of the broadband PIFA with multiband for SAR reduction," *The Journal of Korea Electromagnetic Engineering Society*, Vol. 16, No. 1, 66–77, 2005.

Design of the Dual-band Planner Monopole Antenna for Coupled Rectangular-loop Structure and T-shape Rectangular Patch

J. D. Jang, S. W. Lee, and N. Kim
Chungbuk National University, South Korea

Abstract— In this paper, a broadband planar monopole antenna for mobile communication services is presented. The proposed antenna is composed of a small loop with a T-shaped patch and two rectangular patches for wide bandwidth characteristics. The frequency characteristics are modified and optimized by varying the size of each parameter of the antenna. In the measured result, the impedance corresponding to the 10-dB return loss is 815–977 MHz and 1.43 GHz–3.96 GHz. The designed antenna satisfies the impedance bandwidth for GSM900, DCS1900, WCDMA1900, ISM band/WLAN, WiMAX, and LTE next-generation (3.5 GHz) applications.

1. INTRODUCTION

Recently a variety of devices have been developed due to the rapid growth of mobile communication technology services. Therefore, the demands of dual-band and multiband antennas that can be integrated into a portable wireless communication device for several communication standards have attracted high attention. Some interesting candidates seem to be printed prototype antennas. Various types of antennas have been designed, such the inverted-F antennas [1, 2], the coplanar waveguide CPW-fed antennas [3, 4], and the microstrip line-fed antennas [5–7]. However, most of these designs are either too complex or too large in antenna size for practical applications. The difficulty in designing a simple and compact antenna with broadband or multiband functions still challenges engineers when the complexity and size of the antenna's structure is reduced and the operating frequency bands increase. In this paper, we propose a printed antenna with a simpler structure and a more compact size for dual-broadband operations. The entire antenna including the ground plane is only $40 \times 60 \times 1.6\,\text{mm}^3$.

2. ANTENNA STRUCTURE AND EXPERIMENTAL RESULT

Figure 1 shows the geometry of the designed antenna. The proposed antenna structure is a typical planar monopole antenna, a feed line, and radiating patch of the dielectric. The monopole structure in the form of a rectangular loop antenna size was minimized. Electromagnetic characteristics of a rectangular loop structure folded by the emitter currents in the central part of the loop are close to zero, so a radiator opening the center of the turn inside the loop counteracts the reduction in physical size. The center of the loop inductance values increased by a combination of lines through the capacitance value minimizes the value of the reactance. Due to these characteristics of the

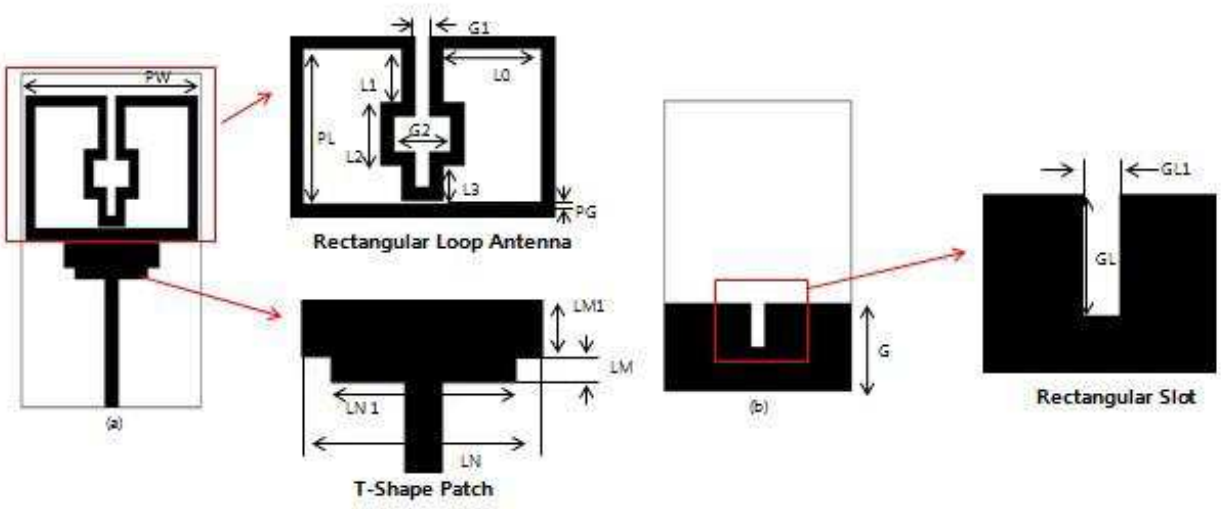

Figure 1: Geometry of the designed antenna.

Table 1: Proposed antenna parameters.

Parameter	Length	Parameter	Length
PW	28	L_2	9
PL	22	L_3	5
LM	2	G	18
LM_1	5	G_1	2
LN	16	G_2	8
LN_1	21	GL	9
L_0	14	GL_1	3
L_1	7.6	P_G	0.4

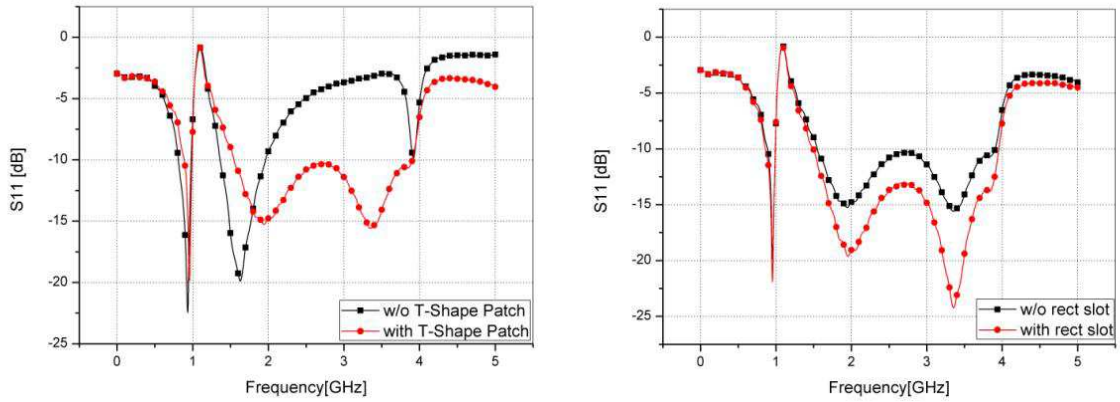

(a) T-shaped patches (b) Existence of rectangular slot

Figure 2: Simulated return loss.

antenna impedance, the entire antenna has increased efficiency. The proposed antenna presents a geometrical configuration of the proposed dual-band antenna design, is 1.6 mm thick, and has a FR-4 substrate with a dielectric constant of 4.4. Details of the antenna design are shown in Table 1.

Figure 1 presents the geometrical configuration of the proposed dual-broadband antenna design. The radiator comprises a rectangular loop-folded strip and T-shape patches. A rectangular loop antenna is used to achieve a frequency as shown in Fig. 2(a), ranging from 810 MHz–960 MHz and 1.3 GHz–1.97 GHz. Also a 3.9 GHz resonance is excited from the coupling effect between the parameters of PG, and then the capacitance according to the change of the resonance point will be moved. The proposed antenna can serve for applications using GSM900, WCDMA1900 and WLAN. The design of the T-shape patch inserts into the feeding line position for the 2.3 GHz–3.2 GHz band to optimize the parameters. The rectangular-loop antenna combined with the T-shape patch structure is used to obtain a wider impedance bandwidth. The corresponding 10-dB return loss bandwidth is 2.51 GHz (1.45 GHz–6.6 GHz) as shown in Fig. 2(a). The proposed antenna creates dual-broadband resonances through a rectangular loop structure and T-shaped patches. Also, the rectangular slot which is in the ground plane enhances the impedance matching without influencing the resonant frequency. These attributes are inserted into the ground plan as a ground, and the direction of the electric field between the radiators is changed. In addition, the rectangular slot width and height of the antenna is lowered according to changes in input resistance.

The simulated results in the form of the rectangular loop antenna frequency result in use of the 810 MHz–960 MHz band, and a relatively high frequency 1.3 GHz–1.97 GHz band. The specific characteristics of the antenna are detailed in Fig. 2(a). In addition, as the T-shape patches are inserted, the frequency characteristics of the 860 MHz–980 MHz and 1.43 GHz–3.96 GHz bands become usable as well. This means the antenna can be used for GSM900 (880–960 MHz), PCS, DCS1900, WCDMA1900 (1850–1990 MHz), WLAN/ISM (2.4 GHz–2.5 GHz), WiMAX (2.4 GHz–2.48 GHz, 3.3 GHz–3.8 GHz) and next generation 3.5 GHz. Fig. 2(b) shows impedance matching an inserted rectangular slot of the ground plane structure.

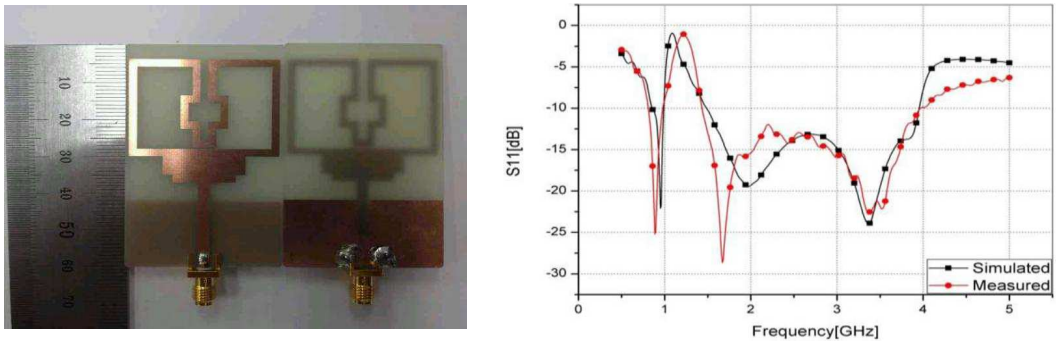

(a) Top and bottom views of the fabricated antenna (b) Measured and simulated return loss

Figure 3: The fabricated antenna.

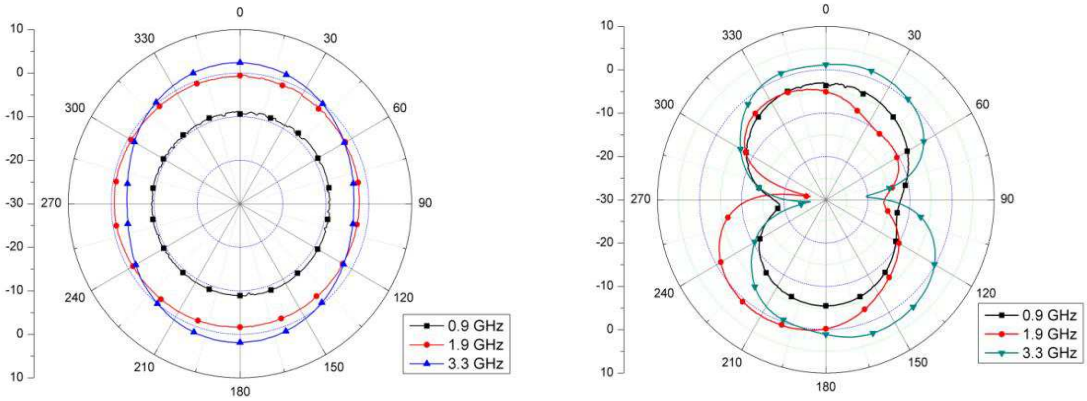

(a) *H*-plane (b) *E*-plane

Figure 4: Measured radiation pattern of the proposed antenna at 0.9 GHz, 1.9 GHz and 3.3 GHz.

3. ANTENNA IS FABRICATED AND MEASURED

Figure 3(a) shows a photograph of the fabricated dual-broadband strip antenna. Fig. 3(b) shows the simulated and measured return losses of the proposed antenna. The simulated and measured results show similar patterns, and the measured result operates at about 815–977 MHz (162 MHz) and 1.43 GHz–3.96 GHz (2.53 GHz).

Figure 4 exhibits the measured radiation patterns of the fabricated antenna in the H-plane (x-z plane) and E-plane (x-y plane) at 0.9 GHz, 1.9 GHz, and 3.3 GHz, respectively. Nearly omnidirectional patterns in the x-z plane are obtained over the desired operating bands.

4. CONCLUSIONS

In this paper, we presented a dual-broadband monopole antenna. The rectangular loop antenna satisfied the bands of 810 MHz–960 MHz and 1.3 GHz–1.97 GHz. In addition, the antenna generated line-coupling effects between the resonances in the 3.9 GHz band. The T-shape the portion is inserted into the feed line. As a result, we obtain a wider impedance bandwidth. Also we inserted the rectangular slot ground plan to improve impedance matching. As can be seen, the simulated and measured result shows reasonable agreement, and dual-broadband at 815–977 MHz and 1.43 GHz–3.96 GHz are with good impedance matching. The measured bandwidth covers both the GSM900 (880–960 MHz), PCS, DCS1900, WCDMA1900 (1850–1990 MHz), WLAN/ISM (2.4 GHz–2.5 GHz), WiMAX (2.4 GHz–2.48 GHz, 3.3 GHz–3.8 GHz), and the next generation 3.5 GHz bands. Moreover, the radiation patterns are omnidirectional shapes, which are appropriate for mobile handsets. Therefore, this antenna can be useful in small multi-band mobile devices.

REFERENCES

1. Zuo, S., Y. Yin, Z. Zhang, and W. Wu, "A compact tri-band PIFA antenna for WLAN and WiMAX applications," *Microwave Opt. Technol. Lett.*, Vol. 52, 919–922, 2010.

2. Ojaroudi, M., M. Hassanpour, C. Ghobadi, and J. Nourinia, "A novel planar inverted-F antenna (PIFA) for WLAN/WiMAX applications," *Microwave Opt. Technol. Lett.*, Vol. 53, 649–652, 2011.
3. Wu, C. M., "Dual-band CPW-fed cross-slot monopole antenna for WLAN operation," *IET Microwave Antennas and Propagat.*, Vol. 1, 542–546, 2007.
4. Yang, Y. J., L. Yang, S. X. Gong, and X. Li, "A novel design of dual-wideband CPW-fed antenna for WLAN/WiMAX applications," *Journal of Electromagnetic Waves and Applications*, Vol. 23, Nos. 8–9, 1191–1200, 2009.
5. Shin, Y.-S. and S.-O. Park, "A compact loop type antenna for bluetooth, S-DMB, Wibro, WiMax, and WLAN applications," *IEEE Antennas Wireless Propagat. Lett.*, Vol. 6, 320–323, 2007.
6. Gupta, R. K. and G. Kumar, "Printed dual band monopole antenna structures for WLAN applications," *Microwave Opt. Technol. Lett.*, Vol. 50, 2483–2487, 2008.
7. Lin, C., F. S. Zhang, G. Zhao, F. Zhang, and Y. Song, "A novel symmetrical monopole antenna for dual-broadband operation," *Microwave Opt. Technol. Lett.*, Vol. 51, 976–979, 2009.
8. Choi, D. G., H. S. Shin, N. Kim, and Y. K. Kim, "Design of the broadband PIFA with multiband for SAR reduction," *The Journal of Korea Electromagnetic Engineering Society*, Vol. 16, No. 1, 66–77, 2005.
9. Shin, C. S., H. S. Shin, N. Kim, J. I. Choi, and J. D. Park, "Internal monopole antenna design for multiband operation and sar analysis," *The Journal of Korea Electromagnetic Engineering Society*, Vol. 15, No. 12, 1190–1198, 2004.
10. Lee, H. M., S. W. Lee, and N. Kim, "The design and SAR analysis of the broadband printed monopole antenna with Z-patch," *The Journal of Korea Electromagnetic Engineering Society*, Vol. 18, No. 12, 1391–401, 2007.
11. Lee, S. M., S. W. Lee, and N. Kim, "Design of dual-band monopole antenna fed-by CPW using asymmetric ground plan," *The Journal of Korea Electromagnetic Engineering Society*, Vol. 27, No. 7, 715–849, 2010.
12. Lee, D. H. and W. S. Park, "Analysis of a T-shaped UWB printed monopole antenna using surface currents," *The Journal of Korea Electromagnetic Engineering Society*, Vol. 16, No. 9, 883–892, 2005.

Design and Relative Permittivity Determination of an EBG-based Wearable Antenna

N. R. Rishani, **M. Al-Husseini**, **A. El-Hajj**, **and K. Y. Kabalan**
ECE Department, American University of Beirut, Beirut 1107 2020, Lebanon

Abstract— This paper presents a simple technique for determining the permittivity of a textile material, and the use of this material in the design of a wearable antenna based on Electromagnetic Band Gap (EBG) structures. Finding the permittivity of some types of textile is usually a challenge. Knowing the exact permittivity value is very important to prevent the operation frequency of textile-based antennas from deviating from the intended design frequency. A patch antenna that resonates at 1.575 GHz is designed on a Cordura fabric dielectric material, assuming a permittivity (ε_r) of 1.9. Copper tapes are used as the conductive material. In the design, an EBG layer is incorporated halfway between the patch and the ground plane. A prototype of the designed antenna is fabricated, and its reflection coefficient measured. Results show a shift in the resonant frequency to 1.74 GHz, implying a lower substrate permittivity than originally assumed. The same design is simulated for several values of ε_r and the attained results show resonance at 1.74 GHz for a permittivity of 1.5. The patch is then redesigned for 1.575 GHz taking $\varepsilon_r = 1.5$, where the measurements of the newly fabricated prototype show agreement with the simulated ones.

1. INTRODUCTION

Recent years have witnessed a great increase in the use of wearable antennas. This is due to the high demand on wireless systems that are mobile, miniaturized, have light weight, and are of low cost. Wearable antennas are the optimal solution since they provide the mobility in different systems that every user desires. They can be used in medical systems, military equipment, entertainment places, and other applications. This usage is also enhanced by the increasing importance of body-centric communications within the sphere of Personal Area Networks (PANs) and Body Area Networks (BANs) [1]. On the other hand, the progress in the textile industry and the fabrication of electro-textiles made it easier for such antennas to invade the market and to be implemented easily into garments and cloths.

Although such antennas are made up of textiles, they still maintain their electromagnetic characteristics and are being used in many fields. Yet, one of the designing challenges lies in finding the permittivity of these textile substrates mainly when several layers of the material are stacked above each other.

In this paper, we propose a simple technique for finding the permittivity of textile material. The fabric under study is Cordura fabric [2] with an extremely tough polyamide 6.6 (nylon) fabric made of a special air-textured yarn with almost a uniform thickness. This material is used to design an EBG-based wearable antenna for operation at 1.575 GHz.

2. ANTENNA DESIGN

A patch antenna that resonates at 1.575 GHz is designed on a Cordura fabric dielectric material, assuming a permittivity (ε_r) of 1.9 [3, 4], and copper tapes are used as the conductive material for the patch and the ground. For this ε_r value of Cordura, the patch dimensions are 66 mm × 69 mm and those of the full ground plane are 106 mm × 108 mm.

Since the antenna is wearable and will be placed in the body vicinity, backward radiation had to be minimized as well as the effect of the body on the antenna behavior. To overcome this, and in addition to the full ground plane mentioned before, an Electromagnetic Band Gap (EBG) layer is incorporated between the patch and the ground plane, as shown in Figure 1. The EBGs used in this design are mushroom EBGs, where a layer of 5 × 5 almost square patches is placed between two Cordura fabric layers, each layer being 3 mm thick. Every patch is 18.5 mm × 19 mm and are placed 2 mm apart.

The EBG layer minimizes backward radiation when transmitting, and keeps the antenna performance steady while operating in the body vicinity. EBGs can also offer major improvements of radiation patterns, radiation efficiency, and impedance bandwidth over conventional microwave antennas and systems [5]. In the work conducted by Bashir in [6], results show that the radiation pattern of an antenna with EBGs has good front radiation and a small back radiation.

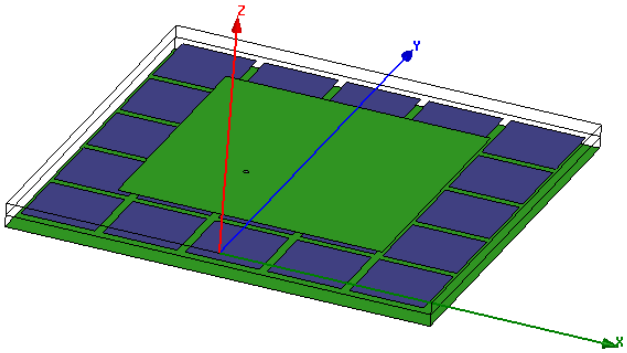

Figure 1: Geometry of the proposed antenna showing patch, EBG layer, and ground plane.

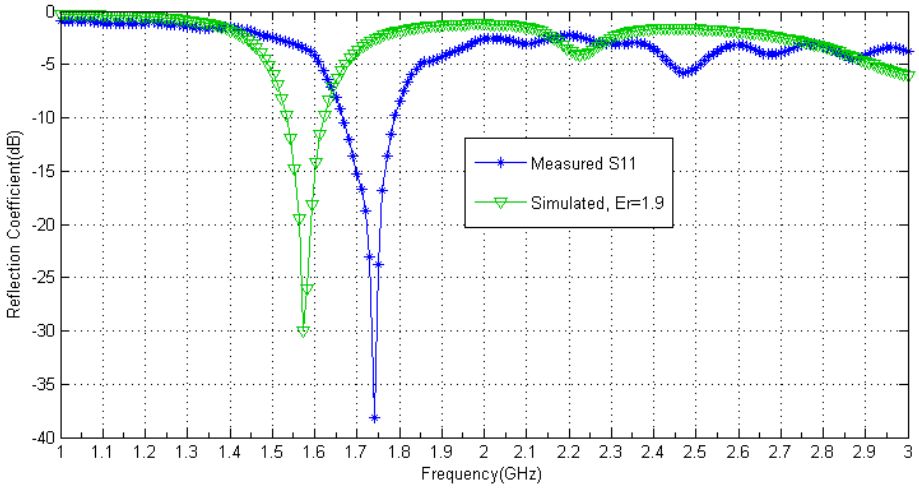

Figure 2: Simulated reflection coefficient assuming $\varepsilon_r = 1.9$, and the obtained measured reflection coefficient. The operation frequency shifted to 1.74 GHz.

Figure 3: Fabricated prototype.

The design was simulated using Ansoft HFSS and the simulated reflection coefficient in Figure 2 shows resonance at 1.575 GHz.

3. PROTOTYPE AND MEASUREMENTS

A prototype of the designed coaxially-fed antenna is fabricated, and its reflection coefficient is measured. A photo of the fabricated prototype is shown in Figure 3.

The measured S_{11} is also shown in Figure 2, which reveals a shift in the resonant frequency from 1.575 GHz to 1.74 GHz, and this implies a lower substrate permittivity.

To find the correct permittivity value, the same design is simulated for several values of ε_r and

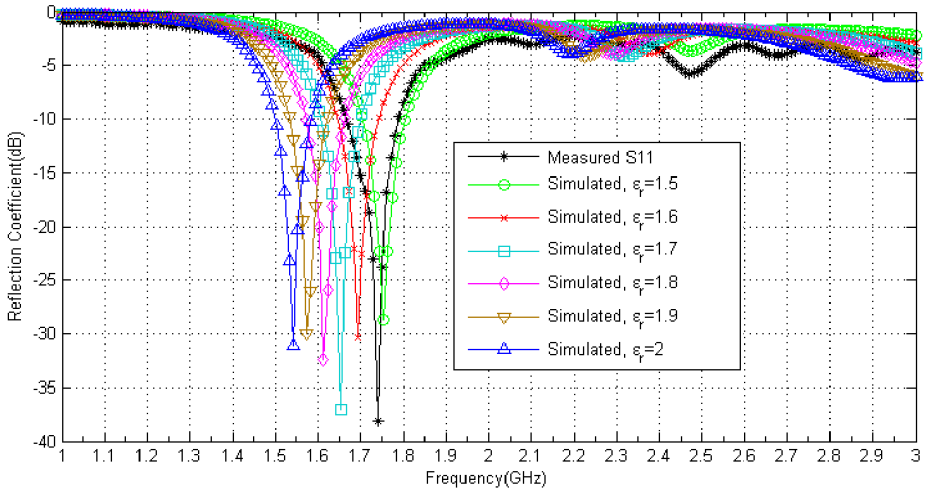

Figure 4: Simulated and measured reflection coefficients for several ε_r values.

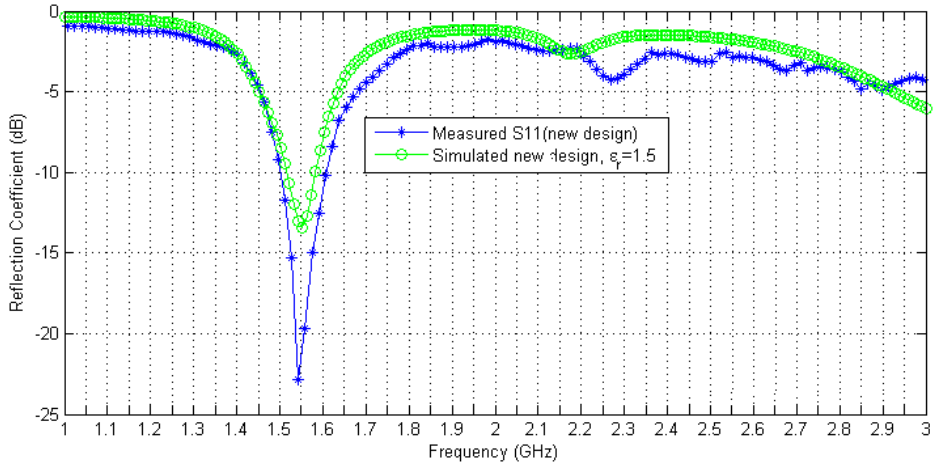

Figure 5: Simulated and measured reflection coefficient of the re-designed antenna.

S_{11} is computed for each of the cases. The attained results show that for a permittivity of 1.5, the antenna resonates at 1.74 GHz being the experimental resonant frequency, as shown in Figure 4.

Considering $\varepsilon_r = 1.5$, the patch is redesigned for an operation frequency of 1.575 GHz. The new patch dimensions are 66 mm × 69 mm. The re-designed antenna is fabricated, and measurements are taken. As illustrated in Figure 5, measured resonance at 1.575 GHz is obtained, and high correlation between simulated and measured reflection coefficient plots is revealed. As a result, it is concluded that the permittivity of the used textile material is 1.5.

4. CONCLUSION

A simple method to find the permittivity of a textile material for wearable antennas was presented in this paper. An antenna with a full ground and an incorporated EBG layer was designed and fabricated for assuming a textile permittivity of 1.9. Measurements showed a deviation from the original resonant frequency. The design was then simulated for several permittivity values, until a permittivity of 1.5 resonated at the same frequency obtain experimentally. The wearable antenna was re-designed and fabricated for $\varepsilon_r = 1.5$, where the results of simulation and measurements were highly correlated.

ACKNOWLEDGMENT

This work was supported by the University Research Board (URB) at the American University of Beirut (AUB).

REFERENCES

1. Rais, N. H. M., P. J. Soh, S. Ahmad, N. B. M. Hashim, and P. S. Hall, "A review of wearable antenna," *Proceedings of Antennas Propagation Conference, LAPC 2009*, 225–228, Loughborough, 2009.
2. Delcotex Germany, www.delcotex.de.
3. Lilja, J. and P. Salonen, "Textile material characterization for SoftWear antennas," *Proceedings of IEEE Military Communications Conference, MILCOM 2009*, 1–7, Loughborough, 2009.
4. Kaivanto, E., J. Lilja, M. Berg, E. Salonen, and P. Salonen, "Circularly polarized textile antenna for personal satellite communication," *Proceedings of the Fourth European Conference on Antennas and Propagation, EuCAP 2010*, 1–4, Apr. 2010.
5. Hall, P. S. and Y. Hao, *Antennas and Propagation for Body-Centric Wireless Communications*, Artech House, 2006.
6. Bashir, S., M. Hosseini, R. M. Edwards, M. I. Khattak, and L. Ma, "Bicep mounted low profile wearable antenna based on a non-uniform EBG ground plane flexible EBG inverted-L (FEBGIL) antenna," *Proceedings of Antennas Propagation Conference, LAPC 2008*, 333–336, Loughborough, 2008.

Antenna Array for IEEE 802.11/a/b MIMO Application

Dau-Chyrh Chang, **Yi-Jhen Li**, **and Chao-Hsiang Liao**
Communication Research Center, Oriental Institute of Technology
No. 58, Sec. 2, Sichuan Rd., Banqiao Dist., New Taipei City 220, Taiwan, R.O.C.

Abstract— In this paper, antenna array for WiFi IEEE 802.11a/b with frequency at 2.4 GHz ∼ 2.5 GHz and 5.2 GHz ∼ 5.8 GHz is implemented. The results from both simulation and measurement are compared. The geometry of the antenna array is simulated by GEMS. Top patch arrays is dual polarizations with frequency at 5.5 GHz. The second layer patch array is dual polarizations with frequency at 2.4 GHz. The 5.5 GHz array is located on the top of 2.4 GHz array. The return loss, power pattern, efficiency for two orthogonal polarizations at 2.4 GHz and 5.5 GHz will be discussed in below section.

1. INTRODUCTION

Most of communication systems should have high performance antenna or antenna system. For indoor Wi-Fi communication, the Access Point (AP) is omni-direction antenna radiation pattern, because it needs to receive signal in each direction. However, for point to point outdoor Wi-Fi communication, it is long distance from AP to client, so the antenna directivity and efficiency are very important. The common way is using antenna array to increase the antenna gain, but some conditions need to be considered, such as element spacing, ground plane size, mutual coupling . . . etc.. If these factors do not considered in the design process, the performance of the antenna will be decreased.

The modern wireless communication systems require higher data throughput and longer propagation range to satisfy user's requirements. Multiple-input and multiple-output (MIMO) technology is proposed to meet these purposes. An antenna for MIMO application has to contain two or more antennas that operate at the same frequency bands. To avoid the interference between antennas, conventional designs keep the antennas with $\lambda/2$ distance [1, 2]. However, the modern wireless devices are required to be small, compact, and portable. Therefore, reducing distance and maintaining good isolation between antennas in MIMO antenna are necessity [3–5].

In this paper, a patch antenna array for IEEE 802.11a/b MIMO application by dual polarization and dual band is presented, the geometry and antenna design method are shown in below section.

2. ANTENNA ARRAY DESIGN

The profile of the proposed antenna shown in Figure 1 is printed on an FR4 substrate with relative permittivity of 4.4, loss tangent of 0.0245, and thickness of 0.4 mm for IEEE 802.11a/b MIMO application. The overall dimensions of $17 \times 7.1\,\mathrm{cm}^2$ consist of two square antenna elements of $5.1 \times 5.1\,\mathrm{cm}^2$ for 2.4 GHz and $2.1 \times 2.1\,\mathrm{cm}^2$ for 5.2 GHz. Top patch arrays is dual polarizations with frequency at 5.5 GHz. The second layer patch array is dual polarizations with frequency at 2.4 GHz. The 5.5 GHz array is located on the top of 2.4 GHz array. Two identical patch antenna

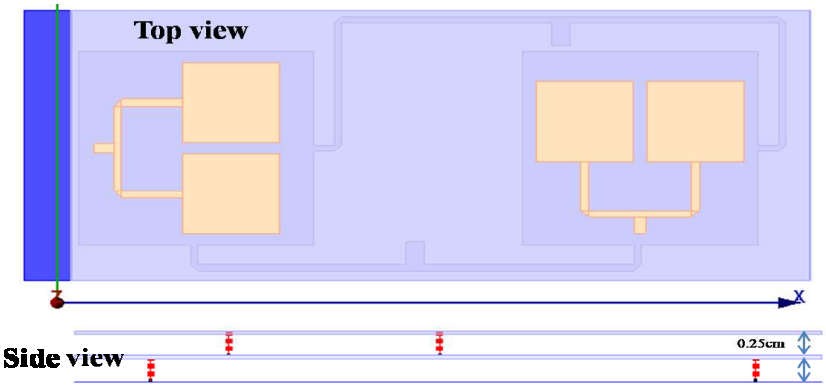

Figure 1: The profile of the proposed antenna array.

arrays by two orthogonal polarizations are designed at top and second planes. The bottom plane is the ground plane and it has 0.25 cm height intervals, the gap of the ground plane is used not only to increase the impedance matching of the antenna array but also to ensure good isolation between them. The patch antenna array is fed by 50 Ω i-pex cable. The hardware implementation for 2.4 GHz and 5.5 GHz is shown in Figure 2.

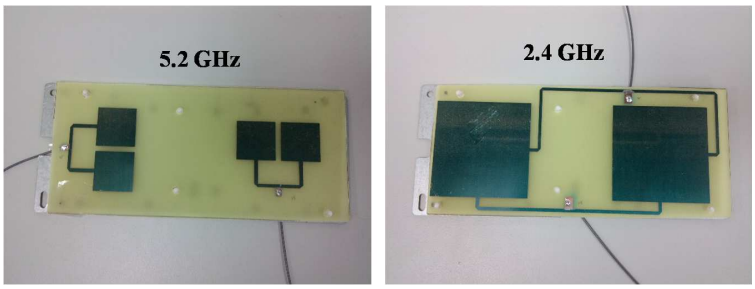

Figure 2: Hardware implementation for 2.4 GHz and 5.5 GHz.

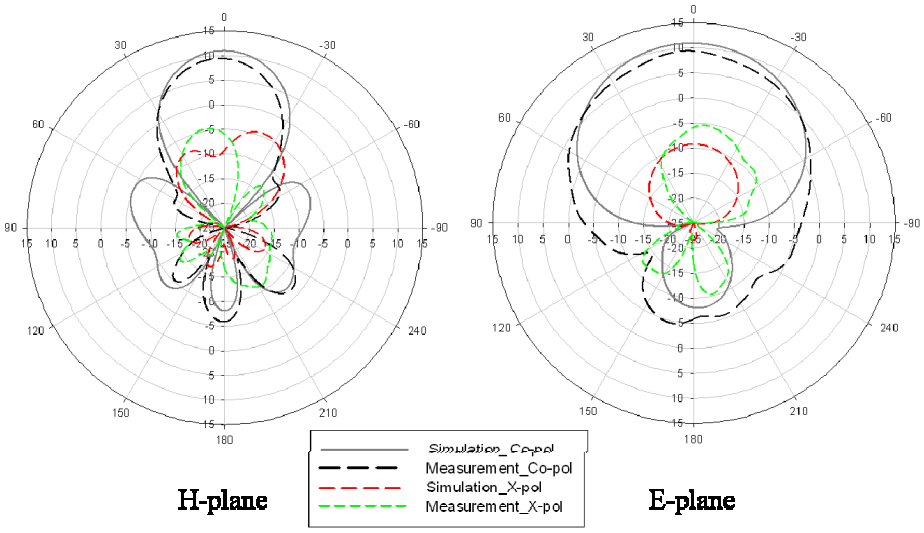

Figure 3: 2D radiation pattern at 2.45 GHz.

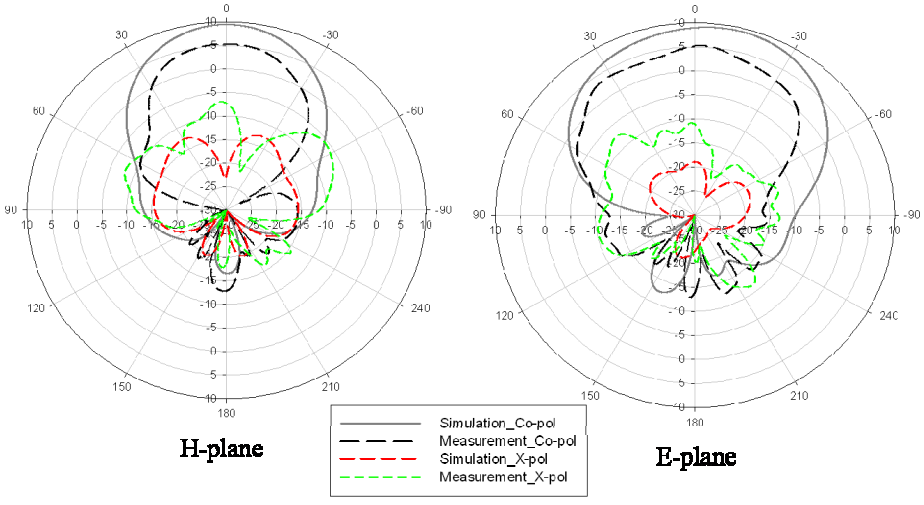

Figure 4: 2D radiation pattern at 5.5 GHz.

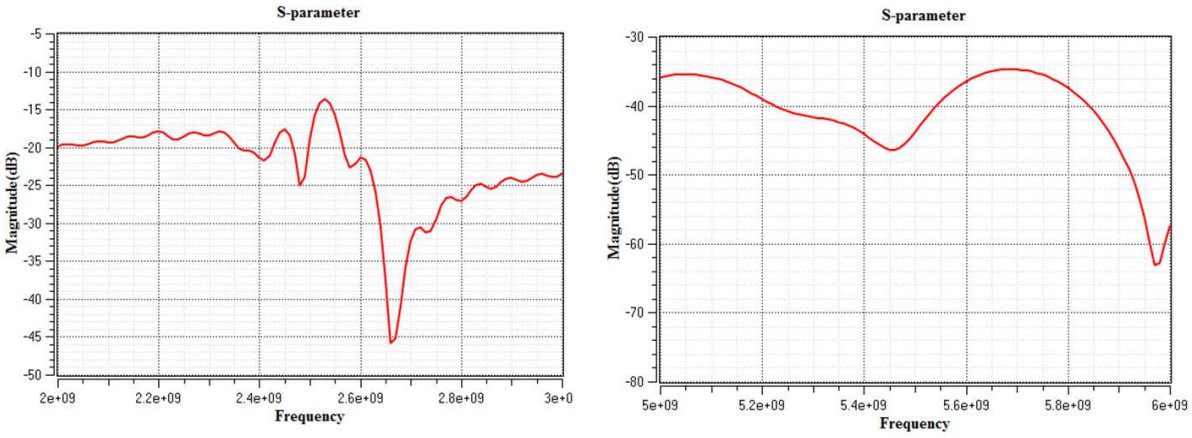

Figure 5: Simulated isolation of the proposed antenna.

3. SIMULATION AND MEASUREMENT RESULTS

Figure 3 is E plane and H plane radiation pattern at 2.45 GHz. The simulated and measured gains are about 11 dBi and 10 dBi. Figure 4 is E plane and H plane radiation pattern at 5.5 GHz. The simulated and measured gains are about 9 dBi and 6 dBi. Minor differences between the simulation and measurement, may be caused by measurement error and defects in the hardware implementation. Figure 5 is simulated isolation between two orthogonal polarizations at 2.4 GHz and 5.5 GHz. The S_{21} is less than -15 dB to ensure good isolation.

4. CONCLUSIONS

A patch antenna array for IEEE 802.11a/b MIMO application is proposed and verified. The results from both simulation and measurement are agreement. Base on the antenna performances and compact dimension, the proposed design can be applied to IEEE 802.11a/b MIMO application.

REFERENCES

1. Gupta, I. J., J. A. Ulrey, and E. H. Newman, "Antenna element bandwidth and adaptive array performance," *Proc. 2005 IEEE AP-S*, 295–298, 2005.
2. Katajamaki, T., "A compact dual-band phased array antenna for outdoor WLAN," *IEEE Vehicular Technology Conference*, 59–63, 2004.
3. Heath, R. W., A. Paulraj, and S. Sandhu, "Antenna selection for spatial multiplexing systems with linear receivers," *IEEE Commun. Lett.*, Vol. 5, 142–144, Apr. 2001.
4. Gesbert, D., H. Boelcskei, and A. Paulraj, "Outdoor MIMO wireless channels: Models and performance prediction," *IEEE Trans. Commun.*, Vol. 50, 1926–1934, Dec. 2002.
5. Gorokhov, A., D. A. Gore, and A. J. Paulraj, "Receive antenna selection for spatial multiplexing: Theory and algorithms," *IEEE Trans. Signal Processing*, Vol. 51, 2796–2807, Nov. 2003.

Analysis of a Dual Frequency Circular Patch Antenna

Sultan Can, K. Yavuz Kapusuz, and Elif Aydın
Department of Electrical and Electronics Engineering, Atılım University, Ankara, Turkey

Abstract— This study demonstrates resonant frequencies of several shorting pin loaded circular antennas, which are dual-frequency antennas. Dual-frequency operation is formed by using a shorting pin, which is connected between ground and the radiated part of the antenna. There are various studies, which are used to produce dual-frequency operation, and among those methods, a shorting pin is used to form dual frequency circular patch antennas since there are rare studies on this issue and size reduction is possible by inserting a pin to an antenna. This study is done to expand the studies in the literature about a shorting pin loaded circular patch antennas. The parameters that affect the resonant frequencies of the antenna are also evaluated. The thickness, permittivity and shorting pin positions are varied and the resonant frequencies are examined according to the change of these parameters. Frequency ratios are determined for each variation and the results are compared.

1. INTRODUCTION

Patch antennas are one of the most important elements in today's communication systems. Microstrip patch antennas, which are resonant antennas, are popular due to their low weight, low profile and cheap for printed circuit construction [1–7]. Efficient design of an antenna can increase the overall performance of the communication systems. Since the efficient design of a patch antenna is crucial, calculating design parameters such as resonant frequency and input impedance is getting more and more important [1–3]. Dual frequency operations are also popular in wireless communications and there are several methods to form a dual frequency such as slot, slit and shorting pin loading [2]. In designing the dual frequency antenna, an important parameter is to achieve higher frequency ratios with lower sizes. The frequency ratio is determined as the ratio of the upper frequency to the lower frequency in literature [3]. Inserting a shorting pin is mostly preferred because it significantly reduces the size of the antenna [3]. In this study, a dual frequency antenna is presented and a shorting pin is used to form a dual circular patch antenna. Inserting a shorting pin to a circular patch is preferred because the studies in literature show that shorting pin loaded circular antennas have larger frequency ratios when compared to the rectangular ones [4]. Frequency ratio characteristics are examined and the ratios are determined for different permittivity, thickness and shorting pin positions.

2. THE GEOMETRY OF THE ANTENNA

The proposed antennas geometry is given in Figure 1. The demonstrated antennas are fed by a coax, and a shorting pin which is inserted to the circular patch antenna in order to form dual frequency operation. The distance of the shorting pin from the centre of the circle is determined

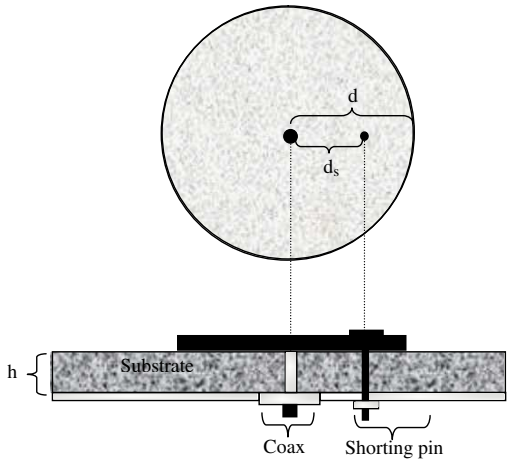

Figure 1: Geometry of a shorting pin loaded microstrip circular patch antenna.

as d_S. The radius of the circle is assigned as d. The thickness and the permittivity of the substrate are denoted as h and ε, respectively. The shorting pin radius is given as Figure 1.

A frequency ratio (r) is defined between the upper and lower resonant frequency and this equation is formulated as in Eq. (1);

$$r = \frac{f_{upper}}{f_{lower}} \tag{1}$$

The variation of r will be presented in the following sections. The effects of all antenna parameters such as permittivity, thickness and pin position values will be mentioned, as well.

3. RESULTS

The upper and lower frequencies are examined for different permittivity values in Figure 2. The variation of frequencies with respect to a ratio of shorting pin position to the radius of the circle is demonstrated for a substrate thickness 0.16 cm. A decrement is observed in the lower frequency with an increase in the position ratio. An increment is also observed in the upper frequency with an increment in the ratio of the positions.

The frequency ratios are also demonstrated according to the permittivity and shorting pin positions in Figure 3. Maximum frequency ratio is observed with an antenna which has a permittivity value $\varepsilon_r = 2.2$ at a position ratio $d_S/d = 0.9$. Minimum frequency ratio is observed with an antenna which has a permittivity value $\varepsilon_r = 4.4$ at a position ratio $d_S/d = 0.1$. The antenna with permittivity $\varepsilon_r = 4.4$ is also compared with the experimental values demonstrated in [6]. All these data prove that the permittivity of the substrate changes the upper and the lower frequencies but the effect of the permittivity value to the frequency ratio is not significant. Besides, the ratio of the radius and the shorting pin position from the centre of the circle (d_S/d) increase the frequency ratio. The antennas with different permittivity values which have a radius = 2.186 cm and a substrate thickness $h = 0.16$ cm achieve a frequency ratio approximately 3.5 at a ratio 0.9 while it was about 2.2 at a ratio was 0.1.

The effect of the thickness to the frequency ratio is also examined for an antenna with a radius 2.186 cm which has a permittivity value of $\varepsilon_r = 4.4$. The results are presented in Figure 4. As shown in aforementioned figure varying the thickness changes the frequency ratio and the lowest thickness value which is 1 mm achieved the maximum frequency ratio.

The studies in the literature demonstrate a null voltage point according to the ratios of the positions in equilateral patches [3]. The null voltage point is determined at a ratio around 0.33. As seen in Figure 4 a null voltage point is observed at a distance ratio around 0.3. Thickness parameter has a negligible effect at that point and the frequency ratio remains around 2.45 for each thickness value.

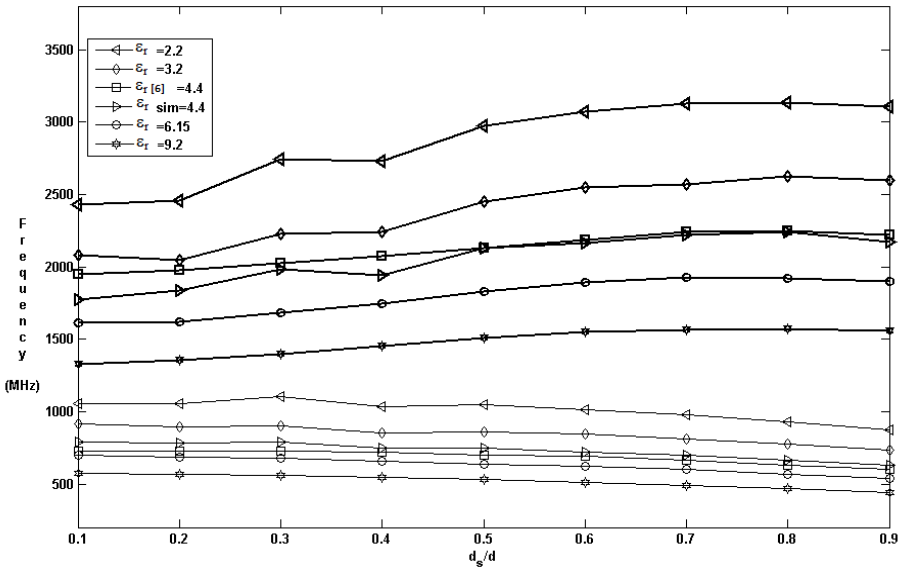

Figure 2: The resonant frequencies variation with permittivity and shorting pin position ratios where $d =$ 2.186 cm and $h = 0.16$ cm.

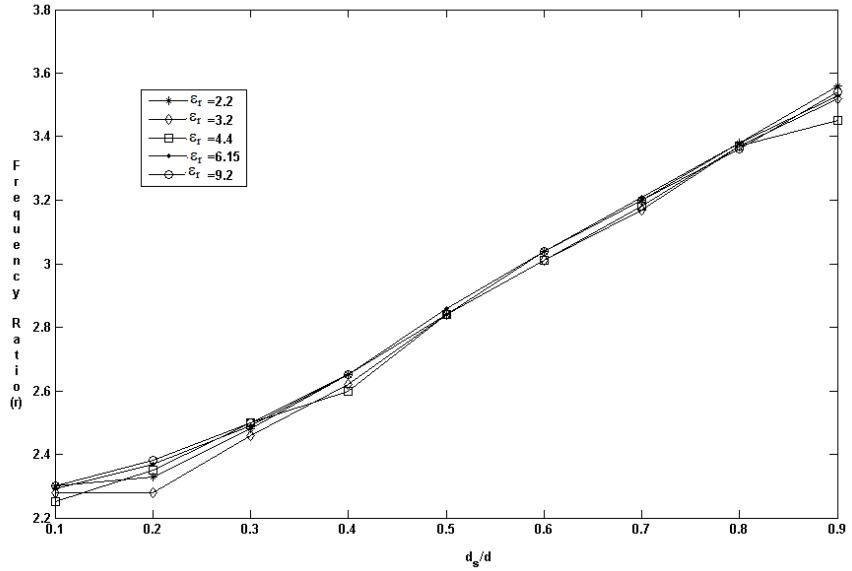

Figure 3: The frequencies ratio variation with permittivity $d = 2.186\,\text{cm}$ and $h = 0.16\,\text{cm}$.

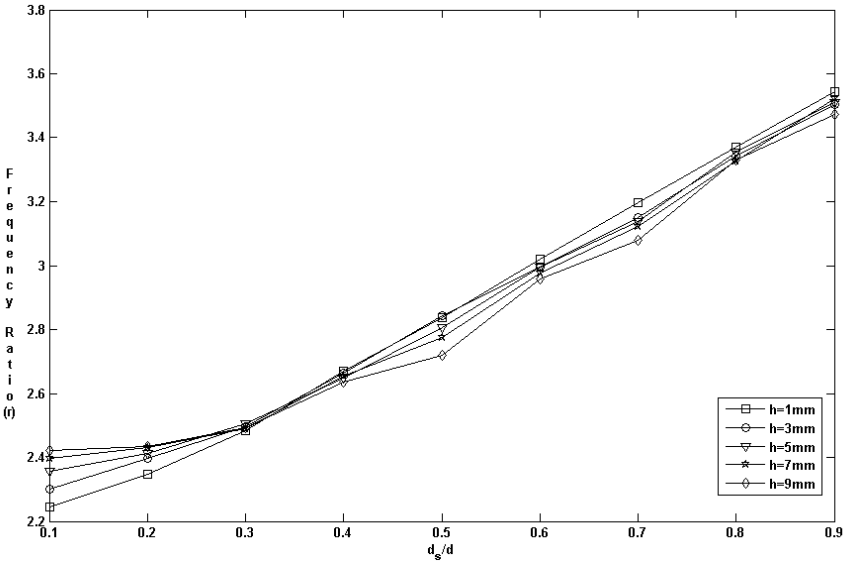

Figure 4: Shorting pin position ratio versus frequency ratio graph for different thickness values $d = 2.186\,\text{cm}$, $\varepsilon_r = 4.4$.

Table 1: Comparison with simulated results of the proposed antennas with ones proposed in [6] and frequency ratio.

Antenna	d (cm)	d_s (cm)	h (cm)	ε_r	f_{lower} (MHz)	f_{upper} (MHz)	f_{lower} error (%)	f_{upper} error (%)	r
A [6]	2.186	2.1	0.16	4.4	568	2176	–	–	3.83
B	2.186	2.1	0.16	4.4	596.9	2190	5.09	0.64	3.66
C	2.186	2.12	0.03	2.08	834.5	3185.6	–	–	3.82

As mentioned before, size of the antenna is a crucial parameter in today's world. For this purpose, reducing the size of the antenna is important for the designers. An antenna (C) with a frequency ratio 3.82 is proposed with a side length 2.186 cm and permittivity value $\varepsilon_r = 2.08$ which has a lower thickness when compared to the one in the literature [6]. However, the antenna C is capable of achieving the same frequency ratio. The antenna proposed in the literature (A) is compared with the antenna (B) and error calculated for both upper and lower frequency. The error

obtained is 5.09% for the lower frequency and 0.64% for the upper frequency.

4. CONCLUSION

Several antennas are proposed for achieving high frequency ratios for dual frequency operations. The frequency ratios are demonstrated for different permittivity values, thickness and position ratios. It is concluded that increasing the distance ratio of the shorting pin to the radius significantly increases the frequency ratio in shorting pin loaded circular patch antennas. It is also obtained that an antenna with lower size and thickness higher frequency ratios are achievable. It is also seen that thickness parameter has a negligible effect on frequency ratio at a critical point where the ratio d_S/d is around 0.3. An antenna is also proposed with smaller size, but achieves the same frequency ratio.

REFERENCES

1. Aydın, E. and S. Can, "Modified resonant frequency computation for tunable equilateral triangular microstrip patch," *IEICE Electronics Express*, Vol. 7, No. 7, 500–505, 2010.
2. Can, S., "Computation of resonant frequency of dual band triangular patch antenna," Master's Thesis in Electrical & Electronics Engineering, Atılım University, Turkey, Jul. 2011.
3. Aydın, E. and S. Can, "Operating frequency calculation of a shorting pin-loaded ETMA," *Microwave and Optical Technology Letters*, Vol. 54, No. 6, 1432–1435, Jun. 2012.
4. Kumar, P. and G. Sing, "Microstrip antennas loaded with shorting post," *Engineering*, Vol. 1, No. 1, 41–45, Jun. 2009.
5. Kumar, P. and G. Sing, "Theoretical computation of input impedance of gap-coupled circular microstrip patch antennas loaded with shorting post," *Journal of Computational Electronics*, Vol. 10, Nos. 1–2, 195–200, Jun. 2011.
6. Tang, C. L., H. T. Chen, and K. L. Wong, "Small circular microstrip antenna with dual frequency operation," *Electronic Letters*, Vol. 33, No. 13, 1112–1113, Jun. 1997.
7. Gurel, Ç. S., E. Aydın, and E. Yazgan, "Computation and optimization of resonant frequency and input impedance of a coax-fed circular patch microstrip antenna," *Microwave and Optical Technology Letters*, Vol. 49, No. 9, 2263–2267, Sep. 2007.

Eigenanalysis of Arbitrarily Shaped 2-D and 3-D Closed and Open-Radiating Structures: A Review

G. A. Kyriacou[1], P. C. Allilomes[1], C. S. Lavranos[1], C. L. Zekios[1], S. J. Lavdas[1], and A. V. Kudrin[2]

[1]Microwaves Lab., Department of Electrical and Computer Engineering
Democritus University of Thrace, Xanthi, Greece
[2]Department of Radiophysics, University of Nizhny Novrogod, Russia

Abstract— A review of our research effort on the eigenanalysis of open-radiating and closed, straight as well as curved, structures is presented herein. Our previous work was focused on two dimensional (2-D) waveguiding structures and particularly on open-radiating waveguides including leaky wave phenomena, as well as curved geometries in the transverse and possibly curved along the propagation direction. Thus, this review deals with, a hybrid Finite Element method for open waveguides, a Finite Difference Frequency Domain method for curvilinear coordinates, a Hybrid Domain Decomposition and Truncation method for closed structures and a Finite Difference Frequency Domain periodic structures eigenanalysis.

1. INTRODUCTION

The modal characteristics of waveguiding structures are essential for the design of a variety of microwave devices. Valuable analytical solutions of canonical cross section closed waveguides are well established since the early days of microwaves. Arbitrary cross-section waveguides, partially or inhomogenously loaded with either isotropic or anisotropic materials can also be studied with the aid of numerical techniques like the Finite Element (FEM) or Finite Difference methods, e.g., our work by P. Allilomes and C. Lavranos [1, 2] as well as an indicative similar work by E. Karchevskiy [3].

Regarding our previous work, a hybrid Finite Element in conjunction with a cylindrical harmonics expansion is established for the analysis of open waveguides. The transparency of the fictitious circular contour truncating the finite element mesh is ensured by enforcing the field continuity conditions according to a vector Dirichlet-to-Neumann mapping [1]. The eigenanalysis of curved waveguides is confronted by a Finite Difference frequency domain method in orthogonal curvilinear coordinates [2]. The latter eliminates the usually encountered stair case effects by making the grid conformal to the material boundaries. Additionally it supports multi-coordinate systems and inhomogeneous grids enabling fine mesh around current carrying conductors and coarse mesh in the area of low field variations. These features offer high accuracy with minimum computer resources.

Aiming at the eigenanalysis of electrically large structures like the reverberation chambers or focused microwave cavities our previous Finite Element Method is extended accordingly [4]. For this purpose the perturbations inside the cavity are enclosed within a canonically shaped fictitious surface and the interior field is described using a vector FEM. Outside these perturbations, within the large canonical cavity, the electromagnetic field is represented through an analytical eigenfunctions expansion. The field continuity across the fictitious surface is exactly enforced according to the DtN formalism to yield an appropriate eigenvalue problem. This is in turn solved for the resonant frequencies and the related quality factors. Within this effort we are currently working toward extending this methodology for the eigenanalysis of open-cavities including various types of cavity backed antennas.

The design of a variety of periodic structures like filters, frequency selective surfaces and traveling wave antennas can be served very efficiently though the knowledge of the associated modes propagation constants and characteristic impedances. Motivated by these requirements, our previous FDFD eigenanalysis methods are now appropriately extended to account for the periodicity by simulating a single unit cell [5]. However, this approach is limited to an ω-formulation where the dispersion curves are evaluated by scanning the propagation constant (β) range of values. But this is possible when β is real and only for certain simple geometries. For arbitrary geometries and anisotropic material loadings (especially regarding leaky and frozen wave modes), β is complex and its range is unknown. For this purpose we put an effort in formulating a β-eigenproblem, which is possible by incorporating the Floquet expansion within the FDFD formulation.

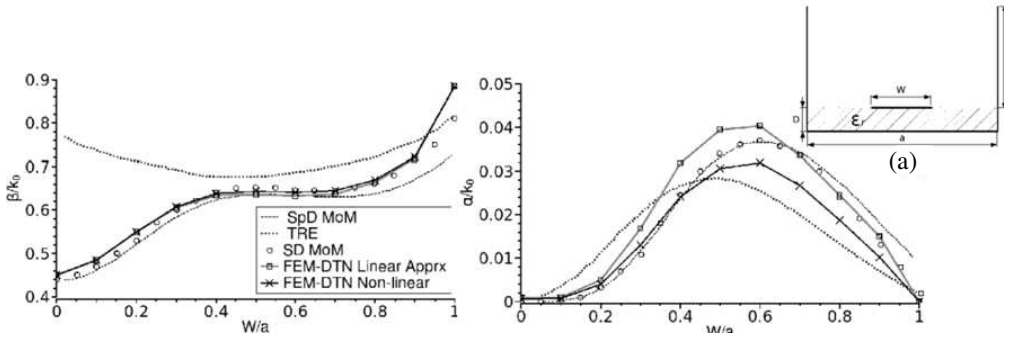

Figure 1: Normalized longitudinal propagation and phase constant (space-domain MoM: SpD MoM; transverse equivalent networktechnique: TRE; spectral-domain MoM: SD MoM; hybrid FEM: FEM-DtN).

2. HYBRID FEM FOR OPEN WAVEGUIDES

This technique is a hybridization of the FEM with a cylindrical harmonics expansion by means of a Dirichlet-to-Newman mapping approach and enables, the modeling of arbitrary cross section open waveguiding structures with inhomogeneous material loading. Keeping the 2-D formulation, the structures are considered homogeneous along the propagation axis. The open waveguide cross section is enclosed within a fictitious circular contour C. A vector FEM is employed for the description of the field in the complicated structure inside C. In the unbounded domain outside the contour C the field is expanded into an infinite summation of TE and TM modes. The latter are explicitly expressed as an infinite expansion of cylindrical harmonics for which Hankel functions of the second kind are chosen. The transparency of the fictitious contour C is ensured by enforcing the field continuity conditions according to the principles of a vector Dirichlet-to-Neumann (DtN) mapping. In turn, the orthogonality of the azimuthal eigenfunctions is exploited to yield a system of equations. This is then formulated as a generalized eigenvalue problem to be solved for the unknown complex propagation constants. However, this is a non-linear problem, since the unknown propagation constant occurs within the argument of the Hankel functions. This is solved employing a matrix Regula Falsi iterative algorithm. The required initial guesses are provided by solving an approximate linear eigenvalue problem again developed in the same work.

3. FDFD METHOD FOR CURVILINEAR COORDINATES

The 2-D Finite Difference Frequency Domain eigenvalue method formulated in orthogonal curvilinear coordinates [2], is a novel eigenvalue method, in which the finite difference discretization is applied by means of an orthogonal curvilinear grid. That leads to an eigenvalue problem formulated for the complex propagation constants and the corresponding fields distributions of curved structures. For this purpose Maxwells Curl equations, are discretized with the aid of a curvilinear grid over the whole solution domain, according to the basic Yee's principles. Following a 2-D scheme, this analysis is restricted to structures uniform along the propagation direction. Its direct implementation in orthogonal curvilinear coordinates leads to an accurate description of curved or bent geometries with an adaptive grid free of the well known stair case effect. The waveguiding structure can be curved in all directions (obeying some limitations with respect to the curvature along the propagation axis) and this constitutes its main advantage. The cross section of the waveguide structure can be of arbitrary shape loaded with inhomogeneous and in general anisotropic materials, such as ferrite, ferroelectric or multiferroic tensors. In addition, the complex matrix-format ability enables the introduction of the well known PML complex tensor, which enables open radiating geometries simulation. Moreover, this method can be formulated with non-uniform grids, which is essential for the description of curvilinear structures with fine geometry features. Finally, for the simulation of geometries with arbitrary cross section the method has been modified to accurately combine more than one orthogonal curvilinear grids. This method has been used to accurately extract the propagation constants of several curved structures, such as curved rectangular, cylindrical or coaxial waveguides. The extracted numerical results are compared either with analytical solutions such as Lewins perturbation theory for curved waveguides [6], with published numerical results or with results obtained from an electromagnetic simulator such as CST MS.

4. HYBRID DOMAIN DECOMPOSITION AND TRUNCATION METHOD FOR CLOSED STRUCTURES

This hybrid technique is directed toward the application of the Finite Element Method, similar to the Bymoment method but extending it so, that an eigenvalue formulation is attained. Each i-th perturbation is enclosed inside a fictitious parallelepiped surface S_f (fictitious box) and the electromagnetic field is expressed employing the finite element method. In the unperturbed cavity domain, outside the surface S_f, the field is expanded into an infinite sum of the analytically available eigenfunctions/eigenmodes of an empty rectangular cavity, obtained considering Perfect Electric Conductor (PEC) walls. The surface integral, appearing in the weak form, provides the means to combine FEM solution with the field expansion in the unperturbed region. However, the most serious difficulty, occurring within this type of hybrid methodologies, is the necessity to decouple the degrees of freedom in the numerical and analytical expansions. For this purpose a type of by-moment approach (an intermediate continuity condition) is employed by considering equivalent electric and magnetic current densities on these fictitious surfaces, which result from Loves equivalence principle. These equivalent currents are expanded into either local (on each surface) or global all over the box (the small empty box eigenfunctions) orthogonal eigenfunctions. According to DtN, first the electric field continuity is enforced in two steps: through the equivalent magnetic current to establish the domain-I solution in terms of that of domain-II. This is then differentiated (through Maxwell curl equation) to obtain the magnetic field in subdomain-I and its continuity is then enforced through the equivalent electric current. This procedure yields a generalized eigenvalue problem with just a few hundreds of degrees of freedom formulated for the cavity resonant frequencies.

5. FDFD PERIODIC STRUCTURES EIGENANALYSIS

An eigenanalysis methodology is adopted using Finite Difference in Frequency Domain (FDFD) in order to evaluate the Floquet wavenumbers. An eigenvalue problem is formulated and solved with Arnoldi iterative Algorithm. Motivated by the requirements FDFD eigenanalysis method is now appropriately extended to account for the periodicity by simulating a single unit cell. The periodicity of the structure is accounted in two alternative approaches. Initially Periodic Boundary Conditions (PBCs) are imposed on the periodic surfaces whose results found in general to be in a very good agreement with analytical ones. However, there is a deviation when the phase difference between periodic surfaces rise above 150 degrees [5]. In order to get more accurate results, a Floquet Field Expansion is incorporated within the FDFD formulation (second approach). The rationale behind this approach is as follows. Floquet expansion is a discrete spatial Fourier transform (series) since the electric/magnetic field of lossless periodic structures is a spatial periodic function. In this sense, the evaluation of the Floquet coefficients requires a linear interpolation between the adjacent nodes of the electric and magnetic field, discretized according to Yees cell. Linear interpolation is being applied only in the direction of the structures periodicity. The discretized Floquet coefficients are similar to Bragg diffraction expressions for the total reflected wave. In this sense the power conservation law in conjunction to the Braggs diffraction law lead to the conclusion that band gap appears when the period of the structure is equal or larger than the $\lambda g/2$. Also, adaptive meshing is employed for the accurate study of very fine discontinuities in particular when periodic structures loaded with anisotropic or isotropic media are simulated in order to reveal the so-called Frozen Modes.

6. NUMERICAL RESULTS

In this section some selected numerical results of the above methodologies are presented.

6.1. Hybrid FEM for Open Waveguides

The normalized complex propagation constant $\gamma/k_0 = \beta/k_0 - j\alpha/k_0$ versus the ratio w/α (w = width of the microstrip line and α = width of the substrate) for a laterally shielded microstip line is presented in Figure 1. The analysis was carried out at the frequency of 50 GHz, and for a structure (Figure 1(a)) with dimensions $\alpha = 45\,\text{mm}$, $D = 1.59\,\text{mm}$, $L = 2\,\text{mm}$, and a dielectric constant $\epsilon_r = 2.56$. For the phase constant, a very good agreement with the classic spectral-domain MoM [7] can be observed for almost all the different ratios. For small w/α, the transverse equivalent network method fails [7], while the present finite-element Dirichlet-to-Neumann method is in a very good agreement with both the space- and spectral-domain MoM [7]. Moreover, for large w/α ratios, the current method is closer to the results obtained from the classic spectral-domain MoM rather

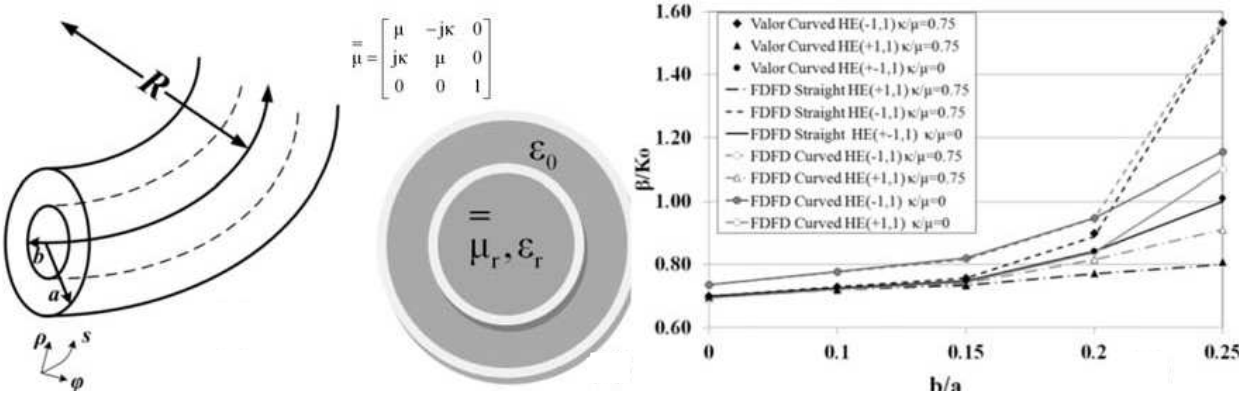

(a) (b) (c)

Figure 2: (a), (b) A curved circular waveguide with a longitudinally concentric ferrite rod ($R/2a = 1.5$). (c) Normalized phase constants for the examined curved circular waveguide, compared with those for the corresponding straight waveguide (FDFD method and Valor [2]).

than the space-domain MoM. For the leakage constant we also notice a good agreement of the finite-element Dirichlet-to-Neumann method with both the spectral and space-domain MoM.

6.2. FDFD Method for Curvilinear Coordinates

The examined structure is a curved circular waveguide with a longitudinally concentric ferrite rod, as shown in Figure 2. Two geometries are studied. Initially, a straight circular waveguide with a longitudinally concentric ferrite rod, as shown in Figure 2(b), is simulated and the results are compared with those given by Valor [8]. The simulation grid is a pure polar grid as used in our previous works, e.g., [2]. The normalized phase constants are extracted versus the ratio b/a for the dominant HE (1, 1) mode with k/μ as a parameter. As, shown, when $k/\mu = 0$ the ferrite rod is simplified to a dielectric rod, where all left- and righthand circularly polarized modes are degenerated, as also analyzed in our previous work [2]. Thus, left and right-hand circularly polarized HE (1, 1) modes have the same dispersion curves. On the other hand when $k/\mu \neq 0$ a degeneration removal phenomenon appears (known as birefringence) and HE (+1, 1), HE (−1, 1) dispersion curves are separated. The computed results for that case (black lines) are almost identical with those obtained by Valor (black triangles, diamonds and circles) [2], following exactly the above theory. Afterwards, the curved waveguiding structure shown in Figure 2(a) was analyzed exclusively with the Curvilinear FDFD method. The waveguide curvature led to some important results, as shown in Figure 2(c). For the $k/\mu = 0$ case a significant (up to 15% at ratio = 2.5) degeneration removal was occurred, as it was expected due to the waveguide's curvature, as explained in our previous work [2]. On the other hand, for $k/\mu \neq 0$ an important eigenvalue (phase constants) increase for both HE (+1, 1) and HE (−1, 1) mode has occurred. This increase rises up to 9% for HE (+1, 1) mode at ratio equal to 2.5 and 6% for HE (−1, 1) mode at ratio equal to 2.

6.3. Hybrid Domain Decomposition and Truncation Method for Closed Structures

A reverberation chamber (RC) (2 [m], 4 [m], 5 [m]) with metallic walls is loaded with two perturbations (the modes stirrers area and the EUTs area). In Figure 3(a) the comparison of the resonant frequencies between a brute force and the proposed DDM formulation is shown. For the computation of the eigenfrequencies a mesh of 1000 tetrahedral elements is considered. The CPU time and memory from brute force and DDM methods is (5 hours and 4 GB) and (20 min and 1 GB) respectively.

6.4. FDFD Periodic Structures Eigenanalysis

The dispersion diagram of a periodic structure loaded with two misaligned dielectric and one gyrotropic ferrite slab is presented in Figure 3(b), where $\phi = B_0 P$ is the product of the fundamental wavenumber B_0 and the period P. It is obvious that the TE_{20} mode is identified as a frozen mode, since its dispersion curve is flat at 100 degrees causing a zero group velocity ($v_g = 0$). Therefore it does not transfer energy, while it is asymmetric, unlike the rest ones of the diagram. Entering the slab of gyrotropic ferrite, the wave slows down dramatically and its amplitude increases enormously, creating unique conditions for nonlinear phenomena.

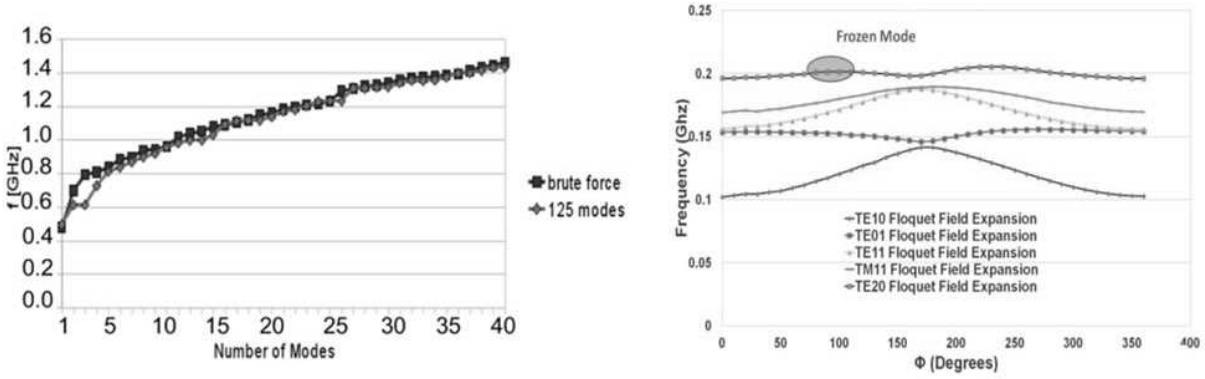

(a) (b)

Figure 3: (a) Resonant frequencies for the case of Brute force technique (squared line) and for the case of the proposed DDM technique (diamond line). (b) Dispersion Diagram of a periodic structure including an anisotropic media to yield a frozen mode.

7. CONCLUSION

A review of our research effort on the eigenanalysis of open-radiating and closed, straight as well as curved, structures was presented herein. During the presentation the basic principles of the above described eigenanalysis methodologies will be presented, along with a series of numerical results as well as validations in comparison to results published by other researchers.

ACKNOWLEDGMENT

This work was financially supported by the Greek Ministry of Education, Lifelong Learning and Religious Affairs through the research project THALIS Design Techniques for Digitally Controlled RF-Microwave Structures Appropriate for Software Defined — Cognitive Radio (RF-EIGEN-SDR).

REFERENCES

1. Allilomes, P. C. and G. A. Kyriacou, "Nonlinear finite-element leaky-waveguide solver," *IEEE Transactions on Microwave Theory and Techniques*, Vol. 55, 1496–1510, Jul. 2007.
2. Lavranos, C. S. and G. A. Kyriacou, "Eigenvalue analysis of curved waveguiding structures employing an orthogonal curvilinear frequency domain finite difference method," *IEEE Transactions on Microwave Theory and Techniques*, Vol. 57, No. 3, 594–611, Mar. 2009.
3. Dautov, R. Z. and E. M. Karchevskiy, "Exact nonlocal boundary conditions in the theory of dielectric waveguides," *PIERS Online*, Vol. 5, No. 5, 436–440, 2009.
4. Zekios, C. L., P. C. Allilomes, and G. A. Kyriacou, "Eigenfunction expansion for the analysis of closed cavities," *2010 Loughborough Antennas and Propagation Conference*, 537–540, UK, Nov. 2010.
5. Lavdas, S., C. S. Lavranos, and G. A. Kyriacou, "Periodic structures eigenanalysis incorporating the floquet field expansion," *Proc. of the ICEAA IEEE ARWC Conference*, Turin, Italy, Sep. 2011.
6. Lewin, L., C. Chang, and E. F. Kuester, *Electromagnetic Waves and Curved Structures*, Peregrinus, London, UK, 1977.
7. Gomez-Tornero, J. L., F. D. Quesada-Pereira, and A. Alvarez-Melcon, "A full-wave space-domain method for the analysis of leaky-wave modes in multilayered planar open parallel-plate waveguides," *Int. J. RF Microw. Comput.-Aided Eng.*, Vol. 15, No. 1, 128–139, Dec. 2005.
8. Valor, L. and J. Zapata, "Efficient finite element analysis of waveguides with lossy inhomogeneous anisotropic materials characterized by arbitrary permittivity and permeability tensors," *IEEE Transactions on Microwave Theory and Techniques*, Vol. 43, No. 10, 2452–2459, 1995.

Introducing Clifford Analysis as the Natural Tool for Electromagnetic Research

G. R. Franssens
Belgian Institute for Space Aeronomy, Belgium

Abstract— Clifford algebra and the thereupon based Clifford Analysis are introduced as the natural mathematical tools to formulate and solve electromagnetic problems. This is a new and powerful approach, which permits to make new progress in both the understanding and computation of electromagnetic fields.

1. INTRODUCTION

The model for electromagnetism, still widely in use today in applied sciences, is a virtually unchanged version that goes back to O. Heaviside, who "sorted out" two earlier models by J. Maxwell (one using the real algebra and the other using the quaternion algebra). Its mathematical formulation is not only very outdated, but also has obscured all this time important intrinsic properties of the underlying physical phenomenon. Responsible for this state of affairs is a vector algebra, invented by J. Gibbs and adopted by Heaviside to build his model, that is entirely inappropriate for describing electromagnetism. The Maxwell-Heaviside equations are considered to be the correct model for (classical) electromagnetism, because they predict numerical values for the magnitudes of the field components that are in agreement with experimental values. However, these equations do not correctly model the geometrical content of the electromagnetic field, nor all its physical invariances (e.g., Lorentz invariance, which is traditionally "proved" by mathematical cheating). Modern physical insight requires that a faithful model not only predict correct magnitudes, but also correctly models the geometric content and invariances that correspond to the physical phenomenon. Once one is willing to give attention to these additional requirements, by changing to a model that is also correct in this broader geometrical sense, fascinating new progress becomes possible.

Electromagnetism has a higher degree of intrinsic simplicity and beauty, than what can be inferred from its classical formulation. This can be brought out more clearly by stating electromagnetism in terms of modern mathematical language and concepts. The here presented reformulation is not yet another fancy way of writing Maxwell's equations, but the result of using an advanced mathematical framework that is also capable of solving them. This new framework severely simplifies the solution of electromagnetic problems and allows us to tackle rather advanced problems in a pure analytical way.

The power of the adopted mathematical formalism stems from the fact that it exploits a, so far overlooked, inherent property of electromagnetism: electromagnetic fields in a region without sources possess a generalized form of holomorphy. This property imposes restrictions on an electromagnetic field in such a way that new progress in electromagnetism by analytical methods becomes possible and this to a much larger extent than what is currently believed achievable.

The next two sections contain a condensed introduction to the mathematical framework that allows us to do electromagnetic research with power and elegance: Clifford algebra and the thereupon based Clifford Analysis (CA). A branch of CA, called hyperbolic CA, is shown to be the natural setting to formulate and solve electromagnetic problems (as well as quantum field problems). In particular, the mathematical model for electromagnetism, when stated in CA as in Section 4, reduces to a single as-simple-as-it-gets equation. This equation is equivalent to the Maxwell-Heaviside model in the narrow sense that both models produce the same field component magnitudes, but this new model now also has the geometrical content right. In Section 5, some examples of new insights and results obtained with CA are summarized.

2. CLIFFORD ALGEBRA

The underlying idea of this new approach to electromagnetism is that we should use that mathematical framework which is best adapted to the structure of the universe that we live in. In our 4-dimensional universe this is, in the absence of gravity, (locally) a pseudo-Euclidean space (Minkowski space) or when gravity is present, a pseudo-Riemannian space. An important aspect

of such spaces is their quadratic inner product structure (called the metric by physicists), which profoundly shapes the form that the laws of physics take. Over the last century, it has become apparent that the laws of physics essentially express geometrical relationships between quantities, which themselves have geometrical content. It thus makes sense to use a number system that is up to this task. By combining these observations we naturally arrive at what are now called Clifford algebras, and which by W. Clifford himself were called geometrical algebras. Clifford algebras make it possible to easily formulate geometrical relationships between the geometrical objects that can exist in a linear space [1, 4, 13, 15].

Over each quadratic inner product space $R^{p,q}$, i.e., R^n together with the canonical quadratic inner product of signature (p,q) and dimension $n \triangleq p+q$, one can define $n+1$ real Clifford algebras, one for each signature (p,q) with q running from 0 to n. Let $\{\mathbf{e}^1, \ldots, \mathbf{e}^n\}$ be an orthonormal basis for the linear inner product space $R^{p,q}$, with canonical quadratic form P of signature (p,q). The real Clifford algebra $Cl_{p,q}$ over $R^{p,q}$ is defined by [2, 4, 13],

$$\left(\mathbf{e}^1\right)^2 = \ldots = (\mathbf{e}^p)^2 = +1, \qquad \left(\mathbf{e}^{p+1}\right)^2 = \ldots = (\mathbf{e}^n)^2 = -1, \tag{1}$$

$$\mathbf{e}^i\mathbf{e}^j + \mathbf{e}^j\mathbf{e}^i = 0, \quad i \neq j, \tag{2}$$

together with linearity over $\mathbb{R}$ and associativity.

Among the infinitely many Clifford algebras one finds several familiar algebras, some of which were independently reinvented in physics. For instance: (i) $Cl_{0,0}$: real numbers $\mathbb{R}$, (ii) $Cl_{1,0}$: split-complex and $Cl_{0,1}$: complex numbers $\mathbb{C}$, (iii) $Cl_{1,1}$: split-quaternion, $Cl_{2,0}$: hyperbolic quaternion and $Cl_{0,2}$: quaternion numbers $\mathbb{H}$, (iv) $Cl_{3,0}$: Pauli numbers and (v) $Cl_{1,3}$: Time-Space algebra [12], and $Cl_{3,1}$: Majorana algebra. Dirac's well-known algebra of gamma matrices is isomorphic to the complex Clifford algebra $Cl_4(\mathbb{C})$.

Each Clifford algebra $Cl_{p,q}$ is a unital, non-commutative, associative algebra over $\mathbb{R}$, which naturally forms a graded linear space of dimension 2^n, $Cl_{p,q} = \oplus_{k=0}^{n} Cl_{p,q}^k$. A real Clifford number (also called "multivector") x is a hypercomplex number over $\mathbb{R}$ with 2^n components of the form (using the implicit summation convention)

$$x = \underbrace{a1}_{1} + \underbrace{a_i\mathbf{e}^i}_{\binom{n}{1}} + \underbrace{\frac{1}{2!}a_{i_1 i_2}\left(\mathbf{e}^{i_1} \wedge \mathbf{e}^{i_2}\right)}_{\binom{n}{2}} + \ldots + \underbrace{a_{1,\ldots,n}\left(\mathbf{e}^1 \wedge \ldots \wedge \mathbf{e}^n\right)}_{1}. \tag{3}$$

With $[x]_k$ the k-grade projector, $x = \sum_{k=0}^{n}[x]_k$. A pure grade component $[x]_k$ represents an oriented subspace segment of dimension k, called a k-vector. A Clifford number thus extends the concept of an oriented line segment (i.e., an ordinary vector) by incorporating all possible oriented subspace segments of R^n, with dimensions ranging from 0 to n. E.g., $[x]_2$ represents an oriented plane segment, whereby its $\binom{n}{2}$ components determine its direction and orientation in R^n and its magnitude corresponds to its surface area (shape is not encoded). By an element of $Cl_{p,q}$ one can represent any ensemble of oriented subspace segments of R^n. The Clifford product encodes the natural geometrical constructions that are possible with oriented subspace segments that result in new oriented subspace segments.

3. CLIFFORD ANALYSIS

Clifford Analysis (CA) is an advanced and recent part of mathematical analysis. It can be regarded as a generalization of the familiar 2-dimensional theory of complex holomorphic functions to an arbitrary number of dimensions [2, 3, 7]. More precisely, real CA is a function theory wherein one studies a subset of functions, with domain in R^n and which take values in a real Clifford algebra. In CA, the algebra of complex numbers is replaced with a Clifford algebra $Cl_{p,q}$ and the classical complex Cauchy-Riemann equation is replaced with a $Cl_{p,q}$-valued equation, which preferably has physical relevance. CA is the proper mathematical setting for studying generalized physics (encoded in the chosen generalized Cauchy-Riemann equation) in universes with an arbitrary number p of time dimensions and an arbitrary number q of space dimensions. The particular case, $p = 1$ and $q = 3$, has direct relevance for the physics in our own universe, and this version of CA provides us with a function theory over Minkowski space in which the functions can be designed to represent electromagnetic or quantum fields.

Of all the concepts associated with complex holomorphic functions (such as monogenicity, complex analyticity, conformal map, etc.) only the property of holomorphy extends to higher dimensions. Consequently we have, in any number of dimensions, a generalized Cauchy kernel (generalizing the complex kernel function $\frac{i}{2\pi}\frac{1}{z}$), Cauchy theorem, Cauchy integral formula, residue theorem, etc..

Real CA can be divided in two branches: (i) elliptic CA, for which $p = 0$ or $q = 0$, now about 30 years old [2, 3], and (ii) a) hyperbolic CA, for which $p = 1$ or $q = 1$, and b) ultra-hyperbolic CA, for which $p > 1$ and $q > 1$. The development of branch (ii) is still ongoing. Branch (i) is rooted in ordinary real function theory, while the much harder branch (ii) requires distribution theory [8]. For instance, the generalized Cauchy kernels in non-elliptic CA are rather complicated distributions [11]. Hence, hyperbolic CA of signature $(1, 3)$ is the type of analysis to be used to describe the physics in our universe.

4. ELECTROMAGNETISM

In terms of the Clifford algebra $Cl_{1,3}$, the model for electromagnetism simplifies to one simple equation [12]:

$$\partial F = -J. \tag{4}$$

Herein is: (i) ∂ the Dirac operator (i.e., the 4-dimensional nabla operator), (ii) $F \in Cl^2_{1,3}$ a bi-vector function representing the electromagnetic field and (iii) $J \in Cl^1_{1,3} \oplus Cl^3_{1,3}$ represents the electric (grade 1 part) and (if necessary) magnetic (grade 3 part) monopole charge-current density field, assumed of compact support $\bar{s}$.

The product between ∂ and F is the Clifford product in $Cl_{1,3}$. This product guarantees that automatically the correct partial derivative operator acts on the correct electromagnetic field component and that the result is equated to the correct component of the charge-current density field. The merit of this model not only lies in its extreme compactness, but especially in its analytical tractability by methods of CA, for solving electromagnetic source problems in vacuum and homogeneous isotropic dielectrics. We can regard (4) as a generalized Cauchy-Riemann equation that singles out a subset of Clifford functions, which now by design represent physical electromagnetic fields.

(i) Our current model for electromagnetism (irrespective of its formulation) has no solution in general! It requires that integrability conditions are fulfilled, which turn out to be exactly the local conservation of electric and magnetic monopole charge-current density. This follows almost readily from (4) and it rigorously explains the consequence of the well-known over-determination enforced by the equation and its relation to charge conservation. This point of view is usually not made clear in the classical literature.

(ii) Let $x_0 \in R^n$ denote the calculation point, $\mathcal{D} \triangleq C^\infty_c(R^n, \mathbb{R})$ the set of smooth real-valued functions with compact support in R^n and $\mathcal{D}'$ the linear space of distributions with support in R^n. By definition, the $Cl_{p,q}$-valued vector distribution $C_{x_0} \in \mathcal{D}' \otimes Cl^1_{p,q}$ satisfying

$$\partial C_{x_0} = \delta_{x_0} = C_{x_0}\partial, \tag{5}$$

with δ_{x_0} the delta distribution with support $\{x_0\}$, is called the *Cauchy kernel* relative to x_0. We do not need to specify boundary conditions for C_{x_0}, any fundamental solution of (5) will do. The significance of C_{x_0} lies in the fact that the (left and right) convolution operator $C_{x_0}*$ is a (left and right) $Cl_{p,q}$-valued and functional inverse of the Dirac operator ∂.

(iii) It can be shown [8], that any Cauchy kernel can be obtained from a scalar distribution $f_{x_0} \in \mathcal{D}' \otimes Cl^0_{p,q}$ as

$$C_{x_0} = \partial f_{x_0}. \tag{6}$$

with f_{x_0} a fundamental distribution of the ultra-hyperbolic equation

$$\Box_{p,q} f_{x_0} = \delta_{x_0}, \tag{7}$$

since $\partial^2 = \Box_{p,q}$, the canonical d'Alembertian of signature (p, q).

(iv) For $(p, q) = (1, 3)$, the causal and anti-causal scalar distributions, $f^+_{x_0}$ and $f^-_{x_0}$ respectively, are obtained from the ordinary wave equation $\Box f^\pm_{x_0} = \delta_{x_0}$ and are given by

$$f^\pm_{x_0} = \frac{\delta_{c^\pm_{x_0}}}{4\pi r}. \tag{8}$$

Herein is $\delta_{c_{x_0}^{\pm}}$ the delta distribution having as support the half null-cone $c_{x_0}^{\pm}$. The action of $f_{x_0}^{\pm}$ on any $\varphi \in \mathcal{D} \triangleq C_c^{\infty}\left(R^4, \mathbb{R}\right)$ is given by [5, p. 249 Eq. (9) and p. 252, Eq. (14') with $k = 0$, and after splitting in causal and anti-causal parts],

$$\left\langle f_{x_0}^{\pm}, \varphi \right\rangle = \frac{1}{4\pi} \int_0^{+\infty} \int_{S_{\mathbf{s}_0}^2} \varphi\left(t_0 \pm r, \mathbf{s}_0 + r\xi\right) dS^2 r dr, \tag{9}$$

with $x_0 = (t_0, \mathbf{s}_0)$, $r \triangleq |\mathbf{s} - \mathbf{s}_0|$ and $\xi \triangleq \frac{\mathbf{s}-\mathbf{s}_0}{|\mathbf{s}-\mathbf{s}_0|} \in S_{\mathbf{s}_0}^2$ the spatial unit 2-sphere centered at $\mathbf{s}_0$. This shows that $f_{x_0}^{\pm}$, $\forall x_0 \in R^4$, are defined $\forall \varphi \in \mathcal{D}$ and are distributions. For our problem, the components of the source function J in (4) play the role of test functions. The causal and anti-causal Cauchy kernels, associated to (8), are

$$C_{x_0}^{\pm} = \frac{\delta_{c_{x_0}^{\pm}}^{(1)}}{4\pi r} dt - \left(\pm \frac{\delta_{c_{x_0}^{\pm}}^{(1)}}{4\pi r} + \frac{\delta_{c_{x_0}^{\pm}}}{4\pi r^2} \right) \xi, \tag{10}$$

with $\delta_{c_{x_0}^{\pm}}^{(1)}$ the generalized derivative of $\delta_{c_{x_0}^{\pm}}$. A rigorous examination reveals that $\delta_{c_{x_0}^{\pm}}^{(1)}$ are partial distributions, only defined for test functions that vanish in a neighborhood of the calculation point x_0. This is a technical complication that is satisfactory handled within distribution theory [11], and then x_0 can also be inside the source region $\bar{s}$.

5. NEW RESULTS

(i) A new integral theorem for the electromagnetic radiation problem with given compact smooth sources in vacuum (or a homogeneous isotropic dielectric) can be derived over an arbitrary region $c \supset \bar{s}$ in time-space (hence also over a moving spatial region enclosing a moving source) and is given by

$$F\left(x_0\right) = \left\langle C_{x_0}^{-}, J \right\rangle + \left\langle C_{x_0}^{-}|_{\delta\bar{c}}, n^*\left(F|_{\delta\bar{c}}\right) \right\rangle_{\delta\bar{c}}, \tag{11}$$

with n^* the dual of the 4-dimensional normal n. Eq. (11) states that the electromagnetic field produced in any point x_0 in c is the result of a contribution from the source field J (given by a "volume" Schwartz pairing) and a contribution from the electromagnetic field present at the boundary $\delta\bar{c}$ (given by a "boundary" Schwartz pairing). The notation $|_{\delta\bar{c}}$ means restriction to the boundary.

(ii) Any electromagnetic field, in a region without sources, is holomorphic. This is expressed by (11) with $J = 0$,

$$F\left(x_0\right) = \left\langle C_{x_0}^{-}|_{\delta\bar{c}}, n^*\left(F|_{\delta\bar{c}}\right) \right\rangle_{\delta\bar{c}}. \tag{12}$$

Holomorphy can be interpreted as an intrinsic form of holography. In physical terms, this means that any such field can be reconstructed inside a region from its values on the boundary of that region. Any field: static, evanescent, transient, etc.!

(iii) The particular solution of the electromagnetic radiation problem follows from (11) as

$$F\left(x_0\right) = \left\langle C_{x_0}^{-}, J \right\rangle. \tag{13}$$

By substituting the expression (10) for $C_{x_0}^{-}$ and splitting the resulting electromagnetic field $F\left(x_0\right)$ in electric and magnetic parts, (13) can be shown to reproduce *Jefimenko's formulas* [6, 14].

We can easily obtain a second expression for $F\left(x_0\right)$ by substituting $C_{x_0}^{-} = \partial f_{x_0}^{-}$ in (13) and using the definition of the distributional derivative. We get

$$F\left(x_0\right) = -\left\langle f_{x_0}^{-}, \partial J \right\rangle. \tag{14}$$

Applying (9) with $\varphi = dJ = \partial \wedge J$, now results in the following equivalent expression for (14),

$$F\left(x_0\right) = -\frac{1}{4\pi} \int_0^{+\infty} \int_{S_{\mathbf{s}_0}^2} \left(\partial \wedge J\right)\left(t_0 - r, \mathbf{s}_0 + r\xi\right) dS_{\mathbf{s}_0}^2 r dr. \tag{15}$$

This is a simple integral representation for the electromagnetic field, generated by a C^1 spatially compact monopole charge-current density source field J. Contrary to the form (13), no special care

is required to evaluate the integrals in (15) when the observation point x_0 lies inside the source region $\bar{s}$. Expression (15) appears to be a new form for the particular solution of the electromagnetic radiation problem.

(iv) A radiation boundary condition can be formulated, by using a Cauchy kernel with appropriate causality. A practical application for such a condition is, e.g., the construction of a perfectly reflection-less grid boundary (without having to introduce locally a dissipating medium), useful for simulating wave propagation in time-space over an arbitrarily truncated discretization mesh.

(v) CA is also applicable to obtain an integral theorem for the electromagnetic radiation problem with given compact smooth sources in a curved background vacuum [10].

6. PROSPECTS

(i) Although it is not yet definitively proved, CA strongly suggests that the problem of electromagnetic scattering by arbitrarily shaped (homogeneous and isotropic) dielectric bodies (i.e., a generalization of Mie's problem) might be analytically solvable in CA.

(ii) A non-homogeneous medium can be taken into account with the current method if it is equivalent to a curved vacuum.

(iii) The incorporation of arbitrary bi-anisotropic media requires a substantial extension of the present method.

REFERENCES

1. Bolinder, E. F., "Clifford algebra, what is it?," *IEEE Ant. and Prop. Soc. Newsletter*, 18–23, 1987.
2. Brackx, F., R. Delanghe, and F. Sommen, *Clifford Analysis*, Pitman, London, 1982.
3. Delanghe, R., F. Sommen, and V. Souček, *Clifford Algebra and Spinor-valued Functions*, Kluwer, Dordrecht, 1992.
4. Doran, C. and A. Lasenby, *Geometric Algebra for Physicists*, Cambridge University Press, Cambridge, 2003.
5. Gel'fand, I. M. and G. E. Shilov, *Generalized Functions*, Vol. I, Academic Press, 1964.
6. Franssens, G. R., "The electromagnetic radiation problem in an arbitrary gravitational background vacuum," *WSEAS Transactions on Mathematics*, Vol. 6, 838–851, 2007.
7. Franssens, G. R., "Introduction to Clifford analysis," *Proceedings of the IKM 2009*, Weimar, Germany, July 2009, http://euklid.bauing.uni-weimar.de/ikm2009/paper.php.
8. Franssens, G. R., "Introduction to Clifford analysis over pseudo-euclidean space," *Proceedings of the IKM 2009*, Weimar, Germany, July 2009, http://euklid.bauing.uni-weimar.de/ikm2009/paper.php.
9. Franssens, G. R., "A physical interpretation of Clifford analysis," *Proceedings of the 18th ICFIDCAA*, Macau SAR, China, August 13–17, 2010.
10. Franssens, G. R., "Clifford analysis solution of the electromagnetic boundary value problem in a gravitational background vacuum," *Advances in Applied Clifford Algebras*, Vol. 20, 587–616, 2010.
11. Franssens, G. R., "The Cauchy kernels of ultrahyperbolic Clifford analysis," *Proceedings of the 9th International Conference on Clifford Algebras (ICCA'11)*, Weimar, Germany, July 2011.
12. Hestenes, D., *Space-time Algebra*, Gordon and Breach, New York, 1966.
13. Hestenes, D. and G. Sobczyk, *Clifford Algebra to Geometrical Calculus*, Reidel, Dordrecht, 1984.
14. Jefimenko, O. D., *Electricity and Magnetism: An Introduction to the Theory of Electric and Magnetic Fields*, Electret Scientific, Star City, 1989.
15. Lounesto, P., *Clifford Algebras and Spinors*, Cambridge University Press, Cambridge, 2001.

Numerical Technique to Calculate Propagation Constants for the Problem of Polarized Wave Propagation in a Layer with Nonlinear Permittivity

D. V. Valovik and E. V. Zarembo
Penza State University, 40 Krasnaya Street, Penza 440026, Russia

Abstract— We consider a plane layered waveguide structure. The layer is located between two half-spaces with constant permittivities. The permittivity inside the layer is an arbitrary function of the electric field intensity. The propagation of polarized TM electromagnetic waves in such a structure is considered. Surface waves propagating along the boundaries of the layer are sought-for. We suggest a numerical approach to calculate propagation constants. Numerical results are presented.

1. INTRODUCTION

During many years problems of TE- and TM-waves propagation through nonlinear layers are intensively investigated. Such problems attract more and more attention due to their importance in different areas such as nonlinear optics, plasma physics, microelectronics etc. [1–3].

We consider a plane layered waveguide structure. The layer is located between two half-spaces with constant permittivities. The permittivity inside the layer is an arbitrary function of the electric field intensity [1, 4]. We consider propagation of polarized TM electromagnetic waves in such a structure (the same approach can be applied for TE waves). The physical problem for surface waves is reduced to the (nonlinear) boundary eigenvalue problem for nonlinear ordinary differential equations. Usually, in such problems, the main goal is to obtain a dispersion equation (DE) for propagation constants (eigenvalues) [4–7]. In spite of the fact that for such a structure formed by a layer with constant permittivity [2] it is easy to find exact DEs it is a serious problem to obtain exact DEs for a layer with nonlinear permittivity. For many physically interesting nonlinear permittivities it is far beyond our abilities to obtain and analyze exact DEs. So it is necessary to develop numerical methods to solve such nonlinear boundary eigenvalue problems. We suggest a numerical approach to calculate propagation constants (eigenvalues) for (nonlinear) layered waveguide structures based on numerical solution of a Cauchy problem in the layer [8]. By means of transmission conditions on the layer boundaries we can define initial data for this Cauchy problem. When this Cauchy problem is solved we construct a function that continuously depends on the spectral parameter. The zeros of this function, which can be effectively calculated are the sought-for propagation constants (eigenvalues).

2. STATEMENT OF THE PROBLEM

Consider electromagnetic waves propagating through a homogeneous anisotropic nonmagnetic dielectric layers The permittivity inside the layer depends on modulus of the electric field intensity by arbitrary law. The layer is located between two half-spaces $x < 0$ and $x > h$ in Cartesian coordinate system $Oxyz$. The half-spaces are filled with homogeneous isotropic nonmagnetic media without any sources and have constant permittivities $\underline{\varepsilon}$ and $\overline{\varepsilon}$, respectively ($\underline{\varepsilon}$ and $\overline{\varepsilon}$ are arbitrary real values). Suppose that everywhere $\mu = \mu_0$ is the permeability of free space.

The electromagnetic field $\mathbf{E}$, $\mathbf{H}$ satisfies the Maxwell equations

$$\mathrm{rot}\mathbf{H} = -i\omega\varepsilon\mathbf{E}; \quad \mathrm{rot}\mathbf{E} = i\omega\mu\mathbf{H}, \tag{1}$$

the continuity condition for the tangential field components on the boundaries $x = 0$, $x = h$, and the radiation condition at infinity: the electromagnetic field exponentially decays as $|x| \to \infty$ in the domains $x < 0$ and $x > h$. Here ω is the circular frequency and $\mathbf{E}$, $\mathbf{H}$ are the complex amplitudes [9]. Geometry of the problem is shown in Fig. 1.

The permittivity inside each layer is described by the diagonal tensor

$$\tilde{\varepsilon}_i = \begin{pmatrix} \varepsilon_{xx} & 0 & 0 \\ 0 & \varepsilon_{yy} & 0 \\ 0 & 0 & \varepsilon_{zz} \end{pmatrix},$$

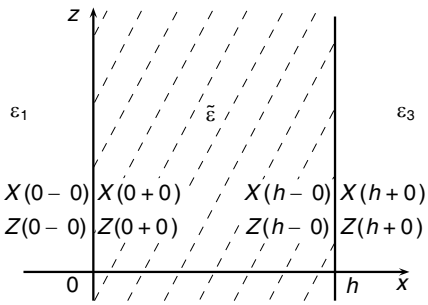

Figure 1: Geometry of the problem.

where $\varepsilon_{xx} = \varepsilon_x + \varepsilon_0 f\left(|E_x|^2, |E_z|^2\right)$ and $\varepsilon_{zz} = \varepsilon_z + \varepsilon_0 g\left(|E_x|^2, |E_z|^2\right)$. Here ε_x, ε_z are constant parts of the permittivities ε_{xx}, ε_{zz}; ε_0 is the permittivity of free space; $f(u, v)$ is a continuously differentiable function w.r.t. both variables, $g(u, v)$ is a continuous function w.r.t. both variables.

Consider TM waves $\mathbf{E} = (E_x, 0, E_z)^T$, $\mathbf{H} = (0, H_y, 0)^T$, where $(\ldots)^T$ is the transposition operation. It is easy to show that the fields components do not depend on y. Waves propagating along the boundaries z depend on z harmonically. So the fields components have the form:

$$E_x = \mathrm{E}_x(x)e^{i\gamma z}, \quad E_z = \mathrm{E}_z(x)e^{i\gamma z}, \quad H_y = \mathrm{H}_y(x)e^{i\gamma z}, \tag{2}$$

where γ is the unknown spectral parameter (propagation constant).

Let $(\ldots)' \equiv \frac{d}{dx}$. Substituting (2) into (1), normalizing accordingly with the formulae $\tilde{x} = kx$, $\frac{d}{dx} = k\frac{d}{d\tilde{x}}$, $\tilde{\gamma} = \frac{\gamma}{k}$, $\tilde{\varepsilon}_x = \frac{\varepsilon_x}{\varepsilon_0}$, $\tilde{\varepsilon}_z = \frac{\varepsilon_z}{\varepsilon_0}$, where $k^2 = \omega^2\mu\varepsilon_0$ with $\mu = \mu_0$, denoting by $Z(\tilde{x}) := \mathrm{E}_z$, $X(\tilde{x}) := i\mathrm{E}_x$ and omitting the tilde we obtain the system (see, for example [4, 10, 11])

$$\begin{cases} -Z'' + \gamma X' = \varepsilon_{zz} Z, \\ -Z' + \gamma X = \gamma^{-1}\varepsilon_{xx} X. \end{cases} \tag{3}$$

It is supposed that

$$\varepsilon = \begin{cases} \underline{\varepsilon}, & x < 0; \\ \tilde{\varepsilon}, & 0 < x < h; \\ \overline{\varepsilon}, & x > h. \end{cases} \tag{4}$$

3. DIFFERENTIAL EQUATIONS IF THE PROBLEM

Denote by $\underline{k}^2 = \gamma^2 - \underline{\varepsilon}$, $\overline{k}^2 = \gamma^2 - \overline{\varepsilon}$.

For the half-space $x < 0$ and $x > h$ we have the permittivity $\varepsilon = \underline{\varepsilon}$ and $\varepsilon = \overline{\varepsilon}$. From formulae (3) and (4) we obtain the linear systems. Its general solutions in according to the condition at infinity are

$$\begin{cases} X(x) = X(0-0)e^{\underline{k}x} \\ Z(x) = \gamma^{-1}\underline{k}X(0-0)e^{\underline{k}x}, \end{cases} \quad \begin{cases} X(x) = X(h+0)e^{-\overline{k}(x-h)} \\ Z(x) = -\gamma^{-1}\overline{k}X(h+0)e^{-\overline{k}(x-h)}, \end{cases} \tag{5}$$

where the constant $X(0-0)$ is supposed to be known (initial condition) and the constant $X(h+0)$ is defined by transmission conditions. From (5) it is easy to see that the inequality $\gamma^2 > \max(\underline{\varepsilon}, \overline{\varepsilon})$ holds.

Inside the layer, where $f'_u = \frac{\partial f}{\partial X^2}$, $f'_v = \frac{\partial f}{\partial Z^2}$, system (3) can be rewritten in the form

$$\begin{cases} \frac{dX}{dx} = \frac{\gamma^2(\varepsilon_z+g)+2(\varepsilon_x-\gamma^2+f)X^2 f'_v}{\gamma(2X^2 f'_u+\varepsilon_x+f)} Z, \\ \frac{dZ}{dx} = \frac{1}{\gamma}\left(\gamma^2 - \varepsilon_x - f\right) X. \end{cases} \tag{6}$$

4. TRANSMISSION CONDITION

Transmission conditions for tangential and normal components of the electromagnetic field imply the following conditions for the functions X and Z

$$[\varepsilon X]|_{x=0} = 0, \quad [\varepsilon X]|_{x=h} = 0, \quad [Z]|_{x=0} = 0, \quad [Z]|_{x=h} = 0, \tag{7}$$

where $[f]|_{x=x_0} = \lim\limits_{x\to x_0-0} f(x) - \lim\limits_{x\to x_0+0} f(x)$.

Definition 1. *The value $\gamma = \overline{\gamma}$ such that nonzero solutions $X(x)$ and $Z(x)$ of system (6) exist under conditions (7), in the half-spaces these solutions are defined by (5) is called an eigenvalue of the problem. The functions $X(x)$ and $Z(x)$ corresponding to the eigenvalue $\gamma = \overline{\gamma}$ are called eigenfunctions of the problem.*

Definition 2. *The conjugation problem in multiply connected domain (problem P_M) is to determine eigenvalues γ such that there are nonzero functions $X(x)$, $Z(x)$ that satisfy the following conditions: if $x < 0$ and $x > h$ then the function X, Z are defined by (5), where $X(0-0)$ is supposed to be known and $X(h+0)$ is defined from transmission conditions (7); if $0 < x < h$ the functions X, Z are solutions of system (6); the functions X, Z satisfy transmission conditions (7).*

We should emphasize that the *problem P_M* depends on the initial condition $X(0-0)$. This is one of the important distinctions between this nonlinear problem and similar linear (if the permittivity inside the layer is constant) problem. The linear problem does not depend on the initial condition.

5. EXISTING OF THE EIGENVALUES

Let P and Q be the right hand-sides of the equations of system (6). Since the solutions of system (3) in the half-spaces $x < 0$ and $x > h$ are known let us go over to the Cauchy problem for nonlinear system (6). Consider system (6) with initial conditions

$$X(0) := X(0+0), \quad Z(0) := Z(0+0), \tag{8}$$

where $X(0+0)$ and $Z(0+0)$ are determined from (7): $X(0+0)$ is a root of the equation $\underline{\varepsilon}X(0-0) = (\varepsilon_x + f(X^2(0+0),\ Z^2(0+0)))X(0+0)$ and $Z(0-0) = Z(0+0)$. As $X(0-0)$ is known, so it is $Z(0-0) = \gamma^{-1}\underline{k}X(0-0)$.

Let $\sqrt{\max(\underline{\varepsilon}, \overline{\varepsilon})} < \gamma_* < \gamma^* < \infty$, $\gamma \in [\gamma_*, \gamma^*]$ and $b_i < \infty$ be a constant. Define the set $\Pi^\gamma := \{(X, Z, \gamma) : |X - X(0+0)| \le b^\gamma, |Z - Z(0+0)| \le b^\gamma, \gamma \in [\gamma_*, \gamma^*]\}$. Let the value M^γ be such that $M^\gamma \ge \max\limits_{\Pi^\gamma} |P|$, $M^\gamma \ge \max\limits_{\Pi^\gamma} |Q|$.

Theorem 1. *The solution $X(x, \gamma)$, $Z(x, \gamma)$ of the Cauchy problem for system (6) with initial conditions (8) exists, this solution is continuously differentiable w.r.t. x, in addition this solution is unique for all $x \in [0, h]$, where $h \le b^\gamma / M^\gamma$ and continuously depends on γ, for all $\gamma \in [\gamma_*, \gamma^*]$.*

From (7) we obtain $(\varepsilon_x + f(h-0))\, X(h-0) = \overline{\varepsilon}X(h+0)$, $Z(h+0) = -\gamma^{-1}\overline{k}X(h+0)$. However the value $X(h+0)$ is an unknown and must be determined. Construct the function

$$F(\gamma) := Z(h-0, \gamma) - Z(h+0, \gamma).$$

Then $F(\gamma) = Z(h-0, \gamma) + \gamma^{-1}\overline{k}X(h+0) = Z(h-0, \gamma) + \overline{\varepsilon}^{-1}\gamma^{-1}\overline{k}\,(\varepsilon_x + f(h-0))\, X(h-0)$. It is easy to see that the value of the function F is calculated through the solution of the Cauchy problem only.

If the value $\gamma = \tilde{\gamma}$ is such that $F(\tilde{\gamma}) = 0$ then $\tilde{\gamma}$ is an eigenvalue of the *problem P_M*.

Theorem 2. *Let the conditions of theorem 1 be satisfied and let the segment $[\underline{\gamma}, \overline{\gamma}] \subset [\gamma_*, \gamma^*]$ be such that $F(\underline{\gamma})F(\overline{\gamma}) < 0$. Then at least one eigenvalue $\tilde{\gamma}$ of the problem P_M exists and $\tilde{\gamma} \in (\underline{\gamma}, \overline{\gamma})$.*

It is easy to describe how to construct a numerical method to determine propagation constants. Let $\gamma \in [\gamma_*, \gamma^*]$. Divide the segment $[\gamma_*, \gamma^*]$ into m pieces. We get the grid $\{\gamma^{(j)}\}$, $j = \overline{0, m}$. Then for each $\gamma^{(j)}$ one must solve a Cauchy problem for system (6) in each layer with initial conditions (8) (initial conditions are defined for each $\gamma^{(j)}$). If there are indexes $0 \ge k < l \le m$ such that $F(\gamma^{(k)})F(\gamma^{(l)}) < 0$ then there is at least one eigenvalue $\tilde{\gamma} \in (\gamma^{(k)}, \gamma^{(l)})$.

Suggested numerical method allows to determine eigenvalues of the considered problem with any prescribed accuracy. With the help of this method the normalized dependence of the propagation constant (normalized by ω^{-1}) γ w.r.t. the layer's thickness (normalized by ω) h will be depicted as well (so called dispersion curve (DC)).

There is an analytical method (*Dispersion Integral Equation Method (DIEM)*) to study such waveguiding problems for a wide range of nonlinearities. However, exact dispersion equations obtained with the help of DIEM are not easy to investigate [4].

6. NUMERICAL EXAMPLE

As an example let us consider a layer and nonlinearity with saturation. We are about to compare linear and nonlinear waveguides. In the case when all 3 media have constant permittivities we can derive exact DE (here for simplicity we consider scalar permittivity inside the layer, for the case of

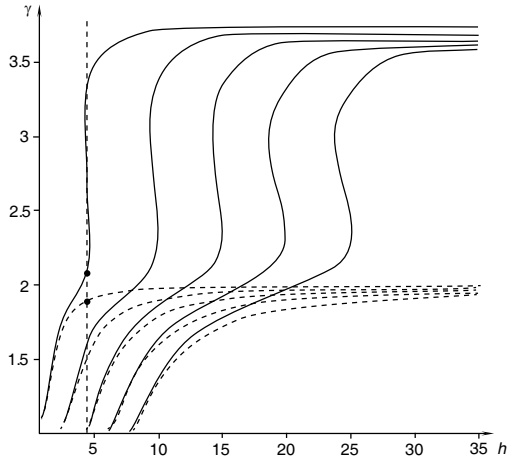

Figure 2: Dispersion curves for the nonlinear (solid) and linear (dashed) problems. The following parameters are used $\underline{\varepsilon} = \overline{\varepsilon} = 1$, $\varepsilon_2 = 3$, $Z(0-0) = 1$, $\alpha = \beta = 0.001$. Horizontal dashed line is the asymptote for the linear DCs. Vertical dashed line corresponds to the layer of thickness $h = 4.4$. Two black circles mark two eigenvalues $\gamma = 1.886$ (linear problem) and $\gamma = 2.075$ (nonlinear problem) correspond to the layer's thickness 4.4.

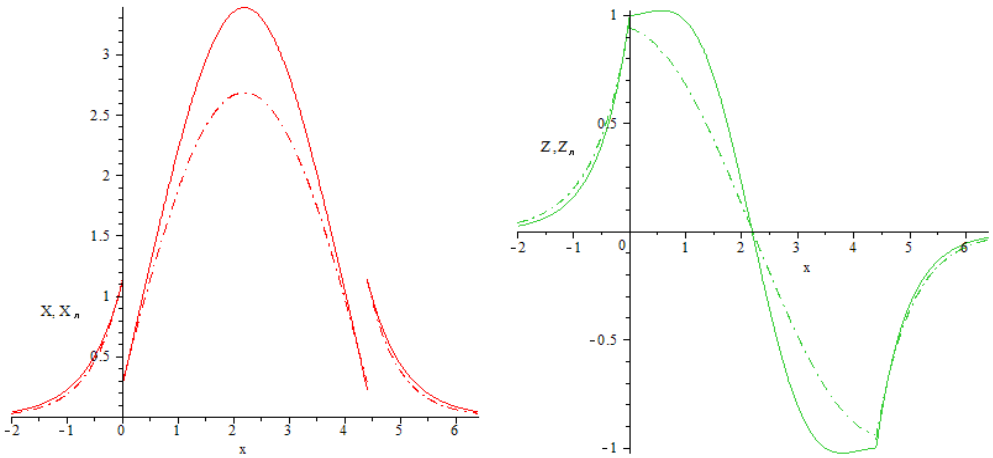

(a) (b)

Figure 3: Eigenfunctions correspond to the marked eigenvalues in Fig. 2. (a) Dashed curve corresponds to X (linear problem) and solid curve corresponds to X (nonlinear problem). (b) Dashed curve corresponds to Z (linear problem) and solid curve corresponds to Z (nonlinear problem). For the linear problem $X(x) = C_1 \sin k_2 x + C_2 \cos k_2 x$, $Z(x) = \gamma^{-1} k_2 (C_1 \cos k_2 x - C_2 \sin k_2 x)$, where $C_1 = 1.678$, $C_2 = 0.285$.

tensor permittivity see, for example, [4]). Here we have no enough space to write down the details of the derivation (see [2], for example). Inside the layer solution of system (5) are expressed in terms of cos and sin. Apply transmission conditions (7) to the solution we can write the DE in the following form (we suppose that $\cos k_2 h \neq 0$)

$$\tan k_2 h = \frac{\varepsilon_2 k_2 (\overline{\varepsilon}\underline{k} + \underline{\varepsilon}\overline{k})}{\underline{\varepsilon}\overline{\varepsilon} k_2^2 - \varepsilon_2^2 \underline{k}\overline{k}}, \tag{9}$$

where the permittivity inside the layer is ε_2 and $k_2^2 = \varepsilon_2 - \gamma^2$.

Some numerical results are presented in Figs. 2, 3. Dispersion curves are shown in Fig. 2. Eigenfunctions are shown in Fig. 3. The nonlinearity inside the layer is described by $\varepsilon = \varepsilon_2 + \frac{\alpha(E_x^2 + E_z^2)}{1 + \beta(E_x^2 + E_z^2)}$, where ε_2 is the constant part of the permittivity ε, α, β are coefficients of the nonlinearity. Dispersion curves for the linear problem are calculated from Equation (9).

Similar results have been already obtained for TE and TM waves and different nonlinearities (see, for example, [10–15]).

7. CONCLUSION

We notice that suggested numerical method is effective to find isolated eigenvalues. Moreover, if $\hat{\gamma}$ is an eigenvalue of the problem. It is easy to understand that the total derivative w.r.t. γ of the function $F(\gamma)$ must not vanish if $\gamma = \hat{\gamma}$.

The numerical method suggested above has several merits:

– the method is rather simple to implement (any known mathsoft can solve Cauchy problems);
– the method allows to determine eigenvalues with any prescribed accuracy;
– the method can be applied to study practically arbitrary nonlinearities;
– suggested approach can be applied to study multilayered nonlinear waveguides.

ACKNOWLEDGMENT

We should like to thank Prof. Yu. G. Smirnov for his advice. The work is partly supported by Russian Federation President Grant (MK-2074.211.1) and the Russian Foundation for Basic Research, project No. 11–07–00330–A.

REFERENCES

1. Akhmediev, N. N. and A. Ankevich, *Solitons, Nonlinear Pulses and Beams*, Chapman and Hall, London, 1997.
2. Adams, M. J., *An Introduction to Optical Waveguides*, John Wiley and Sons, Chichester, NY, Brisbane, Toronto, 1981.
3. Boardman, A. D., et al., "Third-order nonlinear electromagnetics TE and TM guided waves," *Nonlinear Surface Electromagnetic Phenomena*, H.-E. Ponath and G. I. stegeman, Eds., Elsevier Science Publishers B.V., 1991.
4. Smirnov, Y. G. and D. V. Valovik, *Electromagnetic Wave Propagation in Nonlinear Layered Waveguide Structures*, Penza University Press, Penza, 2011.
5. Shürmann, H.-W., V. S. Serov, and Y. V. Shestopalov, *Physical Review E*, Vol. 58, No. 1, 1040–1050, 1998.
6. Joseph, R. I. and D. N. Christodoulides, *Optics Letters*, Vol. 12, No. 10, 826–828, 1987.
7. Leung, K. M., *Physical Review B*, Vol. 44, No. 10, 5007–5012, 1991.
8. Valovik, D. V. and E. V. Zarembo, *Journal of Communications Technology and Electronics*, Approved.
9. Eleonskii, P. N., L. G. Oganes'ants, and V. P. Silin, *Sov. Phys. JETP*, Vol. 35, No. 1, 44–47, 1972.
10. Valovik, D. V. and Y. G. Smirnov, *Journal of Communications Technology and Electronics*, Vol. 56, No. 3, 283–288, 2011.
11. Valovik, D. V., "Electromagnetic TM wave propagation through a nonlinear metamaterial layer with arbitrary nonlinearity," *PIERS Proceedings*, 1676–1680, Kuala Lumpur, Malaysia, Mar. 27–30, 2012.
12. Smirnov, Y. G. and D. V. Valovik, "Nonlinear effects of electromagnetic TM wave propagation in anisotropic layer with kerr nonlinearity," *PIERS Proceedings*, 1670–1675, Kuala Lumpur, Malaysia, Mar. 27–30, 2012.
13. Valovik, D. V., *Journal of Communications Technology and Electronics*, Vol. 56, No. 5, 544–556, 2011.
14. Valovik, D. V., *Journal of Communications Technology and Electronics*, Vol. 56, No. 11, 1311–1316, 2011.
15. Valovik, D. V., "Propagation of TE-waves through a nonlinear metamaterial layer with arbitrary nonlinearity," *PIERS Proceedings*, 193–197, Suzhou, China, Sep. 12–16, 2011.

Electromagnetic TE Wave Propagation in Nonlinear Layered Waveguide Structures. Computational Approach to Determine Propagation Constants

D. V. Valovik
Penza State University, 40 Krasnaya Street, Penza 440026, Russia

Abstract— A plane multilayered waveguide structure is considered. The layers are located between two half-spaces with constant permittivities. The permittivity inside each layer depends on modulus of the electric field intensity by arbitrary law. This structure can be treated as a 1D (nonlinear) photonic crystal [2]. We consider propagation of polarized electromagnetic waves in such a structure. Surface waves are sought for. The physical problem is to determine propagation constants of electromagnetic waves propagating in the waveguide. This problem is reduced to (nonlinear) conjugation eigenvalue problem in a multiply-connected domain. Usually, in such problems, the main goal is to obtain a *dispersion equation* (DE) for propagation constants (eigenvalues). For many physically interesting nonlinear permittivities it is far beyond our abilities to obtain and analyze exact DEs. We suggest a numerical approach to calculate propagation constants (eigenvalues) for (nonlinear) multilayered waveguide structures based on numerical solution of a Cauchy problem in each layer.

1. INTRODUCTION

It is known that exact DEs for plane-layered (including multilayered) waveguides with constant permittivity in each layer can be derived [1]. For one-layer waveguides with constant permittivity in the layer the DE can be completely studied by analytical methods. However for a nonlinear layer such a study can hide a lot of difficulties. When the number of layers is increasing it is getting difficult to find DEs and practically impossible to solve them. In this connection the problem to develop numerical methods for the discussed problems is urgent. In the case of one-layer nonlinear waveguides such numerical methods have been developed (see for example [9]).

2. STATEMENT OF THE PROBLEM

Consider electromagnetic waves propagating through N homogeneous isotropic nonmagnetic dielectric layers. The permittivity in each layer depends on modulus of the electric field intensity by arbitrary law. The layers are located between two half-spaces $x < h_0$ and $x > h_N$ in Cartesian coordinate system $Oxyz$. The half-spaces are filled with homogeneous isotropic nonmagnetic media without any sources and have constant permittivities $\underline{\varepsilon}$ and $\overline{\varepsilon}$, respectively ($\underline{\varepsilon}$ and $\overline{\varepsilon}$ are arbitrary real values). Suppose that everywhere $\mu = \mu_0$ is the permeability of free space.

The electromagnetic field $\mathbf{E}$, $\mathbf{H}$ satisfies the Maxwell equations

$$\mathrm{rot}\mathbf{H} = -i\omega\varepsilon\mathbf{E}; \quad \mathrm{rot}\mathbf{E} = i\omega\mu\mathbf{H}, \tag{1}$$

the continuity condition for the tangential field components on the boundaries $x = h_0$, $x = h_1, \ldots$, $x = h_N$, and the radiation condition at infinity: the electromagnetic field exponentially decays as $|x| \to \infty$ in the domains $x < h_0$ and $x > h_N$. Here ω is the circular frequency and $\mathbf{E}$, $\mathbf{H}$ are the complex amplitudes.

The permittivity inside each layer has the form $\varepsilon = \varepsilon_i + \varepsilon_0 f_i\left(|\mathbf{E}|^2\right)$, $i = \overline{1, N}$, where ε_i is the constant part of the permittivity ε in the ith layer; ε_0 is the permittivity of free space; $f_i(u)$ is a continuous function.

Consider TE waves $\mathbf{E} = (0, E_y, 0)^T$, $\mathbf{H} = (H_x, 0, H_z)^T$, where $(\ldots)^T$ is the transposition operation. It is easy to show that for considered geometry the fields components do not depend on y. Waves propagating along z depend on z harmonically. So the fields components have the form

$$E_y = E_y(x)e^{i\gamma z}, \quad H_x = H_x(x)e^{i\gamma z}, \quad H_z = H_z(x)e^{i\gamma z}, \tag{2}$$

where γ is the unknown spectral parameter (propagation constant).

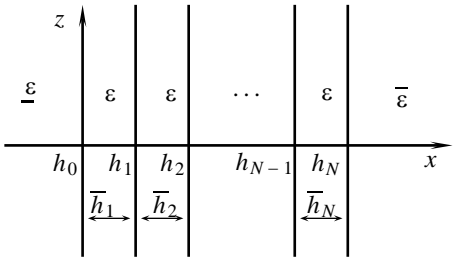

Figure 1: The value h_i denotes the coordinate along x axis, $\overline{h}_i$ denotes the thickness of the ith layer.

Substituting components (2) into (1), normalizing accordingly with the formulae $\tilde{x} = kx$, $\frac{d}{dx} = k\frac{d}{d\tilde{x}}$, $\tilde{\gamma} = \frac{\gamma}{k}$, $\tilde{\varepsilon}_j = \frac{\varepsilon_j}{\varepsilon_0}$, $j = \overline{1,N}$, $\tilde{\varepsilon} = \frac{\varepsilon}{\varepsilon_0}$, $\tilde{\overline{\varepsilon}} = \frac{\overline{\varepsilon}}{\varepsilon_0}$, where $k^2 = \omega^2\mu\varepsilon_0$ with $\mu = \mu_0$, denoting by $E_y(\tilde{x}) \equiv Y(\tilde{x})$ and omitting the tilde, one obtains the equation [3, 5]

$$Y''(x) = \gamma^2 Y(x) - \varepsilon Y(x). \tag{3}$$

It is necessary to find real solutions $Y(x)$ of Equation (3). The value of γ must be real[1] (in order that $|\mathbf{E}|^2$ does not depend on z).

It is supposed that

$$\varepsilon = \begin{cases} \underline{\varepsilon}, & x < h_0; \\ \varepsilon_1 + f_1(Y^2), & h_0 < x < h_1; \\ \cdots & \\ \varepsilon_N + f_N(Y^2), & h_{N-1} < x < h_N; \\ \overline{\varepsilon}, & x > h_N. \end{cases} \tag{4}$$

Geometry of the problem is shown in Fig. 1.

3. DIFFERENTIAL EQUATIONS OF THE PROBLEM

Denote by $\underline{k}^2 = \gamma^2 - \underline{\varepsilon}$, $k_i^2 = \varepsilon_i - \gamma^2$, $i = \overline{1,N}$, $\overline{k}^2 = \gamma^2 - \overline{\varepsilon}$. For the half-spaces $x < h_0$, $x > h_N$ from (3), (4) we obtain linear equations. Its solutions in according to the condition at infinity are

$$Y(x) = \begin{cases} Y(x) = Y(h_0 - 0)e^{\underline{k}(x-h_0)}, & x < h_0 \\ Y(x) = Y(h_N + 0)e^{-\overline{k}(x-h_N)}, & x > h_N. \end{cases} \tag{5}$$

In solutions (5) the constant $Y(h_0 - 0)$ is defined by initial conditions, the constant $Y(h_N + 0)$ is defined by transmission conditions. The inequality $\gamma^2 > \max(\underline{\varepsilon}, \overline{\varepsilon})$ holds (see (5)).

Inside the i-th layer $h_{i-1} < x < h_i$, where $i = \overline{1,N}$ Equation (3) takes the form

$$Y'' = -\left(k_i^2 + f_i(Y^2)\right) Y. \tag{6}$$

4. TRANSMISSION CONDITIONS

Continuity of the tangential components of the electromagnetic field implies the following conditions for the functions Y and Y' (here $[f]|_{x=x_0} = \lim\limits_{x\to x_0-0} f(x) - \lim\limits_{x\to x_0+0} f(x)$)

$$[Y]|_{x=h_i} = 0, \quad \left[Y'\right]\big|_{x=h_i} = 0, \quad i = \overline{0,N}. \tag{7}$$

Definition 1. The value $\gamma = \overline{\gamma}$ such that nonzero solution $Y(x)$ of Equation (6) exists, this solution satisfies (7) and in the half-spaces $x < h_0$ and $x > h_N$ is described by (5) is called an eigenvalue of the problem. The function $Y(x)$ corresponding to the eigenvalue $\gamma = \overline{\gamma}$ is called an eigenfunction of the problem[2].

[1] Let us describe why in this nonlinear problem it is impossible to consider complex values of γ. As $\mathbf{E} = \left(0, E_y(x)e^{i\gamma z}, 0\right) = e^{i\gamma z}(0, E_y(x), 0)$, then $|\mathbf{E}|^2 = |e^{i\gamma z}|^2 \cdot |E_y|^2$. As it is known $|e^{i\gamma z}| = 1$ if $\mathrm{Im}\gamma = 0$. Let $\gamma = \gamma' + i\gamma''$ and $\mathrm{Im}\gamma \neq 0$. Then $|e^{i\gamma z}| = |e^{i\gamma' z}| \cdot |e^{-\gamma'' z}| = e^{-\gamma'' z}$, that is Equation (3) contains the variable z. This means that the function $Y(x)$ therefore the component E_y depend on z. This contradicts the choice of $E_y(x)$. In the linear problem it is possible to consider complex γ.

[2] It is well known that electromagnetic waves in a layer propagate on dedicated frequencies, and there are finite number of such frequencies. Fixed values of the spectral parameter γ correspond to these dedicated frequencies. This situation takes place both for linear cases and nonlinear cases. This is the reason why it is necessary (in the theory and in the applications) to determine eigenvalues γ and eigenfunctions.

Definition 2. The conjugation problem in multiply connected domain (*problem* P_E) is to determine eigenvalues γ such that there are nonzero functions $Y(x)$ that satisfy the following conditions: if $x < h_0$ and $x > h_N$ then the function Y is defined by (5), where $Y(h_0 - 0)$ is supposed to be known and $Y(h_N + 0)$ is defined by (7); if $h_{i-1} < x < h_i$, $i = \overline{1, N}$ the function Y is a solution of Equation (6); the functions Y and Y' satisfy transmission conditions (7)[3].

5. EXISTING OF THE EIGENVALUES

Since the solutions of Equation (3) in the half-spaces $x < h_0$ and $x > h_N$ are known let us go over to the Cauchy problem for nonlinear Equation (6). Rewrite Equation (6) as a system in the normal form. Let $Y_1 := Y$, $Y_2 := Y'$, then

$$\begin{cases} Y_1' = Y_2 \\ Y_2' = -\left(k_i^2 + f\left(Y_1^2\right)\right) Y_1 \end{cases}. \tag{8}$$

Consider system (8) with initial conditions

$$Y_1(h_i + 0) \quad \text{and} \quad Y_2(h_i + 0), \quad i = \overline{0, N-1}. \tag{9}$$

Let $\sqrt{\max(\underline{\varepsilon}, \overline{\varepsilon})} < \gamma_* < \gamma^* < \infty$, $\gamma \in [\gamma_*, \gamma^*]$ and $b_i^\gamma < \infty$ be a constant. For $i = \overline{0, N-1}$ define the sets $\Pi_{i+1}^\gamma := \left\{(Y_1, Y_2, \gamma) : |Y_1 - Y_1(h_i + 0)| \le b_{i+1}^\gamma, |Y_2 - Y_2(h_i + 0)| \le b_{i+1}^\gamma, \gamma \in [\gamma_*, \gamma^*]\right\}$. Let the value M_i^γ be such that $M_i^\gamma \ge \max\limits_{\Pi_i^\gamma} |Y_2|$, $M_i^\gamma \ge \max\limits_{\Pi_i^\gamma} \left|(k_i^2 + f(Y_1^2))Y_1\right|$, $i = \overline{1, N}$.

Theorem 1. The solution $Y_1(x, \gamma)$, $Y_2(x, \gamma)$ of the Cauchy problem for system (8) with initial conditions (9) exists, this solution is continuously differentiable w.r.t. x, in addition this solution is unique for all $x \in [0, h]$, where $h \le b_i^\gamma / M_i^\gamma, i = \overline{1, N}$ and continuously depends on γ, for all $\gamma \in [\gamma_*, \gamma^*]$.

Using transmission conditions (7) we obtain

$$Y_1(h_i - 0, \gamma) = Y_1(h_i + 0, \gamma), \quad Y_2(h_i - 0, \gamma) = Y_2(h_i + 0, \gamma), \tag{10}$$

where $i = \overline{0, N}$. Taking into account formulae (5), (10) we get

$$Y_1(h_N - 0, \gamma) = Y(h_N + 0) \ \text{ and } \ Y_2(h_N - 0, \gamma) = -\overline{k} Y(h_N + 0). \tag{11}$$

On the other hand, the value $Y(h_N + 0)$ is an unknown and must be determined. Let $F(\gamma) := Y_2(h_N - 0, \gamma) - Y_2(h_N + 0, \gamma)$. From the first formula (11) we obtain $Y(h_N + 0) := Y_1(h_N - 0, \gamma)$. Then $F(\gamma) = Y_2(h_N - 0, \gamma) + \overline{k} Y_1(h_N - 0, \gamma)$. If the value $\gamma = \tilde{\gamma}$ is such that $F(\tilde{\gamma}) = 0$ then $\tilde{\gamma}$ is an eigenvalue of the *problem* P_E.

Theorem 2. Let the conditions of theorem 1 be satisfied and let the segment $[\underline{\gamma}, \overline{\gamma}] \subset [\gamma_*, \gamma^*]$ be such that $F(\underline{\gamma}) F(\overline{\gamma}) < 0$. Then at least one eigenvalue $\tilde{\gamma}$ of the *problem* P_E exists and $\tilde{\gamma} \in (\underline{\gamma}, \overline{\gamma})$.

6. NUMERICAL METHOD

The numerical method suggested below allows to determine eigenvalues of the considered problem with any prescribed accuracy. With the help of this method the normalized dependence of the propagation constant (normalized by ω^{-1}) γ w.r.t. the layer's thickness (normalized by ω) h will be depicted as well (so called dispersion curve (DC)).

Let us consider Equation (6). In the first layer $h_0 < x < h_1$ the initial conditions are defined by formulae (9).

Let us suppose that the p-th layer has a variable thickness that is the value h_{p-1} is a constant and the value h_p is varied from h_* to h^*. The thicknesses $\overline{h}_i$ of other layers stay constants for all $i = \overline{1, N}$ except $i = p$ and the values h_i are varied for all $i = \overline{p, N}$ when the value h_p is varied.

Denote by $h := h_p$. Let $0 < h_* < h^* < \infty$ and $\sqrt{\max(\underline{\varepsilon}, \overline{\varepsilon})} < \gamma_* < \gamma^* < \infty$ be constants. Suppose that $h \in [h_*, h^*]$ and $\gamma \in [\gamma_*, \gamma^*]$.

[3] The nonlinear problem under consideration essentially depends on the initial condition $Y(h_0 - 0)$. The similar problem for linear layers (if the permittivity inside each layer is constant) does not depend on the initial condition. This means that in the linear problem the "bundle" of waves with different amplitudes corresponds to each eigenvalue γ. In the nonlinear problem it is not so, eigenvalues depend on amplitudes. This is one of the important differences between these linear and nonlinear problems.

Divide the segments $[h_*, h^*]$ and $[\gamma_*, \gamma^*]$ into n and m pieces respectively. We get the grid $\left\{h^{(i)}, \gamma^{(j)}\right\}$, $i = \overline{0,n}$, $j = \overline{0,m}$; and $h^{(0)} = h_*$, $h^{(n)} = h^*$, $\gamma^{(0)} = \gamma_*$, $\gamma_m = \gamma^*$. Then for each pair of indexes (i, j) we obtain a pair of initial conditions $(Y_{ij}(h_0 + 0), Y'_{ij}(h_0 + 0))$.

Now we can state the Cauchy problem for Equation (6) in the first layer with the initial conditions $Y_{ij}(h_0 + 0)$, $Y'_{ij}(h_0 + 0)$. Solving this problem we obtain the values $Y_{ij}(h_1 - 0) = Y_{ij}(h_1 + 0)$ and $Y'_{ij}(h_1 - 0) = Y'_{ij}(h_1 + 0)$. These values are the initial conditions for Equation (6) in the second layer that is in such a way we state next Cauchy problem. Serially solve the Cauchy problem for each layer we reach the p-th layer. For this layer we have the initial conditions $Y_{ij}(h_{p-1} + 0)$ and $Y'_{ij}(h_{p-1} + 0)$ defined from the solution on the previous layer. Using these initial conditions we state the Cauchy problem for Equation (6) in the p-th layer. Solve this problem we obtain the values $Y_{ij}(h_p - 0) \equiv Y_j(h_p^{(i)} - 0)$ and $Y'_{ij}(h_p - 0) \equiv Y'_j(h_p^{(i)} - 0)$. In the same way as earlier we pass to the next layer and solve a Cauchy problem with the initial conditions defined from the solution on the previous layer. In such a way we reach the final layer. From the solution of the Cauchy problem in the final layer we obtain $Y_{ij}(h_N - 0)$ and $Y'_{ij}(h_N - 0)$. As the function Y is continuous when $x = h_N$ then we can calculate the value $Y_{ij}(h_N + 0) = Y_{ij}(h_N - 0)$. Using the second formula (5) and $Y_{ij}(h_N + 0)$ we can calculate $Y'_{ij}(h_N + 0) = -\sqrt{(\gamma^{(i)})^2 - \overline{\varepsilon}}Y_{ij}(h_N + 0)$. However we know the value $Y'_{ij}(h_N - 0)$ from the solution of the Cauchy problem. Taking into account the continuity of $Y'(x)$ on the boundary $x = h_N$ we construct the function

$$F(\gamma_j) = Y'_{ij}(h_N - 0) - Y'_{ij}(h_N + 0) = Y'_{ij}(h_N - 0) + \sqrt{(\gamma^{(i)})^2 - \overline{\varepsilon}}Y_{ij}(h_N - 0).$$

Function $F(\gamma)$ is a continuous function w.r.t. γ under the assumptions of theorem 1.

Let for given $h_p^{(i)}$ such γ_j and γ_{j+1} exist that $F(\gamma_j)F(\gamma_{j+1}) < 0$. This means that at least one value $\tilde{\gamma}_j \in (\gamma_j, \gamma_{j+1})$ exists and $\tilde{\gamma}_j$ is an eigenvalue of the considered problem. In addition the thicknesses $\overline{h}_1, \ldots, \overline{h}_{p-1}, \overline{h}_p^{(i)}, \overline{h}_{p+1}, \ldots, \overline{h}_N$ correspond to this eigenvalue. The value $\tilde{\gamma}_j$ can be calculated with any prescribed accuracy, for example, by using dichotomy method.

Considered problem for a one-layer waveguide and for Kerr and generalized Kerr nonlinearities can be solved exactly (see [3, 4]): the DE is expressed in elliptic functions. However study of this DE is not an easy problem and will be getting harder with increasing the number of layers.

7. TWO-LAYER WAVEGUIDE. TE WAVES

As an example let us consider two-layer waveguide (to compare with the case of one-layer waveguide see [4–8]. In the case when all 4 media have constant permittivities we can derive exact DE. Here we have no enough space to write down the details of the derivation. Inside the layers solution of Equation (3) are expressed in terms of cos and sin. Apply transmission conditions (7) to the solutions we can write the DEs in any of the following forms (we suppose that $\cos k_1\overline{h}_1 \neq 0$ and $\cos k_2\overline{h}_2 \neq 0$)

$$\tan k_2\overline{h}_2 = \frac{k_2\left[\left(\underline{k}\overline{k} - k_1^2\right)\tan k_1\overline{h}_1 + k_1\left(\underline{k} + \overline{k}\right)\right]}{\left(k_1^2\overline{k} + \underline{k}k_2^2\right)\tan k_1\overline{h}_1 + k_1\left(k_2^2 - \underline{k}\overline{k}\right)}, \quad \tan k_1\overline{h}_1 = \frac{k_1\left[\left(k_2^2 - \underline{k}\overline{k}\right)\tan k_2\overline{h}_2 - k_2\left(\underline{k} + \overline{k}\right)\right]}{k_2\left(\underline{k}\overline{k} - k_1^2\right) - \left(\overline{k}k_1^2 + \underline{k}k_2^2\right)\tan k_2\overline{h}_2}.$$

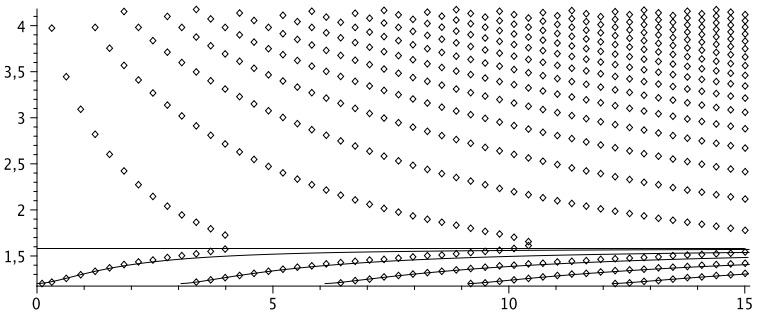

Figure 2: $\underline{\varepsilon} = 1.44$, $\overline{\varepsilon} = 1$, $\varepsilon_1 = 2$, $\varepsilon_2 = 2.5$, $\alpha_1 = 0.01$, $\alpha_2 = 0.02$.

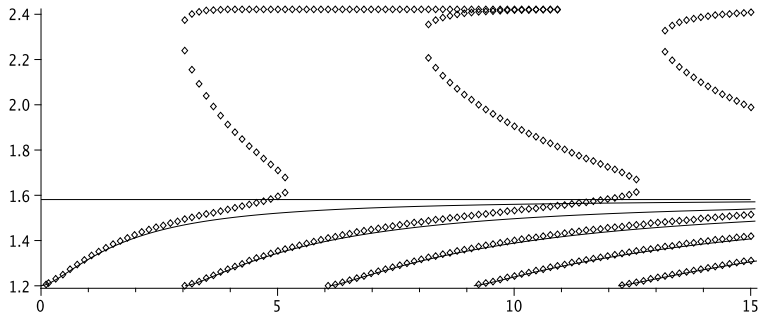

Figure 3: $\underline{\varepsilon} = 1$, $\overline{\varepsilon} = 1.44$, $\varepsilon_1 = 2$, $\varepsilon_2 = 2.5$, $\alpha_1 = 0.03$, $\alpha_2 = 0.01$.

Some numerical results for the two-layer waveguide are presented in Figures 2, 3. For the layers inside the waveguide the permittivities are described by Kerr law $\varepsilon = \varepsilon_1 + \alpha_1 Y^2$ (for the first layer), $\varepsilon = \varepsilon_2 + \alpha_2 Y^2$ (for the second layer). The following parameters are used: $h_0 = 0$, $Y(0-0) = 1$, $\overline{h}_1 = 1$, and $\overline{h}_2$ is varied. In each figure below the vertical axis corresponds to γ, the horizontal axis to h_2. Rhombuses are solutions of the nonlinear problem, lines are solutions of the linear problem ($\alpha_1 = \alpha_2 = 0$, the the latter equations), horizontal line is the asymptote for the linear case.

8. CONCLUSION

We notice that suggested numerical method is effective to find isolated eigenvalues. Moreover, if $\hat{\gamma}$ is an eigenvalue of the problem. It is easy to understand that the total derivative w.r.t. γ of the function $F(\gamma)$ must not vanish if $\gamma = \hat{\gamma}$.

The numerical method suggested above has several merits:

– the method is rather simple to implement (any known mathsoft can solve Cauchy problems);
– the method allows to determine eigenvalues with any prescribed accuracy;
– the method can be applied to study practically arbitrary nonlinearities.

ACKNOWLEDGMENT

I should like to thank Prof. Yu. G. Smirnov for his advice. The work is supported by Russian Federation President Grant (MK-2074.211.1) and the Russian Foundation for Basic Research, project No. 11-07-00330-A.

REFERENCES

1. Adams, M. J., *An Introduction to Optical Waveguides*, John Wiley and Sons, Chichester, NY, Brisbane, Toronto, 1981.
2. Joannopoulos, J. D., S. G. Johnson, J. N. Winn, and R. Meade, *Photonic Crystals: Molding the Flow of Light*, Princeton University Press, Princeton, 2008.
3. Schurmann, H. W., V. S. Serov, and Y. V. Shestopalov, *Phys. Rev. E.*, Vol. 58, No. 1, 1040–1050, 1998.
4. Valovik, D. V., *Journal of Communications Technology and Electronics*, Vol. 56, No. 5, 544–556, 2011.
5. Valovik, D. V., "Propagation of TE-waves through a nonlinear metamaterial layer with arbitrary nonlinearity," *PIERS Proceedings*, 193–197, Suzhou, China, Sep. 12–16, 2011.
6. Valovik, D. V., *Computational Mathematics and Mathematical Physics*, Vol. 51, No. 9, 1622–1632, 2011.
7. Valovik, D. V., *Journal of Communications Technology and Electronics*, Vol. 56, No. 11, 1311–1316, 2011.
8. Valovik, D. V., "Electromagnetic TM wave propagation through a nonlinear metamaterial layer with arbitrary nonlinearity," *PIERS Proceedings*, 1676–1680, Kuala Lumpur, Malaysia, Mar. 27–30, 2012.
9. Valovik, D. V. and E. V. Zarembo, *Journal of Communications Technology and Electronics*, Approved.

Electromagnetic Wave Diffraction on the Conducting Thin Screen Placed on the Isotropic and Anisotropic Media Interface

A. F. Bourganov, E. M. Karchevskiy, and N. B. Pleshchinskii
Kazan Federal University, Russia

Abstract— The over-determined boundary value problem method in the diffraction electromagnetic waves theory is extended to the case of anisotropic media. The solvability conditions of the over-determined boundary value problems for Maxwell equations set in the anisotropic semi-space are obtained in the case of one-axis anisotropy. The representations of solutions of Maxwell equations set by traces of tangential components of the field on the boundary of domain are constructed. The problem on reflection and refraction of the electromagnetic wave on the isotropic and anisotropic media interface is considered. The integral equation is obtained to determine field perturbation of conducting thin screen placed at the media interface.

1. INTRODUCTION

The diffraction problems for the electromagnetic waves on the conducting thin screens belong to classic problems of electrodynamics [1]. By potentials of special form such problems are reduced to integral equations either with weak singularity or to hyper-singular equations. The over-determined boundary value problem method [2] offers to pass from boundary value problems for Helmholtz equation in two-dimensional case or for the Maxwell equations set in the general case to equivalent to them integral equations. By this fundamental solutions or Green functions for the layered medium are not used. In the works [3, 4] the integral equations of different types were obtained to which the electromagnetic wave diffraction problem on the thin screen in isotropic medium is reduced. In the present work, the case is considered when the conducting thin screen is placed on the isotropic and anisotropic media interface.

2. OVER-DETERMINED BOUNDARY VALUE PROBLEM IN THE CASE OF ANISOTROPIC MEDIA

Consider the Maxwell equations set for complex amplitudes E and H of the electric and magnetic vectors of the electromagnetic field harmonically dependent on time

$$\operatorname{rot} H = i\omega\varepsilon E, \quad \operatorname{rot} E = -i\omega\mu H \tag{1}$$

in the upper half-space $z > 0$. Let the traces of tangent components E and H be given on the plane $z = 0$ and

$$[z_0, E](x, y, 0) = e(x, y), \quad [z_0, H](x, y, 0) = h(x, y). \tag{2}$$

This problem is the over-determined one because boundary functions in conditions (2) cannot be given arbitrary.

We call the solution E, H of Maxwell equations set in the domain $z > 0$ outgoing into a half-space if each of its components is the distribution of slow growth not containing harmonics which transfer the energy on infinity (the radiation condition) and the traces (2) are defined correctly in classic sense or in generalized sense.

Let k be a wave number, $k^2 = \omega^2\mu\varepsilon$. Denote

$$\gamma(\xi, \eta) = \left\{\xi^2 + \eta^2 \geq k^2 : i\sqrt{\xi^2 + \eta^2 - k^2};\ \ \xi^2 + \eta^2 \leq k^2 : \sqrt{k^2 - \xi^2 - \eta^2}\right\}.$$

Vector-functions E, H are the solution of the problem (1), (2) in the class of solutions outgoing into the half-space if and only if, when [5] the equality for the Fourier transforms of traces of their components on the plane $z = 0$

$$\begin{aligned} \omega\varepsilon\gamma(\xi, \eta)e_x(\xi, \eta) + \xi\eta h_x(\xi, \eta) + (k^2 - \xi^2)h_y(\xi, \eta) = 0, \\ -\omega\mu\gamma(\xi, \eta)h_x(\xi, \eta)\xi\eta e_x(\xi, \eta) + (k^2 - \xi^2)e_y(\xi, \eta) = 0. \end{aligned} \tag{3}$$

is fulfilled.

In the case of analogues statements for the solutions of the problem outgoing into the lower half-space $z < 0$ one should change a sign of the function $\gamma(\xi, \eta)$ in formulas (3).

3. MAXWELL EQUATIONS SET IN THE ANISOTROPIC SEMI-SPACE

Consider Maxwell equations set

$$\operatorname{rot} H = i\omega\bar{\varepsilon}\, E, \quad \operatorname{rot} E = -i\omega\bar{\mu}\, H \tag{4}$$

in the case when dielectric constant $\bar{\varepsilon}$ is a tensor and permeance $\bar{\mu} = \mu$ is a scalar. To simplify reasoning we will consider only the case of diagonal anisotropy when

$$\bar{\varepsilon} = \varepsilon \begin{pmatrix} \alpha & 0 & 0 \\ 0 & \beta & 0 \\ 0 & 0 & 1 \end{pmatrix}.$$

Let, as well as before, $k^2 = \omega^2\mu\varepsilon$.

Let us redefine the unknown solutions of boundary value problem by zero in the lower semi-plane and consider them as distributions of slow growth at infinity. Let us pass in Equation (4) from classic derivatives to generalized ones and apply the Fourier integral transformation by all variables: $x, y, z \to \xi, \eta, \zeta$. We will use the same denotations for Fourier transforms and for their prototypes.

If we exclude normal components E_z, H_z from obtained equations then we get for Fourier transforms of tangent components a set of four equations in the vector-matrix form

$$\begin{pmatrix} \xi\eta & k^2\beta - \xi^2 \\ \eta^2 - k^2\alpha & -\xi\eta \end{pmatrix} \begin{pmatrix} E_x \\ E_y \end{pmatrix} + \omega\mu\zeta \begin{pmatrix} H_x \\ H_y \end{pmatrix} = i\omega\mu \begin{pmatrix} h_x \\ h_y \end{pmatrix},$$
$$\omega\varepsilon\zeta \begin{pmatrix} E_x \\ E_y \end{pmatrix} - \begin{pmatrix} \xi\eta & k^2 - \xi^2 \\ \eta^2 - k^2 & -\xi\eta \end{pmatrix} \begin{pmatrix} H_x \\ H_y \end{pmatrix} = i\omega\varepsilon \begin{pmatrix} e_x \\ e_y \end{pmatrix}.$$

By this the tangent components of vector E should satisfy equations

$$k^2 \begin{pmatrix} \zeta^2 + \alpha\xi^2 + \eta^2 - k^2\alpha & (\beta - 1)\,\xi\eta \\ (\alpha - 1)\,\xi\eta & \zeta^2 + \xi^2 + \beta\eta^2 - k^2\beta \end{pmatrix} \begin{pmatrix} E_x \\ E_y \end{pmatrix}$$
$$= ik^2\zeta \begin{pmatrix} e_x \\ e_y \end{pmatrix} + i\omega\mu \begin{pmatrix} \xi\eta & k^2 - \xi^2 \\ \eta^2 - k^2 & -\xi\eta \end{pmatrix} \begin{pmatrix} h_x \\ h_y \end{pmatrix}. \tag{5}$$

The determinant of coefficients matrix of this set of equations

$$\Delta = k^4\Big\{\zeta^4 - \left[(\alpha+\beta)k^2 - (1+\alpha)\xi^2 - (1+\beta)\eta^2\right]\zeta^2 + \left(k^2 - \xi^2 - \eta^2\right)\left(\alpha\beta k^2 - \alpha\xi^2 - \beta\eta^2\right)\Big\}$$

can be easily decomposed into multipliers by additional supposition that anisotropy is one-axis, i.e., two of three diagonal elements of matrix are equal, either $\alpha = 1$, or $\alpha = \beta$. By this two first particular cases differ from each other not essentially.

Let us consider the first variant of one-axis anisotropy.

Let $\beta = 1$. Denote by $\gamma_1^2 = k^2 - \xi^2 - \eta^2$, $\gamma_2^2 = \alpha k^2 - \alpha\xi^2 - \eta^2$, by this $\Delta = k^4(\zeta^2 - \gamma_1^2)(\zeta^2 - \gamma_2^2)$. Assume that roots of these complex-valued expressions are extracted in such way that values $\gamma_1 = \gamma_1(\xi, \eta)$ and $\gamma_2 = \gamma_2(\xi, \eta)$ are either negative real numbers or pure imaginary numbers with positive imagine part.

Set of Equation (5) splits into two independent equations of the form

$$\left(\zeta^2 - \gamma_2^2\right)\omega\varepsilon E_x = i\,\varphi_1(\zeta), \quad (\alpha - 1)\xi\eta\,\omega\varepsilon E_x + \left(\zeta^2 - \gamma_1^2\right)\omega\varepsilon E_y = i\,\varphi_2(\zeta). \tag{6}$$

The right-side parts of these equations contain the Fourier transforms of boundary functions.

By theorem Paley-Wiener solutions of Equation (6) should be analytically continued to the upper semi-plane of the complex plane by variable ζ. In addition, boundary functions should be such that after inverse Fourier transformation these solutions should contain no harmonics coming from infinity.

Consequently, distributions $E_x, E_y, E_z, H_x, H_y, H_z$ are the solutions of the boundary value problem (4), (2) for upper semi-space in case of one-axis anisotropy of the first type and satisfy the radiation condition if and only if when conditions

$$\omega\varepsilon\gamma_2 e_x + \xi\eta h_x + \left(k^2 - \xi^2\right)h_y = 0, \qquad -\omega\mu\gamma_1 h_x + \xi\eta e_x + \left(k^2 - \xi^2\right)e_y = 0. \tag{7}$$

are fulfilled for Fourier transforms of boundary functions. By this the Fourier transforms of the unknown distributions

$$\begin{aligned}
&E_x = \frac{i}{\zeta+\gamma_2}\,e_x, \qquad E_y = \frac{i}{\zeta+\gamma_1}\,\frac{\omega\mu\gamma_1}{k^2-\xi^2}\,h_x - \frac{i}{\zeta+\gamma_2}\,\frac{\xi\eta}{k^2-\xi^2}\,e_x,\\
&H_x = \frac{i}{\zeta+\gamma_1}\,h_x, \qquad H_y = -\frac{i}{\zeta+\gamma_1}\,\frac{\xi\eta}{k^2-\xi^2}\,h_x - \frac{i}{\zeta+\gamma_2}\,\frac{\omega\varepsilon\gamma_2}{k^2-\xi^2}\,e_x,\\
&E_z = \frac{i}{\zeta+\gamma_1}\,\frac{\omega\mu\eta}{k^2-\xi^2}\,h_x + \frac{i}{\zeta+\gamma_2}\,\frac{\xi\gamma_2}{k^2-\xi^2}e_x, \qquad H_z = \frac{i}{\zeta+\gamma_1}\,\frac{\xi\gamma_1}{k^2-\xi^2}\,h_x - \frac{i}{\zeta+\gamma_2}\,\frac{\omega\varepsilon\eta}{k^2-\xi^2}e_x.
\end{aligned} \tag{8}$$

For $\alpha = \beta$ (the second variant of one-axis anisotropy) the analogous statement takes place. Distributions $E_x,\ E_y,\ E_z, H_x,\ H_y,\ H_z$ are the solutions of the boundary value problem (4), (2) for upper semi-space in case of one-axis anisotropy of the second type and satisfy the radiation condition if and only if when conditions

$$\gamma_1(\eta\cdot e_x - \xi\cdot e_y) + \omega\mu(\xi\cdot h_x + \eta\cdot h_y) = 0, \qquad \alpha\omega\varepsilon(\xi\cdot e_x + \eta\cdot e_y) - \gamma_2(\eta\cdot h_x - \xi\cdot h_y) = 0, \tag{9}$$

are fulfilled for Fourier transforms of boundary functions. Here $\gamma_1^2 = k^2-\xi^2-\eta^2$, $\gamma_2^2 = \alpha k^2 - \alpha\xi^2 - \eta^2$.

It is easy to show that in the limiting case the solvability conditions (7) and (9) coincide with conditions (3).

4. REFLECTION AND REFRACTION OF WAVES ON THE MEDIA INTERFACE

Let us consider the reflection and refraction problem of electromagnetic waves coming from infinity on isotropic and anisotropic media interface. We should seek a solution of the Maxwell equations set (1) in the lower semi-space and of the Maxwell equations set (4) in the upper semi-space in class of outgoing to infinity solutions satisfying by $z = 0$ the conjugation conditions

$$\left[z_0, E^+ - E^-\right](x,y) = a(x,y), \qquad \left[z_0, H^+ - H^-\right](x,y) = b(x,y). \tag{10}$$

Here the given vector-functions $a(x,y)$ and $b(x,y)$ are the differences of tangent components of electric and of magnetic wave vectors coming to plane $z = 0$ from below and from above. Sign $+$ is valid for upper anisotropic semi-space of the first type and sign $-$ is valid for lower isotropic semi-space.

Problem (1), (4), (10) is a jump problem. Its solution can be considered as a potential of special form which is convenient to use for investigating the electromagnetic wave diffraction problem on a thin conducting screen.

To determine the Fourier transforms of traces of unknown waves we have a set of linear algebraic equations consisting of the solvability conditions for the over-determined problem in the upper semi-space of the form (7)

$$\omega\varepsilon^+\gamma_2^+\cdot e_x^+ + \xi\eta\cdot h_x^+ + \left(k_+^2-\xi^2\right)\cdot h_y^+ = 0, \qquad -\omega\mu\gamma_1^+\cdot h_x^+ + \xi\eta\cdot e_x^+ + \left(k_+^2-\xi^2\right)\cdot e_y^+ = 0,$$

of the solvability conditions for the over-determined problem in the lower semi-space of the form (3)

$$-\omega\varepsilon^-\gamma^-\cdot e_x^- + \xi\eta\cdot h_x^- + \left(k_-^2-\xi^2\right)\cdot h_y^- = 0, \qquad -\omega\mu\gamma^-\cdot h_x^- + \xi\eta\cdot e_x^- + \left(k_-^2-\xi^2\right)\cdot e_y^- = 0,$$

and of conditions of the jump problem (10)

$$e_x^+ - e_x^- = a_x, \quad e_y^+ - e_y^- = a_y, \quad h_x^+ - h_x^- = b_x, \quad h_y^+ - h_y^- = b_y.$$

Solution of this problem can be written down in the explicit form. To get solution of the set of Equation (4) for $z > 0$, it is necessary to substitute expressions of distributions $e_x^+,\ e_y^+,\ h_x^+,\ h_y^+$ into formulas (8) and to carry out the inverse Fourier transformation. To get solution of the set of Equation (1) for $z < 0$, it is necessary to substitute expressions $e_x^-,\ e_y^-,\ h_x^-,\ h_y^-$ into analogous formulas and also to carry out the inverse Fourier transformation.

5. WAVE DIFFRACTION ON THE PLANE SCREEN

Let $\mathcal{M}$ be a conducting thin screen placed in the plane $z = 0$, and $\mathcal{N}$ be its complement to complete plane. Let (E_0^-, H_0^-) be the electromagnetic wave falling down on a screen from isotropic lower semi-space. The diffraction wave problem on a plane screen consists of the following.

It is necessary to seek solutions of set of Equation (1) for $z < 0$ and of set of Equation (4) for $z > 0$ in class of outgoing to infinity solutions satisfying for $z = 0$ conditions

$$\begin{aligned} [z_0, E^+](x,y) &= 0, \quad [z_0, E^- + E_0^-](x,y) = 0, && (x,y) \in \mathcal{M}, \\ [z_0, E^+ - E^- - E_0^-](x,y) &= 0, \quad [z_0, H^+ - H^- - H_0^-](x,y) = 0, && (x,y) \in \mathcal{N}. \end{aligned}$$

We will seek a solution $(E^\pm, H^\pm)$ of the diffraction problem in the form of a sum of two addends. First addend $(E_1^\pm, H_1^\pm)$ is a solution of the reflection and refraction wave problem on the media interface without screen, it can be found as a solution of a jump problem for $a(x,y) = e_0^-(x,y),\ b(x,y) = h_0^-(x,y)$.

Second addend $(E_2^\pm, H_2^\pm)$ is a perturbation from a screen. We will seek it in the form of a solution of a jump problem also. By this $a(x,y) = 0$ everywhere, $b(x,y) = 0$ on $\mathcal{N}$. Vector-function $b(x,y)$ on $\mathcal{M}$ should be found by conditions

$$e_{2,x}^+ = -e_{1,x}^+, \qquad e_{2,y}^+ = -e_{1,y}^+ \quad \text{on} \quad \mathcal{M} \tag{11}$$

or by analogous conditions for traces of tangential components of vector E_2^-.

The expressions of the functions $e_{2,x}^+$ and $e_{2,y}^+$ can be found from complete set of equations of a jump problem. Let us pass in these formulas to prototypes of distribution $b(\xi, \eta)$. Then we obtain the set of integral equations to determine field perturbation from screen.

ACKNOWLEDGMENT

Supported by RFBR 12-01-97012-r-povolzh'e-a.

REFERENCES

1. Hönl, H., A. W. Maue, and K. Westpfahl, *Theorie der Beugung*, Springer-Verlag, Berlin, 1961.
2. Pleshchinskaya, I. E. and N. B. Pleshchinskii, "Over-determined boundary value problems for elliptic partial differential equations and their application to waves diffraction theory," *Uchenye Zapiski Kazanskogo Gosudarstvennogo Universiteta*, Vol. 147, No. 3, 41–32, 2005 (in Russian).
3. Pleshchinskaya, I. E. and N. B. Pleshchinskii, "The over-determined Cauchy problems for the Maxwell equations set and electromagnetic waves diffraction on the metallic screens," *Conf. Proc. 11th Int. Conf. Mathematical Methods in Electromagnetic Theory MMET*06*, 255–257, Kharkov, Ukraine, Jun. 2006.
4. Pleshchinskii, N. B., I. E. Pleshchinskaya, and E. M. Karchevskiy, "The over-determined boundary value problem method in the electromagnetic waves propagation and diffraction theory," *PIERS Proceedings*, 132–1136, Moscow, Russia, Aug. 18–21, 2009.

Parallel Algorithm of Solving the Electromagnetic Wave Diffraction Problem on the Spherical Screen

E. M. Karchevskiy and N. B. Pleshchinskii
Kazan Federal University, Russia

Abstract— The electromagnetic wave diffraction problem on a thin conducting spherical screen is reduced to pair summatorial equation relative to unknown coefficients of expansion into a series of spherical waves. This equation can be transformed to a regular infinite set of linear algebraic equations by integral-summatorial identities method. For all stages of numerical algorithm of solving the problem the parallel calculating processes are possible. At first, if field traces of outside source at the sphere are decomposed onto magnetic and electric parts, then magnetic and electric parts of the unknown field can be found independently. Secondly, if coefficients of field conjugation conditions at the sphere do not depend on longitude coordinate, then calculations also can be fulfilled independently for every number of the series coefficients. Thirdly, if by reduction of infinite set the finite set of linear equations of large dimension is obtained, then it can be solved by one of parallel algorithms. But the most effect can be obtained just at the stage of calculating the auxiliary integrals over screen.

1. INTRODUCTION

The electromagnetic wave diffraction problem on the conducting thin screen is formulated as the boundary value problem for Maxwell equations set. If screen is a part of spherical surface then it is expediently to seek a solution of Maxwell equations in the spherical system of coordinates. In this case it is possible to represent general solution of these equations as an expansion into a series by spherical harmonics. It is necessary to find indeterminate coefficients of expansion in such way that the corresponding boundary conditions and conjugation conditions are fulfilled on a screen and on the remaining part of sphere. In the classical case of the diffraction problem on a complete sphere (see, for example, [1]) these coefficients are found in explicit form. In the case when screen has an arbitrary spherical form the set of equations for determining unknown values becomes rather difficult. Its numerical solving needs large calculating resources.

The purpose of the present work is to determine steps at which the calculating algorithm can be divided into independent subproblems and then realized on the multiprocessor calculating complex.

2. THE FORMULATION OF THE DIFFRACTION PROBLEM

Suppose an infinitely thin ideally conducting plate $\mathcal{M}$ (a screen) is placed in the space and is a part of sphere with radius R. Denote by $\mathcal{N}$ the remaining part of sphere $\mathcal{S}$. It is possible to assume in the general case that media properties are different inside sphere and outside of it. But to simplify reasoning, we assume that space is filled by homogeneous isotropic medium.

Suppose there is a source generating harmonic electromagnetic wave outside of screen. We should seek a field appearing by diffraction of this wave on a screen.

The mathematical formulation of the diffraction problem consists of the following. We should seek solutions of Maxwell equations set (complex amplitudes) inside sphere and outside of it

$$\operatorname{rot} H = i\omega\varepsilon_0\varepsilon\, E, \quad \operatorname{rot} E = -i\omega\mu_0\mu\, H$$

(it is assumed that dependence of field components on time has the form $e^{i\omega t}$). By this solutions should satisfy conditions at infinity, boundary conditions on $\mathcal{M}$ and conjugation conditions on $\mathcal{N}$. Boundary conditions and conjugation conditions are standard: tangent components of vector E vanish on the conducting surface and tangent components of vector E and H are continuous on the two media interface. Conditions at the infinity will be formulated later.

We choose the spherical coordinates system (r, θ, α), $\theta \in [0, \pi]$ is a latitude, $\alpha \in [0, 2\pi]$ is a longitude. In the plane of variables α and θ development of sphere is a rectangle.

3. MAXWELL EQUATIONS IN THE SPHERICAL COORDINATES SYSTEM

Maxwell equations set in the spherical coordinates system is a set of six equations with partial derivatives with respect to six complex-valued functions E_r, E_θ, E_α, H_r, H_θ, H_α by three spatial

variables. Each of the unknown functions can be decomposed (in any domain bounded by spheres with center in the origin of coordinates) into Fourier series by variable α of the form

$$A(r,\theta,\alpha) = \sum_{m=-\infty}^{+\infty} A_m(r,\theta)e^{im\alpha},$$

which converges in the classical (or in the generalized) sense. Set of equations for the Fourier coefficients with number m (to simplify formulas this number is not shown) has the form

$$\begin{aligned}
\frac{\partial(\sin\theta\, H_\alpha)}{\partial\theta} - im\, H_\theta &= i\omega\varepsilon_0\varepsilon\, r\sin\theta\cdot E_r, & \frac{\partial(\sin\theta\, E_\alpha)}{\partial\theta} - im\, E_\theta &= -i\omega\mu_0\mu\, r\sin\theta\cdot H_r,\\
im\, H_r - \sin\theta\,\frac{\partial(r\, H_\alpha)}{\partial r} &= i\omega\varepsilon_0\varepsilon\, r\sin\theta\cdot E_\theta, & im\, E_r - \sin\theta\,\frac{\partial(r\, E_\alpha)}{\partial r} &= -i\omega\mu_0\mu\, r\sin\theta\cdot H_\theta,\\
\frac{\partial(r\, H_\theta)}{\partial r} - \frac{\partial H_r}{\partial\theta} &= i\omega\varepsilon_0\varepsilon\, r\, E_\alpha, & \frac{\partial(r\, E_\theta)}{\partial r} - \frac{\partial E_r}{\partial\theta} &= -i\omega\mu_0\mu\, r\, H_\alpha.
\end{aligned}$$

If boundary conditions and conjugation conditions in the diffraction problem can be divided into independent conditions for the Fourier coefficients of field components also, then this problem splits into set of independent subproblems. At this stage *first possibility* of paralleling of algorithm appears.

Second possibility is connected with the fact that any solution of the set of Equation (2) can be represented as a sum of two partial solutions: of magnetic type for $E_r = 0$ and of electric type for $H_r = 0$.

We have for magnetic field by

$$\begin{aligned}
E_r &= 0, & E_\theta &= \frac{\omega\mu_0\mu m}{\sin\theta}\, u, & E_\alpha &= i\omega\mu_0\mu\,\frac{\partial u}{\partial\theta},\\
H_r &= \Big(\frac{\partial^2(r\, u)}{\partial r^2} + k^2 r\, u\Big), & H_\theta &= \frac{1}{r}\,\frac{\partial^2(r\, u)}{\partial\theta\,\partial r}, & H_\alpha &= \frac{im}{r\sin\theta}\,\frac{\partial(r\, u)}{\partial r},
\end{aligned}$$

where u being a potential function. This function should satisfy the potential equation

$$r\,\frac{\partial^2(r\, u)}{\partial r^2} + \frac{1}{\sin\theta}\,\frac{\partial}{\partial\theta}\Big(\sin\theta\,\frac{\partial u}{\partial\theta}\Big) + \Big(k^2r^2 - \frac{m^2}{\sin^2\theta}\Big)\, u = 0.$$

Potential function v of electric field should satisfy just the same equation, by this field components

$$\begin{aligned}
E_r &= \Big(\frac{\partial^2(r\, v)}{\partial r^2} + k^2 r\, v\Big), & E_\theta &= \frac{1}{r}\,\frac{\partial^2(r\, v)}{\partial\theta\,\partial r}, & E_\alpha &= \frac{im}{r\sin\theta}\,\frac{\partial(r\, v)}{\partial r},\\
H_r &= 0, & H_\theta &= -\frac{\omega\varepsilon_0\varepsilon m}{\sin\theta}\, v, & H_\alpha &= -i\omega\varepsilon_0\varepsilon\,\frac{\partial v}{\partial\theta}.
\end{aligned}$$

4. AXIS SYMMETRICAL FIELD

Suppose that components of electromagnetic field do not dependent on the coordinate α. For $m = 0$ set of Equation (2) has the form

$$\begin{aligned}
\frac{\partial(\sin\theta\, H_\alpha)}{\partial\theta} &= i\omega\varepsilon_0\varepsilon\, r\sin\theta\cdot E_r, & \frac{\partial(\sin\theta\, E_\alpha)}{\partial\theta} &= -i\omega\mu_0\mu\, r\sin\theta\cdot H_r,\\
-\frac{\partial(r\, H_\alpha)}{\partial r} &= i\omega\varepsilon_0\varepsilon\, r\, E_\theta, & -\frac{\partial(r\, E_\alpha)}{\partial r} &= -i\omega\mu_0\mu\, r\, H_\theta,\\
\frac{\partial(r\, H_\theta)}{\partial r} - \frac{\partial H_r}{\partial\theta} &= i\omega\varepsilon_0\varepsilon\, r\, E_\alpha, & \frac{\partial(r\, E_\theta)}{\partial r} - \frac{\partial E_r}{\partial\theta} &= -i\omega\mu_0\mu\, r\, H_\alpha.
\end{aligned}$$

This set of equations splits into two independent subsystems and any its solution can be written down as a sum of two partial solutions as it was in the case $m \neq 0$.

When we consider the axis symmetrical problem, it is convenient to choose another potential functions. The potential function u of magnetic field should satisfy equation

$$r\,\frac{\partial^2(ru)}{\partial r^2} + \frac{\partial}{\partial\theta}\left(\frac{1}{\sin\theta}\,\frac{\partial(\sin\theta\cdot u)}{\partial\theta}\right) + k^2r^2\, u = 0,$$

the potential function v of electric field should satisfy just the same equation. The complete field components are expressed by two potential functions in the following way:

$$E_\alpha = u, \qquad H_r = \frac{-1}{i\omega\mu_0\mu}\frac{1}{r\sin\theta}\frac{\partial(\sin\theta\cdot u)}{\partial\theta}, \qquad H_\theta = \frac{1}{i\omega\mu_0\mu}\frac{1}{r}\frac{\partial(ru)}{\partial r},$$
$$H_\alpha = v, \qquad E_r = \frac{1}{i\omega\varepsilon_0\varepsilon}\frac{1}{r\sin\theta}\frac{\partial(\sin\theta\cdot v)}{\partial\theta}, \qquad E_\theta = \frac{-1}{i\omega\varepsilon_0\varepsilon}\frac{1}{r}\frac{\partial(rv)}{\partial r}.$$

It is easy to find partial solutions of potential equations by Fourier method:

$$u_n(r,\theta) = \frac{1}{\sqrt{kr}}Z_{n+1/2}(kr)\,\Theta_n(\theta), \qquad \Theta_n(\theta) = \text{const}\,P_n^{(1)}(\cos\theta), \quad n = 1, 2, \ldots$$

here $Z_{n+1/2}(\cdot)$ are cylindrical functions (solutions of Bessel equations) and $P_n^{(1)}(\cdot)$ are joint Legendre functions. We choose constant multipliers in such way that functions $\Theta_n(\theta)$ should be normalized with weight $\sin\theta$ on segment $[0,\pi]$.

Let us consider the diffraction problem for axis symmetrical wave at the ring spherical screen $\theta_1 < \theta < \theta_2$. We have for a wave being generated by exterior source, for $r > R$ and for $r < R$

$$u^0(r,\theta) = \sum_{n=1}^{+\infty}\left[\overrightarrow{u}^0_n\frac{1}{\sqrt{kr}}H^{(2)}_{n+1/2}(kr) + \overleftarrow{u}^0_n\frac{1}{\sqrt{kr}}H^{(1)}_{n+1/2}(kr)\right]\Theta_n(\theta),$$
$$v^0(r,\theta) = \sum_{n=1}^{+\infty}\left[\overrightarrow{v}^0_n\frac{1}{\sqrt{kr}}H^{(2)}_{n+1/2}(kr) + \overleftarrow{v}^0_n\frac{1}{\sqrt{kr}}H^{(1)}_{n+1/2}(kr)\right]\Theta_n(\theta).$$

It is assumed that this wave can contain both spherical harmonics coming from infinity and harmonics outgoing to infinity.

Outgoing from sphere waves determine potential functions

$$u^-(r,\theta) = \sum_{n=1}^{+\infty}\overrightarrow{u}^-_n\frac{1}{\sqrt{kr}}H^{(2)}_{n+1/2}(kr)\,\Theta_n(\theta), \qquad v^-(r,\theta) = \sum_{n=1}^{+\infty}\overrightarrow{v}^-_n\frac{1}{\sqrt{kr}}H^{(2)}_{n+1/2}(kr)\,\Theta_n(\theta).$$

The unknown potential field functions inside sphere have the form

$$u^+(r,\theta) = \sum_{n=1}^{+\infty}u^+_n\frac{1}{\sqrt{kr}}J_{n+1/2}(kr)\,\Theta_n(\theta), \qquad v^+(r,\theta) = \sum_{n=1}^{+\infty}v^+_n\frac{1}{\sqrt{kr}}J_{n+1/2}(kr)\,\Theta_n(\theta).$$

5. REGULAR SLAE OF THE DIFFRACTION PROBLEM

It is easy to see that boundary conditions and conjugation conditions on a sphere (for $r = R$) are independent for magnetic field and for electric field. Consider problem for magnetic field. Functions u and $\dfrac{\partial u}{\partial r}$ should be continuous on $\mathcal{N}$, i.e., conditions $u^- = u^+$ and $\dfrac{\partial u^-}{\partial r} = \dfrac{\partial u^+}{\partial r}$ should fulfill, and conditions $u^0 + u^- = 0$ and $u^0 + u^+ = 0$ should fulfill on a screen $\mathcal{M}$.

Note that field from exterior source is given in the whole space, i.e., both inside sphere and outside of it. In the case when spherical surface $r = R$ is a media interface (screen is placed on the surface of the dielectric ball), the diffraction problem should be solved in two stages. At first, it is necessary to find a solution of the reflection (and refraction) problem for given wave from the ball, and then it is necessary to pass to the problem on perturbation of founded in the whole space field by conducting thin screen.

By conditions for $r = R$ it follows that for all n

$$\overrightarrow{u}^-_n\,H^{(2)}_{n+1/2}(kR) = u^+_n\,J_{n+1/2}(kR) = c_n,$$

here c_n are new unknown coefficients. These coefficients should satisfy pair summatorial equation

$$\sum_{n=1}^{+\infty}c_n\,\Theta_n(\theta) = -\sum_{n=1}^{+\infty}\left[\overrightarrow{u}^0_n\,H^{(2)}_{n+1/2}(kR) + \overleftarrow{u}^0_n\,H^{(1)}_{n+1/2}(kR)\right]\Theta_n(\theta), \quad \theta\in\mathcal{M},$$
$$\sum_{n=1}^{+\infty}\gamma_n\,c_n\,\Theta_n(\theta) = 0, \quad \theta\in\mathcal{N}, \qquad \gamma_n = \frac{[H^{(2)}_{n+1/2}]'(kR)}{H^{(2)}_{n+1/2}(kR)} - \frac{[J_{n+1/2}]'(kR)}{J_{n+1/2}(kR)}.$$

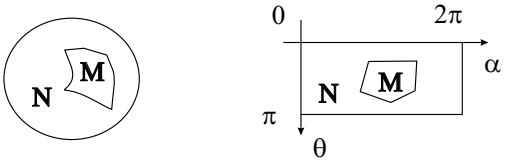

Figure 1: A screen on a sphere and a development of sphere.

Here $\mathcal{M} = [\theta_1, \theta_2]$ and $\mathcal{N}$ is a segment, supplementing $\mathcal{M}$ up to $[0, \pi]$.

This pair equation can be transformed into regular infinite set of linear algebraic equations by integral-summatorial identities [2, 3].

Third possibility of paralleling is the algorithm of solving SLAE, which appears by reduction method.

6. GENERAL CASE

In the case when $m \neq 0$, magnetic and electric potential functions are expressed by cylindrical and joint Legendre functions also,

$$u_n(r, \theta) = \frac{1}{\sqrt{kr}} Z_{n+1/2}(kr)\, P_n^{(m)}(\cos\theta), \quad n \geq |m|.$$

Radial multipliers are chosen in correspondence with required wave orientation. In the case of outgoing from sphere to infinity waves Hankel functions of the 2-nd kind are used, and for coming waves Hankel functions of the 1-nd kind are used. Both these functions should be present in the unknown field inside sphere. Moreover, they should have equal coefficients (as there are no sources of field inside sphere, so only standing waves can exist there).

In general case unknown coefficients of field decomposition have two indexes: m, n. But in the case when plane wave run into the spherical screen

$$E^0 = x_0\, Ae^{-ikz}, \qquad H^0 = y_0\, \frac{A}{W} e^{-ikz},$$

it is necessary to consider only two values of parameter m: $m = -1$, $m = 1$.

In a difference from axis symmetrical case, if the exterior field is only magnetic or only electric wave, then the unknown field contains both magnetic and electric components. Some simplification is possible only in the case when spherical screen is a ring or a spherical segment. To such screens at variables plane α, θ (see Fig. 1) correspond strips $\theta_1 < \theta < \theta_2$ and $\alpha_1 < \alpha < \alpha_2$.

The numerical experiment has shown that the most economy effect of calculating resources is obtained by parallel calculating coefficients of SLAE of the form

$$I_{m,n;p,q} = \iint_{\mathcal{M}} \sin\theta\, S_{m,n}(\theta, \alpha)\, S_{p,q}(\theta, \alpha)\, d\theta\, d\alpha,$$

where $S_{m,n}(\theta, \alpha)$ are spherical functions. This is *fourth possibility* of paralleling of algorithm.

ACKNOWLEDGMENT

Supported by RFBR 12-01-97012-r-povolzh'e-a.

REFERENCES

1. Morse, P. M. and H. Feshbach, *Methods of Theoretical Physics*, Vol. 2, McGraw-Hill Book Company, New York, 1953.
2. Pleshchinskaya, I. E. and N. B. Pleshchinskii, "Over-determined boundary value problems for elliptic partial differential equations and their application to waves diffraction theory," *Uchenye Zapiski Kazanskogo Gosudarstvennogo Universiteta*, Vol. 147, No. 3, 41–32, 2005 (in Russian).
3. Pleshchinskii, N. B., *Models and Methods of Waveguided Electrodynamics*, Kazan State Uuversity, Kazan, 2008 (in Russian).

Integral Equation Methods in Optical Waveguide Theory

A. S. Il'inskii[1] **and E. M. Karchevskiy**[2]

[1]Lomonosov Moscow State University, Russia
[2]Kazan Federal University, Russia

Abstract— The eigenvalue problems for generalized natural modes of an inhomogeneous dielectric waveguide without a sharp boundary and a step-index dielectric waveguide with smooth boundary of cross-section are formulated as problems for the set of time-harmonic Maxwell equations with partial radiation conditions (Sveshnikov radiation conditions) at infinity in the cross-sectional plane. The original problems by integral equations method are reduced to nonlinear spectral problems with Fredholm integral operators. Theorems on spectrum localization are proved, and then it is proved that the sets of all eigenvalues of the original problems can only be some sets of isolated points on the Reimann surface, ant it also proved that each eigenvalue depends continuously on the frequency and dielectric permittivity and can appear and disappear only at the boundary of the Reimann surface. The Galerkin method for numerical calculations of the generalized natural modes are proposed, and the convergence of the method is proved. Some results of numerical experiments are discussed.

1. INTRODUCTION

Optical fibers are dielectric waveguides (DWs), i.e., regular dielectric rods, having various cross sectional shapes, and where generally the dielectric permittivity may vary in the waveguide's cross section [1]. Although existing technologies often result in a dielectric permittivity that is anisotropic, frequently it is possible to assume that the fiber is isotropic [2], which is the case investigated in this work. The study of the source-free electromagnetic fields, called natural modes, that can propagate on DWs necessitates that longitudinally the rod extend to infinity. Since often DWs are not shielded, the medium surrounding the waveguide transversely forms an unbounded domain, typically taken to be free space. This fact plays an extremely important role in the mathematical analysis of natural waveguide modes, and brings into consideration a variety of possible formulations. Each different formulation can be cast as an eigenvalue problem for the set of time-harmonic Maxwell equations, but they differ in the form of the condition imposed at infinity in the cross-sectional plane, and hence in the functional class of the natural-mode field. This also restricts the localization of the eigenvalues in the complex plane of the eigenparameter [3]. All of the known natural-mode solutions (i.e., surface guided modes, leaky modes, and complex modes) satisfy the partial radiation conditions at infinity (see, for example, [4]), which firstly were originally introduced by A. G. Sveshnikov [5] for a scattering problem. The partial radiation conditions in waveguiding problems are connected with the fact that propagation constants β may be complex and may be generally considered on the appropriate logarithmic Reimann surface [6]. For real propagation constants on the principal ("proper") sheet of this Reimann surface, one can reduce the partial radiation conditions to either the Sommerfeld radiation condition or to the condition of exponential decay. The partial radiation conditions may be considered as a generalization of the Sommerfeld radiation condition and can be applied for complex propagation constants. This conditions may also be considered as the continuation of the Sommerfeld radiation condition from a part of the real axis of the complex parameter β to the appropriate logarithmic Reimann surface [7].

2. GENERALIZED NATURAL MODES OF A STEP-INDEX DIELECTRIC WAVEGUIDE

Let the three-dimensional space be occupied by an isotropic source-free medium, and let the dielectric permittivity be prescribed as a positive real-valued function $\varepsilon = \varepsilon(x)$ independent of the longitudinal coordinate and equal to a constant $\varepsilon_\infty > 0$ outside a cylinder. In this section we consider the generalized natural modes of an step-index optical fiber and suppose that the dielectric permittivity is equal to a constant $\varepsilon_+ > \varepsilon_\infty$ inside the cylinder. The axis of the cylinder is parallel to the longitudinal coordinate, and its cross section is a bounded domain Ω_i with a twice continuously differentiable boundary γ (see Fig. 1). The domain Ω_i is a subset of a circle with radius R_0. Denote by Ω_e the unbounded domain $\Omega_e = \mathbb{R}^2 \backslash \overline{\Omega}_i$. Denote by U the space of complex-valued continuous and continuously differentiable in $\overline{\Omega}_i$ and $\overline{\Omega}_e$, twice continuously differentiable in Ω_i and Ω_e functions. Denote by Λ the Riemann surface of the function $\ln \chi_\infty(\beta)$, where $\chi_\infty = \sqrt{k^2\varepsilon_\infty - \beta^2}$.

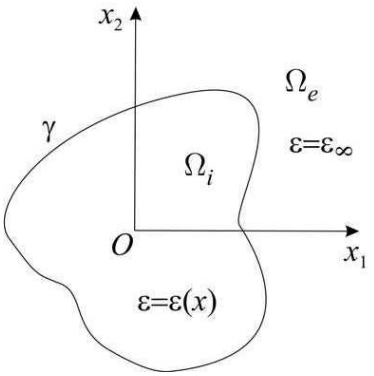

Figure 1: A schematic waveguide's cross-section.

Here $k^2 = \omega^2\varepsilon_0\mu_0$, ω is a given radian frequency; ε_0, μ_0 are the free-space dielectric and magnetic constants, respectively. Denote by Λ_0 the principal ("proper") sheet of this Riemann surface, which is specified by the condition $\mathrm{Im}\chi_\infty(\beta) \geq 0$.

A nonzero vector $\{\mathrm{E}, \mathrm{H}\} \in U^6$ is referred to as generalized eigenvector (or eigenmode) of the problem corresponding to an eigenvalue $\beta \in \Lambda$ if the following relations are valid [8]:

$$\mathrm{rot}_\beta \mathrm{E} = i\omega\mu_0 \mathrm{H}, \quad \mathrm{rot}_\beta \mathrm{H} = -i\omega\varepsilon_0\varepsilon \mathrm{E}, \quad x \in \mathbb{R}^2 \setminus \gamma, \tag{1}$$

$$\nu \times \mathrm{E}^+ = \nu \times \mathrm{E}^-, \quad x \in \gamma, \tag{2}$$

$$\nu \times \mathrm{H}^+ = \nu \times \mathrm{H}^-, \quad x \in \gamma, \tag{3}$$

$$\begin{bmatrix} \mathrm{E} \\ \mathrm{H} \end{bmatrix} = \sum_{l=-\infty}^{\infty} \begin{bmatrix} \mathrm{A}_l \\ \mathrm{B}_l \end{bmatrix} H_l^{(1)}(\chi_\infty r) \exp(il\varphi), \quad r \geq R_0. \tag{4}$$

Here differential operator rot_β is obtained from usual operator by replacing generating waveguide line derivative with $i\beta$ multiplication; and $H_l^{(1)}(z)$ is the Hankel function of the first kind and index l. The conditions (4) are the the partial radiation conditions.

Theorem 1 (see [8]). *The imaginary axis $\mathbb{I}$ and the real axis $\mathbb{R}$ of the sheet Λ_0 except the set $G = \{\beta \in \mathbb{R}: \ k^2\varepsilon_\infty < \beta^2 < k^2\varepsilon_+\}$ are free of the eigenvalues of the problem (1)–(4). Surface and complex eigenmodes correspond to real eigenvalues $\beta \in G$ and complex eigenvalues $\beta \in \Lambda_0$, respectively. Leaky eigenmodes correspond to complex eigenvalues β belonging to an "improper" sheet of Λ for which $\mathrm{Im}\chi_\infty(\beta) < 0$.*

The results of the theorem 1 generalize the well known results on the spectrum localization of the step-index circular dielectric waveguide, which were obtained by separation of variables method (see, for example, [9]).

We use the representation of the eigenvectors of problem (1)–(4) in the form of the single-layer potentials u and v:

$$\mathrm{E}_1 = \frac{i}{k^2\varepsilon - \beta^2}\left(\mu_0\omega\frac{\partial v}{\partial x_2} + \beta\frac{\partial u}{\partial x_1}\right), \quad \mathrm{E}_2 = \frac{-i}{k^2\varepsilon - \beta^2}\left(\mu_0\omega\frac{\partial v}{\partial x_1} - \beta\frac{\partial u}{\partial x_2}\right), \quad \mathrm{E}_3 = u, \tag{5}$$

$$\mathrm{H}_1 = \frac{i}{k^2\varepsilon - \beta^2}\left(\beta\frac{\partial v}{\partial x_1} - \varepsilon_0\varepsilon\omega\frac{\partial u}{\partial x_2}\right), \quad \mathrm{H}_2 = \frac{i}{k^2\varepsilon - \beta^2}\left(\beta\frac{\partial v}{\partial x_2} + \varepsilon_0\varepsilon\omega\frac{\partial u}{\partial x_1}\right), \quad \mathrm{H}_3 = v, \tag{6}$$

$$\begin{bmatrix} u(x) \\ v(x) \end{bmatrix} = \frac{i}{4}\int_\gamma H_0^{(1)}\left(\sqrt{k^2\varepsilon_{+/\infty} - \beta^2}\,|x-y|\right)\begin{bmatrix} f_{+/\infty}(y) \\ g_{+/\infty}(y) \end{bmatrix} dl(y), \quad x \in \Omega_{i/e}, \tag{7}$$

where unknown densities $f_{+/\infty}$ and $g_{+/\infty}$ belong to the space of Hölder continuous functions $C^{0,\alpha}$. The original problem (1)–(4) by single-layer potential representation (5)–(7) is reduced [8] to a nonlinear eigenvalue problem for a set of singular integral equations at the boundary γ. This problem has the operator form

$$A(\beta)w \equiv (I + B(\beta))w = 0, \tag{8}$$

where I is the identical operator in the Banach space $W = (C^{0,\alpha})^4$ and $B(\beta)$: $W \to W$ is a compact operator consists particularly of the following boundary singular integral operators:

$$Lp = -\frac{1}{2\pi}\int_0^{2\pi} \ln\left|\sin\frac{t-\tau}{2}\right| p(\tau)d\tau, \quad t \in [0, 2\pi], \quad L\colon C^{0,\alpha} \to C^{1,\alpha}, \tag{9}$$

$$Sp = \frac{1}{2\pi}\int_0^{2\pi} \operatorname{ctg}\frac{\tau-t}{2} p(\tau)d\tau + \frac{i}{2\pi}\int_0^{2\pi} p(\tau)d\tau, \quad t \in [0, 2\pi], \quad \mathrm{S}\colon C^{0,\alpha} \to C^{0,\alpha}. \tag{10}$$

The original problem (1)–(4) is spectrally equivalent [8] to the problem (8). Namely, suppose that $w \in W$ is an eigenvector of the operator-valued function $A(\beta)$ corresponding to an eigenvalue $\beta \in \Lambda_0 \setminus D$, $D = \{\beta \in \mathbb{I}\} \cup \{\beta \in \mathbb{R}\colon\ \beta^2 < k^2\varepsilon_\infty\}$. Then using this vector we can construct the densities of the single-layer potential representation (5)–(7) of an eigenmode $\{\mathrm{E}, \mathrm{H}\} \in U^6$ of the problem (1)–(4), corresponding to the same eigenvalue β. For other side, any eigenmode of the problem (1)–(4), corresponding to an eigenvalue $\beta \in \Lambda_0 \setminus D$ can be represented in the form of single-layer potentials. The densities of this potentials construct an eigenvector $w \in W$ of the operator-valued function $A(\beta)$ corresponding to the same eigenvalue β.

Theorem 2 (see [8]). *For each $\beta \in \{\beta \in \mathbb{R}\colon\ \beta^2 \geq k^2\varepsilon_+\}$ the operator $A(\beta)$ has the bounded inverse operator. The set of all eigenvalues β of the operator-valued function $A(\beta)$ can be only a set of isolated points on Λ. Each eigenvalue β depends continuously on $\omega > 0$, $\varepsilon_+ > 0$, and $\varepsilon_\infty > 0$ and can appear and disappear only at the boundary of Λ, i.e., at $\beta = \pm k\sqrt{\varepsilon_\infty}$ and at infinity.*

The results of the theorem 2 generalize the well known results on the dependence of the propagation constants β of the step-index circular dielectric waveguide on the wave number k and dielectric permittivity ε (see, for example, [9]).

3. GENERALIZED NATURAL MODES OF AN INHOMOGENEOUS WAVEGUIDE

In this section, we consider the generalized natural modes of an inhomogeneous optical fiber without a sharp boundary. Let the dielectric permittivity ε belongs to the space $C^2(\mathbb{R}^2)$ of twice continuously differentiable in $\mathbb{R}^2$ functions. Denote by ε_+ the maximum of the function ε in the domain Ω_i, let $\varepsilon_+ > \varepsilon_\infty > 0$. A nonzero complex vector $\{\mathrm{E}, \mathrm{H}\} \in (C^2(\mathbb{R}^2))^6$ is referred to as generalized eigenvector (or eigenmode) of the problem corresponding to an eigenvalue $\beta \in \Lambda$ if the following relations are valid [3]:

$$\mathrm{rot}_\beta \mathrm{E} = i\omega\mu_0 \mathrm{H}, \quad \mathrm{rot}_\beta \mathrm{H} = -i\omega\varepsilon_0\varepsilon \mathrm{E}, \quad x \in \mathbb{R}^2, \tag{11}$$

$$\begin{bmatrix} \mathrm{E} \\ \mathrm{H} \end{bmatrix} = \sum_{l=-\infty}^{\infty} \begin{bmatrix} \mathrm{A}_l \\ \mathrm{B}_l \end{bmatrix} H_l^{(1)}(\chi_\infty r) \exp(il\varphi), \quad r \geq R_0. \tag{12}$$

Theorem 3 (see [3]). *The imaginary axis $\mathbb{I}$ and the real axis $\mathbb{R}$ of the sheet Λ_0 except the set $G = \{\beta \in \mathbb{R}\colon\ k^2\varepsilon_\infty < \beta^2 < k^2\varepsilon_+\}$ are free of the eigenvalues of the problem (11), (12). Surface and complex eigenmodes correspond to real eigenvalues $\beta \in G$ and complex eigenvalues $\beta \in \Lambda_0$, respectively. Leaky eigenmodes correspond to complex eigenvalues β belonging to an "improper" sheet of Λ for which $\mathrm{Im}\chi_\infty(\beta) < 0$.*

If vector $\{\mathrm{E}, \mathrm{H}\} \in (C^2(\mathbb{R}^2))^6$ is an eigenvector of problem (11), (12) corresponding to an eigenvalue $\beta \in \Lambda$, then (see [3])

$$\mathrm{E}(x) = k^2 \int_{\Omega_i} (\varepsilon(y) - \varepsilon_\infty)\Phi(\beta; x, y)\mathrm{E}(y)dy + \mathrm{grad}_\beta \int_{\Omega_i} \left(\mathrm{E}, \varepsilon^{-1}\mathrm{grad}\varepsilon\right)(y)\Phi(\beta; x, y)dy, \quad x \in \mathbb{R}^2, \tag{13}$$

$$\mathrm{H}(x) = -i\omega\varepsilon_0 \mathrm{rot}_\beta \int_{\Omega_i} (\varepsilon(y) - \varepsilon_\infty)\Phi(\beta; x, y)\mathrm{E}(y)dy, \quad x \in \mathbb{R}^2. \tag{14}$$

Using the integral representation (13) for $x \in \Omega_i$ we obtain a nonlinear eigenvalue problem for integral equation on the domain Ω_i. This problem has the operator form

$$A(\beta)\mathrm{F} \equiv (I - B(\beta))\mathrm{F} = 0, \tag{15}$$

where the operator $B(\beta)$: $(L_2(\Omega_i))^3 \to (L_2(\Omega_i))^3$ satisfies the right side of the integral representation (13) for $x \in \Omega_i$. For any $\beta \in \Lambda$ the operator $B(\beta)$ is compact [3].

It was proved in the paper [3] that the original problem (11), (12) is spectrally equivalent to problem (15). Namely, suppose that $\{\mathrm{E}, \mathrm{H}\} \in (C^2(\mathbb{R}^2))^6$ is an eigenmode of problem (11), (12) corresponding to an eigenvalue $\beta \in \Lambda$. Then $\mathrm{F} = \mathrm{E} \in [L_2(\Omega_i)]^3$ is an eigenvector of the operator-valued function $A(\beta)$ corresponding to the same eigenvalue β. Suppose that $\mathrm{F} \in [L_2(\Omega_i)]^3$ is an eigenvector of the operator-valued function $A(\beta)$ corresponding to an eigenvalue $\beta \in \Lambda$, and also suppose that the same number β is not an eigenvalue of the following problem:

$$\left[\Delta + \left(k^2\varepsilon - \beta^2\right)\right] u = 0, \quad x \in \mathbb{R}^2, \quad u \in C^2(\mathbb{R}^2), \tag{16}$$

$$u = \sum_{l=-\infty}^{\infty} a_l H_l^{(1)}\left(\chi_\infty r\right) \exp\left(il\varphi\right), \quad r \geq R_0. \tag{17}$$

Let $\mathrm{E} = B(\beta)\mathrm{F}$ and $\mathrm{H} = (i\omega\mu_0)^{-1}\mathrm{rot}_\beta \mathrm{E}$ for $x \in \mathbb{R}^2$. Then $\{\mathrm{E}, \mathrm{H}\} \in (C^2(\mathbb{R}^2))^6$, and $\{\mathrm{E}, \mathrm{H}\}$ is an eigenvector of the original problem (11), (12) corresponding to the same eigenvalue β.

Theorem 4 (see [3]). *For each $\beta \in \{\beta \in \mathbb{R}\colon \beta^2 \geq k^2\varepsilon_+\}$ the operator $A(\beta)$ has the bounded inverse operator. The set of all eigenvalues β of the operator-valued function $A(\beta)$ can be only a set of isolated points on Λ. Each eigenvalue β depends continuously on $\omega > 0$, $\varepsilon_+ > 0$, and $\varepsilon_\infty > 0$ and can appear and disappear only at the boundary of Λ, i.e., at $\beta = \pm k\sqrt{\varepsilon_\infty}$ and at infinity.*

4. NUMERICAL METHOD

Describe a projection method for numerical solution of the problem (8). Denote by N the set of integers. We use the representation of the approximate eigenvector of the operator-valued function $A(\beta)$ in the form

$$w_n = \left(w_n^{(j)}\right)_{j=1}^4, \quad w_n^{(j)}(t) = \sum_{k=-n}^{n} \alpha_k^{(j)} \exp(ikt), \quad n \in N, \quad j = 1, 2, 3, 4. \tag{18}$$

We look for unknown coefficients $\alpha_k^{(j)}$ by Galerkin method

$$\int_0^{2\pi} (Aw_n)^{(j)}(t) \exp\left(-ikt\right) dt = 0, \quad k = -n, \ldots, n, \quad j = 1, 2, 3, 4. \tag{19}$$

The trigonometric functions $\exp(ikt)$ are the orthogonal eigenfunctions of the singular integral operators L: $C^{0,\alpha} \to C^{1,\alpha}$ and S: $C^{0,\alpha} \to C^{0,\alpha}$, corresponding to the following eigenvalues:

$$\lambda_m^{(L)} = \{\ln 2 \text{ if } m = 0,\ (2|m|)^{-1} \text{ if } m \neq 0\},$$
$$\lambda_m^{(S)} = \{i \text{ if } m = 0,\ i\,\mathrm{sign}(m) \text{ if } m \neq 0\}$$

for the operators L and S respectively. Hence, the action of the main (singular) parts of the integral operators in (8) on the basis functions is expressed in the explicit form.

Denote by W_n^T the set of all trigonometric polynomials of the orders up to n. Denote by $W_n \subset W$ the space of the elements $w_n = (w_n^{(j)})_{j=1}^4$, where $w_n^{(j)} \in W_n^T$. Using the Galerkin method for numerical solution of the problem (8), we get finite-dimensional nonlinear spectral problem

$$A_n(\beta) w_n = 0, \quad A_n\colon W_n \to W_n. \tag{20}$$

Theorem 5 (see [10]). *If β_0 belongs to the spectrum $\sigma(A)$ of the operator-valued function $A(\beta)$, then there exists some sequence $\{\beta_n\}_{n\in N}$ with $\beta_n \in \sigma(A_n)$, that $\beta_n \to \beta_0$, $n \in N$. If $\{\beta_n\}_{n\in N}$ is a sequence such that $\beta_n \in \sigma(A_n)$ and $\beta_n \to \beta_0 \in \Lambda$, then $\beta_0 \in \sigma(A)$. If $\beta_n \in \sigma(A_n)$, $A_n(\beta_n)w_n = 0$, and $\beta_n \to \beta_0 \in \Lambda$, $w_n \to w_0$, $n \in N$, $\|w_n\| = 1$ then $\beta_0 \in \sigma(A)$ and $A(\beta_0)w_0 = 0$, $\|w_0\| = 1$.*

Figure 2 shows the dispersion curves for the complex modes (on the left) and for the surface guided modes (on the right) of the step-index waveguides of circular and square cross-section. The numerical results obtained by Galerkin method marked by circles and by squares on the left of the Fig. 2. The dispersion curves for circular waveguide are plotted here by solid line, $\widetilde{\beta} = \beta/(k\sqrt{\varepsilon_\infty})$ and $V = kR\sqrt{\varepsilon_+ - \varepsilon_\infty}$. The right side of the Fig. 2 compares the experimental data [11] for surface waves of square waveguide (marked by squares) with our numerical results (solid lines). Here a is a half of the square's side.

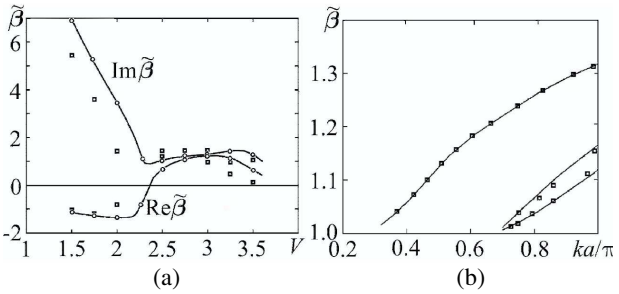

Figure 2: The dispersion curves for (a) the complex modes and (b) surface guided modes of the step-index waveguides of circular and square cross-section.

ACKNOWLEDGMENT

Supported by RFBR 12-01-97012-r-povolzh'e-a.

REFERENCES

1. Marcuse, D., *Theory of Dielectric Optical Waveguides*, Academic Press, New York, 1974.
2. Snyder, A. W. and D. Love, *Optical Waveguide Theory*, Chapman and Hall, London, 1983.
3. Kartchevski, E. M., A. I. Nosich, and G. W. Hanson, "Mathematical analysis of the generalized natural modes of an inhomogeneous optical fiber," *SIAM J. Appl. Math.*, Vol. 65, No. 6, 2033–2048, 2005.
4. Dautov, R. Z. and E. M. Karchevskii, *Integral Equations Method and Exact Nonlocal Boundary Conditions in the Theory of Dielectric Waveguides*, Kazan State University, Kazan, 2009 (in Russian).
5. Sveshnikov, A. G., "The principle of limit absorption for a waveguide," *Dokl. AN SSSR*, Vol. 80, No. 3, 345-347, 1951 (in Russian).
6. Il'inskii, A. S. and Yu. V. Shestopalov, *Application of the Methods of Spectral Theory in the Problems of Wave Propagation*, Moscow State University Press, Moscow, 1989 (in Russian).
7. Shestopalov, Yu. V., Yu. G. Smirnov, and E. V. Chernokozhin, *Logarithmic Integral Equations in Electromagnetics*, VSP, Leiden, The Netherlands, 2000.
8. Karchevskii, E. M., "The fundamental wave problem for cylindrical dielectric waveuides," *Differential Equations*, Vol. 36, 1109–1111, 2000.
9. Veselov, G. N. and S. B. Raevskiy, *Layered Metal-Dielectric Waveguides*, Radio i Sviaz', Moscow, 1988 (in Russian).
10. Karchevskii, E. M., "Mathematical analysis and numerical modeling of the guided modes of the step-index optical fibers," *SIAM J. Appl. Math.*, Vol. 102, 414–419, 2000.
11. Goncharenko, A. M. and V. A. Karpenko, *The Foundations of the Theory of Optical Waveguides*, Nauka i Tekhnika, Minsk, 1983 (in Russian).

TM Wave Propagation in a Cylindrical Waveguide with Kerr Nonlinearity

Yu. G. Smirnov
Penza State University, 40 Krasnaya Street, Penza 440026, Russia

Abstract— We consider three-dimensional space filled by isotropic medium with constant permittivity. In this medium a circle cylindrical waveguide is placed. The waveguide is filled by isotropic nonmagnetic nonlinear medium with Kerr nonlinearity. We consider electromagnetic TM waves propagating along the waveguide axis, that is eigenmodes of the structure.

The problem is reduced to the nonlinear eigenvalue problem for system of integral equations. The iteration method to calculate approximate eigenvalues of the boundary problem is formulated. Existence and convergence (the approximate solution to the exact one) theorems are proved also.

1. STATEMENT OF THE PROBLEM

Let us consider three-dimensional space $\mathbb{R}^3$ with Cartesian coordinate system $Oxyz$. The space is filled by isotropic medium with constant permittivity $\varepsilon \geq \varepsilon_0$, where ε_0 is the permittivity of free space. In this medium a circle cylindrical waveguide is placed. The waveguide is filled by isotropic nonmagnetic medium. The waveguide has cross section $W := \left\{(x, y)\colon x^2 + y^2 < R^2\right\}$ and its generating line (the waveguide axis) is parallel to the axis Oz. We shall consider electromagnetic waves propagating along the waveguide axis, that is eigenmodes of the structure.

Let us consider also cylindrical coordinate system $O\rho\varphi z$ and axis Oz of cylindrical coordinate system coincides with axis Oz of Cartesian coordinate system.

Electromagnetic field depends harmonically on time.

Electromagnetic field $(\mathbf{E}, \mathbf{H})$ satisfies the Maxwell equations

$$\begin{aligned} &\mathrm{rot}\mathbf{H} = -i\omega\varepsilon\mathbf{E}, \\ &\mathrm{rot}\mathbf{E} = i\omega\mu\mathbf{H}, \end{aligned} \tag{1}$$

the continuity condition for the tangential components on the media interfaces (on the boundary of the waveguide) and the radiation condition at infinity: the electromagnetic field exponentially decays as $\rho \to \infty$.

The permittivity inside the waveguide is described by Kerr law

$$\varepsilon = \varepsilon_0 \left(\varepsilon_2 + \alpha|\mathbf{E}|^2\right),$$

where ε_2 is a constant part of the permittivity, α is the nonlinearity coefficient. The values ε_2 and α are supposed to be real constants.

It is necessary to find surface waves propagating along the waveguide axis [1–3].

The solutions to the Maxwell equations are sought in the entire space.

2. TM WAVES

Let us consider TM waves $\mathbf{E} = (E_\rho, 0, E_z)^T$, $\mathbf{H} = (0, H_\varphi, 0)^T$, where $E_\rho = E_(\rho, \varphi, z)$, $E_z = E_z(\rho, \varphi, z)$, and $H_\varphi = H_\varphi(\rho, \varphi, z)$. Waves propagating along waveguide axis Oz depend harmonically on z. This means that the components of the field ($\mathbf{E}$, $\mathbf{H}$) have the form $E_\rho = E_\rho(\rho;\gamma)e^{i\gamma z}$, $E_z = E_z(\rho;\gamma)e^{i\gamma z}$, $H_\varphi = H_\varphi(\rho;\gamma)e^{i\gamma z}$, where γ is the propagation constant (spectral parameter of the problem).

Substituting TM waves into Maxwell's Equation (1) we obtain

$$\begin{cases} i\gamma E_\rho(\rho) - E_z'(\rho) = i\omega\mu H_\varphi(\rho), \\ i\gamma H_\varphi(\rho) = i\omega\varepsilon E_\rho(\rho), \\ \frac{1}{\rho}\left(\rho H_\varphi(\rho)\right)' = -i\omega\varepsilon E_z(\rho), \end{cases} \tag{2}$$

where $(\,\cdot\,)' \equiv \frac{d}{d\rho}$.

Introduce the notation

$$E_\rho(\rho;\gamma) = u_1(\rho,\gamma), \quad iE_z(\rho;\gamma) = u_2(\rho,\gamma). \tag{3}$$

Outside and inside the waveguide $\varepsilon = \tilde{\varepsilon}\varepsilon_0$, where

$$\tilde{\varepsilon} = \begin{cases} \varepsilon_1, & \rho > R; \\ \varepsilon_2 + \alpha\left(u_1^2 + u_2^2\right), & \rho < R, \end{cases}$$

and also let $k_0^2 = \omega^2\varepsilon_0\mu$, where $k_0 > 0$ is the wave number of free space.

We consider that $u_1(\rho;\gamma)$, $u_2(\rho;\gamma)$ are real functions. We will omit argument(s) γ and/or ρ if there are no misunderstandings.

Using (3), from system (2) we obtain

$$\begin{cases} \gamma u_2' + \left(\gamma^2 - k_0^2\tilde{\varepsilon}\right) u_1 = 0, \\ \gamma\frac{1}{\rho}(\rho u_1)' + \frac{1}{\rho}\left(\rho u_2'\right)' + k_0^2\tilde{\varepsilon}u_2 = 0. \end{cases} \tag{4}$$

It is necessary to find eigenvalues γ of the problem that correspond to surface waves propagating along waveguide axis, i.e., the eigenvalues corresponding to the eigenmodes of the structure. We seek the real values of spectral parameter γ, such that the nonzero real solutions u_1 and u_2 to system (4) exist. We suppose that γ is a real value (due to $|\mathbf{E}|^2$ does not depend on z).

Also we assume that functions u_1 and u_2 are sufficiently smooth.

We will seek γ under conditions $\varepsilon_1 < \gamma^2 < \varepsilon_2$. It should be noticed that condition $\gamma^2 > \varepsilon_1$ holds if $\varepsilon_1 > 0$. If $\varepsilon_1 < 0$, then $\gamma^2 > 0$.

3. DIFFERENTIAL EQUATIONS OF THE PROBLEM. TRANSMISSION CONDITIONS

In the domain $\rho > R$ we have $\varepsilon = \varepsilon_1\varepsilon_0$. System (4) takes the form

$$\begin{cases} k_1^2 u_1 + \gamma u_2' = 0, \\ -\gamma\frac{1}{\rho}(\rho u_1)' - \frac{1}{\rho}\left(\rho u_2'\right)' - k_0^2\varepsilon_1 u_2 = 0, \end{cases} \tag{5}$$

where $k_1^2 = \gamma^2 - k_0^2\varepsilon_1$.

Denoting by $k_2^2 := k_0^2\varepsilon_2 - \gamma^2$, from (4) we obtain the system of equations inside the waveguide

$$\begin{cases} -k_2^2 u_1 + \gamma u_2' = f_1, \\ -\gamma\frac{1}{\rho}(\rho u_1)' - \frac{1}{\rho}\left(\rho u_2'\right)' - k_0^2\varepsilon_2 u_2 = f_2, \end{cases} \tag{6}$$

where $f_1 = k_0^2\alpha\left|\mathbf{u}\right|^2 u_1$, $f_2 = k_0^2\alpha\left|\mathbf{u}\right|^2 u_2$ and $|\mathbf{u}|^2 = u_1^2 + u_2^2$, $\mathbf{u} = (u_1, u_2)^T$.

Tangential components of electromagnetic field are known to be continuous at the media interfaces. In this case the tangential components are E_z and H_φ. Hence, we obtain

$$E_z(R+0) = E_z(R-0), \quad H_\varphi(R+0) = H_\varphi(R-0),$$

where the constant $E_z^R = u_2(R) = E_z(R+0)$ is supposed to be known (initial condition).

It is well known that a normal component of electromagnetic field have a finite jump at the medium interface. In this case the normal component is E_ρ. It is also well known that the value $\tilde{\varepsilon}E_\rho$ is continuous at the medium interface. Thus we obtain the transmission conditions for functions u_1 and u_2:

$$\left[\tilde{\varepsilon}u_1\right]_{\rho=R} = 0, \quad \left[u_2\right]_{\rho=R} = 0, \tag{7}$$

where $[f]_{x=x_0} = \lim\limits_{x\to x_0-0} f(x) - \lim\limits_{x\to x_0+0} f(x)$ denotes a finite jump of the function f at the interface.

From the first condition (7) we obtain

$$\varepsilon_2 u_1|_{\rho=R-0} - \varepsilon_1 u_1|_{\rho=R+0} + \alpha u_1|\mathbf{u}|^2\big|_{\rho=R-0} = 0.$$

Let us formulate the transmission problem (*problem P*). *It is necessary to find eigenvalues γ and corresponding nonzero eigenfunctions $u_1(\rho)$ and $u_2(\rho)$ such that $u_1(\rho)$ and $u_2(\rho)$ satisfy to the*

continuity conditions, satisfy to system (6) *on* $(0, R)$, *satisfy to system* (5) *on* $(R, +\infty)$; *transmission conditions* (7) *and the radiation condition at infinity: eigenfunctions exponentially decay as* $\rho \to \infty$. *The spectral parameter of the problem is the real value* γ.

In accordance with the condition at infinity the solution of system (5) has the form

$$u_1 \equiv E_\rho = -\gamma k_1^{-1} C K_0'(k_1\rho), \quad u_2 \equiv E_z = C K_0(k_1\rho),$$

where C is an arbitrary constant; $K_0(z) = \frac{\pi i}{2} H_0^{(1)}(iz)$ is the Macdonald function.

4. NONLINEAR INTEGRAL EQUATION AND DISPERSION EQUATION

Let us consider nonlinear system (6). From the first equation of this system we obtain

$$u_1 = k_2^{-2}\left(\gamma u_2' - f_1\right). \tag{8}$$

Substituting (8) into the second equation of the system (6), we have

$$Lu_2 \equiv \left(\rho u_2'\right)' + k_2^2 \rho u_2 = W, \quad 0 < \rho < R, \tag{9}$$

with linear part $Lu_2 \equiv (\rho u_2')' + k_2^2 \rho u_2$ and $W(\rho) = \frac{k_2^2}{k_0^2 \varepsilon_2}(\frac{\gamma}{k_2^2}(\rho f_1)' - \rho f_2)$.

With the help of the corresponding Green function one can invert the linear part (the differential operator L) and obtain more convenient to studying an integro-differential equation.

The Green function can be obtained in the following form

$$G(\rho, s) = \begin{cases} \frac{\pi}{2} J_0(k_2\rho) \frac{N_0(k_2 s) J_0(k_2 R) - J_0(k_2 s) N_0(k_2 R)}{J_0(k_2 R)}, & \rho < s \le R, \\ \frac{\pi}{2} J_0(k_2 s) \frac{N_0(k_2 \rho) J_0(k_2 R) - J_0(k_2 \rho) N_0(k_2 R)}{J_0(k_2 R)}, & s < \rho \le R, \end{cases} \tag{10}$$

where $J_0(\rho)$ is the zero-order Bessel function; $N_0(\rho)$ is the zero-order Neumann function. The Green function exists if $J_0(k_2 R) \neq 0$.

We obtain *the dispersion equation*

$$\Delta(\gamma) \equiv \varepsilon_2 u_1(R-0) + \alpha u_1(R-0)|\mathbf{u}(R-0)|^2 + \varepsilon_1 \frac{\gamma}{k_1} K_0'(k_1 R) = 0$$

under condition that functions u_1, u_2 are solution of the system

$$\begin{cases} u_1(s) = -\frac{\gamma^2}{k_0^2 \varepsilon_2 k_2^2} \int\limits_0^R \frac{\partial^2 G}{\partial s \partial \rho} \rho f_1 d\rho - \frac{\gamma}{k_0^2 \varepsilon_2} \int\limits_0^R \frac{\partial G}{\partial s} \rho f_2 d\rho - \frac{1}{k_2^2} f_1(s) + h_1(s), \\ u_2(s) = -\frac{\gamma}{k_0^2 \varepsilon_2} \int\limits_0^R \frac{\partial G}{\partial \rho} \rho f_1 d\rho - \frac{k_2^2}{k_0^2 \varepsilon_2} \int\limits_0^R G \rho f_2 d\rho + h_2(s), \end{cases} \tag{11}$$

where $h_1(s) = \frac{\gamma R}{k_2^2} \frac{\partial^2 G(R,s)}{\partial \rho \partial s} K_0(k_1 R)$, $h_2(s) = R \frac{\partial G(R,s)}{\partial \rho} K_0(k_1 R)$.

Let us represent system (11) in the matrix operator form. Introduce the kernel matrix

$$K(\rho, s) = \{K_{nm}(\rho, s)\}_{n,m=1}^2 = -\rho \begin{pmatrix} q_{11} G_{\rho s} & q_{12} G_s \\ q_{21} G_\rho & q_{22} G \end{pmatrix}, \tag{12}$$

where the function G indexes denote partial derivatives. Also introduce the matrix of coefficients

$$Q = \begin{pmatrix} q_{11} & q_{12} \\ q_{21} & q_{22} \end{pmatrix} = \frac{1}{\varepsilon_2} \begin{pmatrix} (\gamma/k_2)^2 & \gamma \\ \gamma & k_2^2 \end{pmatrix}, \tag{13}$$

and the matrix linear integral operator $\mathrm{K} = \{\mathrm{K}_{nm}\}_{n,m=1}^2$ with the operators K_{mn}, associated with system (11), $\mathrm{K}\mathbf{g} = \int\limits_0^R K(\rho, s)\mathbf{g}(\rho) d\rho$, where $\mathbf{g} = (g_1, g_2)^T$.

Then, the system of integral equations can be written in the operator form

$$\mathbf{u} = \alpha \mathrm{K}\left(|\mathbf{u}|^2 \mathbf{u}\right) - \alpha \mathrm{J}\left(|\mathbf{u}|^2 \mathbf{u}\right) + \mathbf{h}, \tag{14}$$

where $\mathbf{h} = (h_1, h_2)^T$ and the operator J is defined by formula $\mathrm{J} = \frac{k_0^2}{k_2^2}\begin{pmatrix} 1 & 0 \\ 0 & 0 \end{pmatrix}$.

We will consider Equation (14) in $\mathbf{C}[0,R] = C[0,R] \times C[0,R]$ with the norm $\|\mathbf{u}\|_{\mathbf{C}}^2 = \|u_1\|_C^2 + \|u_2\|_C^2$, where $\|u\|_C = \max\limits_{x\in[0,R]} u(x)$.

Proposition. *Let* $\mathrm{K} : \mathbf{C}[0,R] \to \mathbf{C}[0,R]$ *be the integral operator with the bounded kernels* $K_{nm}(x,y)$ *in* $[0,R]\times[0,R]$, *defined by formulas* (12) *and* (13). *Then, the operator* K *is bounded and its norm estimation* $\|\mathrm{K}\|_{\mathbf{C}\to\mathbf{C}} \le M$, *holds.*

Approximate solutions $\mathbf{u}^n(s) = (u_1^n(s), u_2^n(s))^T$ of integral equations system (11) can be calculated by means of the iteration process

$$\mathbf{u}^{n+1} = \alpha(\mathrm{K}-\mathrm{J})\left(|\mathbf{u}^n|^2\mathbf{u}^n\right) + \mathbf{h}. \tag{15}$$

Theorem 1. *If* $|\alpha| \le A^2$, *where* $A = \frac{2}{3}\frac{1}{\|\mathbf{h}\|\sqrt{3\|\mathrm{N}_0\|}}$ and $\|\mathrm{N}\| := |\alpha|\|\mathrm{K}-\mathrm{J}\|(>0)$, *then Equation* (14) *has a unique solution* $\mathbf{u}$ *in the ball* $B_{r_*} \equiv \{\mathbf{u} : \|\mathbf{u}\| \le r_*\}$ *for*

$$r_* = -\frac{2}{\sqrt{3\|\mathrm{N}\|}}\cos\left(\frac{\arccos\left(\frac{3\sqrt{3}}{2}\|\mathbf{h}\|\sqrt{\|\mathrm{N}\|}\right)}{3} - \frac{2\pi}{3}\right). \tag{16}$$

Rewrite dispersion Equation (4) in the following form

$$\varepsilon_2 k_1 J_1(k_1R)K_0(k_1R) + \varepsilon_1 k_2 J_0(k_2R)K_1(k_1R) = \alpha F(\gamma), \tag{17}$$

where

$$F(\gamma) = \frac{k_1}{R}\int\limits_0^R \rho\left(\gamma J_1(k_2\rho)u_1(\rho) - k_2 J_0(k_2\rho)u_2(\rho)\right)|\mathbf{u}|^2 d\rho - \gamma\frac{k_1}{k_2}J_0(k_2R)|\mathbf{u}(R-0)|^2 u_1(R-0).$$

Let us consider the left-hand side of Equation (17). It corresponds to the dispersion equation for a linear medium inside the waveguide, i.e., for $\alpha = 0$

$$g(\gamma) \equiv \varepsilon_2 k_1 J_1(k_1R)K_0(k_1R) + \varepsilon_1 k_2 J_0(k_2R)K_1(k_1R) = 0.$$

Introduce the notation $\lambda_{1m} := k_0^2\varepsilon_2 - \frac{j_{1m}^2}{R^2}$, $\lambda_{2m} := k_0^2\varepsilon_2 - \frac{j_{0m}^2}{R^2}$, where j_{0m} is the m-th positive root of the equation $J_0(x) = 0$ and j_{1m} is the m-th positive root of the equation $J_1(x) = 0$; $m = 1, 2, \ldots$.

Before the proving of the existence eigenvalues theorem for the nonlinear boundary problem P, it should be noticed that the points $\sqrt{\lambda_{2i}}$ are poles of Green's function (10). The Green function is not defined at these points. Therefore, we can choose sufficiently small values $\delta_i > 0$ such that the conditions $\operatorname{sign} g\left(\sqrt{\lambda_{2i}} - \delta_i\right) = (-1)^{i+1}$, and $\sqrt{\lambda_{2i}} - \delta_i > \gamma_{0i}$ are fulfilled.

Theorem 2. *Let the values* ε_1, ε_2, α *satisfy the conditions* $\varepsilon_2 > \varepsilon_1 > 0$, $0 < |\alpha| \le \alpha_0$, *where*

$$\alpha_0 = \min\left(\min_{\gamma\in\Gamma} A^2(\gamma), \frac{\min\limits_{1\le l\le 2, 1\le i\le m}\left|g(\sqrt{\lambda_{li}})\right|}{0.3R^2\left(\max\limits_{\gamma\in\Gamma} r_*(\gamma)\right)^3}\right), \tag{18}$$

and the condition

$$\lambda_{1m} > k_0^2\varepsilon_1 \tag{19}$$

holds for certain $m \ge 1$. *Then, there are at least* m *values* $\gamma_i, i = 1, \ldots, m, \sqrt{\lambda_{1i}} < \gamma_i < \sqrt{\lambda_{2i}} - \delta_i$ *such that the problem* P *has a nontrivial solution.*

From Theorem 2, it follows that, under the above assumptions, there exist axially symmetrical propagating TM waves in cylindrical dielectric waveguides of circular cross-section filled with a nonmagnetic isotropic medium with Kerr nonlinearity. This result generalizes the well-known similar statement for dielectric waveguides of circular cross-section filled with a linear medium (i.e., $\alpha = 0$).

5. CONVERGENCE THEOREM OF THE ITERATION METHOD

Let us formulate the iteration method to calculate approximate eigenvalues of the boundary problem P. Also we prove the existence and convergence (the approximate solution to the exact one) theorems.

Theorem 3. *Suppose that* $\varepsilon_2 > \varepsilon_1 > 0$ and $0 < |\alpha| \le \alpha_0$, *where* α_0 *is defined by* (18), *and condition* (19) *holds for certain* $m \ge 1$. *Then, for each* $n \ge 0$ *at least* m *values* $\gamma_i^{(n)}, i = 1, \ldots, m$, *exist. These* $\gamma_i^{(n)}$ *satisfy the inequality* $\sqrt{\lambda_{1i}} < \gamma_i^{(n)} < \sqrt{\lambda_{2i}} - \delta_i$ *and are roots of the equation*

$$k_1^{(n)}\varepsilon_2 K_1\left(k_1^{(n)}R\right) J_0\left(k_2^{(n)}R\right) + k_2^{(n)}\varepsilon_1 K_0\left(k_1^{(n)}R\right) J_1\left(k_2^{(n)}R\right) = \alpha F(\gamma^{(n)}),$$

where $k_1^{(n)} = \sqrt{\left(\gamma^{(n)}\right)^2 - \varepsilon_1}$, $k_2^{(n)} = \sqrt{\varepsilon_2 - \left(\gamma^{(n)}\right)^2}$ *and* $\mathbf{u}^n$ *is defined by* (15).

The following theorem states the convergence of approximate eigenvalues to the exact ones.

Theorem 4. *Let* ε_1, ε_2, a, *satisfy the condition* $\varepsilon_2 > \varepsilon_1 > 0$, $0 < |\alpha| \le \alpha_0$, *where* α_0 *is defined by* (18), *and condition* (19) *holds for certain* $m \ge 1$. *Let* γ_i *and* $\gamma_i^{(n)}$ *be exact and approximate eigenvalues of the problem* P, *respectively in the segment* Γ_i (γ_i, $\gamma_i^{(n)}$ *are roots of the exact and approximate dispersion equations, respectively,* $i \le m$, $m \ge 1$). *Then* $\left|\gamma_i^{(n)} - \gamma_i\right| \to 0$ *as* $n \to \infty$.

The numerical method for calculating approximate eigenvectors and approximate eigenfunctions of the nonlinear boundary problem P is implemented in the following way.

Let us introduce a grid

$$\rho_j = jH_0, \quad j = \overline{0, N-1},$$

where $H_0 = R/N$ in the segment $[0, R]$. All the integrals on the segment $[0, R]$ are calculated by method of rectangles with the nodes $\rho_j^* = jH_0 + H_0/2$. The function $\mathbf{u}^n$ is considered as a mesh function, which is set at the nodes ρ_j^*. To be more precise, $\mathbf{u}^n(\rho) = \mathbf{u}^n(\rho_j^*)$ for $\rho \in \left(\rho_j^* - H_0/2, \rho_j^* + H_0/2\right)$.

Let us introduce a grid $\gamma_{ij} = \sqrt{\lambda_{1i}} + jh_i$, $j = \overline{0, N_i - 1}$, where $h_i = \left(\sqrt{\lambda_{2i}} - \delta_i - \sqrt{\lambda_{1i}}\right)/N_i$ (the step h is sufficiently small) in the segment Γ_i. Then, the values $\Delta(\gamma_{ij})$ are calculated and the segments of signs reversal of $\Delta(\gamma_{ij})$ are defined. In other words, the segments $[\gamma_{ij}, \gamma_{i,j+1}]$ such that $\Delta(\gamma_{ij})\Delta(\gamma_{i,j+1}) < 0$ are defined. In the each of these segments the value of the localized root of equation $\Delta(\gamma) = 0$ is refined by the dichotomy method. Thus the approximate eigenvalues $\widetilde{\gamma}_i^{(n)}$ can be made arbitrary close to the exact roots $\gamma_i^{(n)}$ by means of choosing the steps H_0 and h_i.

Iteration process (15) of solving integral equations system (11) (with fixed γ) begins with the initial approximation $\mathbf{u}^0(s) = (0, 0)^T$ and finishes when the estimation $\max\limits_{0 \le j \le N-1} \left|\mathbf{u}^{n+1}(\rho_j^*) - \mathbf{u}^n(\rho_j^*)\right| < \delta$ is fulfilled for certain sufficiently small $\delta > 0$.

Proofs of the theorems you can find in [4].

ACKNOWLEDGMENT

The work is supported by the Russian Foundation for Basic Research, project No. 11–07–00330–A.

REFERENCES

1. Eleonskii, P. N., L. G. Oganes'Yants, and V. P. Silin, "Cylindrical nonlinear waveguides," *Soviet Physics Jetp.*, Vol. 35, No. 1, 44–47, 1972.
2. Schürmann, H. W., Yu. G. Smirnov, and Yu. V. Shestopalov, "Propagation of TE-waves in cylindrical nonlinear dielectric waveguides," *Phys. Rev. E*, Vol. 71, No. 1, 016614-1–016614-10, 2005.
3. Smirnov, Yu. G., H. W. Schürmann, and Yu. V. Shestopalov, "Integral equation approach for the propagation of TE-waves in a nonlinear dielectric cylindrical waveguide," *J. of Nonlinear Math. Phys.*, Vol. 11, No. 11, 256–268, 2004.
4. Smirnov, Yu. G. and D. V. Valovik, *Electromagnetic Wave Propagation in Nonlinear Layered Waveguide Structures*, Penza Univ. Press, 2011.

X-ray Image Processing in Studying Jawbone Tissues

J. Mikulka and M. Kabrda
Department of Theoretical and Experimental Electrical Engineering
Brno University of Technology, Kolejní 4, Brno 612 00, Czech Republic

Abstract— Image processing in biomedical applications is strongly developing issue. Many methods and approaches for image preprocessing, segmentation and visualization were described. This paper describes X-ray image processing. The aim of processing is to segment regions of jawbone cysts and evaluate their local descriptors. It is necessary to choose suitable segmentation method because of adverse parameters of regions. The regions of the cysts are of low contrast and the pixel intensity distribution is not homogenous. The semiautomatic live-wire method was chosen. This approach to image segmentation is faster and more accurate than manual segmentation. It is very good compromise between simple manual edge tracing and automatic methods such as thresholding, watershed segmentation or other methods whose results must be post-processed. The second step of processing is to evaluate local descriptors of segmented regions which correspond to cysts. Several parameters were chosen to describe these regions — region area, mean gray value of intensities, modal gray value of intensities, standard deviation of intensities, minimal and maximal gray value of intensities, integrated intensity, median of intensities and shape descriptors of region (perimeter, circularity, aspect ratio, roundness and solidity). Values of these parameters will be used in following development of semiautomatic processing method with regard to current assessment of cysts by doctors.

1. INTRODUCTION

Cysts are defined as pathological cavities with their own capsule, epithelium and liquid or mushy content. The cyst wall is formed by fibrous tissue. A typical property of the cyst is its expansive growth. The cyst wall functions as a semipermeable membrane, permeable in one direction for the surrounding liquid. The result is a gradual enlargement of the cyst [1].

Follicular cysts (Fig. 1) arise from the epithelium of tooth germ and develop either between a naked crown and the joined inner and outer epithelium or enamel or between the two layers of epithelium. Their appearance can be triggered by a primary disorder in the development of tooth germs. Follicular cysts can occur individually or multiply [2]. The majority of follicular cysts most frequently appear in the region of lower jawbone. Bulky cysts can lead to face-deforming swelling. Radicular cysts (Fig. 1) belong to the most frequently occurring jawbone cysts. They are believed to appear due to inflammatory excitation of Malasser epithelium remnants of periodontal crevice by the infected content of the root duct of a transversely situated tooth. Cysts are associated with teeth without pulp and they occur in all age categories (mostly 30 and 40 years of age), and are a bit more frequent in males. The follicle of radicular cyst is usually of round or oval shape [1].

To obtain images of the afflicted jawbones, X-ray examination is very often performed in practice using the orthopantomograph, which enables panoramic images of whole jawbones to be obtained.

The paper describes the first steps in proposing methods for the processing of OPG images and their implementation in the automation of the assessment of the two types of cyst. The aim of the proposal is to make and train a model from actual medical data and then to use it for an automatic classification of cysts according to the existing scale used in manual processing.

2. IMAGE PROCESSING CHAIN

The image processing chain currently consists of orthopantomograph detection, segmentation of the cystic region, and description of regions in terms of local properties. The existing solution will

Figure 1: OPG image of follicular cyst on the left and radicular cyst on the right.

later be complemented with the results of a classification based on the physician's knowledge which, together with a selection of local descriptors will be sufficient to train a suitably selected model (Fig. 2). The trained model will subsequently be used for automated computer-aided classification of cysts.

In view of the properties of the regions that represent the jawbone cysts, and the necessity of delineating precisely the given region in order to obtain corresponding local descriptors, the live-wire semi-automatic segmentation method was chosen. The method enables fast manual delineation of the region of interest, using the shortest path algorithm. The image first undergoes convolution using the Sobel filter [6], by means of which the edges in the image are enhanced. The user marks out individual points in the image, between which the optimum shortest path is sought, which will run along the image edges [7]. In our case the shortest path is being sought using the Djikstr algorithm. The algorithm is finite (for any finite input the algorithm will end) because in each cycle run exactly one node is added to the set of visited nodes. Thus there are at most as many cycle runs as there are peaks in the graph. Let us imagine we have a graph $\mathbf{G}$, in which we want to find the shortest path. Let us determine that $\mathbf{V}$ is a set containing all the peaks of graph $\mathbf{G}$ and $\mathbf{E}$ is a set of all edges of graph $\mathbf{G}$. The principle of the algorithm consist in that for each peak v from $\mathbf{V}$ the algorithm remembers the shortest length of path that needs to be taken to get to the peak. Let us denote this value $d[v]$. In the beginning, all the peaks have the value $d[v] = \infty$, excepting the initial peak s, the corresponding value of which is $d[s] = 0$. Infinity expresses an unknown path to the peak. The algorithm further utilizes the sets $\mathbf{Z}$ and $\mathbf{N}$, where $\mathbf{N}$ contains the hitherto unvisited and $\mathbf{Z}$ the visited peaks. The algorithm is repeated cyclically until the set $\mathbf{N}$ is empty. In each algorithm cycle one peak $v_{\min}$ is added from $\mathbf{N}$ into $\mathbf{Z}$. It is the peak with the least value $d[v]$ from all the peaks v from $\mathbf{N}$. For each peak u, with one edge from $v_{\min}$ leading to it (its length expressed as $l(v_{\min}, u)$) the following algorithm is applied: if $(d[v_{\min}] + l[v_{\min}]) < d[u]$, then the value $d[v_{\min}] + l[v_{\min}, u]$ is assigned to $d[u]$. If this condition is not satisfied, nothing will happen. When the algorithm ends, then for each peak v from the set $\mathbf{V}$ the length of its shortest path from the initial peak s will be assigned to $d[v]$ [8]. The live-wire method is suitable for the segmentation of images in which the region of interest is in individual images always in a different position and always has a different shape. This method is thus in our case the most suitable for image segmentation. One or more regions can be marked/delineated simultaneously in the image (Fig. 3).

The aim of further processing the segmented images is to obtain local descriptors of regions that represent jawbone cysts. The Image J program was used to evaluate statistically the distribution of pixel intensities in cystic regions and to establish the shape parameters of these regions. In this phase of research the following parameters were evaluated in the submitted set of images: area,

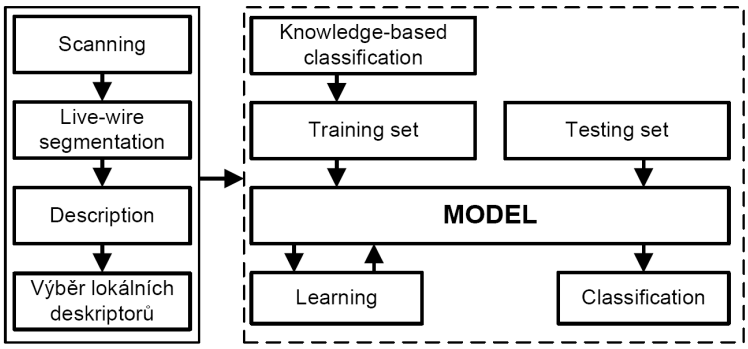

Figure 2: Image processing chain designed for automated classification of follicular and radicular cysts.

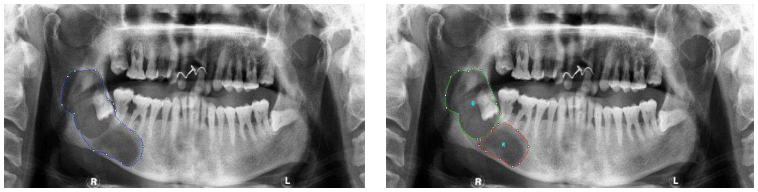

Figure 3: Semiautomatic segmentation using the live-wire method — one delineated region, several delineated regions.

mean intensity value in the region, standard deviation of pixel intensities in the region, median of pixel intensities in the region, modal value of pixel intensities in the region, minimum and maximum values of pixel intensities in the region, and integral of pixel intensities in the region. Also, the shape parameters of segmented regions were established: perimeter of the region, circularity according to (1), ratio of the major and minor half-exes of the inscribed ellipse, roundness according to (2), and convexity according to the relation (3):

$$C = 4 \cdot \pi \cdot \frac{S}{P^2}, \tag{1}$$

$$R = 4 \cdot \frac{S}{\pi \cdot a_{\text{major}}^2}, \tag{2}$$

$$X = \frac{S}{S_C}, \tag{3}$$

where C is the circularity of the region, S is the area of the region, P is the perimeter of the region, R is the roundness of the region, α_{major} is the length of the major half-axis of ellipse inscribed in the region, X is the convexity of the region, and S_C is the area of the convex region described/circumscribed over the region under examination.

3. RESULTS OF PROCESSING

The whole of available database of images, i.e., 13 images with follicular cysts and 18 images with radicular cysts was evaluated using the methodology described. The difference is obvious between follicular and radicular cysts as mentioned in the introductory paragraph. While the follicular cysts are rather of an oblong shape, the radicular cysts are almost always of circular nature. The different circularity of the two types of cyst provides the possibility of classifying cysts into two basic groups:

- follicular cyst — circularity: 0.807 ± 0.149,
- radicular cyst — circularity: 0.932 ± 0.086.

To enhance the quality of cyst classification, it would be appropriate to select a greater number of parameters the probability distributions of which do not overlap in the two types of cyst. One such parameter could, for example, be a parameter giving the ratio of the major and minor half-axis lengths of inscribed ellipse:

- follicular cyst — ratio of half-axes: 1.975 ± 0.613,
- radicular cyst — ratio of half-axes: 1.514 ± 0.401.

Based on subjective assessment of values, the area can also be selected as a suitable candidate for cyst classifier:

- follicular cyst — area: 58029.38 ± 40023.60,
- radicular cyst — area: 30249.54 ± 25048.18.

From the discussion of the values it follows that the automated system can be complemented with a cyst classification according to the cyst type. The next step will be a classification of the level of cystic disorder in jawbone according to a scale currently used by physicians for subjective assessment of OPG images. Images assessed by physicians will be correlated with the values given in the tables, and an appropriate model will be made and trained for cyst classification.

4. CONCLUSIONS

Fundamental research described in the paper concerns the area of processing OPG images of jawbones with the aim of classifying follicular and radicular cysts. The classification of cysts can be divided into two types:

- binary classification of the type of cyst: follicular or radicular,
- classification of the level of jawbone affliction with cyst disorder on the currently used scale of 1–4.

The results of image processing indicated the possibility of using a combination of several parameters for a binary classification of cysts (circularity, ratio of half-axes of inscribed ellipse, and area of cystic region). An algorithm was proposed for the classification of the level of jawbone affliction. The selection of a model and the process of training will be carried out using the Rapid Miner system in a follow-up work and after the available database has been processed by physicians.

ACKNOWLEDGMENT

This work was supported in part by the Grant project GAP102/11/0318, 102/12/1104, project FEKT-S-11-5/1012 and CZ.1.07.2.3.00.20.0175.

REFERENCES

1. Pazdera, J., *Fundamentals of Oral and Maxillofacial Surgery*, UP Olomouc, 2011.
2. Černochova, P., *Diagnostika Retinovaných Zubů*, Grada Publishing, Praha, 2006.
3. Mikulka, J., E. Gescheidtová, K. Bartušek, and Z. Smékal, "Processing of MR slices of temporomandibular disc for 3D visualization," *PIERS Online*, Vol. 6, No. 3, 204–206, 2010.
4. Bartušek, K., E. Gescheidtová, and J. Mikulka, "Data processing in studying biological tissues using MR imaging techniques," *33th the International Conference on Telecommunications and Signal Processing*, 171–175, Asszisztenda Szervezo, Budapešt, 2010.
5. Smékal, Z., O. Liberda, K. Bartušek, and J. Mikulka, "Data processing in studying the temporomandibular joint, using MR imaging and sonographic techniques," *16th International Conference on Digital Signal Processing (DSP 2009)*, 100–106, Santorini, Greece, 2009.
6. Hlaváč, V. and M. Šonka, *Image Processing*, Grada, Praha, 1992.
7. Baggio, D. L., *GPGPU Based Image Segmentation Livewire Algorithm Implemnetation*, Technological Institute of Aeronautics, Sao José dos Campos, 2007.
8. Brassard, G. and P. Bratley, *Algorithmics*, Prentice-Hall, Englewood Cliffs, 1988.

Sensors and Experimental Model Verification on HV Transformers Measurement

P. Drexler, P. Fiala, M. Friedl, P. Marcon, M. Steinbauer, Z. Szabo, and M. Hadinec
Department of Theoretical and Experimental Electrical Engineering,
Brno University of Technology, Kolejni 2906/4, Brno 612 00, Czech Republic

Abstract— One of the problematic phenomena in the field of high-voltage technology, is the occurrence of partial discharge. Several other effects have combined with this notion over time [1]. In consequence of these effects there emerge short electromagnetic pulses with a defined and measurable spectrum in the characteristic frequency band [2]. The group of end products attributable to the emergence of interfering signals involves, for example, displacement current in a dielectric, pulse current on the interface between dielectrics, or the dielectric/metal interface owing to high electric field intensity and structure of the dielectric.

In order to prevent the transformer failure the observation of pulse activity is necessary. The occurrence of discharge with substantial charge transport level can be localized in critical areas of the transformers. Having a possibility to localize the increased discharge activity in some of the critical areas allows us to undertake precautions in order to avoid the critical transformer failure. The discharge activity localization can be determined on the basis of processing of signals from suitable installed sensors. The evaluation of the discharge location utilizes the model of wave propagation inside the transformer, which has been presented in early work [3].

For the experimental verification of localization method a model setup has been built. The model setup is equipped with antenna sensors, RF amplifiers and data acquisition unit. The model setup is described in the paper as a following step of the research. The result of the measurement which has been performed up to the present are presented also.

1. INTRODUCTION

One of the problematic phenomena in the field of high-voltage technology, is the occurrence of partial discharge (PD). Several other effects have combined with this notion over time [1]. In consequence of these effects there emerge short electromagnetic pulses with a defined and measurable spectrum in the characteristic frequency band [2]. The group of end products attributable to the emergence of interfering signals involves, for example, displacement current in a dielectric, pulse current on the interface between dielectrics, or the dielectric/metal interface owing to high electric field intensity and structure of the dielectric.

In order to prevent the transformer failure the observation of pulse activity is necessary. The occurrence of discharge with substantial charge transport level can be localized in critical areas of the transformers. Having a possibility to localize the increased discharge activity in some of the critical areas allows us to undertake precautions in order to avoid the critical transformer failure. The discharge activity localization can be determined on the basis of processing of signals from suitable installed sensors. The evaluation of the discharge location utilizes the model of wave propagation inside the transformer, which has been presented in early work [3]. Large distribution transformers are constructed in such a manner as to have structural measures facilitating oil purification. Also, these transformers are equipped with sensors indicating the initial stage of increase in pulse activity. In the course of this activity, as is well known, there occurs an increase in the boundary value of the applied dielectric breakdown value. Under certain conditions, the separation of chemical compounds incurred by decomposition of the dielectric does not have to occur. Thus, free atoms of carbon, hydrogen and oxygen develop from hydrocarbons, and there also generates a certain percentage of water, other organic compounds and semi-conductive carbon. All of these elements decrease the quality of the di-electric, in addition to that, rapid increase in pulse activity may cause the formation of a hazardous explosive compound of oxygen and hydrogen.

2. MEASUREMENT MODEL SETUP

For the evaluation of PD detection and localization the measurement model has been designed and built. The model is based on the oil filled metal tank which is box-shaped. The tank contains 230 l of transformer oil. Four inserts are assembled on the wall of the tank. The inserts are in the form of cylinder cavity and they allows to put the antennas inside in order to be able to collect

PD radiated RF energy. The oil tank is shown in the left of the Figure 2. In the right of Figure 2 the antennas positions in the tank with their labels are shown also. The tank is equipped with the metal cover which can be removed to insert additional objects with specified material properties $\varepsilon_{r,n}$, $\mu_{r,n}$ and $\gamma_{r,n}$ inside the tank. The insertion of additional objects allows to observe changes in signal time relations which are caused by the additional reflections on the walls and different propagation velocities in the objects and at their boundaries.

The presence of objects with properties different to the oil environment (middle of Figure 2) causes the propagation of waves with different wave numbers $\overline{k}_n$ in compare to the primary wave number $\overline{k}_1$

$$\overline{k}_1 = \sqrt{-j\omega_1\mu_1\left(\gamma + j\omega_1\varepsilon_1\right)}; \quad \overline{k}_n = \sqrt{-j\omega_n\mu_n\left(\gamma + j\omega_n\varepsilon_n\right)}. \tag{1}$$

Considering the known configuration of the model (or the HV transformer) there is a possibility to determine the probability areas of PD occurrence by means of the numerical model evaluation. The example of probabilities $P_1, \ldots, P_n$ areas are shown in the right part of Figure 1 for P_1 and P_2.

3. EXPERIMENTAL TIME DOMAIN MEASUREMENT

We can localize the area of the PD activity by evaluating the time relation of the signal received on antennas. The verification of the time-of-arrival difference in different receiving channels has been made by means of short testing pulse. The testing pulse was applied on the TX antenna and the signals on the remaining RX were captured. The positions of the antennas in the measurement

Figure 1: Examples of local explosion of oxygen and hydrogen in the transformer.

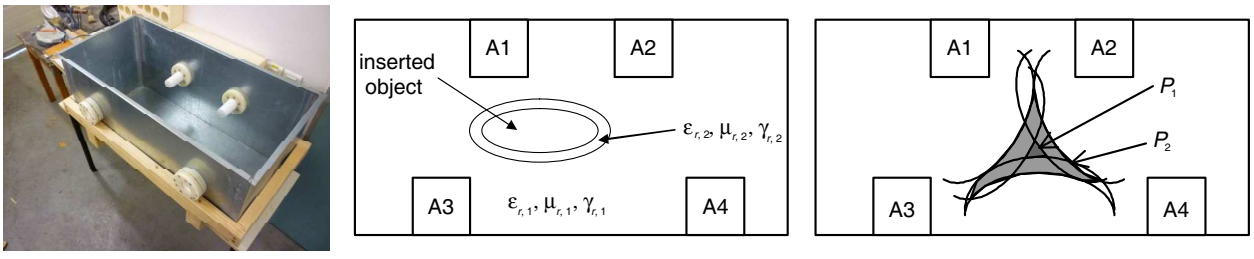

(a) (b) (c)

Figure 2: (a) Tank with inserts for antennas, (b) position of antennas with labels, (c) PD occurence.

Figure 3: Measuring setup in nuclear power plant Dukovany.

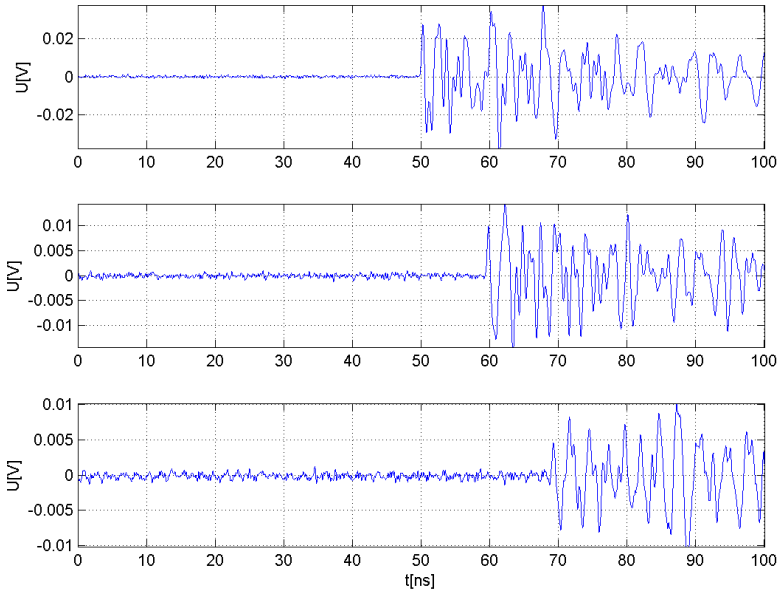

Figure 4: The captured waveforms from RX antennas.

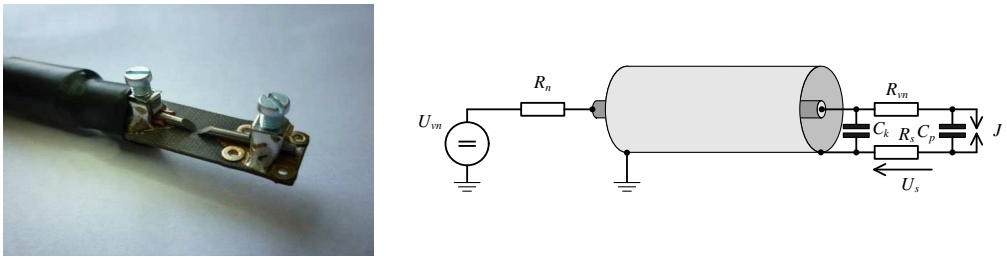

(a) (b)

Figure 5: (a) Spark-gap construction and (b) schematic diagram of spark-gap.

model have been designed in the way that the distances of three RX antennas to the TX antenna are mutually different.

A negative short pulse of electrical voltage with the peak level of approx. -6 V was fed in TX antenna in position A1. The pulse was supplied by the pulse generator based on the avalanche effect in the RF transistor in the transition from saturation into the off-state. The pulse fall time is $t_f = 370$ ps, rise time is $t_r = 880$ ps and the pulse width is $t_w = 650$ ps. The captured waveforms are shown in the right part of Figure 4.

In order to preserve the time-of-arrival differences the cables between the RX antennas and the acquiring device were of the same length. The signals on the receiving antennas were captured by the digital storage oscilloscope with the sampling rate 2 GSa/s and with the analog bandwidth of 1 GHz.

The ground of scanning channels was connected to the body of transformer. Due to the propagation in cavity with conducting walls a considerable amount of multiple reflections can be observed in the RX channels. However, for the signals time relations evaluation the occurrence of the first remarkable transient has to be watched. The solution of the PD occurrence location can be evaluated by means of the numerical model which has been presented in previous work [3]. This effect can be modeled by inserting of additional walls into the oil tank which is the goal of further research.

4. MEASUREMENT OF SIMULATED PARTIAL DISCHARGE

In order to test the designed detection system in the measurement model a need for suitable discharge source occurs. A spark-gap with low breakdown voltage has been proposed. Due to the low level of charge transport during the PD activity in order of 10^{-10} C the low breakdown voltage is required in order to get the similar charge transport level. The spark-gap consists in two tungsten electrodes of sharp-tip shape to maximize the field intensity in the gap. The gap distance has been

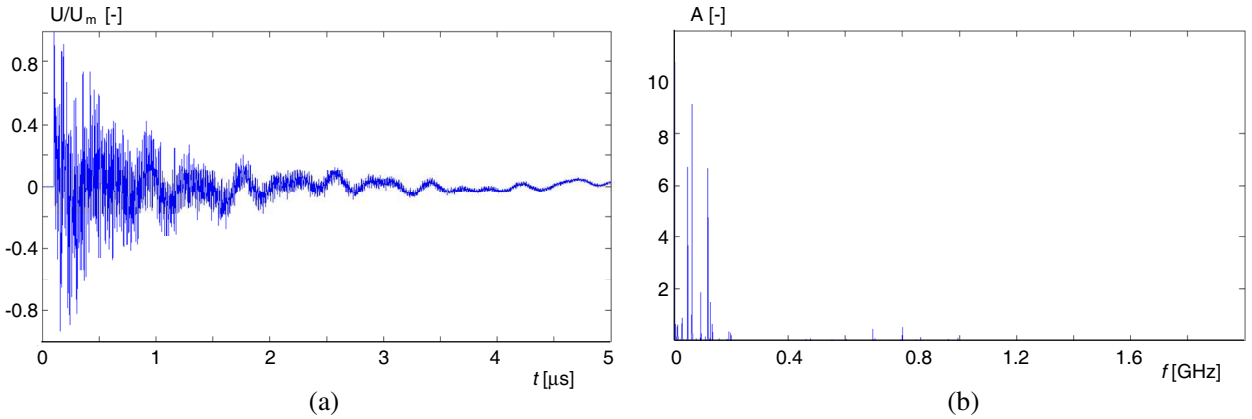

Figure 6: (a) Waveform and (b) spectrum of the PD radiated signal.

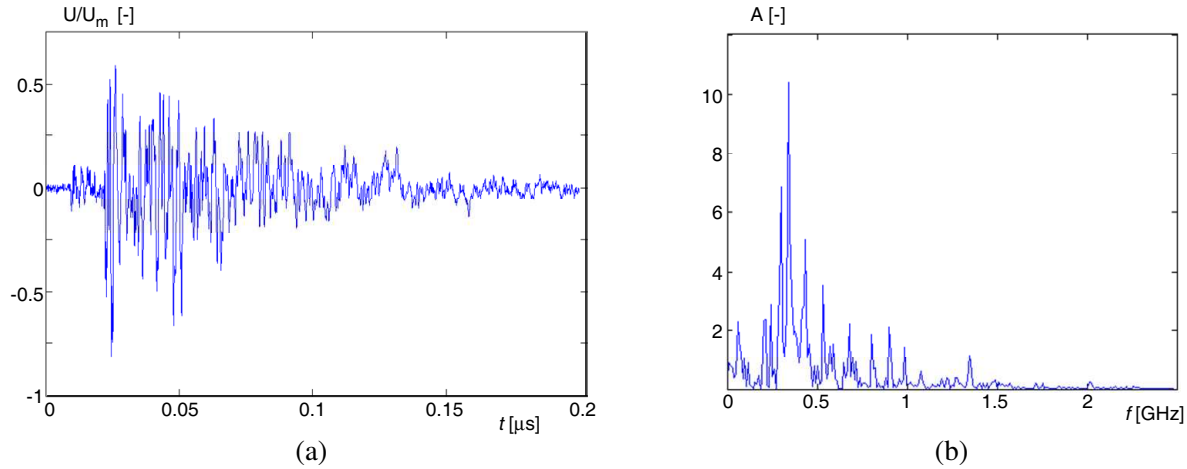

Figure 7: (a) Waveform and (b) spectrum of the spark-gap discharge radiated signal.

set to 0.1 mm.

The spark-gap has been placed in the oil tank and the electromagnetic radiation of the discharge has been captured by means of four antenna sensors. The waveform and the spectrum of the spark-gap discharge should approximate the characteristic of the partial discharge. The waveform and the spectrum of the PD radiation is shown in Figure 6. The signal has been obtained by measurement on real high voltage transformer during the PD.

The characteristics obtained by measurement of the spark-gap discharge in the oil tank are shown in Figure 7. The differences in the characteristics in Figures 6 and 7 are obvious. The PD waveform has longer time duration in compare to spark-gap discharge waveform. The next difference is the content of harmonic components. The most of the power is carried by the harmonic components on frequencies in range 10–200 MHz. While the waveform of the spark-gap discharge has shorter time duration and the frequency content is also different. The most of the signal power is carried by frequencies of hundreds of MHz. Components with frequencies up to 2 GHz are present also.

5. CONCLUSIONS

The description of the measurement model for PD detection and localization method evaluation is presented in the paper. The spectral transmission characteristic of the model equipped with antenna sensor is shown further. In order to demonstrate the ability of transients time-of-arrival resolving the time domain measurement has been performed. Simulated discharge is compared to the real PD acquisition. Regarding to differences another discharge source should be intended which is a part of further research. The designed circuitry for RF signal processing is a point of subsequent publication.

ACKNOWLEDGMENT

This work was supported within project from Education for Competitiveness Operative Programme CZ.1.07.2.3.00.20.0175 and project of the BUT Grant Agency FEKT-S-11-5/1012 and grant Ministry of Industry and Trade FR-TI1/001.

REFERENCES

1. Fiala, P., "Transformer partial discharge modeling, minimal breakdown value set in a critical parts of transformer design," Research Report, Laboratory of Modeling and Optimization Fields in Electromagnetic Systems, FEI VUT and ABB EJF a.s. Brno, No. 2/99, 18.3.1999, Brno, Czech Republic, 1999.
2. Sarathi, R., A. J. Reid, and M. D. Judd, "Partial discharge study in transformer oil due to particle movement under DC voltage using the UHF technique," *Electric Power Systems Research*, Vol. 78, 1819–1825, Elsevier, 2008.
3. Fiala, P., T. Jirku, P. Drexler, and P. Dohnal, "Detection of partial discharge inside of HV transformer, modeling, sensors and measurement," *PIERS Proceedings*, 1013–1016, Cambridge, USA, Jul. 5–8, 2010.

Quantum Hydrodynamics of Charge Carriers in Graphene

P. A. Andreev
Department of General Physics, Physics Faculty, Moscow State University, Russian Federation

Abstract— Graphene is the carbon monolayer. This material has a lot of interesting properties and is in a centre of many present day researches. In literature graphene is considered as independent system *and* as a part of semiconductor geterostructures and field effect transistor. Thus, especially the graphene conductivity properties and properties of graphene carriers have been studied. One of the unusual and important properties of graphene carriers is the carrier dispersion. The energy of free nonrelativistic electron is proportional to the square of the momentum then the dispersion law is quadratic. Novoselov et al. shown that graphene carriers has linear dispersion law and they are massless. This result is analogous to the free ultrarelativistic electrons and massless particles. In quantum case the massless Dirac's equation gives the linear dispersion law. Thereby, the massless Dirac's equation was suggested for description of grapnene carrier dynamics. Instead of speed of light in Dirac's equation the Fermi velocity graphene electron were used.

Properties of single carrier quasi-particle in graphene is a fundamental properties which give us understanding of microscopic carrier dynamics, but for understanding of a graphene role in semiconductor structures we need to study collective dynamics of graphene carriers. For this purpose in literature many-particle massless Dirac's equation including the Coulomb interaction between carriers is used. Feynman's diagram method has been used in many papers for studying collective properties of graphene carriers.

In this paper we present a new method of studying of graphene carriers collective properties. This method is called many-particle quantum hydrodynamics (QHD). One is based on many-particle massless Dirac's equation. QHD method allows us to derive equation which described dynamic of particles in physical space (for graphene it is a two dimensional space) instead of 2N dimensional configuration space where the wave's spinor is defined.

We derive QHD equations for the graphene carriers and use these equations for the calculation of dispersion properties of collective excitations in graphene. We suppose that graphene situated in external uniform magnetic field directed at different angles to the grapheme plane. As the results we present dispersion dependencies for collective excitations in grapheme and make comparison with the results of other authors which they found by other methods.

1. INTRODUCTION

There are a lot of papers where elementary excitations in graphene are considered [1–4] together with transport properties [5, 6]. There are transitions of electrons between Landau levels in graphene in magnetic field directed perpendicular to the sample. These transitions give us a picture of possible elementary excitations and their frequencies. In general this picture is analog of the same in a 2DEG, but in the last case Landau levels are equidistant.

Some of these elementary excitations lead to the formation of collective excitations. Systems of charged particles (plasma or 2DEG) in the absence of external field reveal Langmuir waves as a basic collective excitations. To collective excitations studying a hydrodynamic description can be used [7]. For proper description of quantum effects in plasma or 2DEG the quantum hydrodynamics should be used [8–13].

In this paper we present basic steps of development of graphene quantum hydrodynamics which aimed to study linear and nonlinear collective excitations in graphene.

2. MODEL

In vicinity of Dirac points behavior of electrons may be described by means massless Dirac equation, where instead of speed of light c must be put Fermi velocity $v_F \simeq 10^{-2}c$ [14, 15]. This equation is

$$\imath\hbar\partial_t\psi = \left(\sum_i \left(v_F\widehat{\sigma}^\alpha D_i^\alpha + e_i\varphi_{i,ext}\right) + \sum_{i,j\neq i}\frac{1}{2}e_ie_jG_{ij}\right)\psi, \tag{1}$$

where Coulomb interaction is included. The following designations are used in the Hamiltonian (1): $D_i^\alpha = -\imath\hbar\partial_i^\alpha - e_iA_{i,ext}^\alpha/c$, $\varphi_{i,ext}$, $A_{i,ext}^\alpha$ — are the potentials of external electromagnetic field,

$\mathbf{E}_{i,ext} = -\nabla\varphi_{i,ext} - \partial_t \mathbf{A}_{i,ext}$ is the electric field, $\mathbf{B}_{i,ext} = curl\mathbf{A}_{i,ext}$ is the magnetic field, quantities e_i, m_i-are the charge and mass of particles, $\hbar$ — is the Planck constant, and $G_{ij} = 1/r_{ij}$, — is the Green functions of the Coulomb interaction. The spinor wave function ψ depend on 2N coordinates $R = [\mathbf{r}_1, \ldots, \mathbf{r}_N]$ and time $\psi = \psi(R, t)$, where $\mathbf{r}_i = [x_i, y_i]$ are the 2D coordinates of each particle. Pauli matrices σ_i^α satisfies to the commutation relation

$$[\sigma_i^\alpha, \sigma_j^\beta] = 2\imath\delta_{ij}\varepsilon^{\alpha\beta\gamma}\sigma_i^\gamma. \tag{2}$$

Set of graphene quantum hydrodynamics equations consists of continuity equation

$$\partial_t n + v_F \nabla \mathbf{S} = 0; \tag{3}$$

spin evolution equation

$$\partial_t S^\alpha + v_F \partial^\alpha n = -\frac{2}{\hbar}\varepsilon^{\alpha\beta\gamma} J_M^{\beta\gamma}; \tag{4}$$

equation of spin current evolution

$$\begin{aligned} &\partial_t J_M^{\alpha\beta} + v_F \partial^\alpha J^\beta - \hbar v_F^2 \varepsilon^{\alpha\gamma\delta}\partial^\beta\partial^\gamma S^\delta \\ &= -\frac{e}{c} v_F^2 \varepsilon^{\alpha\beta\gamma} n B^\gamma + \frac{2v_F^2}{\hbar}\varepsilon^{\alpha\mu\nu}\Pi^{\nu\mu\beta} + e v_F S^\alpha E^\beta - e^2 v_F S^\alpha \partial^\beta \int d\mathbf{r}' G(\mathbf{r}, \mathbf{r}') n(\mathbf{r}', t); \end{aligned} \tag{5}$$

and momentum balance equation

$$\partial_t J^\alpha(\mathbf{r}, t) + v_F \partial^\beta J_M^{\beta\alpha} = \frac{e v_F^2}{c}\varepsilon^{\alpha\beta\gamma} S^\beta B^\gamma + e v_F n E^\alpha - e^2 v_F n \partial^\alpha \int d\mathbf{r}' G(\mathbf{r}, \mathbf{r}') n(\mathbf{r}', t), \tag{6}$$

where

$$\Pi^{\alpha\beta\gamma} \cong S^\alpha \frac{J^\beta J^\gamma}{n^2} - \hbar^2 S^\alpha \frac{\partial^\beta\partial^\gamma\sqrt{n}}{\sqrt{n}}. \tag{7}$$

Basic ideas for derivation of the set of quantum hydrodynamics equations described at Ref. [16]. The set of Equations (3)–(6) describes a dynamic of graphene electrons in physical space instead of 2N dimensional configuration space, where the wave function is specified [17, 18].

We going to consider a dispersion of linear waves. So, we consider small perturbations of physical quantities near equilibrium state

$$\begin{gathered} n = n_0 + \delta n, \quad S^\alpha = S_0^\alpha + \delta S^\alpha, \quad \mathbf{S}_0 \parallel \mathbf{B}_0 \\ J^\alpha = 0 + \delta J^\alpha, \quad J_M^{\alpha\beta} = 0 + \delta J_M^{\alpha\beta}, \end{gathered} \tag{8}$$

We suppose what small perturbations δf are harmonic

$$\delta f = f(\omega, \mathbf{k}) \exp(-\imath\omega t + \imath\mathbf{k}\mathbf{r})$$

and obtain an equation $\Lambda^{\alpha\beta}(\omega, \mathbf{k}) S^\beta(\omega, \mathbf{k}) = 0$

Evident form of the matrix $\Lambda^{\alpha\beta}$ is

$$\hat{\Lambda} = \begin{pmatrix} \Lambda_{xx} & \Lambda_{xy} & 0 \\ \Lambda_{yx} & \Lambda_{yy} & 0 \\ \Lambda_{zx} & \Lambda_{zy} & \Lambda_{zz} \end{pmatrix},$$

Dispersion equation to be

$$\det \widehat{\Lambda}(\omega, \mathbf{k}) = 0. \tag{9}$$

This equation splits into two

$$\Lambda_{xx}\Lambda_{yy} - \Lambda_{xy}\Lambda_{yx} = 0, \tag{10}$$

and

$$\Lambda_{zz} = 0. \tag{11}$$

We suppose to consider two contributions, one of them is influence of the magnetic field directed perpendicular to the sample B_z, the second one is contribution of the in plane magnetic field B_x.

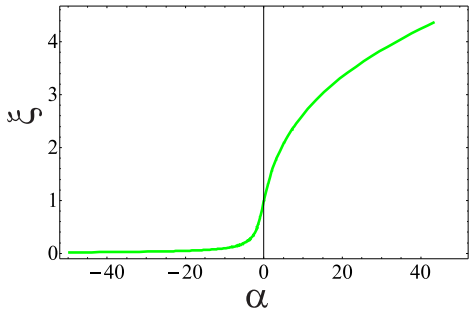

Figure 1: The figure presents a dispersion dependence appearing from Equation (11) at the presence of an in-plane magnetic field. Here $\xi = \omega/kv_F$ and $\alpha = -\frac{|e|}{\hbar c}\frac{B_0}{k^2}\cos\theta$.

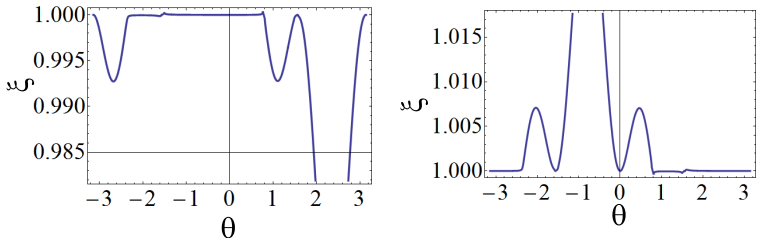

Figure 2: The figure presents two solutions of Equation (10). It shows us angle dependence of $\xi(\theta)$. System parameters are $\kappa = -10^{-6}$, $\chi = 0.1$, and $\mu = 10^{-3}$.

In the absence of external magnetic field Equation (10) has one solution, it is $\omega = kv_F$. If we put sample in external magnetic field perpendicular to the sample we will find no changes. Equation (11) has no solutions in both described cases. Situation change if we switch on in plane magnetic field. Evident form of Equations (10) and (11) becomes complicated, and new solutions are arisen. In this case Equation (11) has one solution which is presented at Fig. 1. From Fig. 1 we can see that at small α the parameter ξ is linearly proportional to α. So, we can write $\xi = \lambda_1\alpha + \lambda_2$, where λ_i are numerical constants. Using evident forms of ξ and α we can find:

$$\omega = -\frac{|e|\lambda_1}{\hbar c}\frac{B_0}{k}\cos\theta + kv_F\lambda_2$$

As for Equation (10), its degree increase to eight, and it has two physically feasible solutions instead of one. Real parts of these solutions are presented at Figs. 2 and 3. The imaginary part of the solutions to four orders of magnitude smaller than their real part, so we neglect it.

Equation (10) is studied in linear on B_x approximation.

In dimensionless variables dispersion properties of system ($\omega(\mathbf{k})$ or $\xi(\mathbf{k})$, where $\xi = \omega/kv_F$) depend on parameter $\alpha = \frac{e}{\hbar c}\frac{\mathbf{kB}}{k^3} = -\frac{|e|}{\hbar c}\frac{B_0}{k^2}\cos\theta$, in the case of Equation (11).

From Equation (10) we find that ξ depends on $\kappa = \frac{eB_{0x}}{c\hbar k^2} < 0$, $\mu = \frac{e^2 S_{0z}}{\hbar v_F k^2}$, $\chi = S_{0x}/n_0$, and θ. The angle θ is defined as $\cos\theta = k_x/k$ and $\sin\theta = k_y/k$.

3. CONCLUSION

In this paper, we have suggested the graphene quantum hydrodynamics equation based on famous massless relativistic Dirac's equation for electrons in graphene. We have described dispersion of collective excitations of electron in graphene. We have shown that where are three type of collective excitations, whose frequencies strongly depend on an angle between direction of wave propagation and direction of in plane external magnetic field.

REFERENCES

1. Roldan, R., J.-N. Fuchs, and M. O. Goerbig, "Collective modes of doped graphene and a standard two-dimensional electron gas in a strong magnetic field: Linear magnetoplasmons versus magnetoexcitons," *Phys. Rev. B*, Vol. 80, 085408(6), 2009.

2. Roldan, R., J.-N. Fuchs, and M. O. Goerbig, "Spin-flip excitations, spin waves, and magnetoexcitons in graphene Landau levels at integer filling factors," *Phys. Rev. B*, Vol. 82, 205418(11), 2010.
3. Roldan, R., M. O. Goerbig, and J.-N. Fuchs, "Theory of Bernstein modes in graphene," *Phys. Rev. B*, Vol. 83, 205406(5), 2011.
4. Goerbig, M. O., "Electronic properties of graphene in a strong magnetic field," *Rev. Mod. Phys.*, Vol. 83, 1193–1243, 2011.
5. Das Sarma, S., S. Adam, E. H. Hwang, and E. Rossi, "Electronic transport in two-dimensional graphene," *Rev. Mod. Phys.*, Vol. 83, 407–470, 2011.
6. Peres, N. M. R., "The transport properties of graphene: An introduction," *Rev. Mod. Phys.*, Vol. 82, 2673–2700, 2010.
7. Akhiezer, I. A., *Plasma Electrodynamics*, Pergamon Press, 1975.
8. Kuz'menkov, L. S. and S. G. Maksimov, "Quantum hydrodynamics of particle systems with coulomb interaction and quantum bohm potential," *Theoretical and Mathematical Physics*, Vol. 118, 227–240, 1999.
9. Marklund, M. and G. Brodin, "Dynamics of spin-1/2 quantum plasmas," *Phys. Rev. Lett.*, Vol. 98, 025001(4), 2007.
10. Kuz'menkov, L. S., S. G. Maksimov, and V. V. Fedoseev, "Microscopic quantum hydrodynamics of systems of fermions: Part 1," *Theoretical and Mathematical Physics*, Vol. 126, 110–120, 2001.
11. Andreev, P. A. and L. S. Kuzmenkov, "Waves of magnetic moment and generation of waves by neutron beam in quantum magnetized plasma," arXiv:1109.3335.
12. Shukla, P. K. and B. Eliasson, "Nonlinear collective interactions in quantum plasmas with degenerate electron fluids," *Rev. Mod. Phys.*, Vol. 83, 885–906, 2011.
13. Andreev, P. A., L. S. Kuzmenkov, and M. I. Trukhanova, "Quantum hydrodynamics approach to the formation of waves in polarized two-dimensional systems of charged and neutral particles," *Phys. Rev. B*, Vol. 84, 245401(13), 2011.
14. Novoselov, K. S., A. K. Geim, S. V. Morozov, D. Jiang, M. I. Katsnelson, I. V. Grigorieva, S. V. Dubonos, and A. A. Firsov, "Two-dimensional gas of massless Dirac fermions in graphene," *Nature*, Vol. 438, 197–200, 2005.
15. Sheehy D. E. and J. Schmalian, "Quantum critical scaling in graphene," *Phys. Rev. Lett.*, Vol. 99, 226803(4) 2007.
16. Andreev P. A., "Collective excitations in graphene in magnetic field," arXiv:1201.0779.
17. Goldstein S., "Quantum theory without observers-part one," *Physics Today*, Vol. 51, No. 3, 42–47, 1998.
18. Goldstein S., "Quantum theory without observers-part two," *Physics Today*, Vol. 51, No. 4, 38–42, 1998.

Microscopic Classic Hydrodynamic and Methods of Averaging

L. S. Kuzmenkov[1] and P. A. Andreev[2]

[1]Department of Theoretical Physics, Physics Faculty, Moscow State University, Russian Federation
[2]Department of General Physics, Physics Faculty, Moscow State University, Russian Federation

Abstract— In classic mechanics there are at least two general methods for hydrodynamic equation derivation. The first one is the consideration of macroscopic parallelogram in a medium and calculation for number of particles, momentum or energy passing through the planes. It is the way of macroscopic hydrodynamics. The second method of the hydrodynamic equations derivation includes the physical kinetics and offers the microscopic method starting from Liouville equation. Using of the physical kinetics as intermediate step leads to additional unnecessary limitation. This method includes derivation of the kinetic equation chain which also called BBGKY chain. The hydrodynamic equation arises as moments of the frequency function.

We present a new method for derivation of the hydrodynamic equation directly from classic motion equations. The first and most important step is the definition of the particles density in vicinity of the point of the physical space. This definition contains generalized function (Dirac's delta function) and represents analytical representation of a notion of the physically infinitesimal volume. The Newton law of motion is used for motion description of each particle in vicinity of point of physical space. Particle density is the first collective variable in our description. Next step is the derivation of equation of temporal evolution for the particle density. In the result new physical quantities are appeared and we can derive evolution equations for these quantities. During derivation a chain of equations is arisen, this chain is an analog of the BBGKY chain, but other framework lies behind.

This method is developed as for the neutral as for the charged particles, but in our presentation we consider charged particles only and we consider non-relativistic limit. However, this method can be used for derivation of equations for relativistic hydrodynamic and kinetic as well. We demonstrate this method, as it has written, for simplest case. One of the interesting consequences is that electric dipole field, electric quadrupole field and etc are arise in equations of collective motion *and* in Maxwell equation as sources of electric field.

1. INTRODUCTION

In abstract we mention two different ways for derivation of hydrodynamic equations. One of them is macroscopic. In this case we need to consider macroscopic physically infinitesimal pies of medium and apply mechanics lows to it [1]. The second way was suggested in the middle of the twentieth century. It includes integration of Liouville equation to obtain kinetic equation, and equations of hydrodynamics appear as consequence of kinetic equation [2–4]. Basic ideas of another method development have been presented in abstract. Below we give a detailed description of this method suggested in Ref. [5], some its applications were also described where.

We also want to note that in last decade a method of many-particle quantum hydrodynamics has been developed for a various physical systems (see for example [6, 7]. Nevertheless, classic hydrodynamics has some benefits. It is a time to describe basic steps for equation derivation.

2. MODEL

We count a number of particles or their mass in vicinity of a point $\mathbf{r}$ of physical space. We suppose that vicinity has volume Δ. So, density of particles $\rho(\mathbf{r}, t)$ equals to

$$\rho(\mathbf{r}, t) = \frac{1}{\Delta} \sum_{i=1}^{N(\mathbf{r},t)} m_i, \tag{1}$$

where $N(\mathbf{r}, t)$ is the number of particles in the vicinity of point $\mathbf{r}$. It is not convenient to work with the sum having a changing limit of summation. There is a way to avoid this problem. We use Dirac delta function to count particles in vicinity of a point $\mathbf{r}$

$$\rho(\mathbf{r}, t) = \frac{1}{\Delta} \int d\xi \sum_{i=1}^{N} m_i \delta(\mathbf{r} + \xi - \mathbf{r}_i(t)), \tag{2}$$

where N is the total number of the particles in a system, and ξ scanning vicinity of a point $\mathbf{r}$. Integral of δ-function gives us 1 if particle in the vicinity and 0 if particle outside of the vicinity.

For simplicity we consider here the Coulomb interaction only, but presenting in the paper method allows us to consider relativistic motion of particles with whole electromagnetic interaction.

If we consider the system of particles with equal masses m we can write $\rho(\mathbf{r},t) = mn(\mathbf{r},t)$. Lets consider time derivative of particles density

$$\begin{aligned}\partial_t\rho &= \frac{1}{\Delta}\int d\xi \sum_{i=1}^{N} m_i \partial_t \delta(\mathbf{r}+\xi-\mathbf{r}_i(t)) \\ &= -\frac{1}{\Delta}\int d\xi \sum_{i=1}^{N} m_i \partial_{\mathbf{r}} \delta(\mathbf{r}+\xi-\mathbf{r}_i(t))\partial_t \mathbf{r}_i = -\partial_{\mathbf{r}}\left(\frac{1}{\Delta}\int d\xi \sum_{i=1}^{N} m_i \mathbf{v}_i \delta(\mathbf{r}+\xi-\mathbf{r}_i(t))\right). \quad (3)\end{aligned}$$

In right-hand side of Equation (3) we put in brackets a quantity which has meaning of particles current. In the results we have continuity equation

$$\partial_t\rho + \nabla\mathbf{J} = 0 \quad (4)$$

where a current of particles

$$\mathbf{J}(\mathbf{r},t) = \frac{1}{\Delta}\int d\xi \sum_{i=1}^{N} m_i \mathbf{v}_i(t)\delta(\mathbf{r}+\xi-\mathbf{r}_i(t)) \quad (5)$$

appears. Using $\mathbf{J}$ we can introduce velocity of center of mass for particles in vicinity of each point $\mathbf{v}(\mathbf{r},t) = \mathbf{J}(\mathbf{r},t)/n(\mathbf{r},t)$. We can also introduce velocity of thermal motion u_i for each particle as difference between a particle velocity and velocity of a local center of mass $\mathbf{u}_i = \mathbf{v}_i(t) - \mathbf{v}(\mathbf{r},t)$.

Analogously to Equation (3) we can find equation for current $\mathbf{J}(\mathbf{r},t)$. So, we come to Euler equation, which describes balance of momentum and has form

$$\partial_t J^\alpha(\mathbf{r},t) + \frac{1}{\Delta}\partial^\beta \int d\xi \sum_{i,k\neq i} v_i^\alpha v_k^\beta \delta(\mathbf{r}+\xi-\mathbf{r}_i(t)) = \frac{1}{\Delta}\int d\xi \sum_{i=1}^{N} e_i E_i^\alpha(\mathbf{r}_i(t),t)\delta(\mathbf{r}+\xi-\mathbf{r}_i(t)) + \Phi^\alpha, \quad (6)$$

where Φ^α presents force field caused by Coulomb interaction. To obtain the terms in right-hand side of Equation (6) Newton equations have been used, which in considered case reads $m_i\dot{\mathbf{v}}_i = e_i\mathbf{E}_{i,ext} - \nabla\sum_{j\neq i} e_i e_j/r_{ij}$. For simplicity, we include external electric field only, but external magnetic field can be treated in the same way. Evident form of last term in right-hand side of Equation (6) is

$$\Phi^\alpha = -\frac{1}{\Delta}\int d\xi \sum_{i,k\neq i} e_i e_k \partial_i^\alpha \left(\frac{1}{|\mathbf{r}_i - \mathbf{r}_k|}\right)\delta(\mathbf{r}+\xi-\mathbf{r}_i(t)). \quad (7)$$

It describes contribution of Coulomb interaction.

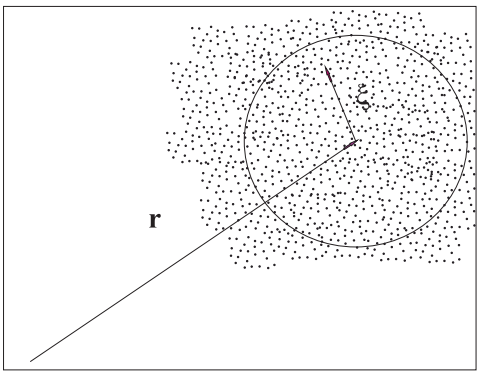

Figure 1: The figure presents a Δ vicinity of a point $\mathbf{r}$ and shows the meaning of vector ξ scanning the vicinity. Points on the picture represent particles.

The second term in the left-hand side has kinematic nature and does not depend on interaction and its nature. To be short we symbolize this term as $\partial_\beta \Pi^{\alpha\beta}$. $\Pi^{\alpha\beta}$ has meaning of tensor of momentum current. It may be presented in the form of $\Pi^{\alpha\beta} = nv^\alpha v^\beta + p^{\alpha\beta}$, where $p^{\alpha\beta}$ is the tensor of kinematic pressure, in most of cases it might be presented as $p\delta^{\alpha\beta}$. $p^{\alpha\beta}$ has the same structure as $\Pi^{\alpha\beta}$, but instead of $\mathbf{v}_i$ we must put thermal velocities. $\mathbf{u}_i$.

Since we present detailed transformation for Φ^α to show its structure in terms of concentration and other physical fields. Lets add integration on $\mathbf{r}'$ and change variables in Coulomb law due to δ-function

$$\begin{aligned}\Phi^\alpha &= -\frac{1}{\Delta}\int d\mathbf{r}' d\xi \sum_{i,k\neq i} e_i e_k \partial_i^\alpha \left(\frac{1}{|\mathbf{r}_i - \mathbf{r}_k|}\right)\delta(\mathbf{r}+\xi-\mathbf{r}_i(t))\delta(\mathbf{r}'-\mathbf{r}_k(t)) \\ &= -\frac{1}{\Delta}\int d\mathbf{r}' \sum_{i,k\neq i} e_i e_k \partial^\alpha \left(\frac{1}{|\mathbf{r}+\xi-\mathbf{r}'|}\right)\delta(\mathbf{r}'-\mathbf{r}_k(t))\delta(\mathbf{r}+\xi-\mathbf{r}_i(t)). \end{aligned} \tag{8}$$

For next step we consider functions $f(\mathbf{r})$ and $\varphi(\mathbf{r})$ connected dy relation

$$f(\mathbf{r}) = \frac{1}{\Delta}\int_\Delta \varphi(\mathbf{r}+\xi)d\xi,$$

for them there is the identity

$$\int f(\mathbf{r})d\mathbf{r} = \int \varphi(\mathbf{r})d\mathbf{r}.$$

Consequently we have that

$$\Phi^\alpha = -\frac{1}{\Delta^2}\int d\mathbf{r}' d\xi d\xi' \sum_{i,k\neq i} e_i e_k \partial^\alpha \left(\frac{1}{|\mathbf{r}+\xi-\mathbf{r}'-\xi'|}\right)\delta(\mathbf{r}'+\xi'-\mathbf{r}_k(t))\delta(\mathbf{r}+\xi-\mathbf{r}_i(t)). \tag{9}$$

Setting it on $\overrightarrow{\xi} - \overrightarrow{\xi}'$, using a fact that the Coulomb law is slowly changing on distances of order ξ, we represent a function Φ^α as a Taylor series. We start from consideration of the first term which has form

$$\Phi^\alpha_{(1)} = -\int d\mathbf{r}' \left(\partial^\alpha \frac{1}{|\mathbf{r}-\mathbf{r}'|}\right)\frac{1}{\Delta}\int d\xi \sum_i e_i \delta(\mathbf{r}+\xi-\mathbf{r}_i(t))\frac{1}{\Delta}\int d\xi' \sum_k e_k \delta(\mathbf{r}'+\xi'-\mathbf{r}_k(t)).$$

The second and third integrals are the charge densities in the vicinity of point $\mathbf{r}$ and $\mathbf{r}'$ correspondingly. So, $\Phi^\alpha_{(1)}$ may be presented in a short form

$$\Phi^\alpha_{(1)} = -\frac{e^2}{m^2}\rho(\mathbf{r},t)\partial^\alpha \int d\mathbf{r}' \left(\frac{1}{|\mathbf{r}-\mathbf{r}'|}\right)\rho(\mathbf{r}',t) = -\frac{e}{m}\rho\cdot\partial^\alpha \varphi_{charge},$$

where φ_{charge} is the potential of electric field caused by the density of charge. We point up on it because below we meet potential caused by electric dipole moment.

After detailed treatment of the first term in the Taylor series for Φ^α we can pay attention for the next terms. To understand some crucial points we need to treat the second term. It appears

in the form

$$\begin{aligned}\Phi^{\alpha}_{(2)} &= -\frac{1}{\Delta^2}\int d\mathbf{r}'\sum_{i,k\neq i}\left(\partial^{\alpha}\partial^{\beta}\frac{1}{|\mathbf{r}-\mathbf{r}'|}\right)(\xi^{\beta}-\xi'^{\beta})e^2\delta(\mathbf{r}'+\xi'-\mathbf{r}_k(t))\delta(\mathbf{r}+\xi-\mathbf{r}_i(t))d\xi d\xi' \\ &= -\int d\mathbf{r}'\left(\partial^{\alpha}\partial^{\beta}\frac{1}{|\mathbf{r}-\mathbf{r}'|}\right)\left(\frac{1}{\Delta}\sum_i \xi^{\beta}e\delta(\mathbf{r}+\xi-\mathbf{r}_i(t))\frac{1}{\Delta}\sum_k e\delta(\mathbf{r}'+\xi'-\mathbf{r}_k(t))\right. \\ &\quad \left.-\frac{1}{\Delta}\sum_i e\delta(\mathbf{r}+\xi-\mathbf{r}_i(t))\frac{1}{\Delta}\sum_k e\xi'^{\beta}\delta(\mathbf{r}'+\xi'-\mathbf{r}_k(t))\right)d\xi d\xi' \\ &= -\frac{e}{m}\int d\mathbf{r}'\left(\partial^{\alpha}\partial^{\beta}\frac{1}{|\mathbf{r}-\mathbf{r}'|}\right)\left(\frac{1}{\Delta}\sum_i \xi^{\beta}e\delta(\mathbf{r}+\xi-\mathbf{r}_i(t))d\xi\cdot\rho(\mathbf{r}',t)\right. \\ &\quad \left.-\rho(\mathbf{r},t)\cdot\frac{1}{\Delta}\sum_k e\xi'^{\beta}\delta(\mathbf{r}'+\xi'-\mathbf{r}_k(t))d\xi'\right). \end{aligned} \tag{10}$$

In this term a new quantity appears, it is a local density of electric dipole moment

$$d^{\alpha}(\mathbf{r},t)=\frac{1}{\Delta}\int d\xi\sum_i \xi^{\beta}e_i\delta(\mathbf{r}+\xi-\mathbf{r}_i(t)). \tag{11}$$

Using notion of charge density (1) and electric dipole density (11) we can rewrite $\Phi^{\alpha}_{(2)}$ as

$$\Phi^{\alpha}_{(2)}=-\frac{e}{m}\int d\mathbf{r}'\left(\partial^{\alpha}\partial^{\beta}\frac{1}{|\mathbf{r}-\mathbf{r}'|}\right)\left(d^{\beta}(\mathbf{r},t)\rho(\mathbf{r}',t)-\rho(\mathbf{r},t)d^{\beta}(\mathbf{r}',t)\right). \tag{12}$$

The density of force can be present in the following form

$$\Phi^{\alpha}=-\frac{e}{m}\rho(\mathbf{r},t)\cdot\partial^{\alpha}\left(\frac{e}{m}\int d\mathbf{r}'\frac{\rho(\mathbf{r}',t)}{|\mathbf{r}-\mathbf{r}'|}-\partial^{\beta}\int d\mathbf{r}'\frac{d^{\beta}(\mathbf{r}',t)}{|\mathbf{r}-\mathbf{r}'|}\right)-\frac{e}{m}d^{\beta}(\mathbf{r},t)\cdot\partial^{\alpha}\partial^{\beta}\int d\mathbf{r}'\frac{\rho(\mathbf{r}',t)}{|\mathbf{r}-\mathbf{r}'|}. \tag{13}$$

In the very last term in formula (13) we can introduce electric field $\mathbf{E}=-\nabla\varphi$ in two different ways $\partial^{\alpha}E^{\beta}$ or $\partial^{\beta}E^{\alpha}$. To solve this mystery we should consider the first term in right-hand side of Equation (6) which caused by external electric field. In this term we can put $\mathbf{r}+\xi$ instead of $\mathbf{r}_i(t)$ in the argument of $\mathbf{E}_{i,ext}$ because of delta-function. After that we represent a function as a Taylor series on ξ assuming that external field change slowly at interatomic distances. In the result we have that a force field $\mathbf{F}$ caused by external electric field appears as $F^{\alpha}(\mathbf{r},t)=(e/m\cdot\rho(\mathbf{r},t)+d^{\beta}(\mathbf{r},t)\partial^{\beta}+\ldots)E^{\alpha}_{ext}(\mathbf{r},t)$. It shows us a proper structure of Φ^{α}.

So far we have considered the two terms in the Taylor series for Φ^{α}, but we can see interesting tendency that Φ^{α} contains contributions of the electric charge, dipole moment and next terms including quadrupole and higher moments of the pies of the medium. On this step we can introduce the potential of electric field caused by particles. We knew that electric field acts on the charge density and corresponding force density has form $\rho\mathbf{E}$. Thus, the bracket behind the charge density is the electric field which connected with the potential of electric field φ in usual way $\mathbf{E}=-\nabla\varphi$ we yield evident form for φ

$$\varphi=\frac{e}{m}\int d\mathbf{r}'\frac{\rho(\mathbf{r}',t)}{|\mathbf{r}-\mathbf{r}'|}-\partial^{\beta}\int d\mathbf{r}'\frac{d^{\beta}(\mathbf{r}',t)}{|\mathbf{r}-\mathbf{r}'|}. \tag{14}$$

Using equality

$$\triangle\frac{1}{|\mathbf{r}-\mathbf{r}'|}=-4\pi\delta(\mathbf{r}-\mathbf{r}')$$

we found equation for φ introduced by formula (14)

$$\nabla\mathbf{E}=-\triangle\varphi=4\pi(e/m)\rho-4\pi\partial^{\beta}d^{\beta}+\ldots \tag{15}$$

We can use evident form of electric field corresponding to potential (14) for short representation of Φ^α in the result we find

$$\Phi^\alpha = (e/m)\rho E^\alpha + d^\beta \partial^\beta E^\alpha + \dots \tag{16}$$

We can see that whole electric field caused by ρ, $\mathbf{d}$ and other moments (15) act on each quantity ρ, $\mathbf{d}, \dots$. Its action includes in Φ^α by means of different terms in (16). Here we should point to a fact that in quantum hydrodynamics a force field acting on density of electric dipole moment has form $d^\beta \partial^\alpha E^\beta$ [7], that diverge from $d^\beta \partial^\beta E^\alpha$ in formula (16).

The paper contains a lot of large formulas, but in fact the simple idea lays behind all of it. One is the analytic representation of notion of averaging on the physically infinitesimal volume.

We gave detailed description for formation electric dipole moment contribution at dynamics of system of charged particles. Formulas (15) and (16) contain series which contains electric quadrupole moment and higher multipole moments along with electric dipole moment of medium.

In described manner we can find equation for energy balance and equations of balance for another additive physical quantities. For example, it might be density of electric dipole moment $\mathbf{d}$ and density of higher multipoles.

3. CONCLUSION

We have presented the method of direct derivation of hydrodynamic equation starting from microscopic picture of motion. We do not need to derive kinetic equation as a middle step. We have find that electric dipole and higher order moments make contribution in hydrodynamic equations along with density of charge.

REFERENCES

1. Landau, L. D. and E. M. Lifshitz, "Hydrodinamics," *Course of Theoretical Physics*, Vol. 6, Pergamon, London, 1981.
2. Pitaevskii, L. P. and E. M. Lifshitz, "Physical kinetics (kinetic theory)," *Course of Theoretical Physics*, Vol. 10, Pergamon, London, 1981.
3. Haug, H. and A. Jauho, *Quantum Kinetics in Transport and Optics of Semiconductors*, 2nd Edition, Springer, Berlin, 2008.
4. Kuhn, T., *Theory of Transport Properties of Semiconductor Nanostructures*, edited by E. Scholl, Springer, New York, 1997.
5. Drofa, M. A. and L. S. Kuz'menkov, "Continual approach to multiparticle systems with long-range interaction. Hierarchy of macroscopic fields and physical consequences," *Theoretical and Mathematical Physics*, Vol. 108, 848–859, 1996.
6. Kuz'menkov, L. S. and S. G. Maksimov, "Quantum hydrodynamics of particle systems with coulomb interaction and quantum bohm potential," *Theoretical and Mathematical Physics*, Vol. 118, 227–240, 1999.
7. Andreev, P. A., L. S. Kuzmenkov, and M. I. Trukhanova, "Quantum hydrodynamics approach to the formation of waves in polarized two-dimensional systems of charged and neutral particles," *Phys. Rev. B*, Vol. 84, 245401(13), 2011.
8. Vlasov, A. A., "The vibrational properties of an electron gas," *Sov. Phys. Usp.*, Vol. 10, 721–733, 1968.

Building NMR/NQR Spectrometer

R. Kubásek and M. Alkhaddour
Department of Theoretical and Experimental Electrical Engineering
Brno University of Technology, Kolejni 4, Brno 612 00, Czech Republic

Abstract— The paper deals with NMR/NQR spectrometer design. Paper describes individual parts of spectrometer and its important technical parameters. The experimental measurement of H_2 by NMR and of $KClO_3$ by NQR are described.

1. INTRODUCTION

NMR (Nuclear Magnetic Resonance) spectroscopy and tomography are common tools used in many applications over all field of technical and humanitarian disciplines. It is not necessary to mention all medicine, chemistry or geology applications. Contrariwise, NQR (Nuclear Quadrupole Resonance) applications are not so common and also well know as NMR. We can find considerable benefit in explosive and drug detection [1] and [2]. NQR is fundamental tool in chemistry description of solid state materials, mainly crystalline structures. Theoretical studies of several elements NQR can be found. Experimental studies and measurement is in many cases at the edge of technical possibilities due to low signal on NQR. Signal level strongly depends on specific element and material structure where is the element contained. This paper shows the limits of spectrometer designed by common tools and electrical components.

2. SPECTROMETER AND ITS PARTS

The block diagram in Figure 1 shows general approach of spectrometer setup. Any components of spectrometer have technical parameters at different levels. Generally we will discus the important ones. The control center, microprocessor, is important to synchronize all measurement processes and it is necessary if multiple averaging acquisitions are performed. We firstly focus on experiments with single excitation and single FID (Free Induction Decay) signal acquisition. All synchronization was made by triggering square pulse for RF amplifier. For simplicity and fast visualization we used oscilloscope Agilent DSO6052A triggered by square pulse. Resolution is only 8-bits, nevertheless enough for demonstration of functionality.

Arbitrary generator Agilent 33250A was used as sine source for excitation. Mainly spectral cleanness, phase noise and harmonic distortion are discussed in many sources. Used generator should match all this requirements. Experiments show, that probe coil tuned with high quality, $Q = 10$ to 50, adjust even not exactly harmonic signal at input of probe to nice sine course. It is due narrow frequency bandwidth of probe. The parameters of sine source are not so tough for hard pulse excitation. Precise tuned probe is absolutely necessary for acquisition. The signal level increase with quality Q.

RF amplifiers should be chosen mainly by its frequency range and maximal power. In excitation, RF amplifier is in pulse mode, then the continuous power it typically fifth-time lower and require higher power supply voltage. We expect needed power approximately 100 to 200 W. RF amplifier TOMCO 2235A was used. Function of power coupler is separation of excitation pulse (RF amplifier to probe) from acquisition of FID (probe to LN preamp). In fact, coupler distinguishes high from low signals [3]. Coupler is tuned typically in not a wide band frequency range. For different frequencies, for example 10 and 28 MHz, we need to use two couplers tuned to theirs frequency. There exists some approach for wide band couple design, but we recommend use of simple filter design coupler.

Probe design can be made in two ways, serial or parallel resonate circuits. Both have some advantages and also disadvantages. Parallel is of simple design, bud need two turning parts. Serial circuit uses transformer for matching circuit, but need only one turning part (commonly capacitor). Turning probe to desired frequency and matching to 50 Ω can be performed by bidirectional coupler, blue part in Figure 1. We can also use reflection meter or spectral analyzer in return loss mode. The additional circuits for transient effect after excitation can be added to probe coil [4]. Transient effect of receiver has to be less then relaxation T_2.

Low noise preamplifier is protected by power coupler, but other prevention from overshoot should be done. There can occurs voltage peaks in hundred of volts. Gain about 40 dB for NMR

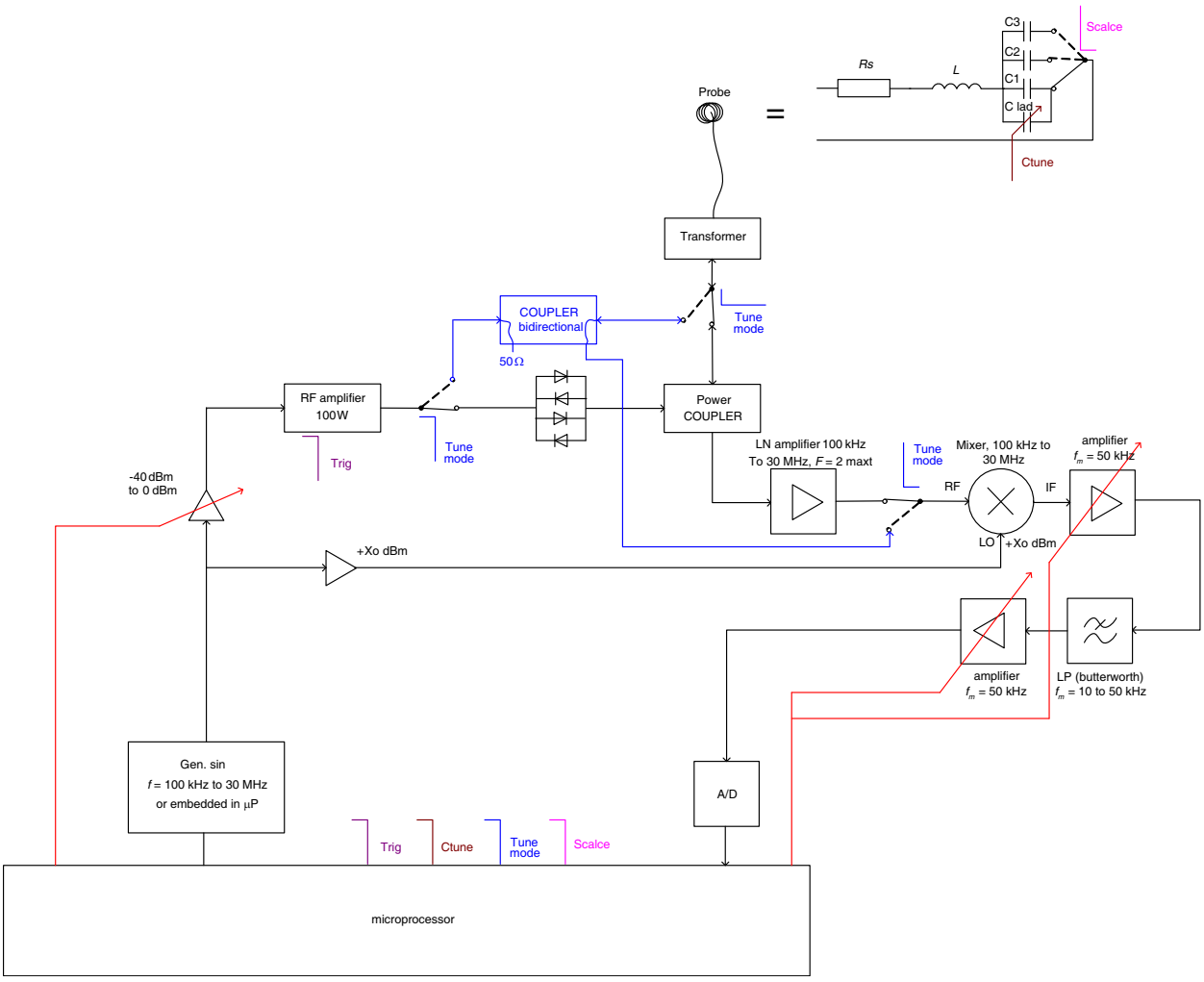

Figure 1: Spectrometer block diagram.

application seems to be enough. Gain in NQR task should be higher, in fact as much as possible with respect to limitation by disturbances and noise level. We use preamplifiers gain up to 80 dB.

Mixer translate FID signal to base band. We need to choose practical parameters of mixer like frequency range and local oscillator power. Major technical parameters are isolations between gates and IP3 cross point. All parameters are frequency depended parameters and for lower frequency have better values. We used mixer Mini-Circuits ZAD-6+. It is advantage to use extra local oscillator sine signal generator to shift FID and for easy level adjustment.

Low pass filter should have better parameters, noise and distortions, then isolation of mixer. The limiting factor is step response of filter, which should be as short as possible. Butterworth or better Bessel approximation are suitable. We used general purpose filter LTC1562 as 8th order Bessel LP with cut off frequency 30 kHz. The step response of that filter is 20 µs long.

3. EXPERIMENTS

The firs NMR experiment was perform with magnet KONSTANTIN. It is the magnet developed at Czech Academy of Science in Brno [3]. The magnet allows for the setting of the field in steps by means of current using superstabilization coils. We setup the strength of flux density to 254.44 mT (10.833 MHz for H_2). The probe coil was turned to this frequency with return loss less then −40 dB. After hour stabilization the measurement was performed. The local oscillator frequency was shifted by 10 kHz to obtain time course of FID signal with envelope. FID signal with excitation pulse envelope is shown in Figure 2(a).

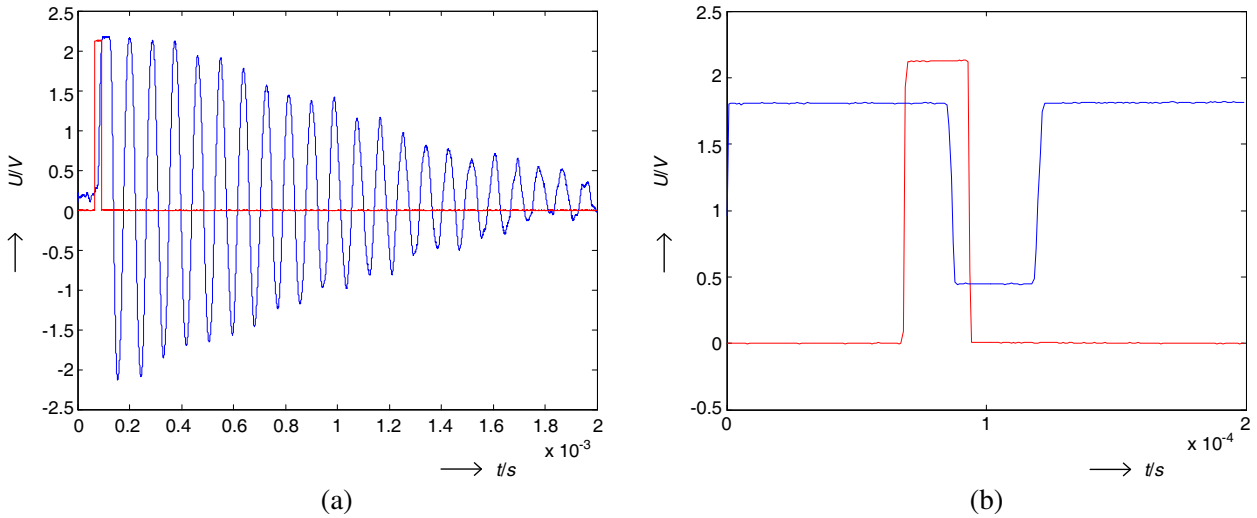

Figure 2: (a) The NMR FID signal and excitation pulse (red), (b) excitation pulse (red) and transient response of whole spectrometer line.

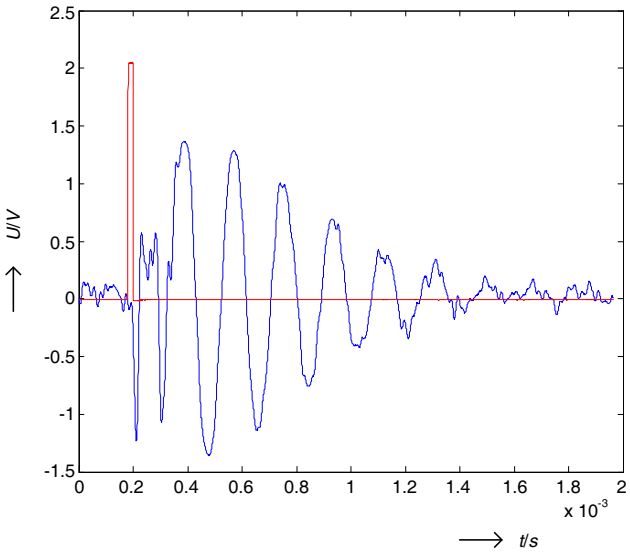

Figure 3: NQR signal of $KClO_3$ and excitation pulse (red).

The FID signal has time constant approximately 1.6 ms. Estimated field inhomogeneity is:

$$\Delta B_0 = \frac{1}{T_2 \gamma} = 2.3\,\mu\mathrm{T} = 9.2 \cdot 10^{-6} B_0, \tag{1}$$

where γ is gyromagnetic ratio of H_2. This inhomogeneity corresponds to assumed inhomogeneity of magnet KONSTANTIN, 10^{-5} of B_0. The RF excitation pulse was 25 µs long with power approximately 10 W. The optimal parameters are hard to find and it is experimental task. Nevertheless, the integral power was slightly lower then estimated one from probe space dimensions and electrical parameters. The total gain of all amplifiers was 100 dB. The noise and interferences in FID signal is suitable low. The transient response after excitation, can be seen in Figure 2(b), was 28 µs long and corresponds to step response of low pass filter. Transient response was measured with maximal (open loop) gain of amplifiers.

The second experiment was made with 10 g of crystalline $KClO_3$ at NQR frequency 28.1 MHz. Chlorine based materials with NQR signal was chosen because its high value of FID signal. The NQR do not need any B_0 field what simplify experiment setup. Probe for 28.1 MHz was also tuned with return loss less then -40 dB. The parameters of excitation pulse for NQR can be expect close to NQR one. Generally, needed energy transmitted to nucleus if similar for NMR and

NQR applications. We used 20 µs long RF excitation pulse of power about 30 W. Only different preamplifiers in signal line in comparison with NMR experiment were used. The total gain of all amplifiers were 120 dB, NQR FID signal was approximately ten times lower than NMR signal of H_2. The FID of NQR can be seen in Figure 3.

The transient effect after excitation is longer due to different preamplifier used. The lower value of signal logically leads to higher noise in FID signal, but it is still at suitable level. The relaxation time about 1 ms corresponds to theoretical relaxations, the exact value is difficult to estimate. The exact relaxations and other NQR parameters strongly depend on many conditions, mainly on crystalline structures and chemical composition of $KClO_3$, temperature, static pressure, and more circumstances.

4. CONCLUSION

The design of the presented technical instruments is advanced enough for realization of NMR/NQR spectrometer in not very complicated way. We can build simple NMR spectrometer with suitable technical parameters by smart choose of any spectrometers par. The challenge is to design all connections and design the whole unit. Success of NQR experiment is granted for material with high level of FID signal. Typically chlorine based materials. For example nitrogen based materials gives much weaker signal, approximately 100 to 1000 times lower then $KClO_3$ signal, and FID signal with single acquisition is buried in noise. The only one way seems to be in low-noise probe design and use of averaging to extract useful signal from noise.

ACKNOWLEDGMENT

This work was supported by/within the project of the Grant Agency of the Czech Republic No. 102/09/0314 and project from Education for Competitiveness Operative Programme CZ.1.07.2.-

3.00.20.0175 (Electro-researcher).

REFERENCES

1. Grechishkin, S. and N. Ya Sinyavskin, "Nuclear quadrupole resonance as an explosive and narcotic detection technique," *IOP Physics Uspekti*, Vol. 40, No. 4, 393–406, 1997.
2. Ostafin, M. and B. Nogaj, "14N-NQR based device for detection of explosives in landmines," *Science Direct Measurement*, Vol. 40, 43–54, 2007.
3. Robinson, F. N. H., "A sensitive nuclear quadrupole resonance spectrometer for 2–60 MHz," *IOP Science Instrument*, Vol. 15, 1982
4. Rudakov, T. N., V. V. Fedotov, A. V. Belyakov, and V. T. Mikhal'tsevich, "Suppression of transient processes in the oscillatory circuit of the NQR spectrometer," *Instruments and Experimental Techniques*, Vol. 43, No. 1, 78–81, 2000.
5. Král, B., "Merení halovými clánky na elektromagnetech spektrometru jaderné magnetické resonance," *Slaborpoudý Obzor*, 32/5 1971.

Magnetic Flux Density Reconstruction Method

M. Hadinec
Department of Theoretical and Experimental Electrical Engineering
Brno University of Technology, Czech Republic

Abstract— This article deals with the measurement of magnetic flux density around copper specimens, which are created using printed circuit board technology. The current that flows in the specimen creates magnetic field. Such magnetic fields can be mapped using magnetic resonance tomography or by Hall probes. The method for reconstruction of magnetic flux density inside the measured volume will be presented and analyzed. The reconstruction method is based on Legendre polynomials approximation, using Least Mean Squares solver programmed in Matlab. This reconstruction method could be usable for acceleration of the mapping process, which is lengthy and can lead to many errors while measuring many points and many planes around the specimen. Using proper approximation coefficients, it is possible to compute individual approximated maps of magnetic flux density, so there is no need of fine mapping and meshing inside desired volume. These coefficients can be obtained from values measured on the edge of desired volume, using Laplaces's equation solution.The measured and approximated maps of magnetic flux density are compared and differences analyzed. The theoretical model of magnetic flux density around measured specimen is made in COMSOL.

1. INTRODUCTION

The magnetic flux density was measured in several planes around specimens, using Hall's probes. The proper mapping of magnetic flux density around these specific specimens is important for electric impedance tomography (EIT) research and other further numerical purposes [1]. The mapping process is usually made manually and can obtain many errors. It would be helpful to speed up this process by approximation and reconstruction of several planes in the desired volume or by making simulation of magnetic flux density distribution in COMSOL. The aim of this work is to show magnetic flux density reconstruction method based on Legendre's polynomials, which could be suitable for computing maps of magnetic flux density inside measured volume [2]. The better speed of mapping process is obvious, but the approximation can put additional errors to expected shape of magnetic field.

2. MATHEMATICAL MODEL

The mathematical model for reconstruction is based on solution of Laplace's equation. We assume, that the field inside analyzed volume is stationary ($d/dt = 0$) and there are no sources of magnetic field. The Maxwell equations are reduced as

$$\nabla \times \mathbf{B} = 0 \tag{1}$$

$$\nabla \cdot \mathbf{B} = 0 \tag{2}$$

Each equation can be combined by application of Nabla operator and the result will be

$$\nabla(\nabla \times \mathbf{B}) = \nabla(\nabla \cdot \mathbf{B}) - \nabla^2 \mathbf{B} = \Delta \mathbf{B} = 0 \tag{3}$$

where Δ is the Laplace's operator and this formula is Laplace's equation. In our model, we assume, that the desired magnetic flux density vector is oriented perpendicular to the surface of the copper specimen.

Now it is suitable to use well known Dirichlet's problem of finding a function, which solves a specified partial differential equation in the desired volume. The solution takes prescribed values measured on the boundary of the volume [3]. The Dirichlet's problem is based on finding a unique continuous function u, which is twice continuously differentiable in the desired volume and continuous on the boundary (if there is given function f that has values everywhere on the boundary of a volume), such that u is harmonic in the interior and $u = f$ on the boundary. The requirement is called Dirichlet boundary condition. In NMR applications, the general solution could be obtained as

$$B(r, \theta, \varphi) = \sum_{n=0}^{\infty} \sum_{m=0}^{m=n} r^n \cdot P_{n,m}(\cos\theta) \cdot [C_{n,m} \cdot \cos(m \cdot \varphi) + D_{n,m} \cdot \sin(m \cdot \varphi)] \tag{4}$$

where r is distance from origin of coordinates, $P_{n,m}(\cos\theta)$ are Legendre's polynomials of first order a nth degree (for $m = 0$), resp. associated Legendre's polynomials (for $m = 1, 2, \ldots n$), m is polynomial degree, θ is half of peak angle, φ is azimuth angle, $C_{n,m}$ and $D_{n,m}$ are approximation coefficients [4]. The solution is converging inside sphere with radius, which is equal to number one.

The formulas for computing of Legendre polynomials for given order and degree were described in [5] and are beyond the scope of this article. To obtain approximation coefficients, the Matlab LSQR solver has to solve system of linear equations, which can be described according this formula

$$\begin{pmatrix} hc_{1,1,1} & hc_{1,1,2} & \cdots & hc_{1,Q,Q} & hd_{1,1,1} & \cdots & hd_{1,Q,Q} \\ hc_{2,1,1} & hc_{2,1,2} & \cdots & hc_{2,Q,Q} & hd_{2,1,1} & \cdots & hd_{2,Q,Q} \\ \vdots & \ddots & & & & & \vdots \\ \vdots & & \cdots & \cdots & \cdots & & \vdots \\ \vdots & & & & & \ddots & \vdots \\ hd_{g,1,1} & hc_{g,1,2} & \cdots & hc_{g,Q,Q} & hd_{g,1,1} & \cdots & hd_{g,Q,Q} \end{pmatrix}^{S}_{g\times 2Q^2} \times \begin{pmatrix} C_1 \\ \vdots \\ C_{Q^2x1} \\ D_1 \\ \vdots \\ D_{Q^2x1} \end{pmatrix}^{K}_{2Q^2\times 1} = \begin{pmatrix} B_{m1} \\ B_{m2} \\ \vdots \\ \vdots \\ \vdots \\ B_{mg} \end{pmatrix}^{Bm}_{g\times 1.} \tag{5}$$

where Q is a degree of approximation, B_m are measured values inside the volume. The left matrix is created according to (4) equation from Legendre's polynomials $P_{n,m}(\cos\theta)$, distance r from origin of coordinates and goniometric functions $\sin(m\varphi)$ and $\cos(m\varphi)$. The approximation accuracy is highly dependant on Q, but it the highest degree of approximation depends on the density of measured points of the volume. There is an analogy with Nyquist-Shannon sampling theorem. The solution is obtained using LSQR method, which is implemented in Matlab. The matrix should be large and sparse.

3. SPECIMENS AND FIELD MAPPING PROCESS

The specimens are realized by printed circuit board technology. The shape of two measured specimens is given by needs of EIT tomography methods. First specimen has full circle shape and second specimen has large central gap. The dimensions of gaped specimen can be seen on Fig. 1(a), photo of non-gaped specimen with Hall probe can be seen on Fig. 1(b). The power cables are attached trough the isolation plate, direction of magnetic field created by the current inside these cables should not influence the measured field.

The mapping of magnetic flux density was realized by Hall probe and fluxmeter F.W.BELL 9550. While measuring magnetic fields up to 100 µT, the resolution is 0.1 µT. Two copper wires, which are used for feeding the specimens are oriented perpendicular to mapping plane. Unfortunately, there are still problems with influence of feeding wires near the specimen, the field is slightly deformed. The input current was 5 A, the field was mapped in 5 planes, equally distributed above the specimen. The mapping area can be seen from Fig. 1(a).

4. RESULTS

Before computing approximation coefficients, it was suitable to create COMSOL model of measured specimen to compare measured fields with simulations. The meshing of this model was quite difficult task, because of the proportions between input wires and specimen. The specimen thickness is about 35 µm. Therefore, the meshing net has to be adjusted manually, especially around the edge

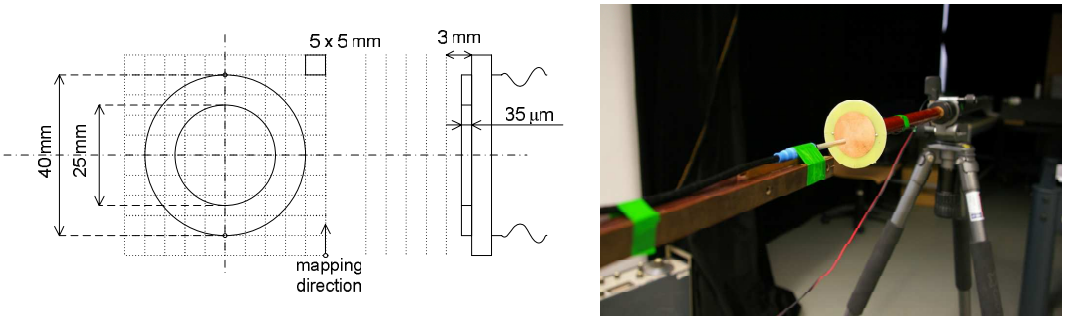

(a) (b)

Figure 1: Copper specimens and dimensions of mapped area.

of specimen. If this optimization is not made, the solution doesn't converge and we can not obtain proper results.

As we can see from Fig. 2(b), the shape of the field has maximum value of magnetic flux density around 64 µT and minimum around −64 µT. These values are in a good agreement with measured fields. The higher value could be caused by absence of isolation desk in the model or just the thickness of copper specimen is not exactly 35 µm.

The results of measuring and approximation can be seen on Fig. 3. The degree of approximation was set to $Q = 10$, because with this degree we obtained the best results. If we raise the approximation degree above $Q = 15$, the convergence of linear equation system solved by LSQR method

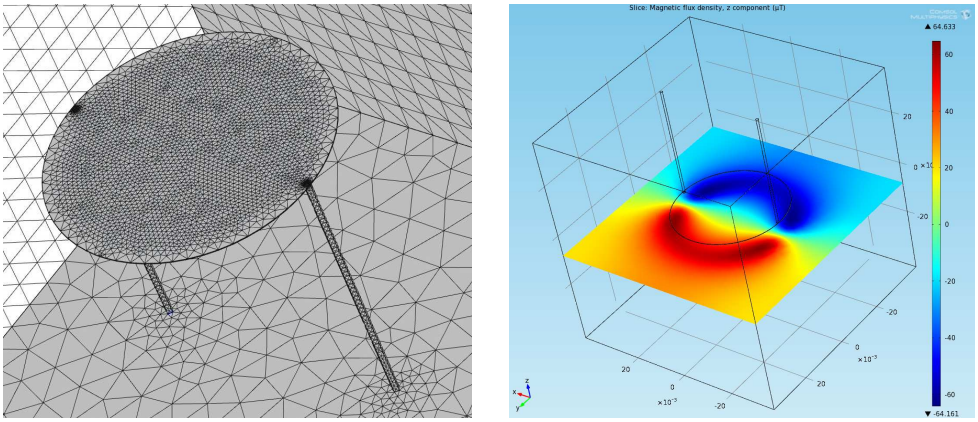

(a) (b)

Figure 2: Copper specimens and dimensions of mapped area.

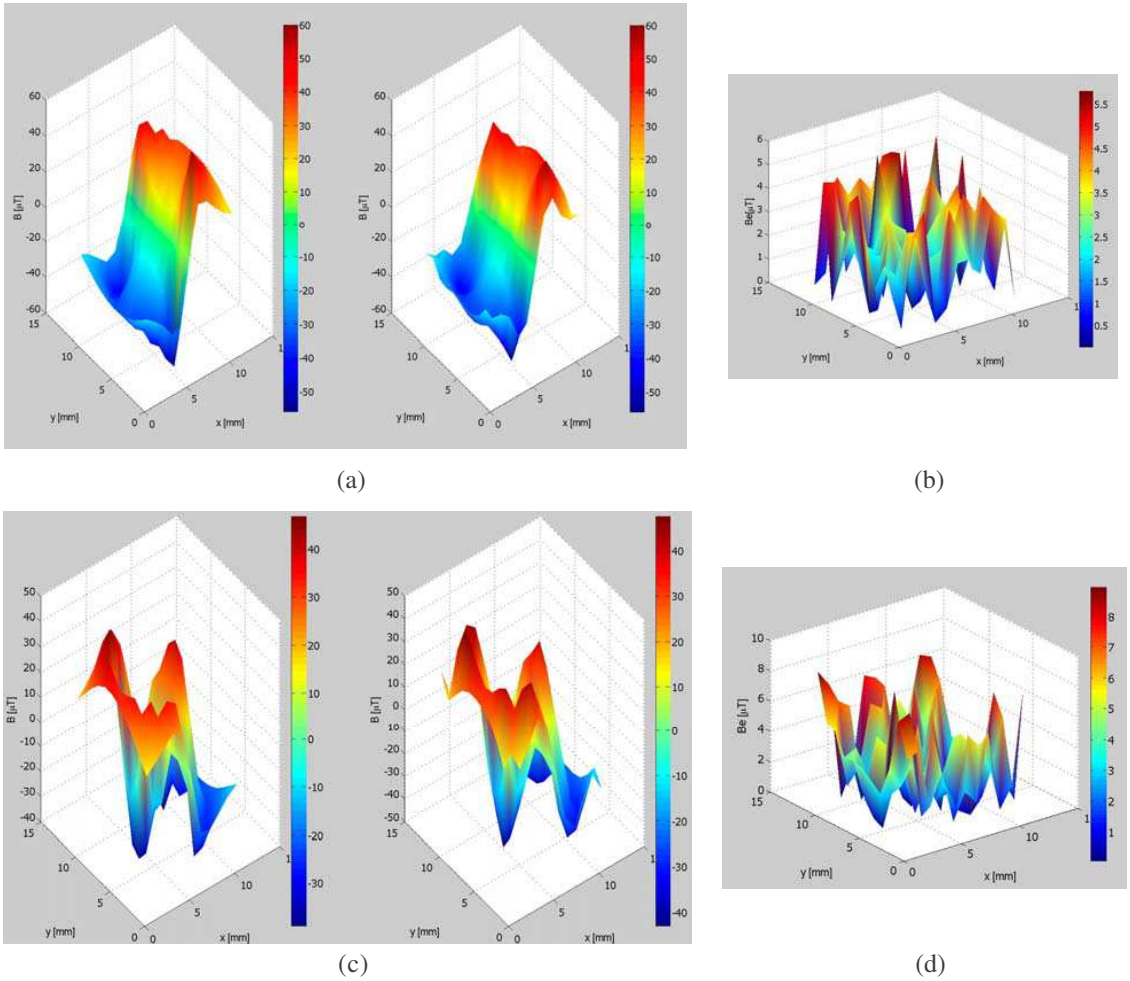

(a) (b)

(c) (d)

Figure 3: Comparison of measured and computed maps for two different specimens.

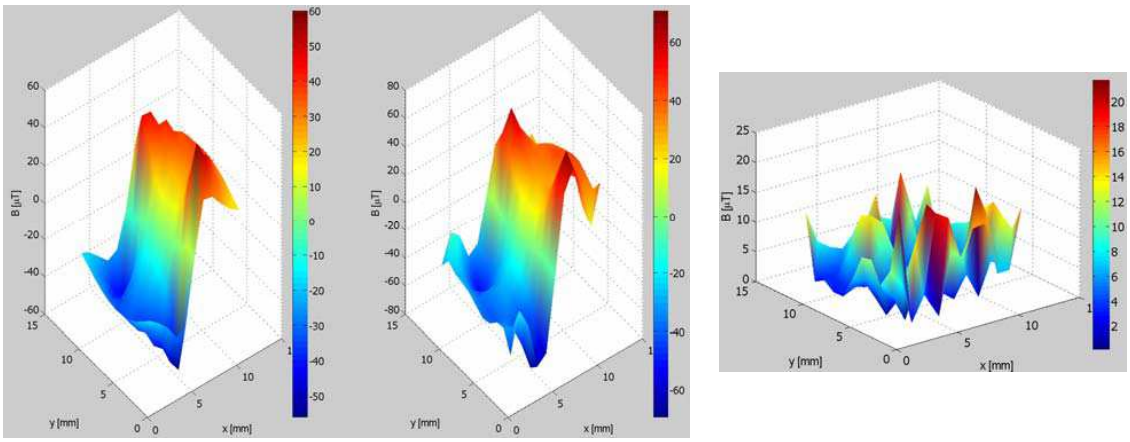

(a) (b)

Figure 4: Comparison of measured and computed maps without one plane for not-gaped specimen.

stagnated. On Fig. 3(a) we can see comparison of measured field map (left) and approximated field map (right) in the plane, which is 6 mm above the specimen. The other measured planes have similar shape. In this case, the coefficients used for computing the approximated map were obtained from all measured points. On Fig. 3(c) we can see field above gaped specimen. Fig. 3(b) and Fig. 3(d) show absolute value of difference between measured and approximated values of magnetic flux density at each measured point. We can see, that the field of gaped specimen is more "complicated" in shape and also the maximum approximation error is nearly twice bigger than error of not-gaped specimen. Therefore is obvious, that shape of magnetic field has big influence on approximation error. On Fig. 4(a) we can see also comparison of measured map and approximated map above non-gaped specimen, but the approximation coefficients are not computed from all five planes, but only from four planes. Therefore, in this case the values of this approximated map are fully reconstructed from other four planes. As we can see, the shape of magnetic field is still very similar to original measured field, but the maximum absolute difference is nearly 20 μT, which is quite big failure and should be better [6]. The error can be caused by unsuitable position of measured volume (size of planes is much bigger than distance between planes), because the approximation obtained on the spherical surface has much better results.

5. CONCLUSIONS

The description of magnetic flux density reconstruction method is presented in this paper. The method has been applied to reconstruction of magnetic flux density fields above different copper specimens. The precision of computed field is highly dependant on the shape of measured field. Although the error of reconstruction seems to be quite big, the shape of reconstructed field is very similar to original. The error should be lower when choosing different distribution of measured points, which is also aim of our future work. The results from simulation in COMSOL are presented and are in good agreement with measured field.

ACKNOWLEDGMENT

This work was supported within project from Education for Competitiveness Operative Programme CZ.1.07.2.3.00.20.0175 and project of the BUT Grant Agency FEKT-S-11-5/1012.

REFERENCES

1. Kříž, T., "Comparison of the methods usage in eit image reconstruct," *Proceedings of the 17th Conference Student EEICT 2011*, Vol. 1, 356–260, Novpress s.r.o., Brno, 2011, ISBN: 978-80-214-4273-3.
2. Dorri, B., M. E. Vermilye, and W. E. Toffolo, "Passive shimming of MR magnets: Algorithm, hardware, and results," *IEEE Transactions on Applied Superconductivity,* Vol. 3, No. 1, 254–257, Mar. 1993.
3. Rektorys, K., *Přehled Užité Matematiky*, Prometheus, Praha, 1995, ISBN 80-85849-72-0.
4. Konzbul, P. and K. Švéda, "Shim coils for NMR and MRI solenoid magnets," *Measurement Science and Technology*, Vol. 6, 1116–1123, 1995.

5. Hadinec, M. and K. Bartušek, "Legendre polynoms application in NMR," *Radioelektronika 2007*, 4, Mj Servis, Brno, 2007, ISBN 1-4244-0821-0.
6. Hadinec, M., P. Fiala, and K. Bartušek, "Mapping technique of basic magnetic field in MR tomography," *PIERS Online*, Vol. 7, No. 4, 321–325, 2011.

Self-consistent Electrodynamics

Konstantin Meyl
Faculty of Computer and Electrical Engineering, Furtwangen University, Germany

Abstract— Even though one usually calculates capacitor losses with a complex epsilon it still offends the principle of a constant speed of light. Maxwell's term $c^2 = 1/\varepsilon \cdot \mu$ suggests a physically inexplicable complex speed. By such an offence against basic principles every physicist is asked to search and to repair the mistake in the textbooks. The contribution clearly explains how vortex losses occur instead of using the postulated and fictive imaginary part of the material constant epsilon. The theory better explains the function of a microwave oven, the welding of PVC foils or how capacitor losses occur. The responsible potential vortices can be derived without postulate them from the established laws of physics. Vortex losses can even be proven experimentally and are clearly shown. The potential vortex is substituted for the vector potential A, which has controlled electrodynamics as "impurity factors" ever since its introduction. A unified theory of all interactions and physical phenomena is missing without potential vortices. This theory justifies the efforts and the rationale for rebuilding electrodynamics and in so doing effectively removes contradictions of the vector potential and loss theory. Consequences are discussed such as the discovery of magnetic monopoles by the German Helmholtz Center [1], the extended Poynting vector, and many more effects involved with the new approach of the potential vortex, that is replacing the vector potential in the dielectric.

1. INTRODUCTION

The error search leads over Poynting's theorem to the vector potential **A**. At this point a new abyss opens. It shows quickly how and where the whole electrodynamics get entangled in contradictions. The vector potential **A** assumes, as everybody knows that no magnetic monopoles exist. Mathematically expressed it should be

$$\operatorname{div} \mathbf{B} = \operatorname{div} \operatorname{rot} \mathbf{A} = 0. \quad \text{(Called the 3rd equation of Maxwell).} \tag{1}$$

On the 16th of October, 2009 sixteen authors reported in the magazine "*Science*" about the discovery of magnetic monopoles [1]. For the vector potential and all derivations constructing it, this new discovery means the final death blow from the mathematical-physical view. However, a new way must be found. A way to electrodynamics free of contradictions, without vector potential **A** and without complex ε. Vortex physics offers such a way free from contradictions, with the derivation of potential vortices by a potential density vector **b** which adequately substitutes for the outdated vector potential. Also the dielectrically losses, from now on as vortex losses of disintegrating potential vortices can be calculated in the electrodynamics free of contradiction without complex ε. Besides, **b** is by no means postulated but is derived from approved physical legitimacies according to textbooks.

2. THE DISCOVERY OF THE LAW OF INDUCTION

In the choice of the approach the physicist is free as long as the approach is reasonable and well founded. In the case of **Maxwell's field equations** two experimentally determined regularities served as basis: On the one hand, **Ampère's law** and on the other hand the **law of induction of Faraday**. Maxwell, the mathematician, thereby gave the finishing touches for the formulations of both laws. He introduced the displacement current **D** and completed Ampère's law accordingly, and doing so without a chance of being able to measure and prove the measure. Only after his death this was possible experimentally, what afterwards makes clear the abilities of this man. In the formulation of the law of induction, **Maxwell** was completely free because the **discoverer Michael Faraday** had done so without specifications. As a man of practice and of experiment the mathematical notation was less important for Faraday. For him the attempts with which he could show his discovery of the induction to everybody (e.g., his unipolar generator), stood in the foreground.

However, his 40 years younger friend and professor of mathematics Maxwell had something completely different in mind. He wanted to describe the light as an electromagnetic wave and doing so certainly the wave description of Laplace went through his mind, which in turn needs a second

time derivation of the field factor. Because Maxwell for this purpose needed two equations with each time a first derivation, he had to introduce the displacement current in Ampère's law and had to choose an appropriate notation for the formulation of the law of induction to get to the wave equation. His light theory initially was very controversial. Maxwell faster found acknowledgement for bringing together the teachings of electricity and magnetism and the representation as something unified and belonging together [2] than for mathematically giving reasons for the principle discovered by Faraday. Nevertheless, questions should be asked.

If Maxwell has found the suitable formulation, if he has understood 100 percent correct his friend Michael Faraday's discovery. If the discovery (1831) and the mathematical formulation (1862) stem from two different scientists, who in addition belong to different disciplines, thus it is not unusual for misunderstandings to occur. It will be helpful to work out the differences.

3. THE UNIPOLAR GENERATOR

If one turns an axially polarized magnet or a copper disc situated in a magnetic field, then perpendicular to the direction of motion and perpendicular to the magnetic field pointer a pointer of the electric field will occur, which everywhere points axially to the outside. In the case of this by **Michael Faraday**, he developed a **unipolar generator** — by means of a brush between the rotation axis and the circumference a voltage is picked off.

The mathematically correct relation

$$\mathbf{E} = \mathbf{v} \times \mathbf{B} \tag{2}$$

I call this the "*Faraday-law*", despite the fact that it appears in this form in textbooks later in time [3]. The formulation usually is attributed to the mathematician **Hendrik Lorentz**, since it appears in the **Lorentz force** in exactly this form. Much more important than the mathematical formalism are the experimental results and the discovery by Faraday, for which the law concerning unipolar induction is named after him the "**Faraday-law**".

Of course we must realize that the charge carriers at the time of the discovery hadn't been discovered yet and the field concept couldn't correspond to that of today. The field concept is an abstracter one, free of any quantization. That of course is also valid for the field concept advocated by Maxwell, which we now contrast with the "*Faraday-law*" (Figure 1). The second Maxwell equation, the law of induction (2), also is a mathematical description between the electric field strength **E** and the magnetic induction **B**. But this time the two aren't linked by a relative velocity **v**.

In place stands the time derivation of **B**, with which a change in flux is necessary for an electric field strength to occur. As a consequence the Maxwell equation doesn't provide a result in the static or quasi-stationary case. In such cases it is usual to fall back upon the unipolar induction according to Faraday (e.g., in the case of the Hall-probe, the picture tube, etc.). The falling back should only remain restricted to such cases, so the normally idea is used. The question then asked: "*Which restriction of the "Faraday-law" to stationary processes is made*?"

The vectors **E** and **B** can be subject to both spatial and temporal fluctuations. In that way the two formulations suddenly are in competition with each other and we are asked to explain the difference, as far as such a difference should be present.

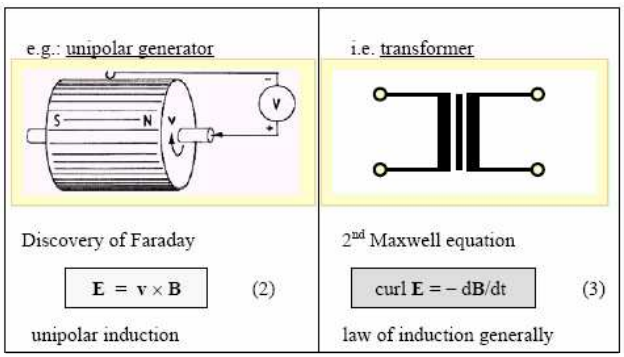

Figure 1: Two formulations for one law. As a mathematical relation between the vectors of the electric field strength **E** and the magnetic flux density **B**.

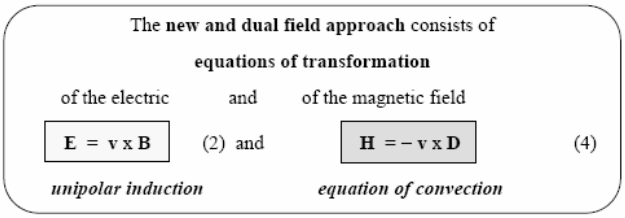

4. DIFFERENT INDUCTION LAWS

For instance, such a difference it is common practice to neglect the coupling between the fields at low frequencies. At high frequencies in the range of the electromagnetic field the **E**- and the **H**-field are mutually dependent. While at lower frequency and small field change the process of induction drops correspondingly according to Maxwell so that a neglect seems to be allowed. Under these conditions electric or magnetic field can be measured independently of each other. Usually it is proceeded as if the other field is not present at all.

That is not correct. A look at the "*Faraday-law*" and immediately it shows that even down to frequency zero both fields are always present. The field pointers however stand perpendicular to each other, so that the magnetic field pointer wraps around the pointer of the electric field in the form of a vortex ring. In this case the electric field strength is being measured and vice versa.

The closed-loop field lines are acting neutral to the outside; so is the normal used idea. However they need no attention. It should be examined more closely if this is sufficient as an explanation for the neglect of the not measurable closed-loop field lines or, if not after all, an effect arises from fields which are present in reality.

Another difference concerns the commutability of **E**- and **H**-field, as is shown by the Faraday-generator, how a magnetic field becomes an electric field and vice versa as a result of a relative velocity v. This directly influences the physical-philosophic question: "*What is meant by the electromagnetic field*?"

5. THE ELECTROMAGNETIC FIELD

The textbook opinion, based on the *Maxwell equations*, names the static field of the charge carriers as cause for the electric field, whereas moving ones cause the magnetic field [4, e.g.]. But that could not have been the idea of **Faraday**, to whom the existence of charge carriers was completely unknown. For his contemporaries, completely revolutionary abstract field concept, based on the works of the **Croatian Jesuit priest Boscovic** (1711–1778). In the case of the field it should less concern a physical quantity in the usual sense, than rather the "*experimental experience*" of an interaction according to his field description.

We should interpret the "*Faraday-law*" to the effect that we experience an electric field if we are moving with regard to a magnetic field with a relative velocity and vice versa. In the commutability of electric and magnetic field a duality between the two is expressed, which in the Maxwell formulation is lost as soon as charge carriers are brought into play. The question then becomes, "*Is the Maxwell field the special case of a particle free field*?" Much evidence points to the answer as "*yes*", because, after all, a light ray can run through a particle free vacuum. As we see, fields can exist without particles but particles without fields are impossible! In conclusion, the field should have been there first as the cause for the particles. The Faraday description should form the basis from which all other regularities can be derived. What do the textbooks say to that?

6. CONTRADICTORY OPINIONS IN TEXTBOOKS

Obviously there exist two formulations for the law of induction (2 and 3), which more or less have equal rights. Science stands for the questions: "*Which mathematical description is the more efficient one? If one case is a special case of the other case, which description then is the more universal one*?" What Maxwell's field equations tell us is sufficiently known so that derivations are unnecessary. Numerous textbooks are standing by, if results should be cited. Let us hence turn to the "*Faraday-law*" (2). Often one searches in vain for this law in schoolbooks. Only in more pretentious books one makes a find under the keyword unipolar induction. If one compares the number of pages which are spent on the law of induction according to Maxwell with the few pages for the unipolar induction, then one gets the impression that the later is only a unimportant special case for low frequencies. Prof. **Küpfmüller** (TU Darmstadt) speaks of a "*special form*

of the law of induction" [4, p.228, Equation (22)], and cites as practical examples the induction in a brake disc and the Hall-effect. Afterwards Küpfmüller derives from the "*special form*" the "*general form*" of the law of induction according to Maxwell, a postulated generalization, which needs an explanation. But a reason is not given. Prof. **Bosse** (as successor of Küpfmüller at the TU Darmstadt) gives the same derivation, but for him the Maxwell-result is the special case and not the Faraday approach [5, p.58]! In addition he addresses the "*Faraday-law*" as an equation of transformation, points out the meaning, and the special interpretation. On the other hand he derives the law from the "*Lorentz force*", completely in the style of Küpfmüller [4] and with that again takes part of its autonomy.

Prof. **Pohl** (University of Göttingen, Germany) looks at that differently. He inversely derives the "*Lorentz force*" from the "*Faraday-law*" [3, p.77]. We should follow this very convincing representation.

7. THE EQUATION OF CONVECTION

If Bosse [5] prompted term "*equation of transformation*" is justified or not is unimportant at first. That is a matter for discussion. If there should be talk about "*equations of transformation*", then the dual formulation (to Equation (2)) belongs to it, and then it concerns a **pair of complementary equations** which describes the relations between the electric and the magnetic field. Written down according to the rules of duality there results an Equation (4), which occasionally is mentioned in some textsbooks. While both equations in the books of **Pohl** [3, p.76 and 130] and of **Simonyi** [6, p.924] are written down side by side having equal rights and are compared with each other, **Grimsehl** [7, p.130] derives the dual regularity (4) with the help of the example of a thin, positively charged, and rotating metal ring. He speaks of "*equation of convection*" as moving charges produce a magnetic field and so-called convection currents. Doing so he refers to workings of **Röntgen** 1885, **Himstedt**, **Rowland** 1876, **Eichenwald** and many others. In his textbook **Pohl** also gives practical examples for both equations of transformation. He points out that one equation changes into the other one, if as a relative velocity v the speed of light c should occur [3, p.77].

8. THE DERIVATION FROM TEXT BOOK PHYSICS

We now have found a field-theoretical approach with the equations of transformation, which in its dual formulation is clearly distinguished from the Maxwell approach. The reassuring conclusion is added: **The new field approach roots entirely in textbook physics**, and are the results from literature research. We can completely do **without postulates**.

As a starting-point and as approach serve the *equations of transformation* of the electromagnetic field, the "*Faraday-law*" of *unipolar induction* (3) and the according to the rules of duality formulated law called *equation of convection* (4).

$$\mathbf{E} = \mathbf{v} \times \mathbf{B} \tag{3}$$

and

$$\mathbf{H} = -\mathbf{v} \times \mathbf{D} \tag{4}$$

If we apply the curl to both sides of the equations:

$$\operatorname{curl} \mathbf{E} = \operatorname{curl} (\mathbf{v} \times \mathbf{B}), \tag{5}$$

$$\operatorname{curl} \mathbf{H} = -\operatorname{curl} (\mathbf{v} \times \mathbf{D}), \tag{6}$$

then according to known algorithms of vector analysis the curl of the cross product each time delivers the sum of four single terms [8]:

$$\operatorname{curl} \mathbf{E} = (\mathbf{B}\operatorname{grad})\mathbf{v} - (\mathbf{v}\operatorname{grad})\mathbf{B} + \mathbf{v}\operatorname{div} \mathbf{B} - \mathbf{B} \operatorname{div} \mathbf{v} \tag{7}$$

$$\operatorname{curl} \mathbf{H} = -\left[(\mathbf{D}\operatorname{grad})\mathbf{v} - (\mathbf{v}\operatorname{grad})\mathbf{D} + \mathbf{v}\operatorname{div} \mathbf{D} - \mathbf{D} \operatorname{div} \mathbf{v}\right] \tag{8}$$

Two of these again are zero for a non-accelerated relative motion in the x-direction with

$$\begin{aligned} \mathbf{v} &= dr/dt \\ \operatorname{grad} \mathbf{v} &= 0 \\ \text{and } \operatorname{div} \mathbf{v} &= 0 \end{aligned} \tag{9}$$

One term concerns the vector gradient $(\mathbf{v}\,\mathrm{grad})\,\mathbf{B}$, which can be represented as a tensor. By writing down and solving the accompanying derivative matrix and giving consideration to the above determination of the $\mathbf{v}$-vector, the vector gradient becomes the simple time derivation of the field vector $\mathbf{B}(\mathbf{r}(t))$,

$$\begin{aligned} (\mathbf{v}\,\mathrm{grad})\,\mathbf{B} &= \frac{d\mathbf{B}}{dt} \\ \text{and} \quad (\mathbf{v}\,\mathrm{grad})\,\mathbf{D} &= \frac{d\mathbf{D}}{dt} \end{aligned} \tag{10}$$

according to the rule:

$$\frac{d\mathbf{B}(\mathbf{r}(t))}{dt} = \frac{\partial \mathbf{B}(\mathbf{r}=\mathbf{r}(t))}{\partial \mathbf{r}} \cdot \frac{d\mathbf{r}(t)}{dt} = (\mathbf{v}\,\mathrm{grad})\,\mathbf{B} \tag{11}$$

For the final not yet explained terms are written down the vectors $\mathbf{b}$ and $\mathbf{j}$ as abbreviation.

$$\mathrm{curl}\,\mathbf{E} = -d\mathbf{B}/dt + \mathbf{v}\,\mathrm{div}\,\mathbf{B} = -d\mathbf{B}/dt - \mathbf{b} \tag{12}$$

$$\mathrm{curl}\,\mathbf{H} = -d\mathbf{D}/dt + \mathbf{v}\,\mathrm{div}\,\mathbf{D} = -d\mathbf{D}/dt + \mathbf{j} \tag{13}$$

With Equation (13) we in this way immediately look at the well-known law of Ampère (1st Maxwell equation).

9. THE MAXWELL EQUATIONS AS A SPECIAL CASE

The result will be the **Maxwell equations**, if: the potential density

$$\mathbf{b} = -\mathbf{v}\,\mathrm{div}\,\mathbf{B} = 0, \tag{14}$$

(Equation (12) $\equiv$ law of induction, if $\mathbf{b} = 0$ resp. $\mathrm{div}\,\mathbf{B} = 0$), and the current density

$$\mathbf{j} = -\mathbf{v}\,\mathrm{div}\,\mathbf{D} = -\mathbf{v} \cdot \rho_{el}, \tag{15}$$

(Equation (13) $\equiv$ Ampère's law, if $\mathbf{j} \equiv$ with $\mathbf{v}$ moved neg. charge carriers; ρ_{el} = electric space charge density).

In addition the comparison of coefficients (15) delivers a useful explanation to the question, "*What is meant by the current density* $\mathbf{j}$"? It is a space charge density ρ_{el} consisting of negative charge carriers, which moves with the velocity $\mathbf{v}$, for instance through a conductor in the x-direction. The current density $\mathbf{j}$ and the dual potential density $\mathbf{b}$ mathematically seen at first are nothing but alternative vectors for an abbreviated notation. While for the current density $\mathbf{j}$ the physical meaning already could be clarified from the comparison with the *law of Ampère*, the interpretation of the potential density $\mathbf{b}$ is still due (14).

From the comparison of Equation (12) with the *law of induction* (Equation (3)) we merely infer, that according to the *Maxwell theory* that this term is assumed to be zero. But that is exactly the **Maxwell approximation** and the restriction with regard to the new and dual field approach, which takes root in Faraday.

10. THE MAXWELL APPROXIMATION

Also the duality gets lost with the argument that magnetic monopoles ($\mathrm{div}\,\mathbf{B}$) in contrast to electric monopoles ($\mathrm{div}\,\mathbf{D}$) do not exist and until today could evade every proof. It has not yet been searched for the vortices dual to eddy currents, which are expressed in the neglected term. Assuming a monopole concerns a special form of a field vortex, then immediately it is clear why the search for magnetic poles in the past had to be a dead end and their failure isn't good for a counterargument. The missing electric conductivity in a vacuum prevents current densities, eddy currents, and the formation of magnetic monopoles. Potential densities and potential-vortices however can occur. As a result, without exception, only electrically charged particles can be found in the vacuum.

Let us record: **Maxwell's field equations can directly be derived from the new dual field approach under a restrictive condition**. Under this condition the two approaches are equivalent and with that also error free. Both follow the textbooks and can, so to speak, be the textbook opinion. The restriction ($\mathbf{b} = 0$) surely is meaningful and reasonable in all those cases in which the Maxwell theory is successful. It only has an effect in the domain of electrodynamics. Here usually a vector potential $\mathbf{A}$ is introduced and by means of the ***calculation of a complex***

dielectric constant a loss angle is determined. Mathematically the approach is correct and dielectric losses may be calculated. Physically the result is extremely questionable since as a consequence of a complex ε a *complex speed of light* in dielectric matter would result,

according to the definition:

$$c = 1/\overline{\sqrt{\varepsilon}} \cdot \mu. \tag{16}$$

With that electrodynamics offends against all specifications of the textbooks, according to which c is constant and not variable and less then ever complex. But if the result of the derivation physically is wrong, then something with the approach is wrong, therefore we ask if the fields in the dielectric perhaps have an **entirely other nature** and then **dielectric losses** perhaps are **vortex losses** of the **potential-vortex decay**?

11. THE EXTENDED POYNTING VECTOR

The Poynting vector $\mathbf{S} = \mathbf{E} \times \mathbf{H}$ stands for the energy flux density of the electromagnetic field. With this usual abbreviation the calculation of the entire energy balance is possible. First the power flux density is determined, using the enlarged field equations [for Equation (12) (curl $\mathbf{E}$) and for Equation (13) (curl $\mathbf{H}$)]:

$$\operatorname{div} \mathbf{S} = \operatorname{div} (\mathbf{E} \times \mathbf{H}) = \mathbf{H} \cdot \operatorname{curl} \mathbf{E} - \mathbf{E} \cdot \operatorname{curl} \mathbf{H} = -\mathbf{H} \cdot d\mathbf{B}/dt - \mathbf{H} \cdot \mathbf{b} - \mathbf{E} \cdot d\mathbf{D}/dt - \mathbf{E} \cdot \mathbf{j} \tag{17}$$

A certain duality between the electric and the magnetic field can't be neglected. There appear two terms of losses $\mathbf{E} \cdot \mathbf{j}$ and $\mathbf{H} \cdot \mathbf{b}$, which require a more exact investigation. One might calculate the loss factor of a capacitor run on alternating currents in this manner [9, p.135]

$$\tan \delta = 1/\omega \cdot R \cdot C \tag{18}$$

but what remains unnoticed is the fact that here exclusively the *Joule effect* is calculated, while an electric conductivity σ forms the basic condition for the realization of the currents and eddy-currents. A good insulator does not fulfill this basic condition any better than standard capacitors. And this is only one **point of critique** among many. If we run the capacitor, for example with AC currents and exchange the dielectric with one of less conductivity, then the time constant will grow and also the losses are supposed to grow to infinity. This never will be true. Of course there is always a complex ε and the implied offence against the constancy of the speed of light hidden behind these loss factors. Thus one mistake causes the other. In the end the whole electrodynamics subject is under heavy critique. Fortunately, there is a solution to all our problems, as the extended *Poynting vector* (17) offers a **new loss term** in addition to the known ones [10–12].

REFERENCES

1. Morris, D. J. P., D. A. Tennant, S. A. Grigera, B. Klemke, C. Castelnovo, R. Moessner, C. Czternasty, M. Meissner, K. C. Rule, J.-U. Hoffmann, K. Kiefer, S. Gerischer, D. Slobinsky, and R. S. Perry, "Dirac strings and magnetic monopoles in the spin ice $Dy_2Ti_2O_7$," *Science*, Vol. 326, No. 5951, 411–414, Oct. 16, 2009.
2. Maxwell, J. C., *A Treatise on Electricity and Magnetism*, Dover Publications, New York, 1873.
3. Pohl, R. W., *Einführung in Die Physik, Band 2 Elektrizitätslehre*, Springer-Verlag, 1975.
4. Küpfmüller, K., *Einführung in Die Theoretische Elektrotechnik*, Springer Verlag, 1988.
5. Bosse, G., *Grundlagen der Elektrotechnik II*, No. 183, BI-Hochschultaschenbücher, 1967.
6. Simonyi, K., *Theoretische Elektrotechnik, Band 20*, Seite 924, VEB Verlag Berlin, 1979.
7. Grimsehl, E., *Lehrbuch der Physik, 2. Bd.*, 130, Teubner Verl, 1967.
8. Bronstein, U. A., *Taschenbuch der Mathematik*, 652, 4. Neuauflage Thun, 1999.
9. Flügge, S., *Rechenmethoden der Elektrodynamik*, Springer Verlag, Berlin, 1986
10. Meyl, K., *Scalar Wave Transponder*, 72–91, INDEL Verlag, 2012, Appendix: K. Meyl, "About the classical electrodynamics and practical applications influenced by the discovery of magnetic monopoles," *Proceedings of the 55th International Scientific Colloquium*, Ilmenau University of Technology, Germany, Sep. 2010
11. Meyl, K., *Self-consistent Electrodynamics*, INDEL Verlag, 2010, ISBN 978-3-940 703-15-6, www.meyl.eu.

Low-level Measurement of Electric Field Intensity

P. Fiala, M. Friedl, and J. Mikulka
Department of Theoretical and Experimental Electrical Engineering
Brno University of Technology, Kolejni 2906/4, Brno 612 00, Czech Republic

Abstract— The authors report on the measurement of electric field intensity in biological structures. The examined problem is a quantity which can be measured remotely without touching the plant and which shows exceptional importance for in-terrain applications. The decisive aspect consists in the possibility of deciphering the information (about a living object) that may be carried by the electric field. Therefore, the most vital problem is to find out whether the electric field will be utilizable for contactless diagnostics. The principle of the described method consists in electric charge measurement on the electrodes of a capacitive sensor, indicating the elimination of interferences and leakage currents. A theoretical analysis is performed for setting the measurement method sensitivity with respect to anticipated magnitudes of the electric field during the day in different weather conditions. The method of measurement using one test tree within the utilized tree stand is examined. Moreover, the authors propose an evaluation of other related aspects; these aspects include modification concepts for the sensor and methodology of measurement, a comparison with the theoretical model, and a direct comparison with the data provided by other laboratory or experimental techniques.

1. INTRODUCTION

Within biological structures, the investigation of properties in cells and higher organizational units such as tissues or organs can be advantageously supported by the monitoring of quantities or aspects that include electric field intensity E, electric potential φ, oxygen density in tissues, and the content and distribution of proteins, enzymes, or insulin [1–3]. For these purposes, however, the researchers need to have a good command of the metrology and measuring methods within low-level measurement. One of the activities subsumed under biological research [4] consists in the measurement of fluid circulation in wood, which is realized at various rates ranging between 0.1–1 m/hour. This activity is further complemented with the monitoring of the electric field intensity distribution in the vicinity of the examined region.

In the described biological materials, electric field intensity must be monitored not only in close vicinity of the tree and its parts (a cell, a tracheid, the root system components, the trunk, branches, leaves, and needles), but also in entire tree groups and stands.

Electric field intensity E in the biological structure of a tree is related to specific density of the fluid and the pace of its flow within the system of the given biological material.

The measurement of fluid concentration and its circulation through tree structure tissues constitutes a rather difficult task that cannot be realized in a simple manner if the planned measurement process is conceived as non-destructive. In this respect, the presented report contains the analysis of an experimental method designed to support the basic evaluation of measurement utilizing electromagnetic sensors [1] to determine the characteristics of fluid flow through different strata of plants. The measurement method is based upon the monitoring of impedance changes that occur within the sensor environment, namely in the sensor resonance area above the porous material [2–4].

Electric field intensity E is a quantity that records the microscopic and macroscopic characteristics of a biologically active system such as a tree, in which the process of growth can be observed [5, 6].

2. SENSORS

A basic concept has been theoretically designed and practically produced to facilitate the relevant research activities. Sensor No. 1 shown in Fig. 1 was realized during the preparations as a simple equivalent capacitor and operated in the static and resonance modes, Fig. 1. During the actual measurement, we applied a static bridge and vector analyzer in order to sample the capacitance and voltage, and we evaluated electric field intensity E.

Another approach to measuring electric field intensity consists in the use of an electro-optical method. This method utilizes the so-called Raman effect, which occurs when a monochromatic electromagnetic wave impinges on and/or passes through the measured sample. Within the spectrum of the reflected electromagnetic wave can be observed not only the basic frequency line of

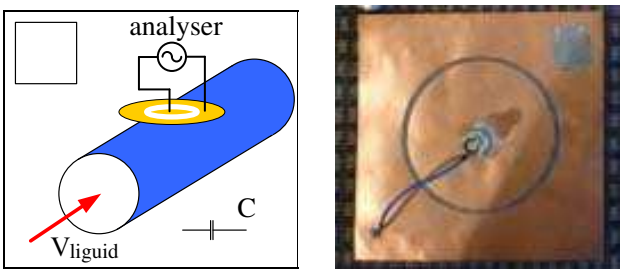

Figure 1: Sensors: capacity sensing.

the emitted monochromatic electromagnetic wave, but also other lateral lines. These lines are dependent on the difference between electric intensities of the sample molecule,

$$f_0 \geq |W_2 - W_1| / h, \tag{1}$$

where f_0 is the frequency of the impinging electromagnetic wave, W_2 and W_1 are energies, or the initial and final states of the molecule irradiated by the impinging electromagnetic wave, and h is the Planck constant. The electric field intensity can be expressed from the energies as

$$W_i = \int\limits_{\Omega} \frac{1}{2} (D_i \cdot E_i)\, dV \quad i = 1, \ldots, N \tag{2}$$

where D, E are the vectors of electrical induction and electrical intensity, Ω is the irradiated sample area, V is the volume interacting with the impinging electromagnetic wave, i is the state index of the excited molecule of the measured environment having a maximum of N. Respecting the law of conservation of energy, the relation to the line shift in the spectrum can be written as

$$f_r h = f_0 h \mp (W_2 - W_1) \tag{3}$$

where f_r is the frequency dependent on the properties of the sample, the upper sign $(-)$ corresponds to the transition from the first state to the second one, and the lower sign $(+)$ corresponds to the transition from the second state to the first one. Thus, the Raman scattering spectrum consists of pairs of lines symetrically distributed around the frequency of the impinging electromagnetic wave having a frequency of f_0. Then, after modification, the expression of the magnitude of the electric field intensity E module as based on relation (2) is

$$E = \sqrt{\frac{2\, dW}{\varepsilon\, dV}} \tag{4}$$

For the determination of the shift within the frequency spectrum and the quantification of the minimum measurable intensity of electric field E, it follows from relation (3) that

$$f_r h = f_0 h \mp \left(\int\limits_{\Omega_2} \frac{1}{2} (D_2 \cdot E_2)\, dV - \int\limits_{\Omega_1} \frac{1}{2} (D_1 \cdot E_1)\, dV \right) \tag{5}$$

If we assume, for the moment of measurement, an approximate magnitude of volume V of regions Ω_1 and Ω_2, the expression changes into

$$\begin{aligned} f_r &= f_0 \mp \frac{1}{2} \frac{\varepsilon}{h} \int\limits_{\Omega_{1,2}} \left(E_2^2 - E_1^2\right) dV \\ f_r &= f_0 \mp \Delta f \end{aligned} \tag{6}$$

If we applied laser having the wavelength of $\lambda = 633\,\text{nm}$, the minimum measurable magnitude of the electric field intensity would be, according to relation (6), as follows:

$$\begin{aligned} f_0 &= 4.7393 \cdot 10^{14}\,\text{Hz}, \quad \Delta f = \frac{1}{2} 1.3362 \cdot 10^{22} \cdot 1 \cdot 10^{-6} \cdot 0.00314|_{\phi=1\,\text{mm}, l=1\,\text{m}, \Delta E=1\,\text{V/m}, p=1\cdot 10^{-6}} \\ \Delta f &= 2.0978 \cdot 10^{11}\,\text{Hz} \end{aligned} \tag{7}$$

with the examined volume diameter of $\phi = 1\,\mathrm{mm}$, $l = 1\,\mathrm{m}$, the anticipated electric field intensity of $E = 1\,\mathrm{V/m}$, and the probability of atom changes of $p = 1.10^{-6}$.

3. EXPERIMENTAL MEASUREMENT

The measurement technique of the first method is based upon the monitoring of capacity or impedance changes of the sensor or, alternatively, upon observing changes of the sensor resonance frequency depending on the through-time changes.

The second method was prepared and tested only in laboratory conditions. A diagram of the task is provided in Fig. 2; the figure presents a task verifying the principle of Raman scattering. Electric potential at frequencies ranging between static and $f_{\max} = 10\,\mathrm{GHz}$ is progressively led to electrodes at the edges of the sample in Fig. 2. The setting of electric field intensity E is carried out, and a device evaluating the spectrum change is connected to the output of the detector.

4. MEASUREMENT WITH A TEST SENSOR

The experimental measurement using a capacity sensor was realized at the outdoor facilities of the Department of Theoretical and Experimental Electrical Engineering [7]. The second method was set up in a research laboratory, and tests were prepared for the verification of accuracy and stability of the technique.

5. MEASUREMENT IN A FOREST

Utilizing the knowledge and observation obtained within the experimental stage of our work, we performed further measurements in a forest utilizing a tree and one sensor. For the purposes of this research activity, these measurements were instrumental towards providing only test results. Fig. 3 shows a capacitive sensor located on a tested tree. The first measurement included calibration and the measurement of capacity as well as electric potential. These data then provided the basis for the evaluation of the desired magnitude of the electric field intensity with a difference formed owing to the influence of fluid circulation in close vicinity of the sensor.

Within the second step, we calibrated the measuring system and started the actual procedure. The experimental measurement proceeded through the resonance frequency and phase reading for the period of approximately three hours. In order to attain results capturing various changes of electric intensity on the tree, it is necessary to repeat the daylong measurement procedure within the given season of the year. Our activities, however, aimed at verifying the measurement method based on laboratory experiments. When fully processed, the obtained results demonstrated the functionality of the sensors from the theoretical electromagnetic point of view.

The forest measurement took place at the grounds of Mendel University in Brno (a university of agriculture and forestry) and was realized using a coniferous tree, the Scots Pine, as the tested object (Fig. 3). The results obtained from the measuring approaches introduced herein have been subject to analysis.

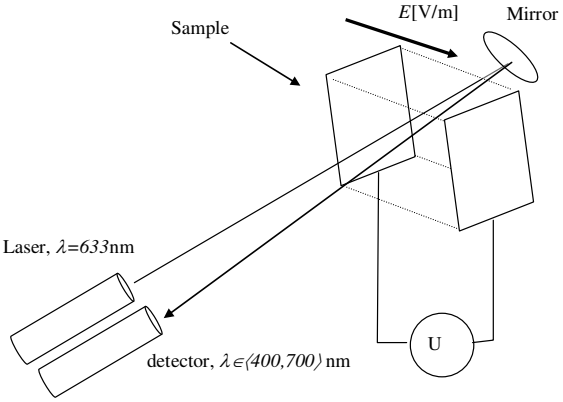

Figure 2: Schematic arrangement of the task.

Figure 3: Tree fixation. Details of the capacity sensors.

6. CONCLUSION

The current trend in the measurement of given quantities is markedly directed towards applying non-destructive methods. This report presents the description of a non-destructive method utilizable for measuring electric field intensity, and the authors focus merely on the laboratory part of the entire process. The measurement method is based on the monitoring of capacity, voltage, and impedance changes of a sensor or, alternatively, on the observation of changes of the Raman shift around a porous material.

The last step realized within the defined tasks was a practical forest measurement. While it is true that the measurement time period would have to be substantially longer in order to provide results with a higher degree of accuracy, we also have to point out that our activities were aimed mainly at verifying the measurement method based on laboratory experiments. The obtained results are analyzed to sustain further development of the described method.

ACKNOWLEDGMENT

The research described in the paper was financially supported by a grant of the Czech Ministry of Industry and Trade No. FR-TI1/001, GACR 102/09/0314, and project of the BUT Grant Foundation No. FEKT-S-11-5/1012.

REFERENCES

1. Meleschenko, S. N., "Nature of changes in electrical properties of plant tissue with change in the external conditions," *Biofyzika*, Vol. 10, No. 3, 507–513, 1965.
2. Brunet, A., "When restriction is good," *Nature*, Vol. 458, 713–714, Apr. 9, 2009, doi:10.1038/458713a; Published Online Apr. 8, 2009.
3. Lubica, K., S. Peter, S. Tomas, et al., "Adiabatic triplet state tautomerization of p-hydroxyacetophenone in aqueous solution," *Journal of Physical Chemistry A*, Vol. 116, No. 11, 2935–2944, Mar. 22, 2012, doi: 10.1021/jp3011469.
4. Friedl, M., P. Fiala, P. Marcon, and I. R. Kubasek, "Measurement of concentration and water flow," *PIERS Proceedings*, 1153–1157, Marrakesh, Morocco, Mar. 20–23, 2011.
5. Aubrecht, L., Z. Stanek, and J. Koller, "Systematic study of the characteristics of the point to-plane corona on natural objects," *Proceedings of the International Congress on Plasma Physics & 25th EPS Conference on Controlled Fusion and Plasma Physics*, 2431–2433, Prague, ECA 22C, 1998.
6. Aubrecht, L., J. Koller, and Z. Staněk, "Onset voltages of atmospheric corona discharges on coniferous trees," *Journal of Atmospheric and Solar Terrestrial Physics*, Vol. 83, 1901–1906, 2001.
7. Steinbauer, M., P. Fiala, K. Bartušek, and Z. Szabó, "Experiments with accuracy of air ion field measurement," *PIERS Proceedings*, 1062–1066, Hangzhou, China, Mar. 24–28, 2008.

Image Reconstruction by EIT Utilizing Magnetic Field

T. Kříž and J. Dědková
Department of Theoretical and Experimental Electrical Engineering
Brno University of Technology, Kolejní 4, Brno 612 00, Czech Republic

Abstract— A possibility of the electric conductivity calculation from a magnetic field obtained outside the measured specimen is described in this paper. Electrical impedance tomography principle is exploited for the conductivity calculation inside a specimen. The standard EIT is using voltage measurement on potential electrodes which are placed on the surface of the specimen whilst the direct current source is connected to a measured object.

1. INTRODUCTION

The electrical impedance tomography (EIT) is a widely investigated problem with many applications in physical and biological sciences. The aim is to reconstruct the internal conductivity or permittivity distributions in two or three dimensional models. The optimization necessitates algorithm that impose regularization and some prior information constraint. The EIT algorithm for a conductivity reconstruction is an inverse and an ill-posed problem. The solution of this problem is described as a minimization of a suitable objective function $\Psi(\sigma)$ which is dependent on a conductivity σ. The least squares method is very often used for a minimization of the objective function. This method converges very fast. The regularization methods are used for better stability of the solution. The Tikhonov regularization method can be used. The regularization term is added to the objective function if the Tikhonov regularization method is used. This term makes the solution stable. The square of the norm of measured voltages and calculated voltages by finite element method is involved in the standard EIT objective function. Objective function in general form can be written

$$\Psi(\sigma) = \frac{1}{2}\sum \left\|\bar{U}_M - \bar{U}_{FEM}(\sigma)\right\|^2 + \alpha \left\|\mathbf{R}\bar{\sigma}\right\|^2 \tag{1}$$

where σ is the unknown conductivity distribution vector in the object, U_M is the vector of measured voltages on the object boundary, $U_{FEM}(\sigma)$ is the vector of peripheral voltages in respect to σ which can be obtained using finite element method, α is a regularization parameter and $\mathbf{R}$ is a regularization matrix connecting adjacent elements of the different conductivities.

2. BASIC THEORY

The EIT problem is recovering the conductivity distribution satisfying continuity equation

$$\mathrm{div}\bar{J} = 0. \tag{2}$$

The current density $\mathbf{J}$ in a linear medium with the interior conductivity σ can be obtain from electric field $\mathbf{E}$ or corresponding potential distribution Φ

$$\bar{J} = \sigma \cdot \bar{E} = -\sigma \cdot \mathrm{grad}\Phi \tag{3}$$

Further we suppose the electric field in very thin layer of electrical conductive medium which can be described by the surface current density $\mathbf{K}$. The surface current density $\mathbf{K}$ inside a specimen produces also a magnetic field. The magnetic flux density $\mathbf{B}$ corresponding to $\mathbf{K}$, can be obtained according to the Biot-Savart Law

$$\bar{B} = \frac{\mu_0}{4\pi}\int_S \frac{\bar{K}\times\bar{R}}{R^3}dS \tag{4}$$

For further numerical simulations we divided the sample into NE triangle elements with centers $[x_t, y_t, z_t]$. We suppose that the current density $\mathbf{K}$ is constant on each element. The magnetic field in general point given by coordinates $[x_i, y_i, z_i]$ we can calculate components of magnetic flux density with using superposition principle

$$\vec{B}_i \approx \frac{\mu_0}{4\pi}\sum_{j=1}^{NE} \frac{\bar{K}_j \times \bar{R}_{ij}}{R_{ij}^3}\Delta S_j \tag{5}$$

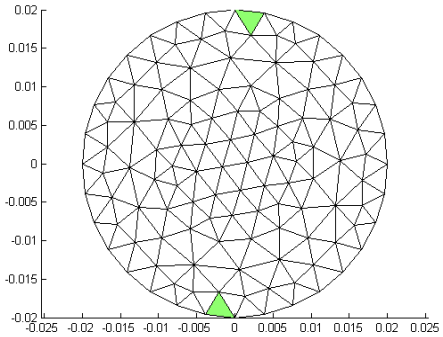

Figure 1: FEM grid with 210 elements and 122 nodes.

The vector $\mathbf{R}$ represents the distance between centre of actual element $[x_t, y_t, z_t]$ and point $[x_i, y_i, z_i]$. If we know certain components of magnetic field we can obtain the current density distribution. If we would like to obtain the NE values of K_x and K_y components of surface current density $\mathbf{K}$, we have to known for example the same number of B_x and B_y components of magnetic field

$$B_{ix} = \frac{\mu_0}{4\pi} \sum_{j=1}^{NE} R_{ijz} \frac{\Delta S_j}{R_{ij}^3} K_{jy}, \quad B_{iy} = -\frac{\mu_0}{4\pi} \sum_{j=1}^{NE} R_{ijz} \frac{\Delta S_j}{R_{ij}^3} K_{jx}, \quad i = 1, \ldots, NE$$

The matrix notation for these $2 \cdot NE$ algebraic equations is

$$\begin{bmatrix} B_{koefx} & 0 \\ 0 & B_{koefy} \end{bmatrix} \begin{bmatrix} K_x \\ K_y \end{bmatrix} = \begin{bmatrix} B_x \\ B_y \end{bmatrix} \quad \Leftrightarrow \quad \mathbf{B}_{koef}\mathbf{K} = \mathbf{B} \tag{6}$$

From system (6) we can obtain very easy wanted current density distribution

$$\mathbf{K} = \mathbf{B}_{koef}^{-1}\mathbf{B} \tag{7}$$

In the following part is shown an example of the magnetic field distribution and the corresponding surface current density distribution and the influence of the non-homogeneity inside tested samples.

The current density is calculated on each element by means of superposition of the outside magnetic field values. We suppose that the current density is constant on elements. The created objective function for the minimization by the least squares method for a conductivity image reconstruction is

$$\Psi(\sigma) = \frac{1}{2} \sum \left\| \bar{J}_M - \bar{J}_{FEM}(\sigma) \right\|^2 + \alpha \left\| \mathbf{R}\bar{\sigma} \right\|^2,$$

where σ is the unknown conductivity distribution vector in the object, J_M is the vector of calculated surfaces current density from measured magnetic flux components outside sample, $J_{FEM}(\sigma)$ is the vector of computed current density in respect to σ which can be obtained using finite element method, α is a regularization parameter and $\mathbf{R}$ is a regularization matrix connecting adjacent elements of the different conductivities.

3. NUMERICAL SIMULATIONS

Numerical models were built for testing of algorithm that calculating conductivity distribution in the investigating samples in Matlab. A numerical model consists of 210 elements and 122 nodes. The linear triangles elements were used for numerical analysis. The FEM grid is shown in Fig. 1. The current electrodes were placed on boundary of investigated samples. Current electrodes are shown in Fig. 1 (green triangles). The current value was adjust to $I = 1$ A. There were defined two values of conductivity for the model. The first material has conductivity 56 MS/m (copper) and the second one has 10 pS/m (cracks).

Three numerical models were built. There were defined regions with different conductivity inside (non-homogenous regions). There is two small non-homogenous regions in the first model, one small

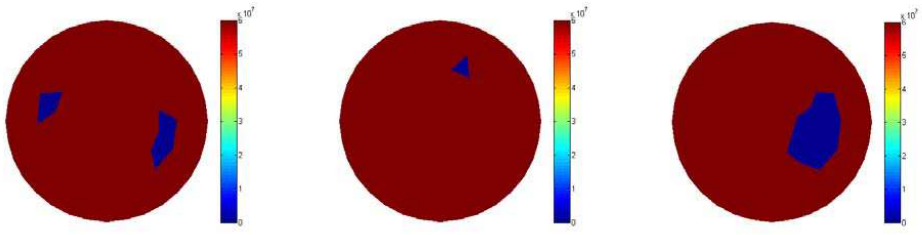

(a) (b) (c)

Figure 2: Original conductivity distribution for (a) sample 1, (b) sample 2 and (c) sample 3.

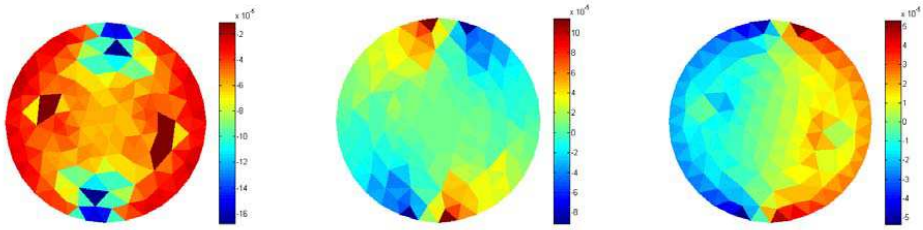

Figure 3: Magnetic flux density components from sample 1.

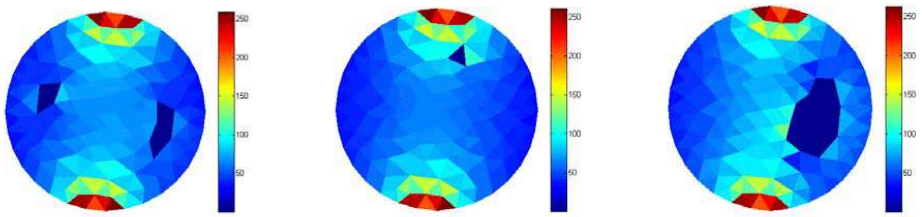

Figure 4: Current density modulus.

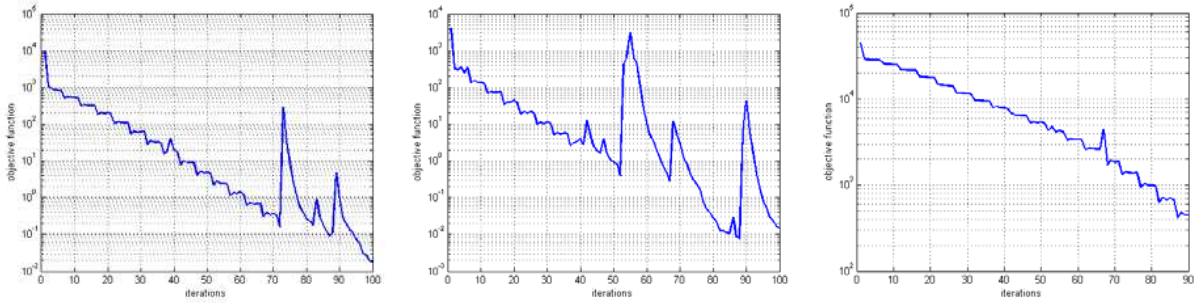

Figure 5: Evolution of objective function.

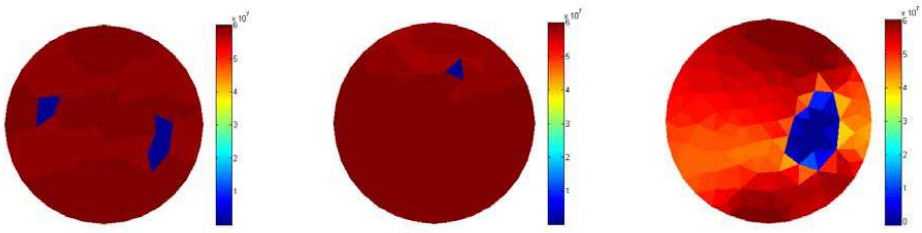

Figure 6: Calculated conductivity distribution for sample 1, sample 2 and sample 3.

non-homogenous region in the second model and one large non-homogenous region in the third one. We can see the original conductivity distribution for all models in Fig. 2.

Surface current density was calculated on each element. We suppose that current conductivity is constant on element. Current density on element is represented by element center with coordinates $[x_t, y_t, z_t]$.

Magnetic flux density components were calculated by Biot-Savart law 1 mm above the sample. Calculated components B_x, B_y and B_z are shown in Fig. 3 for sample 1. These values of magnetic field substitute measured values for reconstruction algorithm testing.

The current density components were computed from magnetic flux components with usage Equation (6). The components B_x and B_y were used to current density. The count of measured (calculated) values of B_y and B_y has to be same as count of elements. Current density modulus was calculated. This modulus was used in the objective function to minimizing solved problem. This current density modulus is marked J_M in the objective function. Computed modulus for all samples is in the Fig. 4.

Current density $J_{FEM}(\sigma)$ is calculated on every iteration. Start value of regularization parameter α very important to stability of reconstruction process. Start value of α was set to $2 \cdot 10^{-12}$. Objective function evolution is watched during minimizing progress. Objective function evolution for all samples is shown in the Fig. 5.

Steps in the graph are due to change value of regularization parameter during minimizing process.

Final values of conductivity are shown in the Fig. 6. Final conductivity values are practically identical with start values for samples 1 and 2.

4. CONCLUSIONS

How, we can see from results in the Fig. 6 algorithm for reconstruction works very good for small cracks. The conductivity values were calculated with highly precision. For large defects resulting value of conductivity is not so accurate. Algorithm designed to calculate the conductivity from the magnetic field is stable and gives very good results.

ACKNOWLEDGMENT

The research described in the paper was financially supported by project of the BUT Grant Agency FEKT-S-11-5/1012 and projekt CZ.1.07.2.3.00.20.0175, Elektro-výzkumník.

REFERENCES

1. Vladingerbroek, M. T. and J. A. Den Boer, *Magnetic Resonance Imaging*, Springer-Verlag, Heidelberg, Germany, 1999, ISBN 3-540-64877-1.
2. Borsic, A., "Regularization methods for imaging from electrical measurement," Ph.D. Thesis, Oxford Brookes University, 2002.
3. Zhang, X., D. Yan, S. Zhu, and B. He, "Noninvasive imaging of head-brain conductivity profiles," *IEEE Engineering in Medicine and Biology Magazine*, Vol. 27, No. 5, 78–83, 2008.
4. Seo, J. K., O. Kwon, and E. J. Woo, "Magnetic resonance electrical impedance tomography (MREIT): conductivity and current density imaging," *Journal of Physics: Conference Series*, Vol. 12, 140–155, 2005.

Optimal Design Approaches for Linear Tubular Actuators

I. Amdouni[1], **L. El Amraoui**[1], **F. Gillon**[2, 3], **M. Benrejeb**[1], **and P. Brochet**[2, 3]

[1]Unité de Recherche LARA Automatique, Ecole Nationale d'Ingénieurs de Tunis
BP. 37, le Belvédère 1002, Tunis
[2]Univ. Lille Nord de France, F-59000 Lille, France
[3]EC-Lille, L2EP, BP48 F-59650 Villeneuve d'Ascq, France

Abstract—An optimal design approach is applied to an incremental linear actuator in the goal to maximize the thrust force. First, parameterized design model is built. Second the optimization problem is formulated. Finally, optimization problem is solved using two developed algorithms.

1. INTRODUCTION

The design of electrical systems is a very complex task which needs experts from various fields of competence. Such difficulties resolution has been the subject of many studies using stochastic and deterministic optimization methods [1, 2]. This paper reports on the optimal design of an incremental linear actuator. At first, one parameterized FE model of the actuator is built [3]. Then, the design parameters of the linear actuator are performed using parallel hybrid Genetic Algorithm (GA) optimization method [4] and parallel hybrid Simulated Annealing (SA) method [5]. In order to solve the optimization problem, two different algorithms are developed.

2. DESCRIPTION OF THE STUDIED ACTUATOR

The electromagnetic structure, on which the optimal design approach is tested, is a linear tubular switched reluctance actuator. It presents four statoric phases and a toothed plunger. Actuator structure is axisymmetric as shown on Figure 1. Non-magnetic separations are set between the statoric phases so that only one statoric phase can be aligned with plunger teeth when it is supplied, Figure 1.

3. MODELING OF THE STUDIED ACTUATOR

A parameterized FE model is developed for the studied actuator under Opera2D® software environment. This model is based on an integral formulation of partial differential equations. Figure 2 shows the mesh of one phase.

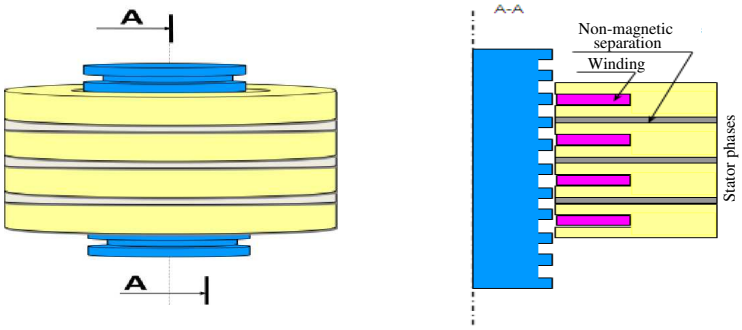

Figure 1: Longitudinal half cross-section of an axisymmetric four phase actuator.

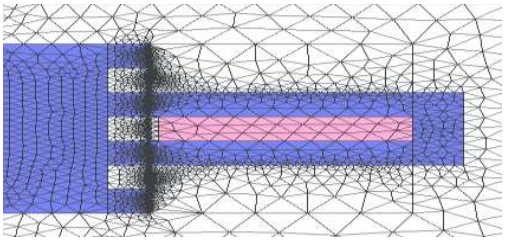

Figure 2: Finite element model of one module of the studied actuator.

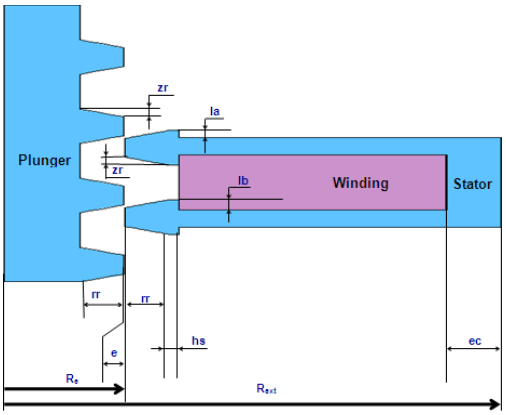

Figure 3: Virtual prototype of the studied actuator.

Table 1: GA factors.

Factors	Values/Types
Generation	10
Population size	4
Crossover probability	0.8000
Mutation probability	0.2000
Crossover type	Scattered
Selection type	Stochastique uniforme
Mutation type	uniforme

Figure 2 shows the parameterized actuator module used as virtual prototype to compute the actuator performances.

4. OPTIMIZATION PROBLEM FORMULATION

The aim of the optimization process is to increase the thrust force level by changing the design parameters of the studied actuator. The finite element model allows determining changes of the thrust force according to dimension variations of three independent parameters.

Considering rr, the stator and rotor tooth height, zr, the tooth inclination and lb, the stator slot width, as optimization problem parameters. The goal of the optimization procedure is to maximize the starting static force, f developed by the actuator, by varying rr, zr and lb under the following constraints: constant heat, constant bulck, constant radius and thickness of the air gap.

The optimization problem is expressed as follow:

$$2\begin{cases} 2.0000\,\text{mm} \leq rr \leq 3.5000\,\text{mm} \\ 0.0508\,\text{mm} \leq zr \leq 1.5700\,\text{mm} \\ 1.0000\,\text{mm} \leq lb \leq 3.5000\,\text{mm} \\ f_{\max} = \max(f(rr,\, zr,\, lb)) \end{cases} \tag{1}$$

The optimization process has been applied using parallel hybrid GA and parallel hybrid SA.

5. ACTUATOR PERFORMANCE OPTIMIZATION

In order to solve the optimization problem, two different methods are developed for the actuator static performance optimization. The first one is based on parallel hybrid GA optimization method and the second one is based on parallel hybrid SA method [4, 5]. Hooke and Jeeves method is used as hybrid solver with these two methods [6]. Figure 5 and Table 3 shows the initial structure of the optimization process.

6. PARALLEL HYBRID GA OPTIMIZATION RESULTS

In this section the optimization is performed using parallel hybrid GA algorithm. First, parallel GA algorithm is started. Then optimal parallel GA parameters are used as initial data for Hooke

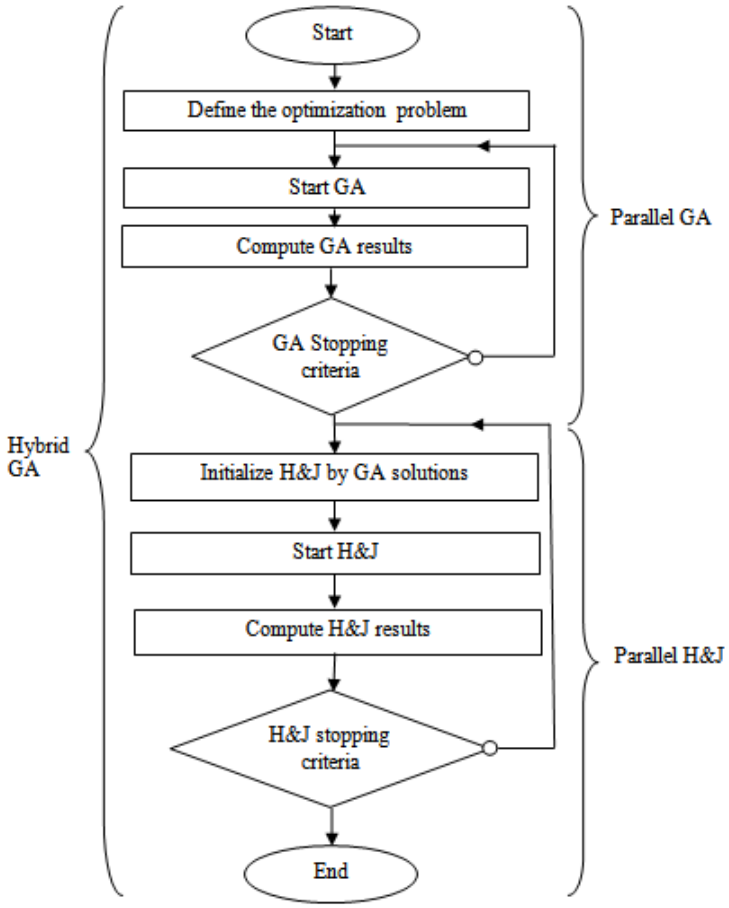

Figure 4: Parallel hybrid GA flowchart.

Table 2: SA factors.

Factors	Values/Types
Max iterations	20
Max function evaluations	20
Function tolerance	0.1000
Annealing function	Fast annealing

Table 3: Initial parameters and hybrid optimization results.

Parameters/Response	Initial Parameters/Response	GA Results	SA Results
rr (mm)	2	2	2
zr (mm)	0.8156	1.1683	1.1683
lb (mm)	1.2902	3.1154	3.1237
$f_{\max}$ (N)	29.3030	41.6750	41.6740
Number of iterations	-	40	20

& Jeeves method, Figure 4.

GA factors are given in Table 1. Optimization result is obtained after 40 iteration, Table 3.

Comparing the initial static force to the optimal GA hybrid solver one, the thrust force has been increased by 42%. The parameters rr is conserved but zr and lb are increased.

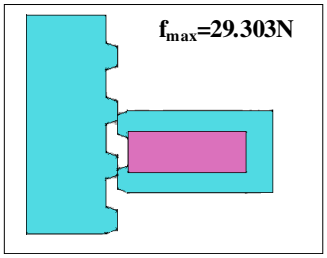

Figure 5: Initial structure of the studied actuator.

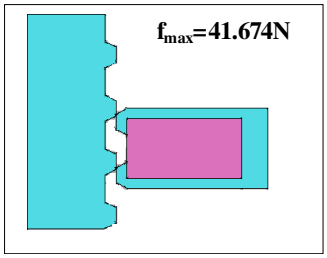

Figure 6: Optimal design structure of the studied actuator_hybrid_SA.

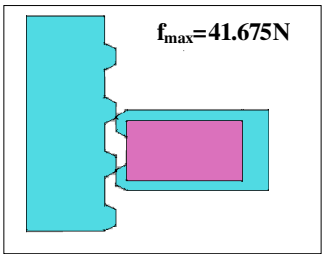

Figure 7: Optimal design structure of the studied actuator_ hybrid_GA.

7. PARALLEL HYBRID SA OPTIMIZATION RESULTS

In this part optimization is applied using parallel hybrid SA method. SA factors are given in Table 2. We start by running SA method then Hooke & Jeeves is initialized with SA result until the optimum is reached, Table 3.

With SA hybrid solver the obtained results show an important increase of the force from 29.300 N to 42.674 N demonstrating the efficiency of the optimization result. Hence, this maximum force is quite the same as that obtained from the parallel hybrid GA. Also, *rr* parameter is remained the same but all other parameters are increased.

Comparing optimal parallel hybrid GA parameters to parallel hybrid SA parameters, only *lb* parameter is increased with the second hybrid method.

The use of this hybrid solver improved the result and found the same optimal force as the parallel hybrid GA solver.

8. INTERPRETATION OF THE RESULTS

The optimization of the actuator design parameters shows that the maximum force obtained from the parallel hybrid SA applied to a Finite Element model of the actuator, is quite the same as that obtained from the parallel hybrid GA applied to the same model.

In addition, achieving the global optimum by hybrid SA method much depends on the initial parameters, Figure 6. If they are well chosen, the optimum is improved and the optimization process consumes less computing time compared to the hybrid GA optimization method, Figure 7.

9. CONCLUSION

Through this paper an optimal design approach is developed for incremental linear actuators. First, a parameterized FE model is developed for the studied actuator. Second, the optimization problem is formulated. The study focuses on the maximization of the static force developed by the actuator.

Finally, the optimization problem is solved using the two hybrid methods developped; parallel hybrid GA optimization method and parallel hybrid SA method. These two methods use Hooke & Jeeves method as hybrid solver. The obtained optimization results show that the hybrid GA optimization method consumes more computing time than the hybrid SA method. Indeed, GA optimization method and SA method are based on randomness, which allows exploring more robust optimization field. In both cases, parallelization leads to a significant reduction of computing time which is halved when using two-core machine.

REFERENCES

1. Xue, X. D., K. W. E. Cheng, T. W. Ng, and N. C. Cheung, "Multi-objective optimization design of in-wheel switched reluctance motors in electric vehicles," *IEEE Transactions on Industrial Electronics*, Vol. 57, No. 9, September 2010.
2. Brisset, S., "Approaches and tools for optimal design of electrical machines," *Empowerment to Supervise Research*, April 2008.
3. Lynch, D. R. and K. D. Plausen, "Time-domain integration of the Maxwell equations on finite elements," *IEEE Transactions on Antennas and Propagation*, Vol. 38, No. 12, 1933–1942, December 1990.
4. Shuohao, K., L. Zhengtian, W. Hanli, and H. Xionghui, "A fault diagnosis method of power systems based on improved objective function and genetic algorithm-tabu search," *IEEE Transactions on Power Delivery*, Vol. 25, No. 3, 1268–1274, July 2010.

5. Weili, Y. and Z. Guansheng, "Adaptive simulated annealing for the optimal design of electromagnetic devices," *IEEE Transactions on Magnetics*, Vol. 32, No. 3, 1214–1217, May 1996.
6. Bath, S. K., J. S. Dhillon, and D. P. Kothari, "Stochastic multiobjective generation allocation using pattern-search method," *IEE Proc.-Gener. Transm. Distrib.*, Vol. 153, No. 4, July 2006.

Analysis of Contactless Power Transfer Systems for Maglev

S. Hasanzadeh and S. Vaez-Zadeh
A Center of Excellence on Applied Electromagnetic Systems and Advanced Motion Systems Research Laboratory, School of Electrical and Computer Engineering, University of Tehran, Tehran, Iran

Abstract— In high power applications of contactless power transfer systems like Maglev, a conflict exists between high efficiency and high transfer power. An equivalent circuit analysis confirmed by FEM, is presented to find acceptable operating frequencies which results high transfer power with improved efficiency.

1. INTRODUCTION

Maglev systems with linear synchronous motors are practical now. They require primary windings distributed along the track, resulting in substantial increase in the construction and maintenance cost. Placing windings on the mover plus a proper contactless power transfer (CPT) system considerably reduces the cost. A suitable structure for CPT system should be designed to satisfy the best performance and meet the requirement of the system. The simplicity of implementation taking into account the practical limitations are essential in selecting the CPT structure.

In the contactless operation, the power transfer apparatus includes a small air gap along the main flux path that links the two coils. The primary coil is located on the stationary base unit while the secondary coil is located on the vehicle. The latter coil effectively receives the power of primary through the air gap and delivers it to the vehicle. The power can be used immediately by the traction motor or can be stored for later use.

Coaxial CPT systems including strait primary wires passing through the center of a cylindrical secondary core with an air gap have already been recognized [1]. Their design and applications has gained attention recently [2]. Needless to say that a solid system design must be established based on a systematic modeling and analysis. The literature lacks such an analysis.

In this work, a coaxial CPT system as in Fig. 1 is chosen for maglev applications with some considerations such as providing high linkage flux and having low volume. A mathematical model is used for the system analysis including the compensating capacitors. Using the model, the analysis including the calculation of power transfer efficiency is carried out. The system parameters can also be obtained based on the system physical specifications. Analytical results are verified by 3D FEM simulations to confirm the modeling and the analysis.

2. CPT MODEL

A physical model of the coaxial CPT system is presented in Fig. 1, where the primary side is a straight wire supplied by a high frequency source on the ground. The secondary side consists of an open hollow cylindrical core of ferrite material and a pickup winding, all mounted on the maglev vehicle. A radial air gap takes the two sides apart.

The system is represented by an equivalent circuit of Fig. 2. The primary wire and the secondary winding are modeled by two coupled RL circuits of impedances $R_1 + j\omega L_1$ and $R_2 + j\omega L_2$ where:

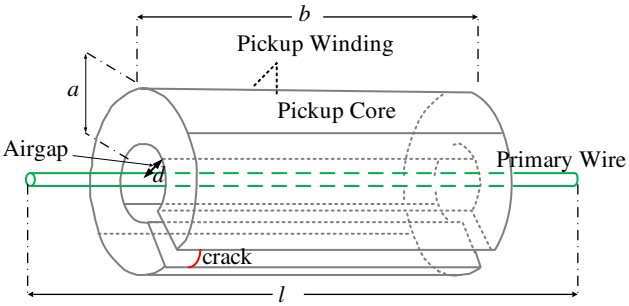

Figure 1: A schematic view of the coaxial CPT system.

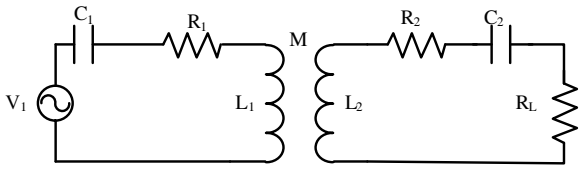

Figure 2: Circuit model of the coaxial CPT system.

$$R_1 = pcu\frac{N_1}{57}\frac{l}{S_1} \tag{1}$$

$$R_2 = pcu\frac{N_2}{57}\frac{2(a+b)}{S_2} \tag{2}$$

$$L_1 = f(N_1, l, S_1) \tag{3}$$

$$L_2 = f(N_2, S_2, a, b) \tag{4}$$

$$M = f(N_1, N_2, S_1, S_2, a, b, d) \tag{5}$$

and a, b, d and l are shown in Fig. 1 with their values given in Table 1 along with N_1, N_2, S_1 and S_2.

The series compensating capacitors C_1 and C_2 are connected to the primary and secondary sides respectively. The capacitances are determined such that a common resonance frequency of ω_0 is provided in two sides as:

$$\omega_0 = \frac{1}{\sqrt{L_1C_1}} = \frac{1}{\sqrt{L_2C_2}} \tag{6}$$

The transferred power passing through the air gap is readily obtained from the equivalent circuit [3]:

$$P_2 = \frac{\omega_0 M^2}{R_L} I_1^2 \tag{7}$$

Also, the system efficiency can be calculated as follows:

$$\eta = \frac{R_L}{R_L + R_2} \frac{1}{1 + \dfrac{R_1\left(R_L + R_2\right)}{\omega_0^2 M^2}} \tag{8}$$

3. SYSTEM ANALYSIS

A CPT system for Maglev applications is analyzed in this section where the system rated values and parameters are listed in Table 1. The input and transfer powers of the system, plus the system efficiency are plotted in Fig. 3. Based on the equations mentioned above, it is seen that the input and transfer powers show the same shape, where their efficiencies at each frequency shows the system loss. There are two frequencies, ω_L and ω_H, over which the input and transfer powers reach their maximum values:

$$\omega_L = \frac{\omega_0}{\sqrt{1+k}}, \qquad \omega_H = \frac{\omega_0}{\sqrt{1-k}} \tag{9}$$

The transfer efficiency is maximum at the resonance frequency, ω_0, located in a frequency boundary of $\omega_L < \omega_0 < \omega_H$. If coupling coefficient, k, is high, the frequency boundary will be wide. A FEM analysis is carried out on a certain resonance frequency as in Fig. 4.

The system analysis on several resonance frequencies are also done by both analytical method and FEM. The corresponding efficiencies at these frequencies are plotted in Fig. 5 for the sake of

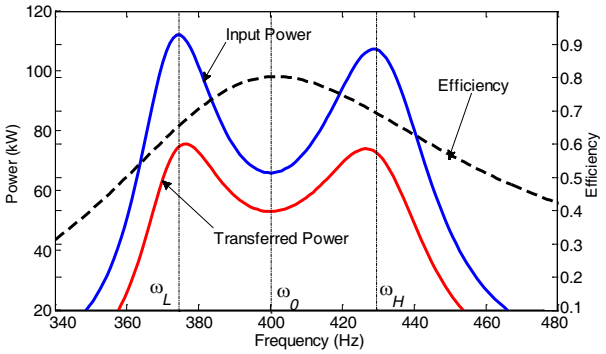

Figure 3: Efficiency, input and transfer power versus frequency.

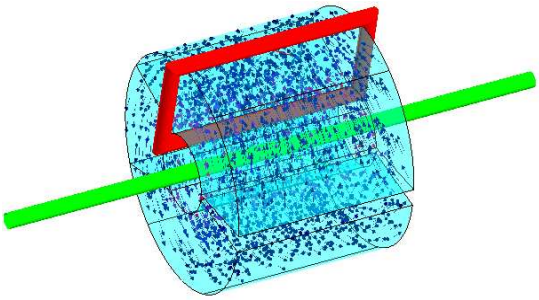

Figure 4: 3D-FEM simulation.

Table 1: Electrical and geometrical parameters of the CPT system.

Parameter Value		Parameter	Value
f_0 (Hz)	400	Width	$a = 10\,\text{cm}$
eta (%)	80	Length	$b = 24\,\text{cm}$
P_{out} (kW)	50	Gap Distance	$d = 5\,\text{cm}$
V_2 (v)	600	Primary Turns	$N_1 = 1$
I_1 (A)	140	Secondary Turns	$N_2 = 10$
I_2 (A)	84	Wire Area	$S_1 = 30\,\text{mm}^2$
L_1 (mH)	1.026	Wire Area	$S_2 = 16\,\text{mm}^2$
L_2 (mH)	16.2	Current Density	$J = 4\,\text{A/mm}^2$
M (mH)	0.6455	Core Material:	Ferrite
C_1 (µF)	154	Maximum Flux Density	$B_{sat} = 0.4\,\text{T}$
C_2 (µF)	9.75	Relative Permeability	$\mu_r = 5000$

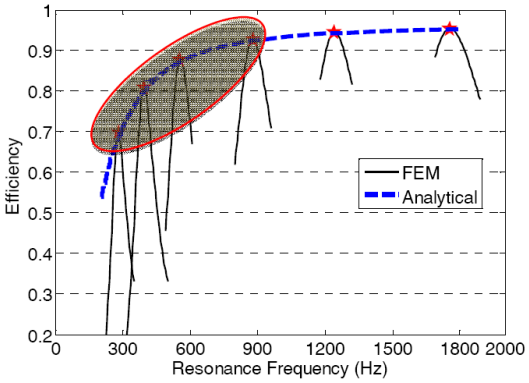

Figure 5: Efficiency versus resonance frequencies.

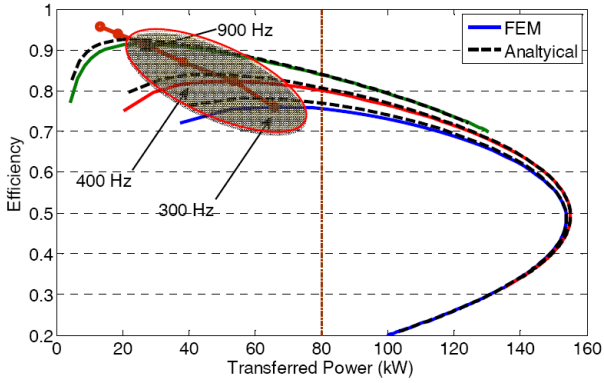

Figure 6: Efficiency versus output power in different operating frequencies.

comparison. The figure confirms the validity of the analytical results as they are close to the FEM results. It also shows that the system efficiency is improved with an increasing resonance frequency.

The system efficiency at the same resonance frequencies is plotted versus the transfer power in Fig. 6. It is seen that almost for all plots, the transfer efficiency drops gradually with the increasing transfer power. Therefore, there is a conflict between high efficiency and high transfer power. However, in high power applications like Maglev both high efficiency and high transfer power are essential. As a result, a compromise between high efficiency and high transfer power is needed.

It is wise to consider the knee of the efficency locus of Fig. 5 as an acceptable operating region, highlighted in Figs. 5 and 6 by a hatched zone. Choosing a desired frequency on the acceptable region, the primary and secondary capacitances are obtained from (6) where L_1 and L_2 are known.

4. CONCLUSIONS

Using a simple equivalent circuit model for a capacitor compensated contactless power transfer system, the transfer power and efficiency are analyzed for Maglev. The model is verified by FEM results. It is shown that a conflict exists between high efficiency and high transfer power. To solve the problem, a compromise is required. A graphical determination of acceptable operating region is also presented. The proposed analysis can be used as a tool for further studies including system design and optimization.

REFERENCES

1. Klontz, K., D. Divan, and D. Novotny, "An actively cooled 120-kW coaxial winding transformer for fast charging electric vehicles," *IEEE Transactions on Industry Applications*, Vol. 31, No. 6, 1257–1263, 1995.
2. Lastowiecki, J. and P. Staszewski, "Sliding transformer with long magnetic circuit for contact-

less electrical energy delivery to mobile receivers," *IEEE Transactions on Industrial Electronics*, Vol. 53, No. 6, 1943–1948, 2006.

3. Villa, J. L., J. Sallán, A. Llombart, and J. F. Sanz, "Design of a high frequency inductively coupled power transfer system for electric vehicle battery charge," *Applied Energy*, Vol. 86, No. 3, 355–363, Mar. 2009.

Dynamic Modeling of Tubular PM Linear Synchronous Actuator Using Multimodal Interpolation of 3D Finite Element Results

I. Ben Salem[1] **and L. El Amraoui**[2]

[1]LARA Automatique Research Laboratory, Ecole Nationale d'Ingénieurs de Tunis, Tunisia
[2]Ecole Supérieure d'Informatique et de Technologie Tunis, Tunisia

Abstract— This paper presents the dynamic modeling of a three phase tubular permanent magnet linear synchronous actuator using multimodal interpolation of 3D finite element results. It gives the advantages of the interpolation application on the self inductance characteristics and improves an accurate dynamic modeling of the actuator.

To achieve this, a two dimensional axi-symmetric finite element model is built, taking into account the magnetic phenomena in the static and the dynamic characterization of this actuator. The force and inductance characteristics are then computed according to plunger position and current densities. The simulation results of the dynamic modeling are provided in two cases: when the finite element results are mathematically interpolated and when they are directly stored on response surfaces.

1. INTRODUCTION

Permanent magnet linear synchronous actuators are carried out to be mostly used in wide range of power systems, thanks to their high massive force. However, its definition can be ambiguous when very saturated devices are to be studied.

This magnetic phenomenon introduces considerable nonlinearities into static, as well as, dynamic behaviors of the actuator [1, 2]. It can cause failure to the control system and constraints the drive system to stop. So, an interpolation method is used to estimate the electro-magnetic parameters in order to perform the dynamic modeling of the actuator.

Using the finite element modeling of the actuator, the electromotive force as well as the statoric inductances is computed from the finite element results [3, 4] and stored on response surfaces using MATLAB functions [5]. These functions are interpolated and included on the dynamic simulation process delivering as final output the mechanical plunger speed. The simulation results of the dynamic model present a comparison between two cases of study: when the finite element results are mathematically interpolated and when they are directly stored on response surfaces.

2. FINITE ELEMENT MODELING

2.1. Actuator Description

The studied structure is a three phase tubular PM linear synchronous actuator equipped with quasi-halbach magnetization and modular stator structure composed of 9 stator slots and 10 armature poles. This actuator provide an axial and bidirectional force that reaches 5 kN for the low speeds. The three stator armature windings of the actuator are shifted from each other by a distance of $2\tau_p/3$. Fig. 1 presents the half cross section of the actuator.

2.2. Finite Element Results

The finite element model of the tubular pm linear synchronous actuator is developed under PC-OPERA® 2D environment. Each part of the actuator is described by one material and geometric parameters. A thin meshing is elaborated in the air-gap zone, to limit the influence of the meshing modification caused by statoric position changing. The zone that around the stator region is

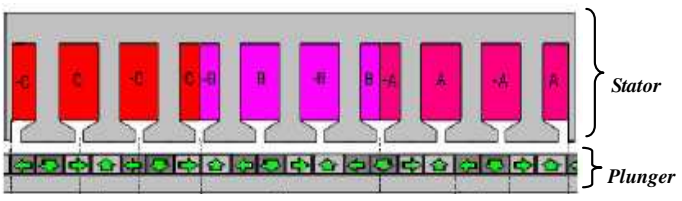

Figure 1: Structure of a linear actuator half cross section.

composed with air, used to conserve a regular meshing around the structure. The complete meshing structure includes 80429 elements with 144 zones including the air-gap [5].

From the finite element results, the inductance characteristics are computed using static points, according to currents and displacement variations, in linear and nonlinear operation cases. Over one pole pitch ($2\tau_p$) and for different current densities J varying from -10 to $10\,\mathrm{A/mm^2}$, the inductances are computed for three phases separately with sinusoidal fed. Fig. 2 and Fig. 3 present the self inductance of phase C.

3. ACTUATOR DYNAMIC MODELING

The magnetic fluxes serve as fundamental quality of the electromagnetic model of the actuator and crossing the air gap constitute the useful flux. Equations system (1) presents superposition of the flux produced by the magnets and the flux due to statoric currents.

$$\begin{bmatrix} \psi_a \\ \psi_b \\ \psi_c \end{bmatrix} = \begin{bmatrix} L_a & 0 & 0 \\ 0 & L_b & 0 \\ 0 & 0 & L_c \end{bmatrix} \begin{bmatrix} i_a \\ i_b \\ i_c \end{bmatrix} + \begin{bmatrix} \psi_{pma} \\ \psi_{pmb} \\ \psi_{pmc} \end{bmatrix} \tag{1}$$

In this model, the inductance matrix is composed only with the self inductances L_a, L_b and L_c because the mutual inductances are neglected. For the electromagnetic force computation, expression (2) is used.

$$F_{em}(i,z) = \sum_{k=a,b,c} \frac{d\psi_k}{dz} i_k \,|_{i_k=cte} \tag{2}$$

As seen, the inductance expression of each phase is required for the electromagnetic force computation. In fact, three multimodal interpolation functions are developed from the inductance characteristics (Equation (3)) shifted from each other by $2\tau_p/3$.

$$\begin{pmatrix} L_a \\ L_b \\ L_c \end{pmatrix} = L_o + L_m \begin{pmatrix} I_{ma}\sin(N_p z) \\ I_{mb}\sin\left(N_p z + \frac{2\tau_p}{3}\right) \\ I_{mc}\sin\left(N_p z + \frac{4\tau_p}{3}\right) \end{pmatrix} \quad \text{with } L_m = \begin{cases} -0.1 \\ -0.12 \\ -0.14 \\ 0.14 \\ 0.12 \\ 0.1 \end{cases} \quad \text{if} \quad \begin{cases} J \in [-10;-8]\ \mathrm{A/mm^2} \\ J \in [-8;-6]\ \mathrm{A/mm^2} \\ J \in [-6;0]\ \mathrm{A/mm^2} \\ J \in [0;6]\ \mathrm{A/mm^2} \\ J \in [6;8]\ \mathrm{A/mm^2} \\ J \in [8;10]\ \mathrm{A/mm^2} \end{cases} \tag{3}$$

L_o is a constant term expressing the average value of the inductances L_a, L_b and L_c. L_m represents the magnetizing parts of the inductances L_a, L_b and L_c, for each current density J.

From the general equation of dynamics, the plunger dynamics can be expressed using Equation (4).

$$\frac{d^2 z(t)}{dt^2} = \frac{1}{M}\left[F_{em} - f_v \frac{dz}{dt} - f_s \mathrm{sign}\left(\frac{dz}{dt}\right) - F_l\right] \tag{4}$$

The dynamic modeling of the PM linear synchronous actuator is expressed as a coupling of the electric, magnetic and mechanic models. It is based on multimodal interpolation functions and it takes into account the nonlinear magnetic effects.

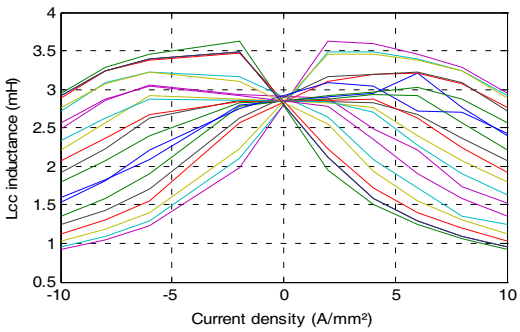

Figure 2: Self inductance of phase C according to current densities over one pole pitch.

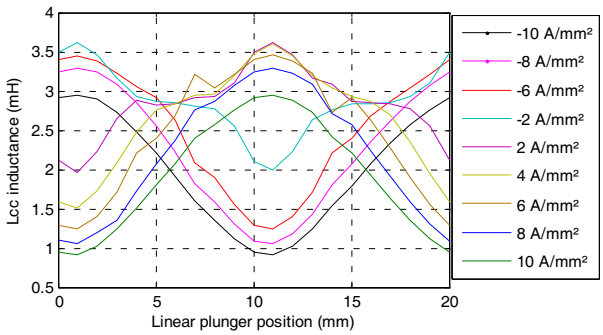

Figure 3: Self inductance of phase C according to the linear position for different current densities.

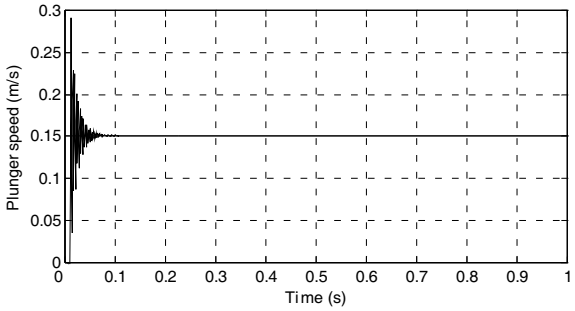

Figure 4: Plunger speed characteristic (case 1).

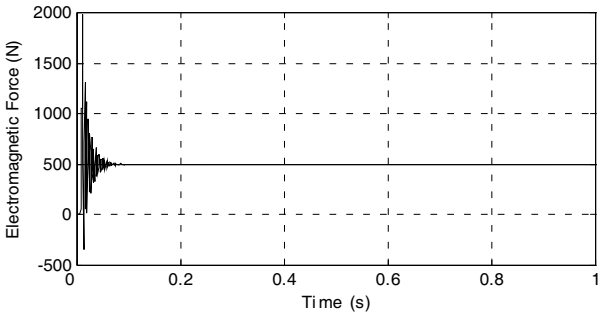

Figure 5: Electromagnetic force (case 1).

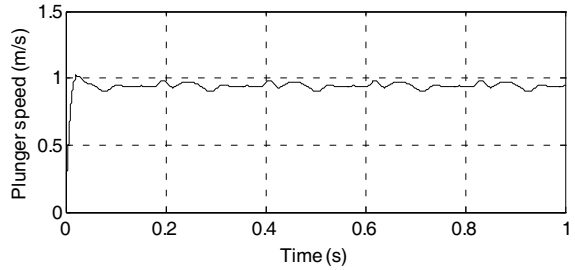

Figure 6: Plunger speed characteristic (case 2).

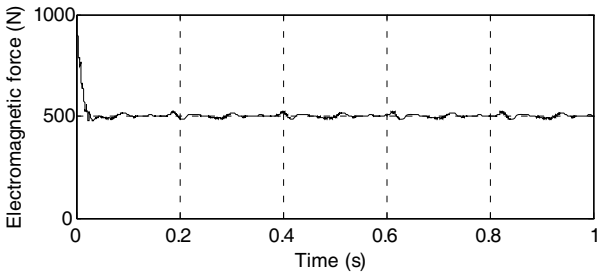

Figure 7: Electromagnetic force (case 2).

The voltage vector u is the actuator model input. Current i and position z are in the same time, state spaces and the model outputs. Nomenclatures of the different abbreviations are presented in appendix (Table 2).

$$\frac{d}{dt}\begin{pmatrix} i_j \\ z \\ v \end{pmatrix} = \begin{cases} [L_j]^{-1}\left[u_j - R_s i_j - e_j\right] \\ v \\ \frac{1}{M}(F_{em} - (f_v v + f_s \text{sign}(v) + F_l)) \end{cases} \tag{5}$$

4. PERFORMANCE ESTIMATION OF THE ELABORATED DYNAMIC MODELING

The elaborated dynamic modeling of the actuator is build and solved numerically under MATLAB® /Simulink environment, to prove the efficiency of the interpolation functions application. The studied actuator is supplied with a three phase voltage vector for a loaded force equal to 500 N. In the first case of simulation, the finite element results are mathematically interpolated and applied to the dynamic modeling as expressed below. In the second case, the finite element results are applied directly to the dynamic modeling using 3D MATLAB functions.

Figures 4, 5, 6 and 7 present the plunger speed and the electromagnetic force generated by the actuator in two cases respectively. In the first case, the fluctuations are observed only in the transient state. They are important but they can be controlled using the current control loop. In the second case, further fluctuations of plunger speed and electromagnetic force are observed in the steady state.

In the first case, the exact derivative of the flux vector is applied to the dynamic modeling. So, it provides a good precision of the force and inductances values and consequently, a best accuracy in the simulated characteristics.

5. CONCLUSIONS

In this paper, the dynamic modeling of a three phase permanent magnet linear synchronous actuator is elaborated using multimodal interpolation of 3D finite element results. This dynamic model is established taking into account the electro-mechanical performances and the magnetic nonlinearity effects.

The axi-symmetric finite element results are used to compute the inductances and forces. These parameters are expressed then using multimodal interpolation functions according to plunger position and current densities.

In the dynamic modeling of the actuator, the application of multimodal interpolation functions insures the exact derivative of the flux vector and guarantees the continuity between the operating

points. That is providing a good precision of force and inductances values and an accurate and malleable dynamic modeling of the actuator.

APPENDIX

Table 1: Geometric parameter dimension of the actuator.

Parameter	Designation	Value
Width pole	τ_p	20 mm
Width between coils	τ_d	22.22 mm
External radius of the stator	R_e	100 mm
Air gap Radius	R_m	55.5 mm
Air gap Thickness	G	1 mm
Statoric resistance	R	0.3 Ω
Masse	M	4.15 kg
Friction force coefficient	f_v	30
Loaded force	F_l	500 N

Table 2: Nomenclature.

Symbol	Quantity	Units
u_j	Supply voltage of phase $j, j = \{a, b, c\}$	V
i_j	Stator current of phase j, $j = \{a, b, c\}$	A
ψ_j	Flux in phase j, $j = \{a, b, c\}$	Wb
ψ_{pm}	Maximum flux linkage due to magnets	mV · s
e_j	Electromotive force of the actuator in phase j	V
L_j	Statoric inductance in phase j, $j = \{a, b, c\}$	H
v	Linear speed	mm/s
z	Linear displacement	mm

REFERENCES

1. Walker, J. A., D. G. Dorell, and C. Cossar, "Flux linkage calculation in permanent magnet motors using the frozen permeabilities method," *IEEE Transactions on Manetics*, Vol. 41, No. 10, October 2005.
2. Bianchi, N. and S. Bolognani, "Magnetic models of saturated interior permanent magnet motors based finite element analysis," *Proceeding of 33rd IAS Annual Meeting*, Vol. 1, October 12–15, 1998.
3. Nakatsugawa, J., Y. Notohara, L. Dongsheng, and Y. Iwaji, "Inductance measurement method for permanent magnet synchronous motors using AC with DC bias," *Proceeding of 18th International Conference on Electrical Machines, ICEM 2008*, 2008.
4. Palinder, H., J. G. Slootweg, J. C. Compter, and M. J. Hoeijmarkers, "Modeling a linear PM motor including magnetic saturation," *Power Electronics, Machines and Drives*, Conference Publication No. 497, ©IEE 2002, April 16–18, 2002.
5. Ben Salem, I., L. El Amraoui Ouni, M. Benrejeb, F. Gillon, and P. Brochet, "Flux linkage approach used for phase inductance computation of a three phase tubular linear PM synchronous actuator," *International Review of Electrical Engineering IREE*, Vol. 4, October 2011.

New Constructions of Kravchenko-Poisson Wavelets and Their Applications for Digital Signal Processing

M. S. Sautbekova and S. S. Sautbekov
Eurasian National University Named after L.N. Gumilyov, Kazakhstan

Abstract—In practice can be useful the finite distributions which are under construction on the basis of Atomic Functions up(x). Recent paper is dedicated to the application of Kravchenko-Poisson distribution in digital signal processing.

1. INTRODUCTION

Wavelet theory has become an active area of research in different fields, including electrical engineering (signal processing, data compression), mathematical analysis (harmonic analysis, operator theory), and physics (fractals, quantum field theory). There are opportunities for further development of both the mathematical understanding of wavelets and a wide range of applications in science and engineering. Consider a complex-valued function ψ satisfying the following conditions:

$$\int_{-\infty}^{+\infty} |\psi(t)|^2 dt < \infty \tag{1}$$

$$C_\psi = 2\pi \int_{-\infty}^{+\infty} \frac{|\hat{\psi}(\omega)|^2}{|\omega|} d\omega < \infty, \tag{2}$$

where $\hat{\psi}$ is the Fourier transform of ψ. The first condition implies finite energy of the function ψ, and the second condition, the admissibility condition, implies that if $\hat{\psi}(\omega)$ is smooth then $\hat{\psi}(0) = 0$. The function ψ is the mother wavelet.

2. CONTINUOUS WAVELET TRANSFORM

If ψ satisfies the conditions described above, then the *wavelet transform* of a real signal $s(t)$ with respect to the wavelet function $\psi(t)$ is defined as:

$$S(b,\, a) = \frac{1}{\sqrt{a}} \int_{-\infty}^{+\infty} \psi' \left(\frac{t-b}{a} \right) s(t) dt, \tag{3}$$

where ψ' denotes the complex conjugate of ψ, and this is defined on the open $(b,\, a)$ half-plane ($b \in \mathbb{R}$, $a > 0$). The parameter b corresponds to the time shift and the parameter a corresponds to the scale of the analyzing wavelet. If we define $\psi_{a,\,b}(t)$ as

$$\psi_{a,\,b}(t) = a^{-1/2} \psi \left(\frac{t-b}{a} \right) \tag{4}$$

which means rescaling by a and shifting by b, then Equation (3) can be written as a scalar or inner product of the real signal $s(t)$ with the function $\psi_{a,\,b}(t)$:

$$S(b,\, a) = \int_{-\infty}^{+\infty} \psi'_{a,\,b}(t) s(t) dt, \tag{5}$$

When function $\psi(t)$ satisfies the admissibility condition, Equation (13), the original signal $s(t)$ can be obtained from the wavelet transform $S(b,\, a)$ by the following inverse formula:

$$s(t) = \frac{1}{C_\psi} \int_{-\infty}^{+\infty} \int_{-\infty}^{+\infty} S(b,\, a) \psi_{a,\,b}(t) \frac{da\; db}{a^2}. \tag{6}$$

3. GAUSSIAN WAVELET FAMILY

In nowadays many kinds of wavelets are known. And one of such families is VMWF (Vanishing Momenta Wavelet Family), sometimes called Gaussian Wavelets.
Functions of this family are derivatives of Gaussian exponent:

$$g_n(x) = (-1)^{n+1}\frac{d^n}{dx^n}e^{-x^2/2}, \quad n \in \mathbb{N} \tag{7}$$

Normalizing coefficient is:

$$C_{g_n} = 2\pi(n-1)!, \quad 0 < n < \infty. \tag{8}$$

Vanishing Momenta Wavelet Family had got such name, because function $g_n(x)$ is equal to zero at first $n-1$ moments:

$$\int\limits_{-\infty}^{\infty} x^m g_n(x)dx = 0\,\forall m, \quad 0 \le m < n, \quad n \in \mathbb{N} \tag{9}$$

In spite of considerable computational consumptions of requirements of CWT, it's using often warrant the best results.

4. PROPERTIES OF GAUSSIAN WAVELETS

Functions of VMWF, as all wavelets, satisfy the admissibility condition

$$\int\limits_{-\infty}^{\infty} \psi(x)dx = 0.$$

Besides this, they have some specific properties. From (7) we can see that the wavelet derivative coincides with greater to one order wavelets:

$$\frac{d}{dx}g_n(x) = -g_{n+1}(x) \tag{10}$$

Respectively, extremum of wavelet $g_n(x)$ coincide with zeros of function $g_{n+1}(x)$. In consideration of (10) we can obtain expression for integration of Gaussian wavelet on any interval:

$$\int\limits_{b_1}^{b_2} g_n(x)dx = g_{n-1}(b_1) - g_{n-1}(b_2). \tag{11}$$

Remark: it holds also for $n = 1$. Function $g_0(x) = -e^{-x^2/2}$ is defined by general expression (7), but it is not a wavelet, because admissibility condition does not hold.
On practice more convenient to modify (11) including scale a and time shift b:

$$\int\limits_{b_1}^{b_2} g_n\left(\frac{x-b}{a}\right)dx = a\left[g_{n-1}\left(\frac{b_1-b}{a}\right) - g_{n-1}\left(\frac{b_2-b}{a}\right)\right]. \tag{12}$$

5. KRAVCHENKO-POISSON DISTRIBUTION AND ITS APPLICATION

Kravchenko-Poisson distribution is a finite solution of equation [2–4]:

$$Lf(x) = \lambda\sum_{k=1}^{M} c(k)f(a_k x - b_k), \qquad |a_k| > 1,$$

where L — linear differential operator with constant coefficients; a_k, b_k — constants, and it has the following expression:

$$p(x) = \begin{cases} \frac{1}{c}\mathrm{up}\left(\frac{x}{b}\right)\exp\left(-\frac{x}{a}\right), & \text{if} \quad x \ge 0, \\ 0, & \text{if} \quad x < 0, \end{cases} \tag{13}$$

where atomic function

$$\mathrm{up}(x) = \frac{1}{2\pi} \int\limits_{-\infty}^{+\infty} \exp(-itx) \prod_{k=1}^{\infty} \mathrm{sinc}\left(t \cdot 2^{-k}\right) dt$$

has the following properties:

1. *supp* $\mathrm{up}(x) = [-1, 1]$
2. $\mathrm{up}(x) \in \mathbb{C}^{\infty}[-1, 1]$
3. $\mathrm{up}(x)$ is an even function: $\mathrm{up}(x) = \mathrm{up}(-x)$
4. $\mathrm{up}(x) = 1 - \mathrm{up}(1 - x)$
5. sum of integers shifts $\mathrm{up}(x)$ identically equals to one

$$\sum_{k=-\infty}^{+\infty} \mathrm{up}(x - k) \equiv 1$$

6. $\mathrm{up}(x)$ has a fast convergent Fourier expansion

$$\mathrm{up}(x) = 0,5 + \sum_{k=-\infty}^{+\infty} \widehat{up}(\pi k) \cos\left(\pi(2k - 1)x\right),$$

7. $\mathrm{up}'(x) = 2\mathrm{up}(2x + 1) - 2\mathrm{up}(2x - 1)$

and c is chosen such that in (13)

$$\int\limits_{\mathbb{R}} p(x)dx = 1.$$

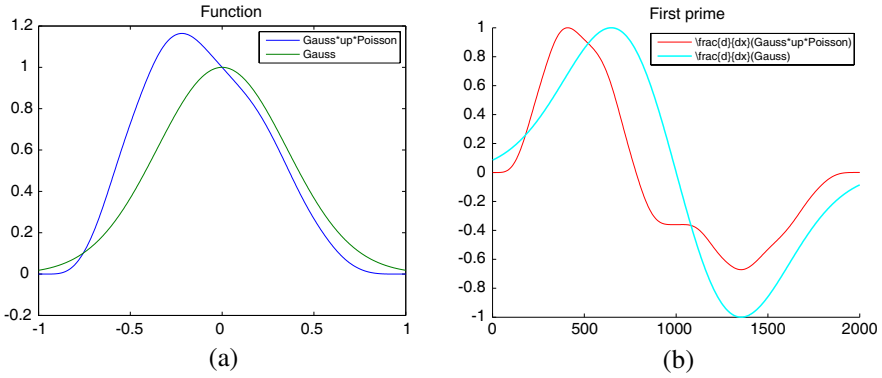

Figure 1: (a) Scaling function $\tilde{p}(x)$, (b) first order wavelet $\tilde{p}'(x)$.

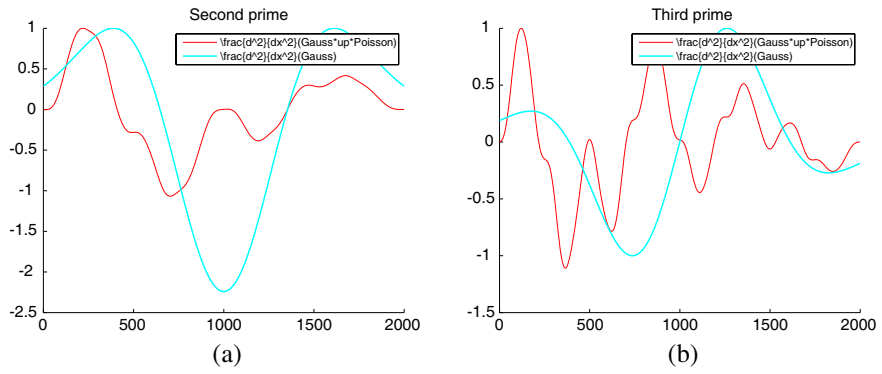

Figure 2: (a) Second order wavelet $\tilde{p}''(x)$, (b) third order wavelet $\tilde{p}'''(x)$.

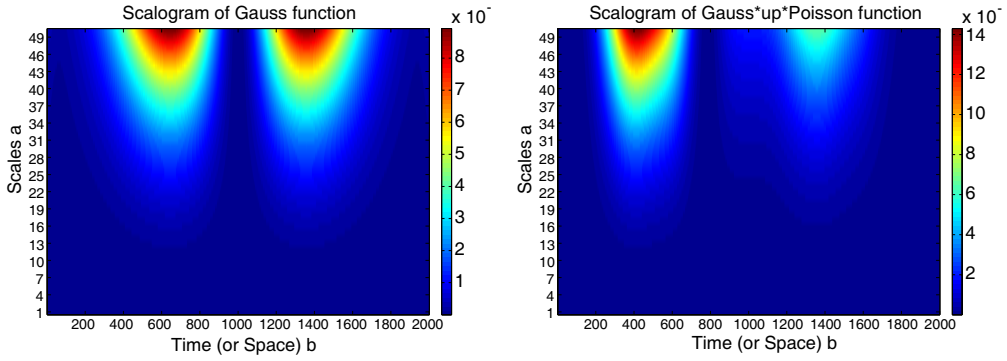

(a) (b)

Figure 3: (a) Scalogram of the Gauss function, (b) scalogram of the $\tilde{p}(x)$ function.

6. COMPUTER SIMULATION

Here we consider a particular case of (13), (3) behaviour under parameters $a = b = 1$. We take into consideration a modified function $\tilde{p}(x) = \mathrm{up}(x)\,\exp(-x)$ on $x \in (-1,\, 1)$. Fig. 1 shows the $\tilde{p}(x)$ and Gauss scaling function and first order wavelet. The wavelets of the second and the third order are shown in Fig. 2. The scalogram of the Gauss function and the $\tilde{p}(x)$ function if shown in Fig. 3.

7. CONCLUSION

The new family of Kravchenko-Poisson wavelets are discussed. The wavelets of the second generation were obtained on the base of Kravchenko-Rvachev structures, etc. The second part is devoted to the computer simulation by the formula (13).

REFERENCES

1. Kravchenko, V. F., O. V. Kravchenko, and A. R. Safin, "Atomic functions in probability theory and stochastic processes," *Uspekhi Sovremennoi Radioelektroniki*, No. 5, 23–38, 2009 (in Russian).
2. Kravchenko, V. F., *Lectures on the Theory of Atomic Functions and Their Some Applications*, Radiotekhnika, Moscow, 2003 (in Russian).
3. Kravchenko, V. F. and V. L. Rvachev, *Algebra of Logic, Atomic Functions and Wavelets in Physical Applications*, Fizmatlit, Moscow, 2006 (in Russian).
4. Kravchenko, V. F., O. S. Labunko, A. M. Lerer, and G. P. Sinyavsky, *Computing Methods in the Modern Radio Physics*, Fizmatlit, Moscow, 2009 (in Russian).

Application of WA-functions of Distribution of Kravchenko-Rvachev for Digital Signal Processing

M. S. Sautbekova and S. S. Sautbekov
Eurasian National University Named after L. N. Gumilyov, Kazakhstan

Abstract— The recent work is dedicated to the application of Kravchenko-Rvachev distribution of digital processing problems of new signal constructions.

1. INTRODUCTION

Wavelet analysis (also called wavelet theory, or just wavelets) has attracted much attention recently in signal processing. It has been successfully applied in many applications such as transient signal analysis, image analysis, communications systems, and other signal processing applications. It is not a new theory in the sense that many of the ideas and techniques involved in wavelets (subband coding, quadrature mirror filters, etc.) were developed independently in various signal processing applications and have been known for some time. What is new is the development of recent results on the mathematical foundations of wavelets that provide a unified framework for the subject.

Within this framework a common link is established between the many diversified problems that are of interest to different fields, including electrical engineering (signal processing, data compression), mathematical analysis (harmonic analysis, operator theory), and physics (fractals, quantum field theory).

Wavelet theory has become an active area of research in this fields. There are opportunities for further development of both the mathematical understanding of wavelets and a wide range of applications in science and engineering.

2. PROBABILITY PROPERTIES OF ATOMIC FUNCTION up(x)

Let $\{\xi_k\}_{k=1}^N$ be sequence of independent discrete random values, taking the meaning -1 or 1 with probability 0.5. Represent the random value ξ^N as

$$\xi^N = \sum_{k=1}^{N} \xi_k 2^{-k}, \quad \xi_k \in \{-1, 1\}. \tag{1}$$

Let $\{\xi_k\}_{k=1}^\infty$ be sequence of independent uniformly distributed random values on $[-1, 1]$. There is a question: what kind of density will have the random value

$$\xi = \sum_{k=1}^{\infty} \xi_k 2^{-k} \, ? \tag{2}$$

For answer we'll use the property of probability density of sum of two random values. Let random value X be a probability density of $p_X(x)$, and random value Y be a probability density of $p_Y(y)$. Then the random value $Z = X + Y$ has the probability density

$$p_Z(z) = \int\limits_{\mathbb{R}} p_X(z - \lambda) p_Y(\lambda) d\lambda \tag{3}$$

We'll use (3) for computation probability density of (2). Function $\mathrm{up}(x)$ inserted as convolution of infinite numbers of rectangular impulses has to satisfy to the next.

Theorem. Probability density $\mathrm{up}(\xi)$ of random value ξ is solution of equation:

$$\mathrm{up}'(\xi) = 2\mathrm{up}(2\xi + 1) - 2\mathrm{up}(2\xi - 1) \tag{4}$$

and has the following analytical expression

$$\mathrm{up}(\xi) = \frac{1}{2\pi} \int\limits_{\mathbb{R}} \prod_{j=1}^{\infty} \mathrm{sinc}\left(t \cdot 2^{-j}\right) e^{it\xi} dt. \tag{5}$$

Definition. Atomic functions are the finite solutions of functional-differential equation

$$Ly(x) = \lambda \sum_{k=1}^{M} c_k y(ax - b_k) \tag{6}$$

where $a > 1$, L is linear differential operator with constant coefficients, b_k — constant. Equation (4) is a particular case of (6).

3. KRAVCHENKO-GAUSS AND KRAVCHENKO-RAYLEIGH DISTRIBUTIONS AND THEIR APPLICATIONS

On practice can be useful finite distributions constructed on a base of Atomic Function up(x) [2, 3]. And some of them are Kravchenko-Gauss, Kravchenko-Rayleigh distributions [1]. They are finite solutions of equation:

$$Lf(x) = \lambda \sum_{k=1}^{M} c(k) f(a_k x - b_k), \qquad |a_k| > 1,$$

where L — linear differential operator with constant coefficients; a_k, b_k — constants, and have the following expression: The recent work is dedicated to the application of Kravchenko-Rvachev [1–3] distribution of digital processing problems of new signal constructions. In the first part the theory of building of the Kravchenko-Gauss, Kravchenko-Rayleigh distributions [1] is represented:

$$p(x) = \frac{1}{\sqrt{2\pi}c} \exp\left(-\frac{x^2}{2a^2}\right) \mathrm{up}\left(\frac{x}{b}\right), \qquad a, b, c \in \mathbb{R}. \tag{7}$$

$$p(x) = \begin{cases} \frac{x}{c} \mathrm{up}\left(\frac{x}{b}\right) \exp\left(-\frac{x^2}{2a^2}\right), & \text{if} \quad x \geq 0, \\ 0, & \text{if} \quad x < 0. \end{cases} \tag{8}$$

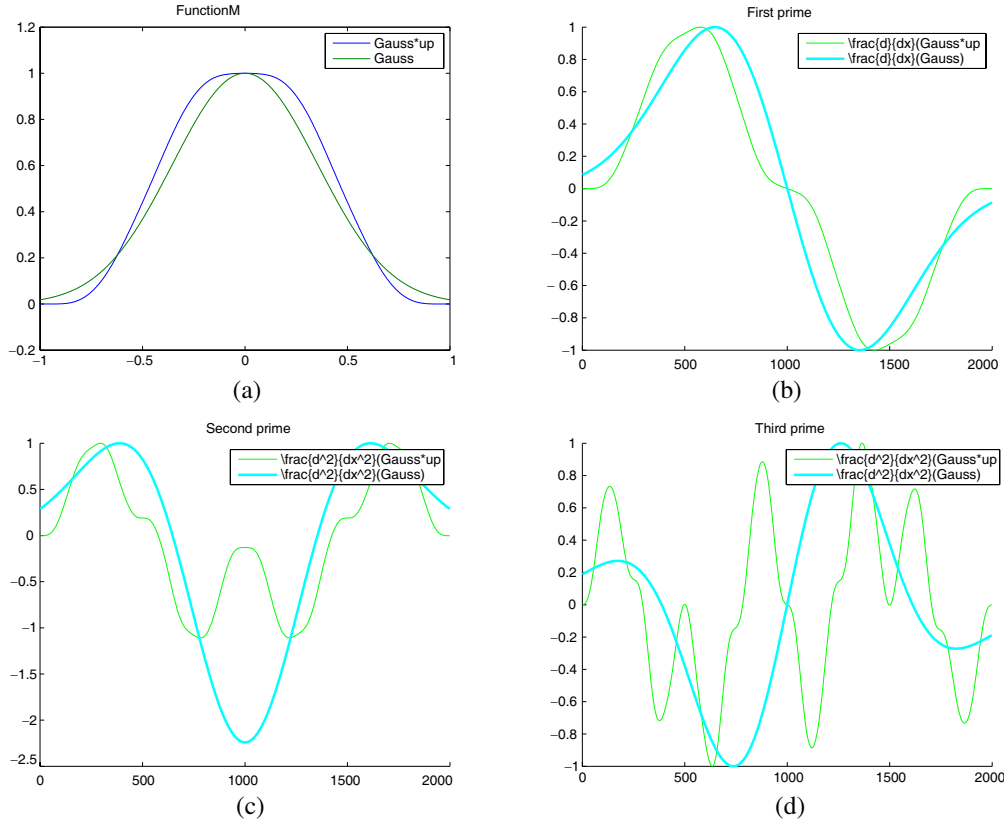

Figure 1: Comparison of the Gauss wavelet with the Kravchenko-Gauss wavelet (a) scaling function, (b) first order wavelet, (c) second order wavelet, (d) third order wavelet.

Here c is chosen such that in (7), (8)

$$\int_{\mathbb{R}} p(x)dx = 1.$$

Nowadays the great number of basis-wavelets is well known. And one of such wavelet-families is VMWF (Vanishing Momenta Wavelet Family), sometimes they called Gaussian wavelets. Functions of this family are the derivatives of gaussian exponents:

$$g_n(t) = (-1)^{n+1}\frac{d^n}{dx^n}e^{-x^2/2}, \quad n \in \mathbb{N}. \tag{9}$$

Normalizing coefficient takes on a value

$$C_{g_n} = 2\pi(n-1)!, \quad 0 < n < \infty.$$

The VMWF family had got its name because of first $n-1$ moments of function $g_n(x)$ is equal to zero:

$$\int_{-\infty}^{+\infty} x^m g_n(x)dx = 0, \quad \forall m, \quad 0 \le m < n, \quad n \in N. \tag{10}$$

Functions of VMWF family as all other wavelets satisfy the acceptability condition:

$$\int_{-\infty}^{+\infty} \psi(x)dx = 0,$$

where $\psi(x) \in L^2(R)$ is a basis wavelet. From (9) we can see that the wavelet derivative coincides with greater to one order wavelets:

$$\frac{d}{dx}g_n(x) = -g_{n+1}(x).$$

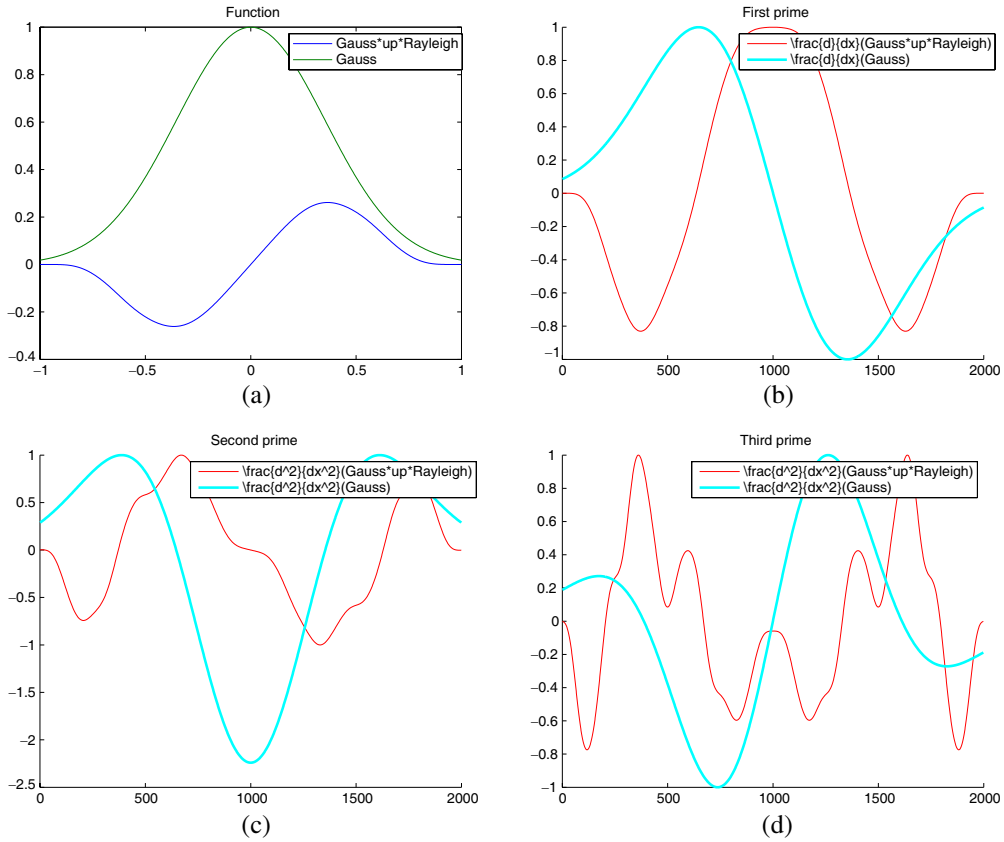

Figure 2: Comparison of the Gauss wavelet with the Kravchenko-Rayleigh scaling function (a) scaling function $\tilde{p}(x)$, (b) first order wavelet $\tilde{p}'(x)$, (c) second order wavelet $\tilde{p}''(x)$, (d) third order wavelet $\tilde{p}'''(x)$.

The new families of Kravchenko-Gauss and Kravchenko-Rayleigh wavelets are discussed. The next physical quantities are considered: wavelet spectra, energy density of the wavelet-skeletons, the scalograms. The second part is devoted to the computer simulation by the formulas (7), (8) and (9).

4. COMPUTER SIMULATION

Here we consider a particular case of (7), (8) behaviour under the parameters $a = b = 1$. We take into consideration a modified Kravchenko-Rayleigh function $\tilde{p}(x) = x\,\mathrm{up}(x)\exp\left(-x^2\right)$ on $x \in (-1, 1)$. Figure 1 shows the comparison of Kravchenko-Gauss and Gauss scaling function and their first three derivative. Comparison of the Kravchenko-Rayleigh versus Gauss function and it's first three derivatives is shown in Figure 2. Figure 3 shows the scalogram of Gauss and $\tilde{p}(x)$ function.

5. APPLICATIONS OF THE WAVELET TRANSFORM

One of the most popular applications of wavelet transform is image compression. The advantage of using wavelet-based coding in image compression is that it provides significant improvements in picture quality at higher compression ratios over conventional techniques. Since wavelet transform has the ability to decompose complex information and patterns into elementary forms, it is commonly used in acoustics processing and pattern recognition. Moreover, wavelet transforms can be applied to the following scientific research areas: edge and corner detection, partial differential equation solving, transient detection, filter design, electrocardiogram (ECG) analysis, texture anal-

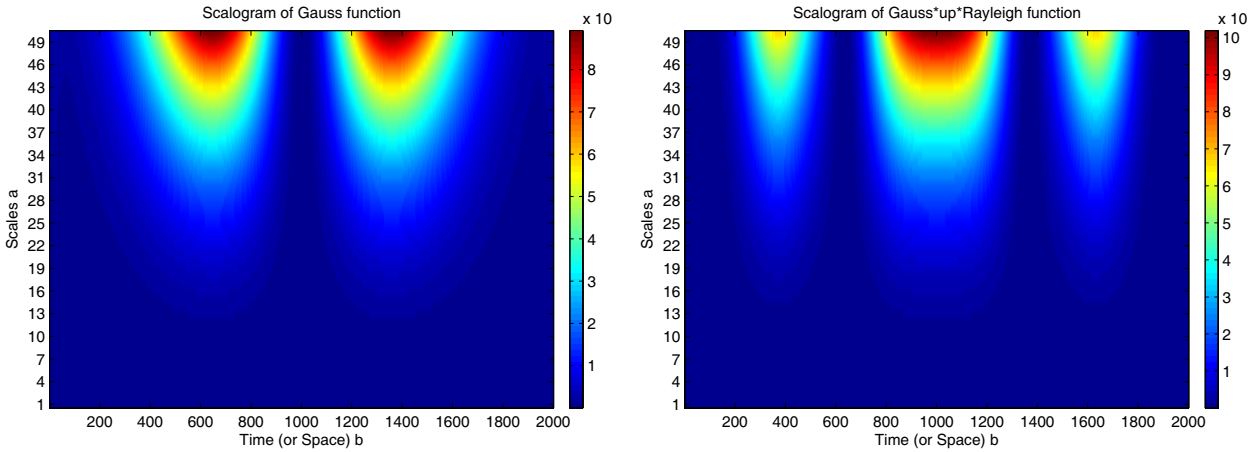

(a) (b)

Figure 3: (a) Scalogram of Gauss's function, (b) Scalogram of $\tilde{p}(x)$ function.

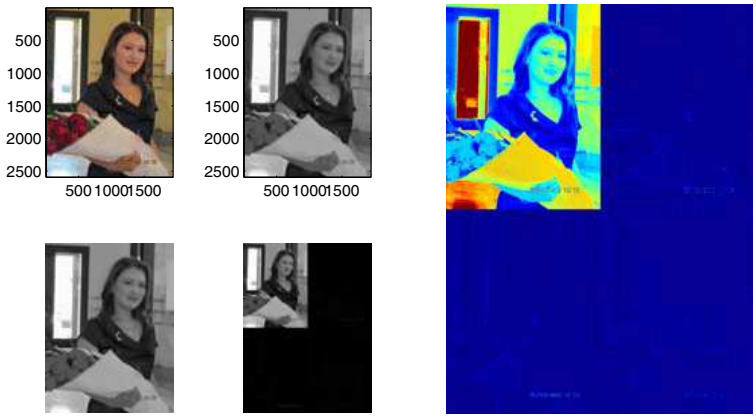

(a) (b)

Figure 4: (a) Compression of the image with 1944×2592 pixels resolution, (b) compressed image.

ysis, business information analysis and gait analysis. Figure 4 shows the compression of the image with 1944×2592 pixels resolution, sRGB color representation bit depth 24.

REFERENCES

1. Kravchenko, V. F., O. V. Kravchenko, and A. R. Safin, "Atomic functions in probability theory and stochastic processes," *Uspekhi Sovremennoi Radioelektroniki*, No. 5, 23–38, 2009 (in Russian).
2. Kravchenko, V. F., *Lectures on the Theory of Atomic Functions and Their Some Applications*, Radiotekhnika, Moscow, 2003 (in Russian).
3. Kravchenko, V. F. and V. L. Rvachev, *Algebra of Logic, Atomic Functions and Wavelets in Physical Applications*, Fizmatlit, Moscow, 2006 (in Russian).

Embedded Object Detection by Using Planar Antenna Measurement System

O. Kurnaz, S. Helhel, and S. Ozen
Department of Electrical and Electronics Engineering, Akdeniz University, Turkey

Abstract— In this study, planar near-field antenna measurement system has been used as a controlled radar setup and bistatic wave scattering conditions have been formed. A metal having 1 cm × 5 cm dimensions has been buried in a non-conductive cylinder having a diameter of 5 cm and height of 10 cm. Then, electromagnetic scattering pattern of cylinder has been obtained by using S_{21} parameter. Using some image processing techniques on obtained pattern, detection of the metal buried in cylinder has been realized.

1. INTRODUCTION

The detection of buried objects in other mediums is important since there are many related applications such as security, military, and medical applications. This issue force scientists to conduct researches on similar issues [1–3].

Marr et al. [1] investigated the scattering characteristic of the metallic sphere by using cylindrical near field scanning system. They investigated the radar cross section and pattern of the sphere by putting it in the center of the scanner They compared numerical solutions with far field data computed from measured near field.

Amineh et al. [2] investigated the capabilities and limits of the horn antennas first and then they proposed a microwave imaging setup by using planar aperture raster scanning. They used blind de-convolution algorithm and tested the performance of their technique.

Burkholder et al. [3] used model-based imaging method instead of conventional imaging approaches and they investigated the detection of objects inside a room.

Since the topic has many applications, it is important to develop an efficient technique. In this study, buried metal detection has been realized by using a planar near field antenna measurement system, which is mainly used for measuring and testing antennas, as a bistatic radar setup. Also, image processing techniques have been used.

2. THEORY

2.1. Scattering Pattern

In a linear electrical system, the relationship between the input/output terminals is expressed in terms of S parameters. In a two port network system, there are totally four S parameters, which are S_{11}, S_{12}, S_{21} and S_{22}, S_{21} represents the ratio of incident electric field power in port one to transmitted electric field power in port two. If

$$S_i = |S_i|e^{j\theta_1} \tag{1}$$

represents the power of incident wave, and

$$S_t = |S_t|e^{j\theta_2} \tag{2}$$

represents the power of transmitted field, then the forward complex transmission coefficient S_{21} can be expressed as

$$S_{21} = |S_{21}|e^{j\theta_3} \tag{3}$$

where $|S_{21}| = \frac{|S_t|}{|S_i|}$ and $\theta_3 = \theta_2 - \theta_1$. Using the information that metallic surfaces reflect the electromagnetic wave more than dielectric materials do [4], scattering pattern of the objects can be obtained by using $|S_{21}|$ parameter.

2.2. Image Processing on Obtained Patterns

Two measurements are required in order to obtain the scattering pattern of the desired object: one for the object and the background medium, and another measurement for only background medium. The difference gives the approximated pattern of the desired object. The method of taking difference is generally used for antenna measurement experiments since the background reflections from the chamber walls and supporting structure may be quite strong [1].

If $F_F(i,j)$ is defined as the measured field on each data grid points (i,j) in presence of both background and object, and $F_B(i,j)$ is defined as the measured field on each data grid points (i,j) in presence of only background where $i = 1,2,3,\ldots,(\frac{a}{\Delta y}+1)$ and $j = 1,2,3,\ldots,(\frac{b}{\Delta x}+1)$, then the difference field can be expressed as

$$F_D(i,j) = \left\{ \begin{array}{ll} F_F(i,j), & [F_F(i,j) - F_B(i,j)] \geq T \\ 0, & \text{otherwise} \end{array} \right\} \tag{4}$$

by using the threshold method. T is the threshold value and is manually determined in this study.

In order to remove the blur effect on the obtained pattern, median filter can be applied to the F_D matrix. If values of each n by n data blocks of matrix F_D are arranged as

$$\begin{aligned} F_{D_1}(i \pm ((n-k)/2), j \pm ((n-k)/2)) &< F_{D_2}(i \pm ((n-k)/2), j \pm ((n-k)/2)) \\ &< \ldots < F_{D_{(n^2)}}(i \pm ((n-k)/2), j \pm ((n-k)/2)) \end{aligned} \tag{5}$$

where n is an odd number and is generally chosen as a small number for computational purposes, and $k = 1,3,\ldots,n$. After the arrangement, the filtered matrix F_{DF} can be obtained on each (i,j) point as the following:

$$F_{DF}(i,j) = F_{D_{((n^2+1)/2)}}(i,j) \tag{6}$$

At a final stage, the dimensions of the pattern image are doubled to increase the resolution of the image. The values of the new data matrix are found according to the following relations,

$$F'_{DF}(2i,2j) = (F_{DF}(i,j) + F_{DF}(i,j+1) + F_{DF}(i+1,j) + F_{DF}(i+1,j+1))/4, \tag{7a}$$

$$F'_{DF}(2i-1,2j) = (F_{DF}(i,j) + F_{DF}(i,j+1))/2, \tag{7b}$$

$$F'_{DF}(2i,2j-1) = (F_{DF}(i,j) + F_{DF}(i+1,j))/2, \tag{7c}$$

$$F'_{DF}(2i-1,2j-1) = F_{DF}(i,j). \tag{7d}$$

3. LABORATORY AND EXPERIMENTAL SETUP

Measurements were made in Near Field Antenna Measurement Laboratory, inside Industrial and Medical Application Based Microwave Research Center (EMUMAM) at Akdeniz University. The laboratory contains one vector network analyzer operating in 10 MHz–9 GHz frequency range (Anritsu MS4624B), 3 step motors (Velmex), 2 stepping motor controllers (Velmex VXM), planar near field antenna measurement system, a computer and 9 pyramidal shaped radiation absorbent materials (RAM), each of which has 60 cm × 60 cm dimensions. There is additional absorbent material surrounding measuring probe to avoid reflections from mechanical parts of the system and laboratory walls. The laboratory and the experimental setup are shown in Fig. 2 and Fig. 3.

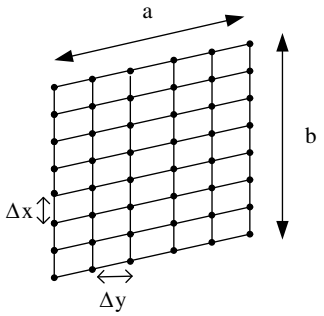

Figure 1: Data grid of planar antenna measurement system.

Figure 2: Near field laboratory and setup.

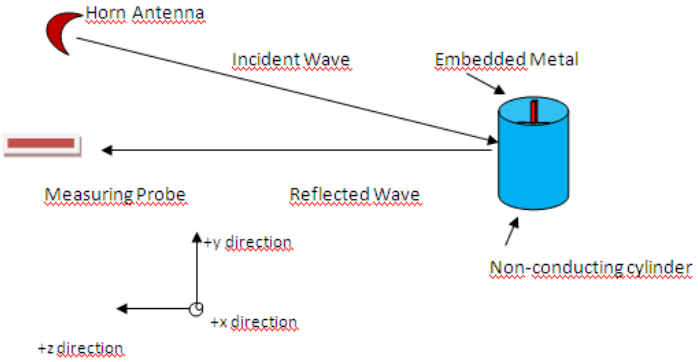

Figure 3: Graphical representation of experimental setup.

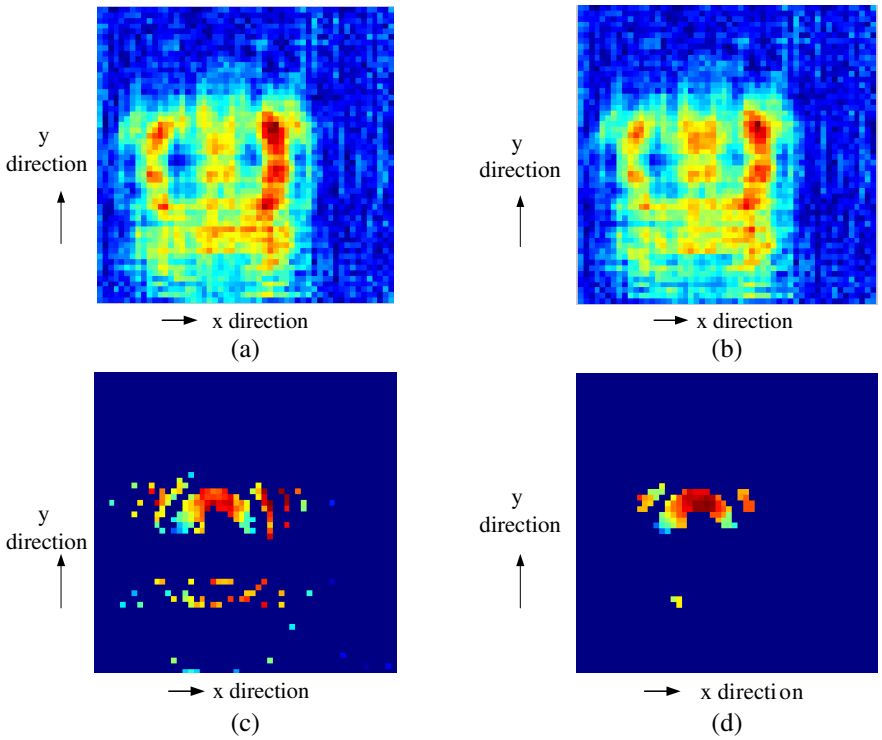

Figure 4: (a) Pattern of object and background. (b) Pattern of only background. (c) Pattern after threshold is applied. (d) Pattern after median filter.

If z-direction is considered to be the direction from measuring probe through the target, one of the step motors provides movement in x-direction and another one provides movement in y-direction, thus a square shaped area can be scanned by the probe. An open ended rectangular shaped waveguide is used as the measuring probe. Vector network analyzer is used for near field measurements, and synchronization of network analyzer and mechanical scanner system has been realized [5].

A metallic ribbon was put within a non-conducting cylinder which has 5 cm diameter and 10 cm height. The ribbon has 1 cm × 5 cm dimensions and it is put at the top of the cylinder block as shown in Fig. 3. The cylinder block was put at 100 cm away from the measuring probe in $-z$ direction. The scanning system scanned an area of 90 cm × 90 cm dimensions and half wavelength ($\lambda/2$) resolution was used.

4. RESULTS AND CONCLUSION

The obtained pattern of the scanned whole setup is shown in Fig. 4(a) and the pattern of the background field is shown in Fig. 4(b). Since the measurement is in the far field range (100 cm), the difference of two patterns is not clear.

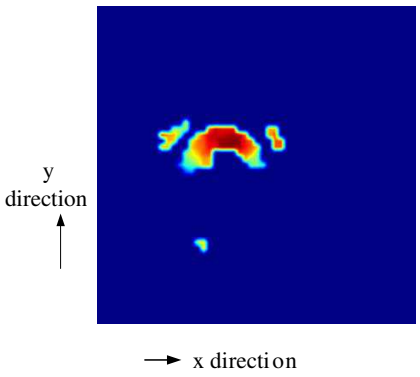

Figure 5: The final pattern obtained after Eq. (7) has been applied 3 times.

On the other hand, the approximated desired pattern is obtained as in Fig. 4(c) after applying Eq. (4) and as in Fig. 4(d) after filter operation. The final image after applying the procedure defined in Eq. (7) 3 times is obtained in Fig. 5.

At a first glance, it is not possible to detect the sole pattern of the metal ribbon from Fig. 4(a), however, the detection of the metal has been realized after applying the method described in the paper.

On the other hand, it has been observed that the measured field decrease as frequency increases. The measurements were made between 7.6 GHz and 9 GHz. The field at 7.8 GHz has been observed nearly two times that at 9 GHz. The result leads us to the conclusion that the accuracy of detection process would be low at very high frequencies or the distance at z-direction should be reduced to get accurate results at very high values.

ACKNOWLEDGMENT

This project was supported by Akdeniz University, Scientific Research Projects Supporting Unit (BAPYB), Grant Number: 2012.02.0121.008 and 2012.05.0102.024.

REFERENCES

1. Marr, R. A., U. H. W. Lammers, T. B. Hansen, T. J. Tanigawa, and R. V. McGahan, "Bistatic RCS calculations from cylindirical near-field measurements — Part II: Experiments," *IEEE Trans. Antennas and Propagation*, Vol. 54, No. 12, 3857–3864, Dec. 2006.
2. Amineh, R. K., M. Ravan, A. Trehan, and N. K. Nikolova, "Near field microwave imaging based on aperture raster scanning with TEM horn antennas," *IEEE Trans. Antennas and Propagation*, Vol. 59, No. 3, 928–940, Mar. 2011.
3. Burkholder, R. J., P. Chang, Y. Bayram, R. J. Marhefka, and J. L. Volakis, "Model-based near-field imaging of objects inside a room," *2007 Antennas and Propagation Society International Symposium*, Jun. 9–15, 2007, Paper DOI: 10.1109/APS.2007.4395783.
4. Balanis, C. A., *Advanced Engineering Electromagnetics*, John Wiley & Sons, 1989.
5. Ozturk, Y. and F. Ustuner, "Düşük maliyetli bir düzlemsel yakın alan anten ölçüm sisteminin tasarlanması ve gerçeklenmesi," *5th URSI Turkish Scientific Congress*, 223–226, Güzelyurt, KKTC, 2010.

Electromagnetic Object Recognition for Dielectric Coated Conductors Based on WD-PCA Type Fused Feature Extraction

G. Turhan-Sayan[1] **and E. Ergin**[1,2]

[1]Department of Electrical-Electronics Engineering
Middle East Technical University (METU), Ankara, Turkey
[2]Turkish Aerospace Industries, Inc. (TAI), Ankara, Turkey

Abstract— This paper presents the application of a real-time electromagnetic object classification technique to recognize dielectric coated conducting objects using their wideband scattered signals received at arbitrary combinations of aspect and polarization. The suggested classifier design technique depends on the use of Singularity Expansion Method (SEM) to represent a given electromagnetic scatterer by its natural resonances. A quadratic time-frequency transformation, the Wigner distribution (WD), is used to extract pole-related feature vectors from scattered signals, and the Principal Components Analysis (PCA) is further used to obtain a fused feature vector for each object of concer

1. INTRODUCTION

Electromagnetic object recognition is a complicated problem due to the aspect and polarization dependent nature of scattered data. Based on the Singularity Expansion Method (SEM), an object can be approximately modeled as a linear time-invariant system and its complex natural resonance (CNR) frequencies can be computed as the poles of system function in complex frequency domain [1]. These poles are determined by the size, shape and material properties of a given object and they are totally independent of aspect angle and polarization conditions. In other words, a complete set of system poles can describe the related finite-size object uniquely in an aspect and polarization independent manner. Although system poles are perfect features in that respect, their extraction from measured scattered data is highly susceptible to noise. Extraction of pole information indirectly turns out to be a more feasible approach in classifier design. Use of late-time signals is especially important in this process as the early time scattered signals are extremely sensitive to aspect and polarization variations. A recently suggested method using this approach is the WD-PCA method [2, 3] where the extracted pole-related object features describe the spectral content of natural response over a properly chosen late-time interval. This technique is based on the use of Wigner Distribution (WD), a quadratic time-frequency transformation, to extract pole-related object features at each available aspect/polarization combination. Then, the Principal Component Analysis (PCA) is used for data reduction and feature fusion. In WD-PCA method, electromagnetic scattered data measured or simulated at only a few different combinations of aspect and/or polarization would be enough to design the classifier for a library of preselected objects. Each library object is represented in the classifier's feature database by a single aspect/polarization invariant fused feature vector. In the real-time object recognition phase, on the other hand, a scattered signal received at a single (arbitrary and unknown) combination of aspect and polarization would be sufficient to classify the test object.

In literature, the WD-PCA technique has been successfully applied to recognize perfect conductor or perfect dielectric objects so far [2–4]. In this paper, this technique will be demonstrated for a more challenging object library that is composed of dielectric coated conducting spheres which have the same overall size and the same coating material but varying sizes of conducting spheres inside.

2. THEORY

Basic theory and fundamental design steps of the WD-PCA based object classification technique are briefly described in this section. In the first step of this design procedure, a database of electromagnetic scattered signals must be generated to contain a total of $K \times M$ different time-domain scattered signals at K reference combinations of aspect angle/polarization for each one of M library targets. Scattered signals can be either measured or synthesized by numerical simulations over a common preselected frequency band in resonance region. Next, the auto Wigner-Ville

distribution (WD) is computed for each design signal $x(t)$ as

$$W_x(t,f) = \int_{-\infty}^{\infty} e^{-j2\pi f\tau} \times (t+\tau/2) \times^* (t-\tau/2) d\tau \tag{1}$$

where the output represents an energy density function over the joint time-frequency plane, in approximate sense. To characterize the natural response behavior of the target, it is needed to partition the total time span T_0 of the signals into Q equally-wide intervals and use the WD output over a selected late time interval [3] to construct a late-time feature vector (LTFV) defined as $\bar{e} = [\bar{E}_{q^*} \;\; \bar{E}_{q^*+1}]$ where $\bar{E}_q$ is the qth partition vector of length $(N/2)$ defined on the qth time interval with its entries computed as

$$E_q(f_p) = \int_{(q-1)\frac{T_0}{Q}}^{q\frac{T_0}{Q}} W_x(t,f_p)\, dt \quad \text{for} \quad q = 1,2,\ldots,Q, \quad p = 1,2,\ldots,\tfrac{N}{2} \quad \text{for} \quad f_p = (p-1)\,\tfrac{1}{T_0} \tag{2}$$

where N is the number of samples of the discrete time domain scattered signal. The methods for choosing parameters Q and q^* are discussed in detail in [3].

Then, the PCA technique is used to extract main patterns common to moderately excitation dependent LTFV features computed at K different aspect/polarization combinations for a given library object. To implement the PCA based multi-aspect feature fusion technique, a real valued feature matrix F of size $K \times N$ is formed for each object having the late-time feature vectors $\bar{e}_k$, $k = 1,\ldots,K$ as its rows. Then, the covariance matrix S_{F} of this feature matrix F is computed which is a $K \times K$ nonsingular, symmetric matrix. Next, an orthonormal matrix $U = [u_1 \; u_2 \; \ldots \; u_K]$ is formed where u_i's are the normalized eigenvectors (of size $K \times 1$) corresponding to the eigenvalues λ_i of the covariance matrix S_F. In this process, the U matrix is formed after ordering the computed eigenvalues such that $\lambda_1 > \lambda_2 > \ldots > \lambda_K$ and it can be used to diagonalize the covariance matrix and to transform the correlated feature vectors $\bar{e}_1, \bar{e}_2, \ldots, \bar{e}_K$ into a set of uncorrelated vectors $z_1, z_2, \ldots, z_K$ by

$$Z = \begin{bmatrix} z_1 \\ z_2 \\ \vdots \\ z_K \end{bmatrix} = U^T \begin{bmatrix} \bar{e}_1 - \mathrm{mean}(\bar{e}_1)\; I_N \\ \bar{e}_2 - \mathrm{mean}(\bar{e}_2)\; I_N \\ \vdots \\ \bar{e}_K - \mathrm{mean}(\bar{e}_K)\; I_N \end{bmatrix} \tag{3}$$

where I_N is an all-ones row vector of length N, the superscript T denotes the transpose operator and the resulting matrix Z (of size $K \times N$) is composed of transformed vectors, z_{i}'s which are the principal components of the feature matrix F. Each principal component z_i is a zero-mean vector with variance λ_i. Then, the fused feature vector (FFV) can be constructed as a weighted sum of principal components to characterize the associated target in the classifier's feature database.

The same procedure is repeated for each object in the classifier library to completely design the classifier's feature database. Then, during the real-time classification phase, the LTFV of the measured test signal is computed as described above and its correlation coefficient with respect to each FFV in the classifier library is computed to determine the library target with the highest matching score.

3. APPLICATIONS AND RESULTS

In this section, we will demonstrate the design of an object classifier to recognize $M = 5$ different dielectric coated conducting spheres S_1, S_2, S_3, S_4 and S_5. These spheres have exactly the same external radius ($r_{\mathrm{out}} = 10\,\mathrm{cm}$), the same relative permittivity of $\varepsilon_r = 7$ but different internal radii ($r_{\mathrm{in}} = 2$, 4, 7, 8 and 9 cm, respectively) for the inner conducting spheres. Far field (at $r \gg r_{\mathrm{out}}$) scattered responses for these library objects are computed in frequency domain (in response to an x-polarized uniform plane wave propagating in $+z$-direction as described in Figure 1) using the Mie series over the frequency range from DC to 19.1 GHz at $\phi = 90$ degrees azimuth angle and for 12 different bistatic aspect angles with $\theta = 15$, 30, 45, 60, 75, 90, 105, 120, 135, 150, 165 and 179 degrees. Also, a noisy signal database is prepared by adding Gaussian noise to these synthesized data to produce scattered signals with signal-to-noise ratio levels of SNR = 20, 15, 10

and 5 dB levels at all 12 aspects for each of the library objects. Out of these 12 bistatic aspects, only $K = 5$ reference aspects at $\theta = 15$, 45, 90, 135 and 179 degrees are chosen to be used in classifier design. Accordingly, a total of $K \times M = 25$ scattered time-domain signals at 20 dB SNR level are used in classifier design after being transformed into time domain by using IFFT. The classifier is designed over the optimum time interval [16.8 ns–20.1 ns] using the design parameters $N = 1024$, $T_0 = 26.81$ ns, $Q = 16$ and $q^* = 11$. As an example, the contour plot for the modified WD output computed for the object S_3 at the aspect angle of $\theta = 105$ degrees is shown in Figure 2. The LTFV extracted over this optimal late-time interval for the object S_3 at the reference aspects at $\theta = 15$, 45, 90, 135 and 179 degrees are plotted in Figure 3. Finally, the fused feature vectors (FFV's) obtained by the PCA method for each library object are given in Figure 4 together with the LTFV of a "test signal" that actually belongs to the object S_3 at the aspect angle of $\theta = 165$ degrees.

After the classifier's FFV database is obtained, this classifier is tested in real-time against $(5 \times 5 \times 12) - 25 = 275$ scattered signals (for 5 targets at 12 aspects and at 5 different noise levels) which are not used in the classifier design phase. The correct decision rates of the classifier are found to be 98 percent in the case of noise-free test data, 95 percent at 20 dB SNR, 93 percent at 15 dB SNR, 85 percent at 10 dB SNR and 75 percent at 5 dB SNR test cases.

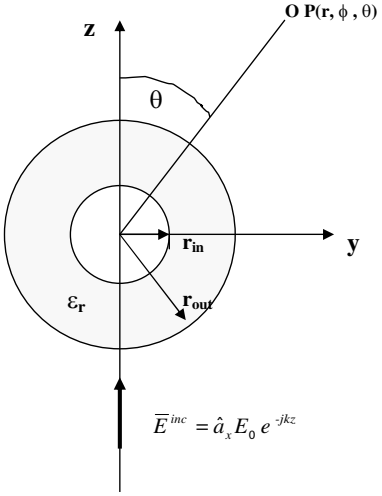

Figure 1: Simulation setup for scattered signal computations under plane wave excitation.

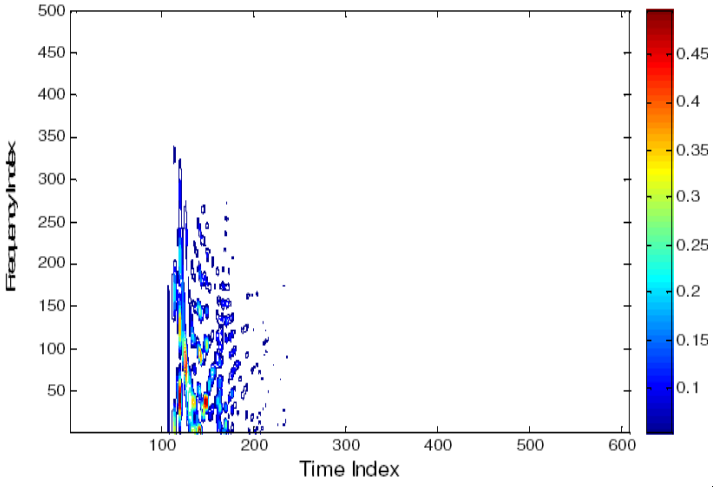

Figure 2: Contour plot for the modified WD output for the object S_3 at the aspect angle $\theta = 105$ degrees.

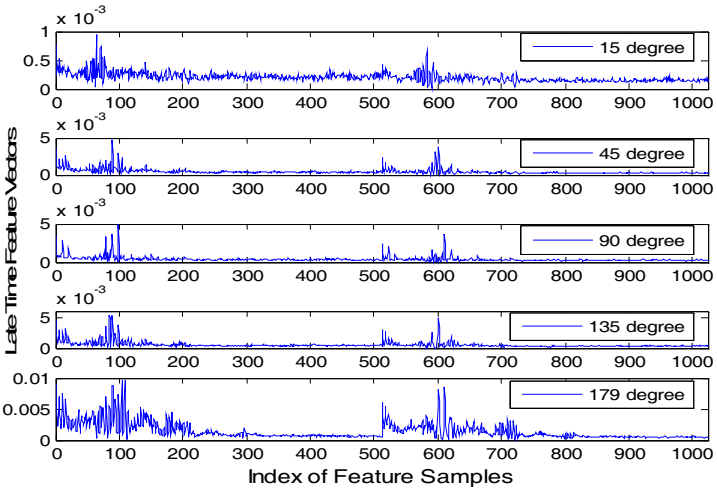

Figure 3: Late time feature vectors (LTFV) for the object S_3 at reference aspects at 20 dB SNR level.

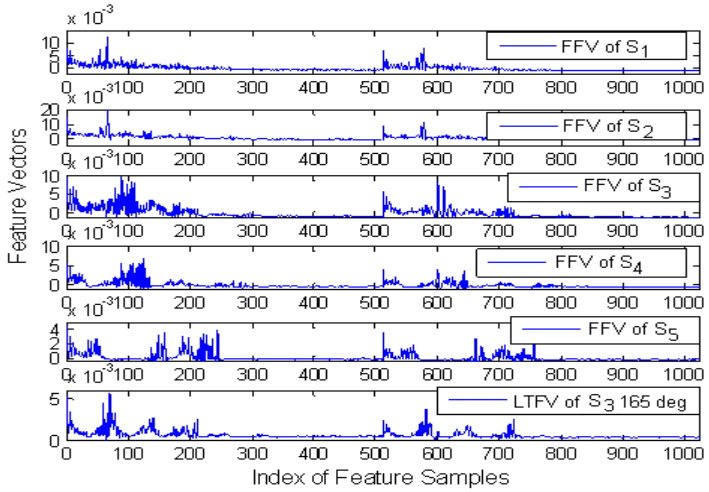

Figure 4: FFVs for each library object and the testing LTFV belonging to the object S_3 at $\theta = 165$ degrees.

4. CONCLUSION

In this paper, design of a WD-PCA based object classifier for five different dielectric coated conducting spheres is demonstrated together with performance testing with noise-free and noisy data. The accuracy rate of the classifier is found to be almost perfect (98 percent) when it is tested by noise-free test data. This accuracy rate is decreased from 95 percent to 75 percent, as expected, as the SNR level of the testing database decreases from 20 dB to 5 dB. Almost all of the wrong decisions made by the classifier have occurred in the recognition of objects S_1 and S_2 which have smaller size conducting spheres inside with $r_{\text{in}} = 2$ cm and $r_{\text{in}} = 4$ cm, respectively.

REFERENCES

1. Baum, C. E., E. J. Rothwell, K. M. Chen, et al., "The singularity expansion method and its application to target identification," *Proc. IEEE*, Vol. 79, No. 10, 1481–1492, Sept. 1991.
2. Turhan-Sayan, G., "Natural resonance-based feature extraction with reduced aspect sensitivity for electromagnetic target classification," *Pattern Recognition*, Vol. 36, No. 7, 1449–1466, Jul. 2003.
3. Turhan-Sayan, G., "Real time electromagnetic target classification using a novel feature extraction technique with PCA-based fusion," *IEEE Transactions on Antennas and Propagation*, Vol. 53, No. 2, Feb. 2005.
4. Ergin, E., "Investigation of MUSIC algorithm based and WD-PCA method based electromagnetic target classification techniques for their noise performances," M.S. Thesis, METU, Turkey, Oct. 2009.

Accurate Measurement of Power Transfer to an RFID Tag with On-chip Antenna

Philipp K. Gentner[1], **Günter Hofer**[2], **Arpad L. Scholtz**[1], **and Christoph F. Mecklenbräuker**[1]

[1]Institute of Telecommunications, Vienna University of Technology
Gusshausstrasse 25/389, Vienna 1040, Austria
[2]Infineon Technologies Austria AG, Contactless and RF Exploration
Babenberger Strasse 10, Graz 8020, Austria

Abstract— Dramatically decreasing the size of an RFID tag is possible by using on-chip antennas, so-called OCAs [1, 2]. For the applications in mind, such as identifying goods in the food supply chain or in medical supply, the systems on chip need to be externally powered. This is challenging due to the small aperture available and because the antenna typically resides on a lossy substrate such as silicon.

Accurate measurement of the power inductively transferred to the tag is impossible using bond wires or probes, because both would introduce severe distortions of the electromagnetic field. Questionable results concerning the voltage induced into the on-chip antenna would be such obtained.

We present a novel method to accurately measure the voltage induced into an on-chip antenna and demonstrate its application in the UHF band at 850 MHz. To verify the proposed method we have designed and manufactured a system on chip. This chip consists of a loop antenna (similar design as reported in [1] and [2]), a rectifier, and a voltage controlled oscillator [3]. The latter modulates the energy backscattered by the chip with a frequency proportional to the voltage delivered by the rectifier. Hence, by measuring the modulation frequency the exact value of the voltage induced into the chip's antenna can be revealed.

In this paper, comprehensive measurements of the inductive coupling between an elaborate reader station and an RFID tag with on-chip antenna will be shown. The silicon is moved in planes above an excitation coil, and the modulation frequency of the signal backscattered is measured. With the relation between the voltage induced into the chip's antenna and the backscattered signal's modulation frequency being calibrated, the energy received by the chip as a function of its position in space is mapped.

1. INTRODUCTION

In an asymmetric or hybrid RFID communication system, the tag consists of an ultra-wideband (UWB) impulse radio transmitter and an UHF receiver [4]. A reader station transmits a UHF carrier for powering and synchronizing the tag. In general, the UWB transmitter allows for higher data rates, while consuming less power. This is an ideal scenario for RFID or wireless sensor applications. If the size of the system is of importance, on-chip antennas (OCAs) are an option. Considering a typical size of a few square millimeters of the chip, the highly reduced antenna efficiency of course yields to a reduction of the feasible communication range.

The contactless powering method in this contribution is inductive coupling. It is important for system design to know the amount of power available for the functionality of the chip. There are three major aspects that influence the power drawn by an integrated chip from the electromagnetic field. These are the performance of the on-chip antenna, the rectifier, and the performance of the reader antenna exciting the magnetic field. We propose an evaluation method to characterize the performance of the OCA and rectifier by measurements, without the need of wired connections to the chip. Thus, compared to other methods we ensure that the electromagnetic field of the excitation coil and the OCA itself is not affected.

The inductive coupling scenario is shown in Figure 1. Furthermore, a microphotograph of the on-chip loop antenna (similar design as reported in [1] and [2]) is displayed. The silicon substrate carrying the OCA is placed at a fixed distance in z-direction above the excitation coil. The coil is a magnetic loop antenna printed on a standard FR4 PCB, fed by a sinusoidal signal at 850 MHz with variable power level P_{in}. The FR4 substrate the loop antenna is printed on has a thickness of 1.5 mm (copper thickness 35 µm). The ground planes on the top and bottom layers are connected by vias to form a coplanar waveguide feed. The loop consists of two turns of conductors (width 0.5 mm). The overall diameter of the spiral coil is 4.2 mm and the inner diameter is 1.5 mm.

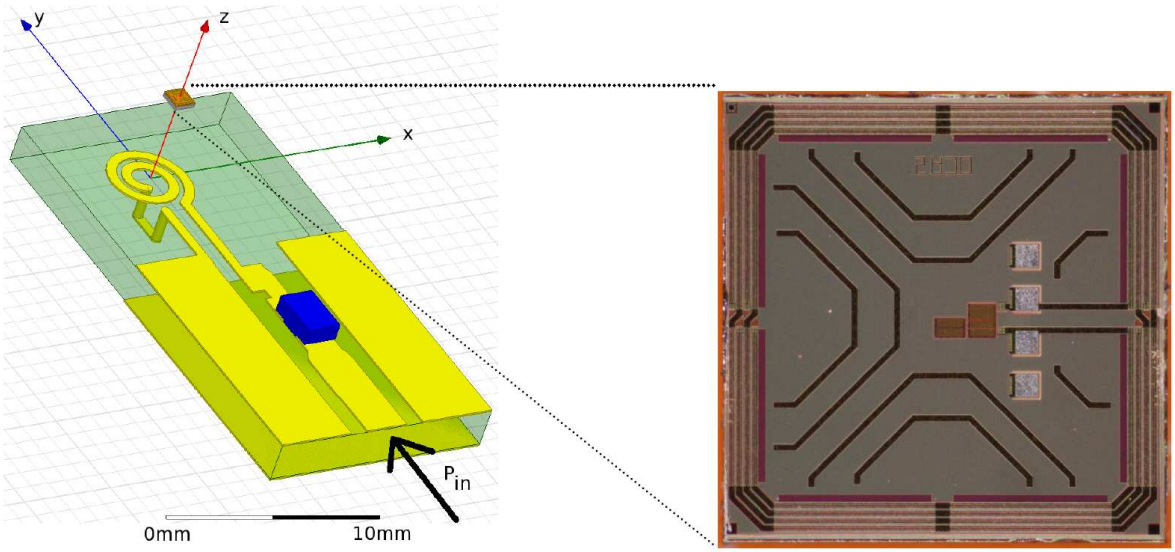

Figure 1: Inductive coupling scenario. The silicon chip with the OCA is placed in close distance in z-direction directly above the center of the excitation coil. On the right side, a microphotograph of the chip with a 4-turn coil antenna is shown.

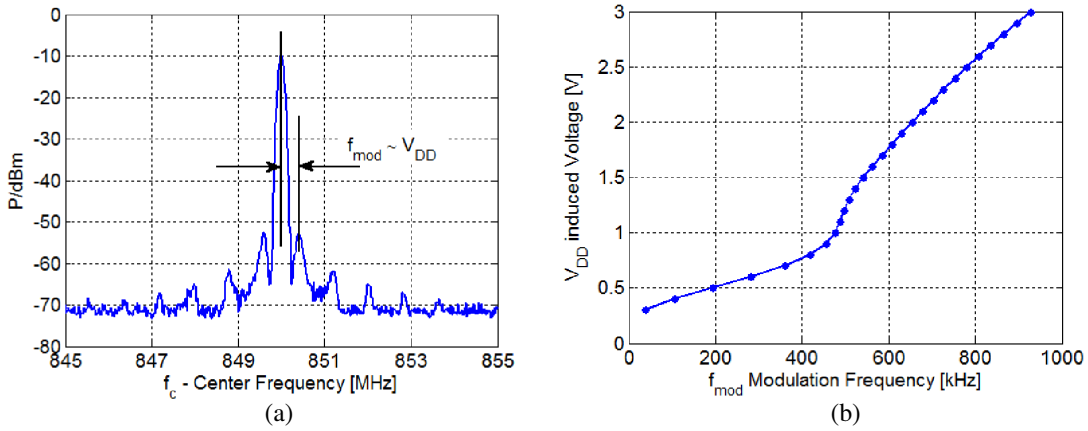

Figure 2: (a) The backscattered signal of the chip in the frequency domain, and (b) simulated proportionality between the modulation frequency f_{mod} and the induced voltage V_{DD}, delivered by the rectifier.

The PCB is designed to make possible on-board impedance matching with concentrated elements. For our experiments, we preferred to use an external impedance tuner. Therefore a jumper replaces the inline matching element on the PCB.

2. DEVICE UNDER TEST

The loop OCA investigated has an overall size of 1 mm^2 with four conductor turns. This type of on-chip antenna is commonly used for inductive coupling and is well known from literature (see [1] and [2]). Our antenna is manufactured with standard 130 nm CMOS technology without any post processing. The conductor width of each turn is 15 µm with a spacing of 2.6 µm between the turns. Two metal layers are utilised for the loop, which are connected by vias. The metal stripes in the loop's inner section prevent the silicon from breaking. The bonding pads inside the OCA (see photograph in Figure 1) are not required for the measurements presented in this paper.

The circuit on the silicon chip features a rectifier [5], a voltage controlled oscillator [3], and a logic part. The rectifier powers the chip. The oscillator and the logic part generate a modulated output signal that is fed to the OCA. Figure 2(a) shows the corresponding measured output spectrum. The peaks in the backscattered signals' spectrum are offset from the sinusoidal carrier at 850 MHz by multiples of the modulation frequency f_{mod}. The modulation frequency f_{mod} is proportional to the chip voltage V_{DD} (induced by the excitation antenna) after the rectifier.

The proportionality between f_{mod} and the chips' V_{DD} is calculated by transient simulation of the oscillator (see Figure 2(b)). The simulation, performed with Cadence, incorporates the parasitic effects of the substrate. This method to conclude from the measured f_{mod} to V_{DD}, allows to determine the performance of the OCA and the rectifier without the need of wired connections.

3. MEASUREMENTS

To show the feasibility of our method several experiments were carried out. The setup for all measurements consists of two styrofoam elements, one carrying the excitation coil and the other carrying the device under test. The excitation coil (see Figure 1) was matched with a tuner to the RF source. The matching process was done without the chip being in the excitation coil's vicinity. The chip was fixed with a double-faced adhesive tape on one end of a dedicated long styrofoam board. The other end of the styrofoam board was mounted on a multi axis platform, which can be moved in x, y and z direction via micrometer screws.

To get a first insight into the power transfer properties, the following initial experiment was performed. For constant input power $P_{in} = +8.6\,\text{dBm}$ at the excitation coil and constant z-position, the chip was moved in the x-y plane, until the measured f_{mod} reached its maximum. The coordinates such obtained are used as the origin $x = y = 0\,\text{mm}$. Now, the chip was moved in the x-y plane in equidistant steps of 0.5 mm. For each of these steps the modulation frequency was measured, and used to calculate the induced voltage V_{DD}. This measurement was carried out for two different z values (0.5 mm and 1.5 mm). Figure 3 shows the corresponding results. The

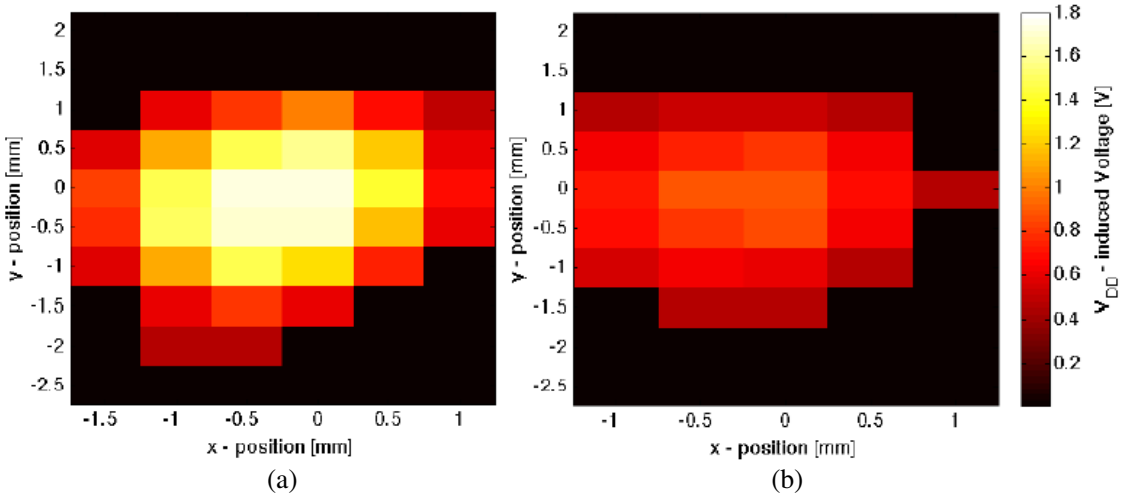

Figure 3: Measured V_{DD} for two different heights above the excitation coil. (a) $z = 0.5\,\text{mm}$ and (b) $z = 1.5\,\text{mm}$.

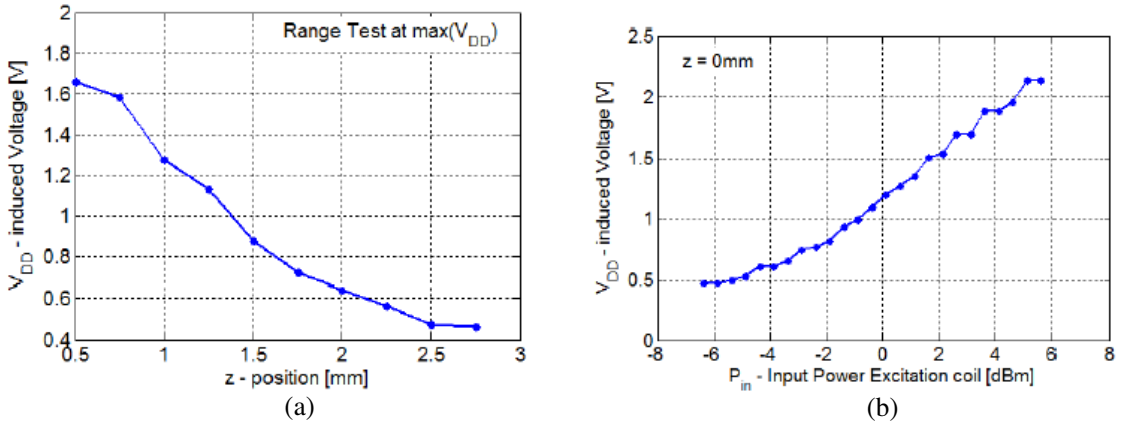

Figure 4: Range test in z-direction with $P_{in} = 8.6\,\text{dBm}$ at (a) max V_{DD} position and (b) input power sweep at $z = 0\,\text{mm}$.

induced voltage V_{DD} decreases with distance in z-direction as expected. Keeping in mind that chip operation requires a certain minimum V_{DD} level, the area of sufficient induced power decreases with height, as can be deduced from Figure 3 in accordance with expectation.

Next, a distance sweep in z-direction at $x = y = 0\,\text{mm}$ was carried out. For this range test, the styrofoam arm with the chip under test was moved from $z = 0.5\,\text{mm}$ to $z = 2.75\,\text{mm}$, while the input power P_{in} was kept constant. The V_{DD} values resulting from the measured f_{mod} are shown in Figure 4(a). The induced voltage decreases with increasing distance from the excitation coil, from $1.66\,\text{V}$ at $z = 0.5\,\text{mm}$ to $0.47\,\text{V}$ at $z = 2.75\,\text{mm}$.

Finally, the chip was brought into contact with the excitation coil ($x = y = z = 0\,\text{mm}$), and the input power P_{in} of the excitation coil was varied from $-6.4\,\text{dBm}$ to $+5.6\,\text{dBm}$. This was done to see how much power can be transferred into the chip in an ideal scenario. We observe that the induced voltage V_{DD} increases from $0.5\,\text{V}$ to $2.13\,\text{V}$ (see Figure 4(b)).

4. CONCLUSION

In this paper we presented a contactless method to determine the voltage induced by an excitation coil to an OCA. The modulation frequency of the signal backscattered from the tag is proportional to the induced voltage V_{DD} after the rectifier. This method was verified by measurements on an RFID chip prototype with an OCA. The tags operational area at constant heights above the excitation coil, as well as the behavior with increasing distance was successfully measured. Also, the voltage provided by the rectifier in an ideal scenario, with zero distance to the excitation coil was measured. This information will help in optimally designing inductively powered RFID chips with on-chip antennas.

ACKNOWLEDGMENT

This work was performed as part of the project 'Smart Data Grain' and 'Contactless Sensing' which are embedded into the program 'Forschung, Innovation, Technologie-Informationstechnologie' (FIT-IT) of the 'Bundesministerium für Verkehr, Innovation und Technologie' (BMVIT). This program is funded by the 'Österreichische Forschungsförderungsgesellschaft' (FFG). This work is partly supported by the Christian Doppler Laboratory for Wireless Technologies for Sustainable Mobility.

REFERENCES

1. Xi, J., N. Yan, W. Che, X. Wang, H. Jian, and H. Min, "On-chip antenna design for UHF RFID," *Electronics Letters*, Vol. 45, No. 1, 14–16, 2009.
2. Guo, L., A. Popov, H. Li, Y. Wang, V. Bliznetsov, G. Lo, N. Balasubramanian, and D. Kwong, "A small OCA on a $1 \times 0.5\,\text{mm}^2$ 2.45 GHz RFID tag — Design and integration based on a CMOS — Compatible manufacturing technology," *IEEE Electron Device Letters*, Vol. 27, No. 2, 96–98, 2006.
3. Klapf, C., A. Missoni, W. Pribyl, G. Holweg, and G. Hofer, "Analyses and design of low power clock generators for RFID TAGs," *Proc. Ph.D. Research in Microelectronics and Electronics PRIME 2008*, 181–184, 2008.
4. Zheng, L.-R., M. B. Nejad, Z. Zou, D. S. Mendoza, Z. Zhang, and H. Tenhunen, "Future RFID and wireless sensors for ubiquitous intelligence," *Proc. NORCHIP*, 142–149, 2008.
5. Reinisch, H., S. Gruber, M. Wiessflecker, H. Unterassinger, G. Hofer, W. Pribyl, and G. Holweg, "An electro-magnetic energy harvester with 190 nW idle mode power consumption for wireless sensor nodes," *Proc. ESSCIRC*, 234–237, 2010.

A Reduced-size Antipodal Vivaldi Antenna with a Reconfigurable Band Notch

L. Safatly, M. Al-Husseini, A. El-Hajj, and K. Y. Kabalan
ECE Department, American University of Beirut, Beirut 1107 2020, Lebanon

Abstract— The paper presents the design and the implementation of a reduced-size antipodal Vivaldi antenna with a reconfigurable band notch. The antenna could be mainly used for UWB applications since it covers a very wide frequency band. It is also suitable for Cognitive Radio (CR) systems because it is capable to sense the spectrum to determine the bands used by primary users, and to communicate pulses that ensure interference avoidance to primary users. For that, a reconfigurable band stop filter, based on three nested complementary split-ring resonators (CSRRs), is integrated on the ground plane. The band notch occurs at 3.5 GHz, 5.2 GHz or 7.3 GHz, and is controlled using electronic switches.

1. INTRODUCTION

The emerging broadband wireless communications and the huge number of medical and military applications have put increasing demand on a technology suitable for high data rates in small distances. For that, the Ultra-Wide Band (UWB) [1] protocol has been gaining a lot of attention. According to FCC regulations, UWB spectrum is limited between from 3.1 to 10.6 GHz. In the UWB environment, the transmitter and receiver antennas must be compact and lightweight and characterized by a gain stability, low distortion and low delays. Vivaldi antennas represent an adequate candidate to these types of communications [2, 3] since they are listed as frequency independent antennas. In [4], the antipodal Vivaldi antenna is introduced and its broadband characteristic is highlighted. Although antipodal Vivaldi antennas satisfy UWB requirements, their dimensions are normally greater than 10 cm. Therefore, size reduction of those UWB antennas is very challenging and was investigated by several researchers to include further enhancement on the size and on the bandwidth. In [5], a compact directive antipodal Vivaldi antenna is designed with dimensions of $52 \times 52\,\text{mm}^2$. Also, a miniaturized $32 \times 35\,\text{mm}^2$ antipodal Vivaldi antenna is introduced in [6].

On the other hand, the current crowding of unlicensed spectra necessitates urgent solutions. Cognitive Radio (CR) [7] is a promising technology to solve the shortage problem and exploit the existing spectrum in a revolutionized way. In a CR environment, unlicensed users are allowed to share the frequency resources with the licensed or primary users. For that, CR implementations pave the way to new challenges in reconfigurable antenna design and RF front ends in general. The essential requirement in reconfigurability is to maintain a constant gain at different resonant frequencies. This could be achieved by integrating a reconfigurable filter within the antenna structure [8]. The antenna surface current distribution will not be affected and hence the radiation pattern will be preserved. The filter will modify adequately the bandwidth of the antenna by adding frequency nulls at desired frequencies.

In this paper, the design and the implementation of a reduced-size antipodal Vivaldi antenna is presented. The antenna is equipped by a reconfigurable filter engraved on its feed line. The overall filter-antenna system provides a UWB response with a reconfigurable frequency band notch.

2. ANTENNA CONFIGURATION

As depicted in Figure 1, the designed Vivaldi antipodal antenna is printed on a $60 \times 35 \times 1.6\,\text{mm}^3$ FR4-epoxy substrate with a relative permittivity $\varepsilon_r = 4.4$. The dual-sided structure of the antenna is designed from the intersection of the quarter of two ellipses. The major and the secondary radii of these ellipses are calculated according to [5]. The dimensions of the different parts are optimized for an impedance bandwidth covering frequencies starting from 1.5 GHz as shown in Figure 2.

To induce the band notch and achieve reconfigurability, a reconfigurable band stop filter, based on three nested complementary split-ring resonators (CSRRs) is integrated on the ground plane. CSRRs are used in the literature to design reconfigurable and tunable bandstop and bandpass filters, which in turn will be embedded in antennas used for cognitive radio applications [9]. In [10], a bandstop filter implemented in the patch of a UWB antenna and based on nested CSRRs is presented. Compared to the work in [10], this proposed design has the advantage of implementing

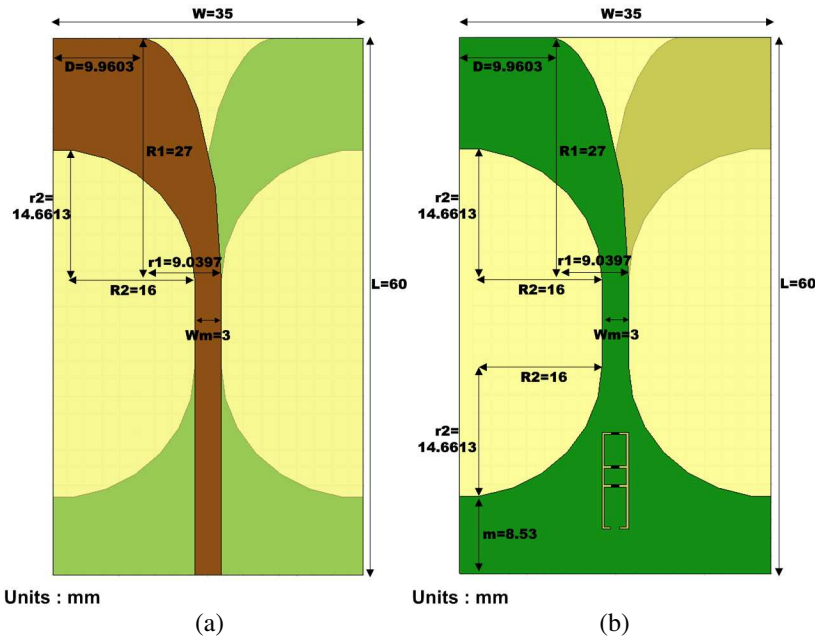

Figure 1: Antenna configuration. (a) Patch. (b) Ground plane.

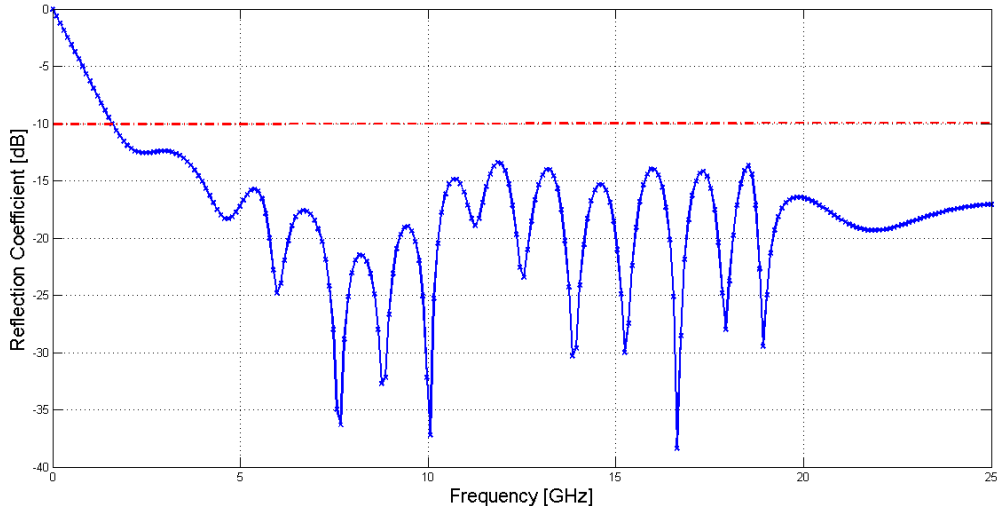

Figure 2: Reflection coefficient of the antenna without the filter.

the notching mechanism as a filter, in the ground plane, which makes connecting the biasing lines a simple task and limit their degrading effect on the antenna performance. The filter is equipped with three electronic switches S1, S2 and S3 having a size of $1 \times 0.25\,\mathrm{mm}^2$. Depending on the state of a switch, the corresponding split-ring slot does or does not induce a band notch. When a switch is activated, the functioning of a larger CSRR is launched, and thus a notch at a lower frequency occurs. The CSRR sizes, depicted in Figure 3, are optimized so that the notch occurs at 3.5 GHz, 5.2 GHz or 7.3 GHz. The following switching cases are considered: Case 1 when all three switches are ON, Case 2 when only switch S3 is deactivated, Case 3 when S2 and S3 are deactivated, and Case 4 when all switches are OFF.

3. RESULTS AND DISCUSSION

The proposed antenna is designed and simulated using Ansoft HFSS [11]. A prototype is fabricated and shown in Figure 3, and the reflection coefficient is measured for the possible operation scenarios. As illustrated in Figures 4 and 5, adequate analogy is shown between the simulated and measured results. For Case 1, in which all switches are ON, a UWB notch-free response is obtained. The results for Cases 2, 3 and 4, where the switches are sequentially activated, reveal

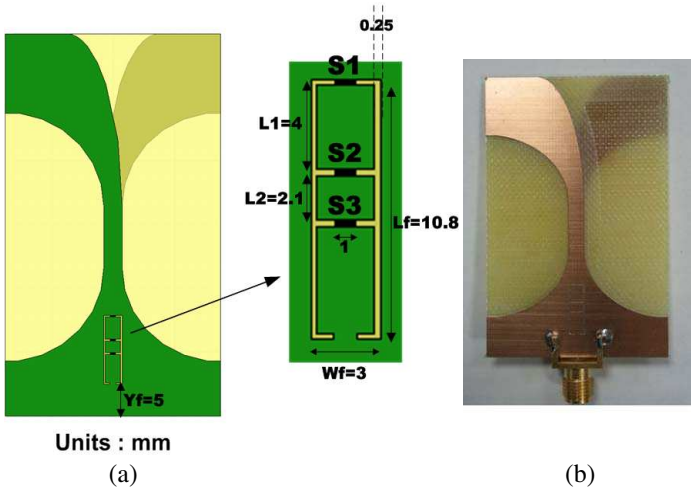

Figure 3: (a) Filter configuration. (b) Fabricated antenna photo.

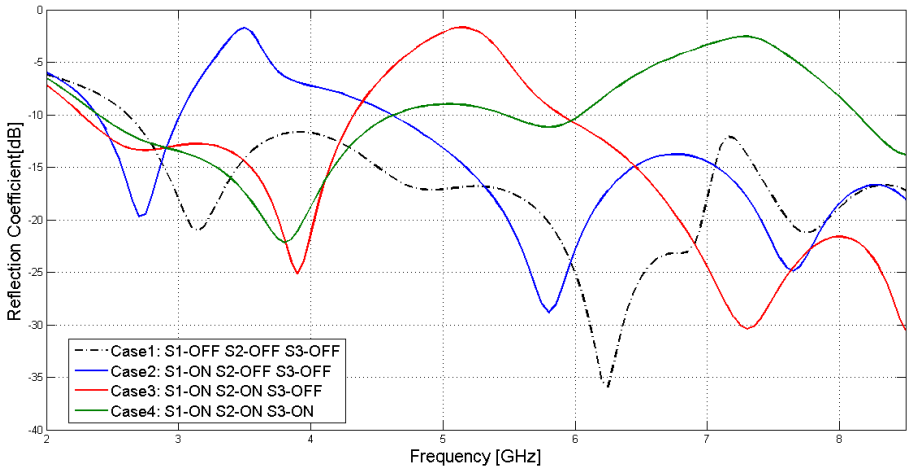

Figure 4: Computed reflection coefficient for the different switching cases of the antenna.

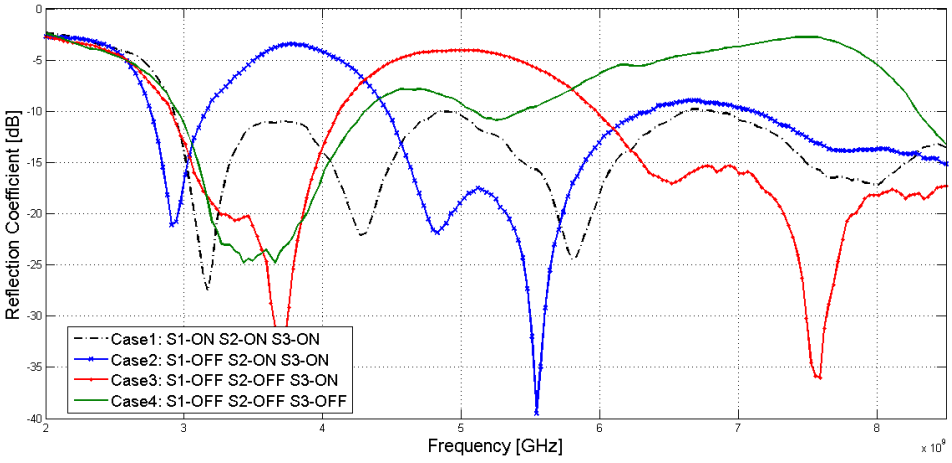

Figure 5: Measured reflection coefficient for the different switching cases of the antenna.

a single notch in the 3.5 GHz, 5.2 GHz or 7.3 GHz band, respectively. A notch in a certain band helps to prevent interference to a licensed user or the service operated in that band. The antenna has an omnidirectional pattern and good gain values in its operation band. However, the patterns

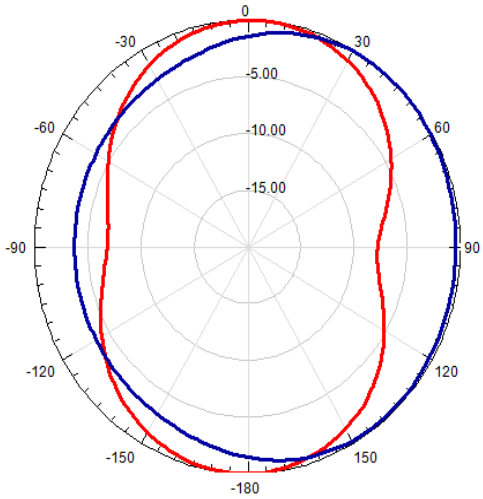

Figure 6: Radiation patterns at 3.5 GHz for Case 2 in the H-plane (blue) and E-plane (red).

are subject to slight degradation at high frequencies. The normalized computed radiation patterns for Case 2, at 3.5 GHz, are shown in Figure 6. A clear omnidirectional pattern is revealed.

4. CONCLUSION

In this work, an antipodal Vivaldi antenna was proposed. It is compact-size and can operate over a very wide bandwidth, starting from 1.5 GHz. Due to the integrated filter on its feed line, the antenna has a reconfigurable band notch induced by CSRRs and controlled by electronic switches. Such design can be a possible candidate to be utilized in CR systems or in UWB applications.

ACKNOWLEDGMENT

This work was supported by the University Research Board (URB) of the American University of Beirut (AUB).

REFERENCES

1. Win, M. Z. and R. A. Scholtz, "Ultra-wide bandwidth (UWB) time hopping spread-spectrum impulse radio for wireless multiple access communications," *IEEE Trans. Commun.*, Vol. 48, No. 4, 679–689, 2000.
2. Mehdipour, A., K. Mohammadpour-Aghdam, and R. Faraji-Dana, "Complete dispersion analysis of Vivaldi antenna for ultra wideband applications," *Progress In Electromagnetics Research*, Vol. 77, 85–96, 2007.
3. Hood, A. Z., T. Karacolak, and E. Topsakal, "A small antipodal Vivaldi antenna for ultrawideband applications," *IEEE Antennas and Wireless Propagat. Lett.*, Vol. 7, 656–660, 2008.
4. Gazit, E., "Improved design of the Vivaldi antenna," *IEE Proceedings H*, Vol. 135, No. 2, 89–92, 1988.
5. Abbosh, A. M., H. K. Kan, and M. E. Bialkowski, "Design of compact directive ultra wideband antipodal antenna," *Microwave and Opt. Tech. Lett.*, Vol. 84, No. 12, 2448–2450, 2006.
6. Jolani, F., G. Dadashzadeh, M. Naser-Moghadasi, and A. M. Dadgarpour, "Design and optimization of compact balanced antipodal Vivaldi antenna," *Progress In Electromagnetics Research C*, Vol. 9, 183–192, 2009.
7. Mitola, J. and G. Q. Maguire, "Cognitive radio: Making software radios more personal," *IEEE Pers. Commun.*, Vol. 6, No. 4, 13–18, 1999.
8. Al-Husseini, M., L. Safatly, A. Ramadan, A. El-Hajj, K. Y. Kabalan, and C. G. Christodoulou, "Reconfigurable filter antennas for pulse adaptation in UWB cognitive radio systems," *Progress In Electromagnetics Research B*, Vol. 37, 327–342, 2012.
9. Al-Husseini, M., A. Ramadan, A. El-Hajj, K. Y. Kabalan, Y. Tawk, and C. G. Christodoulou, "Design based on complementary split-ring resonators of an antenna with controllable band notches for UWB cognitive radio applications," *Proceedings of IEEE International Symposium on Antennas and Propagation, APSURSI*, 1120–1122, Spokane, USA, Jul. 2011.

10. Al-Husseini, M., J. Constantine, C. G. Christodoulou, S. E. Barbin, A. El-Hajj, and K. Y. Kabalan, "A reconfigurable frequency-notched UWB antenna with split-ring resonators," *Proceedings of Asia-Pacific Microwave Conference, APMC*, 618–621, Yokohama, Japan, Dec. 2011.
11. Ansoft HFSS, Pittsburg, PA 15219, USA.

Effect of Small Size Antenna inside Complex PCB

Dau-Chyrh Chang[1], **Cheng-Wei Chen**[2], **Hsiao-Bin Liang**[2], **Chi-Hsiung Wang**[2], **and Tsan-Hung Wu**[2]

[1]Oriental Institute of Technology, Taiwan
[2]Climax Technology Co., Ltd, Taiwan

Abstract— In general, there are many communication antennas inside GSM PCB (Print Circuit Board) for various applications. The radiation of smaller size of antenna will not only radiate to the outside system, but also radiate inside the system. This effect will cause the serious EMI problem. In this paper, on board modified PIFA is used to reduce the EMI effect due to complex PCB environment. The EM simulation tool, GEMS [1], is used to design and analyze the performance of antenna and 3D EM environment in this work. The measured results of TRP/TIS (total radiation power/total isotropic sensitivity) for GSM module of the PCB for wireless home security system verifies the improvement of this proposed on board modified PIFA.

1. INTRODUCTION

For the PCB (printed circuit board) of a wireless product, there are always several wireless solutions on it due to the need of versatile application. For examples, ISM band (868/433 MHz), GSM, WiFi, Zigbee, Z-wave and so on. In addition to those HW (hardware) devices, brilliant ID (industrial design) and ME (mechanical) design make EM environment complex for PCB, which complicate and limit the performance of internal antennas. In this paper, we demonstrate that a GSM antenna designing internally inside the case of a wireless home security product has better performance after a copper strip is properly attached inside the case. The copper strip modifies the radiation pattern of GSM antenna, and further decreases the reflected EM wave by complex PCB environment from GSM antenna itself. That is, a simple reflection plane forming by copper strip reduces EMI (electromagnetic interference) for the GSM antenna [2, 3].

This internal GSM antenna is designed in form of on-board PIFA (printed inverted-F antenna) structure with the PCB of 2-layer FR4, 4.4 dielectric constant and 1.6 mm thickness [4–8], which can operate the frequency ranges of E-GSM 900 (880 MHz ∼ 960 MHz) and DCS 1800 (1710 MHz ∼ 1880 MHz) bandwidth. The passive performances (radiation efficiency, peak gain and pattern) and active performances (TRP/TIS, total radiation power/total isotropic sensitivity) of this GSM PIFA cooperating in a wireless home security product are measured by fast antenna measurement system, SATIMO. The details will be presented and discussed in the following sections.

2. DESIGN OF ON-BOARD GSM PIFA

In this work, a wireless module is designed for upgrading a wired home security system toward wireless system. For the purpose of easy-to-install for customers, an on-board GSM PIFA is designed and implemented on the RF module. The picture of wireless home security product, which is composed of RF module plugging into a wired home security deck, is shown in Fig. 1. The dimension of GSM PIFA is described in Fig. 2. In order to deal with the EMI problem, a copper strip is attached on the case to modify the radiation pattern, which is shown in the left down side of Fig. 1.

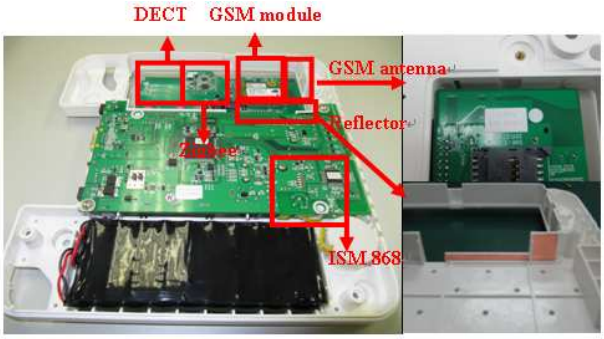

Figure 1: The GSM PIFA in a wireless home security product.

3. MEASUREMENT AND DISCUSSION

The measured return loss, radiation efficiency, peak gain, XY-cut 2D pattern, XZ-cut 2D pattern and YZ-cut 2D pattern of on-board GSM PIFA with/without copper strip are shown in Figs. 3–8, respectively. From those measured results, it can be observed that the GSM PIFA with/without copper strip performs almost the same return loss (S_{11}) but different radiation efficiency, peak gain and radiation pattern. Furthermore, the TRP/TIS showing in Fig. 9 and Fig. 10 reveal that the GSM PIFA with copper strip has much more compromised active results (TRP $\geqq$ 27 dBm and TIS $\geqq$ 100 dBm for E-GSM 900, TRP $\geqq$ 24 dBm and TIS $\geqq$ 100 dBm for DCS 1800) than that without copper strip, especially for TIS [9]. This is because the copper strip serves as a reflector for modifying the radiation pattern of GSM PIFA while the distant between copper strip and antenna is properly decided ($\sim \lambda/8$). Then the radiation pattern is concentrated in front of the reflector, isolating the EMI noise from PCB and eliminating EM wave power reflected by complex PCB environment behind the reflector. This is the reason why the TIS can be substantially improved in E-GSM 900 band. Furthermore, TRP is generally enhanced during the frequency band of E-GSM 900 and DCS 1800.

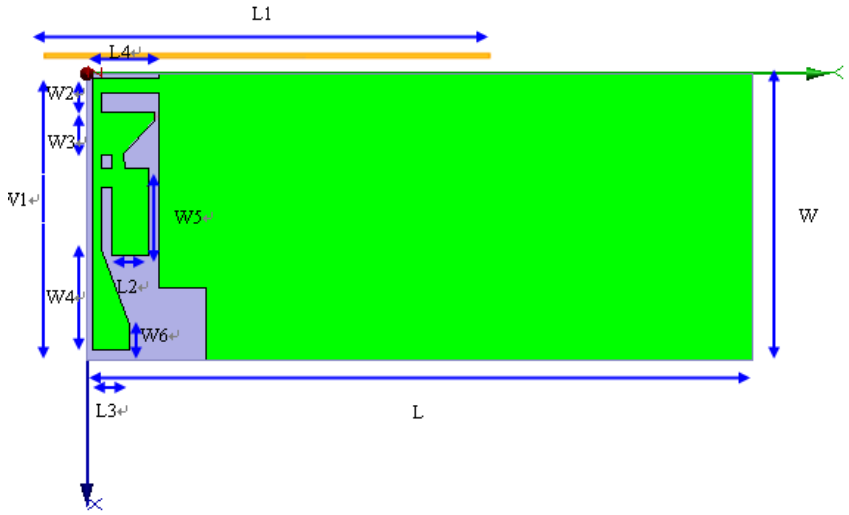

Name	W	W1	W2	W3	W4	W5	W6	L	L1	L2	L3	L4	H
Size	60	57	7	9	21	18	6	140	100	8	5	14	1.6
Unit	mm	mm	mm	mm	mm	mm	mm	mm	mm	mm	mm	mm	mm

Figure 2: The dimension of on-board GSM PIFA.

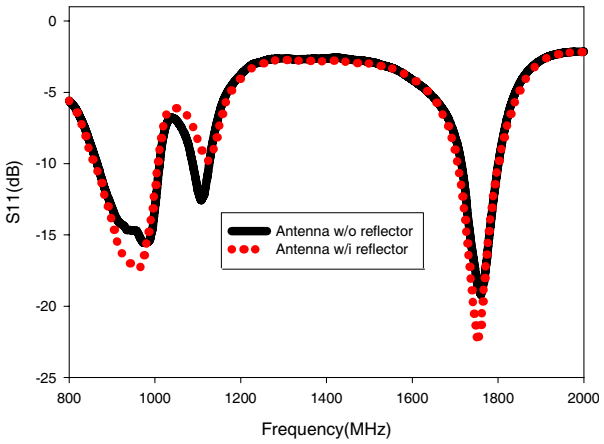

Figure 3: Measurement of S-parameter.

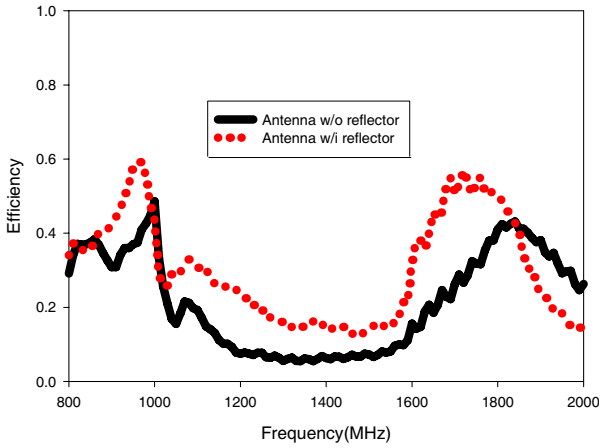

Figure 4: Measurement of radiation efficiency.

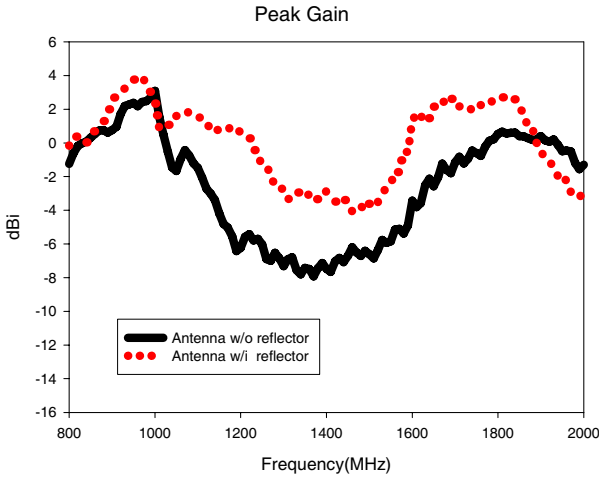

Figure 5: Measurement of peak gain.

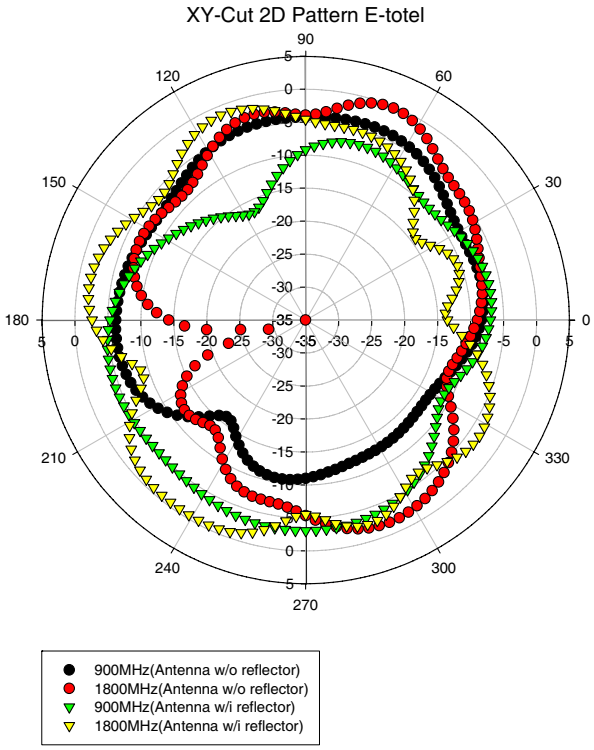

Figure 6: Measurement of XY-cut 2D pattern.

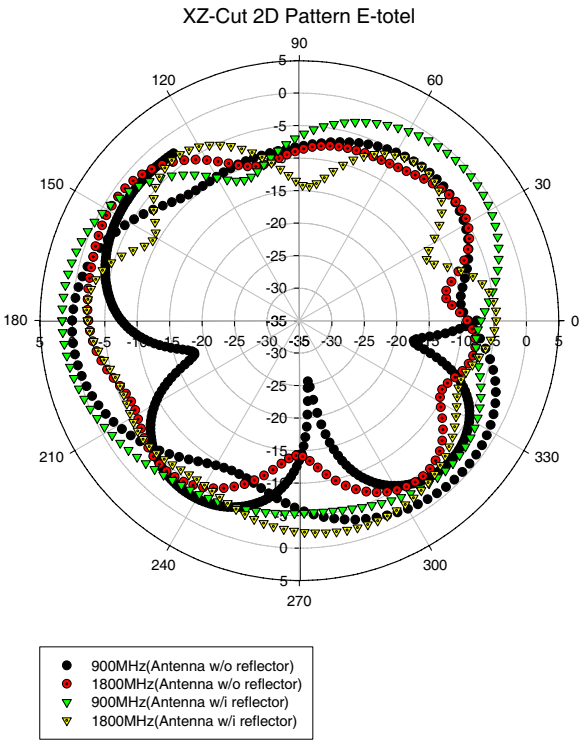

Figure 7: Measurement of XZ-cut 2D pattern.

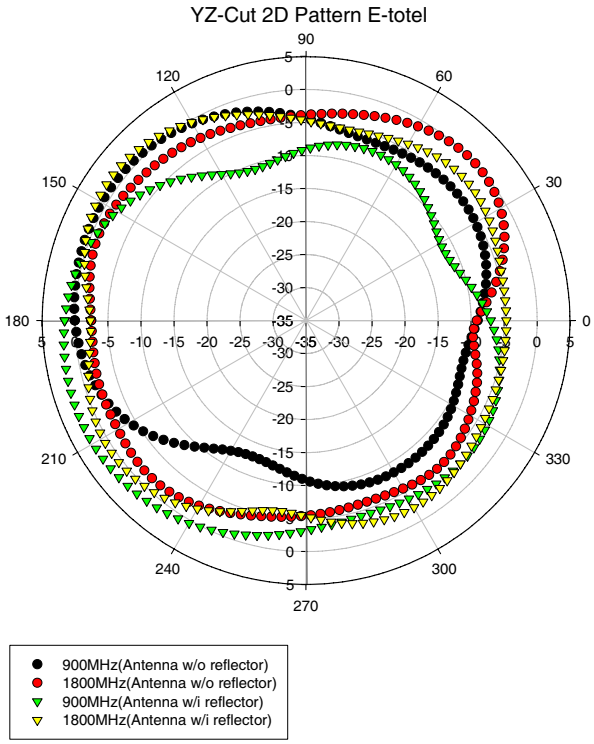

Figure 8: Measurement of YZ-cut 2D pattern.

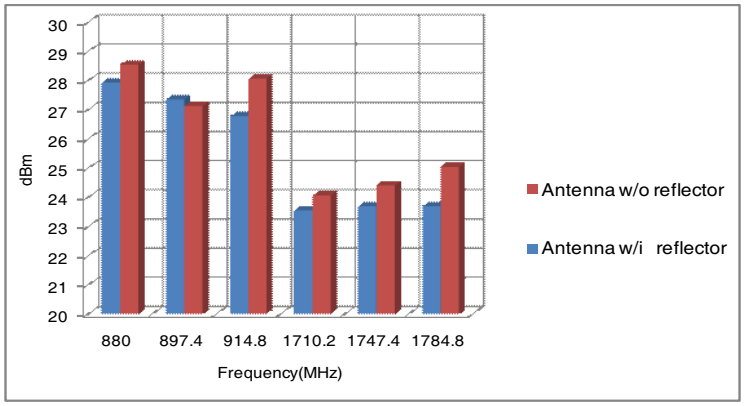

Figure 9: Measurement of TRP of antenna.

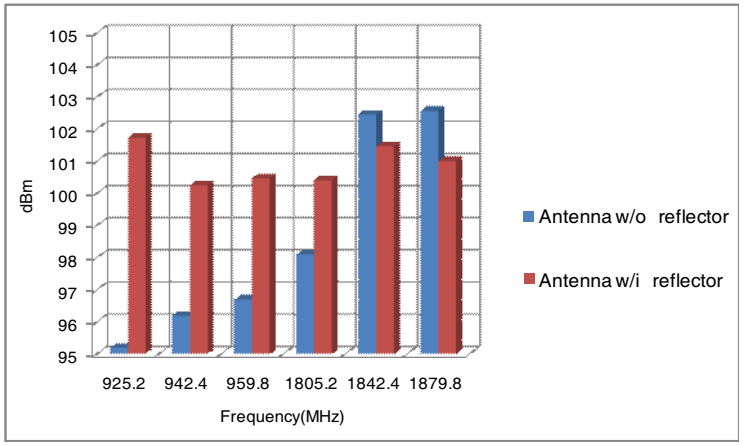

Figure 10: Measurement of TIS of antenna.

4. CONCLUSION

The comprehensive measurement and comparison of on-board GSM PIFA with and without copper strip are presented. The passive measured results of GSM PIFA present that the radiation efficiency and peak gain can be obviously enhanced while the copper strip, i.e., reflector, is attached. Furthermore, the active measurement also verifies that the communication quality of this GSM-based wireless home system product is effectively improved while the reflector is attached. Those experiments reveal that the reflector made by a simple copper strip make great improvement in GSM wireless communication quality due to the isolation of EMI noise from PCB and modification of antenna pattern.

REFERENCES

1. GEMS, 3-D High Performance Parallel EM Simulation Software, www.2comu.com.
2. Wu, C.-F., "MC control and prevention," 2008.
3. Chen, Y.-Z. and R.-Y. Gu, "The study of measurement theorem and prevention over electromagnetic interference environment and RF noise," Da-Yeh University, 2005.
4. Lee, W.-S. and Y.-S. Chen, "900/1800 MHz dual-band ceramic chip antenna bandwidth improvement and equivalent circuit simulation and analysis," National Cheng Kung University, 2005.
5. Hung, W.-L., "Design and study of small PIFA structures," 18–32, Jun. 2007.
6. Chang, Y.-H., "Design of compact printed dual-band and ultra-wideband monopole antenna," 26–33, Jul. 2008.
7. Lai, K.-C., "Design and measurement of ultra wide band antenna," 21–37, Jul. 2008.
8. Chen, W.-S., "Studies of dual-band and broadband printed slot antennas," 57–69, Jan. 2001.
9. Alpaslan, A., "Global test specification for terminals for performance measurements — Performance TST — Radiated performance VF_Ant_Req_V2.2," Vodafone Global.

An Evaluation of Capacitive Feed Methods for Electrically Small and Low-profile Meander Line Antennas

T. Fukusako, Y. Saito, and H. Maema
Computer Science and Electrical Engineering
Graduate School of Science and Technology, Kumamoto University, Japan

Abstract—Effects of feed methods among electrically small and low-profile meander line antennas using a capacitive feed structure are presented. The meander line has a length of one quarter-wavelength with a shorted end, and the capacitive feed structure is installed at the other end. A back conductor, which works as a ground plane, is located at a distance of $0.01\lambda_0$ to the meander line element forming in the area of $0.121\lambda_0 \times 0.075\lambda_0$, which satisfies the condition of electrically small antennas ($ka = 0.435 < 0.5$, wave number: k, radius of a sphere surrounding the antenna: a, and wavelength at the resonance frequency: λ_0). The fabricated antenna has successfully achieved a peak gain of 0.62 dBi and exhibits a higher radiation efficiency of more than 30% compared to an inverted-F antenna of the same dimension.

1. INTRODUCTION

In recent years, many antenna researchers have studied on electrically small and lowprofile antennas (ESLA) [1–6]. An antenna which is close to a back conductor can reduce the electrical effects from the backing material when installed on lossy materials. However, typical electrically and low-profile antennas have low radiation efficiency resulting in a difficulty of impedance matching to 50 Ω.

In a designing of ESLA, a capacitive feed (C-feed) technique has been proposed in [7] for a meander line antenna with a length of half-wavelength. Using the C-feed structure, the imaginary part of the input impedance of the antenna can be easily controlled by varying the size of the feed plate which is installed in between the radiating element and ground plane. Furthermore, a modified quarter-wavelength capacitive-feed meander line antenna (QCFMA) has been proposed in [8] for gain improvement satisfying $ka = 0.435 < 0.5$, k: wave number, a: radius of a sphere surrounding the antenna.

The QCFMA is compared in this paper with the same dimension of meander line antenna with an inverted-F antenna structure (IFMA) in order to evaluate the performance of C-feed structure. As a result, QCFMA shows better radiation characteristics than IFMA, and the two fabricated antennas show good agreement with the simulated results. The feed structure is also compared with a modified QCFMA.

2. ANTENNA STRUCTURE

Figures 1(a) and (b) show the top and side view of the C-feed structure (QCFMA). This antenna has a height (the distance between the antenna and the back conductor) of 2 mm ($0.010\lambda_0 \ll 0.25\lambda_0$), and uses RT/Duroid 5880 substrate with a permittivity (ε_r) of 2.2 and dielectric loss

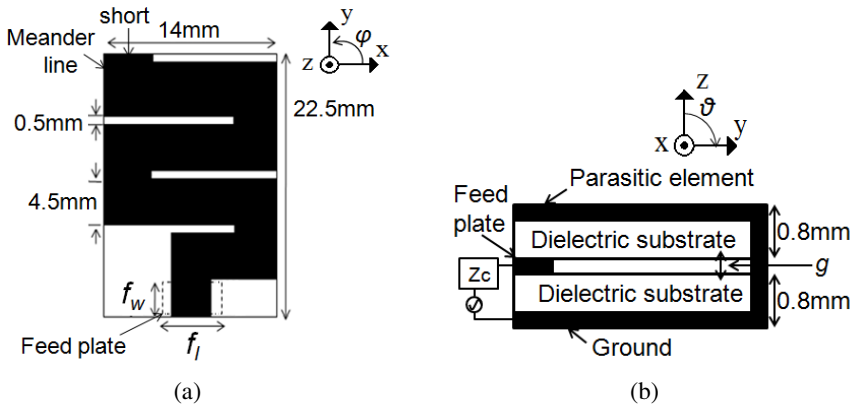

Figure 1: Capacitive feed structure (QCFMA), (a) top view, (b) side view.

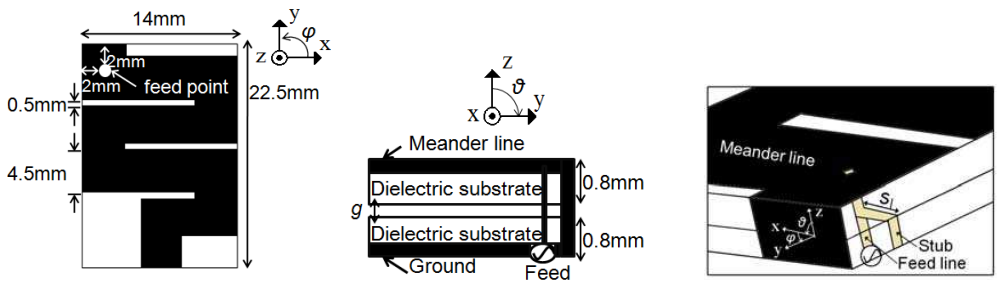

(a) (b) (c)

Figure 2: Inverted-F meander line antenna (IFMA), (a) top view, (b) side view, (c) a shorted stub.

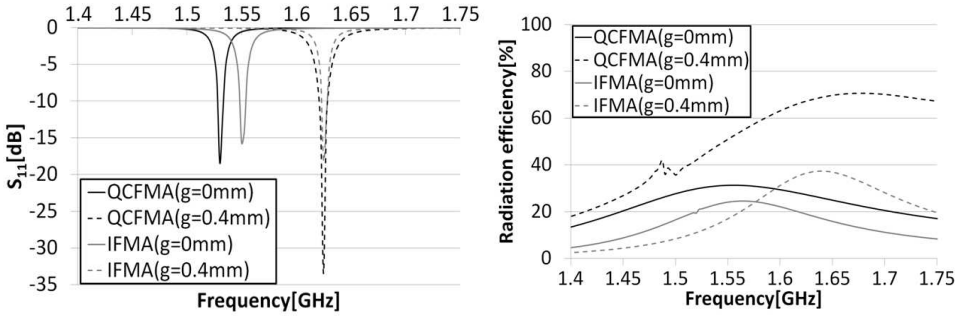

(a) (b)

Figure 3: Comparison of the antennas (Simulation), (a) S_{11} characteristics, (b) radiation efficiency.

($\tan\delta$) of 0.001. The dimension of the substrate and the back conductor are 22.5 mm × 14 mm ($0.121\lambda_0 \times 0.075\lambda_0$). The meander line has a width of 4.5 mm and shorted at the far end with a total length of around $\lambda_0/4$. The metallic feed plate in the figure, which is installed in between the meander line and the back conductor, provides capacitance to the input impedance. The meander line is electromagnetically coupled from the feed plate. The feed plate has a length (f_l) of 5 mm and width (f_w) of 2 mm for impedance matching. Furthermore, effect of the gap between the two dielectric substrates is considered. The thickness of the gap (g) is chosen to 0.4 mm for fabrication.

QCFMA is compared with an inverted-F meander line antenna (IFMA) which is shown in Fig. 2. The dimensions and the shape of the IFMA are the same as those in QCFMA for comparison. The meander line of IFMA is fed as shown in Fig. 2(c), however, a shorted stub is necessary for impedance matching as shown in the figure since the feed structure does not give sufficient inductivity to cancel the capacitance at the resonance frequency of such a low-profile meander line antenna. The shorted stub has a length in the x direction (s_l) of 2 mm. Effect of the gap between the two dielectric substrates is considered and the g is chosen to 0.4 mm as similar to QCFMA.

3. RESULTS

The simulated results of antenna characteristics of QCFMA and IFMA are shown in Fig. 3. The QCFMA and IFMA resonate at approximately the same frequency as shown in Fig. 3(a). In both antennas, the structure with the gap g of 0.4 mm has a higher resonance frequency compared with when there is no gap. It is due to decrease in the capacitance between the meander line and the back conductor. The radiation efficiency of QCFMA is higher than that of IFMA by around 31% at the resonance frequency. It is also noticed that the radiation efficiency of the antennas with the gap is better than when there is no gap. Whether there is or not the gap, the radiation efficiency of QCFMA is higher than IFMA. The two antennas are fabricated and measured. Table 1 shows the simulated and measured results of radiation efficiency at the resonance frequency. The radiation efficiency of the antenna is estimated with the Wheeler cap method [9]. In both antennas, the measured radiation efficiency is close to the simulated results. Fig. 4 shows the radiation patterns in y-z and x-z plane of QCFMA and IFMA. The directivity of these antennas in the y-z plane is different between QCFMA and IFMA.

Figure 5 shows a modified QCFMA, where the feed plate is at the same level as the meander line.

Table 1: Simulated and measured radiation efficiency at the resonance frequency.

	Resonance frequency [GHz]	Radiation efficiency [%]
QCFMA (Sim)	1.63	67.28
QCFMA (Mea)	1.56	65.78
IFMA (Sim)	1.63	36.48
IFMA (Mea)	1.57	31.02

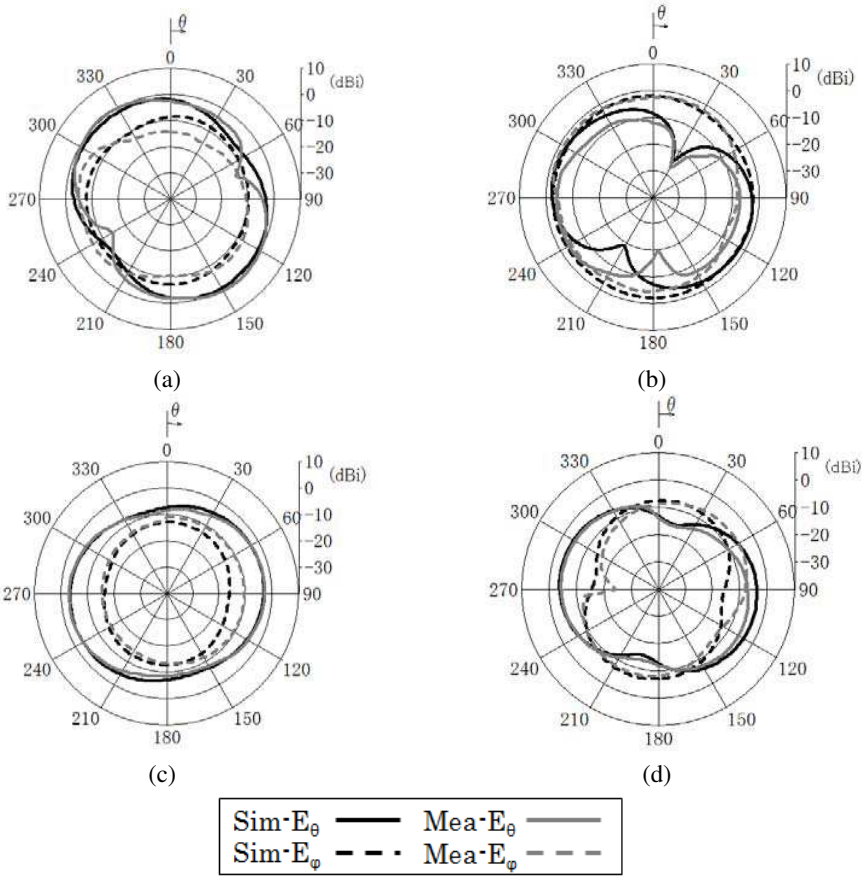

Figure 4: Simulated and measured radiation patterns in y-z plane and x-z plane, (a) QCFMA (y-z plane), (b) QCFMA (x-z plane), (c) IFMA (y-z plane), (d) IFMA (x-z plane).

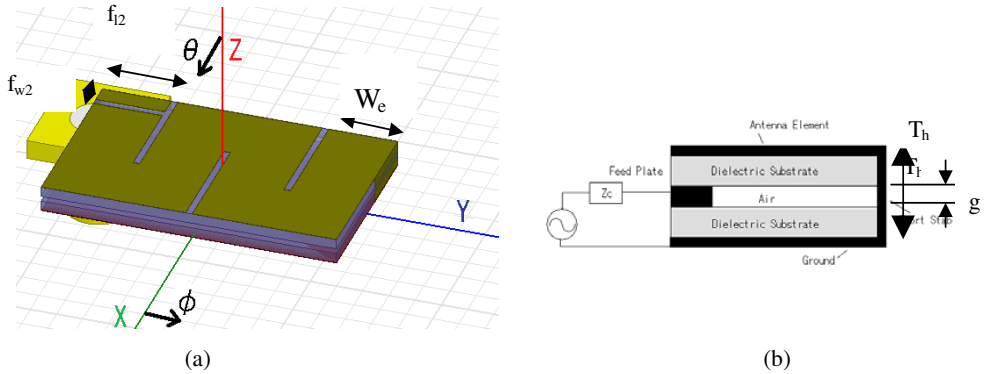

Figure 5: Modified QCFMA. The substrate area is the same as QCFMA with $f_{w2} = 1\,\text{mm}$ and $f_{l2} = W_e$, (a) 3 dimensional view, (b) side view.

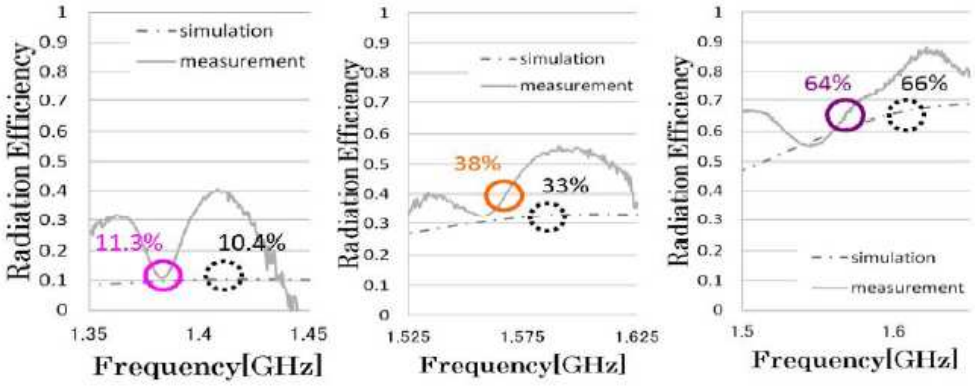

(a) (b) (c)

Figure 6: Simulated and measured radiation efficiency for different T_h with $g = 0\,\text{mm}$, (a) $T_h = 0.8\,\text{mm}$, (b) $T_h = 1.6\,\text{mm}$, (c) $T_h = 3.2\,\text{mm}$.

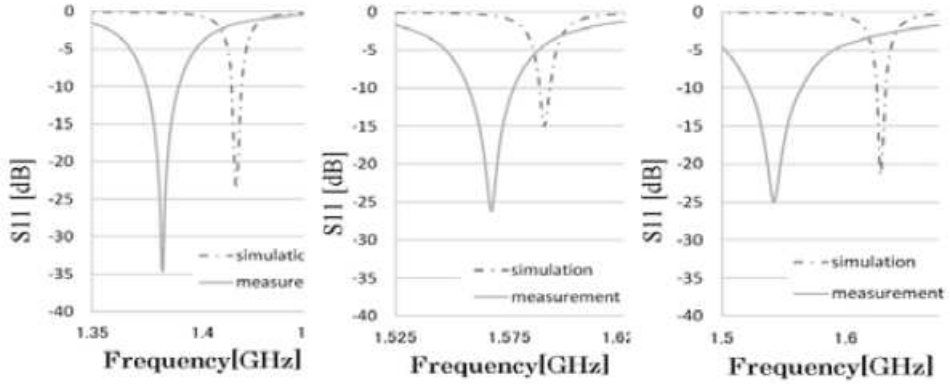

(a) (b) (c)

Figure 7: Simulated and measured S_{11} characteristics for different T_h with $g = 0\,\text{mm}$, (a) $T_h = 0.8\,\text{mm}$, (b) $T_h = 1.6\,\text{mm}$, (c) $T_h = 3.2\,\text{mm}$.

This structure could avoid having a layered structure. As a result, when $W_e = 4.5\,\text{mm}$, a simulated radiation efficiency = 17% is obtained for $g = 0\,\text{mm}$, whereas the efficiency of 40% is obtained for $T_h = 0.8\,\text{mm} + 0.8\,\text{mm} + g\,(g = 0.4\,\text{mm})$. The results of radiation efficiency are lower than the QCFMA because the electric field around the feed plate in the modified QCFMA is parallel to the ground.

Another structure with $w_e = 5.25\,\text{mm}$ is considered for $g = 0\,\text{mm}$. Fig. 6 shows the radiation efficiency for different $T_h s$. In this structure, only two metallic layers are required resulting in a simple structure. Compared with QCFMA, we can conclude that the radiation efficiency of the modified QCFMA with $T_h = 3.2\,\text{mm}$ and $g = 0\,\text{mm}$ are comparable with that of the QCFMA. Fig. 7 shows the S_{11} characteristics for different $T_h s$ and $g = 0$. The differences between measured and simulated results from 28 MHz to 85 MHz are obtained which is probably due to the differences of permittivity, because the strong electric field is concentrated in the substrate and is easily effected by the differences.

4. CONCLUSION

The QCFMA shows higher radiation efficiency than IFMA. Especially, the radiation efficiency of the QCFMA is improved very sensitively by making a small gap (air layer with a thickness of 0.4 mm) compared to that of IFMA. These planar shape antennas are very useful to install devices with limited space. Furthermore, modified QCFMA with a single substrate has been discussed compared to the QCFMA. Therefore, the antenna can find its applications in mobile terminals and RFIDs.

ACKNOWLEDGMENT

The present study was supported by the Ministry of Education, Culture, Sports, Science and Technology (MEXT) of Japan with a Grant-in-Aid for Scientific Research (C) and the Telecommunications Advancement Foundation.

REFERENCES

1. Best, S. R., "A discussion on the properties of electrically small self-resonant wire antennas," *IEEE Antennas and Propagation Magagine*, Vol. 46, No. 6, 9–22, 2004.
2. Erentok, A. and R. W. Ziolkowski, "Metamaterial-inspired efficient electrically small antennas," *IEEE Antennas Transactions on Antennas and Propagation*, Vol. 56, No. 3, 691–707, 2008.
3. Jung, J. H. and I. Park, "Electromagnetically coupled small broadband monopole antenna," *IEEE Antennas Wireless Propag. Lett.*, Vol. 2, 349–351, 2003.
4. Thumvichit, A., T. Takano, and Y. Kamata, "Ultra low profile dipole antenna with a simplified feeding structure and a parasitic element," *IEICE Transactions on Communications*, Vol. E89-B, No. 2, 576–579, 2006.
5. Thumvichit, A., T. Takano, and Y. Kamata, "Impedance matching of a half-wavelength dipole in procimity to a PEC plane," *Proceedings of the IEICE General Conference*, B-1-129, March 2004.
6. Chen, H. D. and Y. H. Tsao, "Low-profile meandered patch antennas for RFID tags mountable on metallic objects," *IEEE Antennas Wireless Propag. Lett.*, Vol. 9, 118–121, 2010.
7. Ide, K. and T. Fukusako, "Low-profile, electrically small meander antenna using a capacitive feed structure," *Microwave and Optical Technology Letters*, Vol. 52, No. 10, 2269–2274, October 2010.
8. Saito, Y. and T. Fukusako, "A novel low-profile electrically small meander line antenna for gain improvement," *Korea-Japan Microwave Conference*, TH2-5-2, November 2011.
9. Mongia, R. K., A. Ittipiboon, and M. Cuhaci, "Measurement of radiation efficiency of dielectric resonator antennas," *IEEE Microwave and Guided Wave Letters*, Vol. 4, No. 3, 80–82, March 1994.

Broadband Circularly Polarized Moxon Based Antennae for RFID and GPS

Haojiong Liu[1], **Oksana Manzhura**[1], **İbrahim Tekin**[2], **and Edip Niver**[1]

[1]Electrical Engineering, New Jersey Institute of Technology, Newark, NJ, USA
[2]Electronics Engineering, Sabancı University, İstanbul, Turkey

Abstract— Novel circularly polarized (CP) VHF SATCOM antenna which was based on Moxon antenna (bent dipole element over a ground plane) has been extended for RFID and GPS applications. A sequence of topologies starting from a single vertical element to two vertical elements of the Moxon arms, then widened strip arm elements were investigated to understand the effects on impedance match over the widened bandwidth. The logic in this evolution was to obtain maximized gain based on Fano-Chu limits, which suggests that more metallization in the radiating configuration that fill the volume would yield higher gain for electrically small antenna. Extending the width of the strip of the equivalent dipole elements lead to a wider bandwidth and improved cross-polarization ratio. Furthermore, splitting the tapered bow tie elements increased the volume filled with radiating elements leading to improved overall performance. Ultimately extended bends at the tip of the tapered sections parallel to the ground plane helped to improve overall performance. In overall, the antenna presented here produced lower physical height, higher gain, wider bandwidth, better cross-polarization and lower back lobe radiation compared to commercial counterparts such as an eggbeater currently used in SATCOM practice as well as similar antennas in RFID and GPS applications.

Here, the concept is extended to cover RFID (850–1050 MHz) and GPS (centered at 1227 and 1575 MHz) bands leading to new applications at a significant cost and size reductions and much improved performance. Prototype antennas were built based on HFSS simulations yielded better than −25 dB return loss. During simulations attention was paid to identify the effects of individual antenna elements as an optimization parameter on the overall input impedance matching over the extended bandwidth. Simulated and measured results yielded higher than industrial counterpart antenna gain, bandwidth and cross-polarization for much reduced physical dimensions.

1. INTRODUCTION

Novel circularly polarized (CP) VHF SATCOM antenna [1] which was based on Moxon antenna [2] (bent dipole element over a ground plane) has been extended for RFID and GPS applications. For RFID mobile applications [3], tag reader antenna is required to have high performance including a broadband operation, circular polarization as well as a large angular coverage from horizon to zenith. For systems at these frequencies, wavelength could be on the order of third to quarter of a meter and conventional antennas may be "too big" for commercial use. For GPS applications [4], antennas are required to have very precise narrow band performance at specific frequency bands (L1 and L2 bands). Novel tag reader RFID antenna and another dual band GPS antenna based on extended Moxon antenna were proposed. Moxon antenna is basically a two-element Yagi-Uda antenna [5], with a bent dipole element to reduce its height and is commonly preferred antenna for HAM operators due to its size, forward gain and wide band impedance match. A systematic sequence of topologies starting from a single vertical element to two cross vertical elements of the Moxon arms fed through a hybrid coupler to achieve Circular Polarization is implemented. Then widened strip arm elements were investigated to understand the effects on widening the bandwidth. The logic in this evolution was to obtain maximized gain based on Fano-Chu limits, which suggests that more metallization in the radiating configuration that fills the volume would yield higher gain for electrically small antenna [6, 7]. Extending the width of the strip into tapered shape and splitting of the equivalent dipole elements with additional bends at the extended tips of these tapered bowtie [8] arms lead to a wider bandwidth and improved cross-polarization ratio. In overall, the antenna presented hereafter experimental measurements produced lower physical height, higher gain, wider bandwidth, cross-polarization and lower back lobe radiation compared to commercial counterparts such as an eggbeater currently used in SATCOM practice as well as similar antennas in RFID and GPS applications.

Table 1: Optimization of geometrical parameters in numerical simulations. Only 9 out of 14 parameters used are presented here. (◄► — longer (larger), ►◄ — shorter (smaller), ▲ — higher (increase), ▼ — lower (decrease)).

No:	Description	RFID	GPS
1	Wedge cutout length	Moving wedge tip closer to the Z axis, effectively makes the first section of the wedge ◄►, shifts central frequency ▼ and ►◄BW	
2	Wedge cutout spread angle	►◄the angle, i.e., sharpening the wedge cutout, ◄► BW and shifts central frequency (or resonance) ▲	
3	Vertical length Changing the length ◄►	Low resonance point ▼ in frequency but ▲ in S_{11}, high resonance point ▼ in frequency and ▼ in S_{11}. Total bandwidth decreases.	
	►◄	Low resonance point ▲ in frequency but ▼ in S_{11}, high resonance point ▲ in frequency and ▲ in S_{11}. Total bandwidth increases.	
4	Length of the first bend ◄►	Low resonance point ▼ in frequency but ▲ in S_{11}, high resonance point ▼ in frequency and ▲ in S_{11}. Total BW▲	Low resonance point ▼ in frequency but ▲ in S_{11}, high resonance point ▼ in frequency and ▲ in S_{11}. Total BW▼
	►◄	Low resonance point ▲ in frequency but ▼ in S_{11}, high resonance point ▲ in frequency and ▼ in S_{11}. Total BW▼	Low resonance point ▲ in frequency but ▼ in S_{11}, high resonance point ▲ in frequency and ▼ in S_{11}. Total BW ▲.
5	Outer angle of the first bend Bigger:	Low resonance point ▼ in frequency but ▲ in S_{11}, high resonance point ▼ in frequency and ▼ in S_{11}. Total BW▼	Low resonance point ▲ in frequency but ▼ in S_{11}, high resonance point ▼ in frequency and ▼ in S_{11}. Total BW▼
	Sharpen	Low resonance point ▲ in frequency but ▼ in S_{11}, high resonance point ▲ in frequency and ▲ in S_{11}. Total BW▲ .	Low resonance point ▼ n frequency but ▲ in S_{11}, high resonance point ▲ in frequency and ▲ in S_{11}. Total BW ▲ .
6	Outer angle of the vertical section (90 degrees)	►◄ outer angle of the vertical section, i.e., sharpening the angle, improves Reflection Impedance around lower resonance frequency, while looses some match around higher resonance frequency. No significant loss of bandwidth is observed with sharper outer angle.	
7	Inner angle of the vertical section ◄►	Low resonance point ▼ in frequency but ▼ in S_{11}, high resonance point ▼ in frequency and ▼ in S_{11}. Total BW stays	Low resonance point ▲ in frequency but ▼ in S_{11}, high resonance point ▼ in frequency and ▲ in S_{11}. Total BW▼.
	►◄	Low resonance point ▲ in frequency but ▲ in S_{11}, high resonance point ▲ in frequency and ▲ in S_{11}. Total BW stays.	Low resonance point ▼ in frequency but ▲ in S_{11}, high resonance point ▲ in frequency and ▼ in S_{11}. Total BW ▲.
8	Horizontal length (no tip) ◄►	Low resonance point ▼ in frequency but ▲ in S_{11}, high resonance point ▼ in frequency and ▼ S_{11}. Total BW ▼ .	
	►◄	Low resonance point ▲ in frequency but ▼ S_{11}, high resonance point ▲ in frequency and ▲ in S_{11}. Total BW ▲ .	
9	Outer angle of the horizontal section ◄►	Low resonance point ▲ in frequency but ▼ S_{11}, high resonance point ▼ in frequency and ▲ in S_{11}. Total BW▼ .	
	►◄	Low resonance point ▼ in frequency but ▲ in S_{11}, high resonance point ▲ in frequency and ▼ in S_{11}. Total BW ▲	

2. DESIGN AND OPTIMIZATION PARAMETERS OF THE MOXON BASED ANTENNA

The proposed antenna consists of two bent Moxon type split bowtie antennas. The two bent antennas are located perpendicular to each other as shown in Figure 1 and are fed at the center via differential input through a hybrid coupler to produce Right Hand Circular Polarization (RHCP).

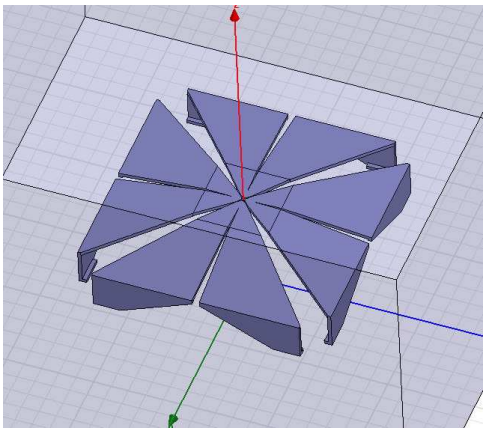

Figure 1: Moxon based RFID tag reader antenna in 3D space.

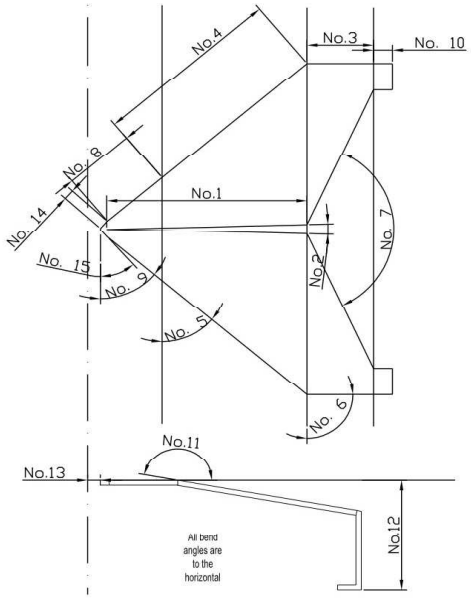

Figure 2: Single triangular shaped antenna arm.

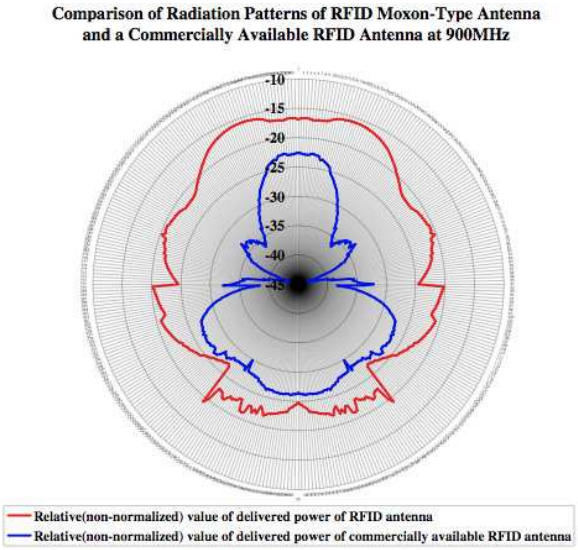

Figure 3: RFID measured antenna pattern comparison.

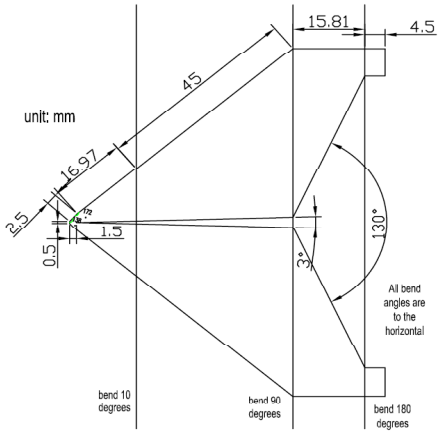

Figure 4: Dimensions of a single triangular shaped RFID tag reader antenna arm.

An expanded view of an arm (petal) is shown in Figure 2 marked with numbers to identify the optimization parameters used in numerical simulations.

The detailed optimization observations are given in Table 1 based on numerical simulations carried out using ANSOFT High Frequency Structure Simulator (HFSS).

3. MOXON BASED RFID TAG READER ANTENNA

RFID tag reader antenna is designed to operate in 850 MHz to 1050 MHz range. Characteristic dimensions of a single triangular shaped antenna conductor are shown on Fig. 4. Assembled antenna over a ground plane is shown on Fig. 5. The Return Loss of the RFID antenna is simulated (Fig. 6) and compared to measured performance of the prototype (Fig. 7). RFID antenna has simulated S_{11} 3 dB range of 710 MHz to 1200 MHz. Measured S_{11} is better then 10 dB in 800 MHz to 1180 MHz. Antenna gain is simulated to be approximately 7 dB and front to rear ratio is -15 dB. When assembled antenna is measured over a small (compared to the size of the antenna) ground plane

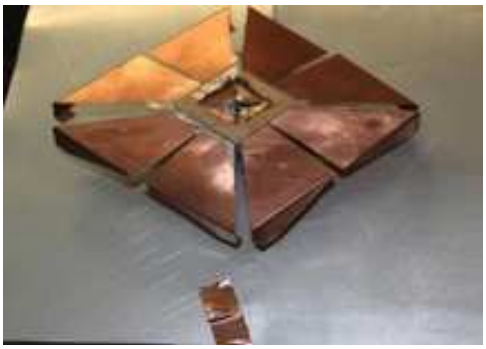

Figure 5: Assembled RFID tag reader antenna over a ground plane.

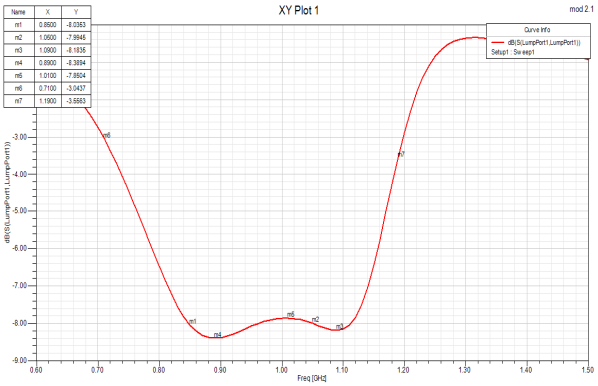

Figure 6: Simulated return loss of the RFID antenna.

Figure 7: Measured return loss of the RFID antenna.

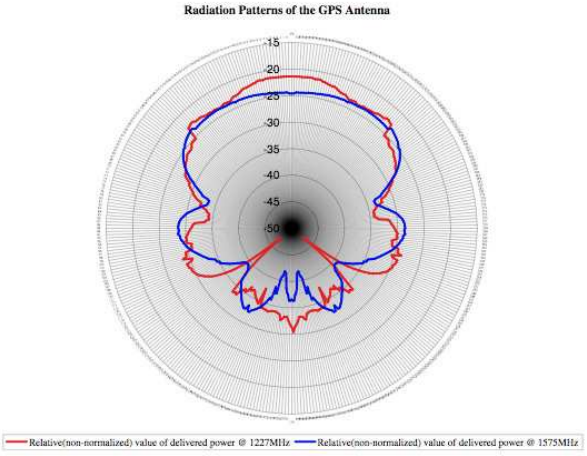

Figure 8: Measured radiation patterns of the GPS antenna at L1 and L2 bands.

Figure 9: Assembled GPS antenna over ground plane.

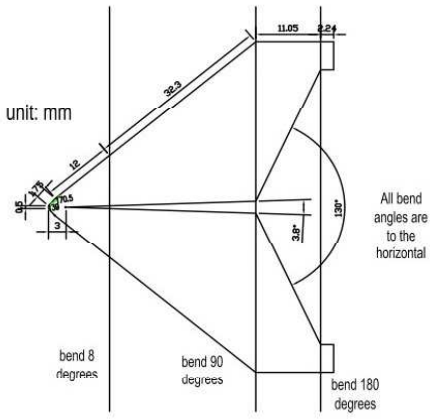

Figure 10: Dimensions (in mm) of a single antenna arm.

and compared with a commercially available RFID of known gain, the measured gain of the Moxon type RFID antenna (4Xin area than the antenna developed here) can be judged to be around 15 dB to 17 dB.

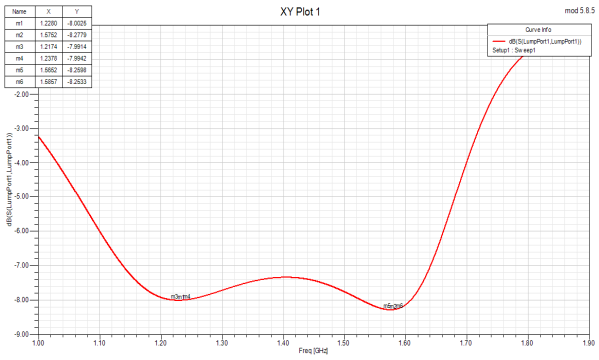

Figure 11: Simulated return loss of the GPS antenna.

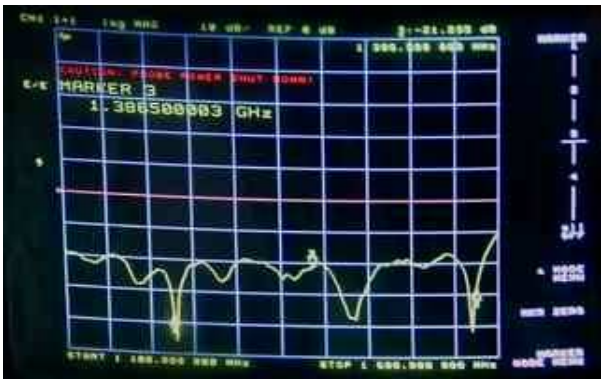

Figure 12: Measured return loss of the GPS antenna.

4. MOXON BASED GPS ANTENNA

Moxon based type antenna for GPS applications is designed to work in two GPS bands, $1227 +/- 10.23$ MHz and $1575 +/- 10.23$ MHz. Characteristic dimensions of a single triangular shaped antenna arm are shown in Fig. 10. Assembled antenna over a ground plane is shown on Fig. 9. The Return Loss of the GPS antenna is simulated (Fig. 11) and compared to measured performance of the prototype (Fig. 12). GPS antenna has simulated S_{11} 3 dB range of. 1000 MHz to 1720 MHz. Measured S_{11} is better then 10 dB in 1000 MHz to 1600 MHz and features deep resonances around both bands of interest, where RL is better then -30 dB. Antenna gain is simulated to be approximately 6.6 dB at 1227 MHz and 8.25 dB at 1575 MHz, while front to rear ratio is better then -14 dB. Measured relative power delivered by the antennna is shown on Fig. 8 for both ranges. Higher band shows somewhat lower power then the lower band due to mismatch and alignment issues during the experiment.

5. CONCLUSIONS

Moxon based RFID and GPS antennas were proposed. Extensive numerical simulations based on optimization of various parameters on the antenna structure were carried out to achieve higher gain, wide band impedance match, high cross-polarization and low profile. Prototype antennas were built and tested confirming good agreements between simulation and experimental results. Furthermore, prototype antennas were compared with commercial counterparts and were observed that RFID tag reader antenna was almost 4 times smaller in physical dimensions for a higher gain of 17 dB. In case of GPS antenna the overall gain was observed to increase for the comparable dimensions.

REFERENCES

1. Tekin, I., O. Manzhura, and E. Niver, "Broadband circularly polarized antennas for UHF SATCOM," *2011 XXXth URSI, IEEE General Assembly and Scientific Symposium*, Aug. 13–20, 2011.
2. Moxon, L., *HF Antennas for All Locations*, 2nd Edition, Radio Society of Great Britain, 2002.
3. Marrocco, G., "The art of UHF RFID antenna design: Impedance-matching and size-reduction techniques," *IEEE Antennas and Propagation Magazine*, Vol. 50, No. 1, 66–79, 2008.
4. Parkinson, B. W. and J. J. Spilker, Jr., "Global positioning system: Theory and applications," *AIAA*, Vols. 1–2, Washington, DC, 1996.
5. Elliott, R. S., *Antenna Theory and Design*, Prentice-Hall, Inc., Englewood Cliffs, NJ, 1981.
6. Schwering, F., "Workshop on electrically small antennas: Background and purpose," *Proceedings of the ECOM-ARO Workshop on Electrically Small Antennas*, Fort Monmouth, NJ, May 6–7, 1976.
7. Chu, L. J., "Physical limitations on omni-directional antennas," *J. Appl. Phys.*, Vol. 19, 1163–1175, 1948.
8. Nagatoshi, M., S. Tanaka, S. Horiuchi, and H. Morishita, "Downsized bow-tie antenna with folded elements," *IEICE Trans. Electron.*, Vol. E93-C, No. 7, Jul. 2010.

Bended Rectangular Slotted Waveguide Antenna

Dana Baz Radwan[1], **Ali Harmouch**[2], **and Mustapha Ziade**[2]

[1]American University of Science & Technology, Beirut, Lebanon
[2]Faculty of Engineering, Lebanese University, Lebanon

Abstract— Rectangular slotted waveguide antennas have been widely used in many areas of telecommunications from plane antennas to wireless internet applications due to their high directivity, compactness and feasibility. One of the major drawbacks of such antennas is that the side lobe level is significant since the slots are placed on a finite conducting plate which consequently leads to a decrease in the overall directivity of such radiators. In this paper, a bended slotted rectangular waveguide antenna is presented. The antenna provides a narrow beamwidth in addition to a significant decrease in the Sidelobe level. FEKO Simulations and experimental tests performed on bended slotted waveguide antenna have shown a significant improvement in the directional characteristics for about 4 dB without any increase in the overall antenna's dimensions.

1. INTRODUCTION

Spreading information over large or small areas is now human's concern all over the world. The most important means implemented in the information is the wireless communication system. Wireless communication continues to present challenges to designers, in particular in the area of slotted waveguide antennas design. Slotted Waveguides Antennas, SWA are one of the competent network applications due to their compactness, their electrical and their mechanical characteristics that make them easy to work with, and flexible to changes that might be made on them. They can work in different ways with respect to their frequencies of operation, sizes, and their number of slots. These waveguides are typically evaluated according to their radiation pattern in the E and H field which relate to their directivity [1, 6]. The major drawback of rectangular slotted waveguide antennas is their reduced directivity; in addition their side lobe levels are usually higher due to the finite dimension of the waveguide conductive surface over which the slots are placed.

Antenna terminals are one of the basic components of wireless communication system. Through different antennas' terminals information is transmitted and received. These antennas radiate the electromagnetic wave towards a designated receiver with maximum radiation efficiency; such a process requires the designed antenna to have advanced electrical and mechanical characteristics such as high directivity, radiation efficiency, high wind resistance and preferably low cost and weight.

The above mentioned requirements are to be taken into consideration, since most of the already existing antennas in the wireless market either are comprised of all these characteristics or promote one characteristic over another; a fact that limits the usage of these antennas as radiating elements in wireless networks. For instance, corner reflector and other types of directive antennas have been used as transmitting elements of wireless networks for many years since they provide high enough directivity (up to 10 dB) over the frequency band; however, the finite size of the conducting reflector compromises the antenna's wind resistance and also results in a high level of side lobes which negatively affect antennas' performance. Parabolic reflector antennas are also used for the same purpose and have almost the same drawbacks, except for their very high directivity [3, 4].

2. SLOTTED WAVEGUIDE ANTENNAS

Slotted waveguide antennas have also been used in the market in many different applications as an antenna for aircrafts due to their compactness, which fits well with the aerodynamic characteristics of flying objects. [x] Recently these antennas have also become a better choice as transmitting elements in network applications since they offer extra high directivity, compactness, high wind resistance and consequently excellent reliability. The most commonly used shapes of slotted waveguide antennas are rectangular and circular configurations. The circular one is widely used for military applications when designing missiles, submarines and space shuttles because of its suitable geometry. Rectangular waveguides are hollow-pipes that consist of conducting walls, filled by dielectric material within which the electromagnetic wave propagates. The upper wall of the guide consists of a finite number of slots that are arranged together in a specific way to provide a

desirable radiation from the slots. The number, shape, size and position of the slots indicate the performance of this antenna; therefore these characteristics are selected according to the specific situation under consideration [1, 2].

The major drawback of rectangular waveguide antennas is that the conducting wall on which the slots are placed is finite, which causes the side lobe levels to increase and consequently reducing directivity. The reduction of the antenna's directivity causes interference problems with neighboring antennas. In spite of all the aforementioned disadvantages, waveguide antennas are the most suitable for wireless applications among others [8, 11, 12].

The aim of this study is to enhance the electrical and mechanical attributes of the already existing waveguide antennas by simply changing its form to a new bended form that electromagnetically provides an in-phase addition of waves radiated by the slots in the far-field. Such a modification is expected to result in an increase in the directional properties, and simultaneously, in a decrease in the side lobe levels.

The increase in the directivity makes the antenna capable of transmitting the same electromagnetic energy for longer distances and consequently enhancing their area of coverage. In addition, the decrease of the side lobe levels makes the antenna less vulnerable to noise sources produced by adjacent radio stations operating in a close area or at a close carrier frequency [6]. The bended rectangular waveguide antenna offers a broadside radiation pattern over the frequency band which is normal to the plane containing the slots. The angle of bending which was selected theoretically, within the interval of 2° to 15°, shows a significant change in the radiation pattern. Simulation and experimental results have shown that an angle bending of 3°, provides an increase of 3 dB in the directivity compared to the regular slotted waveguide antenna. This increase in the directivity is accompanied by a decrease of the side lobe level which makes the designed antenna competitive in the antenna market.

3. ANTENNA DESIGN

3.1. The Straight Waveguide

In this part, we show the different parts of the antenna design, including the description of the FEKO program components that we used. First we performed our calculations using free space inside the waveguide in order to determine its dimensions for a 2.4 GHz center frequency. The main goal is to achieve a gain of 15 dB. The calculations used in this paper are as follows [1]:

In order to calculate the wavelength:

$$\begin{aligned} \lambda &= v/f = \left(3 \times 10^9\right) / \left(2.4 \times 10^9\right) = 0.125\,\mathrm{m} \\ d &= \lambda/2 = 0.125/2 = 0.0625\,\mathrm{m} \\ a &= d = 0.0625\,\mathrm{m} \\ b &= 0.7 \times a = 0.7 \times 0.0625\,\mathrm{m} = 0.0437\,\mathrm{m} \end{aligned}$$

where: a is the height of the waveguide and b is its width.

The experiment's desired directivity was 15 dB, which allowed the number of slots N to be calculated.

$$N = (D \times \lambda)/(2 \times d) = \left(10^{0.5} \times 0.125\right)/(2 \times 0.0625) = 31.622$$

Finally, the Length of the waveguide was determined as follow:

$$N \times d = 31.622 \times 0.0625 = 1.97\,\mathrm{m}$$

According to the above calculations we had a waveguide with wavelength of 0.125 m, width of 0.0625 m, height of 0.0437 m, 31 slots, and a length of 1.97 m which is obviously considered as a long antenna. In order to reduce the dimensions of this antenna, we considered changing the substance inside the waveguide and substitute it with a higher permittivity material such as glass. Glass has an effective permittivity, $\varepsilon_{eff} \approx 6$.

The new calculations became:

$$v = c/\sqrt{(\varepsilon\mu)} = 3 \times 10^9/\sqrt{6} = 1.224 \times 10^9$$

In order to calculate the wavelength v was used:

$$\begin{aligned}\lambda &= v/f = 1.224 \times 10^9/2.4 \times 10^9 = 0.051\,\text{m}\\ d &= \lambda/2 = 0.051/2 = 0.0255\,\text{m}\\ a &= d = 0.0255\\ b &= 0.7 \times a = 0.7 \times 0.0255 = 0.01785\,\text{m}\end{aligned}$$

With a desired directivity of 15 dB, this allowed for the number of slots to be again calculated:

$$N = (d \times \lambda)/(2 \times d) = 10^{15} \times 0.051/2 \times 00.0255 = 31.622$$

The length of the waveguide is then calculated:

$$N \times d = 31.622 \times 0.0255 = 0.806\,\text{m}$$

According to the new calculations we had wavelength of 0.05 m, width of 0.0255 m, height of 0.01785 m, 31 slots (Length of each slot is $\lambda/2 = 0.0255$ and the width is $\lambda/16 = 0.003187$), and a length of 0.806 m. These results are much better considering the size of the antenna, our dimensions decreased by more than one half of the previous dimensions.

After using these dimensions and simulating the designed antenna at the operating frequency on FEKO we obtained the radiation pattern in both planes from which the directivity has been calculated and summarized in the table below.

3.2. The Bended Waveguide

After reaching a good size for the antenna, we started to search for ways to get a better performance in increasing directivity and decreasing side lobes. The idea was by bending the antenna at different degrees and checking whether bending gives better results or not. Starting our experiment we chose 2 degrees, doing the same procedure that we did in the first experiment by putting the model on FEKO and simulating it getting new results concerning wave pattern, directivity, and side lobes. As results we get much better results see Table 1. Having performance made us proceed with our choices in order to get the best performance that we can get between the different bendings. Moreover, we took the 3, 4, 5, 8, 10, and 15 degrees, simulate every object alone and observe its result see Table 1.

As you can see in the table above concerning the different bendings, the results showed improvement on the straight waveguide. The directivity improved then started degrading as we increased the bending angle. We stopped our trials when we saw that the result is decreasing to the first result that is the straight waveguide. We show the results of the best design with 3° bending. We obtained the best directivity, wave pattern, and by that the smaller side lobes is the three degrees bending Figure 2. And later on this is the bending that we used in our practical experiments. As a conclusion bending the waveguide by 3°, gave us a better results as by this tiny bending we made the slots have similar distance from destination in order to direct the wave in a better way.

Figure 1: Rectangular straight slotted waveguide.

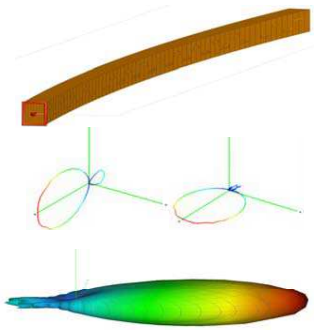

Figure 2: 3-D pattern of the three degrees bended waveguide antenna.

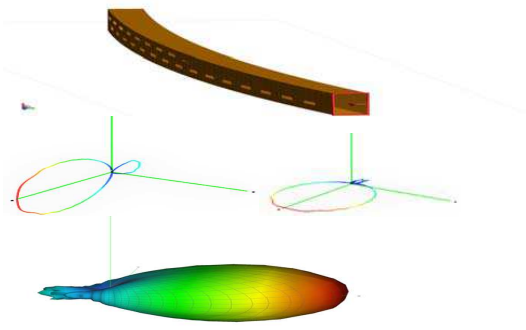

Figure 3: 3-D image for the horizontal, vertical and overall patterns of −3 degrees bending.

Table 1: Straight and bended waveguides.

Waveguide	Vertical pattern, degrees	Horizontal pattern, degrees	Directivity, dB
Straight	40	90	10.564
2 degrees	45	56.5	12.075
3 degrees	44	55	12.289
4 degrees	46	63	11.075
5 degrees	45	56	12.113
8 degrees	53	61	11.031
10 degrees	57	62	10.645
15 degrees	55	65	10.595

Table 2: Straight and opposite bended waveguide.

Waveguide	Vertical pattern, degrees	Horizontal pattern, degrees	Directivity, dB
Straight	40	90	10.564
-2 degrees	45.5	56	12.065
-3 degrees	46	55	12.096
-5 degrees	46	56	12.018

3.3. Opposite Bended Waveguide

As the third application that we wanted to apply here and since our waveguide is meant to be used on airplanes and as we all know that the bottom of the airplane takes a belly shape, but as we want to put the waveguide in it, the slots should be directed to the bottom toward earth, so in the shape that we have, we will face a problem. However, we reached to an idea to bend the waveguide in the opposite way and check if we will lose our wave or if we have a slight difference.

Looking at the previous results we chose the best three results in order to use them for the new experiment. We took the 2, 3, and 5, and recalculated them when bent in the opposite direction so we get -2, -3, and -5 and simulate them on FEKO. The results are shown below in the Table 2.

As a conclusion, waveguides bent at three degrees and minus three degrees gave the best results for the two applications, with the best directivity and the smallest side lobes. The new bended form electromagnetically provides an in-phase addition of waves radiated by the slots in the far-field. The increase in the directivity makes the antenna able to transmit electromagnetic energy for long distances and therefore enhances its ability to provide a bigger area of coverage. In addition, the decrease of the side lobe level makes the antenna less vulnerable to noise and interference.

Figure 3 shows the FEKO results obtained on the minus three degrees bent waveguide slotted antenna.

4. EXPERIMENTAL RESULTS

Three copper waveguides, one straight, one bended to the inside and a one bended to the outside were built in the dimensions calculated and simulated earlier.

Two of the waveguides were bended; one to the inside and the other to the outside at an angle of 3 degrees. After the coaxial cable was fixed in its proper place, the waveguide was filled with silicon. As previously mentioned, the waveguide was filled with silicon because it was then impossible, using the tools available, to fill the waveguide with solid glass or melted glass, as this procedure required advanced manufacturing tools. Also for the bent antennas it was impossible to use solid glass, which is why silicon was used since silicon quickly changes to a solid substance after it is melted. At this point the manufacturing step was completed; the next step was to perform the testing.

Figure 4 shows the test setup that we used to test the antenna at 2.4 GHz. We used a transmitter and a spectrum analyzer. The measured antenna was positioned as a receiver. Blue absorbent sponges containing carbon were positioned around the antenna to eliminate unwanted reflections.

The first consideration was that since the waveguides were filled with silicone instead of glass, the relative permittivity would be different from that of the initial calculation. If the relative permittivity is now lower then according to the calculation a higher frequency would be needed,

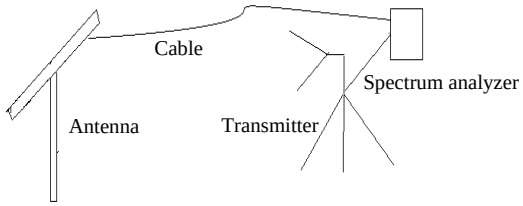

Figure 4: Test setup.

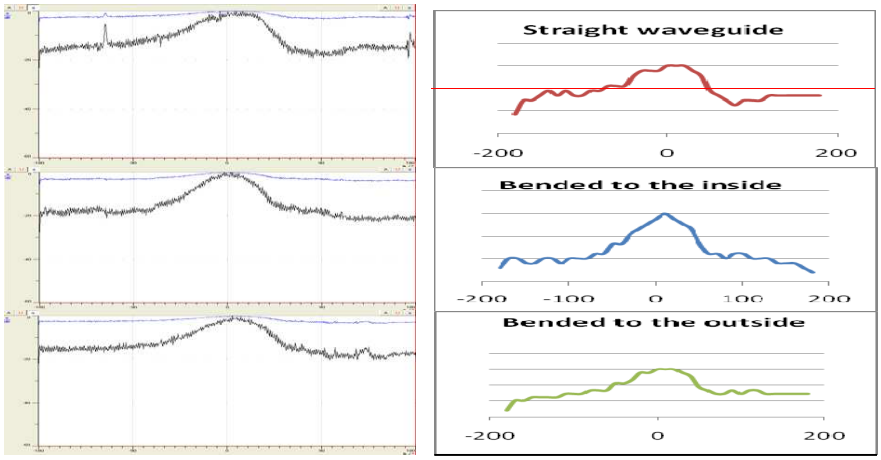

Figure 5: Antenna patterns of each antenna plotted separately.

as by using the previous frequency (2.4 GHz) with silicon (which is expected to have a lower relative permittivity) the waveguide would be excited below the cutoff frequency, which is impossible and would thus, never yield good results. The relative permittivity for silicone was researched, and silicone was found to have different types with different relative permittivity. Furthermore waveguides follow the reciprocity theory, which states that as the frequency varies, the wave pattern will remain constant relative to itself, although its size will change [1].

Waveguides are excited according to the cutoff frequency, so as long as they are excited above the cutoff frequency then the wave propagation and the differences between one antenna and another can be seen. This is the point of this experiment, which is designed to verify if the bent waveguide will have a better performance than a straight waveguide. As long as the performance can be measured then a comparison can be made.

Measurements were taken using software called "Cassy" which reads the wave propagation every half degree. The trial was started by giving an order to the software with all the necessary conditions, at which point the automatic rotator began to rotate and the software began recording the results. This was repeated for every antenna and graphs were created and shown in the figures below. The bent waveguide gave the best results; the side lobes of the bent waveguide had the lowest values. The values for directivity for each antenna were plotted separately in Figure 5.

As mentioned before the results showed the wave propagation for every half degree, so in order to have a clear graph the results of every two, four and ten degrees were taken. Normalization was applied for every group of results (ranging from 0 to 360 degrees), where every ten degrees wave propagation showed the clearest figures for the three antennas, in addition to highlighting the differences among them.

The graphs of the radiation pattern were superimposed on the same figure to give a clear view of the three waves and how the antenna bent to the inside had the best results, than the one bent to the outside, and last the straight waveguide. This is what was expected during the simulation phase. The waveguide which was bent to the inside had the best results among the three antennas Figure 6 and Figure 7 give a clear explanation of these results. Here the results were normalized in order to allow an easy comparison of the performance of the best antenna. All the results on every angle were normalized to 1 in such that the highest level is equal one and all the other points were

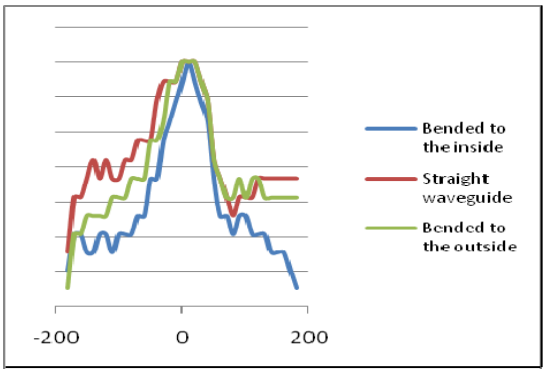

Figure 6: Comparative graphs for the three antennas.

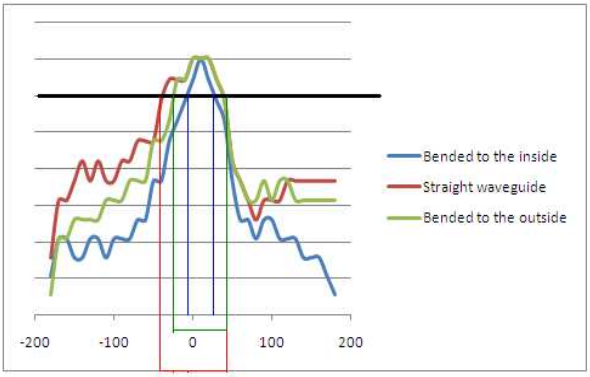

Figure 7: Directivity comparison.

below one; by this the main lobe can be clearly seen as well as the side lobes on both sides. The angles are shown from -200 to 200 because on the rotator this is how the angles are distributed (from 0 to 180° and from 0 to $-180°$. Since the values are taken in V, the following formula was used in order to normalize:

$$V_{\mathrm{dB}} = 20 \log V \qquad \log_{10} V = V_{dB}/20 \Rightarrow V = 10^{V_{dB}/20}$$

This formula gave a set of values of V, then the maximum value was taken and all the values were divided by this number to achieve normalization. This formula was repeated on all three sets in order to have the three peaks on one graph, so Figure 6 shows the pattern of each antenna at every angle for a clear comparison. This procedure was performed not only to show where the side lobes began and ended, but especially to show that the directivity increases for the bended waveguides. The simulation indicated that the directivity increases as the angle of the wave propagation decreases. This was also demonstrated through the practical results. Figure 7 depicts the angle vs. the radiated energy from the designed antenna. The blue graph shows the pattern of the waveguide which was bent inward by three degrees, the green graph shows the wave propagation waveguide which was bent outward by minus three degrees, and the red graph shows the wave propagation of the straight waveguide. The graph depicts a point for comparison (black line) with lines indicating the directivity of each angle for each waveguide (blue, green, red lines). The figure shows that the blue graph has the smallest half-power beamwidth, then the green graph, and then the red graph. The rule of directivity used in this article is calculated according to [1, 6]:

$$D = 41000/\theta_E \times \theta_H$$

According to the figure above the half power beamwidth of the antenna bent inward by three degrees (blue) is the smallest which means the directivity is the highest. In addition the side lobes are the lowest also in the blue graph, which means the side lobes decreased. This was a better result than in the simulation, where the side lobes did not decrease to that extent, meaning that the practical experiment gave better results concerning the side lobes.

5. CONCLUSION

Waveguides are very wide range antennas and commonly used in the market. They are flexible to use and work on a wide range of frequencies. Due to the reciprocity theory, changes are repeated when the frequency is varied. Waveguide antennas are used in many applications such as for the internet, airplanes, and military devices.

In this work, we combined waveguide theory and dish parabolic theory to bend the antenna at various angles, and determine the optimum bend that provides best directivity and lower sidelobes. This bend represent a situation where the distances from the slots to the receiver are nearly equal.

Moreover FEKO simulations found that using a 3 degree angle gave the best directivity, reaching 3 dB, the simulation results were supported by actual measurements at 2.4 GHz. The reduction of the waveguide dimensions were achieved by filling the waveguide with silicone.

Finally we demonstrated that bending the waveguide by three degrees inward or three degrees outwards provides higher directivity without affecting negatively the cost of the antenna system.

REFERENCES

1. Balanis, C. A., *Antenna Theory: Analysis and Design*, 3rd Edition, New Jersey, John Wiley & Sons, Inc., 2005.
2. Sadiku, M. O., *Elements of Electromagnetics*, 2nd Edition, John Wiley & Sons, New York, 1989.
3. "The corner reflector antenna," http://www.antennatheory.com/antennas/reflectors/corner-reflector.php.
4. "The parabolic reflector antenna (satellite dish)," http://www.antennatheory.com/antennas-/dishparabolic.php.
5. "Microstrip (patch) antennas," http://www.antenna-theory.com/antennas/patch.php.
6. Saunders, S. R., *Antennas and Propagation for Wireless Communication Systems*, John Wiley & Sons, England, 1999.
7. Marshall, T., "802.11b WLAN waveguide antenna, unidirectional and omnidirectional, high gain, simple construction," Oct. 2001, http://www.trevormarshall.com/waveguides.htm.
8. Zhong, S. S., W. Wang, and X. L. Liang, "Compact ridge waveguide slot antenna array fed by convex waveguide divider," *IEEE Electronic Letters*, Vol. 41, No. 21, Oct. 13, 2005.
9. Cheng, S., H. Yousef, and H. Kratz, "79 GHz slot antenna based on substrate integrated waveguides (SWI) in a flexible printed circuit board," *IEEE Trans. on Antennas and Propagation*, Vol. 57, No. 1, Jan. 2009.
10. Eldek, A. A., A. Z. Elsherbeni, C. E. Smith, and K.-F. Lee, "Wideband rectangular slot antenna for personal wireless communication system," *IEEE Trans. on Antennas and Propagation,* Vol. 44, No. 5, Oct. 2002.
11. Kim, Y. H. and H. J. Eom, "Radiation from longitudinal slots on the narrow wall of a rectangular waveguide," *IEEE Antennas and Wireless Propagation Letters*, Vol. 7, 2008.
12. Venus Research and Development Site, "Deep space network, new beam-waveguide antenna," Goldstone, California, http://deepspace.jpl.nasa.gov/dsn/antennas/arrays.html.
13. "70 microwave circuit design, introduction to rectangular waveguides," 2010, http://conocimientosmwcircuitddesign.blogspot.com/2010/05/introduction-to-rectangular waveguides.html.

Leaky Wave Radiation for Body-centric Wireless Communications

Xenofon M. Mitsalas[1], **Alexander V. Kudrin**[2], **and George A. Kyriacou**[1]

[1]Microwaves Laboratory, Department of Electrical & Computer Engineering
Democritus University of Thrace, Xanthi, Greece
[2]Department of Radiophysics, University of Nizhny Novrogod, Russia

Abstract— A substantial problem of the emerging field of "Body-Area Communications" refers to the very high losses of electromagnetic waves propagating through biological tissues. Given the abilities of leaky waves to carry energy away (radiate) from dielectric structures, this work examines this possibility by modeling the human body as an infinite lossy dielectric cylinder. The whole human body is modeled by an equivalent homogeneous electrolyte where the frequency dispersion of the dielectric constant and the corresponding conductivity is considered through a Debye model proposed by Ito and Haga [1]. The characteristic equation is solved for both surface and leaky waves in the frequency range of 3 MHz up to 3 GHz. It was found that indeed this model may support leaky (as well as surface) waves. Hence leaky modes should be appropriately excited by appropriately implanted antennas for an efficient transfer of electromagnetic energy outwards or inwards to the human body.

1. INTRODUCTION

In recent years, body-centric wireless communications have become an active area of research because of their various applications such as e-healthcare and personal communications. For example, Ito and Haga [1] have studied with the aid of finite difference time domain method the frequency dependent bioelectromagnetic models of bodycentric wireless communication channels in the range of HF to UHF (3 MHz–3 GHz). Extensive numerical studies have been performed by an impressive number of researchers aiming at the characterization of the human body as an electromagnetic signal channel. Even though such analysis could be highly accurate, especially when realistic human body models are employed, however they are just snapshots (samples) of a very extended physical phenomenon. Theoretical analysis is thus inevitable to understand physical mechanism, and to reveal their hidden characteristics. A step toward this direction was indeed tried by Prof. Hall group [2] with a simplified analysis aiming to characterize the important role of surface and creeping waves on body communication channels. In this paper, an analytical study of the electromagnetic waves propagation along a cylindrical model of the human body is attempted in order to understand the specific characteristics of the possible excited waves. For this purpose the human body is considered as an infinitely extended open radiating cylinder filled with a highly lossy dielectric fluid media ($\epsilon_r \approx 80$, $\sigma = 1.2\,\mathrm{S/m}$ and the diameter = 40 cm). Both surface and leaky waves are supported by such a cylindrical structure which is extensively studied in the past, especially by Kim [3], but only for a low loss and non-dispersive dielectric media. It was suspected and indeed verified herein that very high losses of the human electrolytes may completely change the excited waves characteristics. Besides losses the human tissues (electrolytes) present a very high frequency dispersion by means of a complicated variation of both dielectric constant (ϵ_r) and conductivity (σ) versus frequency.

The Debye model given in [1] is employed herein for the characterization of the whole human body. Actually the Debye equation is adopted with different parameters for the frequency ranges (3–30, 30–300, 300–3000 MHz) as given in [1]. Explicitly, based on Kim's [3] approach the characteristic equation for both surface and leaky modes is extracted and numerically solved. A very efficient technique proposed by the group of Berral, Mesa & Medina [4] is adopted in order to circumvent the numerical difficulties introduced by the involved branch cut singularity. In turn dispersion curves are obtained for both leaky and surface wave modes for three different cases of an infinite dielectric cylinder with 40 cm diameter: (i) low losses dielectric column $\epsilon_r \approx 80$, $\tan\delta = 0.01$, (ii) lossy dielectric column $\epsilon_r \approx 80$, $\sigma = 1.2\,\mathrm{S/m}$, and (iii) a dielectric fluid column described by the Debye model. Only the third case resembles the human body characteristics and the first two are considered just as reference cases in order to understand the phenomena resulting from the high losses and the frequency dispersion. Hence, the resulting dispersion curves are compared in order reveal the underlined physical phenomena in the 3 MHz to 3 GHz range. Additionally, for selected surface and leaky wave modes which constitute candidates for practical operation of

communication channels the electric and magnetic field eigenfunctions are calculated and plotted on a cross-section of the structure. Particular attention is devoted to leaky modes, since these are well established to behave as non-uniform (attenuated) waves along a specific direction in the unbounded space outside the cylinder. This is actually the direction along which the leaky waves excited along lossless dielectric cylinders present their maximum radiation (beam maximum). It is along this direction that the leaky modes eigenfuction is plotted. Unfortunately, it is herein found that leaky modes present very large attenuation constants which basically include all the attractive features of leaky waves. This unexpected radiation phenomenon is mainly caused by the large losses (high conductivity) of the human body electrolytes. The next essential step of this research is to identify proper excitation techniques of the desired modes. Ultimately this analysis will be utilized as a guide to repeat the study on realistic human modes with the aid of numerical techniques.

2. FORMULATION OF THE PROBLEM

Leaky mode studies strongly depend on the determination of the complex propagation constant. Explicitly the phase (β) and attenuation (or leakage) constant (α) are two of the most important parameters revealing the property of leaky waves. The resulting complex characteristic equation cannot be solved analytically traditional complex root search algorithms, such as the Newton-Raphson method or Davidenko method, have been utilized [7, 8]. However, these methods require a careful selection of the initial starting point. It is well known that open waveguides support both slow ($v_p < c$) or surface waves for $\beta > k_0$ as well as fast ($v_p > c$) or leaky waves for $\beta < k_0$, e.g., Collin [6]. The corresponding regimes for the general case of the open waveguide comprised of a media $(\epsilon_{r1}, \mu_{r1})$ embedded in an unbounded medium $(\epsilon_{r2}, \mu_{r2})$ is shown in Fig. 1.

Considering time harmonic dependence as $e^{+j\omega t}$ and propagation along the axial z-direction the general solutions of the wave equation for an open cylindrical waveguide (Fig. 2) can be laid out starting from the axial components as:

$$\begin{cases} E_{z1} = A_{mn} J_m(k_1\rho) e^{j(\omega t - m\theta - \gamma z)} & \text{inside the dielectric cylinder} \quad (1) \\ H_{z1} = B_{mn} J_m(k_1\rho) e^{j(\omega t - m\theta - \gamma z)} & \text{region 1: } 0 \le \rho \le \alpha \quad (2) \end{cases}$$

$$\begin{cases} E_{z2} = C_{mn} H_m^{(2)}(k_2\rho) e^{j(\omega t - m\theta - \gamma z)} & \text{for the unbounded region} \quad (3) \\ H_{z2} = D_{mn} H_m^{(2)}(k_2\rho) e^{j(\omega t - m\theta - \gamma z)} & \text{region 2: } \rho \ge \alpha \quad (4) \end{cases}$$

where ω, m and $\gamma = \beta - j\alpha$ are the angular frequency, azimuthal mode index and propagation constants respectively. J_m and $H_m^{(2)}$ are cylindrical Bessel and second kind Hankel functions of order m, $k_1 = k_0\sqrt{\mu_{r1}\epsilon_{r1} - \gamma^2}$ and $k_2 = k_0\sqrt{\mu_{r2}\epsilon_{r2} - \gamma^2}$ are the radial wavenumbers in regions 1 and 2 respectively, k_0 is the free space wavenumber, and A_{mm}, B_{mm}, C_{mm} and D_{mm} are unknown coefficients to be determined. Expressions for the radial and azimuthal field components for both the bounded region 1 and the unbounded free space (region 2) are given in Kim's Ph.D. thesis [3, p. 174]. Applying the boundary conditions for the tangential electric and magnetic field components at $\rho = \alpha$ (Fig. 2), yields a system of four equations for the unknown coefficients. A 4×4 coefficient matrix is constructed and the characteristic equation is derived from the condition that the determinant of the matrix should be zero to avoid nontrivial solutions. The resulting characteristic equation as it is mentioned in Kim's Ph.D. Thesis [3], reads:

$$\left[\frac{\epsilon_{r1}}{k_1}\frac{J_m'(k_1\alpha)}{J_m(k_1\alpha)} - \frac{\epsilon_{r2}}{k_2}\frac{H_m^{'(2)}(k_2\alpha)}{H_m^{(2)}(k_2\alpha)}\right]\left[\frac{\mu_{r1}}{k_1}\frac{J_m'(k_1\alpha)}{J_m(k_1\alpha)} - \frac{\mu_{r2}}{k_2}\frac{H_m^{'(2)}(k_2\alpha)}{H_m^{(2)}(k_2\alpha)}\right] = \left[\frac{m\gamma}{k_0\alpha}\left(\frac{1}{k_1^2} - \frac{1}{k_2^2}\right)\right]^2 \quad (5)$$

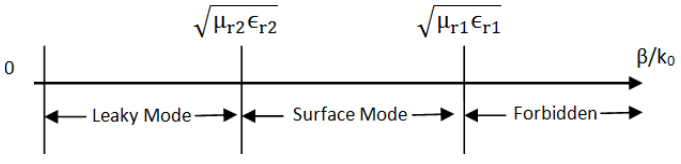

Figure 1: Surface and leaky mode regimes.

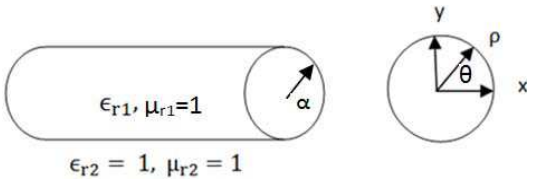

Figure 2: Geometry and cylindrical coordinate system (ρ, θ, z) for an open circular wave guiding structure embedded in free space.

For the particular case of axially symmetric modes $m = 0$, the characteristic equation is separated into distinct equations. Specifically the hybrid modes are reduced to TM^z and TE^z modes for the axial symmetric case $m = 0$:

$$\frac{\epsilon_{r1}}{k_1}\frac{J_1(k_1\alpha)}{J_0(k_1\alpha)} - \frac{\epsilon_{r2}}{k_2}\frac{H_1^{(2)}(k_2\alpha)}{H_0^{(2)}(k_2\alpha)} = 0 \quad \text{for } TM_{0n}^2 \tag{6}$$

$$\frac{\mu_{r1}}{k_1}\frac{J_1(k_1\alpha)}{J_0(k_1\alpha)} - \frac{\mu_{r2}}{k_2}\frac{H_1^{(2)}(k_2\alpha)}{H_0^{(2)}(k_2\alpha)} = 0 \quad \text{for } TE_{0n}^2 \tag{7}$$

Figures 3-4 are obtained by solving numerically the Equations (6) and (7) for TM_{0n} and TE_{0n} respectively by using the Davidenko method.

3. MODELLING THE HUMAN BODY

Dielectric properties of human tissue are depended on frequency. An average complex permittivity for the whole human body was proposed by Ito and Haga [1], which could be approximated by the Debye model [1]:

$$\epsilon_r(\omega) = \epsilon_\infty + \frac{\epsilon_s - \epsilon_\infty}{1 + j\omega\tau} + \frac{\sigma}{j\omega\epsilon_0} \tag{8}$$

where ϵ_0 is the free space permittivity, ϵ_s is the static permittivity at zero frequency, ϵ_∞ is the infinite-frequency permittivity $\omega = 2\pi f$, τ is the relaxation time and σ is the static electric conductivity. The parameters are individually defined in three ranges of 3–30 MHz, 30–300 MHz and 300 MHz–3 GHz, as shown in Table 1. This subdivision into three bands was necessary since Debye equation cannot approximate the actual value of muscle over the whole 3 GHz range.

Exploiting this Debye modeling the human body was approximately considered as a cylindrical column of an electrolyte fluid. In turn, theoretical analysis is inevitable to understand the involved physical mechanisms. Explicitly the human body is considered as an infinitely extended open radiating cylinder with 40 cm diameter. In order to understand the effects of increasing the losses on the excited modes three different cases are analyzed: (i) low losses dielectric column $\epsilon_r \approx 80$, $\tan\delta = 0.01$ (ii) lossy dielectric column $\epsilon_r \approx 80$, $\sigma = 1.2\,\mathrm{S/m}$ and (iii) a dielectric fluid column

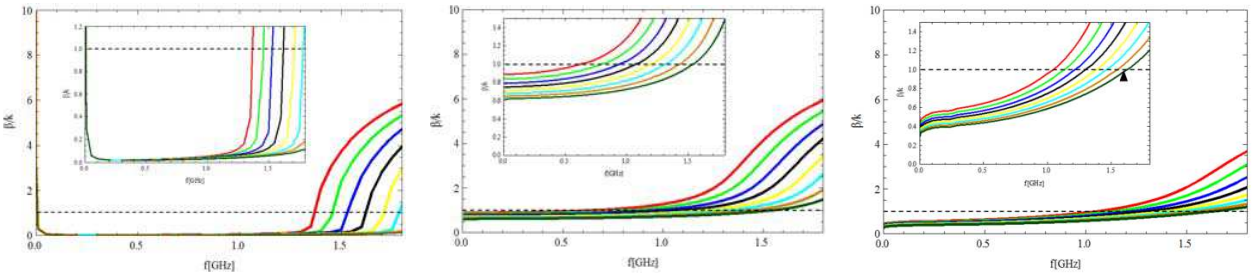

(a) (b) (c)

Figure 3: Dispersion curves for TM_{016}-TM_{023} modes for three models: (a) (i) low losses ($\epsilon_r \approx 80$, $\tan\delta = 0.01$), (b) (ii) lossy ($\epsilon_r \approx 80$, $\sigma = 1.2\,\mathrm{S/m}$), (c) (iii) a dielectric fluid described by the Debye model.

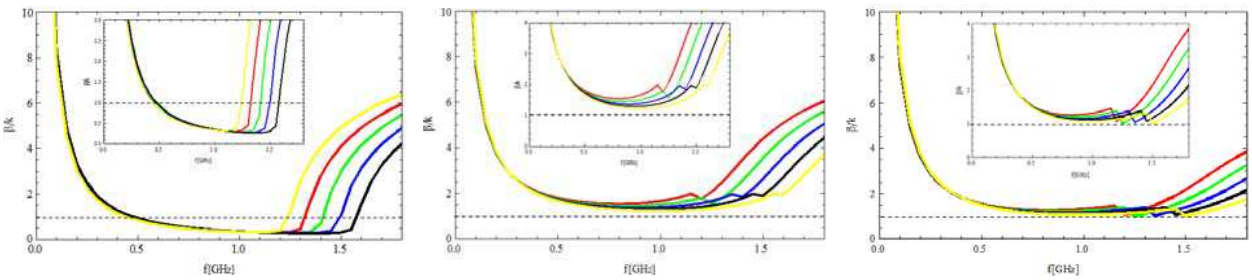

(a) (b) (c)

Figure 4: Dispersion curves for TE_{016}-TE_{020} modes for three models: (a) (i) low losses ($\epsilon_r \approx 80$, $\tan\delta = 0.01$), (b) (ii) lossy ($\epsilon_r \approx 80$, $\sigma = 1.2\,\mathrm{S/m}$), (c) (iii) a dielectric fluid described by the Debye model.

Table 1: Human body average dielectric parameters per frequency range to be utilized in the Debye model of Equation (8), [1].

	3 MHz–30 MHz	30 MHz–300 MHz	300 MHz–3 GHz
Static permittivity ϵ_r	706	101	58.3
Optical permittivity ϵ_∞	81.0	57.0	35.5
Relaxation time τ	3.98×10^{-8} s	3.18×10^{-9} s	3.54×10^{-11} s
Static conductivity σ	0.52 S/m	0.63 S/m	0.75 S/m

described by the Debye model. The dispersion curves that are obtained from the above models are compared in order to reveal the physical phenomena and are further discussed in the next paragraphs.

4. DISPERSION CURVES FOR THE WAVES

Figures 3 and 4 show the normalized phase and normalized attenuation constants of a cylindrical dielectric rod waveguide for the leaky and guided TM and TE modes respectively, for the three considered models (i, ii, iii).

In Fig. 4 at low frequencies near zero (negative slope dispersion), the normalized phase constants for TE modes exceeded unity and is proved in [3] that this spectral range is nonphysical. Above these frequency limits, as seen in Figs. 3–4, the normalized phase constants decreased to a minimum point, then increased again up to unity. This regime corresponds to the physical leaky mode, as $0 \leq \beta/k_0 \leq 1$ as defined in Fig. 1. According to Kim [3], this physical leaky mode regime can be divided into two distinct regions:

i. The antenna mode region ($\beta/k_0 < 1$ and $\beta/k_0 > \alpha/k_0$), where the energy of the guided wave is continuously leaked into the free space, and
ii. Reactive mode region ($\beta/k_0 < 1$ and $\beta/k_0 < \alpha/k_0$), where the energy of the wave is stored as a form of reactive energy.

The negative slope dispersion occurring for TE modes (Fig. 4) at low frequencies (non-physical mode regime) did not exist for TM modes (Figs. 3(b), 3(c)) when high losses are considered. It seems here that the introduction of high media losses eliminates the nonphysical low frequency spectral range. Moreover, the low order TE modes in Figs. 3(b), 3(c) (lossy models ii, iii) exhibit only surface wave behavior, as their normalized phase constants do not extend below unity. These phenomena occurred because of the high losses and the dependency of dielectric permittivity and conductivity on frequency (Table 1). The normalized phase constants of these modes decreased to a minimum point above unity and then increased again up to infinity as frequency is decreased. The normalized attenuation constants are not presented due to space limitations, but it is crucial to estimate which part of them is due to energy leakage rather than cut-off or material losses. This will be tried with the aid of the above Kim's observations, namely to locate the antenna region.

5. FIELD CALCULATION

A leaky wave is expected to radiate continuously as it propagates along the dielectric-air interface. Note, that their amplitude increases exponentially in the direction perpendicular to this interface. However, it is by now well understood that leaky waves are not improper modes but they are rather inhomogeneous (attenuated) waves propagating at a specific angle (θ) with respect to the air-dielectric interface. It is along this specific direction that they were found to exhibit maximum radiation-leakage, namely this the direction of beam maximum. This direction is defined by the leaky mode complex propagation constant, e.g., Jasik [5, p. 16-7]:

$$\cos\theta = \frac{\beta_z}{\beta} = \frac{\beta_z}{\sqrt{\beta_z^2 + \beta_{tr}^2}} \tag{9}$$

where $\beta_z = \mathrm{Re}(\gamma)$ and $\beta_{tr} = \mathrm{Re}(k_2)$ which are previously defined (below Equations (1)–(4)) and calculated from the solution of the characteristic equation. In order to present these phenomena, specific operating frequencies (marked points in Fig. 3(c)) on the dispersion curves are selected for the mode TM_{023} and a frequency $f = 1.6$ GHz. The corresponding roots are substituted in the field expressions of E_z in the Equations (1)–(4) and these are plotted in Figs. 5–6.

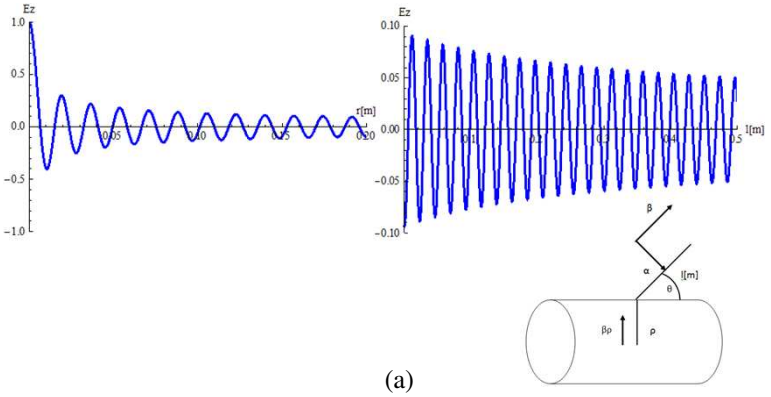

(a)

f (GHz)	βz	β_{tr}	θ (degrees)
1.5	0.890224	8.99302	84.347°
1.55	0.934134	8.51559	83.79°
1.6	0.981598	8.05979	83.056°

(b)

Figure 5: TM_{023} leaky mode characteristics. (a) Electric field E_z at $f = 1.6\,\text{GHz}$ (left) inside the waveguide and (right) outside the waveguide along the direction defined by an angle $\theta \approx 83.056°$, (b) leaky wave angular direction θ (degrees) versus frequency.

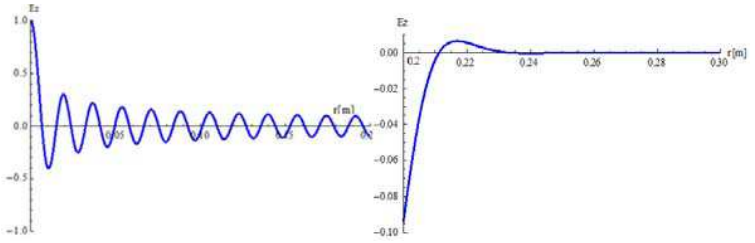

(a) (b)

Figure 6: Electric field E_z of the surface mode TM_{023} (a) inside the dielectric column waveguide and (b) outside the waveguide at $f = 2.4\,\text{Hz}$.

Surface waves behave as proper waves and they attenuate in the transverse direction, as it shown in Fig. 6

The electric field E_z is obtained using the Equations (1) and (3).

6. CONCLUSIONS

The human body is model as a lossy dielectric cylinder filled with an electrolyte equivalent to the whole body average dielectric constant and conductivity. It was found that this structure can indeed support leaky waves which allow energy to flow at a specific direction away from the body. Hence, there is a challenging possibility to appropriately excite leaky mode which could carry electromagnetic energy at larger distances away from the body event with significantly lower power fed to the implanted to antenna.

ACKNOWLEDGMENT

This work was financially supported by the Greek Ministry of Education, Lifelong Learning and Religious Affairs through the research project THALIS Design Techniques for Digitally Controlled RF-Microwave Structures appropriate for Software Defined-Cognitive Radio (RF-EIGEN-SDR).

REFERENCES

1. Ito, K. and N. Haga, "Basic characteristics of wearable antennas for body-centric wireless communications," *Loughborough Antennas & Propagation Conference*, 42–47, Nov. 8–9, 2010.
2. Akhoondzadeh-Asl, L., Y. Nechayev, and P. S. Hall, "Surface and creeping waves excitation by body — Worn antennas," *Loughborough Antennas & Propagation Conference*, 48–51, Nov. 8–9, 2010.
3. Kim, K. Y., "Guided and leaky modes for circular open electromagnetic waveguides: Dielectric, plasma and metamaterial column," Ph.D. Thesis, Dec. 2004.
4. Berral, R. R., F. Mesa, and F Medina, "Appropriate formulation of the characteristic equation for open non-reciprocal layered waveguides with different upper and lower half-spaces," *IEEE Transactions on Microwave Theory and Techniques*, Vol. 53, 1613–1623, May 2005.

5. Jasik, H., *Antenna Engineering Handbook*, McGraw-Hill, 1961.
6. Collin, R. E., *Field Theory of Guided Waves*, McGraw-Hill, New York, 1960.
7. Voitovich, N. N., B. Z. Katsenelenbaum, A. N. Savov, and A. D. Shatrov, "Characteristic propagation modes of dielectric waveguides with a composite cross section," *Radio Engineering and Electronic Physics*, Vol. 24, 1–16, Jul. 1979.
8. Hanson, G. W. and A. B. Yakovlev, "An analysis of leaky wave dispersion phenomena in the vicinity of cutoff using complex frequency plane singularities," *Radio Science*, Vol. 33, No. 4, 803–819, 1998.

Full Wave Maxwell's Equations Solver EMWSolver3D

A. P. Smirnov and A. N. Semenov
Lomonosov Moscow State University, Moscow, Russia

Abstract— In this work, we are introducing 3-dimensional FDTD solver EMWSolver3D. Based on Maxwell equations approximation in integral form on Yee lattice, it provides numerical solution in time domain. EMWSolver3D supports multi-core single processors machines and provides hybrid MPI/OpenMP support for IBM BlueGene/P series. Large-scale electromagnetic and optical problems with size of the order of 400 wavelengths in every dimension for a problem with arbitrary complex geometry structure can be solved. The parallel implementation on MSU BlueGene/P supercomputer, based on asynchronous operations, provides good scalability factor for large problems. Solver supports Dirichlet and periodic boundary conditions on any boundary interface. Uniaxial perfect matched layer conditions also implemented in solver, so wide range of problems in unbounded region can be solved. Effective layer parameters obtained for a particular class of unbounded problems. Comparison of solutions for infinite layers and half-spaces of materials with different permittivity and permeability is shown. Numerical solution of point hard source problem verified with Hankel function analytical solution. For dispersive materials problems EMWSolver3D uses Drude model and can be used in modeling of metamaterials with specific parameters. The illustration of electric field component of plane wave impinging on left-handed material half-space with $\varepsilon = \mu = -1$ are shown. Numerical solution of metamaterial perfect lens problem with point source is provided.

1. INTRODUCTION

Recently a great deal of attention has been paid to the research of artificial electromagnetic materials. Theoretical existence of such materials were introduced by V. G. Veselago in [1]. First real experiments were introduced in [2].

Computational modeling of metamaterials requires a numerical solver for 3D system of Maxwell equations that can handle dispersive media with negative values of dielectric permetivitty and magnetic permeability and can obtain numerical solution for complex structures. Problems in unbounded region require special conditions on a boundaries. In this work, we use perfectly matched layer conditions, that is based on artificial layer which absorbs scattered waves.

One of the most widespread numerical methods for Maxwell equations solving is finite-difference time-domain (FDTD) method. FDTD is based upon Yee lattice and Maxwell equations in integral form and differentional relations from which finite-difference approximation is obtained.

In this work, EMWSolver3D three-dimensional Maxwell equations numerical FDTD solver is developed. Using EMWSolver3D effective layer parameters obtained for a particular class of unbounded problems. Comparison of solutions for infinite layers and half-spaces of materials with different permittivity and permeability is shown. Numerical solution of metamaterial perfect lens problem with point source is provided. The illustration of electric field component of plane wave impinging on left-handed material half-space with $\varepsilon = \mu = -1$ will be shown lately.

2. NUMERICAL MODELLING OF DISPERSIVE MATERIALS

Describing the properties of materials with negative refraction index key fact is the frequency dispersion nature of such materials. Left handed materials can be effectively described by dispersive material Drude model:

$$\begin{aligned} \varepsilon(\omega) &= \varepsilon_0 \left(1 - \frac{\omega_{pe}^2}{\omega^2 - i\omega\gamma_e}\right) \\ \mu(\omega) &= \mu_0 \left(1 - \frac{\omega_{pm}^2}{\omega^2 - i\omega\gamma_m}\right) \end{aligned} \tag{1}$$

where ω_{pe}, ω_{pm} — electric and magnetic plasma frequencies and γ_e, γ_m are electromagnetic losses respectively.

Lets consider numerical FDTD scheme with dispersive materials Drude model. The implementation is based on introduction of additional differentional equation. The materials equation between E and D can be written as:

$$(\omega^2 - i\omega\gamma_e)\vec{D}_\omega = \varepsilon_0(\omega^2 - i\omega\gamma_e - \omega_{pe}^2)\vec{E}_\omega. \tag{2}$$

Applying inverse Fourier transform gives next relation:

$$\left(\frac{\partial^2}{\partial t^2} + \frac{\partial}{\partial t}\gamma_e\right)\vec{D} = \varepsilon_0\left(\frac{\partial^2}{\partial t^2} + \frac{\partial}{\partial t}\gamma_e + \omega_{pe}^2\right)\vec{E}. \tag{3}$$

Discretizing this equation with second order accuracy for the first and second order derivatives we obtain:

$$\begin{aligned} &\frac{D_w^{n+1} - 2D_w^n + D_w^{n-1}}{\Delta t^2} + \langle\gamma_e\rangle\frac{D_w^{n+1} - D_w^{n-1}}{2\Delta t} \\ &= \varepsilon_0\left[\frac{E_w^{n+1} - 2E_w^n + E_w^{n-1}}{\Delta t^2} + \langle\gamma_e\rangle\frac{E_w^{n+1} - E_w^{n-1}}{2\Delta t} + \langle\omega\rangle_{pe}^2\,\frac{E_w^{n+1} + 2E_w^n + E_w^{n-1}}{4}\right], \end{aligned} \tag{4}$$

where $w = x, y, z$, and $\langle\omega\rangle_{pe}^2 = \omega_{pe(i,j,k)}^2 + \omega_{pe(i,j+1,k)}^2 + \omega_{pe(i,j,k+1)}^2 + \omega_{pe(i,j+1,k+1)}^2/4$; $\langle\gamma_e\rangle = \gamma_{e(i,j,k)} + \gamma_{e(i,j+1,k)} + \gamma_{e(i,j,k+1)} + \gamma_{e(i,j+1,k+1)}/4$.

3. UPML ANALYSIS

General formulation of UPML as anisotropic material, were introduced in [5]. Amphere's law for harmonic wave $E(x,y,z,t) = E_\omega e^{-i\omega t}$, $H(x,y,z,t) = H_\omega e^{-i\omega t}$ in UPML described by next equations:

$$\begin{bmatrix} \frac{\partial H_{z_\omega}}{\partial y} - \frac{\partial H_{y_\omega}}{\partial z} \\ \frac{\partial H_{x_\omega}}{\partial z} - \frac{\partial H_{z_\omega}}{\partial x} \\ \frac{\partial H_{y_\omega}}{\partial x} - \frac{\partial H_{x_\omega}}{\partial y} \end{bmatrix} = i\omega\varepsilon \begin{bmatrix} \frac{s_y s_z}{s_x} & 0 & 0 \\ 0 & \frac{s_x s_z}{s_y} & 0 \\ 0 & 0 & \frac{s_x s_y}{s_z} \end{bmatrix} \begin{bmatrix} E_{x_\omega} \\ E_{y_\omega} \\ E_{z_\omega} \end{bmatrix} \tag{5}$$

Let:

$$D_x = \varepsilon\frac{s_z}{s_x}E_x\ ; \qquad D_y = \varepsilon\frac{s_x}{s_y}E_y\ ; \qquad D_z = \varepsilon\frac{s_y}{s_z}E_z. \tag{6}$$

then

$$s_x = 1 + \frac{\sigma_x}{i\omega\varepsilon}\ ; \qquad s_y = 1 + \frac{\sigma_y}{i\omega\varepsilon}\ ; \qquad s_z = 1 + \frac{\sigma_z}{i\omega\varepsilon}. \tag{7}$$

So

$$\begin{bmatrix} \frac{\partial H_z}{\partial y} - \frac{\partial H_y}{\partial z} \\ \frac{\partial H_x}{\partial z} - \frac{\partial H_z}{\partial x} \\ \frac{\partial H_y}{\partial x} - \frac{\partial H_x}{\partial y} \end{bmatrix} = \frac{\partial}{\partial t}\begin{bmatrix} 1 & 0 & 0 \\ 0 & 1 & 0 \\ 0 & 0 & 1 \end{bmatrix}\begin{bmatrix} D_x \\ D_y \\ D_z \end{bmatrix} + \frac{1}{\varepsilon}\begin{bmatrix} \sigma_y & 0 & 0 \\ 0 & \sigma_z & 0 \\ 0 & 0 & \sigma_x \end{bmatrix}\begin{bmatrix} D_x \\ D_y \\ D_z \end{bmatrix} \tag{8}$$

This equations can be discretized on a standard Yee lattice. Parameter σ defines absorbtion in layer.

For $\sigma_x(x)$, reflection coefficient can be written as [3]:

$$R(\theta) = e^{-2\eta\cos\theta\int_0^d \sigma_x(x)dx} \tag{9}$$

where $\eta = \sqrt{\frac{\mu}{\varepsilon}}$. So, for the polynomial profile of losses:

$$\sigma_x(x) = (x/d)^m\sigma_{x,\max}. \tag{10}$$

Value of $\sigma_x(x)$ increasing from zero value on UPML interface $x = 0$, to $\sigma_{x,\max}(x)$ when $x = d$ on a Dirichlet outer boundary. Putting (9) in (7) we obtain:

$$R(\theta) = e^{-2\eta\sigma_{x,\max}d\cos\theta/(m+1)}, \tag{11}$$

where $\sigma_{x,\max}(x)$ based on selection of initial error value $R(0)$. Then $\sigma_{x,\max}(x)$ can be calculated as:

$$\sigma_{x,\max} = -\frac{(m+1)\ln[R(0)]}{2\eta d}. \tag{12}$$

Lets consider 2d square region with point source in the center for the TM waves. Excitation hard-source is sinusoidal function: $E_z(x_0, y_0, t) = -2(t-t_0)/t_w \cdot e^{-((t-t_0)/t_w)^2} \sin(\omega t)$. Size of a region is $1.6\lambda \times 1.6\lambda$ with spatial step $h = 0.016\lambda$ and times step $\Delta t = h/(2C)$. The calculation is compared with numerical solution obtained on $16\lambda \times 16\lambda$ with same parameters as initial problem.

On a Figure 1 the relative error comparison in point (0.8λ, 0.032λ) is shown for different UPML parameters that introduced in [3]. Parameters $R(0), m, p$ where $p = d/h$ is number of cells in layer.

So, increasing the size of absorbing layer is always cause better reflectionless absorbtion. Also from specific time period error stops growing.

4. EXAMPLES

Considering example of perfect lens [2] numerical modeling with EMWSolver3D, we will use model presented in [4]. The perfect lens is metamaterial slab with next parameters of Drude model. For the sake of simplicity, the plasma frequencies are assumed to be equal $\omega_{pe} = \omega_{pm} = \sqrt{2}\omega$ where ω is the operating frequency and zero losses: $\gamma_e = \gamma_m = 0$. This Drude model parameters gives following electromagnetic media properties: $\varepsilon = \mu = -1$, so slab is matched to the free space at this frequency in simulations.

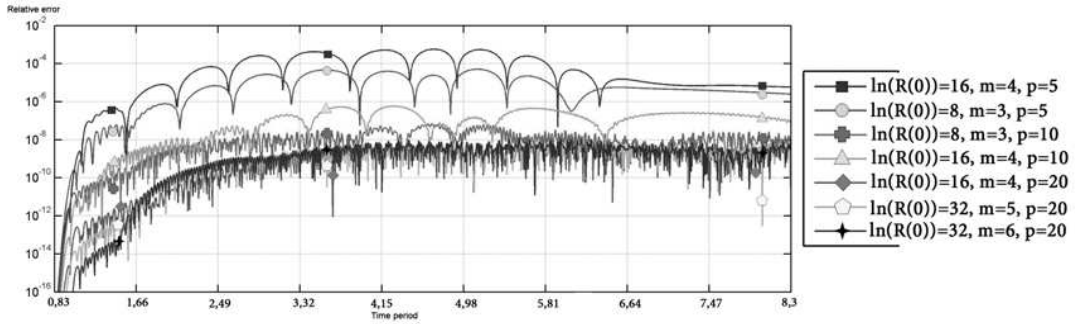

Figure 1: Relative error in (0.8λ, 0.032λ) point for different $R(0)$; m; p parameters.

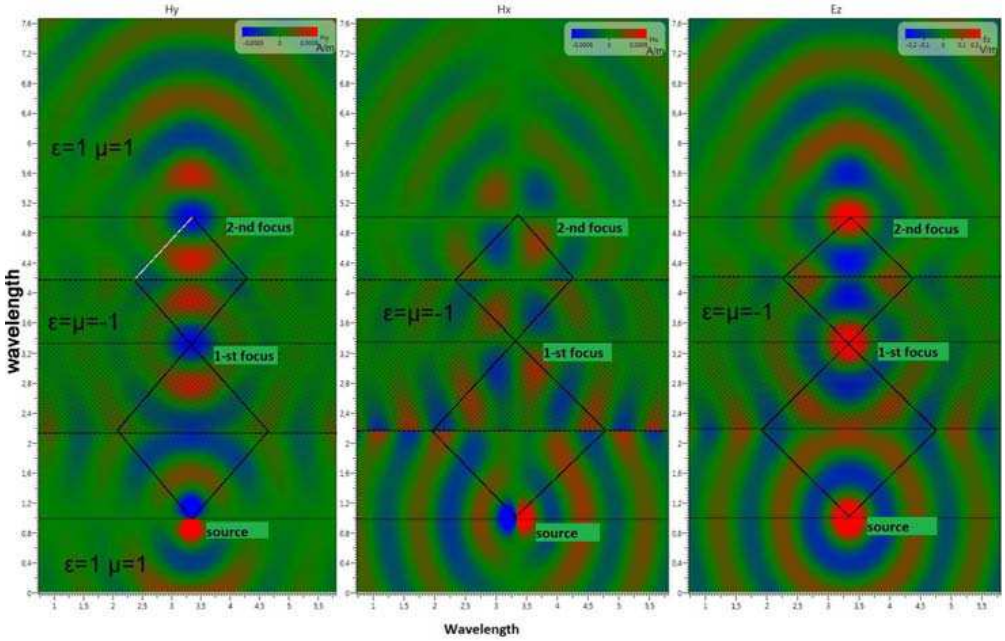

Figure 2: Electric and magnetic field TM components distribution of perfect lens.

For the TM mode we use point sinusoidal hard-source for wave excitation. The computation domain is bounded by UPML absorbing layer. Metamaterial slab is finite and not continued on UPML layer.

On Figure 2, the results of numerical simulation are presented. The snapshot of field distribution is taken after 100τ periods, when the steady state appears. From the distribution we can see, that two focuses appeared as it proposed in [1].

5. PARALLEL IMPLEMENTATION

Introduced early EMWSolver3D were implemented on Lomonosov Moscow State University IBM BlueGene/P supercomputer. Using 1D data decomposition for highly elongated problems and 3D data decomposition for general problems together with asynchronous transfer operations between nodes of supercomputer we enabled to solve problems up to 10^9 computational points on 2048 nodes. We achieved good speed up and scalability on BlueGene/P [6]

6. CONCLUSION

In this work, we are introducing 3-dimensional FDTD solver EMWSolver3D. Large-scale electromagnetic and optical problems with size of the order of 400 wavelengths in every dimension for a problem with arbitrary complex geometry structure can be solved. The parallel implementation on MSU BlueGene/P supercomputer, based on asynchronous operations, provides good scalability factor for large problems. Solver supports Dirichlet and periodic boundary conditions on any boundary interface.

Uniaxial perfect matched layer conditions also implemented in solver, so wide range of problems in unbounded region can be solved. Effective layer parameters obtained for a particular class of unbounded problems. Comparison of solutions for infinite layers and half-spaces of materials with different permittivity and permeability is shown.

Numerical solution of point hard source problem verified with Hankel function analytical solution. For dispersive materials problems EMWSolver3D uses Drude model and can be used in modeling of metamaterials with specific parameters. The illustration of electric field component of plane wave impinging on left-handed material half-space with $\varepsilon = \mu = -1$ are shown. Numerical solution of metamaterial perfect lens problem with point source is provided.

REFERENCES

1. Veselago, V. G., *Usp. Fiz. Nauk*, Vol. 92, No. 3, 517, 1967.
2. Pendry, J. B., *Phys. Rev. Lett.*, Vol. 85, 3966, 2000.
3. Taflove, A. and S. C. Hagness, *Computational Electrodynamics: The Finite-Difference Time-Domain Method*, Norwood, 2000.
4. Zhao, Y., P. Belov, and Y. Hao, *Phys. Rev. E*, Vol. 75, No. 37, 602, 2006.
5. Gedney, S. D., *IEEE Trans. Antennas Prop.*, Vol. 44, 1630–1639, 1996.
6. Semenov, A. N., "Parallelnaya realizacia chislennogo resheniya uravneniy Maksvella FDTD metodom dly bolshih zadach," *Nauchniy Servis v Seti Internet*, 530, Novorossiysk, Russian Federation, September 2011.

New Mathematical Model and Measurement Scheme of Electrical Tomography and Its Fast Resolution by General Ray Method

Alexandre Grebennikov
Facultad de Ciencias Físico Matemáticas, Benemérita Universidad Autónoma de Puebla
Av. San Claudio y Río verde, Ciudad Universitaria, CP 72570, Puebla, Pue., México

Abstract— Computer Tomography consists in the image reconstruction of an interior of a body using the measurements on its surface of characteristics of some external field. Very often this reconstruction can be posed mathematically as a coefficient inverse problem for a differential equation describing the distribution of the field in considered region. Coefficients are functions of the space variables and characterize properties of a media. Well known are X-rays, ultrasonic, radioisotopes, infrared and electrical impedance tomography. For example, X-rays tomography leads to the linear mathematical model and for its resolving can be used corresponding linear fast algorithms, but the know methods for the electrical impedance tomography imaging are non-linear, that leads to algorithms which require a large time of calculations on computer.

We propose here another approach for the mathematical modelling and the measurement scheme for the external data. We explain it for the plane case and describe adaptation for space case. We construct the mathematical model on the basis of General Ray Principle, proposed by the author for distribution of different, in particular electromagnetic, fields. Proposed model leads to the classic Radon transformation that appears as specific element in new General Ray Method, constructed and realized by the author as a simple linear fast numerical algorithm. This approach and algorithms are justified with the numerical experiments on the simulated model examples in MATLAB system.

1. TRADITIONAL MATHEMATICAL STATEMENT OF ELECTRIC TOMOGRAPHY

In a plane case EIT can be mathematically described as a coefficient inverse problem for the Laplace equation, written in the divergent form

$$\frac{\partial}{\partial x}\left(\varepsilon(x,y)u'_x(x,y)\right)+\frac{\partial}{\partial y}\left(\varepsilon(x,y)u'_y(x,y)\right)=0, \tag{1}$$

where $(x,y)\in\Omega$ some limited open region on a plane, $u\,(x,y)$ is potential, the function $\varepsilon=\varepsilon(x,y)$ characterize the conductivity or permittivity of a media.

In traditional statement [1] it is supposed also that functions $J_n\,(x,y)$, $u^0\,(x,y)$ are known on the curve Γ and the next boundary conditions are satisfied:

$$\varepsilon(x,y)\frac{\partial u(x,y)}{\partial n} = J_n(x,y), \quad (x,y)\in\Gamma, \tag{2}$$

$$u(x,y) = u^0(x,y), \quad (x,y)\in\Gamma, \tag{3}$$

where $\frac{\partial}{\partial n}$ is the normal derivative in the points of the boundary curve Γ.

Equations (1)–(3) serve as the model of EIT when there is a family of potential and boundary conditions that corresponds to different angles of scanning scheme. Traditional approach for solving EIT leads to nonlinear ill-posed problem.

2. NEW MEASUREMENT SCHEME FOR ELECTRIC TOMOGRAPHY

We propose here another variant of the Electrical Tomography, when the external electromagnetic field $\vec{V}(l)$, is produced by active electrodes, located outside of the Ω, initiates some distribution of the electric potential inside the domain Ω. At that, we propose that measurements of necessary values would be realized on the boundary curve Γ with another, no active electrodes. For simplicity we put bellow Ω as a circle of radius r. The corresponding scheme is presented at Figure 1, where active electrodes are marked with arcs on the external circle A of radius R and inactive electrodes are marked as arcs on the internal circle B, which is the board of the domain.

We will consider the parallel scanning beam at an angle φ. Let the external field in scanning scheme be electrostatic homogeneous in the direction orthogonal to the line l. We suppose that we

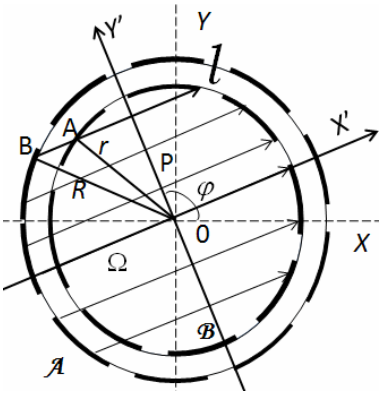

Figure 1: The measurement scheme of the external data.

have a charge in the point B of the external circle, so the potential in the point A of the border can be calculated by the formula: $u = \frac{Q}{4\pi\varepsilon_a d}$, where ε_a is the permittivity of the space out of domain, d is the distance between points A and B at Figure 1, $d = \sqrt{R^2 - p^2} - \sqrt{r^2 - p^2}$, Q is the charge volume. So, we can calculate electrical induction $J(p, \varphi)$ in the point A by formula: $J(p, \varphi) = -\frac{Q}{4\pi d^2}$.

There is the sufficient difference of the proposed scheme with the electric resistance (ERT) or capacitance tomography (ECT) schemes. In ERT the function $J_n(x, y)$ is given, function $u^0(x, y)$ is measured. In ECT the function $u^0(x, y)$ is given, the value of the normal component of electric induction $J_n(x, y)$ is related with measured mutual capacitances [1]. In both ERT and ECT schemes the electric field is produced by the same electrodes that serve as measuring elements, i.e., the electrodes are active. May be this activity of electrodes, which provokes its mutual influence, is the cause of impossibility to use a great number of electrodes and obtain the sufficiently large number of measurements. It is very important that in proposing scheme electrodes on the boundary Γ do not produce the external electric field (are not active) and serve only for measurement of data. Therefore, the proposed approach gives in principal the possibility to use a large number of electrodes and measurements of the input values of data and reconstruct the desired image more perfectly.

3. GENERAL RAY METHOD AND FAST ALGORITHM

We will use General Ray Principle [2], i.e., to consider the electric field as the stream flow of "general rays". Each one of these rays corresponds to some straight line l. The main idea of the General Ray Principle consists in reduction a Partial Differential Equation to a family of Ordinary Differential Equations. Let the line l has the parametric presentation: $x = p\cos\varphi - t\sin\varphi$, $y = p\sin\varphi + t\cos\varphi$, where $|p|$ is a length of the perpendicular, passed from the centre of coordinates to the line l, φ is the angle between the axis X and this perpendicular [3]. Hence, using this parameterization for the line l, we shall consider the potential $u(x, y)$ and function $\varepsilon(x, y)$ for $(x, y) \in l$ as functions (traces) $\bar{u}(t)$ and $\bar{\varepsilon}(t)$ of variable t. Considering the Equation (1) on the line l we obtain for every fixed p and φ the ordinary differential equation for traces

$$\left(\bar{\varepsilon}(t)\bar{u}'_t(t)\right)'_t = 0, \quad |t| < \bar{t}, \quad \bar{t} = \sqrt{r^2 - p^2}. \tag{4}$$

We suppose that functions $v(p, \varphi)$ and $J(p, \varphi)$ are given and we can write boundary conditions

$$\bar{\varepsilon}(-\bar{t})\bar{u}'_t\left(-\bar{t}\right) = J(p, \varphi), \tag{5}$$

$$\bar{u}\left(\bar{t}\right) - \bar{u}\left(-\bar{t}\right) = v(p, \varphi) \tag{6}$$

Equations (4)–(6) are considered as the basic mathematical model for proposing type of electrical tomography.

If different components in the considered structure have the smooth distribution, such as functions $\bar{\varepsilon}(t)\bar{u}'_t(t)$ and $\bar{u}'_t(t)$ are continuous. Integrating twice the Equation (4) on t and using boundary conditions (5)–(6), we obtain for $\varepsilon(x, y)$ the next formula for Scanning General Ray (GR) method

$$\varepsilon(x, y) = 1/R^{-1}\left[\frac{v(p, \varphi)}{J(p, \varphi)}\right], \tag{7}$$

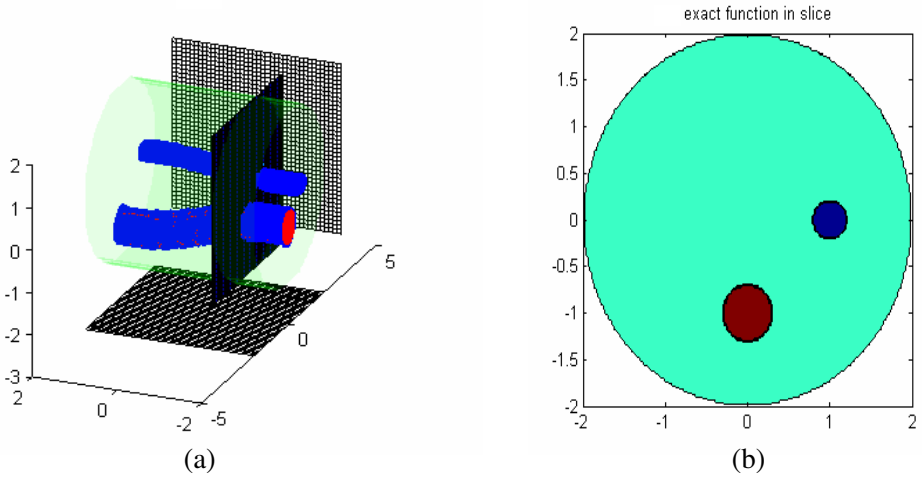

Figure 2: Illustration for synthetic example: (a) space distribution with one intersection; (b) exact distribution in the section.

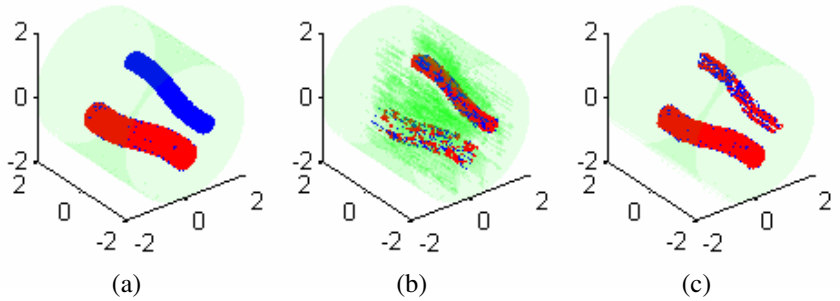

Figure 3: Reconstruction of space structure.

where R^{-1} is the inverse Radon transform operator [3]. *GR*-method gives the explicit solution of the inverse coefficient problem for considering case. It is generalized and applied also for structures with piecewise constant characteristics.

We have constructed the numerical realization of formula (7) that we call "*GR*-algorithm". This algorithm is fast, because it does not require solving any equation and the Radon transform can be inversed by fast manner using discrete Fast Fourier Transform algorithm (FFT).

4. NUMERICAL EXPERIMENTS

We tested scanning *GR*-algorithm on mathematically simulated model examples for space structure with piecewise-constant permittivity. We considered inside the cylinder of radius 2 two different internal long elements S_1, S_2 of different permittivity, as it is shown at part (a) of Figure 2 with one plane intersection orthogonal of the axe of cylinder. This intersection give a plane unit circle Ω with two different internal elements Ω_1, Ω_2 of different permittivity, as it is shown at part (b) of Figure 2.

The scheme of solution of the corresponding example consists in the next steps:

1) consideration of some sections of space object at the planes parallel to plane XZ;

2) simulation of measurement data for the plane case in every considering section in correspondence to the scheme, proposed in [4], that includes: analytic solution the direct Cauchy problem for Equation (4) with known values of functions $J(p,\varphi)$ and $\bar{u}(-\bar{t})$ for every fixed angle φ and parameter p; calculation the value $\bar{u}(\bar{t})$ and explicit form of $v(p,\varphi)$; numerical realization of formula (7);

3) space interpolation of recuperated plane structures and its graphic imagine.

At Figure 3 we present reconstruction of space structure by proposed scheme. For this problem we use Recursive Spline Smoothing method (*RSS*) [5, 6] even for the exact data. Graph (a) — exact solution; graph (b) — approximate solution, reconstructed on exact data without *RS*S; graph (c) — approximate solution, reconstructed on exact data with *RSS*.

5. CONCLUSIONS

A new measurement scheme for electric tomography is proposed. To resolve this scheme a new mathematical model is considered on the base of the *GRP* and is reduced to coefficient inverse problem for the Laplace type equation with piecewise constant coefficient. The plane version of *GR*-method for the solution of this inverse problem is adapted to the space structures. The properties of the constructed algorithms and computer programs are illustrated by numerical experiment.

ACKNOWLEDGMENT

The author acknowledges to VIEP of Merited Autonomous University of Puebla, Mexico for the support of the part of this investigation in the frame of the Project No GRA-EXC12-I.

REFERENCES

1. Williams, R. A. and M. S. Beck, *Process Tomography: Principles, Techniques and Applications*, Butterworth-Heinemann, Oxford, 1995.
2. Grebennikov, A. I., "A novel approach for solution of direct and inverse problems for some equations of mathematical physics," *Proceedings of the 5th International conference on Inverse Problems in Engineering: Theory and Practice*, ed., D. Lesnic, Vol. II, 1–10, Chapter G04, Leeds University Press, Leeds, UK, 2005.
3. Radon, J., "Uber die Bestimmung von Funktionen durch ihre integrawerte langs gewisser Mannigfaltigkeiten," *Berichte Sachsische Academic der Wissenschaften, Leipzig, Math.-Phys.*, K1, Vol. 69, 262–267, 1917.
4. Reyes Mora, S. and A. I. Grebennikov, "Unicidad de solución del problema inverso de identificación de coeficiente en ecuación de tipo laplace con condiciones de contorno parcialmente reducidos," *Boletín de la sociedad cubana de Matemática y Computación*, Numero especial Editorial de Universidad de Ciencias Pedagógicas "Enrique Jose Varona", M-99, 2009.
5. Morozov, V. A. and A. I. Grebennikov, *Methods for Solution of Ill-Posed Problems: Algorithmic Aspects*, Moscow University Press, Moscow, 1992 (English edition in 2005).
6. Grebennikov, A. and C. Gamio, "Fast post-processing algorithm for improving electrical capacitance tomography image reconstruction," *Inverse Problems in Science and Engineering*, Vol. 14, No. 1, 64–74, Jan. 2006.

Noise Influence of Magnetic Field to Conductivity Image Reconstruction

T. Kříž
Department of Theoretical and Experimental Electrical Engineering
Brno University of Technology, Kolejní 4, Brno 612 00, Czech Republic

Abstract— The paper presents a conductivity calculation from values of the magnetic flux density measured outside the specimen. There is described the analysis of the noise influence that is presented in the measured values of a magnetic field. A conductivity calculation is based on the electrical impedance tomography (EIT) algorithm. The standard EIT exploited measured voltage values on electrodes placed at specimen boundaries to a conductivity calculation. The direct current source or the low frequency current source is connected to a specimen. A conductivity calculation is based on a minimizing of a suitable objective function. The least squares method is very often used for a minimization of an objective function. The Tikhonov regularization method is used in order to ensure the stability of an algorithm. The stability and the accuracy are dependent on an accuracy of measured voltage values.

1. INTRODUCTION

The electrical impedance tomography (EIT) is a widely investigated problem with many applications in physical and biological sciences. The aim is to reconstruct the internal conductivity or permittivity distributions in two or three dimensional models. The optimization necessitates algorithm that impose regularization and some prior information constraint. The EIT algorithm for a conductivity reconstruction is an inverse and an ill-posed problem. The solution of this problem is described as a minimization of a suitable objective function $\Psi(\sigma)$ which is dependent on a conductivity σ. The least squares method is very often used for a minimization of the objective function. This method converges very fast. The regularization methods are used for better stability of the solution. The Tikhonov regularization method can be used. The regularization term is added to the objective function if the Tikhonov regularization method is used. This term makes the solution stable. The square of the norm of measured voltages and calculated voltages by finite element method is involved in the standard EIT objective function. Objective function in general form can be written

$$\Psi(\sigma) = \frac{1}{2}\sum \left\|\bar{U}_M - \bar{U}_{FEM}(\sigma)\right\|^2 + \alpha \left\|\mathbf{R}\bar{\sigma}\right\|^2 \tag{1}$$

where σ is the unknown conductivity distribution vector in the object, U_M is the vector of measured voltages on the object boundary, $U_{FEM}(\sigma)$ is the vector of computed peripheral voltages in respect to σ which can be obtained using finite element method, α is a regularization parameter and $\mathbf{R}$ is a regularization matrix connecting adjacent elements of the different conductivities.

2. BASIC THEORY

The EIT problem is recovering the conductivity distribution satisfying continuity equation

$$\mathrm{div}\mathbf{J} = 0. \tag{2}$$

The current density $\mathbf{J}$ in a linear medium with the interior conductivity σ can be obtain from electric field $\mathbf{E}$ or corresponding potential distribution Φ

$$\mathbf{J} = \sigma \cdot \mathbf{E} = -\sigma \cdot \mathrm{grad}\Phi \tag{3}$$

Further we suppose the electric field in very thin layer of electrical conductive medium which can be described by the surface current density $\mathbf{K}$. The surface current density $\mathbf{K}$ inside a specimen produces also a magnetic field. The magnetic flux density $\mathbf{B}$ corresponding to $\mathbf{K}$, can be obtained according to the Biot-Savart Law

$$\bar{B} = \frac{\mu_0}{4\pi}\int_S \frac{\bar{K}\times\bar{R}}{R^3}dS \tag{4}$$

For further numerical simulations we divided the sample into *NE* triangle elements with centers $[x_t, y_t, z_t]$. We suppose that the current density $\mathbf{K}$ is constant on each element. The magnetic field in general point given by coordinates $[x_i, y_i, z_i]$ we can calculate components of magnetic flux density with using superposition principle

$$\vec{B}_i \approx \frac{\mu_0}{4\pi} \sum_{j=1}^{NE} \frac{\bar{K}_j \times \bar{R}_{ij}}{R_{ij}^3} \Delta S_j \tag{5}$$

The vector $\mathbf{R}$ represents the distance between centre of actual element $[x_t, y_t, z_t]$ and point $[x_i, y_i, z_i]$. If we know certain components of magnetic field we can obtain the current density distribution. If we would like to obtain the *NE* values of K_x and K_y components of surface current density $\mathbf{K}$, we have to known for example the same number of B_x and B_y components of magnetic field

$$B_{ix} = \frac{\mu_0}{4\pi} \sum_{j=1}^{NE} R_{ijz} \frac{\Delta S_j}{R_{ij}^3} K_{jy}, \quad B_{iy} = -\frac{\mu_0}{4\pi} \sum_{j=1}^{NE} R_{ijz} \frac{\Delta S_j}{R_{ij}^3} K_{jx}, \quad i = 1, \ldots, NE$$

The matrix notation for these $2 \cdot NE$ algebraic equations is

$$\begin{bmatrix} B_{koefx} & 0 \\ 0 & B_{koefy} \end{bmatrix} \begin{bmatrix} K_x \\ K_y \end{bmatrix} = \begin{bmatrix} B_x \\ B_y \end{bmatrix} \quad \Leftrightarrow \quad \mathbf{B}_{koef}\mathbf{K} = \mathbf{B} \tag{6}$$

From system (6) we can obtain very easy wanted current density distribution

$$\mathbf{K} = \mathbf{B}_{koef}^{-1}\mathbf{B} \tag{7}$$

In the following part is shown an example of the magnetic field distribution and the corresponding surface current density distribution and the influence of the nonhomogeneity inside tested samples.

The current density is calculated on each element by means of superposition of the outside magnetic field values. We suppose that the current density is constant on elements. The created objective function for the minimization by the least squares method for a conductivity image reconstruction is

$$\Psi(\sigma) = \frac{1}{2} \sum \|\mathbf{J}_M - \mathbf{J}_{FEM}(\sigma)\|^2 + \alpha \|\mathbf{R}\sigma\|^2, \tag{8}$$

where σ is the unknown conductivity distribution vector in the object, J_M is the vector of calculated surfaces current density from measured magnetic flux components outside sample, $J_{FEM}(\sigma)$ is the vector of computed current density in respect to σ which can be obtained using finite element method, α is a regularization parameter and $\mathbf{R}$ is a regularization matrix connecting adjacent elements of the different conductivities.

3. DESCRIPTIONS OF TESTED MODELS

Numerical models were built in Matlab. Numerical models consists of 210 elements and 122 nodes. The linear triangles elements were used for numerical analysis. The FEM grid is shown in Fig. 1. The current electrodes were placed on boundary of investigated sample. Current electrodes are shown in Fig. 1. (green triangles). The current value was adjust to $I = 1\,\mathrm{A}$. There were defined two values of conductivity for the model. The first material has conductivity 56 MS/m (copper) and the second one has 1 pS/m (crack). There were defined regions with different conductivity inside (non-homogenous regions). There is one non-homogenous region in the first and two non-homogenouin the second model. There are location of non-homogenous regions in these models. The noise has been pushed in the models. Results of noise influence analysis were examined in all of the three models. We can see the conductivity distribution for both models in Fig. 2.

Magnetic flux density components were computed by Biot-Savart law. The noise has been added. Noise magnitudes were 0.5%, 1%, 2%, 3%, 5% and 10% of magnetic flux component values.

4. NUMERICAL SIMULATIONS

Results of numerical simulations are presenting in this part. The components of magnetic flux density were computed 1 mm above the samples. Distribution of magnetic flux components for sample 2 is in Fig. 3.

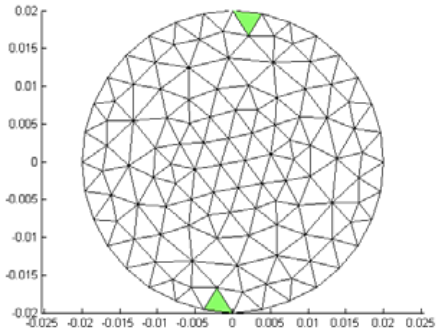

Figure 1: FEM grid with 210 elements and 122 nodes.

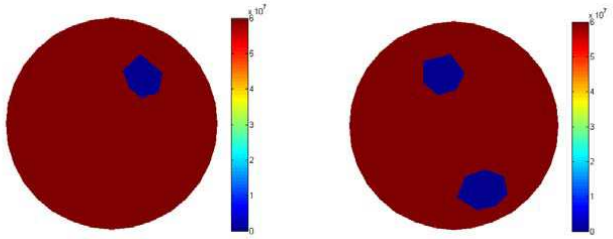

Figure 2: Original conductivity distribution (a) sample 1 and (b) sample 2.

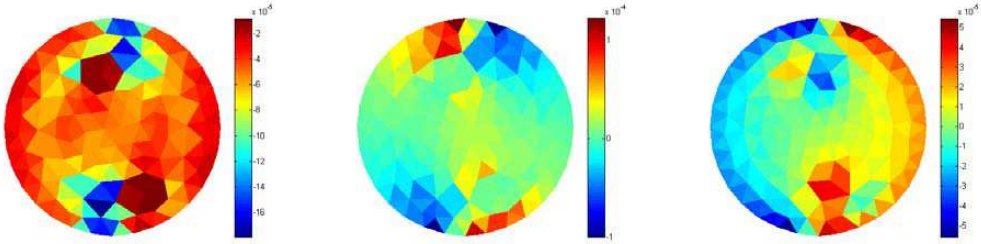

Figure 3: Magnetic flux density components B_x, B_y and B_z — sample 1.

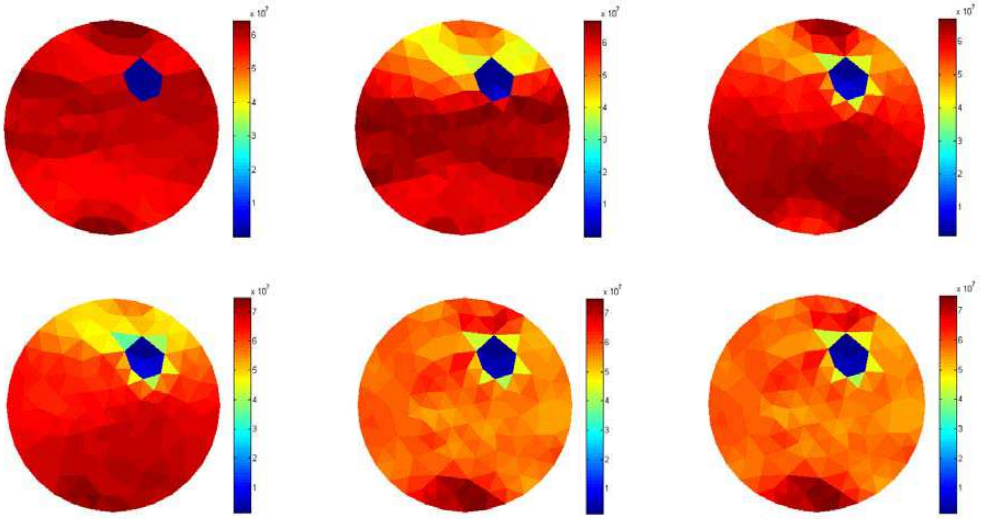

Figure 4: Final value of conductivity for noise 0.5%, 1%, 2%, 3%, 5% and 10% — sample 2.

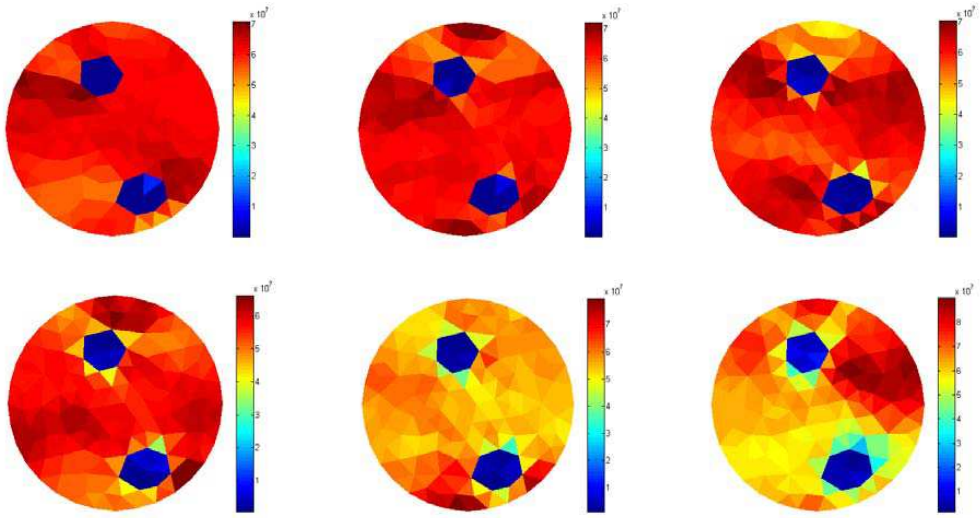

Figure 5: Final value of conductivity for noise 0.5%, 1%, 2%, 3%, 5% and 10% —- sample 1.

The results of calculated conductivity for sample 1 are shown in Fig. 4. This results are for different noise level (0.5%, 1%, 2%, 3%, 5% and 10%). Smallest noise 0.5% is in figure in firs row and first column and 10% noise is in second row and third column.

The results of calculated conductivity for sample 1 are shown in Fig. 4. This results are for different noise level (0.5%, 1%, 2%, 3%, 5% and 10%). Smallest noise 0.5% is in figure in firs row and first column and 10% noise is in second row and third column.

5. CONCLUSIONS

Noise influence were tested to conductivity reconstruction from magnetic field based on EIT in the paper. If the noise level is less than 5% algorithm for conductivity reconstruction can be used to determinate conductivity value and position of non-homogenous region. If the noise level is higher than 5% algorithm can be used only for location of non-homogenous regions.

ACKNOWLEDGMENT

The research described in the paper was financially supported by project of the BUT Grant Agency FEKT-S-11-5/1012 and projekt CZ.1.07.2.3.00.20.0175, Elektro-výzkumník.

REFERENCES

1. Vladingerbroek, M. T. and J. A. Den Boer, *Magnetic Resonance Imaging*, Springer-Verlag, Heidelberg, Germany, 1999, ISBN 3-540-64877-1.
2. Borsic, A., "Regularization methods for imaging from electrical measurement," Ph.D. Thesis, Oxford Brookes University, 2002.
3. Zhang, X., D. Yan, S. Zhu, and B. He, "Noninvasive imaging of head-brain conductivity profiles," *IEEE Engineering in Medicine and Biology Magazine*, Vol. 27, No. 5, 78–83, 2008.
4. Seo, J. K., O. Kwon, and E. J. Woo, "Magnetic resonance electrical impedance tomography (MREIT): Conductivity and current density imaging," *Journal of Physics: Conference Series*, Vol. 12, 140–155, 2005.

Electric and Magnetic Components of Waves on the Interface

R. Kadlec, **E. Kroutilová**, **and P. Fiala**
Department of Theoretical and Experimental Electrical Engineering
Brno University of Technology, Kolejní 2906/4, Brno 612 00, Czech Republic

Abstract— The paper presents an analytic solution of propagation, reflection and refraction of broadband electromagnetic signals on field of multilayer optical materials in Matlab program, which is suitable for specific purposes of detail analysis of a general issue.

Generally, the inhomogeneities and regions with different parameters appear even in the cleanest materials. During the electromagnetic wave passage through a material there occur an amplitude decrease and the wave phase shift, owing to the material characteristics such as conductivity, permittivity, or permeability. If a wave impinges on an inhomogeneity, a change of its propagation there occurs. This change materializes in two forms, namely the reflection and refraction. In addition to this process, polarization and interference may appear in the waves. The paper includes a theoretical analysis and references to the generated algorithms, which are verified using numerical models. Numerical models are applied to facilitate the calculation process, and a wide range of programs like ANSYS, Comsol.

The paper deals with the problem of complex angle of refraction in the losing medium. Methods describe in this paper are suitable for the analysis of beam refraction to the other side from the perpendicular line during the passage through the interface. This phenomenon is occur in metamaterials.

1. INTRODUCTION

Generally, inhomogeneities and regions with different parameters appear even in the cleanest materials. During the electromagnetic wave passage through a material there occur an amplitude decrease and a wave phase shift, owing to the material characteristics such as conductivity, permittivity, or permeability. If a wave impinges on an inhomogeneity, a change of its propagation there occurs. This change materializes in two forms, namely in reflection and refraction. In addition to this process, polarization and interference may appear in the waves.

Algorithms were generated in the Matlab program environment that simulates reflection and refraction in a lossy environment on the interface between two dielectrics. The reflection and refraction is in accordance with Snell's law for electromagnetic waves as shown in Figure 1 and Figure 2. The form of Snell's law is [1]:

$$\frac{\sin\theta_0}{\sin\theta_2} = \frac{\mathbf{k}_2}{\mathbf{k}_1} = \frac{\sqrt{j\omega\mu_2 \cdot (\gamma_2 + j\omega\varepsilon_2)}}{\sqrt{j\omega\mu_1 \cdot (\gamma_1 + j\omega\varepsilon_1)}}, \tag{1}$$

where $\mathbf{k}$ is the wave number, γ is the conductivity, ε the permittivity and μ the permeability. Relation (1) is defining for the boundary line between the dielectrics medium. Interpretation of the Fresnel equations and Snell's laws is simple in the case of the refraction on boundary line between the dielectrics medium. In case of refraction in a lossy medium, according to relation (1), angle θ_2 depends on wave numbers $\mathbf{k}_1$ a $\mathbf{k}_2$, which are generally complex; then, in medium 2 an inhomogeneous wave is propagated. An electromagnetic wave is understood as the electric field strength and the magnetic field strength.

For simplicity, we will analyze separately the $\mathbf{E}$ vector parallel to the interface (also known as TE wave) as shown in Figure 1 and $\mathbf{H}$ vector parallel to the interface (also known as TM wave) as shown in Figure 2. For **TE wave** and electric intensity of reflection beams and the intensity of refraction beams are expressed according to the formula:

$$\mathbf{E}_r = \mathbf{E}_1 e^{-jk_1\mathbf{u}_{n1}\times\mathbf{r}}, \quad \mathbf{E}_t = \mathbf{E}_2 e^{-jk_2\mathbf{u}_{n2}\times\mathbf{r}}, \tag{2}$$

where $\mathbf{E}_1$ is calculated from the intensity on boundary line $\mathbf{E}_0$ and reflection coefficient ρ_E, and $\mathbf{E}_2$ is calculated from the intensity on boundary line $\mathbf{E}_0$ and transmission factor τ_E. For numerical

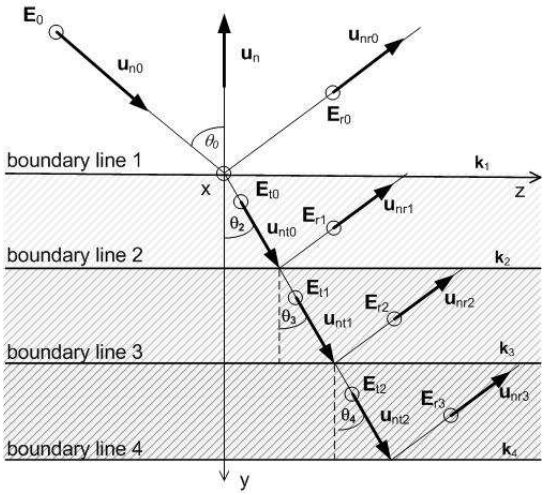

Figure 1: Reflection and refraction of electric component on a layered medium for TE wave.

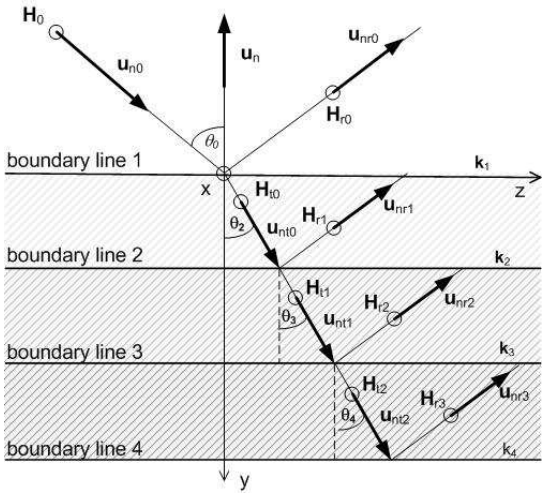

Figure 2: Reflection and refraction of magnetic component on a layered medium for TM wave.

modelling, there is a suitable relation in the form:

$$\begin{aligned}\mathbf{E}_r &= \frac{\mu_2 k_1 \cos\theta_0 - \mu_1\sqrt{k_2^2 - k_1^2\sin^2\theta_0}}{\mu_2 k_1 \cos\theta_0 + \mu_1\sqrt{k_2^2 - k_1^2\sin^2\theta_0}}\mathbf{E}_0 \cdot e^{-j\mathbf{k}_1\,\mathbf{u}_{n1}\times\mathbf{r}},\\ \mathbf{E}_t &= \frac{2\mu_2 k_1 \cos\theta_0}{\mu_2 k_1 \cos\theta_0 + \mu_1\sqrt{k_2^2 - k_1^2\sin^2\theta_0}}\mathbf{E}_0 \cdot e^{-j\mathbf{k}_2\,\mathbf{u}_{n2}\times\mathbf{r}}.\end{aligned} \tag{3}$$

These relations are calculated from the basic variable and they facilitate an acceleration of the calculation process. We use atypical formulas for calculating the magnetic components:

$$\begin{aligned}\mathbf{H}_r &= \frac{\frac{\mu_2}{\mu_1}\mathbf{k}_1 \cos\theta_0 - \sqrt{\mathbf{k}_2^2 - \mathbf{k}_1^2\sin^2\theta_0}}{\mu_2\cos\theta_0 + \frac{\mu_1}{\mathbf{k}_1}\sqrt{\mathbf{k}_2^2 - \mathbf{k}_1^2\sin^2\theta_0}}\frac{\mathbf{E}_0}{\omega} \cdot e^{-j\mathbf{k}_1\,\mathbf{u}_{n1}\cdot\mathbf{r}},\\ \mathbf{H}_t &= \frac{2\mathbf{k}_2 \cos\theta_0}{\mu_2\cos\theta_0 + \frac{\mu_1}{\mathbf{k}_1}\sqrt{\mathbf{k}_2^2 - \mathbf{k}_1^2\sin^2\theta_0}}\frac{\mathbf{E}_0}{\omega} \cdot e^{-j\mathbf{k}_2\,\mathbf{u}_{n2}\cdot\mathbf{r}}.\end{aligned} \tag{4}$$

Sometimes it is easier to deduce the magnetic component from the electrical component, according to these formulas:

$$\mathbf{H}_r = \frac{\mathbf{u}_{n1}\times\mathbf{E}_r}{\mathbf{Z}_{v1}}, \quad \mathbf{H}_t = \frac{\mathbf{u}_{n2}\times\mathbf{E}_t}{\mathbf{Z}_{v2}}. \tag{5}$$

Situation of incident of **TM wave** is shown in Figure 2. For TM wave and magnetic intensity of reflection beams and the intensity of refraction beams are expressed according to the formula:

$$\mathbf{H}_r = -\mathbf{H}_1 e^{-j\mathbf{k}_1\mathbf{u}_{n1}\cdot\mathbf{r}}, \quad \mathbf{H}_t = -\mathbf{H}_2 e^{-j\mathbf{k}_2\mathbf{u}_{n2}\cdot\mathbf{r}} \tag{6}$$

where $\mathbf{H}_1$ is calculated from the intensity on boundary line $\mathbf{H}_0$ and reflection coefficient ρ_H, and $\mathbf{H}_2$ is calculated from the intensity on boundary line $\mathbf{H}_0$ and transmission factor τ_H.

For numerical modelling, there is a suitable relation in the form:

$$\begin{aligned}\mathbf{H}_r &= -\frac{\mu_2\mathbf{k}_1\sqrt{\mathbf{k}_2^2 - \mathbf{k}_1^2\sin^2\theta_0} - \mu_1\mathbf{k}_2^2\cos\theta_0}{\mu_2\mathbf{k}_1\sqrt{\mathbf{k}_2^2 - \mathbf{k}_1^2\sin^2\theta_0} - \mu\mathbf{k}_2^2\cos\theta_0}\mathbf{H}_0 \cdot e^{-j\mathbf{k}_1\,\mathbf{u}_{n1}\cdot\mathbf{r}},\\ \mathbf{H}_t &= -\frac{2\mu_1\cos\theta_0}{\mu_2\mathbf{k}_1\sqrt{\mathbf{k}_2^2 - \mathbf{k}_1^2\sin^2\theta_0} + \mu_1\mathbf{k}_2^2\cos\theta_0}\mathbf{E}_0 \cdot e^{-j\mathbf{k}_2\,\mathbf{u}_{n2}\cdot\mathbf{r}}.\end{aligned} \tag{7}$$

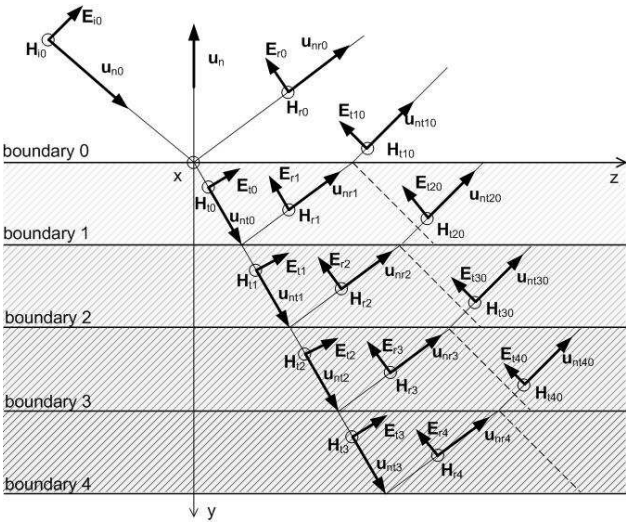

Figure 3: Reflection and refraction of electromagnetic wave on a layered medium for TM wave.

These relations are calculated from the basic variable and they facilitate an acceleration of the calculation process. Sometimes it is easier to deduce the electric components from magnetic components according to these relations:

$$\mathbf{E}_r = \mathbf{Z}_{v1}(\mathbf{H}_r \times \mathbf{u}_{n1}), \quad \mathbf{E}_t = \mathbf{Z}_{v2}(\mathbf{H}_t \times \mathbf{u}_{n2}) \tag{8}$$

2. ELECTROMAGNETIC WAVES IN LAYERED HETEROGENOUS MEDIA

For a layered heterogeneous medium, an algorithm is deduced for the reflection of electric component on several layers, according to Figure 1. The interpretation of propagation of electromagnetic waves on a layered heterogeneous medium is according to relation:

$$\mathbf{E}_{rl} = \mathbf{E}_{il}\rho_{El} \cdot e^{-j\mathbf{k}_l \mathbf{u}_{nrl} \times \mathbf{r}_l}, \quad \mathbf{E}_{tl} = \mathbf{E}_{il}\tau_{El} \cdot e^{-j\mathbf{k}_l \mathbf{u}_{nrl} \times \mathbf{r}_l}, \tag{9}$$

where $\mathbf{E}_{rl}$ a $\mathbf{E}_{tl}$ are the reflection and refraction electromagnetic waves on the boundary line ($l = 1, \ldots, \max$) according to Figure 3, $\mathbf{E}_{il}$ is the amplitude electric field strength on boundary line l, ρ_{El} a τ_{El} are the reflection coefficient and transmission factor on boundary line l, $\mathbf{k}_l$ is the wave number of layer, $\mathbf{r}_l$ is the electromagnetic wave positional vector on boundary line l, $\mathbf{u}_{ntl}$ and $\mathbf{u}_{nrl}$ are the unit vectors of propagation direction.

Magnetic component of electromagnetic waves is deduced for the reflection on several layers, according to Figure 2. The interpretation of propagation of electromagnetic waves on fist layer is according to relation:

$$\mathbf{H}_{r0} = -\mathbf{H}_{i0}\rho_{H0} \cdot e^{-j\mathbf{k}_1 \mathbf{u}_{nr0} \times \mathbf{r}_0}, \quad \mathbf{H}_{t0} = -\mathbf{H}_{i0}\tau_{H0} \cdot e^{-j\mathbf{k}_2 \mathbf{u}_{nr0} \times \mathbf{r}_0}. \tag{10}$$

By modifying the relation for the layer number l (as shown Figure 2) we obtain the relation:

$$\mathbf{H}_{rl} = -\mathbf{H}_{il}\rho_{Hl} \cdot e^{-j\mathbf{k}_{l+1} \mathbf{u}_{nrl} \times \mathbf{r}_l}, \quad \mathbf{H}_{tl} = -\mathbf{H}_{il}\tau_{Hl} \cdot e^{-j\mathbf{k}_{(l+2)} \mathbf{u}_{nrl} \times \mathbf{r}_l}, \tag{11}$$

where $\mathbf{H}_{rl}$ a $\mathbf{H}_{tl}$ are the reflection and refraction magnetic component of electromagnetic waves on the boundary line ($l = 1, \ldots, \max$) according to Figure 2, $\mathbf{H}_{il}$ is the amplitude magnetic field strength on boundary line l, ρ_{Hl} a τ_{Hl} are the reflection coefficient and transmission factor on boundary line l, $\mathbf{k}_l$ is the wave number of layer, $\mathbf{r}_l$ is the electromagnetic wave positional vector on boundary line l, $\mathbf{u}_{ntl}$ and $\mathbf{u}_{nrl}$ are the unit vectors of propagation direction. Figure 3 shows both components of the electromagnetic wave for the reflection on several layers.

3. CONE TRASE METHOD

Figure 5 shows that the wave reflected from a layered medium generates a large number of waves on the surface of the media. The calculation according to non-simplified ray-tracing method (as shown in Figure 4) is too cumbersome. One of the possible methods of simplification is cone trace

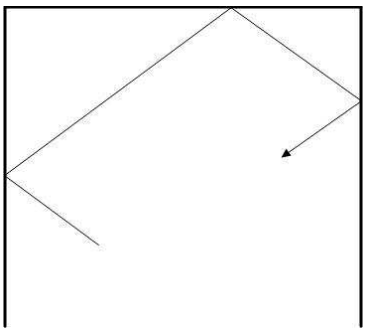

Figure 4: Simple ray trace method [2].

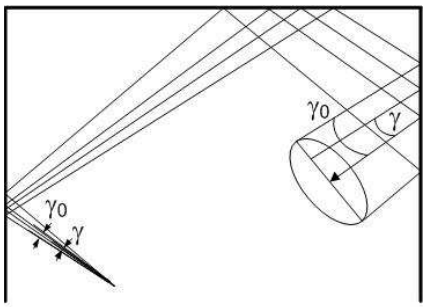

Figure 5: Cone trace method and angles used for calculating gain within cone.

method [2] (as shown in Figure 5). The cone trace method was developed in an attempt to maintain the simplicity of the ray trace model for higher-order reflections, while ensuring that lower-order reflections were not omitted due to quantization of the angular directions of the wave radiation. In this procedure, rather than using discrete rays emanating from the wave source at specific angles, a series of H overlapping cones are calculated with a gain function which is dependent on the relationship between the angular spread of the cone:

$$\gamma_0 = 1.05\sqrt{\frac{4\pi}{H}} \tag{12}$$

and the location of the receiver at angle γ. This gain, G_γ is calculated using equation:

$$G_\gamma = \cos^2\left(\frac{\gamma}{\gamma_0}\right). \tag{13}$$

4. CONCLUSIONS

The paper includes a theoretical analysis and references to the generated algorithms, which are verified using numerical models. Analytic solution of propagation, reflection and refraction of wideband electromagnetic signals on field of multilayer optical materials in Matlab program is very time demanding, according to Figure 3 which shows both components of the electromagnetic waves.

This method is suitable for specific purposes of detail analysis of general issue. Algorithms created in the Matlab environment are verified by the help of programs based on the finite element method, namely programs such as Comsol and ANSYS.

Methods describe in this paper are suitable for analysis of beam refraction to the other side from the perpendicular line during the passage through the interface. This phenomenon is occur in metamaterials.

ACKNOWLEDGMENT

The research described in the paper was financially supported by the research program of Ministry of Industry and Trade of the CR (Diagnostics of Superfast Objects for Safety Testing, FR-TI1/368), Czech Science Foundation (102/09/0314), project of the BUT Grant Agency FEKT-S-11-5/1012 and project from Education for Competitiveness Operative Programme CZ.1.07.2.3.00.20.0175, (Electro-researcher).

REFERENCES

1. Dedek, L. and J. Dedková, *Elektromagnetismus, 2*, 232, VITIUM, Brno, 2000, ISBN 80-214-1548-7.
2. Martin, G. G., "A hybrid model for simulating diffused first reflections in two-dimensional acoustic environments," Ph.D. Thesis, Faculty of Music, McGill University, 2001.
3. Kadlec, R., P. Fiala, and D. Nespor, "Electromagnetic wave propagation in heterogeneous structures," *PIERS Online*, Vol. 6, No. 7, 613–616, 2010.
4. Fiala, P., R. Kadlec, and P. Drexler, "Tuned periodical structures in THz band applied in safety applicatins," *PIERS Proceedings*, 1500–1504, Xi'an, China, March 22–26, 2010.

Mixed Signal Processing for Cable Diagnostics

M. Hadinec
Department of Theoretical and Experimental Electrical Engineering
Brno University of Technology, Kolejní 2906/4, Brno 612 00, Czech Republic

Abstract— Aging of cables is important problem for manufactures of cars, planes and power distribution systems. This topic is highly desired in many industry branches, where aging of cable insulation is a serious problem, especially in point of view of reliability. It is also common problem in telephone cables, where it is important to locate water failures or just to find topology of network. There are many reflectometry methods for locating of open or short circuits at the end of wire, but it is very complicated to detect small anomalies caused by water or other aging of wire isolation. This article describes principles of present frequency domain reflectometry (FDR) methods and time domain reflectometry (TDR) methods, which are compared, advantages or disadvantages are discussed. Experimental part of the article deals with locating of cable failures using TDR techniques, which are compared to the PSpice or Microcap simulations. The small anomalies are then implemented into the measured cable and studied with FDR method. The experiment is based on mixed signal reflectometry method, where measured DC voltage is extracted from the sum of incident and reflected sine waves. The advantage of this method is low demand for measuring circuit hardware, but it has quite high demands for post-processing of results. The measuring is automated by HP-VEE, obtained values are processed with FFT in Matlab. The detection of anomalies and accuracy of MSR method is discussed.

1. INTRODUCTION

The cables are subjected to a various stresses including electrical, mechanical, chemical or thermal stress. Each of these stresses can lead to many function errors, their localization and detection is difficult to recognize. For example, the thermal stress can lead to degradation of cable insulation, the chemical composition and physical morphology changes. These changes allow further degradation with water influence (so called water treeing). To prevent problems and to save repair expenses, there is need for diagnostic technique, which could identify the faults on the cable and recognize the location of these faults. Present localization methods are able to locate hard defects (open or short), but it seems to be very difficult to locate small anomalies or defects, which are caused by degradation of insulation (water) or just mechanically. These soft failures are especially dangerous, because their occurrence is in most cases unpredictable. The other demand laid on cable diagnostics is non-destructivity. There is lots of cable diagnostic approaches [1, 2], but most of them are either destructive or need special laboratory environment. It is obvious, that non-destructive electrical based techniques are the most effective and desirable for cable diagnostics. In the present state, it is possible to categorize methods as time domain analysis methods (TDR) [3], frequency domain analysis methods (FDR) [4] or joint-time frequency analysis methods (JTFDR) [5].

2. REFLECTOMETRY METHODS DESCRIPTION

The exact classification of reflectometry methods is quite difficult task, because there are many specialized subsets of methods, based on TDR or FDR principles. The main idea of TDR is quite simple. A properly shaped electrical pulse is sent through the cable and any discontinuity of impedance generates a reflection. The impedance of fault can be measured by reflected pulse amplitude and the time delay is used for location of fault. The longer the wire, the bigger energy has to be transmitted. The reflection can be characterised by well known reflection coefficient defined as

$$K = \frac{Z_r - Z_0}{Z_r + Z_0} \tag{1}$$

where Z_0 is the characteristic impedance of the cable and Z_r is the impedance of the fault. In theory, it seems to be easy to locate soft faults, but in practice it is very difficult to separate small reflections from the noise or to recognize reflections due to insulation degradation from mechanical parameters of metallic cable core, which are caused by manufacturing tolerances. Another TDR common problem is the interpretation of multiple faults and multiple reflections on single cable. Generally, the TDR method is usable to located harder faults, requires professional experience to interpret the results and the whole measuring system is not small smart package. The advantage of TDR

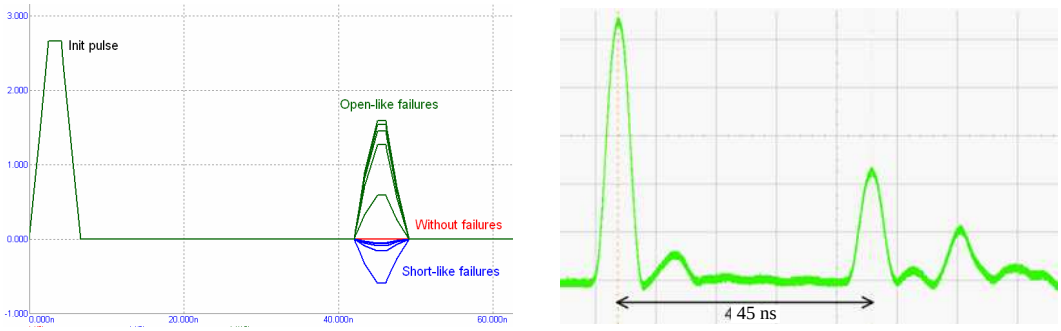

Figure 1: Microcap TDR and measuring TDR comparison.

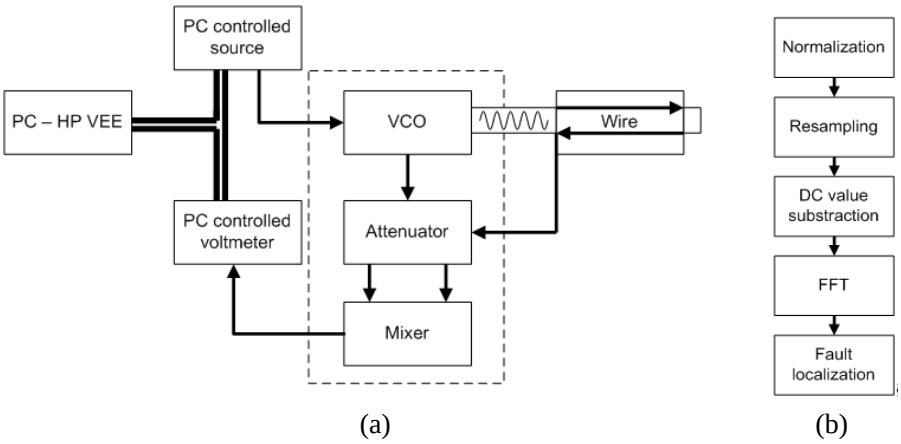

Figure 2: (a) System diagram and (b) post-processing diagram.

methods is the fact, that results can be easily simulated in PSpice or Microcap circuit simulators, which provide models of transmission lines based on RLCG parameters. These simulations provide a possibility to estimate RLCG cable parameters from comparison of measured and simulated pulses, as can be seen on Fig. 1.

The FDR method uses a set of properly stepped-frequency sinusoidal signals as the incident signal, which enables a very good frequency localization ability. The bandwidth of FDR methods is smaller in opposite to TDR. This leads to smaller distortion of reflected signal, but the defect must be exhibited at the impedance spectrum. The impedance spectrum is converted from the frequency domain into the time domain via the inverse Fourier transform [6]. The incident and reflected signals have to be separated by couplers, which can cause unwanted attenuation of signals. Therefore, the FDR systems usually contain of couplers, amplifiers and impedance matching components.

JTFDR methods combine the advantages of TDR and FDR methods. The type of incident signal has to be customized according to type of cables and post-processing. The reflected signal is received and localized in the time and frequency domains simultaneously. It is necessary to consider centre frequency of the reference signal (higher frequencies leads to bigger attenuation, but we get higher spatial resolution), frequency bandwidth (higher bandwidth leads to higher resolution) and time duration of the signal (the shorter reference signal duration enables measuring of shorter cables).

3. MIXED SIGNAL REFLECTOMETRY METHOD DESCRIPTION

The separation of incident and reflected signal is necessary in most FDR methods. However, the directional couplers are expensive instruments, which also require quite good impedance matching with measuring cables. There are also problems with high attenuation of measured signals. The mixed signal reflectometry method [7] is based on mixing the incident and reflected sine waves, which are then analyzed in PC. If the transmitted harmonic signal is $\sin(wt)$, then the reflected signal will be $\alpha(\tau)K\sin(\omega t+\tau)$, where ω is frequency of VCO, $\alpha(\tau)$ is attenuation of cable, τ is

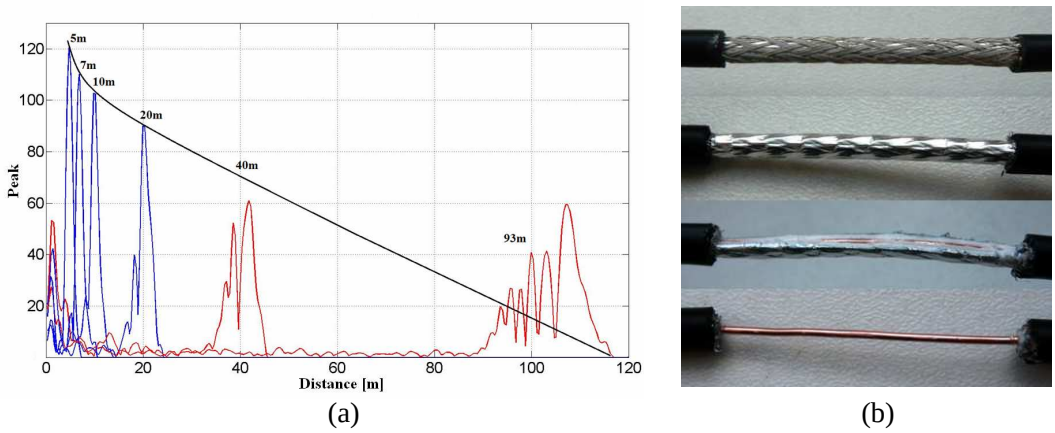

Figure 3: (a) System responses for different cable lengths (cable RG-58U), (b) artificial faults on cables.

time delay for cable loop. Signal for mixer is described as

$$A[\sin(\omega t) + \alpha(\tau)K\sin(\omega(t+\tau))]. \tag{2}$$

The output signal from mixer is described as sum of transmitted and reflected signal as

$$\begin{aligned} &\{A[\sin(\omega t) + \alpha(\tau)K\sin(\omega(t+\tau))]\}^2 \\ &= A^2\Bigg\{\left[\frac{1}{2}\left(1+\alpha^2(\tau)K^2\right) + \alpha(\tau)K\cos(\omega\tau)\right] \\ &\quad -\frac{1}{2}\left[\cos(2\omega t) + \alpha^2(\tau)K^2\cos(2\omega(t+\tau)) + 2\alpha(\tau)K\cos(2\omega t+\omega\tau)\right]\Bigg\}. \end{aligned} \tag{3}$$

This equation contains variables which has frequency equal to one two times bigger than frequency of the transmitted signal and DC value given by

$$A^2\left[\frac{1}{2}\left(1+\alpha^2(\tau)\mathrm{K}^2\right) + \alpha(\tau)K\cos(\omega\tau)\right]. \tag{4}$$

This signal will be measured by voltmeter, which contains A/D convertors, which can be described like low band filters. Therefore, we will measure only DC value. These values are function of VCO frequency.

The frequency of measured trace is in scale to time delay τ. After removing DC value from signal (4), and FFT transform of the signal (Blackmann windowing), we should see peaks corresponding to faults or reflections from the end of line.

4. FAULT DETECTION AND FAULT LOCALIZATION

For experiments, we used coaxial cable RG-58U, characteristic impedance of cable is 50 Ω and maximum length of cable was 53 m. First, we used the measuring system just for detecting the end of cable, which was open ended. As can be seen from Fig. 3(a), the system was able to measure cables up to 40 m with satisfactory precision, but the result of the longest cable is mismatch. The longer cable is measured, the more attenuated peaks are obtained. In this situation the maximum measurable cable length was approximately around 80 m.

Next experiments were performed with artificial faults on cable, as can be seen on Fig. 3(b). The cable was 40 m long, the faults were localized at distance 10 m from measuring system. The end of cable was open-ended.

On the Fig. 4(a) we can see peaks situated only on the beginning of the measured cable and at distance 40 m, because there are reflections from cable connectors and open end of the cable. When we removed part of the cable shielding at distance 10 m, the peak on the beginning of cable disappeared and there is a very small peak around 10 m distance (Fig. 4(b)). When we removed the shielding completely, there is a very big peak at 10 m, but the peak from the end of cable disappeared. There is also a peak around 20 m, which shouldn't be there. When the failure

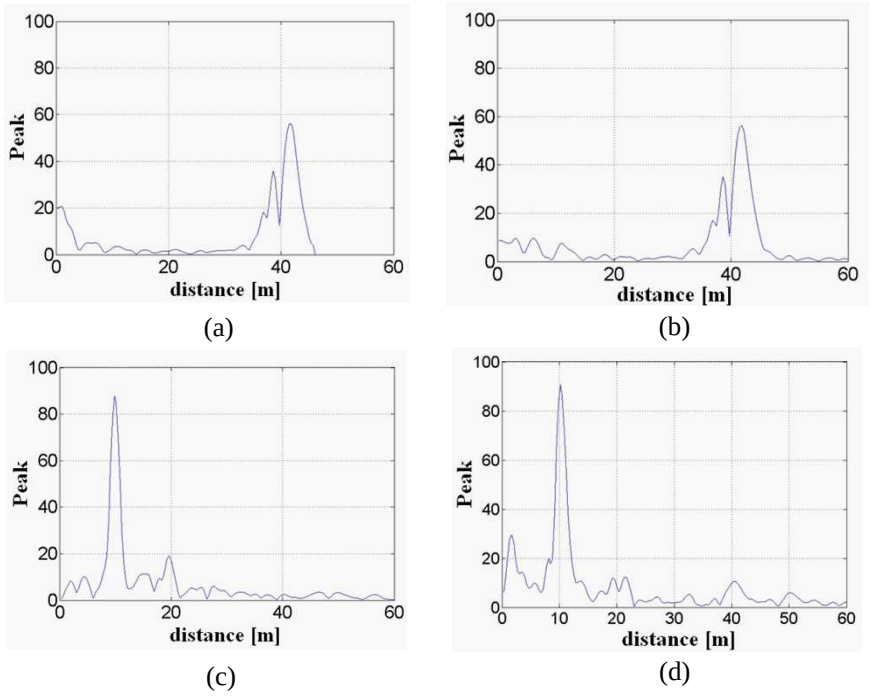

Figure 4: Fault localization results for (a) cable without failure, (b) cable without part of shielding at 10 m, (c) cable without shielding at 10 m, (d) cable without shielding at 10 m inserted into the water.

was inserted into the water, we can see, that transmission of signal is better and there are more reflections at corresponding distances. However, it seems to be quite difficult to locate soft failures of isolation or scratches on shielding.

5. CONCLUSIONS

The brief description of present TDR and FDR principles was presented. The method based on mixing transmitted and reflected harmonic signals of different frequencies was presented and experimental measuring system with RG-58U cable was tested. The obtained signals are processed in Matlab. The calculation of cable lengths based on detection of open-ended cables using mixed signals was presented. The possibility of localization the different artificial faults was tested on RG-58U cable. The method of mixing transmitted and reflected harmonic signals seems to be used for harder faults localization, the soft faults are still difficult to locate.

ACKNOWLEDGMENT

This work was supported within project from Education for Competitiveness Operative Programme CZ.1.07.2.3.00.20.0175 and project of the BUT Grant Agency FEKT-S-11-5/1012.

REFERENCES

1. Cygan, S. P. and J. R. Laghari, "Effects of multistress aging (radiation, thermal, electrical) on polypropylene," *IEEE Transcations on Nuclear Science*, Vol. 38, No. 3, 906–912, 1991.
2. Leguenza, E. L., R. Robert, and J. A. Giacometti, "Dielectric and viscoelastic properties of cross-linked polyethylene aged under multistressing conditions," *IEEE Transactions on Dielectric and Electric Insulation*, Vol. 11, No. 3, 406–417, 2004.
3. Meltzer Hansen, B., J. Ranvholt Ovesen, and K. Kolle, "Characteristics measurements using TDR and modelling of the transmission channel," *IEEE International Symposium on Power Line Communications and Its Applications, ISPLC' 07*, 319–323, March 26–28, 2007.
4. Dodds, D. E. and T. Fretz, "Parametric analysis of frequency domain reflectometry measurements," *Canadian Conference on Electrical and Computer Engineering CCECE 2007*, 1034–1037, April 22–26, 2007.
5. Wang, J., P. E. C. Stone, Y.-J. Shin, and R. A. Dougal, "Application of joint time-frequency domain reflectometry for electric power cable diagnostics," *IET Signal Processing*, Vol. 4, No. 4, 395–405, August 2010.

6. De La Torre, B. C., "DSL line tester using wideband frequency domain reflectometry," online, Saskatoon, 2004, Available at: http://library.usask.ca/theses/available/etd-07052006-094509/unrestricted/b_celaya.pdf.
7. Tsai, P., L. Chet, C. C. You, and C. Furse, "Mixed-signal reflectometer for location of faults on aging wiring," *IEEE Sensors Journal*, Vol. 5, No. 6, 1479–1482, December 2005.

Light Scattering from Nanostructured Media

Gerard Berginc
Thales Optronique, France

Abstract— In this paper, we present some considerations concerning the field of nanophotonics. The light scattering from random structures is discussed. The consequences of the nanostructure of thin films on their optical properties are also described. This last problem is described by random volume and surface scattering. Useful phenomena in the optical range can be produced by random media with randomly rough surfaces. Designing these disordered slabs with rough surfaces can produce new optical components, which can transmit or scatter optical field with specified angular, spatial or spectral properties.

1. INTRODUCTION

New formulations have been developed for a three-dimensional disordered medium with randomly rough interfaces [1, 2]. This structure can describe a device based on metallic nano-particles embedded in insulators or dielectric media. We present a theory of transport based on the Bethe-Salpeter equation. For a three-dimensional system composed of a random medium bounded by two randomly rough surfaces, the Bethe-Salpeter equation is constructed in order that the medium and the boundaries are treated on the same footing. With this unified Bethe-Salpeter equation, a general expression is obtained, whatever the choice of the scattering operators used at the boundaries. The calculation of the intensities scattered by the considered structure for the ladder and most-crossed contributions is given by a Green tensor. Diagrammatic expansions are very useful for investigation of mesoscopic effects. These calculations were performed with the Mueller matrices taking into account the different polarization components. For 3-dimensional slabs with nanoscale roughness and nano-particles, the enhanced backscattering is produced by different mechanisms, the wave scattering by the same boundary, the wave coupling by the two boundaries or the wave scattering by the nano-particles. The different simulations can give some experimental conditions and specifications to realize highly integrated optical devices that use metallic or metallo-dielectric nanoscale structures.

2. SPECIFIC INTENSITY

The main characteristic we must study for the scattering from a random slab is the specific intensity $\boldsymbol{\mathcal{I}}(\boldsymbol{R}, \boldsymbol{k})$. If we take into account the polarization of the wave, the specific intensity is defined as a Stokes vector or a tensor which gives the intensity at the point $\boldsymbol{R}$ in the direction $\hat{\boldsymbol{k}}$. If particles are inside a slab with a permittivity different from the outside medium, boundaries condition must be added to the radiative transfer equation in order to calculate the specific intensity. For rough surfaces, these boundaries condition are expressed in function of scattering operators, where several approximate analytical expressions exist depending on the roughness of the surface. It can be shown that the specific intensity can be deduced from the Wigner function of the electrical field. After having determined the relation between the electromagnetic field and the specific intensity, we can derive the radiative transfer equation from the Maxwell equations. The procedure is to write the Maxwell equations in an integral form with the help of Green functions and to apply the Wigner transform to the equation obtained. The main advantage to start from wave equations is that we are able to take into account new contributions to the scattered intensity such as the enhanced backscattering and the correlations between the scatterers that cannot be obtained from phenomenological radiometric considerations. The objective of this paper is to derive the radiative transfer equations from the wave equations in taking into account rough boundaries. In our approach, we use scattering operators which are a unified way to describe how electromagnetic waves interact with scatterers and boundaries. To use these operators, we have introduced two kinds of Green functions. The first one $\bar{\boldsymbol{G}}_{SV}$ describes the field scattered by the volume (V), which contains the scatterers, and by the rough surfaces (S). The second type of Green function is $\bar{\boldsymbol{G}}_{S}$, which gives the field scattered by a slab with rough boundaries where the scatterers have been replaced by an homogeneous medium described by an effective permittivity. With these Green functions, we can separate the contributions of the surfaces and the volume. The Quasi-Crystalline Coherent Potential Approximation (QC-CPA) is taken into account for the contribution of the random medium, which

is made of spherical nanoparticles of given permittivity in a homogeneous dielectric background medium. The main advantage of our approach is that the equation obtained are similar to the equations generally used to describe the wave scattered by an infinite random medium. For a random layer with rough interfaces, the incoherent specific intensity can be decomposed into four parts.

$$\bar{\boldsymbol{I}}^{incoh} = \bar{\boldsymbol{I}}^{incoh}_{L=0} + \bar{\boldsymbol{I}}^{incoh}_{L=1} + \bar{\boldsymbol{I}}^{incoh}_{Ladder} + \bar{\boldsymbol{I}}^{incoh}_{Crossed}\,, \tag{1}$$

The first term $\bar{\boldsymbol{I}}^{incoh}_{L=0}$ gives the scattering by the slab with rough boundaries and defined by an effective permittivity ϵ_e given by the QC-CP approximation [1]. In order to take into account scattering effects, quantum multiple scattering theory has been transposed in the electromagnetic case , but as a rigorous analytical answer is unreachable, several approximation schemes have been developed. One of the most advanced is the Quasicrystalline Coherent Potential Approximation (QC-CPA) which takes into account the correlation between the particles to determine ϵ_e, we use the fact that the effective medium is not spatially dispersive, it can be shown, using a diagrammatic technique, that the coherent part of the field $< \bar{\boldsymbol{E}} >_V$ which propagates inside an infinite random medium behaves as a wave in an homogeneous medium with a renormalized effective permittivity.

The Quasi-Crystalline Approximation (QCA) is strictly valid when the particles have a fixed position, as in a crystal. The quasi-crystalline approximation is equivalent to neglect the fluctuation of the effective field on a particle located at r_j, due to a position deviation of a particle located at r_i from its average position.

Under the (QC-CPA) approach, for Rayleigh scatterers, an approximate formula for ϵ_e can generalize the usual Maxwell-Garnett formula. We can also obtain an approximate formula for the effective permittivity, which contains the Maxwell-Garnett formula and the Keller approximation. The main result is that we have a tractable formula for the effective permittivity.

The equation of ϵ_e is given by the following expression:

$$\epsilon_e = \epsilon_1 + \frac{3(\epsilon_d - \epsilon_1)\,\epsilon_e\, f_{vol}}{(\epsilon_d - \epsilon_1)\left(1 - f_{vol} - \frac{2\,\mathrm{i}}{3}\,(K_{vac}\,r_d)^3\,\epsilon_e^{3/2}\,w\right) + 3\,\epsilon_e}\,, \tag{2}$$

where ϵ_1 is the permittivity of the slab, ϵ_d the permittivity of the scatterers, f_{vol} the volume fraction of the scatterers and r_d the radius of the scatterers, K_{vac} is the vacuum wavenumber. The function w is the Percus-Yevick distribution.

$$w = \frac{(1 - f_{vol})^4}{(1 + 2\,f_{vol})^2}\,. \tag{3}$$

With a development at the first order of (2) we obtain:

$$\begin{aligned}\epsilon_e \;=\; \epsilon_1 &+ \frac{\epsilon_1(\epsilon_d - \epsilon_1)\,(1 - f_{vol}) + 3\epsilon_1\epsilon_e + 3(\epsilon_d - \epsilon_1)\epsilon_e - f_{vol}}{(\epsilon_d - \epsilon_1)\,(1 - f_{vol}) + 3\epsilon_e} \\ &+ 2\,\mathrm{i}\,\frac{(K_{vac}\,r_d)^3\,(\epsilon_d - \epsilon_1)^2 w\, f_{vol}\,\epsilon_e^{5/2}}{\left[(\epsilon_d - \epsilon_1)\,(1 - f_{vol}) + 3\epsilon_e\right]^2}\,.\end{aligned} \tag{4}$$

If we suppose that the real part of ϵ_e is larger than the imaginary part, we obtain an approximate solution of (4)

$$\begin{aligned}\mathrm{Re}(\epsilon_e) =& \frac{1}{6}\left[-\{(\epsilon_d - \epsilon_1)\,(1 - f_{vol}) - 3\epsilon_1 - 3(\epsilon_d - \epsilon_1) f_{vol}\} + \sqrt{\Delta}\right]\,, \\ \mathrm{Im}(\epsilon_e) =& 2\,\frac{(K_{vac}\,r_d)^3\,(\epsilon_d - \epsilon_1)^2 w\, f_{vol}\, Re(\epsilon_e)^{5/2}}{\left[(\epsilon_d - \epsilon_1)\,(1 - f_{vol}) + 3Re(\epsilon_e)\right]^2}\,,\end{aligned} \tag{5}$$

where

$$\Delta = \left[(\epsilon_d - \epsilon_1)\,(1 - f_{vol}) - 3\epsilon_1\epsilon_e + 3(\epsilon_d - \epsilon_1)\epsilon_e - f_{vol}\right]^2 + 12\epsilon_1(\epsilon_d - \epsilon_1)\,(1 - f_{vol})\,.$$

The second term $\bar{\boldsymbol{I}}^{incoh}_{L=1}$ is related to the first approximation where only one process of scattering by a particle is taken into account.

The two last terms $\bar{\boldsymbol{I}}^{incoh}_{Ladder}$ and $\bar{\boldsymbol{I}}^{incoh}_{Crossed}$ correspond respectively to the ladder approximation and the most-crossed approximation. Figures 1 and 2 show the different processes of scattering for the ladder and most-crossed approximations.

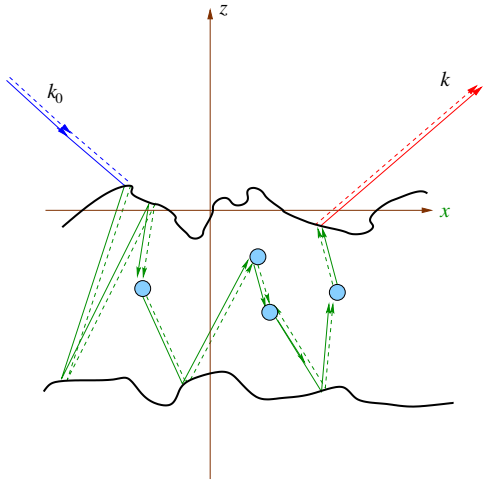

Figure 1: Scattering contributions of the ladder diagrams.

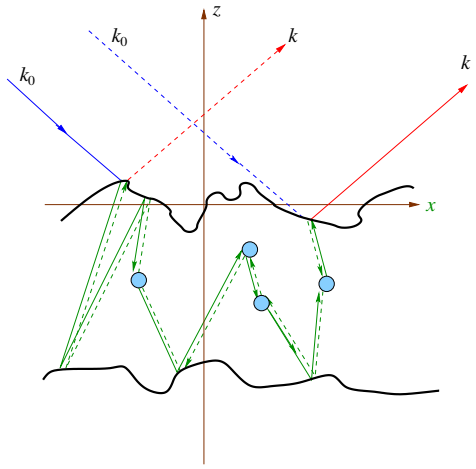

Figure 2: Scattering contributions of the most-crossed diagrams.

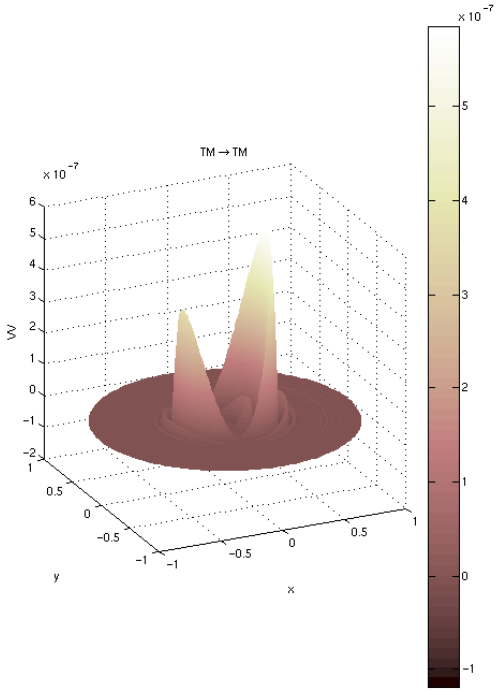

Figure 3: Three-dimensional profile of the TM-TM scattering coefficient.

3. SCATTERING FROM FILM WITH DISCRETE NANOPARTICLES

In this section, we study the coherent backscattering and the pattern of the cross-section from slabs illuminated by plane waves. This phenomenon produces a peak in the backscattering direction $\hat{\boldsymbol{k}} = \hat{\boldsymbol{k}}_0$ due to the interference of waves following the same path but in opposite directions in a scattering medium composed of fixed, randomly placed spherical scatterers as shown in the schematic illustration. We apply the theory of transport based on Bethe-Salpeter equations discussed in the previous sections. We obtained numerically the solutions of the cross-section involving laser light reflection from disordered samples in which coherent backscattering may directly be observed. We consider a dielectric slab with two plane interfaces. The depth of the layer is $H = 15\lambda$. The permittivity of the medium of the layer is $\epsilon_1 = 1.2$, this layer contains scatterers which are located randomly in the slab. The permittivity of the scatterers is $\epsilon_d = 2$, they are considered as spherical nanoparticles of radius $r_d = 0.035\lambda$. We consider a laser wavelength $\lambda = 632\,\text{nm}$. The fractional volume of scatterers is $f_{vol} = 0.01\%$. The layer is deposited on a semi-infinite medium

of permittivity $\epsilon_2 = 16$. The angle of incidence is $\theta_i = -20°$.

We can study the three-dimensional profile of the coherent backscattering. In Fig. 3, we plot the 3D TM-TM scattering coefficient. The axes of the figure represent $x = \sin\vartheta_d \cdot \cos\phi_d$, $y = \sin\vartheta_d \cdot \sin\phi_d$. An important point to be noted is that the three-dimensional profile of the coherent backscattering has a cylindrical pattern.

4. CONCLUSION

By starting from the Maxwell equations, we are able to give an unambiguous definition of the specific intensity as a function of the electric field, and thus clarify the meaning of this quantity. Furthermore, we can take into account the correlations between the scatterers by multiplying the scattering operator of one particle by a structure factor which is identical to those used to describe the scattering of X-rays by crystals. Finally, we have also incorporated the most crossed contributions in our theory to estimate the enhanced backscattering phenomenon.

REFERENCES

1. Soubret, A. and G. Berginc, "Electromagnetic wave scattering from a random layer with rough interfaces II: Diffusive intensity," arXiv: physics/0312136, 2003.
2. Berginc, G. and C. Bourrely, "Light scattering from 3-D nanoscale disordered media," *PIERS Online*, Vol. 6, No. 8, 730–734, 2010.

Technological Aspects of Obtaining Gradient Optical Metamaterial

O. D. Volpian[1], **A. I. Kuzmichev**[2], **and Yu. A. Obod**[3]

[1]Federal State Unitary Enterprise "M. F. Stelmakh Research Institute — Polyus"
Vvedensky Str. 3, Moscow 117342, Russian Federation
[2]Electron Device Department, National Technical University "Kiev Polytechnical Institute"
Pobedy Pr. 37, KPI-2230, Kiev 03056, Ukraine
[3]Scientific-Manufacturing Enterprise "Fotron-Auto Ltd."
Novodanilovskaya Naberezhnaya 8, Moscow 117105, Russian Federation

Abstract— Different technological approaches to fabrication of gradient metamaterials have been considered. Perspectives of applying the precisely controlled reactive pulse magnetron sputtering for obtaining gradient optical metamaterials/metacoatings are shown that is confirmed by obtaining excellent antireflection gradient coatings for visible and infrared light.

1. INTRODUCTION

Optical materials or media, which acquire unusual properties due to their micro- or nanostructure, are called today as optical and photonic metamaterials. These metamaterials are mostly manufactured by thin layers on substrates, therefore they present themselves as coatings (metacoatings). Thin film coatings are employed in optical apparatus and photonic devices practically of all types and for many years since namely they often provide spectral, energetic, polarization and spatial characteristics. The use of metacoatings can enhance parameters of mirrors, filters, polarizators, splitters and allow to create photon barriers, harmonic generators, optical sensors, plasmon optical antennas, subdiffraction superlenses, cloak of invisibility and other devices. The important application of optical metamaterials must be solar energetics.

Traditionally, the optical coating design is based on a multilayer with steeply alternating high n_h and low n_l refraction indexes and it presents interference system of a kind. Certain functional possibilities are given by another type of thin film systems based on gradient coatings, where the refraction index n is gradually, sometimes sinuously (for instance, as in rugate filters), varied in the coating media [1]. Accordingly, the branch of optics, where gradient media are used, is called as GRIN (gradient index) optics. Note, optical phenomena in bulk gradient medium (in the atmosphere) are known many years ago (XIX century, Rayleigh). The thickness of layers in the common interference systems is order of wave length λ. On the contrary, there is an interest in optical gradient coatings, as new metamaterials, with period of n variation less than λ [2]. Such coatings may be considered as nanogradient ones if the length of n variation ≤ 100 nm. The technology of obtaining the gradient optical coatings is of great interest today and will be considered in the given paper.

2. GENERAL CONSIDERATION

Gradient optical metamaterials may be divided into different sorts by the following features: kind of constitutive materials (metal, dielectric or composite), microstructure (discrete or continuous), length of n or ε, or μ variation (relatively λ and absolute value), dimension of gradient (1D, 2D or 3D) and direction of gradient (along what coordinate axis or axes and relatively the line of wave propagation).

The first gradient metamaterials (forming lenses) were the microwave composites for the GHz-frequency range on the base of split ring resonators (SRRs) [3]. Those were manufactured by printed circuit board technology and had the discrete structure of spatial "crystalline" array kind. The resonator parameters of mm-dimensions were changed in the radial direction that was transverse relatively the line of wave propagation. Hence, those metamaterials were $1D_r$ ones. The spatial array from SRRs with radial gradient of μ was built by the same technology for research of cloaking at frequency of ~ 10 GHz [4]. The analogous technology, but with higher resolution due to UV-lithography, was used in [5] for manufacturing the metamaterial-based gradient index lens for strong focusing in range near 1 THz. In this case, the discrete spatial structure was composed from annual slot resonators with dimensions ~ 20 μm. The resonators were etched in 200 nm thick copper layers on dielectric disk substrate. The lens contained 3 disks with resonators. The metamaterial was of $1D_r$ type.

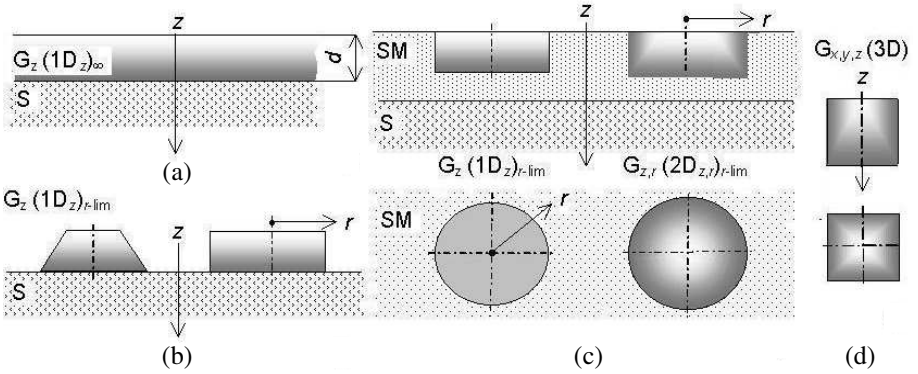

Figure 1: Optical structures with (a), (b), (c) longitudinal $1D_z$, (c) longitudinal/radial $2D_{z,r}$ and (d) 3D gradients. G — gradient layer, S — substrate, SM — medium, surrounding gradient layer, d — thickness of gradient layer, z — direction of wave propagation.

Gradient metamaterials with the discrete composite structure and the period of spatial array $p \ll \lambda$ for optical range, which described in literature, present virtual constructions and only on the paper; such "metamaterials" are used mainly for computer simulation of the invisibility cloak effect [6, 7]. This is explained by severe technological difficulties to fabricate spatial gradient composites with nanoscale dimensions of structure elements. However, there are gradient optical coatings with discrete nanostructures, which do not strictly meet the condition $p \ll \lambda$ for true metamaterials; rather they meet the condition $p < \lambda$ [8]. The latter coatings are formed by layers of random distributed dielectric nanorods inclined under different angles relatively substrate surface. The inclined nanorods are fabricated by GLAD (glancing angle deposition) technology with electron beam evaporation of source material [8]. Variation of n is obtained due to changing the deposition angle. Such metacoatings are proposed to use as antireflection ones. Unfortunately, they contain many voids; this leads to mechanical instability of the coatings and their sensitivity to environmental factors.

The gradient metacoatings with dense continuous structure without voids are more suitable for lasers and, moreover, their technology may be simpler. Fig. 1 presents several examples of such dense antireflection structures with longitudinal and transverse gradients. "Longitudinal gradient" means a gradient along wave propagation direction. In Fig. 1, the more dark tone corresponds to the bigger value of refraction index n.

Figure 1(a) depicts simplest gradient material $G_z(1D_z)_\infty$, which is not confined in the transverse direction, but Fig. 1(b) shows the same gradient material $G_z(1D_z)_{r\text{-lim}}$ as mesastructures with two variants of confining in the transverse direction. Fig. 1(c) depicts confined gradient materials immersed into a special medium SM (e.g., into photosensitive semiconductor material). Herein, the right structure in Fig. 1(c) of $G_{z,r}$ $(2D_{z,r})_{r\text{-lim}}$ type has $2D_{z,r}$ gradient and the incident wave goes simultaneously down to the substrate and to the side. Fig. 1(d) depicts the $3D_{x,y,z}$ gradient material for optoelectronic devices.

Distribution of index n along z-axis (and the others), and value of thickness d (Fig. 1(a)) depend on function of gradient material. For instance, in the case of antireflection coatings, as in Fig. 1, the function is the matching of air medium impedance with substrate material impedance and $n(z)$ profile is defined by a monotonic polynomial curve. For rugate notch filters, the distribution $n(z)$ is a sin-like function. For photon barrier, the profile of $n(z)$ is needed as it is shown in Fig. 2. Gradient material with transverse variation of n (e.g., along radius r) has focusing or defocusing effect (the right part of Fig. 1(c) relates to $n(z,r)$ with defocusing effect). The focusing effect is often employed in waveguide (fiber) optics and laser mirrors. The general advantage of employing gradient materials is the excellent media matching in wider ranges of λ and incident angles than in ordinary interference systems.

Thus, one can conclude that obtaining the gradient distribution of refraction index is a challenge for current optical technology, especially in the case of nanoscale gradient.

3. DEMANDS TO TECHNOLOGY OF OPTICAL NANOGRADIENT METACOATINGS

The nature gives us limited number of substances with specific indexes of refraction, therefore the technology must allow mixing different substances to provide the suitable values of n (or ε, or

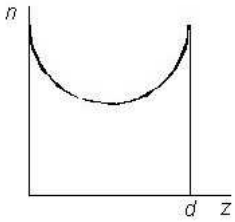

Figure 2: Longitudinal index profile of $n(z)$ for the photonic barrier; $d \leq 100\,\text{nm}$ [2].

μ). Herein, the fabrication processes for obtaining the required nanoscale index variation must be precise, reproducible and reliable.

Gradient coatings must have minimal optical losses and, as a consequence, minimal surface roughness and density of structure defects. Lowering optical losses (light scattering) enhances stability against high intensive light (laser) radiation. Since optical metamaterials are fabricated as deposited on substrates, the technology must ensure good adhesion of the metamaterials. In the case of employing temperature-sensitive substrates, the deposition processes should be low-temperature ones.

Common demands are mechanical, thermal and chemical stability of metamaterials as well as their non-sensitivity to environmental media.

The vacuum plasma-assisted deposition methods meet the said demands and, on our opinion, the most suitable method is one based on reactive magnetron sputtering of metal targets in pulse mode of operation (RPMS) [9]. This method provides high energy activation of synthesis of metamaterials with needed composition on the substrates and its dense microstructure, good adhesion, prevention of arcing on the metallic targets in reactive gas medium. Also, a set-up for RPMS is simpler than electron-beam evaporation installations also containing ion guns for assistance, which traditionally used in the optical industry.

4. EXPERIMENTS WITH MAGNETRON SPUTTERING SYSTEM FOR GRADIENT DEPOSITION

An automatic multi-target magnetron sputtering system with computer control and *in situ* monitoring has been developed and has been successfully employed for obtaining different gradient multi-wave antireflection coatings and other types of coatings with subwavelength thickness of partial layers. Fig. 3 depicts the diagram of magnetron set-up for deposition of longitudinal $1D_z$ gradient metacoatings. Coordinates X_1, X_2 and X_3, algorithm of substrate movement over the magnetron targets, as well as sputtering power of each magnetron, determine composition of material layers deposited on the substrate. Therefore, variation of $n(z)$ is received by regulation of the deposited material composition in conditions of differently sputtered target materials (M1 — Si and M2 — Ti) in reactive gas mixture Ar + O_2. Ar is used as a sputtering gas. O_2 is used for oxide synthesis (accordingly, SiO_2 and TiO_2) on the substrate surface. Oxygen is chemically activated in magnetron discharge plasma as well as in a special activator and due to UV laser radiation directed towards the substrate surface (the activator and the laser are not shown in Fig. 3). The mid-frequency pulse mode of magnetron operation is used. The monitoring *in situ* system (spectrovisor) allows to test optically the deposited coatings directly during the fabrication process and to make corrections of operation parameters, if it is necessary. For obtaining 2D and 3D gradient metamaterial, the substrates do complex movement by two axes; also, a slotted shield is used. Apparatus for testing of ready gradient coatings has been developed, too.

To characterize the gradient metamaterial, produced by this RPMS set-up, let us consider the results of fabrication of nanogradient antireflection coatings, intended for using in optical devices. The first coating contains one homogeneous layer with high value of n, located on the substrate, another homogeneous layer with low index n, bordering with the air, and the intermediate gradient layer with the linear variation of index n (Fig. 5). The measurements of reflection spectrum of this coating indicate the transmittance, exceeding 90% in the wide band (in the visible and near-IR ranges).

The second manufactured gradient coating is one on the Ge substrate with high transmission (antireflection) in the hyperwide band and it is intended for work in IR range. The coating was obtained due to realization of the index profile $n(z)$, depicted in Fig. 6. One can see the experimental

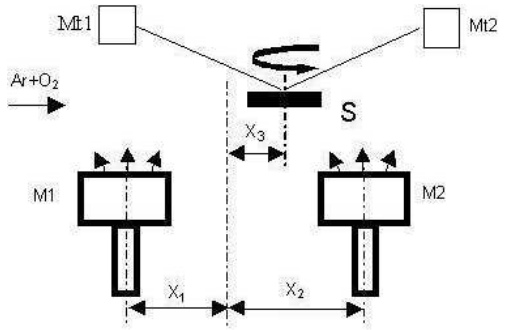

Figure 3: Diagram of multi-target magnetron sputtering system; M1, M2 — sputtering magnetrons with Si and Ti targets, Mt1, Mt2 — optical parts of monitoring *in situ* system, S — rotating substrate; the arrows over M1 and M2 show sputtered target material ejection.

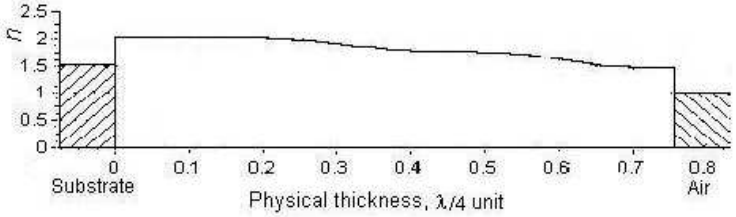

Figure 4: Longitudinal gradient profile of refraction index $n(z)$ for antireflection coating.

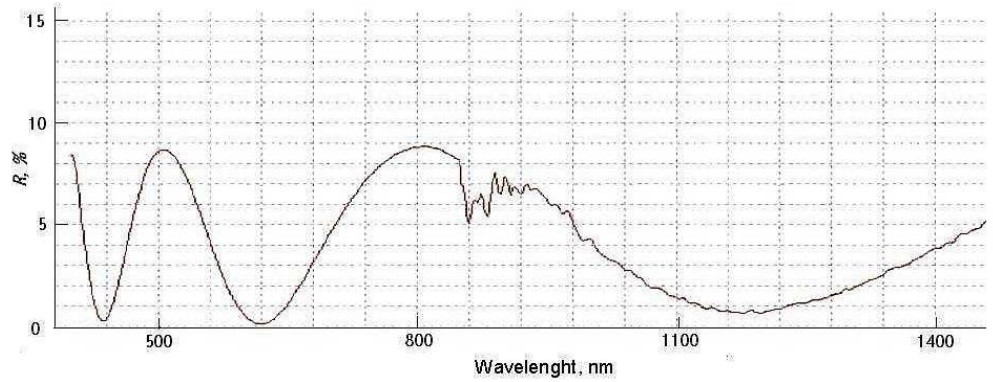

Figure 5: Experimental reflection spectrum of the coating with gradient profile of $n(z)$ shown in Fig. 4.

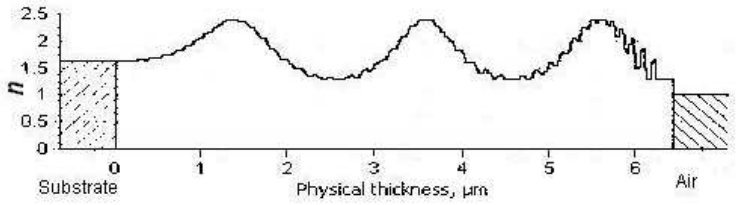

Figure 6: Longitudinal gradient profile of refraction index $n(z)$ for high transmission in hyperwide band.

transmission spectrum (Fig. 7) confirms obtaining transmittance near 100% in very wide band.

It is important to note the presented gradient coatings, produced by RPMS technology, have dense structure and are very stable against mechanical, radiation and environmental factors. Also, they have advantage as their thickness is less than the thickness of multilayer interference coatings with similar spectral characteristics.

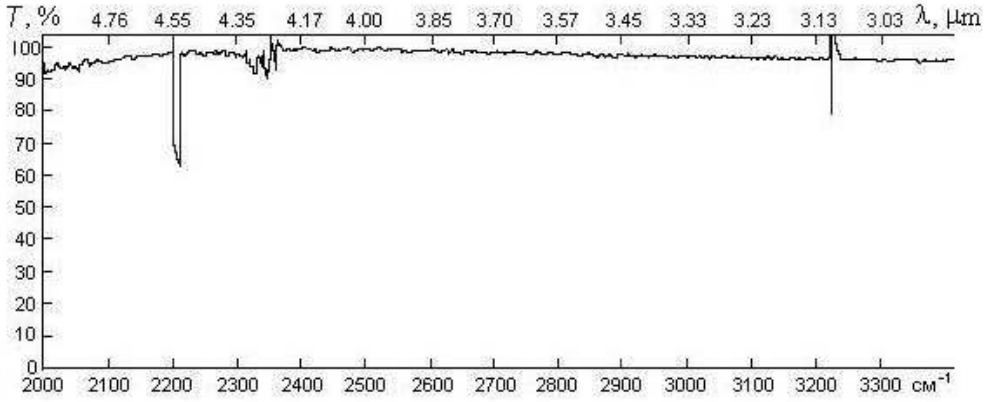

Figure 7: Experimental transmission spectrum of the coating with gradient profile of $n(z)$ shown in Fig. 6.

5. CONCLUSION

Different technological approaches to fabrication of gradient metamaterials have been considered. Although obtaining optical gradient metamaterials with complex nanoscale and multi-dimension variation of refraction index as well as high stability to external factors is a challenge for current technology, the method of precisely controlled reactive pulse magnetron sputtering has high potential in this field. It has been confirmed by successful fabrication of some gradient metacoatings, in particular ones with excellent antireflection properties in very wide band in the visible and IR ranges. However, this method needs further development, especially to provide fabrication of nanoscale multi-dimension gradient with high productivity.

REFERENCES

1. Macleod, H. A., *Thin-film Optical Filters*, CRC Press, 2010.
2. Shvartsburg, A. B., V. Kuzmiak, and G. Petite, "Optics of subwavelength gradient nanofilms," *Physical Reports*, Vol. 452, 33–88, 2007.
3. Smith, D. R., J. J. Mock, A. F. Starr, and D. Schurig, "Gradient index metamaterials," *Phys. Rev. E*, Vol. 71, 036609-1–6, 2005.
4. Schurig, D., J. J. Mock, B. J. Justice, S. A. Cummer, J. B. Pendry, A. F. Starr, and D. R. Smith, "Metamaterial electromagnetic cloak at microwave frequencies," *Science*, Vol. 314, 977–980, 2006.
5. Neu, J., B. Krolla, O. Paul, B. Reinhard, R. Beigang, and M. Rahm, "Metamaterial-based gradient index lens for strong focusing in the THz frequency range," *Proc. 5th Int. Cong. Adv. Electromagn. Mater. in Microwave and Optics — Metamaterials' 2011*, 955–957, Barcelona, Spain, Oct. 2011.
6. Cai, W. and V. Shalaev, *Optical Metamaterials: Fundamentals and Applications*, 200, Springer, New York, 2010.
7. Semouchkina, E., D. H. Werner, G. B. Semouchkin, and C. Pantano, "An infrared invisibility cloak composed of glass," *Appl. Phys. Lett.*, Vol. 96, 233503-1–3, 2010.
8. Kennedy, S. R. and M. J. Brett, "Porous broadband antireflection coating by glancing angle deposition," *Appl. Opt.*, Vol. 42, 4573–4579, 2003.
9. Volpian, O. D., A. I. Kuzmichev, Y. A. Obod, and P. P. Yakovlev, "Optical nanogradient coating deposition by reactive pulse magnetron sputtering," *Abstr. Book of 3rd Central Eur. Symp. Plasma Chem.*, 146–147, Kiev, Ukraine, Aug. 2009.

Measurers' Exposure to Extremely Low Frequency Magnetic Fields at 400 kV Substations

L. Korpinen[1], **H. Kuisti**[2], **H. Tarao**[1,3], **and R. Pääkkönen**[4]

[1]Environmental Health, Tampere University of Technology, Finland
[2]Fingrid Oyj, Helsinki, Finland
[3]Department of Electrical and Computer Engineering
Kagawa National College of Technology, Japan
[4]Finnish Institute of Occupational Health, Tampere, Finland

Abstract— The aim of this paper is to present levels of a measurers' personal magnetic field (MF) exposure at 400 kV substations. Measurements were obtained using a portable Radians Innova ML-1 meter (at the wrist). The maximum values obtained varied from 6.2 μT to 481 μT (average 2.0 μT to 67.9 μT). The maximum and average values do not exceed the 2010 MF occupational exposure level guidelines of International Commission on Non-Ionizing Radiation Protection.

1. INTRODUCTION

The International Commission on Non-ionizing Radiation Protection (ICNIRP) has published guidelines, for limiting the exposure to time-varying EMFs (1 Hz–100 kHz) [1]. According to the guidelines, the reference levels (50 Hz) for general public exposure to varying EMFs [unperturbed root mean square (RMS) values] are 5 kV/m and 200 μT. For occupational exposure, the reference levels (50 Hz) are 10 kV/m and 1000 μT (ICNIRP, 2010). According to these guidelines, the basic restrictions of the internal electric fields (at 50 Hz) for occupational exposure are 0.1 V/m (for the central nervous system (CNS) tissues of the head) and 0.8 V/m (for all tissues of the head and body).

A proposed EC directive (2011/0152) on the minimum health and safety requirements regarding the exposure of workers to risks arising from physical agents (electromagnetic fields), is currently going through a process of debate and approval within the European Union [2].

In earlier studies, we have presented a range of measurement results, drawn from the occupational exposure to extremely low frequency (ELF) electric fields at 400 kV substations and under 400 kV power lines [3–5]. Occupational magnetic field exposure has been only briefly studied at 400 kV substations, so the aim of this work is to present the levels of a measurers' personal MF exposure at 400 kV substations.

Table 1: A summary of the substations, where measurers worked.

Station	Busbar type	Reactors	Main busbar phase-to-phase spacing, m	Bay busbar phase-to phase spacing, m	Main busbar distance from ground, m	Bay busbar distance from ground, m
Station 1	Duplex	(3)	5.0	5.5	11.8	6.7
Station 2	1 MB	1	5.0	5.5	12.3	6.5
Station 3	2 MB + TB	2	5.0	5.5	12.3	6.2
Station 4	1 MB	-	5.0	5.5	12.3	6.9
Station 5	Duplex	2	5.0	5.5	12.3	6.9
Station 6	1 MB	1	5.0	6.0	12.3	6.2
Station 7	2 MB + TB	2	5.0	5.5	12.3	6.3
Station 8	2 MB + TB	3 + (1)	6.0	10.0	15.0	6.9

(MB and TB refer to the main busbar and transfer busbar respectively.)

2. MATERIALS AND METHODS

For the measurement of magnetic field exposure at eight 400 kV outdoor air-insulated substations, two measurers used small, portable Radians Innova ML-1 (accuracy ±10%) MF loggers (at the wrist). The measuring ranges of meters were 0.01–100 μT (Meter 1) and 0.1–1000 μT (Meter 2), with a measurement interval of 10 seconds. Measurements were taken over 16 working days, of which 15 had two measurers and the remaining day only one.

Both of the meters were 15.2 cm × 8.3 cm × 3.4 cm in size and were quite easily transported by the measurer, moving and working on the 400 kV substations and in the vicinity of the reactors. The meter was also able to measure the low frequency magnetic fields in a frequency range of 30 Hz–2 kHz.

Table 1 shows a summary of the substations where the measurers worked. Parentheses around the number of reactors, indicates that the reactor has an iron core and thus the magnetic field is

Table 2: Results of measurers' exposure at substations.

Station	Measurers	Maximum meter value	Magnetic fields, μT				
			Minimum	Maximum	Average	Median	S.D
Station 1	1	1 mT	0.3	13.5	2.1	1.6	1.9
Station 1	2	100 μT	0.3	10.8	2.0	1.6	1.8
Station 1	2	1 mT	0.0	13.0	2.6	2.1	2.0
Station 1	1	100 μT	0.3	8.2	2.7	2.7	1.5
Station 2	1	1 mT	0.1	481	23.8	2.6	58.2
Station 2	2	100 μT	0.1	over 100	25.3	2.5	38.8
Station 2	2	1 mT	0.0	13.1	3.3	2.3	3.1
Station 2	1	100 μT	0.2	13.5	3.3	2.1	3.4
Station 3	1	1 mT	0.1	357	7.8	1.3	31.0
Station 3	2	100 μT	0.1	over 100	6.8	1.2	21.0
Station 3	2	1 mT	0.0	7.3	2.6	2.6	1.7
Station 3	1	100 μT	0.1	6.2	2.4	1.7	1.7
Station 4	2	1 mT	0.3	9.1	3.1	2.7	2.0
Station 4	1	100 μT	0.1	7.9	3.0	2.6	1.9
Station 5	1	1 mT	0.1	14.1	2.9	2.6	1.8
Station 5	2	100 μT	0.1	14.3	2.9	2.6	1.8
Station 5	1	1 mT	0.1	299	18.3	7.0	41.3
Station 5	2	100 μT	0.1	over 100	12.7	6.7	21.3
Station 6	2	1 mT	0.1	300	10.8	2.5	41.1
Station 6	1	100 μT	0.0	102	6.8	3.0	17.9
Station 7	2	1 mT	0.1	20.3	7.8	6.6	4.6
Station 7	1	100 μT	0.6	21.2	8.2	6.6	4.9
Station 7	1	1 mT	0.4	22.9	10.4	11.1	5.6
Station 7	2	100 μT	0.3	24.8	9.7	10.7	5.0
Station 7	2	1 mT	1.0	290	67.9	15.0	91.7
Station 7	1	100 μT	1.2	over 100	30.8	14.6	36.0
Station 8	1	1 mT	0.1	8.0	3.1	2.7	1.6
Station 8	2	100 μT	0.2	7.1	2.9	2.6	1.5
Station 8	2	1 mT	0.1	10.5	2.7	2.3	1.9
Station 8	2	1 mT	0.3	300	46.5	13.6	66.2
Station 8	1	100 μT	0.3	over 100	28.0	6.7	35.5

weak around them. Tubular busbars are normally used in such facilities, but at the older substation in the sample (8), flexible busbars are used. Fuller details of the substations have been reported in an earlier paper [5].

The measurers kept a diary of exposure situations, so that it is possible to determine their precise location for each of the 5 minutes periods. The diary records the number of the meter used and where they worked at the 400 kV substation, for example near the fence of the reactor, at the capacitors or perhaps in their car, when there was rain.

3. RESULTS

Table 2 shows the results of measurers' exposure at the substations. In the table, stations 2, 3, 5, 6, 7 and 8 show the results of the magnetic field measurements around the fence of the reactor. In one meter, the maximum value of the measurements highest range is 102.3 μT in which the meter is completely saturated in the vicinity of the reactor wall. The maximum values obtained varied from 6.2 μT to 481 μT (average 2.0 μT to 67.9 μT). The highest average of magnetic field exposure during a working day, measured with ML-1 meters, was 67.9 μT and median 15.0 μT.

At five substations, Meter 1 (measuring range 0.01–100 μT) could not be used to take measurements, because the values exceeded the maximum value of the meter used. In those substations, Meter 2 measured the follow maximum values: (1) substation 2; max 481 μT, (2) substation 3; max 357 μT, (3) substation 5; max 299 μT, (4) substation 7; max 290 μT and (5) substation 8; max 300 μT. During those days when magnetic flux densities were measured around the reactors, the recorded values were higher than at other times of exposure. On these occasions, the highest MF exposure averaged close to 70 μT.

4. DISCUSSION AND CONCLUSION

The study shows that the measured maximum magnetic fields at 400 kV substations did not exceed the guidelines of ICNIRP [1]. Exposure at the 400 kV substations was quite low. On measuring days, when measurers worked only at the 400 kV switchyard, the average MF exposure reached up to 3 μT. However at substation 7, the magnetic field exposure was seen to be slightly higher than at other substations. In the switchyard of this facility, the maximum exposure was just over 10 μT. The reason for this is assumed to be that the measurements were conducted when a higher power level was transferred than at times of measurement in other substations. The physical structures of the facility however, do not differ from the other substations.

During the measuring days, when measurements were made around the reactor, higher average values were recorded than at other times. In this situation, the highest magnetic field exposure was close to 70 μT. In other cases, the average exposure was between 10 μT–50 μT. The average magnitude of exposure depended on the duration of the measurements, taken at the reactor. At some substations only one reactor was measured although as at others three reactors were measured. This, of course, raises the measurer's exposure near reactor.

In conclusion, whilst the average magnetic field exposure fell between 10 μT–50 μT, both the maximum and average values do not exceed the MF exposure levels, as laid out in the guidelines of the ICNIRP [1].

ACKNOWLEDGMENT

The assistance of the staff of Department of Energy and Process Engineering (Environmental Health), Tampere University of Technology (Tapani Karjanlahti, Riku Koski, Jussi Kurikka-Oja, Riitta Lehtelä, Leena Luoma, Jari Latva-Teikari and Toni Långsjö) is gratefully acknowledged.

REFERENCES

1. International Commission on Non-Ionizing Radiation Protection (ICNIRP), "Guidelines for limiting exposure to time-varying electric and magnetic fields (1 Hz to 100 kHz)," *Health Physics*, Vol. 99, No 6, 818–836, Dec. 2010.
2. European Commission, "Proposal for a directive of the european parliament and of the council on the minimum health and safety requirements regarding the exposure of workers to the risk arising from physical agents (electromagnetic fields) (XXth individual directive within the meaning of article 16(1) of directive 89/391/EEC)," http://eur-lex.europa.eu/LexUriServ/LexUriServ.do?uri=COM:2011:0348:FIN:EN:PDF.
3. Karjanlahti, T., "Measuring occupational exposure to electric and magnetic fields at 400 kV substations," Tampere University of Technology, 2004 (in Finnish).

4. Korpinen, L. H., J. A. Elovaara, and H. A. Kuisti, "Evaluation of current densities and total contact currents in occupational exposure at 400 kV substations and power lines," *Bioelectromagnetics*, Vol. 30, No. 3, 231–240, 2009.
5. Latva-Teikari, J., T. Karjanlahti, J. Kurikka-Oja, J. Elovaara, T. Långsjö, and L. Korpinen, "Measuring occupational exposure to electric and magnetic fields at 400 kV substations," *Proceedings of IEEE/PES Transmission and Distribution Conference and Exposition,* 1–4, 2008.

The Possible Exposure of Children to Extremely Low Frequency Magnetic Fields in the Home

F. Gobba[1], **R. Pääkkönen**[2], **H. Tarao**[3,4], **and L. Korpinen**[3]

[1]Department of Public Health Sciences, University of Modena and Reggio Emilia, Italy
[2]Finnish Institute of Occupational Health, Tampere, Finland
[3]Environmental Health, Tampere University of Technology, Finland
[4]Department of Electrical and Computer Engineering
Kagawa National College of Technology, Japan

Abstract— This paper aims to analyze common magnetic field exposure situations to children in the home, to determine possibly relevant sources. Part of the data presented here derives from measurements performed in projects in Finland and Italy. In the home, the important sources of children's exposure are electrical systems and devices. In conclusion we can say that it is quite easy to find exposure levels that exceed 0.3–0.4 μT in the home.

1. INTRODUCTION

Extremely low frequency (ELF) magnetic fields (MF) are considered as suspected carcinogens (Group 2B IARC), based on consistent epidemiological data on childhood leukemia, although the biological evidence is considered weak. An increase in risk was observed at exposure levels exceeding 0.4 μT. The International Commission on Non-ionizing Radiation Protection (ICNIRP) has published guidelines for limiting exposure to time-varying EMFs (1 Hz–100 kHz) [1].

These guidelines include basic restrictions and reference levels for the protection against acute adverse health effects. Suspected chronic effects such as leukemia however are not considered, as

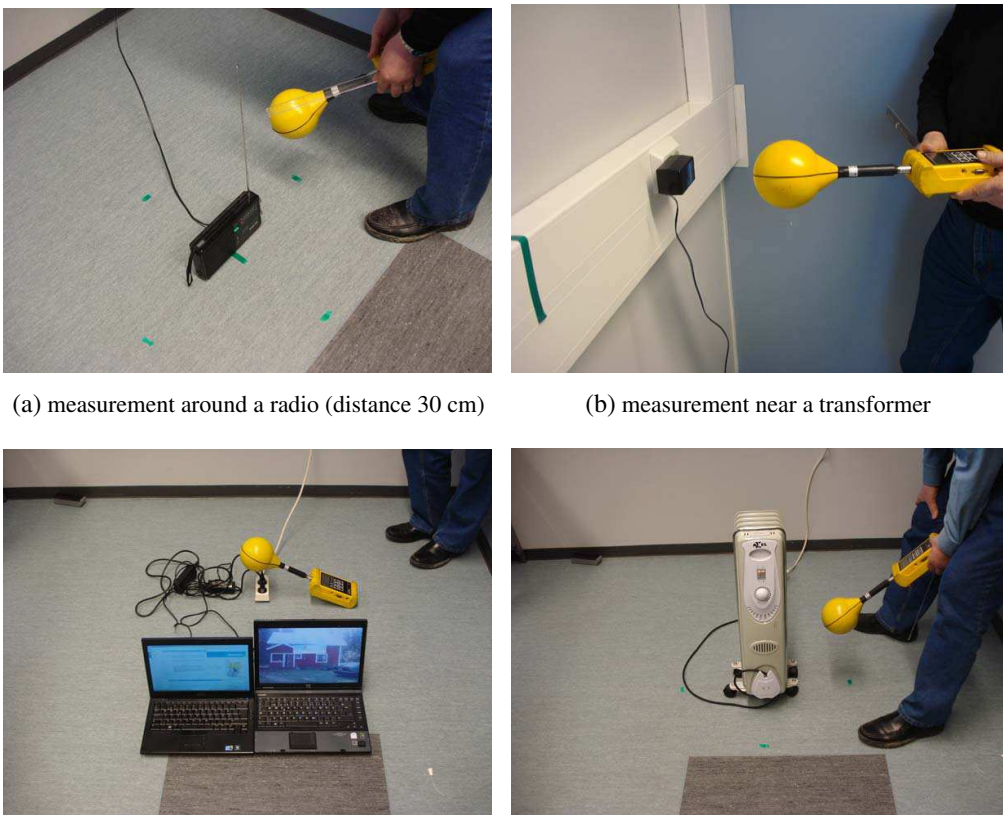

(a) measurement around a radio (distance 30 cm)

(b) measurement near a transformer

(c) measurement near an extension lead

(d) measurement around a heater

Figure 1: Examples of measurements around different devices.

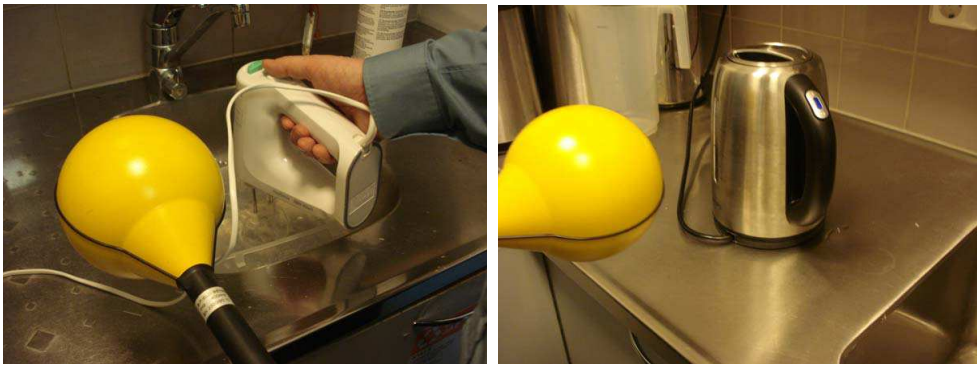

Figure 2: Examples of measurements near a food mixer and an electric kettle.

Table 1: Measurement results taken around devices.

Device	**point 1, μT**	**point 2, μT**	**point 3, μT**	**point 4, μT**
Radio	0.25	0.31	0.33	0.30
CD-player	0.24	0.23	0.23	0.23
MP3-player	0.24	0.23	0.23	0.23
Charger-camera	0.24	0.24	0.24	0.24
Charger + phone 1	0.24	0.24	0.24	0.24
Charger + communicator 1	0.24	0.24	0.23	0.23
Charger + phone 2	0.24	0.24	0.24	0.24
Charger + phone 3	0.24	0.24	0.24	0.24
Phone 3. radio	0.24	0.24	0.24	0.24
Charger + phone 4	0.24	0.24	0.24	0.24
Charger + phone 5	0.24	0.24	0.23	0.23
Charger + Ipad (support structure)	0.24	0.24	0.23	0.23
Extension lead 1 + 2 PCs	0.24	0.24	0.24	0.24
Extension lead 2 + 2 PCs	0.24	0.24	0.23	0.23
Extension lead 2 + 2 PCs + heater	0.24	0.24	0.24	0.24
Heater	0.24	0.24	0.24	0.25

according to the ICNIRP, the causal relationship with electro-magnetic fields (EMF) is not established [1]. The ICNIRP reference levels for general public exposure to 50 Hz EMFs [unperturbed root mean square (RMS) values] are 5 kV/m and 200 μT. For occupational exposure, the reference levels (50 Hz) are given as 1000 μT and 10 kV/m [1].

Previously, we have measured the MF exposure, derived from some new devices (e.g., laptops etc). At home however, the important sources of children's exposure are electrical systems and devices. In a detached house, the exposure was measured to be 0.1 μT. In apartments, the maximum exposure was usually > 0.4 μT (8 apartments), but in those located above the indoor distribution point, the average (max) exposure reached 6.5 μT. In the kitchen, the MF levels were measured at 0.3–0.5 μT and 2.5–4.2 μT in front of the oven and microwave oven respectively. All data was derived from spot measurements obtained using instantaneous RMS meters.

In Italy, the median Time Weighted Average exposure measured using personal meters in 513 homes was 0.03 μT and levels were below 0.4 μT in 97% of the homes sampled. These levels are also most likely representative of the potential exposures of multiple children living in the same house.

This paper aims to analyze common exposure situations to children in the home, to determine possibly relevant sources and part of the data presented here derives from measurements performed in our earlier projects.

Table 2: Results from different devices in the kitchen.

Kitchen Device Measurements	MF, μT	distance	place/height
Mixer with whisks. power 1–3	0.40–0.45	20 cm	place 1
Mixer with whisks. power 1–3	0.76–0.85	20 cm	place 2
Mixer with whisks. power 1–3	0.55–0.67	20 cm	place 3
Mixer with dough hooks. power 1–3	0.89–1.05	20 cm	place 1
Mixer with dough hooks. power 1–3	0.56–0.58	20 cm	place 2
Mixer with dough hooks. power 1–3	0.50–0.60	20 cm	place 2
Microwave oven 1	14.00	20 cm	
Microwave oven 2	6.70	20 cm	
Refrigerator 1	0.24	20 cm	height 0.5 m
Refrigerator 2	0.31	20 cm	height 0.5 m
Electric kettle	0.28–0.29	20 cm	sides 1, 2, 3,

2. MF MEASUREMENT METHODS

The magnetic field density was measured with a Narda ELT-400 meter (L-3 Communications, Narda Safety Test Solutions, Hauppauge, NY, USA — accuracy ±4% RMS). This meter has a frequency range of 1 Hz–400 kHz. Figures 1 and 2 show examples of measurements undertaken. Each household device was measured either on its surface or at four points (at a distance of 30 cm) around the device.

3. RESULTS

The measurement results around devices (4 points) are shown in Table 1. The Table 2 shows the results obtained from different devices in a household kitchen.

Magnetic fields measured at 0.4–1.1 μT around the mixer and varied between 0.2–0.3 μT around the remaining equipment. In proximity to the microwave ovens, the magnetic flux density was 6–14 μT. All measured values however, were clearly below the recommended values provided by ICNIRP.

4. DISCUSSION AND CONCLUSIONS

There are inaccuracies in the measured values, caused for example because the sensor size (diameter 100 mm), the measurement set-up and the background value of the meter (about 0.2 μT). The measured values however, were at least one order of magnitude lower than the reference values for general populations, as proposed by ICNIRP [1]. Considering the suspected chronic effects of ELF-MF, the proposed threshold (0.4 μT) can be easily exceeded in the kitchen (e.g., near the microwave oven or the food mixer), but all the other measured devices fell below this level (Table 1). Even if the ELF-MF exposure in children is usually low, various common household situations were identified as inducing ELF-MF levels that easily exceeded 0.4 μT, such as proximity to central domestic electrical systems and also to some devices in the home (e.g., the microwave oven).

Our results suggest that, in usual conditions, ELF-MF levels in the home are largely below the thresholds deemed causative of acute effects. Furthermore, with some attention (e.g., moving away during the use of certain devices), it seems possible to reduce the risk of exposure below the threshold presented for suspected chronic effects.

REFERENCES

1. International Commission on Non-Ionizing Radiation Protection (ICNIRP), "Guidelines for limiting exposure to time-varying electric and magnetic fields (1 Hz to 100 kHz)," *Health Physics*, Vol. 99, No. 6, 818–836, Dec. 2010.

Electrical Impedance of Plasma Filled Waveguides in the MHz Range

D. Melazzi[1], **D. Curreli**[2], **M. Manente**[1], **and D. Pavarin**[1]

[1]CISAS "G. Colombo" Centro Interdipartimentale Studi Attività Spaziali
University of Padova, Italy
[2]Deptartment of Nuclear, Plasma and Radiological Engineering
University of Illinois Urbana Champaign, USA

Abstract— The Maxwell wave Equations have been numerically solved for the case of a cylindrical plasma-filled waveguide with perfectly conductive walls. The calculations have been done using the SPIREs code, which solves the electromagnetic propagation in frequency domain along the radius of the waveguide by means of a mixed spatial-spectral method (1D-space along radius, spectral domain along azimuthal and axial directions). The waveguide contains a column of plasma, magnetized along the axis of the cylinder, and an antenna, comprised in the gap between the plasma and the conducting wall. The antenna forces an oscillating current at radio-frequency in the Megahertz range. The electromagnetic response of the plasma is described by the Stix dielectric tensor plus the Fried-Conte Z dispersion function for finite-temperature Maxwellian effects. From the numerical solutions of the fields, the electrical impedance of the waveguides has been derived, and showed for a wide range of plasma parameters and waveguide radial sizes. The plasma density ranges from 10^{17} to 10^{21} particles/m^3, the magnetic field is below $B < 0.1$ Tesla, the frequencies are 13.56 and 27.12 (MHz), and the plasma cylinders have radius < 5 cm. The electrical resistance per unit length of the plasma is reported for each case. For a given geometry, the trends allow to find the maximum load conditions, corresponding to the maximum power coupling between the antenna and the plasma load. The results are relevant for many applications, ranging from the electrical design of the plasma-wave coupling in actual plasma devices, to the optimization of the RF plasma sources commonly used in industry. The method can also be proficiently applied to the design of high efficiency plasma sources used on board of spacecrafts for RF plasma thrusters.

1. INTRODUCTION

Among a variety of inductively and capacitively plasma sources, helicon plasma sources have been recognized to be much more effective in generating dense plasma and they are of considerable current interest for a variety of applications, including material surface modification, etching of semiconductors, basic and applied laboratory research. Thanks to their high efficiency and to the production of high density plasma, three main projects have been using helicon sources for space propulsion: the high-power VAriable Specific Impulse Magnetoplasma Rocket (VASIMR), the medium-power Helicon Double Layer Thruster (HDLT) at ANU and the low-power European Helicon Plasma Hydrazine COmbined Micro (HPH.COM). The evaluation of the electromagnetic fields propagating inside the plasma source and the plasma-wave coupling fundamental quantities, like the specific deposited power and the electrical impedance, are fundamental for the optimization of industrial plasma source, for the quantitative interpretation of experiments, for the theoretical investigation and for the electrical design of such a plasma system. The fast and reliable algorithm implemented in SPIREs [1] allows the evaluation of the electrical impedence of helicon sources over a wide range of plasma parameters useful for different applications.

The paper is structured as follows. Section 2 gives a brief overview of the numerical method, whose results are presented in Section 3.

2. NUMERICAL MODEL

Plasma sources used in semiconductor manufacturing, laboratory experiments and in spacecraft plasma thrusters often deal with a plasma cylinder of radius r_a surrounded by an antenna placed at radius r_b, and enclosed inside a conducting tube of radius r_c, as showed in the axial section of Fig. 1. The cylindrical symmetry of the system suggests the use of cylindrical coordinates (r, θ, z). A magnetostatic field $\bar{B}_0$ is directed along the z axis, $\bar{B}_0 = B_0\hat{z}$, perpendicular to the (r, θ) plane.

Quantities along θ and z directions are Fourier transformed in the corresponding spectral modes, so that wave quantities have an harmonic dependence as $\exp[i(m\theta + k_z z - \omega t)]$, where m is the

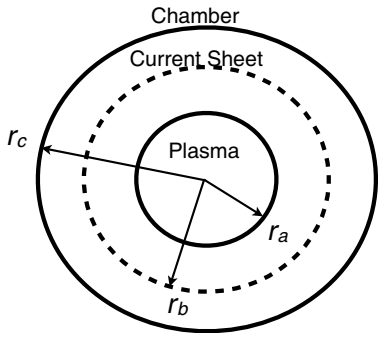

Figure 1: Geometry in the (r, θ) plane of the plasma system considered; r_a is the plasma radius, r_b is the antenna radius, r_c is the conductive chamber radius. The z axis points outward perpendicular to the (r, θ) plane.

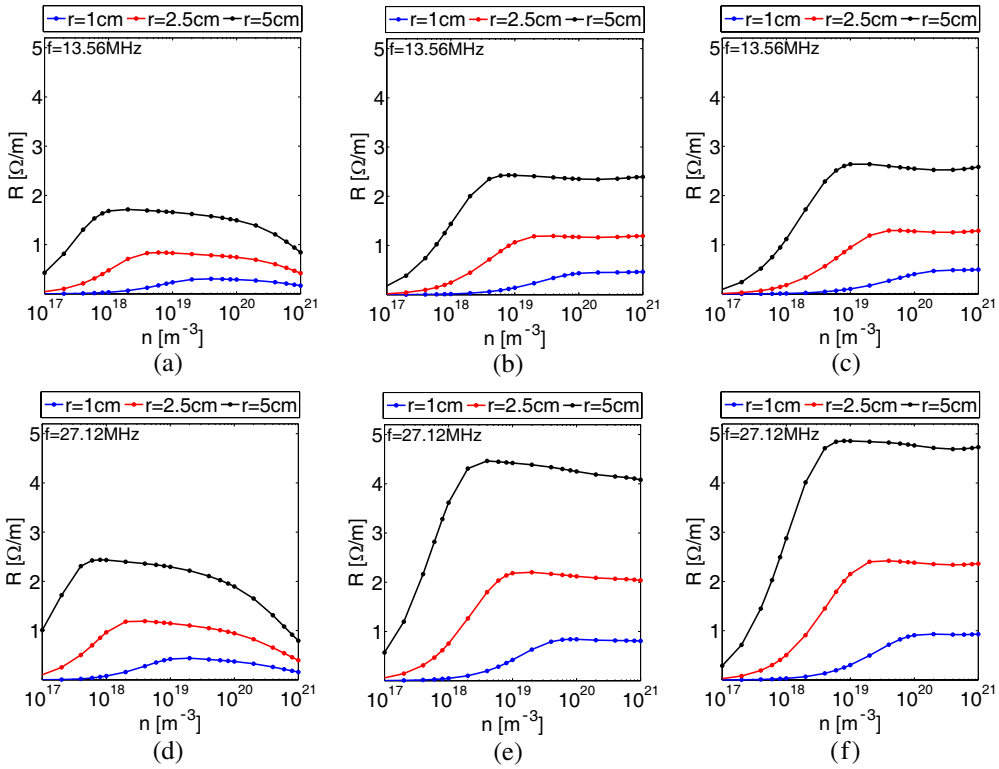

Figure 2: Electrical resistance as a function of the plasma density for three ($r_a = 1.0{\cdot}10^{-2}$ m, $r_a = 2.5{\cdot}10^{-2}$ m, $r_a = 5.0 \cdot 10^{-2}$ m) homogeneous magnetized plasma sources: (a), (d) $B_0 = 100$ G, (b), (e) $B_0 = 500$ G, (c), (f) $B_0 = 1000$ G at $f = 13.56$ MHz and $f = 27.12$ MHz, respectively. Parameters are: $m = 0$ antenna, $I_0 = 1.0$ A and neutral pressure $p_n = 2.0$ Pa.

azimuthal mode, k_z is the parallel wave number and ω is the angular frequency of the wave. The wave-plasma coupling inside the system is regulated by the two wave Maxwell equations [2], plus the constitutive relations Eqs. (3) and (4) of the materials for low fields amplitude, by means of the dielectric tensor ϵ and the magnetic permeability tensor μ, which relate the fields $\bar{E}$ and $\bar{B}$ to the electric displacement $\bar{D}$ and the magnetic field $\bar{H}$:

$$\nabla \times \bar{E} = i\omega t \bar{B} \tag{1}$$

$$\nabla \times \bar{H} = -i\omega t \bar{D} + \bar{J} \tag{2}$$

$$\bar{D} = \epsilon \bar{E} \tag{3}$$

$$\bar{B} = \mu \bar{H} \tag{4}$$

In the thin wire approximation, the antenna current can be treated with negligible extension along the radial direction, and it is represented by an infinite set of current sheets, which are

harmonic functions with respect to time and space [3]. The electrical response of a magnetized plasma is represented by a non-diagonal tensor ϵ with five non-zero elements [5], which looses validity when non-linear effects of wave-particle interaction become relevant:

$$\boldsymbol{\epsilon} = \epsilon_0 \begin{bmatrix} S & -iD & 0 \\ iD & S & 0 \\ 0 & 0 & P \end{bmatrix} \tag{5}$$

where S, D and P are function of the plasma frequency $\omega_{p\alpha} \equiv \sqrt{n_\alpha q_\alpha^2/\epsilon_0 m_\alpha}$, the gyrofrequency $\omega_{c\alpha} \equiv \epsilon_\alpha q_\alpha B_0/m_\alpha$ with ϵ_α the particle charge sign, the particle thermal velocity $v_\alpha \equiv \sqrt{2T_\alpha/m_\alpha}$, the collision frequency ν_α, and the plasma dispersion function Z tabulated by Fried and Conte [4]; the superscript α referes to the index of the plasma species. The tensor ϵ has been assumed to be a function of radius, so that radial variation of plasma density, magnetic field, electron temperature, and neutral pressure can be taken into account. SPIREs solved for the propagation of plasma waves and evaluated the electrical impedance of an uniform magnetized plasma column forced by an $m = 0$ and $m = 1$ antenna at frequencies in the megahertz range. The propagation involves the coupling of two plasma waves, namely the Helicon (H) and the Trivelpiece-Gould (TG), with different transverse wavelength as expressed by the following dispersion relation [6]:

$$\lambda_{\perp_{H,TG}}(n_\parallel) = 2\pi \left[n_\parallel^2 \frac{\omega_{ce}^2}{4c^2} \left(1 \mp \sqrt{1 - 4\frac{\omega_{pe}^2}{\omega_{ce}^2}\frac{1}{n_\parallel^2}} \right)^2 - n_\parallel^2 \frac{\omega^2}{c^2} \right]^{-1/2}, \tag{6}$$

where $n_\parallel$ is the parallel wave number, defined as $n_\parallel = k_z/k_0$, where $k_0 = \omega/c$ is the vacuum wave number. Once that the electromagnetic propagation inside the plasma column is solved, the electrical impedance due to the power coupled to the plasma by the antenna can be evaluated by

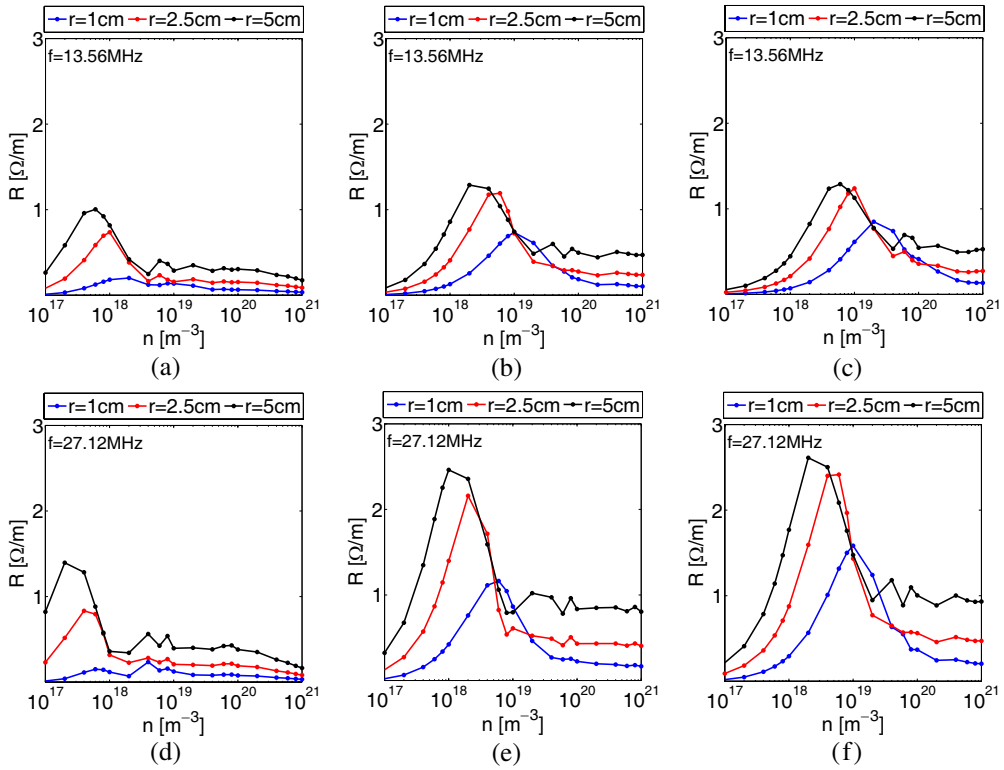

Figure 3: Electrical resistance as a function of the plasma density for three ($r_a = 1.0{\cdot}10^{-2}$ m, $r_a = 2.5{\cdot}10^{-2}$ m, $r_a = 5.0 \cdot 10^{-2}$ m) homogeneous magnetized plasma sources: (a), (d) $B_0 = 100$ G, (b), (e) $B_0 = 500$ G, (c), (f) $B_0 = 1000$ G at $f = 13.56$ MHz and $f = 27.12$ MHz, respectively. Parameters are: $m = 1$ antenna, $I_0 = 1.0$ A and neutral pressure $p_n = 2.0$ Pa.

means of:

$$P = \frac{1}{2}\int_{V_{plasma}} \bar{E}^* \cdot \bar{J}_{plasma} dV = \frac{|I_0^2|}{2}\left(R + iX\right), \tag{7}$$

where I_0 is the antenna current, R and X are the plasma resistance and reactance, respectively.

3. RESULTS

Figure 2 shows the plasma resistance for the $m = 0$ mode excited by means of a single loop antenna.

Figure 3 shows the plasma resistance for the $m = 1$ mode excited by means of a 0.1 m long Nagoya type III antenna.

4. CONCLUSION

SPIREs has been used for the numerical solution of the Maxwell wave Equations in a cylindrical plasma-filled waveguide with perfectly conductive walls; the plasma column is magnetized along the axis of the waveguide, and an antenna comprised in the gap between the plasma and the conducting wall forces an oscillating current at 13.56 MHz and 27.12 MHz, respectively. The electrical impedance of the waveguides has been derived, and the plasma resistance has been showed for a wide range of plasma parameters and waveguide radial sizes; specifically, the plasma density ranges from 10^{17} to 10^{21} particles/m^3, the magnetic field is below $B < 0.1$ Tesla, and the plasma cylinders have radius < 5 cm. The electrical resistance per unit length of the plasma is reported for different azimuthal excitation modes, $m = 0$ and $m = 1$.

Considering the plasma resistance R showed in Fig. 2 in the $m = 0$ excitation case, a maximum load condition can be identified for each working frequency and B_0 magnetic field. In the low magnetic field configurations showed in Figs. 2(a), (d), a maximum plasma resistance can be easily identified whereas in the higher confinement magnetic field configurations showed in Figs. 2(b), (c), (e), (f), a plateau develops for a given density value, which depends on the specific B_0 considered and gets higher for decreasing values of the plasma radius.

As a rule of thumb, the plasma resistance gets higher for higher working frequency, given a source geometry and confinement magnetic field. Similar considerations can be done for the $m = 1$ case showed in Fig. 3, where the forementioned rule works as well. Differently than the $m = 0$ case, in Fig. 3 there is a drop in the plasma resistance instead of a plateau as soon as a certain density value is reached; given the geometry, this value is higher for lower working frequency while it gets higher as soon as the confinement magnetic field increases.

Given a geometry, working frequency, confinement magnetic field and antenna azimuthal excitation mode, these plasma resistance trends allow to identify the maximum load conditions, corresponding to the maximum power coupling between the antenna and the plasma load. Depending upon the operative range considered, the results are relevant for many applications, ranging from the electrical design of the plasma-wave coupling in actual plasma devices, to the optimization of the RF plasma sources commonly used in industry, and finally to the design of high efficiency plasma sources used on board of spacecrafts for RF plasma thrusters. Furthermore, once that one among many source parameters is given, all the others can be chosen so as to optimize the power delivered by the antenna to the plasma.

REFERENCES

1. Melazzi, D., D. Curreli, M. Manente, J. Carlsson, and D. Pavarin, "SPIREs: A finite-difference frequency-domain electromagnetic solver for inhomogeneous magnetized plasma cylinders," *Computer Physics Communication*, Vol. 183, No. 6, 1182–1191, 2012.
2. Jackson, J. D., *Classical Electrodynamics*, John Wileyt and Sons Inc., 1999.
3. Vey, B. D., "Antena user guide," *Plasma Fusion Ctr.*, Rep. PFC/RR-84-13, Massachusetts Institute of Technology, 1984.
4. Fried, B. D., S. D. Conte, and J. D. Jackson, *The Plasma Dispersion Function*, Academic, New York, 1961.
5. Stix, T. H., *Plasma Waves*, Springer-Verlag, New York, 1992.
6. Chen, F. F. and D. Arnush, "Generalized theory of helicon waves. I. Normal modes," *Physics of Plasmas*, Vol. 4, No. 9, 3411–3421, 1997.

Equilibrium Conditions of Radiofrequency-heated Plasma Cylinders

D. Curreli[1], **D. Melazzi**[2], **M. Manente**[2], **and D. Pavarin**[2]

[1]Department of Nuclear, Plasma and Radiological Engineering
University of Illinois Urbana Champaign, USA
[2]CISAS "G. Colombo" Centro Interdipartimentale Studi Attività Spaziali
University of Padova, Italy

Abstract— The equilibrium conditions of radiofrequency heated plasma cylinders have been calculated by solving the two coupled problems of the electromagnetic power deposition and the macroscopic transport of charged and neutral species. The two Maxwell wave equations have been finite-differenced along the radius of the cylinder (SPIREs code), providing the input source terms for the transport problem. The continuity and momentum equations of a single-ionized cold plasma, together with energy conservation, have been solved along the same radial direction (EQM code). An iterative procedure has been used between the two problems in order to evaluate the profiles at equilibrium. The method allows the prediction of the profiles of plasma density, electron temperature and neutral density in RF heated plasma cylinders. Calculations have been done for typical conditions encountered in low-pressure helicon discharges, where the plasma is magnetized with an external field directed along the axis of the cylinder. The plasma density profiles are peaked at the center, even if most of the RF deposition occurs at the edge of the discharge. The increase of plasma density with the RF power has been calculated for a direct comparison with Langmuir probe measurements in helicon experiments. The electron temperature remains constant with the increasing power, but increases at the edge of the cylinder where the RF wave is strongly dumped via the Trivelpiece-Gould mode. Neutrals are depleted at the center of the discharge, where the plasma density reaches its maximum.

1. INTRODUCTION

In the present paper, we present numerical calculations of the equilibrium conditions of a magnetized plasma cylinder heated by means of a radio frequency (RF) antenna. The case is relevant for a number of applications, ranging from semiconductor processing to RF plasma thrusters for spacecrafts [13–15].

The method allows the evaluation of all the relevant quantities commonly measured for the characterization of a plasma discharge, i.e., the value of the oscillating electric and magnetic field, the profiles of plasma density, electron temperature and neutral density. In order to evaluate the equilibrium, two coupled problems have been iteratively solved up to the convergence on the profiles, (1) the solution of the plasma-wave coupling problem, and (2) the solution of the macroscopic transport of plasma and neutral species. For the solution of the first problem, the electromagnetic fields have been solved using a finite-difference discretization of the macroscopic Maxwell equations on a standard Yee mesh, implemented in the SPIREs code [11]. The anisotropic behavior of the magnetized plasma column is modeled using the classical Stix dielectric tensor [3], comprising the extra-diagonal terms and thermal effects [2]. The solution of plasma and neutral profiles (problem 2) has been done using a theory recently proposed for the evaluation of the equilibrium conditions of plasma cylinders of finite-length [9]. The theory, implemented in the EQM code [9], is based on the short-circuit effect originally proposed by Simon [1]. The theory developed in [9] has recently received an independent verification from dedicated two-dimensional Particle-in-Cell simulations [12], confirming the violation of the classical ambipolar cross-field transport due to the short circuiting of electrons at the axial boundaries of finite-extension cylinders. Here we summarize the method and we show an example of numerical calculation after the convergence between the two problems. Most notably, the method allows an evaluation *a priori* of the absolute values of plasma density and electron temperature, quantities that usually have to be measured from the particular experiment, being considered as an input for electromagnetic calculations.

The paper is organized as following. Section 2 gives a brief review of the methodology adopted. For more details we suggest the two previous works [9] and [11]. Section 3 presents the numerical results, showing the equilibrium profiles of plasma and RF fields for the case of a coil antenna fed at 13.56 MHz and 200 Gauss of axial magnetostatic field. The RF power of 250, 500 and 750 watt spans over the range of common helicon applications.

2. METHODOLOGY

A common way to obtain a cold weakly-ionized plasma is to excite a low-pressure gas (from 10^{-1} to 10^{1} Pa) contained in a cylinder with a radio frequency antenna in the MHz range wrapped around the cylinder. The method is experimentally simple and reliable, and it's nowdays one of the most widespread technique for making a plasma source. A stable quiescent plasma at low density (10^{16}–10^{18} particles/m^3) can be obtained with these kind of sources. The addition of a magnetostatic field, with the magnetic induction vector directed preferably along the axis of the cylinder, allows (under the opportune conditions of wave frequency, field intensity and plasma density) the propagation of bounded plasma waves, capable to enhance the RF coupling and increase the plasma density up to the rage of 10^{19} particles/m^3. This condition, typical of helicon experiments, is what we have analyzed with our model.

The calculation of the equilibrium condition of a RF heated magnetized plasma source requires the solution of two intimately connected problems. The first, how the electromagnetic wave launched by the antenna propagates into the plasma and is absorbed by this anisotropic medium. The second, how the plasma configures itself under the forcing action of the RF wave. Past studies [5–7] have demonstrated that the propagation of the electromagnetic waves into the plasma can excite two coupled plasma modes, usually referred as: (H) *helicon* mode (the fast wave of fusion plasmas), and (TG) *Trivelpiece-Gould* mode (slow wave), with different transverse wavelengths expressed by the following dispersion relation [5]:

$$\lambda_{\perp_{H,TG}}\left(n_{\|}\right) = 2\pi\left[n_{\|}^2\frac{\omega_{ce}^2}{4c^2}\left(1 \mp \sqrt{1-4\frac{\omega_{pe}^2}{\omega_{ce}^2}\frac{1}{n_{\|}^2}}\right)^2 - n_{\|}^2\frac{\omega^2}{c^2}\right]^{-1/2}, \tag{1}$$

where $n_{\|} = k_z/k_0$ is the wave number in direction parallel to the magnetic field, $k_0 = \omega/c$ the wave number of vacuum, ω the antenna angular frequency, ω_p the electron plasma frequency, ω_c the electron cyclotron frequency, and c the speed of light. In Eq. (1) the minus sign refers to the Helicon mode, and the plus to the Trivelpiece-Gould mode. Figure 1 shows a plot of Eq. (1) for three different cases: low-field-low-density, medium-field-medium-density and high-field-high-density (frequency is constant at 13.56 MHz). Here the terminology low, medium and high is relative to the sources commonly adopted in the laboratory practice and semiconductor industry. For each case, the two branches corresponding to each mode is depicted with different colors. The helicon branch can be excited only for an interval of $\lambda_{||}$. A minimum $\lambda_{||}$ is required to avoid the evanescent condition of the helicon branch, giving constraints on the antenna design.

The electromagnetic fields propagating inside the plasma cylinder has been calculated with the code SPIREs [11], obtaining the local values of the electric field, magnetic field, and plasma currents. From the local value of the fields, the RF power coupled with the plasma has been calculated by

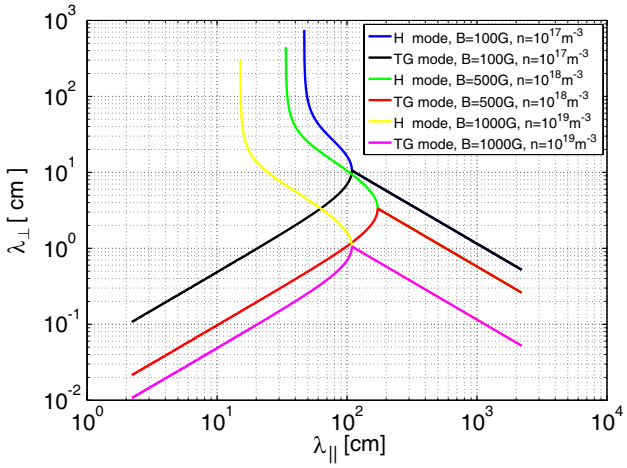

Figure 1: Dispersion relation of a cold magnetized plasma. Wavelength of the perpendicular modes $\lambda_\perp$ vs. wavelength of the parallel mode $\lambda_{||}$, for three cases (1) low field and low plasma density, (2) medium field and medium plasma density, and (3) high field and high plasma density. Magnetic field is in Gauss. Frequency is constant and equal to 13.56 MHz.

integrating the electrical work, $E^* \cdot J_{pl}$, done by the electric field E on the plasma currents J_{pl}, the integration being done over the volume V of propagation.

The calculated RF power deposited into the plasma is then used as an input in the problem of the macroscopic transport. A detailed description of the physical model can be found in [9], here we will summarize the main points. The local input power given at each location by the RF propagation is used by the plasma to overcome particle and inelastic losses. The particle losses are given by the convective fluxes of particles, and the inelastic losses come from the details of the atomic physics of the particular gas, and consists mostly of radiative losses. The coupling with the boundaries plays an important role in the final macroscopic configuration of the discharge, since electrons are short circuited at the end walls of the cylinder, where the magnetic lines intersect the walls. The model has been implemented in a code called EQM.

The two codes SPIREs and EQM have been iterated together until convergence on the profiles. Convergence is usually obtained after few iterations. Figure 2 shows an example, showing the convergence on the profile of plasma density and deposited power for one case.

3. RESULTS

3.1. Axial Symmetric RF Antenna

The method briefly summarized in Section 2 has been used to evaluate the radial profiles at equilibrium of a cylindrical helicon discharge at low pressure, assumed of 18 mTorr (2.4 Pa) of Argon. A dielectric tube of 5 cm of internal diameter has been considered, with a magnetostatic field of 200 Gauss along the axis of the cylinder. The numerical results have been reported in Fig. 3. The figure shows the radial profiles at equilibrium for a $m = 0$ antenna, made with an axis-symmetric coil wrapped around the discharge tube. The origin of the radial coordinate is placed at the axis of the cylinder. The figure shows (a) module of the RF electric field, (b) module of the RF magnetic field, (c) deposited power, (d) plasma density, (e) electron temperature, (f) density of the neutral gas, all at equilibrium and for three different power levels. The amplitude of the fields is shown here per Ampere of current flowing on the antenna, at the location $z = 0$ at the antenna center. The calculation shows that the plasma density increases for an increasing RF power. Furthermore, the

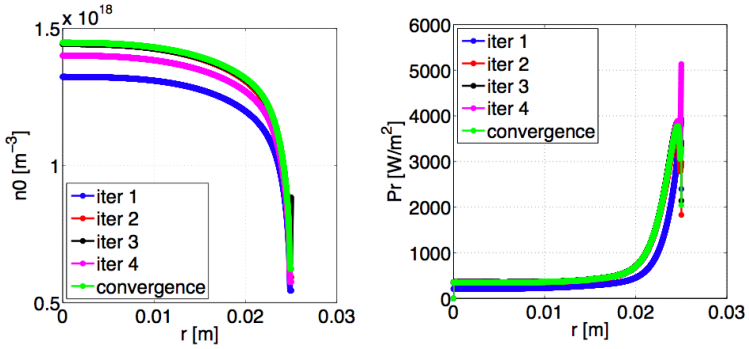

(a) (b)

Figure 2: Example of convergence on the profile of (a) plasma density, (b) deposited power, obtained from the iteration of the two codes SPIREs and EQM.

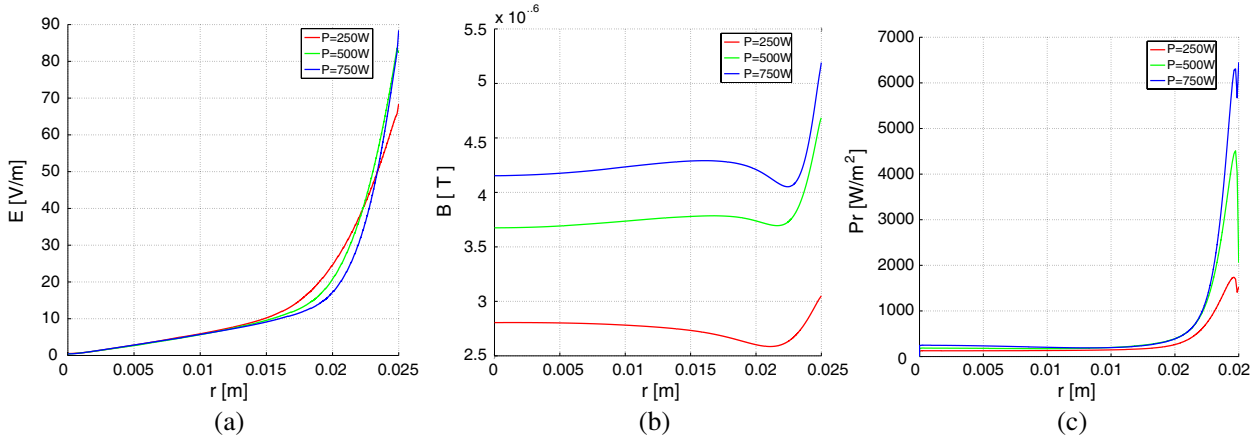

(a) (b) (c)

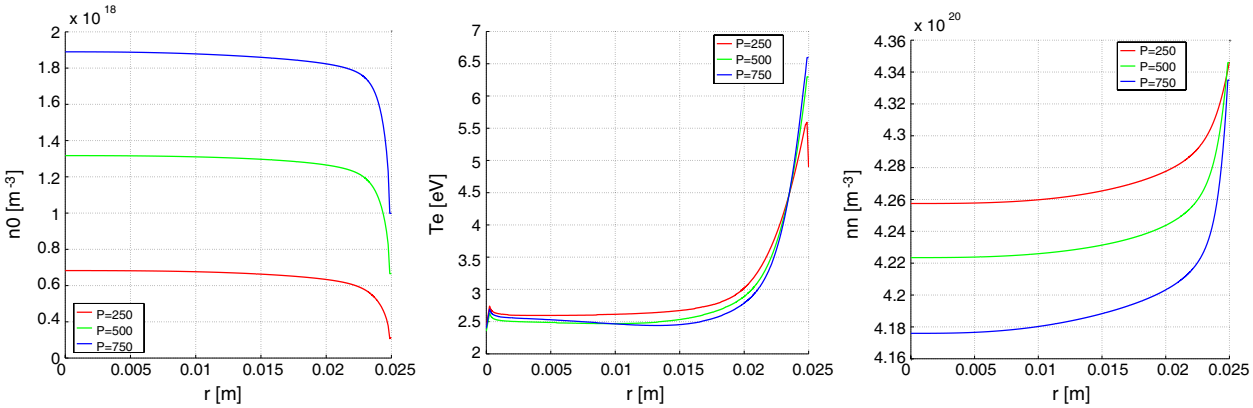

(d) (e) (f)

Figure 3: Radial profiles at equilibrium of a magnetized positive column of Argon plasma sustained by an $m = 0$ RF antenna. Gas pressure before the discharge $p_0 = 18$ mTorr, antenna frequency 13.56 MHz, axial magnetostatic field 200 Gauss. (a) Module of the RF electric field, (b) module of the RF magnetic field, (c) deposited RF power, (d) plasma density, (e) electron temperature, (f) density of the neutral gas.

density profile is peaked at the center even if the power deposition occurs mostly near the edge of the cylinder. The electron temperature remains approximatively constant vs. the power. Electron temperature increases only at the edge of the discharge, where the field intensity is larger and where the specific power Pr is higher. The neutral gas is depleted at the center of the discharge, in agreement with the observations, and it is accumulated at the side of the cylinder where neutrals recombines.

3.2. Discussion on RF Heating

The deposition of RF power occurs mainly at the edge of the plasma cylinder, where the Trivelpiece-Gould mode is rapidly dumped by collisional processes. The conditions for having a transition from edge-localized to center-localized power deposition have been shown elsewhere [10]. As a result from the power deposition calculations, it has also been possible to evaluate the contribution of different physical processes concurring to the dumping of the RF wave. It has been found that the dumping of the electromagnetic wave into the plasma occurs mostly by collisional processes of electrons with charged species, and in minor part of electrons with neutrals. At low pressures of few Pascals the Coulomb collision frequency usually dominates over the electron-neutral contribution. A smaller contribution also comes from the Landau dumping of the RF wave due to wave-particle interaction, accounted by means of the Z plasma dispersion function [2] into the dielectric tensor. The Landau term is usually negligible for cold plasmas at electron temperatures of few electronvolts. It becomes relevant only after that the electron temperature is increased (hot case).

In Argon discharges, and all high-Z gases, most of the RF power is used to counteract the inelastic losses. This holds until the atom is completely ionized (4.426 keV for Ar^{+18}), i.e., in all the cases of practical interest for the applications. At a given pressure, an increase of RF power involves a small increase of the electron temperature, since the power is mostly expended in the generation of new plasma particles, with a resulting increase of plasma density. This property of cold plasmas is particularly attractive for making plasma sources to be used in industrial processing, where low electron temperatures are desirable, to reduce the substrate damage due to ion bombardment. In spacecraft thrusters using RF plasma sources as a main propulsion stage, the opposite condition of high Te's is desirable, thus suggesting the use of low-Z gases (like hydrogen) or the addition of a second stage specifically devoted to heating (like an ICRH stage, Ion Cyclotron Resonance Heating).

4. CONCLUSION

An iterative procedure among two existing codes named SPIREs and EQM has been used to evaluate the equilibrium conditions of a radio frequency heated plasma cylinder. The first code, SPIREs, solves the two macroscopic Maxwell wave equations (Faraday and Ampere-Maxwell) for a magnetized plasma cylinder. The dielectric tensor of the plasma is a Stix dielectric tensor comprising the Z plasma dispersion function for finite-temperature effects. The second code, EQM, solved the transport of charged and neutral species as forced by a non-uniform input of RF power. From

the iteration of the codes together the equilibrium profiles of plasma density, electron temperature, neutral density, and electromagnetic fields are found as a function of the cylinder radius. The convergence is usually obtained after few iterations. Explicit calculations for a varying RF power are shown. The effect of the RF heating on the plasma properties has been discussed, in relation to the use of cold plasma sources for semiconductor processing and spacecraft RF thrusters.

REFERENCES

1. Simon, A., "Ambipolar diffusion in a magnetic field," *Phys. Rev.*, Vol. 98, No. 2, 317–318, 1955.
2. Fried, B. D. and S. D. Conte, *The Plasma Dispersion Function*, Academic, New York, 1961.
3. Stix, T. H., *Plasma Waves*, Springer-Verlag NewYork Inc., 1992.
4. Jackson, J. D., *Classical Electrodynamics*, John Wiley and Sons Inc., 1999.
5. Chen, F. F. and D. Arnush, "Generalized theory of helicon waves. I. Normal modes," *Phys. Plasmas*, Vol. 4, No. 9, 3411–3421, 1997.
6. Arnush, D. and F. F. Chen, "Generalized theory of helicon waves. II. Excitation and absorption," *Phys. Plasmas*, Vol. 5, 1239, 1998.
7. Arnush, D., *Phys. Plasmas*, Vol. 7, 3042, 2000.
8. Chen, F. F., *Introduction to Plasma Physics and Controlled Fusion, Plasma Physics*, 2nd Edition, Springer, New York, 2006.
9. Curreli, D. and F. F Chen, "Equilibrium theory of cylindrical discharges with special application to helicons," *Phys. Plasmas*, Vol. 18, 113501, 2011.
10. Curreli D., "Transition from edge-localized to center-localized power deposition in helicon discharges," *The European Physical Journal Applied Physics*, Vol. 56, 24007, 2011.
11. Melazzi, D., D. Curreli, M. Manente, J. Carlsson, and D. Pavarin, "SPIREs: A finite-difference frequency-domain electromagnetic solver for inhomogeneous magnetized plasma cylinders," *Comput. Phys. Comm.*, Vol. 183, No. 6, 1182–1191, 2012.
12. Lafleur T. and R. W. Boswell, "Particle-in-cell simulations of ambipolar and nonambipolar diffusion in magnetized plasmas," *Phys. Plasmas*, Vol. 19, 053505, 2012.
13. http://www.adastrarocket.com/aarc/.
14. http://prl.anu.edu.au/SP3/research/HDLT/.
15. http://www.hphcom.eu/.

LogicView: An Open Source Software for 3D Visualization of Models and Fields in Electromagnetics

A. O. Rodrigues[1], **J. J. Viana**[2], **and J. A. Ramirez**[1]

[1]Universidade Federal de Minas Gerais, Belo Horizonte, Minas Gerais, Brazil
[2]Independent Consultant, Logic Style, Belo Horizonte, Minas Gerais, Brazil

Abstract— The visualization of the results in three dimensional (3D) electromagnetic problems, which may involve the distribution of vector field quantities, is not well exploited and still poses some challenges. Existing softwares for the visualization of scientific data are either expensive or offers only a small set of features. We present LogicView, an open source software available under a public domain license which offers several tools and useful features for the visualization of scientific data, physical model and fields, in particular in electromagnetics. LogicView was developed in Java, allowing its use in multiple platforms (Windows, Unix or Mac). It allows 3D visualization of any set of data presented in a matrix of values. It can, therefore, be used to visualize physical models and field quantities, such as electromagnetic field distributions, the specific absorption rate (SAR) distribution and hot spots temperature distributions. The paper describes the software architecture and the computing platform. It explains in a step by step example how LogicView reads any set of values. It also presents usages of LogicView through 3D visualization of two open source models of the human body.

1. INTRODUCTION

The calculation of electromagnetic fields using numerical methods has become an important step in the solution of many engineering problems. The fast development of portable computers with growing processing capabilities has played an important role in contributing to consolidate numerical simulation as a complementary methodology to measurements. The applications cover a wide range of the electromagnetic spectrum, varying from power frequency problems, including the design of electrical machines and transmission lines, the design of antennas, and the calculation of radar cross section, amongst others.

If on one hand, several numerical techniques such as the finite difference time domain (FDTD) method, the finite element method, the method of moments, amongst others [1], are available for the field calculation, on the other hand, the visualization of the results especially in three dimensional (3D) is not well exploited and still poses a real challenge.

It is recognized that in the analysis of the results of many problems, the 3D visualization presents several advantages:

- 2D visualization of vector fields and scalar values restrains the analysis to cuts or points. Location of maximum values (hot spots), for example, is much easier in 3D visualization of equipotential surfaces.
- 3D models allow a better representation, considering that most problems are 3D in nature. 3D visualization allows visualization of how the field propagates inside the model, a result that can not be obtained in any single 2D cut. In addition, 3D visualization of specific materials also helps avoiding discontinuity when the 2D cuts are assembled.
- Visualization is an essential ingredient for understanding. Research conducted into learning processes concluded that people learn up to 83% of new information through sight [2].

The existing softwares for visualization of scientific data are expensive and offers only a small set of features, particularly in 3D such as surface plot, rotate and zoom. Other tools, such as material selection or cuts, which are important in certain analysis are normally not available. More complex visualization software offer other tools for visualization, but are expensive and are usually targeted to other purposes such as visual graphic animations.

We present LogicView, an open source software available under a public domain license [3] which offers several tools and useful features for the visualization of scientific data, physical model and fields. LogicView was developed in Java, allowing its use in multiple platforms (Windows, Unix or Mac). It allows 3D visualization of any set of data presented in a matrix of values. It can, therefore, be used to visualize physical models, such as human head models, and field quantities, such as electromagnetic fields, SAR and temperature distributions.

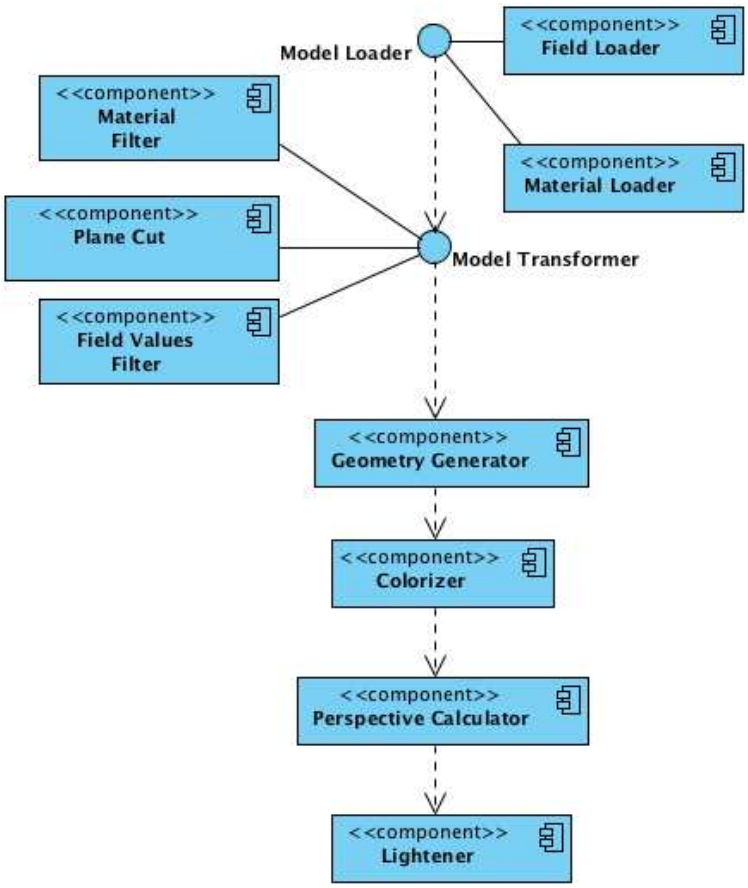

Figure 1: Software architecture diagram.

2. SOFWARE ARCHITECTURE AND PLATFORM

This section is divided in two parts. First, the architecture of LogicView is discussed. Second, the computing platform used is presented.

2.1. Software Architecture

LogicView was developed using a component-based architecture. Applications build using this architecture are composed by a number of loosely connected subsystem cooperating to implement features. In LogicView this collaboration takes the form of a pipeline that has a *Model File* as input and a specific 3D visualization as output. Figure 1 shows how the software architecture is structured.

Model processing starts with loading, which consists interpreting a model representation from disk to memory. Currently the software supports *Material Models* (descriptions of materials and surrounding space) and *Field Models* (descriptions of field values in each model voxel over time). Next comes filtering, in which components such as plane cutter, material selector or field value selector decide which voxels must be passed down the pipeline in order to generate the view requested by the user. The next phase is geometry generation in which the voxels to be rendered are analyzed and transformed into hexahedrons. After that, an optimization step removes invisible geometry faces.

Once geometry generation is completed, the color component sets the color of each visible geometry face according to the scene and the type of model being displayed. Model processing is completed by the lighting and point of view calculation steps. After the model visualization is shown, it can be interactively changed by the users. Any change in scene parameters triggers the computing of a new scene by the visualization pipeline.

2.2. Computing Platform

LogicView was developed using Java3D and the Java Media Framework. The Java platform enables LogicView to run in any operating system where the Java virtual machine and the Java 3D library

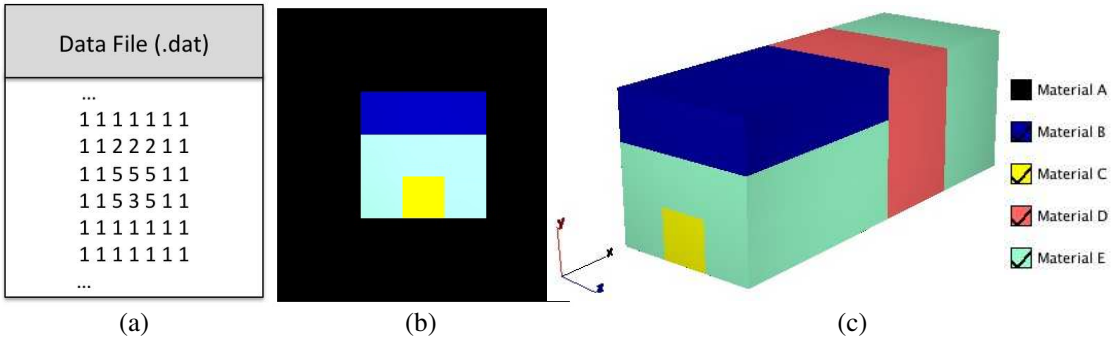

Figure 2: Poly model.

are available. This list includes among other operating systems: Linux, Mac OS, Solaris, and Windows. The Java Media Framework enables LogicView to export visualizations in JPEG, GIF, PNG and QuickTime (mov) formats.

Java3D is an open-source object-oriented API for 3D software. It contains high-level abstractions that makes it easier to write code that render 3D scenes. Java3D also allows the developer to concentrate on the application logic instead of dealing with the low-level graphic primitives of the underlying platform (OpenGL or Direct 3D).

3. FORMATTING A 3D MODEL FOR LOGICVIEW

To visualize any set of 3D matrix of values in LogicView, three steps are necessary:

1. Write the 3D matrix in a text file. Each value must be separated by a space. The values must be written in the file in x-y slices separated by a line break for each new value of z. Each value will represent one of the materials in the physical model. This file must have a .dat extension and is called the *Data Source File*.
2. Create another text file, with a .3dm extension. This file will describe the properties of the model and materials and will be called the *Model File*.
3. Open LogicView, choose "Model", "Open Model", and then choose the *Model File*.

The next subsection exemplifies the construction of the *Data Source File* and the *Model File*.

3.1. Example of a Model File: Poly Model

This example is available for download at [3]. Poly is a 3D matrix of integer values, with $10 \times 7 \times 7$ values in x, y and z directions, respectively. Each integer value on the matrix represents a different material. Poly has five different materials, represented by the integer values of 1 to 5. This matrix is in a text file, named Poly.dat, that is called the *Data Source File*, detailed in the next.

The Data Source File: In the Poly Model, the integer values of 1 to 5 represent different materials A to E, respectively. Figure 2(a) shows an extract of Data Source File for the slice $z = 2$, and Figure 2(b) indicates the corresponding 2D picture of the model (1 = A is black, 2 = B is blue, 3 = C is yellow and 5 = E is light green). To read this Data Source File, LogicView needs a Model File that is described next.

The Model File: This file, with extension .3dm, describes the materials and geometry of the model and provides a pointer to the *Data Source File*. The data in the Model file is composed of four Sections: *Heading*, *Materials*, *Data Source* and *End of File*.

The *Heading Section* contains comments (⟨?xml version...?⟩⟨!-Created by...-!⟩), and information of the model, such as the name of the model (⟨MaterialModel name = "Poly"), dimension ("dimension = number of cubes in x, y and z directions") and size of each cube in x, y and z direction in meters ("deltas = 0.02, 0.02, 0.02, 0.02"). The *Materials Section* describes each of the materials in the model inside the ⟨material...⟩⟨/material⟩ tag, using the following properties: code ("material code = integer associated with each material"), color ("color = RGB code for the color of the material"), name of the material, transparency (0 means no transparency), visible (true shows the material, false it is not shown) and finishes with the end material tag (⟨/material⟩). The *Data Source* Section is a pointer to the *Data Source File* described before. The *End of File Section* is the final line of the file, that must contain the tag that ends of the material model (⟨/MaterialModel⟩).

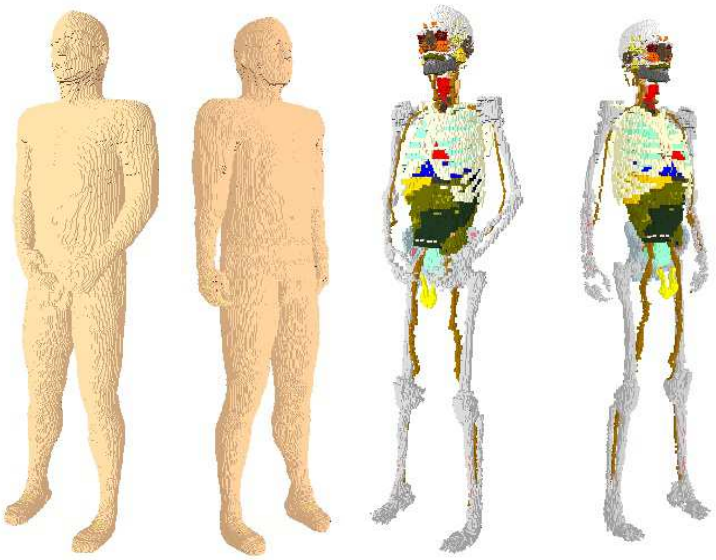

Figure 3: Zubal Phantom with arms folded and arms down — complete and without skin and muscles.

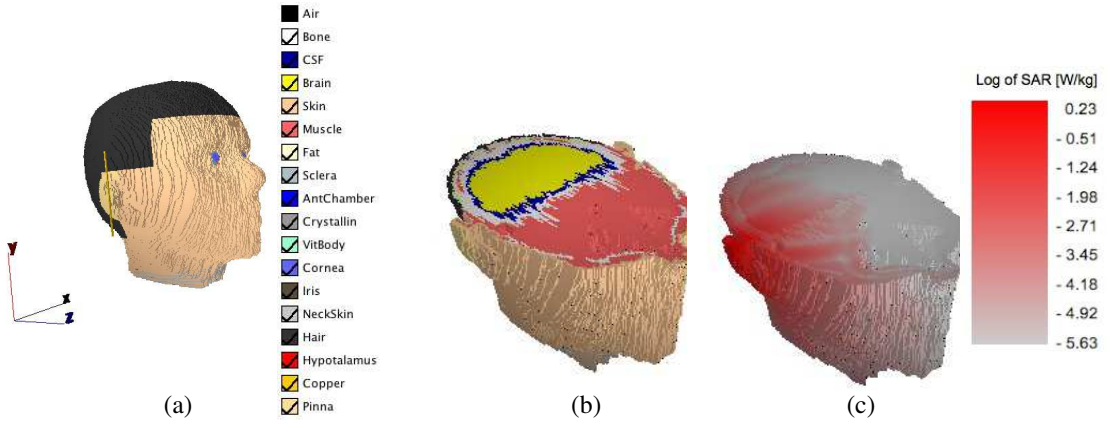

Figure 4: John3Doe model.

Visualization of the Model: Figure 2(c) shows the Poly Model without material A. Material A (value = 1) is used to simulate air and surrounds the other materials.

Example of Field File: Poly.3df LogicView allows the user to associate field quantities, such as electric or magnetic fields, specific absorption rate (SAR) distribution, temperature distributions, and others quatities to a physical model. In order to do that, the user must provide LogicView an input file with extension .3df, called *Field File*. Similarly to the *Model File*, the data inside the *Field File* is composed of *Heading*, *Field Data*, *Material Model Associated* and *End of File*.

4. VISUALIZATION OF OPEN SOURCE MODELS

This section shows some of the features LogicView for the visualization of more complex models which are available under public domain licenses. It also shows the visualization of field quantities.

4.1. Zubal Models — Body, Head and Torso [4]

The Zubal phantoms are a group of human phantoms that are used in several researches, which were developed from a segmented computed tomography (CT) of the torso and head, and magnetic resonance images (MRI) of the head slices of two living human males [4]. All of these volume arrays represent high resolution models of the human anatomy and can serve as a voxel-based anthropomorphic phantom suitable for many computer-based modeling and simulation calculations. The phantom data was modified using a Matlab program to re-arrange the data in the x; y; z order required by LogicView, as described in Section 2, which is available at [3]. Figure 3 illustrates the

Zubal phantoms created by LogicView.

4.2. John3Doe — Human Head Model [5]

The head model is composed of 17 different materials: air, bone, cerebrospinal fluid (CSF), brain, skin, muscle, fat, eye (subdivided in sclera, anterior chamber, crystallin, vitreous body, cornea and iris), neck skin, hair, hypothalamus and pinna. The head is surrounded by a layer of air from $x = 0$ to $x = 20$ (3.7 cm), $x = 127$ to $x = 150$ (4.3 cm), $y = 0$ to $y = 29$ (3.2 cm), $y = 250$ to $y = 258$ (8.9 cm), $z = 0$ to $z = 45$ (5.0 cm) and $z = 237$ to $z = 258$ (2.3 cm). The model size is 151 cells in x, 259 cells in y and 259 cells in z, resulting in approximately 10 million cubic cells (10,129,231) and a total size of 28.09 cm × 28.75 cm × 28.75 cm. The cell size ($\Delta x \times \Delta y \times z$) is 1.86 mm × 1.11 m × 1.11 mm in x, y and z directions, respectively.

Figure 4(a) shows a complete view of the human head model whereas Figure 4(b) illustrates the internal tissues within the head and Figure 4(c) the SAR distribution due to a cellular phone.

5. CONCLUSION

This paper has introduced LogicView, an open source software available under public domain license that allows 3D visualization of physical models and field quantities. LogicView was developed in Java and can be used in multiple operating systems, which confers to it portability. A simple example was used to illustrate how it can read any set of values. In addition, two more complex examples were used to show the features of the software, a complete human phantom and a heterogeneous human head model. LogicView offers important features for the visualization of models and fields in 3D and is particularly suited to electromagnetics.

ACKNOWLEDGMENT

This work was supported by the National Council for Scientific and Technological Development — CNPq, Brazil, under grant: 306.910/2006-3, and by The State of Minas Gerais Research Foundation — FAPEMIG, Brazil, under grants: TEC 251/09 and Pronex APQ 01075/09.

REFERENCES

1. Jin, J. M., *Theory and Computation of Electromagnetic Fields*, IEEE Press, John Wiley and Sons, New Jersey, USA, 2010.
2. Carvajal, A., "Quantitative comparison between the use of 3D vs 2D visualization tools to present building design proposals to non-spatial skilled end users," *Proceedings of the Ninth International Conference on Information Visualisation*, 291–294, London, UK, Jul. 2005.
3. Rodrigues, A. O., J. J. Viana, and J. A. Ramirez, "LogicView — An open source software for 3d visualization of human phantoms, electromagnetic fields and temperature distributions," LogicView 3D is an open source software available under a public domain license at [http://www.logicstyle.com], 2010.
4. Gindi, G., M. Lee, A. Rangarajan, and I. G. Zubal, "Bayesian reconstruction of functional images using anatomical information as priors," *IEEE Trans. on Med. Imag.*, Vol. 12, No. 4, 670–680, 1993.
5. Rodrigues, A. O., J. J. Viana, and J. A. Ramirez, "A head model for the calculation of SAR and temperature rise induced by cellular phones," *IEEE Trans. on Magn.*, Vol. 44, No. 6, 1446–1449, 2008.

A Method to Model a Spindle System with an Electromagnetic Actuator

Jong Hyun Kim, **Gyu Ha Kim**, **and Sun-Kyu Lee**
School of Mechatronics, Gwangju Institute of Science and Technology
Oryong-dong, Buk-gu, Gwangju 500-712, Republic of Korea

Abstract— The goal of this research is to model a spindle system with an electromagnetic actuator. This model will be applied to a spindle run-out control and a tool motion control. The spindle system is consisted of ball bearing units and four electromagnetic actuators. The electromagnetic actuator is used to compensate the run-out error of the spindle in this system. A bondgraph modeling method is used to model the spindle system including the electromagnetic forces. The dynamic mechanical model of the spindle system is represented and the dynamic equations are specified based on the model. In bearing units, bidirectional bearing compliance expresses the fact that a certain load on a spindle does not only induce compliance in the load direction but also induce relatively small compliance in the orthogonal direction due to the bearing structure. The electromagnetic forces are acted at the end of the shaft and considered as the external load on the shaft. The bondgraph model of the spindle system considered all the relations between electrical systems and mechanical systems. Therefore it is respected that it is easy to model the spindle system using the bondgraph modeling method and apply the model to the spindle control.

1. INTRODUCTION

Recently, many designers have attempted to create "structured, textured or engineered" surfaces that provide novel functions or combinations of functions [1, 2]; these may include mechanical contact, hydrodynamics, and metrology artifacts. Many functions used in applications rely on the wettability, friction, adhesion, and optical properties of textured surfaces. Micro-surfaces are generated using a variety of manufacturing methods, such as cutting, laser machining, electron beam writing, and lithographic methods. These manufacturing methods have been adapted so that they control the trajectory motion of the cutting tool using lead zirconate titanate (PZT) actuators [3, 4]. Research on micro-topography generation using trajectory motion control has been performed by Wada et al. [5], who used a fixed tool controlled by piezoelectric actuators on three axes.

The current paper presents a tool mounted on an actively controlled rotational shaft using an electromagnetic actuator (EMA) which is used to generate the surface micro-topography. Spindle control using the EMA has been investigated by the author's research group for several years [6–8]. The spindle system consists of a spindle shaft supported by two pairs of ball bearings, the EMA, and an AC motor with a flat belt. The EMA is installed at the front part of the spindle to compensate both the run-out error and the thermal displacement in the radial direction. The EMA consists of 8 magnetic poles and it controls the motion of the spindle in the x-y plane. A bondgraph modeling method is used to model the spindle system including the EMA. The bondgraph modeling method has an advantage to model the system (consisted of an electrical and mechanical part) easily and also is easy to modify the model according to the various condition of the system. The bondgraph model is applied to control the spindle system in order to compensate the run-out error and control the tool trajectory motion. In the spindle control system, the values of control parameters are changed according to the model and the performance is determined by the difference between the model and the real system. So the accurate model is needed in order to control the real system precisely. The comparison results between the model and real system is represented and shows it can be applied to the spindle control system.

2. SPINDLE SYSTEM

The spindle bearing system consists of a spindle shaft supported by two pairs of ball bearings, the EMA, and an AC motor with a flat belt. The EMA, installed at the front of the spindle shaft, consists of 8 magnet poles enabling it to be controlled in the radial direction. The x-y displacements are measured by two capacitance sensors located at the end of the spindle shaft, and the values are transferred to a dSPACE controller board. The control signals, which are calculated by a PC, are transferred to linear current amplifiers.

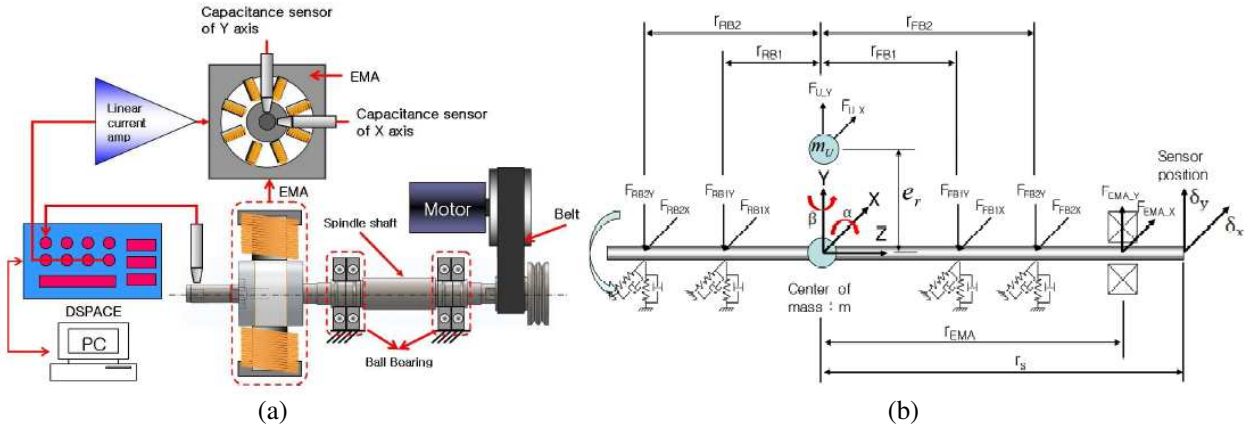

Figure 1: Structure of spindle system: (a) schematic diagram, (b) mechanical model.

The bondgraph modeling method is used to model the spindle system including the electromagnetic forces. The dynamic mechanical model of the spindle system is shown in Figure 1(b). Assuming that the spindle shaft is a rigid body, its motion is constrained by the elasticity of the ball-race. The equations of translational motion are

$$\begin{aligned} m \cdot \ddot{x} &= F_{U\_X} + F_{EMA\_X} - F_{FB1X} - F_{FB2X} - F_{RB1X} - F_{RB2X} \\ m \cdot \ddot{y} &= F_{U\_Y} + F_{EMA\_Y} - F_{FB1Y} - F_{FB2Y} - F_{RB1Y} - F_{RB2Y} \\ \begin{bmatrix} m & 0 \\ 0 & m \end{bmatrix} \begin{bmatrix} \ddot{x} \\ \ddot{y} \end{bmatrix} &= \begin{bmatrix} F_{U\_X} \\ F_{U\_Y} \end{bmatrix} + \begin{bmatrix} F_{EMA\_X} \\ F_{EMA\_Y} \end{bmatrix} - \begin{bmatrix} F_{FB1X} \\ F_{FB1Y} \end{bmatrix} - \begin{bmatrix} F_{FB2X} \\ F_{FB2Y} \end{bmatrix} - \begin{bmatrix} F_{RB1X} \\ F_{RB1Y} \end{bmatrix} - \begin{bmatrix} F_{RB2X} \\ F_{RB2Y} \end{bmatrix} \end{aligned} \tag{1}$$

The equations of rotational motion are

$$\begin{aligned} I \cdot \ddot{\alpha} = & - r_{EMA} \cdot F_{EMA\_Y} + r_{FB1} \cdot F_{FB1Y} + r_{FB2} \cdot F_{FB2Y} \\ & - r_{RB1} \cdot F_{RB1Y} - r_{RB2} \cdot F_{RB2Y} \\ I \cdot \ddot{\beta} = & \, r_{EMA} \cdot F_{EMA\_X} - r_{FB1} \cdot F_{FB1X} - r_{FB2} \cdot F_{FB2X} \\ & + r_{RB1} \cdot F_{RB1X} + r_{RB2} \cdot F_{RB2X} \\ \begin{bmatrix} I & 0 \\ 0 & I \end{bmatrix} \begin{bmatrix} \ddot{\alpha} \\ \ddot{\beta} \end{bmatrix} = & \, r_{EMA} \begin{bmatrix} 0 & -1 \\ 1 & 0 \end{bmatrix} \begin{bmatrix} F_{EMA\_X} \\ F_{EMA\_Y} \end{bmatrix} - r_{FB1} \begin{bmatrix} 0 & -1 \\ 1 & 0 \end{bmatrix} \begin{bmatrix} F_{FB1X} \\ F_{FB1Y} \end{bmatrix} \\ & - r_{FB2} \begin{bmatrix} 0 & -1 \\ 1 & 0 \end{bmatrix} \begin{bmatrix} F_{FB2X} \\ F_{FB2Y} \end{bmatrix} + r_{RB1} \begin{bmatrix} 0 & -1 \\ 1 & 0 \end{bmatrix} \begin{bmatrix} F_{RB1X} \\ F_{RB1Y} \end{bmatrix} \\ & + r_{RB2} \begin{bmatrix} 0 & -1 \\ 1 & 0 \end{bmatrix} \begin{bmatrix} F_{RB2X} \\ F_{RB2Y} \end{bmatrix} \end{aligned} \tag{2}$$

where

F_U: unbalanced force

F_{FB}, F_{RB}: reaction force of the bearing

x, y: displacement at a center of mass

α, β: angle at a center of mass

r: distance from a center of mass to each element.

The electromagnetic force generated from the EMA and transferred to the spindle shaft is expressed as follows. The transfer function of the linear current amplifier is

$$G_a(s) = K_a \cdot \frac{\omega_a}{s + \omega_a} \ (\mathrm{A/V}) \tag{3}$$

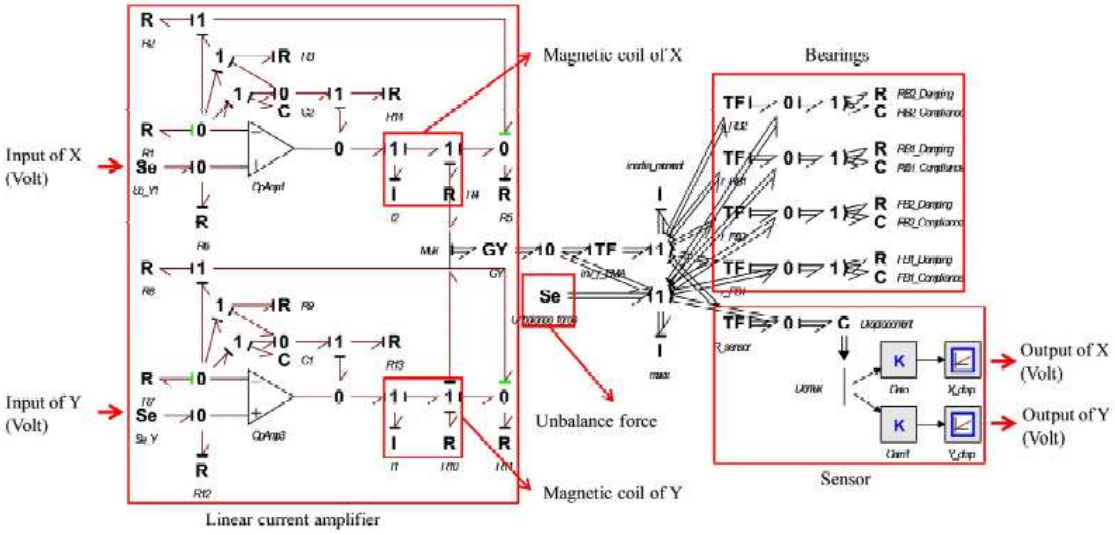

Figure 2: Bondgraph model of the spindle system.

The electromagnetic force acting on the spindle shaft is

$$F_{EMA} = 4 \cdot \cos(\alpha) \cdot \frac{\mu_0 \cdot A_p \cdot N^2 \cdot i_0 \cdot i}{g_0^2} \text{ (N)} \tag{4}$$

The current gain, defined here as the ratio of the electromagnetic force to the input current, is

$$K_i = 4 \cdot \cos(\alpha) \cdot \frac{\mu_0 \cdot A_p \cdot N^2 \cdot i_0}{g_0^2} \text{ (N/A)} \tag{5}$$

From (3) and (5), the electromagnetic force can be expressed as

$$G_{EMA}(s) = K_i \cdot G_a(s) \text{ (N/V)} \tag{6}$$

The reaction force of the ball bearings acting on the spindle shaft is given as

$$\begin{bmatrix} F_{BX} \\ F_{BY} \end{bmatrix} = \begin{bmatrix} k_x & k_{xy} \\ k_{yx} & k_y \end{bmatrix} \begin{bmatrix} x \\ y \end{bmatrix} + \begin{bmatrix} c_x & c_{xy} \\ c_{yx} & c_y \end{bmatrix} \begin{bmatrix} \dot{x} \\ \dot{y} \end{bmatrix} \tag{7}$$

where k is stiffness of the bearing and c is damping of the bearing. According to the above equations, the whole spindle system model is obtained as follows.

3. COMPARISON RESULTS

The parameters of the spindle system are represented in Table 1. The stiffness, damping and current gain are obtained from the frequency analysis of the system.

According to the Table 1, the transfer function of the spindle system is calculated from the bondgraph model. In this model, it is assumed that the value of cross-coupled damping factors is zero. For the x-axis,

$$G_p(s) = \frac{6.8 \cdot 10^{10} s^3 + 1.4 \cdot 10^{16} s^2 + 2.3 \cdot 10^{19} s + 3.8 \cdot 10^{23}}{s^6 + 2.1 \cdot 10^5 s^5 + 1.9 \cdot 10^9 s^4 + 10^{13} s^3 + 5.5 \cdot 10^{16} s^2 + 6.3 \cdot 10^{19} s + 2.5 \cdot 10^{23}} \tag{8}$$

For the y-axis,

$$G_p(s) = \frac{5.8 \cdot 10^{10} s^3 + 1.2 \cdot 10^{16} s^2 + 10^{19} s + 3.2 \cdot 10^{23}}{s^6 + 2.1 \cdot 10^5 s^5 + 1.7 \cdot 10^9 s^4 + 8.4 \cdot 10^{12} s^3 + 5.1 \cdot 10^{16} s^2 + 4.8 \cdot 10^{19} s + 2.4 \cdot 10^{23}} \tag{9}$$

The following presents the results comparing the frequency responses of the spindle system model and the real system.

According to the results, the frequency response obtained from the bondgraph model of the spindle system is similar to that of the real system. Therefore the bondgraph model can be applied to the spindle control system.

Table 1: System parameters used in the bondgraph model.

Parameters	Description	Values	units
m	mass of shaft	2.278	kg
I	inertia of shaft	0.024	kg*m^2
r_FB1	distance from mass center	0.014	m
r_FB2	distance from mass center	0.028	m
r_RB1	distance from mass center	0.072	m
r_RB2	distance from mass center	0.086	m
r_EMA	distance from mass center	0.091	m
r_Tool	distance from mass center	0.161	m
C_x	X-damping of bearing	943	Nsec/m
C_y	Y-damping of bearing	464	Nsec/m
K_x	X-stiffness of bearing	16.9	N/μm
K_y	Y-stiffness of bearing	16.6	N/μm
K_{xy}	cross-coupled stiffness	−1.07	N/μm
K_{yx}	cross-coupled stiffness	−1.89	N/μm
K_{ix}	current gain of X axis	126	N/A
K_{iy}	current gain of Y axis	103	N/A

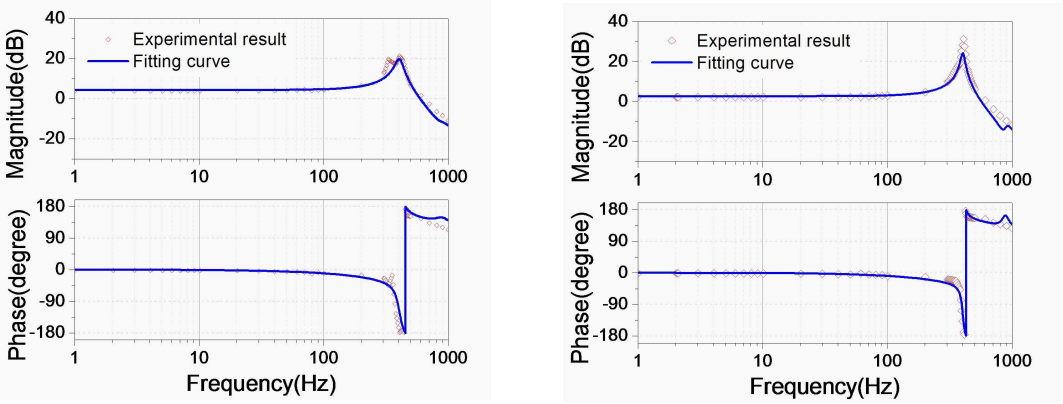

Figure 3: Frequency response of the spindle system, (a) x axis. (b) y axis.

4. CONCLUSIONS

In this paper, a spindle system with the EMA is represented in order to compensate each run-out error and thermal displacement in radial direction and control the tool trajectory motion. The bondgraph modeling method is used in order to model the spindle system. It is easy to make and modify a model easily. The bondgraph model is obtained from the electrical and mechanical relations of the spindle system. The parameters are obtained from the frequency response of the spindle system. According to the comparison results between the model and real system, the frequency response of the model is similar to that of the real system. Therefore the bondgraph model can be applied to the spindle control system. It is respected that it is easy to model the system using the bondgraph modeling method and apply to the control system.

ACKNOWLEDGMENT

This work was supported by a National Research Foundation of Korea (NRF) NRL Program grant funded by the Korean government (MEST) (No. 20120018621), as well as the Ministry of Knowledge Economy (MKE) of the Korean government (No. 10033595-2011-13 and 2010-H-003-00030100-2010).

REFERENCES

1. Evans, C. J. and J. B. Bryan, "Structured, textured, or engineered surface," *Cirp Annals-Manufacturing Technology*, Vol. 48, No. 2, 541–556, National Institute of Standards and Technology, Gaithersburg, USA, 1999.
2. De Chiffre, L., P. Lonardo, H. Truumpold, D. A. Lucca, G. Goch, C. A. Brown, J. Raja, and H. N. Hansen, "Quantitative characterization of surface texture," *CIRP Annals, Manufacturing Technology*, Vol. 49, No. 2, 635–652, 2000.
3. Kwok, T. C., C. F. Cheung, L. B. Kong, S. To, and W. B. Lee, "Analysis of surface generation in ultra-precision machining with a fast tool servo," *Proc. IMechE, Part B: Journal of Engineering Manufacture*, Vol. 224, 1351–1367, 2010.
4. Araki, T., W. Gao, S. Kiyono, M. Sudoh, and M. Mito, "Generation of large-area microstructured surface by diamond turning with a fast tool servo," *Proc. of the 17th Annual Meeting, ASPE*, 538–541, 2002.
5. Wada, T., M. Takahashi, T. Moriwaki, and K. Nakamoto, "Development of a three axis controlled fast tool servo for ultraprecision machining (1st report) — Development of 3-axis FTS unit and evaluation of its characteristics," *JSPE*, Vol. 73, No. 12, 1345–1349, 2007.
6. Ahn, J.-S., S.-M. Kim, and S.-K. Lee, "Compensation of spindle unbalance-induced vibration using an electromagnetic exciter," *Proc. ASPE 16th Annual Meeting Conference*, 2001.
7. Ahn, J.-S., S.-M. Kim, and S.-K. Lee, "Micro machining using an electro magnetic excitor," *Proc. 2nd Euspen International Conf.*, 2001.
8. Zhao, S., T.-H. Kim, W.-S. Kim, and S.-K. Lee, "Modeling of an electromagnetically actuated spindle system considering bidirectional bearing compliance," *International Conference on Mechatronics and Information Technology 2005*, Vol. 1, 2006.

A Direct Experimental Inspection of Displacement Currents

Zi-Hua Weng[1], **Jing-Yan He**[1], **Jin-Pan Zhu**[1], **and Ying Weng**[2]

[1]School of Physics and Mechanical & Electrical Engineering
Xiamen University, Xiamen 361005, China
[2]College of Chemistry & Chemical Engineering, Xiamen University, Xiamen 361005, China

Abstract— J. C. Maxwell was first to describe the electromagnetic features with two methods, the quaternion and the vector. And it inspires other scholars to depict the electromagnetic theory with the octonion. The most conclusions of the electromagnetic theory described with octonion are the same as that with the vector, except for the orientation of displacement currents etc.. In recent years, along with the evolution of measurement technologies, the researchers are attempting to validate directly the displacement current in the experiment. The paper proposes and fulfills one phase measurement experiment to scrutinize the orientation of displacement currents. The test results do not coincide with theoretical values of the classical electromagnetic theory. While part test results are close to the theoretical values of the electromagnetic theory described with the octonion, although it cannot explain all of test results yet. The study indicates that the recent measurement technology is capable of inspecting directly the amplitude, the phase value, and the orientation of displacement currents.

1. INTRODUCTION

J. C. Maxwell was first to mix two methods, the quaternion and the vector terminology, to describe the electromagnetic features. The quaternion is divided into the scalar part and the vectorial part. And the latter was evolved into the conventional vector. Up to the present, the electromagnetic theory described by the vector is quite successful, and it seems to hint at that it may be feasible to accept the quaternion and the octonion to represent the electromagnetic features [1, 2]. Unfortunately it is not successful to adopt the quaternion directly to depict electromagnetic features.

The octonion is decomposed into the quaternion and the S-quaternion. The S-quaternion can be used to describe the electromagnetic equations, and that the equations are capable of transforming into the electromagnetic equations in the 3-dimensional vector space equivalently. The electromagnetic equations described with the S-quaternion are the same as Maxwell's equations in the classical electromagnetic theory, except for the orientation of the displacement current [3].

H. R. Hertz discovered firstly the electromagnetic waves, thereby confirmed indirectly the conceptual validity of the displacement currents. Subsequently other scholars repeated and modified the Hertz's experiment [4, 5], but none of them verified directly the orientation of displacement currents. Along with the recent development of measurement technologies, S. M. Godin etc originate to scrutinize directly the accuracy of displacement currents [6].

During the recent years, A. Chakrabarty etc are making an attempt at verifying directly the amplitude of magnetic effects induced by the displacement current [7]. They brought forward one experimental proposal of the parallel-plate capacitor. On the basis of some scholars' studying, the paper brings forward and fulfills one experimental proposal with the phase measurement method. The experiment is capable of inspecting directly the orientation of displacement currents, by means of measuring the amplitude and the phase value of the induced electromotive force which produced from the magnetic effect of displacement currents.

2. PHASE DIFFERENCE

In the parallel-plate air dielectric capacitor (Figure 1), it appeals to apply the alternating voltages across the capacitor plates, in order to yield the induced electromotive force large enough to be capable of measuring. In the capacitor plates, the alternating voltage with the frequency f is,

$$V_1 = V_{10} \exp(j\omega t), \tag{1}$$

and it forms the electric field $\mathbf{E}_1$ between the plates, while its electric displacement $\mathbf{D}_1$ is,

$$\mathbf{D}_1 = \varepsilon_0 \mathbf{E}_1 = \mathbf{i}_z (V_{10}/d) \exp(j\omega t), \tag{2}$$

where ε_0 is the air dielectric coefficient, d is the interval between two plates, $\omega = 2\pi f$. $\mathbf{i}_z$ is the unit vector of the normal of plate. j is imaginary unit, and $j^2 = -1$.

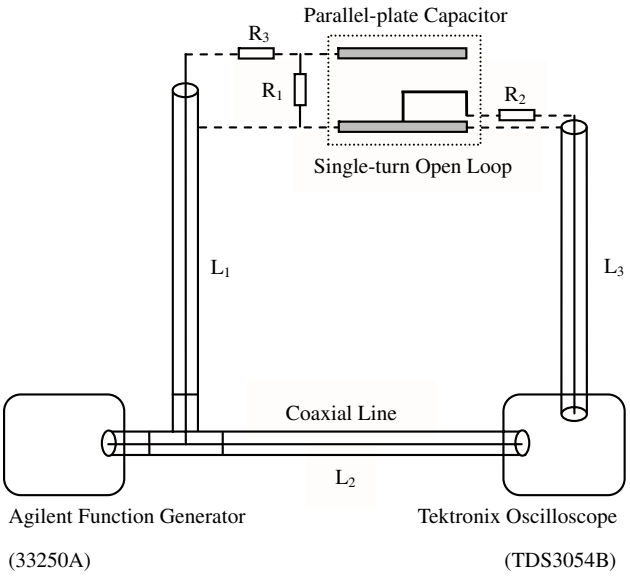

Figure 1: The proposal experimental scheme for the phase measurement of the magnetic effect produced by the displacement current.

The displacement current in the capacitor is,

$$\mathbf{J}_d = \partial \mathbf{D}_1/\partial t = \mathbf{i}_z(j\omega\varepsilon_0 V_{10}/d)\exp(j\omega t), \tag{3}$$

The displacement current is along the direction of $\mathbf{i}_z$, and the magnetic field H_φ produced by $\mathbf{J}_d$ surrounds the direction of $\mathbf{i}_z$. According to the Ampere-Maxwell equation in the electromagnetic theory described with the S-quaternion,

$$\oint \mathbf{H} \cdot d\mathbf{l} = -I, \tag{4}$$

where the closed curvilinear integral of the magnetic field $\mathbf{H}$ is $2\pi r H_\varphi$, the electric current I in the round cross-section with the radius r is $\pi r^2 J_d$, with $\mathbf{J}_d = \mathbf{i}_z J_d$. a is the radius of plate, with $r \le a$. $d\mathbf{l}$ is the oriented line.

The above deduces the annular magnetic field,

$$H_\varphi = rJ_d/2 \quad (r < a). \tag{5}$$

The annular magnetic field H_φ produced by the displacement current induces the magnetic flux, $\Psi = \int \mu_0 H_\varphi h dr$, in the open loop,

$$\Psi = -\left(j\omega\mu_0\varepsilon_0 a^2 h V_{10}/(4d)\right)\exp(j\omega t). \tag{6}$$

According to the Faraday's law, the induced magnetic flux density is $V_2 = -\partial\Psi/\partial t$, and

$$V_2 = -\left(\pi^2 h a^2 f^2 V_{10}/(c^2 d)\right)\exp(j\omega t), \tag{7}$$

where $c^2 = 1/(\mu_0\varepsilon_0)$, and h is the height of rectangular single-turn open loop.

Contrasting Eq. (1) and Eq. (7) reveals that, the phase difference between the induced electromotive force V_2 and the applying voltage V_1 is π. That is, two of them have opposite phase in the electromagnetic theory with the S-quaternion.

In the electromagnetic theory with the vector, Eq. (4) is rewritten as, $\oint \mathbf{H} \cdot d\mathbf{l} = I$, therefore the phase difference between the induced electromotive force V_2 and the applying voltage V_1 is 0 (or 2π). That is, two of them are in phase in the classical electromagnetic theory.

3. EXPERIMENTAL SCHEME

In the experiment, the interval of two plates is $d = a$, and the height of the rectangle single-turn open loop is $h = d/2$. The applying voltage across the capacitor plates is $V_1 = V_{10}\sin(\omega t + \varphi_1)$,

while the outputting induced electromotive force is $V_2 = V_{20}\sin(\omega t + \varphi_2)$. If the inputting power is too low, the outputting voltage will be on the verge of the error range. Thereby the signal source should adopt either the function generator or the signal generator combined with the power amplifier, while the inputting voltage is $V_{10PP} = 10\,\mathrm{V}$.

When the radius is $a = 100\,\mathrm{mm}$, there is one constant k_1 depending solely on the geometrical structure of the capacitor and of the single-turn open loop,

$$k_1 = V_{20}/\left(V_{10}f^2\right) = \left(\pi^2 h a^2\right)/\left(c^2 d\right) = 55 \times 10^{-20}.$$

If V_{20} is in millivolt, V_{10} is in volt, and f is in MHz, the above can be rewritten as,

$$k_2 = V_{20(mv)}/\left(V_{10(v)}f^2_{(\mathrm{MHz})}\right) = k_1 \times 10^{15} = 55 \times 10^{-5},$$

further the above can be magnified to constant A, in order to calculate and compare expediently,

$$A = k_2 \times 10^5 = 55.$$

In the experiment, the measured value of A is one curve with sharp undulating amplitudes, and its function value is A_m. The phase difference between the V_2 and the V_1 is varied along with the increasing of frequencies. Because the coaxial lines L_1 and L_2 have the same one length, the phase difference is equals to zero when same one signal inputs into two lines. The measured phase difference includes mainly the phase difference caused by the coaxial line $L_3 = 0.53\,\mathrm{m}$, and its phase correction formula is, $\Delta\varphi = 360^\circ \times (L_3/\lambda) = 90.86^\circ \times f/100$. Herein the wavelength is $\lambda = c'/f$, c' is the speed of electromagnetic waves in the coaxial line and is about $2.1 \times 10^8\,\mathrm{m/s}$, the signal frequency is in MHz.

4. RESULTS

4.1. Experiment A

In the experiment, the capacitor plates are the brass with the radius 100 mm, and the measured frequency range is within 1 MHz $\sim$ 80 MHz. The parallel-connected resistor $R_1 = 50\,\Omega$, and the

Table 1: The phase difference of the applied voltage and the induced electromotive force ($a = 100\,\mathrm{mm}$, $R_1 = 50\,\Omega$, $R_2 = R_3 = 200\,\Omega$. V_{PP10}, V_{PP20}, f are in volt, millivolt, and MHz respectively).

f	V_{PP10}	V_{PP20}	$\Delta\varphi(^\circ)$	A	f	V_{PP10}	V_{PP20}	$\Delta\varphi(^\circ)$	A
41	16.39	89.55	120	325.03	61	16.10	88.88	−158	148.36
42	16.52	85.53	125	293.50	62	16.15	98.25	−150	158.26
43	16.62	82.13	128	267.26	63	16.14	92.14	−138	143.83
44	16.77	85.16	130	262.30	64	16.32	91.20	−132	136.43
45	16.91	88.01	132	257.02	65	16.61	76.48	−124	108.98
46	17.21	87.37	137	239.92	66	16.70	66.12	−120	90.89
47	17.28	89.81	140	235.28	67	17.18	65.62	−115	85.09
48	17.25	91.87	142	231.15	68	17.57	56.06	−105	69.00
49	17.21	93.41	152	226.06	69	17.98	47.80	−108	55.84
50	17.16	90.28	163	210.44	70	18.31	40.77	−110	45.44
51	17.37	89.14	170	197.30	71	18.84	29.97	−120	31.56
52	17.31	89.41	170	191.02	72	19.61	27.83	−135	27.38
53	17.19	91.99	172	190.51	73	20.40	33.28	−160	30.61
54	16.89	94.09	170	191.04	74	22.40	39.11	170	31.88
55	16.75	97.01	170	191.46	75	23.40	48.01	168	36.47
56	16.45	97.55	180	189.10	76	24.42	57.26	168	40.60
57	16.33	96.32	−175	181.54	77	24.87	69.72	165	47.28
58	16.18	96.62	−170	177.51	78	25.46	80.22	165	51.79
59	16.30	104.30	−162	183.82	79	25.83	103.10	160	63.96
60	16.05	93.20	−154	161.30	80	24.96	125.00	162	78.25

serial-connected resistors $R_2 = R_3 = 200\,\Omega$. In the lower frequency range, such as the 1 MHz $\sim$ 40 MHz, the function value A_m is quite high and is deviated severely from the theoretical value $A = 55$. When the signal frequency approaches the frequency range 60 MHz $\sim$ 80 MHz, the function value A_m has the chance to be able to close to the theoretical value $A = 55$. The test results reveal that the curve A_m has two cross points with the line $A = 55$ (Table 1). Before the phase value correcting, the phase difference of the cross point with the higher frequency is near to π. After the phase value correcting, the phase difference of the cross point with the lower frequency is near to π.

The above measured result states that the phase difference φ of cross points between the measured curve A_m and the theoretical value $A = 55$ is close to $-\pi$ or $\pi/2$. The measured result φ is deviated severely from the theoretical value 2π of the classical electromagnetic theory. Meanwhile a part of results which the phase difference φ is close to $-\pi$ in the above can be explained by the electromagnetic theory described with the octonion. When the serial-connected resistors $R_2 = R_3$ vary from $50\,\Omega$ to $300\,\Omega$, there are the same conclusions in the experiments.

4.2. Experiment B

In the experiment, the capacitor plates are the brass with the radius 150 mm, and the measured frequency range is within 40 MHz $\sim$ 80 MHz. The parallel-connected resistor $R_1 = 50\,\Omega$, and the serial-connected resistors $R_2 = R_3 = 200\,\Omega$. The measured results reveal that the curve A_m has two cross points with the theoretical value $A = 123.75$ (Table 2). After the phase correcting, the phase differences of cross points are located on the span from $-3\pi/4$ to $-5\pi/4$.

The above measured results state that the phase difference φ of cross points between the measured curve A_m and the theoretical value $A = 123.75$ is close to $-\pi$. The measured results φ are deviated severely from the theoretical value 2π of the Maxwell's classical electromagnetic theory. Meanwhile the result which the phase difference φ is close to $-\pi$ in the above can be explained by the electromagnetic theory with octonions. When the serial-connected resistors $R_2 = R_3$ vary from $150\,\Omega$ to $350\,\Omega$, the experiments conclude the same inferences.

Table 2: The phase difference of the applied voltage and the induced electromotive force ($a = 150$ mm, $R_1 = 50\,\Omega$, $R_2 = R_3 = 200\,\Omega$. V_{PP10}, V_{PP20}, f are in volt, millivolt, and MHz respectively).

f	V_{PP10}	V_{PP20}	$\Delta\varphi(^\circ)$	A	f	V_{PP10}	V_{PP20}	$\Delta\varphi(^\circ)$	A
41	17.02	91.10	71	318.41	61	15.90	110.40	−130	186.60
42	17.21	98.87	84	325.68	62	16.12	113.80	−125	183.65
43	17.19	95.60	95	300.78	63	16.39	123.00	−115	189.08
44	17.22	94.88	100	284.60	64	16.54	118.20	−108	174.47
45	17.41	91.32	103	259.03	65	16.54	121.20	−95	173.44
46	17.50	91.73	108	247.72	66	16.62	112.30	−90	155.12
47	17.76	93.42	110	238.12	67	17.11	99.14	−80	129.08
48	17.91	103.40	112	250.58	68	17.61	85.34	−82	104.80
49	17.63	113.60	115	268.37	69	18.03	70.62	−80	82.27
50	17.58	122.00	118	277.59	70	18.50	63.45	−85	69.99
51	17.51	123.80	130	271.83	71	19.04	62.82	−100	65.45
52	17.38	140.70	133	299.39	72	19.87	64.93	−110	63.04
53	17.19	154.90	140	320.79	73	20.60	81.22	−120	73.99
54	16.90	171.20	152	347.40	74	22.39	99.57	−125	81.21
55	16.68	182.60	165	361.89	75	23.66	128.10	−130	96.25
56	16.65	180.90	180	346.46	76	24.51	151.50	−128	107.01
57	16.54	182.90	−160	340.35	77	24.74	181.20	−125	123.53
58	16.28	166.50	−150	304.02	78	24.77	207.20	−125	137.49
59	16.52	135.30	−138	235.28	79	24.40	250.70	−145	164.63
60	16.14	121.40	−130	208.94	80	23.48	277.60	−140	184.73

5. CONCLUSIONS

In the range of classical electromagnetic theory, it has not been finished the direct inspection of displacement currents yet. Based on previous research on displacement currents inspection, the paper proposes and fulfills an experiment proposal adopting the phase measurement method, to scrutinize directly the amplitude and orientation of displacement currents.

It should be noted that the study for the phase measurement of displacement currents has examined only some simple cases, of which the radii of capacitor plates are 100 mm and 150 mm respectively and the frequency range is only within 40 MHz $\sim$ 80 MHz. Despite its preliminary character, this study can clearly indicate that each measured phase value, of which the cross points of the measured curve A_m with the theoretical value A, does not coincide with the theoretical value of classical electromagnetic theory described with the vector. A striking difference is that, part measured phase values locate on the range near the prediction value of the electromagnetic theory described with the S-quaternion, although it cannot explain all of the results yet. It is undoubted that the above results enrich the understanding to the physical features of displacement currents. For the future experimental study, the research will concentrate on only the adopting large radii of plates to achieve precise measured phase values.

ACKNOWLEDGMENT

This project was supported partially by the National Natural Science Foundation of China under grant number 60677039.

REFERENCES

1. Gogberashvili, M., "Octonionic electrodynamics," *Journal of Physics A*, Vol. 39, No. 22, 7099–7104, 2006.
2. Chanyal, B. C., P. S. Bisht, and O. P. S. Negi, "Generalized octonion electrodynamics," *International Journal of Theoretical Physics*, Vol. 49, No. 6, 1333–1343, 2010.
3. Weng, Z.-H., "Displacement current and experimental inspection in the octonion space," *Scientific Journal of Physical Science*, Vol. 2, No. 1, 1–13, 2012 (in Chinese).
4. Arthur, J. W., "An elementary view of Maxwell's displacement current," *IEEE Antennas and Propagation Magazine*, Vol. 51, No. 6, 58–68, 2009.
5. Rizzotto, M. G., "Visualizing displacement current — A classroom experiment," *The Physics Teacher*, Vol. 37, No. 7, 398–399, 1999.
6. Godin, S. M. and V. V. Botvinovskii, "Measurement of displacement current by a fammeter," *Journal of Communications Technology and Electronics*, Vol. 54, No. 9, 1092–1095, 2009.
7. Sanyal, G. S. and A. Chakrabarty, "A direct experimental proof of displacement current," *Resonance*, No. 11, 1065–1073, 2008.

Analysis of the Forbidden Regions for Multilayer Planar Waveguide with LHM

Yaw-Dong Wu[1], **Ming-Shiung Cheng**[1], **Shih-Yuan Chen**[2], **and Tien-Tsorng Shih**[1]

[1]Department of Electronic Engineering
National Kaohsiung University of Applied Sciences, Kaohsiung, Taiwan, R.O.C.
[2]Department of Electric Engineering
National Sun Yat-Sen University, Kaohsiung, Taiwan, R.O.C.

Abstract— In recent years, the planar waveguides with Left-Handed Medium (LHM) have been widely studied and proposed. A feature of the LHM has both the permittivity ε and permeability μ less than zero. There always exist two forbidden regions for guided modes in the three-layer planar waveguide with LHM guiding layer. Most of the multilayer planar waveguides with the LHM films were supposed to have an enough width of the interaction layer and the same forbidden region as the three-layer planar waveguide with LHM film to discuss optical modes. The forbidden region was not reported previously to the multilayer planar waveguide with the narrow interaction layer. In this study, the modal theory and the boundary condition were used to analyze the forbidden region of the five-layer planar waveguide with LHM film in the narrow interaction layer. The numerical results show that the forbidden regions are separated and differ from the three-layer planar waveguide with LHM film. The variation of the forbidden region depends on the narrow width of the interaction layer and the ratio value of the permeability of the guiding layer and the interaction layer. We also show a phenomenon that the forbidden region and the dispersion cure of the effective refraction in five-layer planar waveguide with LHM film are almost similar to that of the three-layer planar waveguide with LHM film when the width of the interaction layer is wide enough. The simulation results would be very useful for designing waveguide devices with the LHM films.

1. INTRODUCTION

The left-handed material had been presented by veselago in 1968 and frabricated in experiment by Shelby et al. [1, 2]. The material possesses simultaneously negative dielectric permittivity and permeability [3, 4] and thus has a negative refractive index. Some analyses of the three-layer planar waveguide with LHM film have been proposed [5]. By using the graphical method, the optical modes in the symmetric slab waveguide structure with a core of LHM was investigated [6] and the forbidden region of the three-layer planar waveguide with LHM film had been analyzed [7].

Here we investigate the forbidden region of the multilayer planar waveguide with the LHM film by using the modal theory [8–11]. The model theory is used to explain the forbidden region in the planar waveguide with LHM. By solving Maxwell's equation and matching the boundary, the field of the transverse electric polarized wave and dispersion curves will be obtained. We used the dispersion curves to compare the forbidden region of the three-layer and five-layer planar waveguide with LHM film. Form simulation results, we show the forbidden region between three-layer and multilayer is different when the interaction layer is thin and almost the same in the enough width of interaction layer. The numerical results would be very useful for designing multilayer waveguide devices with the LHM films.

2. ANALYSIS

In this section, we use the model theory to drive the TE-polarized field of the multilayer planar waveguide with LHM guiding film. The structure of the multilayer is composed of guiding film with LHM, interaction film, cladding, substrate, as shown in Figure 1. We consider the transverse electric polarized waves propagating along the z direction. The wave equation can be reduced to

$$\nabla^2 E_{yj} = \frac{n_j}{c^2}\frac{\partial^2 E_{yj}}{\partial t^2}, \quad j = i, f, c, s \tag{1}$$

With solutions of the Equation (1)

$$E_{yj}(x, z, t) = E_j(x)\exp[j(\omega t - \beta k_o z)], \quad j = i, f, c, s \tag{2}$$

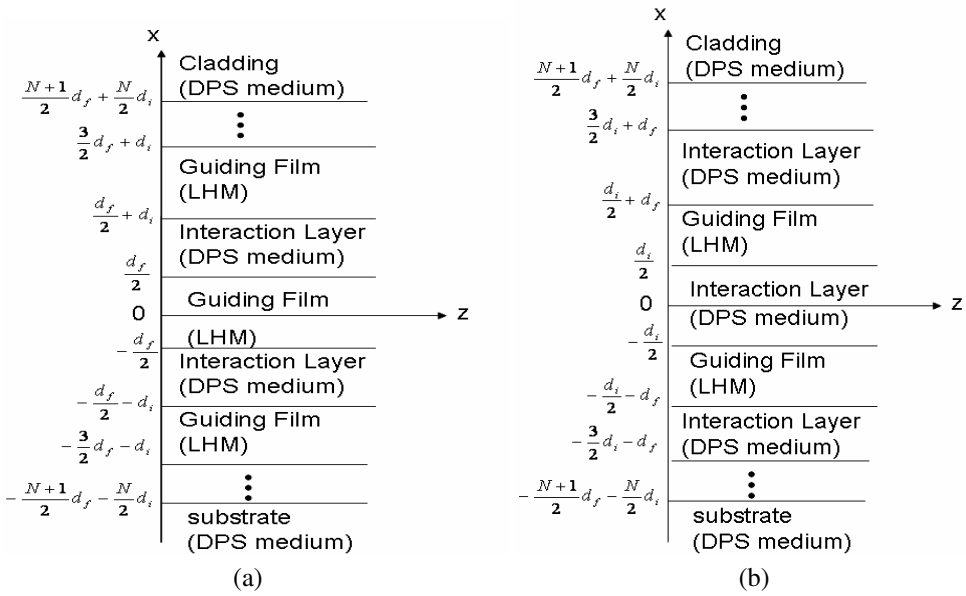

Figure 1: The structure of the multilayer planar waveguides with LHM film: (a) for N = even and (b) for N = odd.

The subscripts i, f, c and s in Equations (1), (2) are used to denote the interaction layer, guiding film, cladding, and substrate, respectively. In Equation (2), β is the effective refractive index, ω is the angular frequency, and k_0 is the wave number in the free space. By substituting Equation (2) into the wave equation, the transverse electric fields in each layer has the general form

$$E_c(x) = A_c \exp(-k_o q_c x), \quad \text{in the cladding} \tag{3a}$$
$$E_f(x) = A_f(m) \cos\{k_0 Q_f (x - x_f(m))\}, \quad \text{in the guiding film} \tag{3b}$$
$$E_i(x) = A_i(m) \cosh\{k_0 q_i (x - x_i(m))\}, \quad \text{in the interaction layer} \tag{3c}$$
$$E_s(x) = A_s \exp(k_0 q_s x), \quad \text{in the substrate} \tag{3d}$$

where the subscripts $m = 1, 2, \ldots, N$. The A_c, $A_f(m)$, $A_i(m)$, A_s, q_c, Q_f, q_i, q_s, $x_f(m)$, and $x_i(m)$ are all constants, these constants can be obtained by matching the boundary conditions. For the linear case, the constant A_c is arbitrary. The amplitude parameters $A_f(m)$, $A_i(m)$ and A_s are proportional to A_c.

The q_i and Q_f can be expressed as

$$q_j = \sqrt{\beta^2 - \varepsilon_j \mu_j}, \quad j = i, c, s \tag{4a}$$
$$Q_f = \sqrt{\varepsilon_f \mu_f - \beta^2} \tag{4b}$$

For simplicity, we considered $\varepsilon_i = \varepsilon_c = \varepsilon_s$ and $\mu_i = \mu_c = \mu_s$ so that $q_i = q_c = q_s = q$. It can be noted that in Equations (4a) and (4b) that q_j and Q_f are given in term of a single unknown, the effective index β. By matching the boundary conditions, we obtained the following dispersion equations [7]:

$$\tan(k_0 Q_f d_f) = \frac{\frac{\mu_f}{\mu_c} Q_f q (1 + \tanh\phi)}{Q_f^2 - \left(\frac{\mu_f}{\mu_c} q\right)^2 \tanh\phi} \quad \text{for} \quad N = \text{even} \tag{5a}$$
$$\tan(k_0 Q_f d_f) = \frac{\frac{\mu_f}{\mu_c} Q_f q (1 + \tanh\varphi)}{Q_f^2 - \left(\frac{\mu_f}{\mu_c} q\right)^2 \tanh\varphi} \quad \text{for} \quad N = \text{odd} \tag{5b}$$

where $\phi = k_0 q[d_f/2 + (\frac{N-1}{2})d_f + \frac{N}{2} d_i - x_i(1)]$ and $\varphi = k_0 q[d_i/2 + (\frac{N-1}{2})d_i + \frac{N}{2} d_f - x_i(1)]$ is for N = even and N = odd,respectively.The dispersion equations can be solved numerically when the

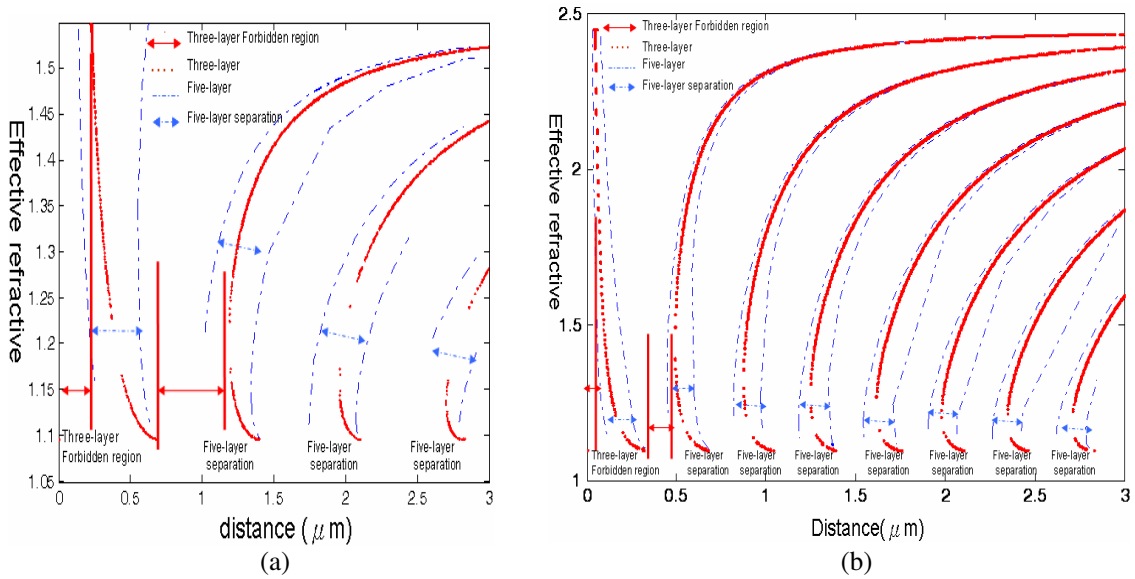

(a) (b)

Figure 2: The forbidden region of a three-layer and five-layer planar waveguide (for $N = 0$): (a) $di = 0.1\,\mu\text{m}$ and $\mu_f/\mu_c = -2$, (b) $di = 0.1\,\mu\text{m}$ and $\mu_f/\mu_c = -5$.

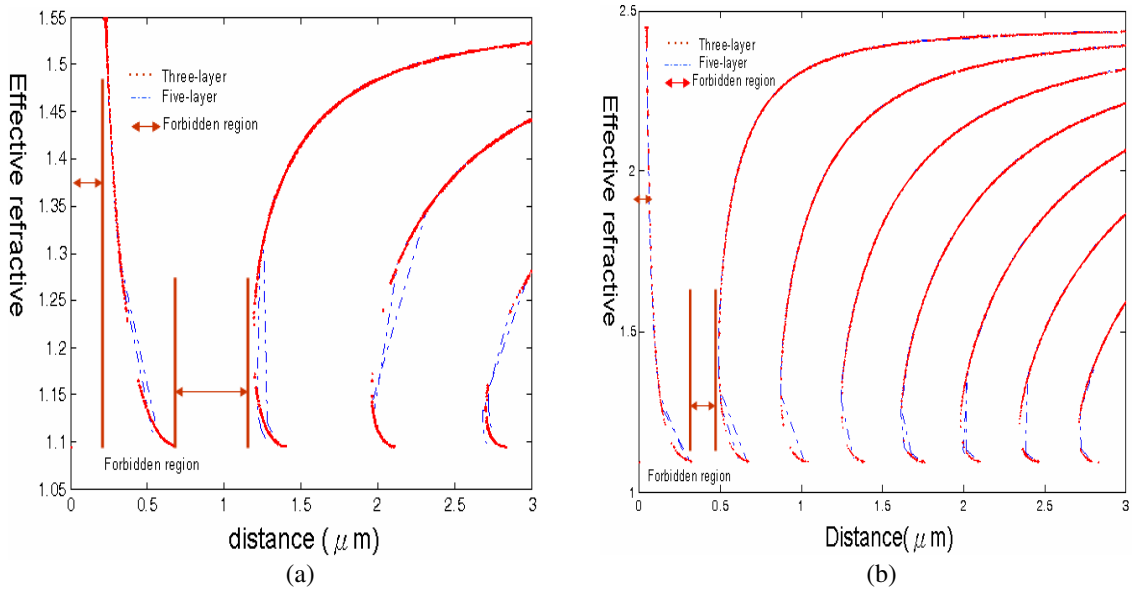

(a) (b)

Figure 3: The forbidden region of a three-layer and five-layer planar waveguide (for $N = 1$): (a) $di = 2\,\mu\text{m}$ and $\mu_f/\mu_c = -2$, (b) $di = 2\,\mu\text{m}$ and $\mu_f/\mu_c = -5$.

constant β is determined. The forbidden region can be gotten by the relation of plotting β versus d_f.

3. NUMERICAL RESULTS

In this section, we used the general formulas derived in Section 2 to solve the dispersion equation. The two numerical examples are presented as follows: when $N = 0$ and 1, we can simplify the dispersion equation to analyze the forbidden region of the three-layer and five-layer planar waveguide with LHM, respectively.

The numerical results are shown in Figures 2 and 3. Figure 2 shows the dispersion cure of the three-layer and five-layer planar waveguide with the wavelength in free space $\lambda = 1.55\,\mu\text{m}$, $\varepsilon_f = -\varepsilon_c = -\varepsilon_s$. In Figure 2(a), the forbidden of the three-layer and five-layer is plotted with the parameters $di = 0.1\,\mu\text{m}$ and $\mu_f/\mu_c = -2$. In Figure 2(b), the forbidden of the three-layer and five-layer planar waveguide is plotted with the parameters $di = 0.1\,\mu\text{m}$ and $\mu_f/\mu_c = -5$. As the

ratio of the permeability of the guiding layer and the interaction layer gets increasing, the forbidden region gets decreasing. No matter what the ratio is, the forbidden region of three-layer waveguide always existed tow forbidden region in the figure and that of the five-layer waveguide is separated.

In Figure 3(a), the forbidden of the three-layer and five-layer planar waveguide is plotted with the parameters $di = 2\,\mu\text{m}$ and $\mu_f/\mu_c = -2$. In Figure 3(b), the forbidden of the three-layer and five-layer planar waveguide is plotted with the parameters $di = 2\,\mu\text{m}$ and $\mu_f/\mu_c = -5$. The forbidden region and the dispersion cure of the of five-layer planar waveguide are similar to three-layer waveguide when the interaction layer is enough wide.

4. CONCLUSION

In conclusion, we used the modal theory and boundary condition to obtain a dispersion equation of the multilayer planar waveguide with LHM film. By taking numerical method, the forbidden region can be determined with graphical method. The simulation result, the forbidden region of the five-layer planar waveguide with a narrow interaction layer is different from three-layer planar waveguide and similar to three-layer planar when the interaction film is enough width. We also show that the thickness of the interaction layer would effect the size of the forbidden region in the multilayer planar waveguide with LHM film.

REFERENCES

1. Shelby, R. A., D. R. Smith, S. Schultz, *Science*, Vol. 292, 77, 2001.
2. Veselago, V. G., *Sov. Phys. Usp.*, Vol. 10, 509, 1968.
3. Ziolkowski, R. W. and E. Heyman, "Wave propagation in media having negative permittivity and permeability," *Phys. Rev. E*, Vol. 64, 056625, 2001.
4. Milonni, P. W. and G. J. Maclay, "Quantized-field description of light negative-index media," *Opt. Commun.*, Vol. 228, 161–165, 2003.
5. Peacock, A. C. and N. G. R. Broderick, "Guided modes in channel waveguides with a negative index of refraction," *Opt. Express*, Vol. 11, 2502–2510, 2003.
6. He, Y., Z. Cao, and Q. Shen, "Guided optical modes in asymmetric left-hand waveguides," *Opt. Commun.*, Vol. 245, 125–135, 2005.
7. Kuo, C.-W., S.-Y. Chen, Y.-D. Wu, and M.-H. Chen, "Analyzing the multilayer optical planar waveguides with double-negative metamateral," *Progress In Electromagnetics Research*, Vol. 110, 163–178, 2010.
8. Doer, C. R. and H. Kogelnik, "Dielectric waveguide theory," *J. Lightwave Technol.*, Vol. 26, 1176–1187, 2008.
9. Wu, Y. D. and M. H. Chen, "Method for analyzing multilayer nonlinear optical waveguide," *Opt. Express*, Vol. 13, 7982–7995, 2005.
10. Kuo, C. W., S. Y. Chen, M. H. Chen, C. F. Chang, and Y. Wu, "Analyzing multilayeroptical waveguide with all nonlinear layers," *Opt. Express*, Vol. 15, 2499–2516, 2007.
11. Wu, Y. D., M. H. Chen, C. K. Kuo, S. Y. Chen, and C. F. Chang, "The study ofmultilayer planar optical waveguide structure with nonlinear cladding," *Optical and Quantum Electronics*, Vol. 40, 495–512, 2008.

On the Geometric Representations of Electromagnetism

S. L. Vesely[1] **and A. A. Vesely**[2]

[1]I.T.B. — C.N.R., Italy
[2]Via L. Anelli 13, Milano, Italy

Abstract— When the information conveyed by signal reception is presented in a visual form, the backing of geometry may be more usable than one based on probability theory. Since H. Hertz started telecommunications centering on the analogy between electromagnetic waves and light, a geometric model of electromagnetism can improve both visual representation and interpretation of signals. Here we succinctly revisit some interpretations given to electromagnetism and their relationship with geometry.

1. INTRODUCTION

According to Euclid, geometry was the expression of mathematics, and its graphical aspects, limited to straightedge and compass constructions, assisted logical reasoning. In today's mathematics, algorithmic reasoning has largely sidestepped the need of graphical methods, while in physics geometry may play different roles, according to the task at hand. Here we outline four frequent ones.

Newton held that Euclidean geometry is a sort of simplified topography; that is, a model describing objective properties of the space where we live. Let's call (1) this conception of geometry. Gauss' epoch marked a scrutiny of Euclidean geometry trueness, as a follow-up to developments in calculus in connection with quantitative use of rangefinders. That involved a reexamination of relationships that had been silently assumed up to then among the extension of real world, our senses, and geometry. That subject, called the *Problem of Space*, determined a differentiation between Newton's conception and that of subsequent physical theories. In particular, the recognition that the parallel postulate was not logically necessary[1] induced various scientists, also including H. Helmholtz and A. Einstein, to ascertain by measurements which axioms related to geometrical extensions hold.

According to the philosopher I. Kant, geometrical properties depend on the apperception; that is, on our connatural conception of space[2]. Although he criticized empiricism, Kant was not a mathematician, and his relevant ideas on space theorizations, which we tag (2), had to be reworked by physicists. H. Poincaré, for example, observed that mathematical expressions of physical laws depend on the chosen coordinate system; e.g., Cartesian coordinates may sometime result in simpler formulas than spherical coordinates, and vice versa. Accordingly the laws don't allow to uniquely determine space properties. Along that line of thought, E. Kretschmann criticized the physical meaning that Einstein had attributed to general covariance, holding that any law can be put in covariant form as long as the complicated mathematical expressions that may result are tolerated. In quantum mechanics, Kantian philosophy surfaces in various degrees. There is a wide consensus that the measuring apparatus affects measurements, but the observer can influence the process too. In any case, Heisenberg's uncertainty principle, by limiting the possibility to simultaneously know all particles' properties, implies giving up *a priori* the licitness of microscopic measurements, because they are not connatural to macroscopic devices/observers. Thereupon, experimental discovery of the shape of the physical space faded out.

As a further theoretical way, Plato's theory of Ideas, illustrated by the Allegory of the Cave, was reevaluated. A meaning often attributed to the Allegory is that objects described by mathematical means are clear and distinct whereas sensorial perception may be fuzzy. Physical realism avails of mathematical proofs to understand and validate physical laws numerically. Although it makes use of spaces and manifolds, it favors geometric algebra over drawn diagrams, which are considered informal. Let's tag (3) the conception just sketched.

[1]As Euclid's fifth postulate is pivotal in discerning geometries with Euclidean metrics from those with non-Euclidean metric, it is worth noting that the postulate doesn't extend well to three-dimensional space, where straight lines are skew to one another in the general case.

[2]In practice, Kant means that the space's shape is whatever our brains attribute to it. Presently, his point of view is generally agreed, and psychological contributions to spatial perception is a discussed topic. However, it makes sense to distinguish the perception of celestial space's shape from sense experiences related to interactively reachable objects.

Application areas, such as information processing and communications, remote sensing, control systems, call for conveying large amounts of data, typically by means of graphical representations. In order to interpret visual data while still preserving consistency, graphical rendering should be based upon — and justified by — a purposely developed geometrical model. A geometry suitable for such task can be based on groups of movements, in the geometrical sense of relations between positions. F. Klein in his "Erlangen program" highlighted the *relational* aspect of geometry; that is, the fact that different geometries can be built by choosing different groups of transformations[3]. We tag (4) the latter conception.

In the following, we are going to sketch how electromagnetism can be represented geometrically and the role that the four conceptions we introduced play in such representations.

2. THE SPATIAL INTERPRETATIONS OF THE FIELDS

Currently, the mathematical framework describing the electromagnetic field in terms of the vectors **E**, **D**, **H** and **B** doesn't attach any physical meaning to their geometrical representation. Indeed, there are whole theories, such as bivector and spinor fields, developed without bothering about conditions for isomorphism at all. Maxwell himself introduced that leaning, using unrelated formalisms. However, physical reality is attributed to the electromagnetic field chiefly because of its spatial extension. In electrostatics and magnetostatics, experimental determination of the extension of **E** and **H** depends on the static concept of force applied to a body's points. The relevant mathematical background is missing, as at the times when the experiments that shaped such physical meaning of the fields were first carried out, representations used graphical statics only. Later, statics was extended to space, as *null system*, and put on a sound mathematical basis. But, by then, experience with electric currents had already led researchers toward some theory capable of doing the time variations of fields[4]. The spatial statics was discarded because it didn't conform with conception (1); that is, it didn't allow to represent electromagnetic fields in the framework of Newtonian dynamics. Numerous analogies between electrical and mechanical systems notwithstanding, no satisfactory Newtonian explanation was found either[5]. Indeed, Faraday's and Ampère-Maxwell's equations give a mathematical account of the interdependent variations of **E**, **D**, **H** and **B**. They, as H. Hertz showed, describe the electromagnetic phenomena that are relevant for developing electronics and telecommunications. The applicability of Newtonian conceptions to electromagnetism declined after classical electrodynamics faced the problems resulting from relativity of motion[6] and interaction with matter. Those problems lead respectively to Einstein's relativity, and quantum mechanics.

The microscopic study of electric and magnetic properties of the matter brought some degree of convergence between electrodynamics and statistical thermodynamics toward a common model of the matter. Starting from the theory of electrons, and continuing with all subsequent treatments of wave-particle interactions, a sequel of theories based upon inferential statistics focused on the representations using phase space, that are akin to the Platonic conception (3). Relaxing the requirement to adhere to the space of conception (1), and taking up sample space representations allows to deal homogeneously with generalized coordinates and momenta, so as to treat radiative, thermal, acoustical, chemical, and other aspects, irrespectively of whether they bear extensive or intensive quantities. Quantum field theories, that mathematically formalize and extend electrodynamics, often treat interactions according to perturbation theory. The wave-particle duality allows to develop a physical kinetics that includes particles as well as interactions among them, such as gravitons, phonons, photons, plasmon-polaritons, et cetera[7] [1]. There is a wide variety of subsequent developments, each characterized by an outstanding mathematical effectiveness of calculative approximations. For example, that palette includes R. Feynman's quantum electrodynamics, which avails of space-time, and E. Wigner's time-frequency representation, that introduces

[3]We bring to mind that Moritz Pasch raised a question whether measuring infinitesimals is possible. As a consequence, a group of infinitesimal generators could not generate a geometry with metric properties. In particular, that is relevant for generating geometries from infinitesimal motions of mechanisms.

[4]In that historical context, *quasi static* fields mark the conceptual turning point from static mechanical modeling to the dynamical one of waves.

[5]We are going to expand on the interpretation of the transforms of spatial statics in Section 4. For now, let's just mention that the geometric figures resulting from point-mass dynamics indeed correspond to trajectories and equations of motions.

[6]In gravitation theory, E. Mach pioneered the first line of approach to the relativity of motion related to rotation.

[7]Pure particle — or action-at-a-distance — theories have been revived by J. Wheeler and R. Feynman. Those theories have been studied at the quantum as well as at the classical level. It has been shown that they are mathematically equivalent to pure field theories. So (quasi)-particles are considered to mediate the action among bodies much like fields do. In other words, particle pictures are used also for describing energy dissipation.

wavelets transforms. However, the pervasive deployment of probabilistic models as a base for all physical theories, including information theory, can be considered a weakness. It seems that the more the mathematical sophistication increases, the more schematic and prototypical the experimental representations become. That tendency might be a symptom of a difficulty inherent in the Platonic conception (3); that is, the vigor of mechanical reductionism was relinquished away together with its original, conception (1) representations[8].

3. PROPAGATION

There are traveling solutions of Maxwell's equations that describe time varying electromagnetic fields. These solutions are usually interpreted according to one of three main ways: one is concerned with energy propagation, another one deploys mechanical analogies, and a further one extends geometric optics toward lower frequencies.

A renown energetic, space-based model is the one by J. H. Poynting. According to it, energy has the spatial extension of the static fields around electric components of circuits, and current and tension variations cause the energy flow through the space, as described by the Poynting vector. When propagating solutions can be related to some frequencies, the conveyed energy or momentum are usually associated to the corresponding waves or particles. In addition, the problem can be tackled as a radiometric one in the framework of thermodynamics, according to Kirchhoff's formulation of Huygens-Fresnel principle.

The analogy between small oscillations in the aether at the passage of an electromagnetic disturbance and their mechanical counterparts involves the stress and the mass density of the media, by means of the propagation constant. In the first approximation the disturbance characteristics play no role, and even less those of the space which is supposed to be homogeneous, isotropic, and infinite. If there are boundary conditions, the solutions of the wave equation may not satisfy Maxwell's equations.

Finally, despite the fact that light phenomena are a subset of electromagnetic ones, when stemming from geometric optics its framework prevails. The so-called *geometric optics* was developed beside graphical statics, and similarly uses straight lines for its constructions. A pioneer of analytical geometry, G. Monge considered light beams to be better represented by cones. In order to give an account of diffraction, he associated a cone to the envelope of solutions to a first order partial differential equation. Nowadays, wavefronts are associated to the rays equations, which can be derived from the eikonal method using contact transformations to carry wavefronts into wavefronts, or from canonical transformation using Hamilton's characteristic function [2]. The latter, modern formalizations exhibit a shift to an analytic geometrical representation of optics of conception (3). Thus we may say that representations based on analytical geometry, albeit very handy for refining computation methods, don't suggest interpretations of electromagnetism different from those that had been posed originally for optics.

4. GEOMETRIES FEATURING AN INVARIANT QUADRIC

Around the end of 1800s it was suggested that the motion of a test body not subject to forces lead to determining the properties of conception (1)'s space. Thus, for example, a space such that a rigid body can rotate around a plane so as to reach its mirrored image must have properties different from the space that we live in, irrespectively of the coordinate system being used to describe such motion. During the early 1900s, the quest for graphical representations of non-Euclidean geometry aired the possibility to confer some reality to the shape of the void[9]. In such scenario, the presence of physical fields could manifest itself as a deformation of the void's shape. If determinations about the test body depend on light signals, special relativity theory asserts that the reality is not Newtonian in this case. The type of space depends on the reciprocal motion of the so-called inertial reference frames, as a consequence of two postulates: (i) invariance of laws of motion, including expressions like $\nabla^2\Psi = \frac{\partial^2\Psi}{\partial x^2} + \frac{\partial^2\Psi}{\partial y^2} + \frac{\partial^2\Psi}{\partial z^2} = 1/c^2\frac{\partial^2\Psi}{\partial t^2}$ corresponding to *plane waves*[10], (ii) the invariance of the propagation speed of light signals, that is expressions like $(dx)^2 + (dy)^2 + (dz)^2 = c^2(dt)^2$, for

[8]Originally E. Schrödinger interpreted solutions to his equation as electronic charge density in the configuration space. E. Madelung gave a hydrodynamic formulation for the flow of one electron. However, that interpretation cannot be extended to many electrons, and M. Born eventually interpreted the square of those Schrödinger functions as a probability density.

[9]There is an abysmal difference between setting out to determine geometrical and dynamical properties of aether and ascribing such physical properties to the void. Indeed, if the void is void, it is not a subject of physical interest by definition.

[10]From a purely mathematical point of view, infinitesimal relationships are compatible with multiple topologies; this topic was discussed in connection with Riemannian geometries.

fronts propagating radially from a finite central point[11]. H. Minkowski gave an analytic geometrical interpretation of the theory in a pseudo-Euclidean four-dimension space, attributing to expression (ii) the meaning of a metric differential form[12]. As a consequence, the relativistic effect turns out to belong to the Kantian conception (2): The shape of the space depends on the metric, and for slow speeds the analytical representation resembles that given in mechanics[13].

As an alternative to the Riemannian metric as introduced by Minkowski, one can be defined basing on a finite projective quadric form. F. Bolinder pragmatically considered that kind of quadric for stationary applications to transmission lines at microwave range. He noticed that both impedance transformation formulas and scattering matrices of two-port networks often have a bilinear form, and hence used non-Euclidean representations, such as Cayley-Klein's, to plot the measurements in the complex impedance (admittance) plane and the complex reflection-coefficient plane in a compact manner. Besides those plotting problems, the fact that Moebius' bilinear transforms admit infinity as input and/or output may lead also to *interpretive* problems. On the contrary, infinite elements are indistinguishable from the others in projective geometry. Moreover in projective geometry the Moebius transform may be equivalently expressed as a linear coordinate substitution with an invariant quadric. The latter entails F. Klein's conception (4): It doesn't imply a shape of the vacuum that a signal travels through, but — unlike mechanical motion — a relationship between a receiver's input and output. We want to stress that this projective geometry with an invariant quadric, that corresponds to the movement problem posed during the late 1800s, is different from the non-Euclidean geometrical approach taken in the early 1900s, that pertains to conception (2)[14].

Now for electromagnetism's invariant quadric. It is possible to represent Maxwell's equations in the analytical style of "force free" Beltrami fields using the null system [5]. The terms **E**, **D**, **H** and **B**[15] of source-free fields can be thought of as forces and couples in the sense of graphical statics, in which it can be shown that the applied forces can always be reduced to a force and a couple. Those decompositions are invariant under symmetry transformations of the space, which consist of right or left screws in the null system. A force-and-couple pair can be expressed as two skew lines of action, identified by their coordinates that transform according to Maxwell's equations. So, for any given assignment of coordinates of two skew lines it is possible to construct equivalent decompositions. The null system's invariant is a ruled quadric surface containing two families of generators. Since the generators are straight lines, this geometry shares with spaces of lines systems the property that it is possible for two tetrahedrons to be inscribed and circumscribed into/around one another at the same time [3, 4]. For that reason, in the framework of conception (4), the emphasis is on the transformations between the coordinates **E**, **D**, **H** and **B**.

To interpret the projective geometric model, let's point out that an antenna does not measure — and a signal is not — a force nor a couple. The physical phenomena that we experimentally ascertain *are* received signals rather than the fields, and they are empirical evidence as long as they are related to material objects. According to conception (4) we focus on the relationships between signals. The bilinear part of the input-to-output transfer function can be interpreted geometrically as a projective transformation with an invariant quadric. That is to say, as if the channel+receiver pair transforms a spatial extension projectively, where the quadric depends on the receiver. Received signals that carry information have a spatial extension, as exemplified by those received by a concave mirror or by a pinhole camera[16]. Furthermore, it may happen that not all the information carried by a signal can be resolved by the receiver. In general, operations analogous to the reduction to a force and a couple over the whole space are ill-defined, although multiple surveys

[11] The relationship between the two kind of electromagnetic *objects* seems to be the same that Huygens and others hypothesized between primary (i) and secondary (ii) sources.

[12] The geometrical interpretation is the renown hypercone, a degenerate quadric, according to F. Klein.

[13] The time coordinate becomes independent of spatial coordinates.

[14] The unit circle in the Cayley-Klein diagram, as used by Bolinder is *an* auxiliary geometric figure introduced in order to represent a non-Euclidean geometry. The null system, instead, is a field; that is, a cover of the whole space with quadrics. Like a metric quadric is not itself metrizable, neither projective quadrics are. The interpretation of an *inversion* operation, e.g., with respect to a circle, is also different depending on whether the circle is intended as metrical conic (as in F. Bolinder's applications) rather than a reference conic of the projective plane (in Theodor Reye's sense).

[15] When **B** and **H** are interpreted as magnetic fields, one implies a mechanical transduction effect specific of some material at low frequencies.

[16] Usually, the fact that a pupil *quantizes* a signal is interpreted as if the original message were encoded, and each light ray transferred an object point to an image point, even though radiation doesn't have such characteristic. If the emitter is not a physical point, there are other effects — besides *spatial projective transformations* of signals that we are doing here, that can be calculated based on linear reception. For example, collimation and color.

from different positions can determine the "electromagnetic image" of a body. On the other hand, signals involving infinity in the input/output relation, as it often happens, can be represented on a plane surface. In such cases, Maxwell's equations can be interpreted as holomorphy conditions [6]. The geometric model of the equations of electromagnetism replaces all the interpretations that involve dynamical models. In fact, as geometry is not concerned with power issues of signals it becomes pointless to reinterpret electromagnetism in the framework of some "more physical" theory, as well as to attribute mass or energy to signals [7]. Rather, geometry provides relationships which are useful for interpreting signals, and is alternative to statistical interpretations.

5. CONCLUSIONS

We reviewed some approaches to geometric representations of electromagnetism, and highlighted their having recourse to mechanical models. The mathematical formulations of impedance transformations and scattering matrices seem to attest that electromagnetism admits autonomous geometrical models that also support interpretative needs. Such models relate visual representations and their transformations in a logically consistent framework. We mentioned the null system as a workable geometrical model belonging to the conception that we tagged (4). The theoretical reach of geometrical modeling is related to the role that visual methods play in signal reception, and also to the weight that telecommunications and electronics carry in detecting phenomena in other fields of study.

REFERENCES

1. Ganguly, A. K. and J. L. Birman, "Theory of lattice Raman scattering in insulators," *Phys. Rev.*, Vol. 162, 806–816, 1967.
2. Geiges, H., "A brief history of contact geometry and topology," *Expo. Math.*, Vol. 19, 25–53, 2001.
3. Moebius, A. F., "Kann von zwei dreiseitigen Pyramiden eine jede in Bezug auf die andere um- und eingeschrieben zugleich heissen?," *Crelle's Journal*, Vol. 3, 273–278, 1828.
4. Moebius, A. F., "Ueber die Bestimmung des Inhaltes eines Polyëders," *Ber. Verh. Königl. Sächs. Ges.*, Vol. 17, 31–68, 1865.
5. Reed, D., "Foundational electrodynamics and Beltrami vector fields," *Advanced Electromagnetism: Foundations, Theory and Applications*, T. W. Barrett and D. M. Grimes, Eds., 217–249, World Scientific Publishing Co., Singapore, 1995.
6. Silberstein, L., "Elektromagnetische Grundgleichungen in bivektorieller Behandlung," *Ann. Phys.*, Vol. 327, No. 3, 579–586, 1907.
7. Mishchenko, M. I., "Gustav Mie and the fundamental concept of electromagnetic scattering by perticles: A perspective," *JQSRT*, Vol. 110, 1210–1222, 2009.

Study on the Human Effect of a Wireless Power Transfer Device at Low Frequency

Ji-Yeon Mun[1], **Min-Gyeong Seo**[1], **Woo-Geun Kang**[2], **Hae-Young Jun**[3], **Yong-Ho Park**[3], **and Jeong-Ki Pack**[1]

[1]Department of Radio Science and Engineering
Chungnam National University, Daejeon, Korea
[2]Electromagnetic Environment Research Center, Korea
[3]DMC R&D Center, SAMSUNG Electronics, Korea

Abstract— In this paper, we analyzed the human effect of a wireless power transfer (WPT) device operating at 6.74 MHz. A commercial simulator, XFDTD Ver. 7.2 based on the finite difference time domain (FDTD) method, was applied to the analysis of the specific absorption rate (SAR) and the induced electric field inside of the Korean human model and a flat phantom. The human model used is a numerical phantom developed by Electronics and Telecommunications Research Institute (ETRI) and the size of the flat phantom model is based on the human model's bust. The simulation results were compared with the Korean Guideline and the ICNIRP 2010 Guideline. The SAR values averaged over 1-g and 10-g were maximum in the groin of the human model, and the maximum SAR values at 5 cm distance were $3.41 * 10^{-3}$ W/kg (1-g averaged SAR) and $1.92 * 10^{-3}$ W/kg (10-g averaged SAR) for 1 W input power. The maximum allowed input power compared to the SAR limit is about 470 W. The calculated value of the maximum induced electric field was 11.1 V/m at the same position, and it is far below the exposure limit of 909.9 V/m. So, the SAR value is the limiting factor of the human exposure of the WPT device. The results for the flat phantom were about a half of the human model. Since the nominal input power of the WPT device is 10 W, it can be concluded that the exposure level of the device is well within the exposure limit of the ICNIRP 2010 guideline.

1. INTRODUCTION

WPT systems can be classified into 3 types: radiation (long/short distance), magnetic resonance and inductive coupling, and each method has its own distinct characteristics [1]. Recently, wireless charging devices for mobile phones have been actively developed, mostly using magnetic resonance or inductive coupling methods.

Regulations for the protection of the human body from EMF exposure are available at national and international levels. The effect of a WPT system on human body varies greatly depending on the operating frequency and the input power. Thus, the SAR as well as the induced electric field inside a human body due to the EMF from the WPT devices must be assessed before the commercialization of the developed devices. Internationally, ICNIRP (International Commission on Non-ionizing Radiation Protection) revised ELF guideline in 2010, and it can be extended up to 10 MHz for certain effects [2]. In Korea, the SAR limits for workers and for body, limbs and whole-body average are newly adopted in January 2012, and it will be effective from January 2013 [3].

In this paper, SAR values and induced electric field strengths were calculated for the EMF exposure from a wireless charging device for mobile phone, operating at 6.74 MHz, and the results were compared with exposure limits of the Korean guideline and the ICNIRP guideline. Tables 1 and 2 summarize the basic restrictions for time varying electric and magnetic fields at 6.74 MHz.

2. SIMULATION CONDITIONS AND BACKGROUNDS

For numerical simulation, the Korean human body model developed by Electronics and Telecommunications Research Institute (ETRI), was used. The model was obtained from the MRI image

Table 1: Basic restrictions for time varying electric and magnetic fields at 6.74 MHz (ICNIRP).

Whole-body average SAR (W/kg)	Localized [head and trunk/limbs] (W/kg)	Tissue mass (g)	Internal electric field (V/m)
0.08	2/4	10	909.9

Table 2: Basic restrictions for time varying electric and magnetic fields at 6.74 MHz (Korea).

Whole-body average SAR (W/kg)	Localized [head and trunk/limbs] (W/kg)	Tissue mass (g)	Internal electric field (V/m)
0.08	1.6/4	1	-

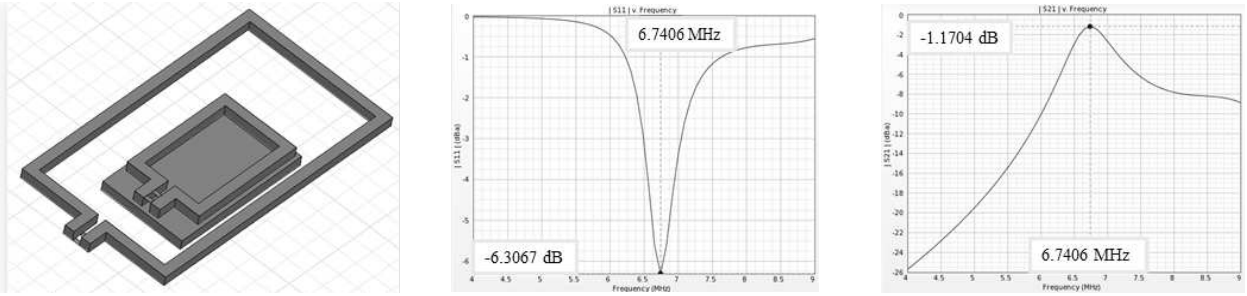

(a) Structure of resonator (b) S_{11} (c) S_{21}

Figure 1: The structure and S-parameters of the WPT device.

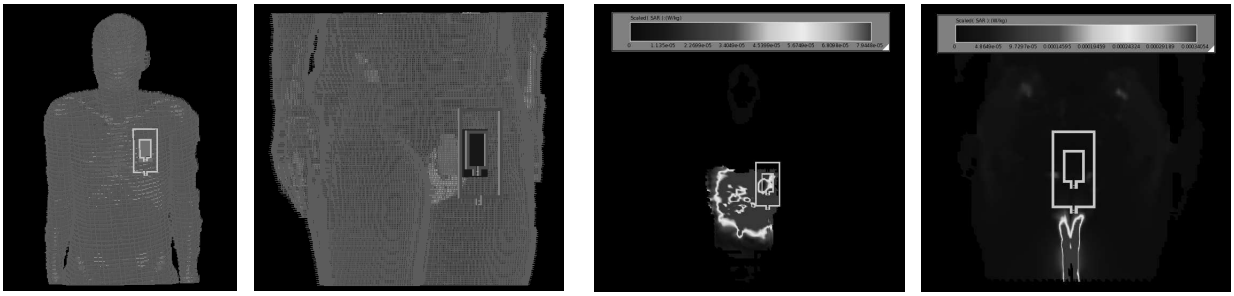

(a) Heart (b) Grion

Figure 2: Typical examples of the layout of the device for simulation.

(a) Heart (b) In front of the Groin

Figure 3: 1 g SAR distributions.

of a volunteer with the height of 176 cm and the weight of 67 kg, very close to the standard man in Korea. The voxel size of the human body model is 3 mm, and it consists of 29 human tissues. For the values of electrical parameters of each tissue, the data provided by FCC was used.

Figure 1 shows the structure of the WPT device. It is composed of the transmitting loop, the receiving loop, and magnetic shielding material. The loops are made of copper. Two loops are magnetically coupled resonate at 6.7406 MHz as shown in Fig. 1. The values for S_{11} and S_{21} are -6.31 dB and -1.17 dB, respectively.

Simulations were performed for all possible cases: 12 locations at the distance of $1 \sim 10$ cm from the human body, as shown in Table 3. In each case, the SAR values (maximum, 1 g average, 10 g average) and the induced E-field values were calculated. The layout of the device around the heart and groin is shown in Fig. 2.

3. RESULTS OF SIMULATION

The simulation results are summarized in Table 3. Max. 1 g SAR was maximum in front of the groin, and it was also large at the position of next to the arm and heart, except limbs for which SAR limits are larger than body. In case of groin, 1 g SAR was maximum in the fat tissue, 122 mm from the skin, and for heart position, it was maximum in the muscle tissue, 22.9 mm from the skin. Fig. 3 shows the 1 g SAR distributions around heart and groin, in the coronal plane which contains the maximum 1 g SAR point. The position of the WPT device was also shown just for reference.

Max. 10 g SAR was also maximum in front of groin. We can see that max. 1 g SAR and max. 10 g SAR values in the worst cases do not exceed the exposure limits of the relevant guidelines for the nominal 10 W input.

Table 3: SAR values and induced electric field strengths for 1 W input.

Case	Distance (cm)	Max. E-field (V/m)	Max. 10 g SAR (W/kg)	Max. 1 g SAR (W/kg)
In front of the face	10	0.26	$3.66 * 10^{-5}$	$9.54 * 10^{-5}$
Next to the face	5	0.61	$6.43 * 10^{-5}$	$1.72 * 10^{-4}$
Heart	5	0.83	$3.33 * 10^{-4}$	$7.95 * 10^{-4}$
Next to the head	5	0.21	$8.59 * 10^{-5}$	$1.77 * 10^{-4}$
Overhead	5	4.17	$1.37 * 10^{-4}$	$3.24 * 10^{-4}$
In front of the groin	5	11.1	$1.92 * 10^{-3}$	$3.41 * 10^{-3}$
Inclined plane of the groin	5	9.39	$1.10 * 10^{-3}$	$3.00 * 10^{-3}$
Pelvis	10	0.87	$2.54 * 10^{-5}$	$8.23 * 10^{-5}$
Next to the arm	5	1.45	$2.19 * 10^{-4}$	$1.37 * 10^{-3}$
Under the arm	5	0.8	$6.39 * 10^{-4}$	$1.46 * 10^{-3}$
Next to the foot	1	0.61	$2.62 * 10^{-4}$	$5.83 * 10^{-4}$
In front of the foot	1	0.36	$2.75 * 10^{-5}$	$8.17 * 10^{-5}$

4. CONCLUSIONS

In this paper, the safety of a wireless charging device for mobile phones operating at 6.74 MHz was investigated. The SAR values averaged over 1 g and 10 g were maximum in front of the groin of the human model. The maximum SAR values at 5 cm distance were $3.41 * 10^{-3}$ W/kg (1-g averaged SAR) and $1.92 * 10^{-3}$ W/kg (10-g averaged SAR) for 1 W input power. The maximum allowed input power compared to the 1 g SAR limit of Korea is about 470 W and that for the 10 g SAR limit of ICNIRP is 1042 W. We thought that 5 cm distance corresponds to the worst case in usual environment. However, if the distance is reduced, SAR values can be drastically increased. The maximum induced electric field was 11.1 V/m in front of the groin, which is far below the basic restriction of ICNIRP. So, the SAR value is the limiting factor for the human exposure from the WPT device. This study was performed for the preliminary design of the device. The design and the characteristics of the device for commercialization can be changed. Further investigation is ongoing for the different design of the device which is more efficient and carries more current.

ACKNOWLEDGMENT

This research was supported by the DMC R&D Center, SAMSUNG Electronics.

REFERENCES

1. Jang, B.-J., "Technical review of wireless power transfer," *Journal of the Korean Institute of Power Electronics*, Vol. 15, No. 6, 27–31, 2010.
2. ICNIRP, "ICNIRP guidelines for limiting exposure to time-varying electric and magnetic fields (1 Hz–100 kHz)," *Health Physics*, Vol. 99, No. 6, 818–836, 2010.
3. Korea Communication Commission, "Guidelines for limiting exposure to electromagnetic fields (KCC Notification 2012-2)," 2012.

Design of Novel Artificial Magnetic Conductor as Reflector and Its SAR Analysis

S. Lee[1], **N. Kim**[1], **and S.-Y. Rhee**[2]

[1]Chungbuk National University, South Korea
[2]Chonnam National University, South Korea

Abstract—A novel artificial magnetic conductor is designed and measured as a reflector to reduce the specific absorption rate. We designed a transformed symmetrical mushroom-like surface without via holes in the cells. Each slot in the structure plays a key role in modeling the desired frequencies. The structure of the unit cell is focused on the wireless local area network band (2.4 GHz). The antenna on the artificial magnetic conductor's reflector is working within one-quarter of a wavelength. For simulated and measured results, reflection coefficients show similar patterns between the artificial magnetic conductor's reflector close to the antenna and the perfect electric conductor's reflector separated at a quarter-wavelength from the antenna. The designed reflector has broad bandwidth, small size, and is easy to fabricate, because the proposed structure has no via holes. The human effect is analyzed by applying the designed reflector. The calculated peak specific absorption rate averaged over 1 g is only 0.002 W/kg when the input power is 1 W. For analyzing more serious status, if 12.8 W of input power is injected, which shows the maximum reference level of 1.6 W/kg, the calculated peak SAR is only 0.0078 W/kg. In conclusion, the designed reflector should block the electromagnetic waves from going to the human body.

1. INTRODUCTION

In modern wireless communication systems, light weight, small size, and low profile antennas with good radiation efficiency are desired, due to how easily they are integrated with RF and microwave circuits [1, 2]. New types of ground planes, which are artificial magnetic conductors (AMCs), perfect magnetic conductors (PMCs), electromagnetic band gap (EBG) material, or high impedance surfaces (HISs), have been studied extensively and have led to significant advancements in many applications. The AMCs are one type of electromagnetic band gap material with a magnetic conductor surface for a specified frequency band. AMC structures are typically realized based on periodic dielectric substrates and various metallization patterns. The AMC has an unusual boundary condition. Therefore, the AMC is able to use a new type of ground plane. The realization of new ground planes instead of perfect electric conductors (PECs) for antennas or microwave applications has been an active area due to a back-radiation shield and a gain increase [3].

The most important characteristic of the AMC structure is that the reflection phase changes from $+180^\circ$ to -180° as the frequency linearly decreases. When we compare the AMC and PEC reflector with a dipole antenna, the AMC reduces the antenna's profile to about $\lambda/10$ without affecting its performance. However, the PEC separates a quarter-wavelength for optimized radiation because of the reverse image currents, which reduce the radiation efficiency [4–6]. Synthetically, these surfaces have two special characteristics. The first is to behave as perfect magnetic conductors, so the parallel image currents appear in-phase rather than out-of-phase. Therefore, this structure could possibly be efficient in radiation close to antennas or surfaces. The second is to control the propagation from electromagnetic waves at the frequency band, so that the multipath interference is eliminated and the radiation patterns are clear.

Usually, the HIS geometry consists of a periodic AMC structure printed on a grounded dielectric slab. Although a metallic via hole in a conventional AMC structure connects the designed patch to the ground plane, sometimes the via hole can be removed. In this paper, we present a novel AMC structure which is a mushroom-like surface without via holes. To verify the properties of the designed AMC, the structure of a unit cell is simulated and analyzed. Also, the dipole antenna above the designed AMCs is simulated and analyzed.

2. DESIGN AND CHARACTERIZATION OF AMCS

Depending on the structure of the unit cell used to implement the high impedance surfaces, the behaviors of the AMCs should result in the desired frequency band. We designed a novel EBG structure that operates at a frequency of 2.4 GHz. We have compared the proposed AMC structure

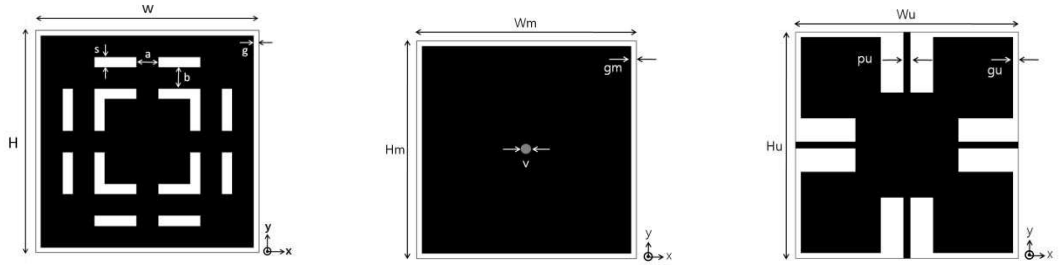

(a) (b) (c)

Figure 1: The geometries of the AMC surfaces. (a) Proposed EBG. (b) Mushroom-like EBG. (c) UC-EBG.

Table 1: The specific values of the patches.

Section	Values (mm)	Section	Values (mm)	Section	Values (mm)	Section	Values (mm)
W	21	H	21	gm	0.5	v	0.5
a	2	b	2	Wu	21	Hu	21
s	1	g	0.5	gu	0.5	pu	0.6
Wm	23	Hm	23				

to the conventional mushroom-like EBG and the uniplanar compact EBG (UC-EBG) structures presented in [1] and [4], respectively. The geometry of the basic cells is shown in Figure 1. Both unit cells are printed on a 2.6 mm thick FR4 PCB (dielectric constant = 4.6, losstangent = 1).

Figure 1(a) shows the proposed EBG structure possessing a bandwidth of 12.5% (2.26–2.56 GHz at 2.4 GHz). Figure 1(b) shows the conventional EBG structure, which has a bandwidth of 11.5% (2.27–2.55 GHz at 2.42 GHz). Figure 1(c) shows the UC-EBG, which has a bandwidth of 4.0% (2.4–2.5 GHz at 2.45 GHz). The designed AMC has a $3X$ wider bandwidth than the conventional UC-EBG. The specific details of the three different patches are shown in Table 1.

The frequency in which the reflected phase for all cases is 0° is fixed to the same value. Using a simulation tool employing the FDTD method, we designed all of the structures to contain in-phase reflection on their surfaces for their normal incident planes at 2.4 GHz. In order to obtain the desired resonant frequency, the proposed AMC cell size is required to be about $0.16\lambda \times 0.16\lambda$ (for a wavelength of 2.4 GHz) or at least 20 mm × 20 mm. The distance between the cells is 0.008λ and 0.008λ in the x and y directions, respectively. The complete array is 294 mm × 294 mm or $2.352\lambda \times 2.352\lambda$, and employs 14×14 cells. In comparison, the conventional AMC cell needs a size of $0.176\lambda \times 0.176\lambda$ with the via hole (diameter = 0.004λ).

The reflection phase determines the frequency range in which the characteristics of AMC can be observed. Figure 2 shows the simulated reflection phases of the designed AMC, the mushroom-like surface employing the via hole, and the UC-EBG. For a frequency of 2.4 GHz, an in-phase reflection is observed in all of the surfaces. When the patches are connected to other patches, that is, the AMC surfaces becomes a planar type, the zero degree reflection phases move to higher frequency bands. Otherwise the frequency band will have a small and short period.

In the case of the via hole, there is a negligible difference between the presence of the via hole or lack thereof in the proposed models. Although the performance with and without the via hole are almost the same, the fabrication of a surface without a via hole is easier and cheaper than that found with a via hole. Therefore, the proposed AMC structure has several advantages: broad bandwidth, small size, simple structure, low price, and easy fabrication. In addition, each slot in the structure plays a key role in tuning the desired frequencies. Resonant frequencies from 2 GHz to 3 GHz can be controlled by the length or width of the slots.

3. MEASUREMENT AND ANALYSIS

A basic dipole antenna exhibits very poor performance when close to a conventional metallic reflector, close being defined as a distance smaller than a quarter-wavelength. The image currents appear out-of-phase rather than in-phase, so that the radiation in the antenna is cancelled out by the currents. However, the performance is greatly improved when the AMC surface is used as the

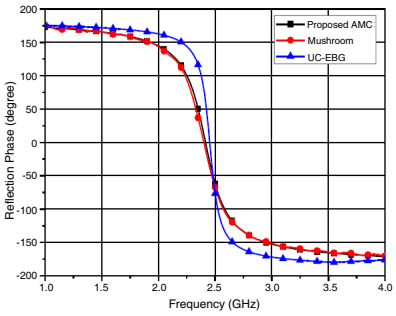

Figure 2: Simulated reflection phase.

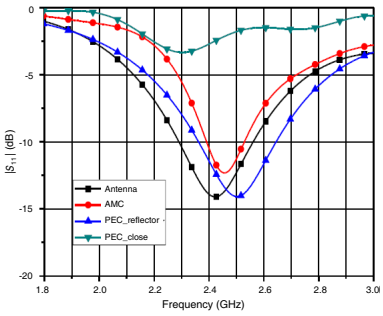

Figure 3: Simulated reflection coefficient.

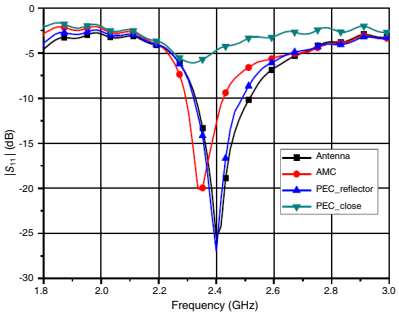

Figure 4: Measured reflection coefficient.

reflector. In order to verify this, we simulated and measured the reflection coefficients of dipole antennas placed above PEC and AMC reflectors. We calculated the length of the dipole antenna to be about 62.5 mm at 2.4 GHz. A vector network analyzer (HP8510c) was used for the measurement of the reflection coefficient in the laboratory. Before any calculations or measurements could be performed, we needed to determine some numerical formulas.

We can calculate the reflection coefficient if we consider a normally incident plane wave that scatters from a semi-infinite dielectric-magnetic slab of a certain depth in free-space. When the permittivity and permeability are ε and μ, the corresponding impedance and the wave number are $\eta = \sqrt{\mu/\varepsilon}$ and $k = \omega\sqrt{\mu}\sqrt{\varepsilon}$. In the free-space the parameters are, respectively, ε_0, μ_0, $\eta_0 = \sqrt{\mu_0/\varepsilon_0}$, and $k_0 = \omega\sqrt{\mu_0}\sqrt{\varepsilon_0}$. Therefore, the relative permittivity and permeability are derived by the expressions $\varepsilon = \varepsilon_0\varepsilon_\Gamma$ and $\mu = \mu_0\mu_\Gamma$. The authors of [7] derived the reflection and transmission coefficient values. Usually, the reflection (S_{11}) and transmission (S_{21}) values are given by:

$$S_{11} = \frac{\eta - \eta_0}{\eta + \eta_0} \frac{1 - e^{-j2kd}}{1 - \left(\frac{\eta-\eta_0}{\eta+\eta_0}\right)^2 e^{-j2kd}} \tag{1}$$

$$S_{21} = \frac{4\eta\eta_0}{(\eta + \eta_0)^2} \frac{e^{-jkd}}{1 - \left(\frac{\eta-\eta_0}{\eta+\eta_0}\right)^2 e^{-j2kd}} \tag{2}$$

Metamaterials have been shown to exhibit very large wave impedances, so the corresponding impedance will approach infinity. The reflection and transmission coefficient values from (1) and (2) therefore become:

$$\lim_{|\eta\to\infty|} S_{11} = +1 \tag{3}$$

$$\lim_{|\eta\to\infty|} S_{21} = 0 \tag{4}$$

A slab having large impedance will use the AMC reflector, which has a broad bandwidth and in-phase reflection. However, although the permeability is not extremely large and the permittivity is near zero, the impedance can be made to be extremely large, that is, the reflected index, $n = \sqrt{\mu/\mu_0}\sqrt{\varepsilon/\varepsilon_0}$, will become small. Therefore, a high impedance and low reflected index are needed for an AMC.

We first confirmed the antenna performance through computer simulation. Figure 3 shows the simulated return loss of the antenna according to the reflectors. There are four symbols: Antenna, AMC, PEC_reflector, and PEC_close. Antenna denotes the reflection characteristic without a reflector in the free space. When the antenna and the PEC reflector are placed closely together (PEC_close), there is no reflecting effect. If the wavelength of the driving source in the free-space is $\lambda 0$, the resonant distances were found to be $\lambda 0/10$. At that time, the antenna is about 12.5 mm away from the PEC reflector. When the distance between the antenna and the PEC reflector becomes a quarter-wavelength, the PEC surface reflects an inverse radiation wave. In the case of the AMC surface, it is not necessary to keep a quarter-wavelength distance. Although they are located closely together (about 12 mm), the antenna works as a perfect reflector.

The measured reflection coefficient results are shown in Figure 4. As can be seen, the measured results are similar to the simulation results. When the PEC reflector is near the antenna, the reflector does not reflect the radiated wave. However, both the PEC reflector separated from the

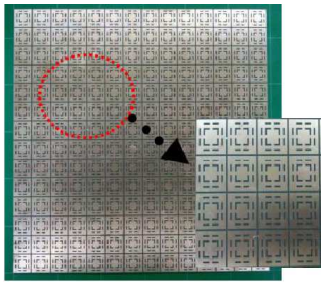

Figure 5: Photograph of the fabricated reflector.

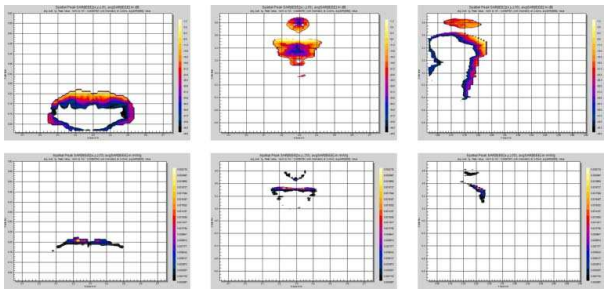

Figure 6: Simulated SAR distribution.

antenna by a quarter-wavelength and the AMC reflector near the antenna performed well. The fabricated reflector is shown in Figure 5. The reflector size is 294 mm by 294 mm. The human effect is analyzed by applying the designed reflector. Figure 6 shows the simulated SAR distribution. The calculated peak SAR averaged over 1 g is only 0.002 W/kg when the input power is 1 W.

4. CONCLUSIONS

We designed and investigated a novel artificial magnetic conductor structure in this paper. The AMC structure was designed to be a reflector. From the simulated and measured results of the reflection phase, the designed structure performed at 2.4 GHz with a 12.6% bandwidth. The proposed AMC structure has several advantages: broad bandwidth, small size, simple structure, and cheap and easy fabrication due to the absence of a via hole. For the simulated and measured tests of the reflection coefficient, both the dipole antenna and the proposed reflector were placed close together (≈ 12 mm). The antenna operated identically to the PEC reflector at a quarter-wavelength. Therefore, this reflector can be used to decrease the size of systems employing a reflector. The designed reflector has broad bandwidth, small size, and ease of fabrication, because the proposed structure has no via holes. The human effect is analyzed by applying the designed reflector. The calculated peak SAR averaged over 1 g is only 0.002 W/kg, when the input power is 1 W. For more serious analysis, if 12.8 W of input power is injected, which shows a maximum reference level of 1.6 W/kg, the calculated peak SAR is only 0.0078 W/kg. In conclusion, the designed reflector should block electromagnetic waves from entering a human body.

REFERENCES

1. Sievenpiper, D., L. Zhang, R. F. J. Broas, N. G. Alexopolous, and E. Yablonovitch, "High-impedance electromagnetic surfaces with a forbidden frequency band," *IEEE Trans. Microwave Theory Tech.*, Vol. 47, No. 11, 2059–2074, 1999.
2. Al-Nuaimi, M. K. T. and W. G. Whittow, "Novel planar AMC for low profile antenna applications," *2009 Loughborough Antennas & Propagation Conference*, 145–148, November 2009.
3. Tomeo-Reyes, I. and E. Rajo-Iglesias, "Comparative study on different AMC ground planes and its applications to low profile wire antennas," *Antennas and Propagation Society International Symposium 2009*, 1–4, June 2009.
4. Sohn, J. R., K. Y. Kim, H.-S. Tae, and H. J. Lee, "Comparative study on various artificial magnetic conductors for low-profile antenna," *Progress In Electromagnetic Research*, Vol. 61, 27–37, 2006.
5. Hampel, S. K., O. Schmits, O. Klemp, and H. Eul, "Design of sievenpiper HIS for use in planar broadband antennas by means of effective medium theory," *Advances in Radio Science*, Vol. 5, 87–94, 2007.
6. Niyomjan, G. and Y. Huang, "Investigation of high impedance surface structure with different patch shapes using a new improved enhanced effective medium method," *2008 International Workshop on Antenna Technology*, 187–190, 2008.
7. Stutzman, W. L., G. A. Thiele, and Stutzman, *Antenna Theory and Design*, John Wiley & Sons, 2000.

A Broadband Active Integrated Microstrip Antenna Array Design in Millimeter Wave Frequency Band

Mohammad Mahdi Honari, **Abdolali Abdipour**, **and Gholamreza Moradi**
Microwave/Millimeter Wave and Wireless Communication Research Lab
Department of Electrical Engineering, Amirkabir University of Technology
Tehran 15914, Iran

Abstract— The design of a broadband active integrated antenna array in millimeter wave frequency band is presented. The output matching network is omitted then the microstrip antenna operates as an output matching network of the power amplifier and radiator. For operating in broadband, both the power amplifier and the antenna array are designed as broadband components. The simulated results of the power amplifier confirm circuit operation. The output power of the amplifier is obtained almost 20 dBm for optimized load. Due to broad bandwidth and isolation with the power amplifier by the ground, the aperture coupled antenna array is employed. The simulated results of the impedance matching, radiation pattern, side-lobe level, and cross-polarization are suitable within the impedance bandwidth of the power amplifier of 24.5 to 31.5 GHz.

1. INTRODUCTION

Active integrated antennas (AIA) constitute a growing area of research in recent years. An AIA can be considered as an active microwave circuit in which the output or input port is directly connected to the antenna probe without any matching network [1, 2]. Integration of the antenna can result in smaller size and weight, lower insertion loss, lower cost and greater efficiency as compared to conventional system. In recent years, one of the main issues of the research is the amplifier-type active antenna [2]. In [3], a novel fully integrated active antenna using the direct integration between power amplifier and antenna is proposed to obtain high PAE and compact RF-front end because of omitting interconnecting elements between the amplifier and antenna. There is a growing interest in communication systems to operate in the mm-wave frequencies in order to obtain wider bandwidth. In a broadband AIA, the antenna and amplifier design in the wide bandwidth. In recent years, many efforts have been devoted on the advance of wideband antenna for modern communication systems [4]. The aperture antennas increase bandwidth because of the coupling between the patch and feed line [4]. Array antennas are being widely used in many wireless applications, such as satellite communication systems but an efficient design along with the fabrication of planar array antenna with proper side-lobe level and wide matching bandwidth are challenging tasks [5].

In this paper, the design of a broadband AIA array in millimeter wave band is presented. For more integration, the transistor of the power amplifier is connected to the array antenna directly. The goal of our design is wide bandwidth then the both of the power amplifier and array antenna are designed as broadband components. We analyze the designed power amplifier by ADS software and matlab. A new antenna array is designed to operate as load of the amplifier. The structure of the antenna array consists of a 3-dB 180°-phase shifter, two 1-port's and two 2-port's aperture-coupled microstrip antennas. Finally, the simulations of the antenna array are done with a frequency domain simulator (HFSS) and a time domain simulator (CST) to be sure about the results. The simulated impedance matching, radiation pattern, side-lobe level, and cross-polarization are suitable throughout the matching bandwidth.

2. CONFIGURATION AND DISCUSSIONS

There are two main parts in AIA. These two are the power amplifier and antenna array that treated as a single unit. In this paper, we design the class-A power amplifier and antenna array as AIA for broadband application at the center frequency of 28 GHz. The amplifier and antenna array are designed on Rogers's TMM 4 substrate with 4 mil substrate height and dielectric constant of 4.5.

2.1. The Power Amplifier

The transistor of amplifier is TRW's 0.15-μm InGaAs/AlGaAs/GaAs pseudomorphic high electron-mobility transistor (pHEMT). The linear equivalent-circuit parameters and asymmetric Curtice nonlinear model of the transistor are in [6]. To achieve the maximum PAE and output power,

we do load pull analysis at the centre frequency of 28 GHz then we optimize the input matching network and the load impedance for broadband operation [2]. The optimum value of the load is obtained $Z_{load} = 36 + j50$ ohm. The overall schematic of designed broadband amplifier structure is shown in Fig. 1. It is seen that the power amplifier is connected to the antenna directly. Fig. 2 shows the output power and gain of the amplifier as function of frequency that are almost stable throughout the bandwidth. Fig. 3 depicts the PAE versus the input power at the center frequency of 28 GHz. Finally as shown in Fig. 4, the drain voltage and load power calculated by ADS software and matlab that are in a good agreement.

2.2. The Antenna Array

The aperture coupled structure is selected for antenna array in view of its intrinsic advantages in active device integration as compared to the other feed structures. On the other hand, this structure has wide bandwidth. The structure of the antenna array consists of a 3-dB 180°-phase shifter, two 1-port's and two 2-port's aperture-coupled microstrip antennas [5]. Fig. 5 shows the configuration of the antenna array. There are three substrates in antenna's structure. The substrates 1 and 3 are the same as power divider one (Rogers's TMM 4) and the substrate 2 is foam. The main idea of designing this antenna array is the generating the wide impedance bandwidth of the 2-port aperture coupled antennas by coupling mechanism [5]. The geometry of the 3-dB 180°-phase shifter is also illustrated in Fig. 5 which contains a Wilkinson power divider and an 180°-broadband Schiffman phase shifter. Wilkinson power is designed for the optimum load of the power amplifier ($Z_{load} = 36 + j50$ ohm) [8]. The 2-port antenna includes two microstrip lines: the feeding port and the coupling port. When power enters to feeding port, a part of it is coupled to the patch through the aperture on the ground plane and radiated into the free space, and the other part of it is then coupled back to coupling port radiated by 1-port aperture coupled antennas. Fig. 6 shows the transmission power ratio and the impedance matching of 2-port antenna. It is seen that the proposed coupling structure can be used in aperture coupled antenna array over the frequency range from 24 to 32 GHz, because in this range of the frequency the suitable power form feeding

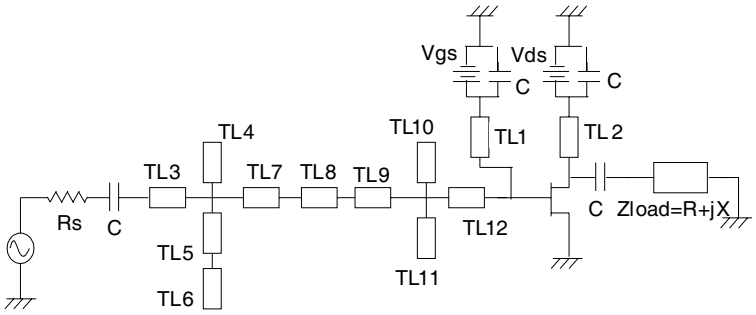

Figure 1: The schematic of broadband class-A power amplifier.

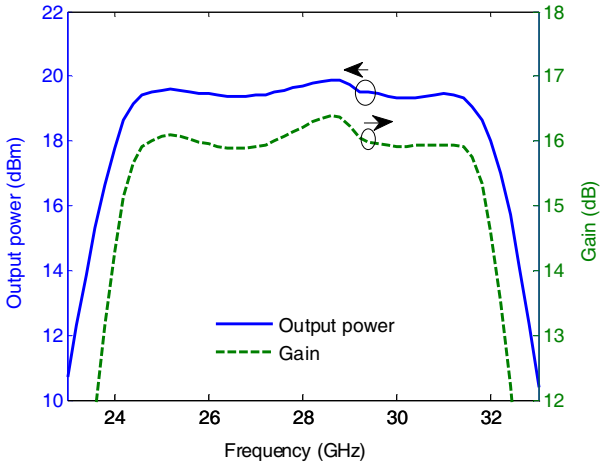

Figure 2: The output power and gain of the amplifier.

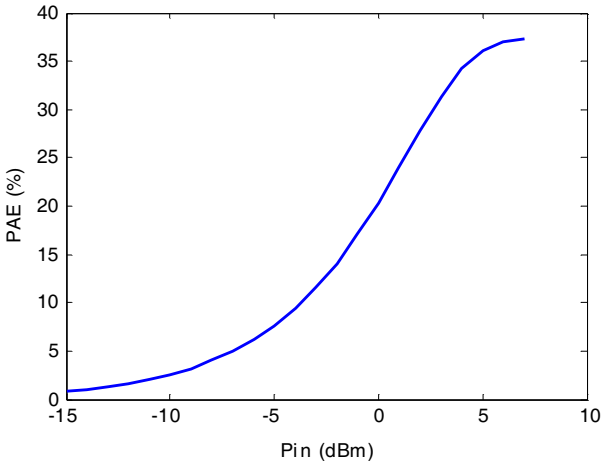

Figure 3: PAE versus the input power at the centre frequency of 28 GHz.

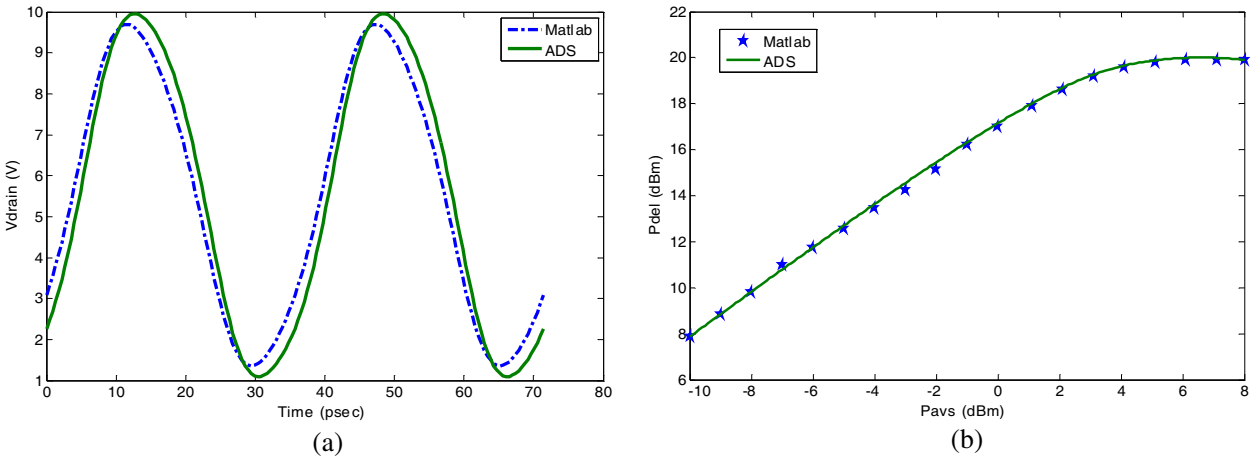

Figure 4: (a) The drain voltage, (b) the power delivered to load as function of the input power, by ADS software and matlab.

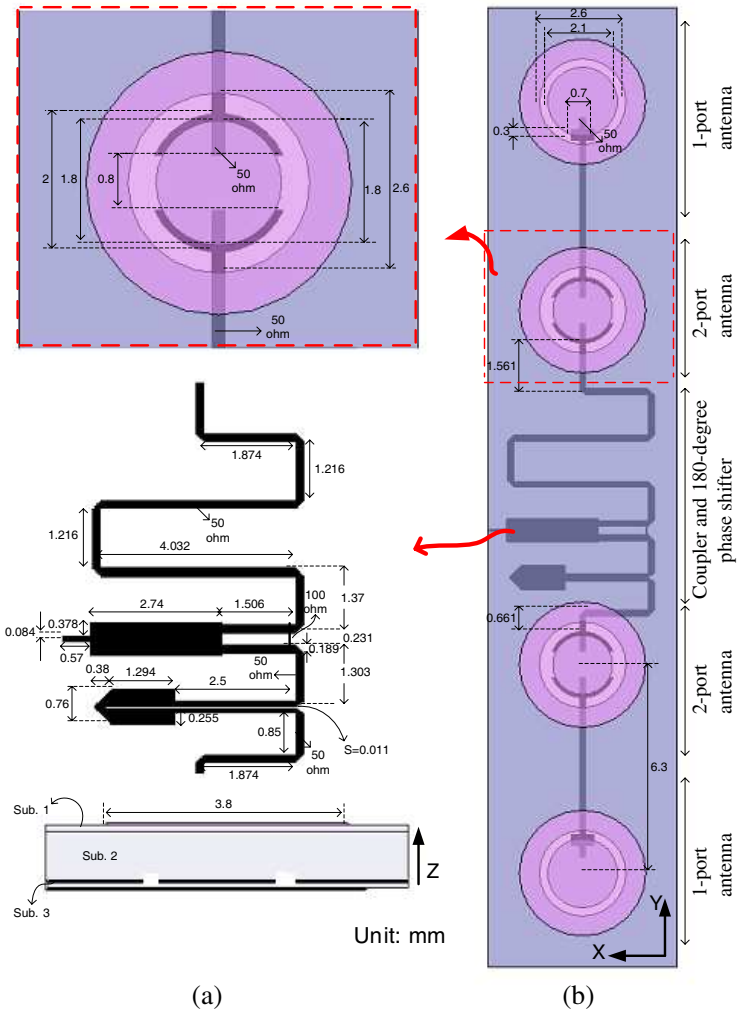

Figure 5: The antenna array (a) side view, (b) top view.

port is coupled to the coupling port [7] and also the matching bandwidth is suitable. Fig. 7 depicts the input impedance of the array antenna. This input impedance of the array antenna is load impedance of the power amplifier that is close to the optimum load. The peak gain is suitable and stable over the bandwidth of the amplifier as shown in Fig. 8. The peak gain is about 11.8 dBi

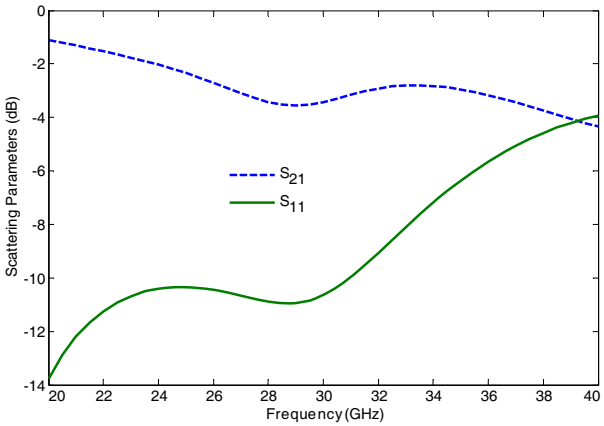

Figure 6: The scattering parameters of 2-port aperture coupled antennas.

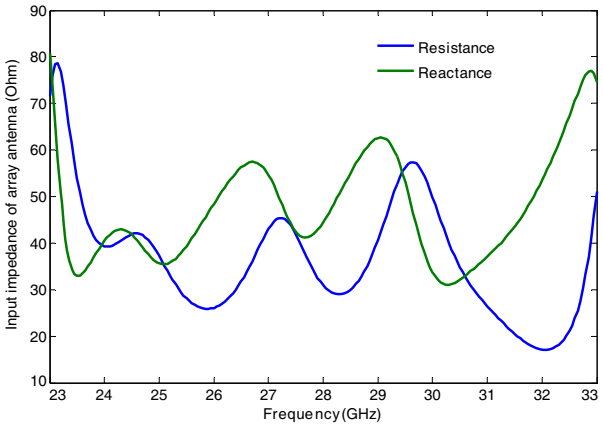

Figure 7: The input impedance of the array antenna.

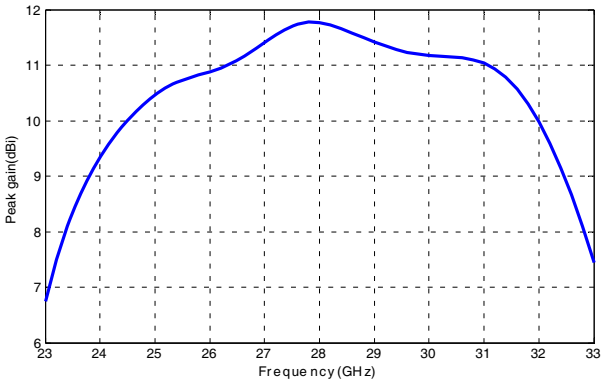

Figure 8: Peak gain of the antenna array.

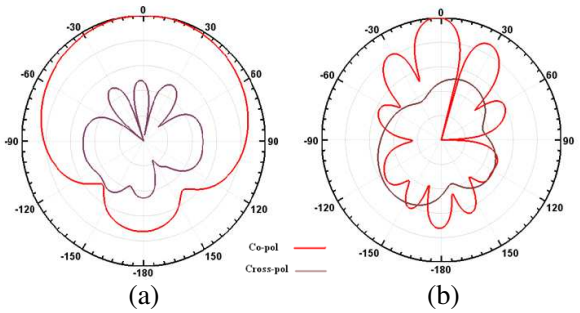

Figure 9: The radiation pattern of the antenna array at the center frequency of 28 GHz, (a) H-plane, (b) E-plane (every sector: 10 dB).

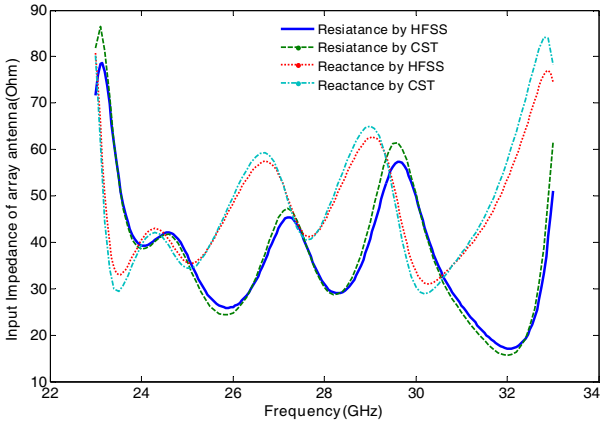

Figure 10: Input impedance of the antenna array calculated by CST and HFSS simulators.

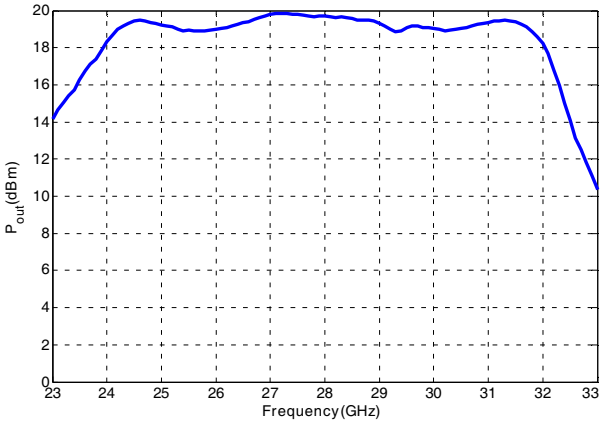

Figure 11: The load power of AIA.

at the center frequency of 28 GHz. Fig. 9 depicts the radiation patterns of the antenna array at 28 GHz. A good radiation pattern is obtained in E-plane and H-plane. Cross-polarization in the 3-dB beamwidth is nearly 25 dB below the co-polarization in the E-plane and 26 dB below the co-polarization in the H-plane for the antenna array. Also there is an acceptable side-lobe level of 6.5 dB. Finally, we compare the simulation results of the antenna array between a frequency domain simulator (HFSS) and a time domain simulator (CST) to be sure about the results. Fig. 10 shows

the input impedance of the antenna array calculated by CST and HFSS simulator that are in good agreement.

2.3. The AIA

The AIA consists of the designed power amplifier and antenna array. Due to the input impedance of the antenna array is not the optimum of load impedance of amplifier, the bandwidth of amplifier is reduced. Fig. 11 illustrates the load power of AIA (load is antenna array). A 1-dB ripple bandwidth of 25% is achieved between 24.5 to 31.5 GHz.

3. CONCLUSION

In this paper, a broadband active integrated antenna array in millimeter wave was presented. The power amplifier was design to operate in broad bandwidth. The antenna array was designed to operate as the load of the power amplifier. The gain, radiation pattern and cross-polarization of the antenna array were adequate in the bandwidth. A 1-dB bandwidth of 25% was achieved.

REFERENCES

1. Vargas, D. S., D. C. Galan, L. E. G. Monuz, and V. G. Posadas, "Broadband active receiving patch with resistive equalization," *IEEE Trans. Microwave Theory & Tech.*, Vol. 56, No. 1, 56–64, Jan. 2008.
2. Honari, M. M., A. Abdipour, and G. Moradi, "Millimeter-wave design of broadband active integrated microstrip patch antenna," *PIERS Proceedings*, 1501–1505, Kuala Lumpur, Malaysia, Mar. 27–30, 2012.
3. Kim, H., I. J. Yoon, and Y. J. Yoon, "A novel fully integrated transmitter front-end with high power-added efficiency," *IEEE Trans. Microwave Theory & Tech.*, Vol. 53, No. 10, 3206–3214, Oct. 2005.
4. Honari, M. M., A. Abdipour, and G. Moradi, "Bandwidth and gain enhancement of an aperture antenna with modified ring patch," *IEEE Antennas and Wireless Propagation Letters*, Vol. 10, 1413–1416, 2011.
5. Honari, M. M., A. Abdipour, and G. Moradi, "Design of wide-band aperture-stacked patch microstrip antennas," *IEICI Electronics Express*, Vol. 9, No. 4, 250–255, Feb. 2012.
6. Siddiqui, M. K., A. K. Sharma, L. G. Callejo, and R. Lai, "A high-power and high-efficiency monolithic power amplifier at 28 GHz for LMDS applications," *IEEE Trans. Microwave Theory & Tech.*, Vol. 46, No. 12, 2226–2232, Dec. 1998.
7. Wincza, K., S. Gruszczynski, and J. Borgosz, "Microstrip antenna array with series-fed 'through-element' coupled patches," *Electron. Lett.*, Vol. 43, No. 9, 487–489, 2007.
8. Wu, Y. and Y. Liu, "An unequal coupled-line Wilkinson power divider for arbitrary terminated impedances," *Progress In Electromagnetics Research*, Vol. 117, 181–194, Jun. 2011.

Three-dimensional Finite Element Modelling of Current Density in Maternal Transthoracic Defibrillation

A. Jeremic[1], **J. Pots**[2], **and E. Khosroshahli**[3]

[1]Department of Electrical and Computer Engineering, McMaster University, Hamilton, ON, Canada
[2]Department of Medicine, McMaster University Hospital, Hamilton, ON, Canada
[3]Department of Biomedical Engineering, McMaster University, Hamilton, ON, Canada

Abstract— Although resuscitation during pregnancy is relatively uncommon and rarely cause deaths they have a particularly large impact in terms of the mortality of the unborn child and long-term effects on families and society as whole. Although modelling of current density distribution and conductive anatomy of the human transthoracic defibrillation has been subject of certain research interest the attempts to model this phenomenon in pregnant women using 3D finite element have been nonexistent. In this paper, we present simplified 3D finite element model of a pregnant female torso and calculate current density distribution in the uterus. We evaluate the current density a function of voltage difference in order to obtain maximum allowed voltage. The purpose of our study therefore is to evaluate maximum possible voltage for a given position of electrodes which can still be considered safe for a fetus.

1. INTRODUCTION

Although it has been acknowledged that the cardiac arrest in pregnancy is a rare event [1] it can have significant impact in terms of age of mother, mortality of unborn children (especially with potential loss of two lives) and consequently long-term effect on a family. However it has been demonstrated that the clinical staff who treat pregnant women have rather limited knowledge of protocols for treating maternal cardiac arrest. One of the commonly used procedures in resuscitation is defibrillation which is routinely used for treating ventricular arrhythmias.

With recent advances in understanding pathophysiologies behind electrical shock in pregnant women [2] it became more obvious that previous studies of current conduction in human body should be extended to account adequately for changes in maternal body that affect conduction pathways. Namely it has been shown [3] that physiological changes in pregnancy affect transthoracic impedance and thus affect transmyocardial current which depolarizes heart (myocardium) as a part of resuscitation. However due to the physiological changes (e.g., size of uterus, increased intra- and extra-cellular fluid, increased blood volume, increased thoracic volume, and presence of amniotic liquid) the transthoracic impedance changes may affect current pathways in an unpredictable way.

In this paper, we present a three-dimensional simplified model for finite-element analysis of maternal transthoracic defibrillation. In this procedure an electrical pulse is applied to the torso through electrodes commonly called paddles. One of the most important aspects is the energy or current density generated on the surface (aforementioned transthoracic current) and corresponding current density in the heart (transmyocardial current) which needs to be above certain threshold, sufficient for stimulation of myocytes that are inexcitable [4]. Three-dimensional models of human defibrillation have been previously studied and quit extensive list of previous reports is listed in [6]. However to the best of our knowledge this is a first attempt to model defibrillation in pregnancy. In this preliminary work, we propose the simplified model in which the uterus and stomach are modelled as a single area with larger conductivity. In order to account for frequency dependent properties of biological tissues we decompose the biphasic pulse into frequency component and perform frequency-domain analysis resulting in corresponding current harmonics. We then calculate the amplitude of the current density harmonics in the lower abdomen and analyze these values with respect to position of electrodes and/or energy delivered by defibrillator.

The organization of the paper is as follows. In Section 2, we present frequency dependent mathematical equations and electric properties of physiological tissues. In Section 3, we discuss finite-element implementation using COMSOL. In Section 4, we present numerical results. Finally in Section 5, we discuss our results and future research directions.

2. MATHEMATICAL MODEL

In order to describe the mathematical model of the defibrillation we first describe the electric pulse that is applied to the patient's torso. Commonly used defibrillators commonly apply rectilinear

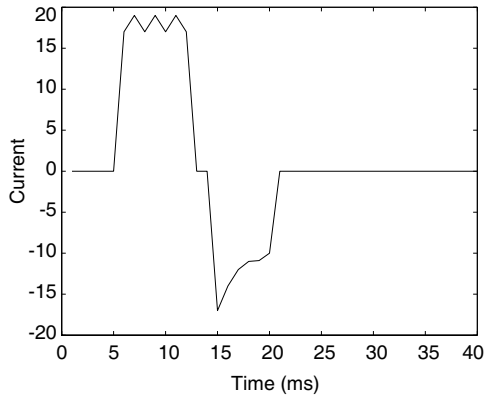

Figure 1: Time waveform of rectilinear pulse.

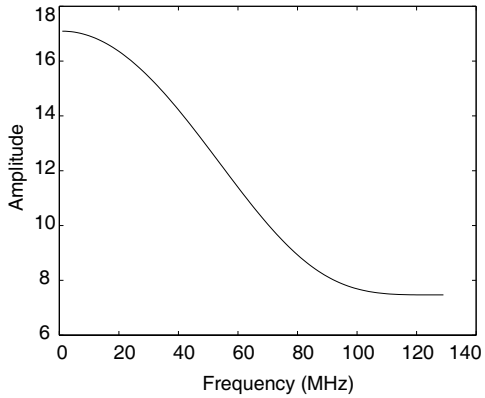

Figure 2: Short-time Fourier transform of the pulse.

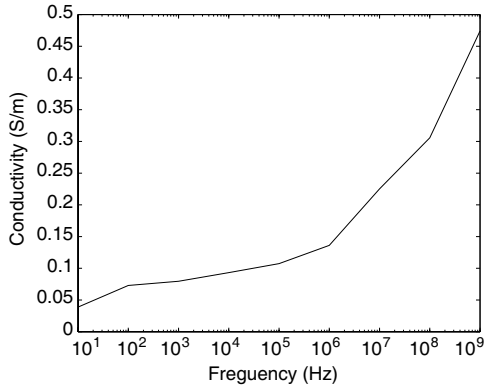

Figure 3: Average conductivity of lungs.

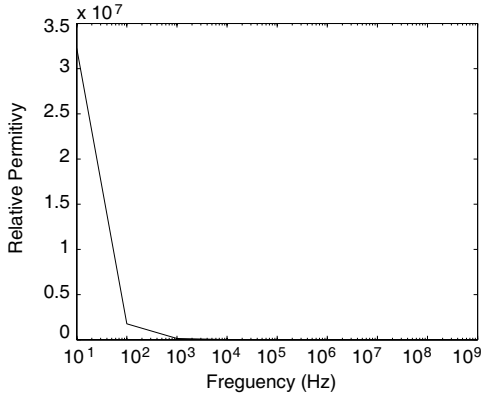

Figure 4: Average permittivity of lungs.

biphasic pulse which consists of constant current pulse followed by truncated exponential decay pulse. In Figure 1, we show typical waveform of a rectilinear biphasic form for energy of 120 kJ into 50 Σ load (common value for standardly used defibrillator pads).

Due to the time-dependant nature of the problem the current propagation is governed by Maxwell's equations

$$\nabla \times \vec{E}(\vec{r},t) = -\frac{\partial \vec{B}(\vec{r},t)}{\partial t} \tag{1}$$

$$\nabla \times \frac{\vec{B}(\vec{r},t)}{\mu} = \vec{J} + \epsilon \frac{\partial \vec{E}(\vec{r},t)}{\partial t} \tag{2}$$

Note that in the above equations the electric properties (conductivity and permittivity) depend on frequency. In this paper, we use several different types of tissue: left and right lung, interstice, diaphragm, equivalent lower torso and skin/fat tissue. We approximate tissues of the abdominal compartment (liver, gut, spleen, uterus) using a homogeneous equivalent tissue with slightly larger conductivity. For illustrational purposes in Figures 3 and 4 we illustrate frequency dependence of lung conductivity and permittivity. Similarly Figures 5 and 6 show same values for human skin. These values were selected from reported estimates of tissue properties [5].

It has been shown [7] that using a piecewise homogeneous torso model consisting of the closed surfaces $S_i,\ i = 1, \ldots, M$ can be obtained in the analytical form. Let σ_i^- and σ_i^+ be the conductivities of the layers inside and outside S_i respectively. We will denote by G_i the regions of different conductivities, and by G_{M+1} the region outside the torso, which behaves as an insulator.

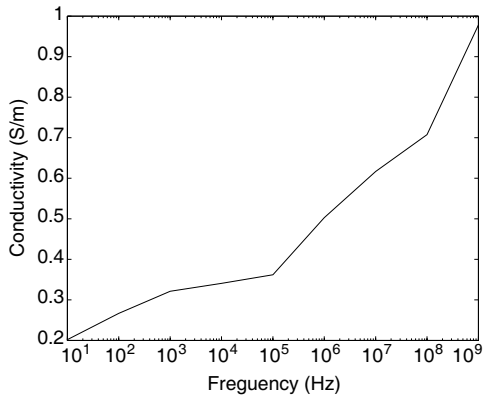

Figure 5: Average conductivity of muscle.

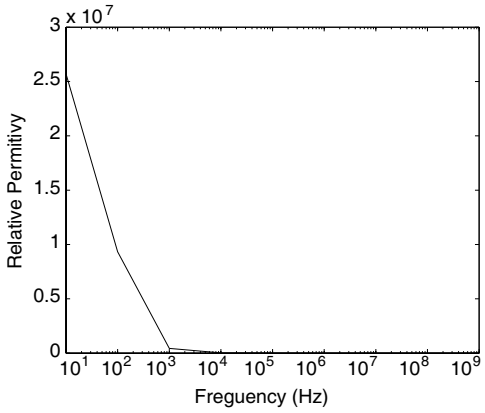

Figure 6: Average permittivity of muscle.

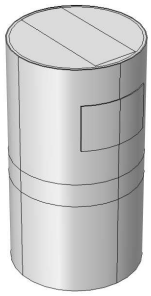

Figure 7: Model geometry.

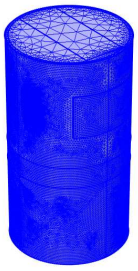

Figure 8: Finite-element mesh.

Therefore, in our model $\sigma_{M+1}^- = \sigma_M^+ = 0$. The magnetic field and potentials are then given by

$$\begin{aligned}\vec{B}(\vec{r},t) &= \vec{B}_0(\vec{r},t) + \frac{\mu_0}{4\pi}\sum_{i=1}^{M}(\sigma_i^- - \sigma_i^+)\int_{S_i}\phi(\vec{r}',t)\frac{(\vec{r}-\vec{r}')}{\|\vec{r}-\vec{r}'\|^3}\times \mathrm{d}S(\vec{r}'),\\ \vec{B}_0(\vec{r},t) &= \frac{\mu_0}{4\pi}\int_G \frac{\vec{J}(\vec{r}',t)\times(\vec{r}-\vec{r}')}{\|\vec{r}-\vec{r}'\|^3}\mathrm{d}^3r', \end{aligned} \tag{3}$$

where μ_0 is the magnetic permeability of the vacuum.

Similarly, the potential $\phi(\vec{r},t)$ is given by [7]

$$\begin{aligned}\frac{\sigma_k^- + \sigma_k^+}{2}\phi(r,t) &= \phi_0(\vec{r})(\sigma_i^- - \sigma_i^+) + \frac{1}{4\pi}\sum_{i=1}^{M}(\sigma_i^- - \sigma_i^+)\int_{S_i}\phi(\vec{r}',t)\frac{(\vec{r}-\vec{r}')}{\|\vec{r}-\vec{r}'\|^3}\cdot \mathrm{d}S(\vec{r}'),\\ \phi_0(\vec{r},t) &= \frac{1}{4\pi}\int_G \frac{\vec{J}(\vec{r}',t)\cdot(\vec{r}-\vec{r}')}{\|\vec{r}-\vec{r}'\|^3}\mathrm{d}^3r', \end{aligned} \tag{4}$$

where we use subscript k is such that $\vec{r}\in G_k$.

The above equations are amenable to inverse modelling and signal processing techniques when estimation of certain unknown parameters is needed. In this paper, we focus our attention on so called forward modelling in which all the parameters are to be known. In this case due to the complexity of the geometry it is more beneficial to calculate solution directly using commercially available software such as COMSOL.

3. FINITE-ELEMENT MODEL

In this section, we discuss model construction and solution. As mentioned before in this paper we use a cylindrical model consisting of the following compartments: left and right lung, interstice, diaphragm, equivalent lower torso and skin/fat tissue. We approximate tissues of the abdominal

compartment (liver, gut, spleen, uterus) using a homogeneous equivalent tissue with 30% larger conductivity to account for the presence of amniotic fluid.

Defibrillation pads were simulated as groups of nodes on torso surface that were constrained with the same potential. No elements were used to simulate the physical structure of the pads. Solutions were obtained for the potential and current density distribution in the lower abdomen (uterus). In order to model different boundaries within the torso we enforced continuity conditions for all the interior boundaries. To properly model exterior boundary we place the torso model in a large (significantly larger than torso) volume and enforce zero potential on the external boundary. We then apply adaptive meshing in which we enforce very coarse mesh for the sphere which ensures reasonable computational time. The resulting mesh consists of approximately 16000 nodes with 21000 degrees of freedom and was implemented using AC/DC module in COMSOL Multiphysics software.

4. NUMERICAL RESULTS

In order to illustrate the applicability of the proposed model in Figures 9 and 10 we illustrate the current density in the lower abdomen at frequencies of 1 kHz and 1 MHz respectively. Observe that the current density at higher frequency is smaller when compared to the current density at lower frequencies. This is a consequence of two opposite effects: decreasing power amplitude of biphasic waveform and increasing conductivity at higher frequencies.

To evaluate the effect of the pad position we perform the analysis for two different positions: anterior-posterior (AP) and anterior-apex (AA). For a maximum voltage difference of 1000 V (peak-to-peak of the biphasic waveform) we obtain maximum values of current density at 18 mA and 32 mA respectively.

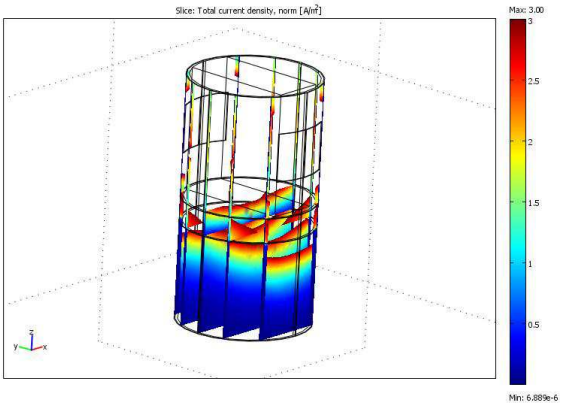

Figure 9: Current density at 1 kHz.

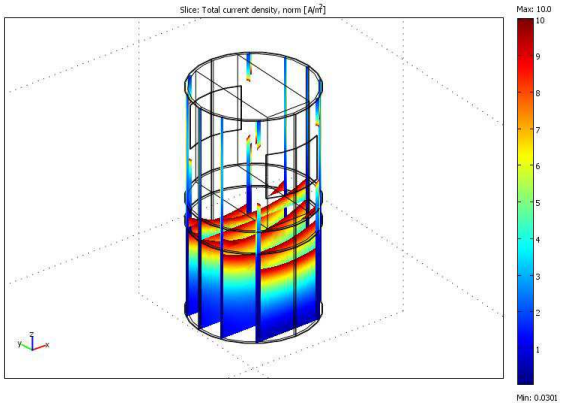

Figure 10: Current density at 1 MHz.

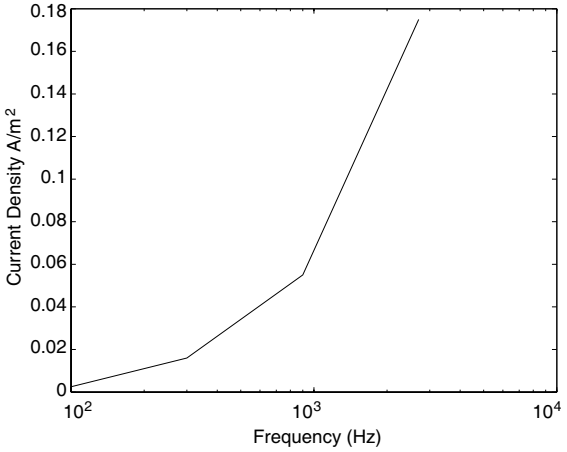

Figure 11: Current density as a function of voltage.

In Figure 11, we illustrate the maximum current density as a function of peak-to-peak voltage. These result can be potentially used to determine maximum allowed voltage which can still produce myocardial current density above inexcitability threshold.

5. CONCLUSION

In this paper, we presented a three-dimensional finite-element model for calculating current density distribution during pregnancy. We approximated presence of uterus by increasing conductivity of lower abdomen for 30% to account for the presence of amniotic fluid. These result can be potentially useful for analyzing if energy requirements for defibrillation of pregnant women should be potentially changed. Future research will include more precise geometry with respect to detail resolution (e.g., including uterus as a separate compartment) as well as anatomically correct torso. Our preliminary results indicate that the current density distribution in lower abdomen may become significant since the levels that are considered potentially dangerous for the fetus are low and therefore warrant further investigation of this topic.

REFERENCES

1. Tiberiu, E., et al., "Cardiopulmonary resuscitation in the pregnant patient — An update," *The Israel Medical Association Journal*, Vol. 13, May 2011.
2. Fatovich, D., "Electric shock in pregnancy," *The Journal of Emergency Medicine,* Vol. 11, 175–177, 1993.
3. Nanson, J., et al., "Do physiological changes in pregnancy change defibrillation energy requirements?," *British Journal of Anaesthesia*, Vol. 87, No. 2, 237–239, 2001.
4. Zipes, D. P., et al., "Termination of ventricular fibrillation in dogs by depolarizing a critical amount of myocardium," *Amer. J. Cardiol.*, Vol. 36, 37–44, 1975.
5. Gabriel, S., et al., 'The dielectric properties of biological tissues: II. Measurements in the frequency range 10 Hz to 20 GHz," *Phys. Med. Biol.,* Vol. 41, 2251–2269, 1996.
6. Camacho, M. A., et al., "A three-dimensional finite element model of human transthoracic defibrillation: Paddle placement and size," *IEEE Trans. on Biomedical Engineering,* Vol. 42, No. 6, Jun. 1995.
7. Gulrajani, R., *Bioelectriciy and Biomagnetism*, John Wiley & Sons, 1998.

Evaluation of Tissue Properties in MR Images

J. Mikulka[1], **E. Gescheidtová**[1], **P. Marcoň**[1], **K. Bartušek**[2], **and A. Šprláková**[3]

[1]Department of Theoretical and Experimental Electrical Engineering
Brno University of Technology, Kolejni 4, Brno 612 00, Czech Republic
[2]Institute of Scientific Instruments of the ASCR, v.v.i
Královopolská 147, Brno 612 64, Czech Republic
[3]Radiological Clinic, The University Hospital Brno
Jihlavská 20, Brno 625 00, Czech Republic

Abstract— Image processing in biomedical applications is strongly developing issue. Many methods and approaches for image preprocessing, segmentation and visualization were described. This paper deals with image evaluation obtained by magnetic resonance tomography. Soft tissues can be observed in these images and their characteristics can be used to further processing and to diagnose diseases. Intensity distribution (mean, maximum, minimum, standard deviation and area) in regions of human head tissues are evaluated and compared for two healthy persons. The obtained values will be compared with the same parameters of unhealthy persons in studying jawbone diseases. The aim of this research is to find relations between tissue parameters which can be observed by often available magnetic resonance measuring sequences (T1/T2 weighted images, diffusion weighted images). The relations and similarity of some tissues and regions in mentioned images could help to increase yield of data obtained by magnetic resonance tomography and thus use of MR to pathological tissues and diseases recognition which must currently be diagnoses by other, often invasive, methods.

1. INTRODUCTION

Magnetic resonance (MR) tomography is nowadays used in medical practice exclusively to soft tissues imaging in the patient's body. Its main advantage is that only strong static magnetic field and radio frequency electromagnetic field is used. This modern diagnostic method for patients bears no risks caused by radiation, unlike computed tomography using X-rays. Imaging of hard tissues (bone) is not possible by MRI [1]. Healthy bone on MR images appears as an area in which no signal is detected. There are several diseases (bone fibrous dysplasia, giant cell tumors, osteonecrosis) for which the bones are distorted, their shape is expanded and this leads to detection of pathological signal in bone marrow. In the skeleton there is a change of their internal structure, which changes in soft tissue. Such bones can be detected by MR tomography. Distribution of healthy tissues is shown in Fig. 1(a). Dark areas on the bottom represent the jawbone. Fig. 1(b) the pathological tissue is visible (green colored). The aim of the MR images processing is classification of a type and stage of disease [2–4] and thus increase the yield of data acquired by MR tomography. To enable the classification of affected hard tissues by MR tomography, the detailed description of both healthy and affected tissues in a wide patient database has to be created. For this purpose, the

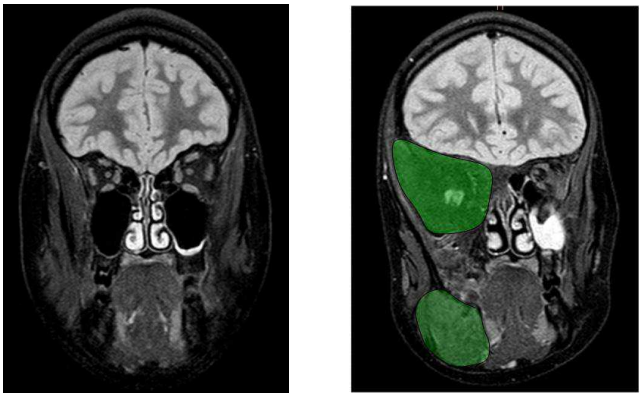

Figure 1: MR image example of a human head, (a) shown one slice with visible jaw bone without pathological tissues, (b) marked area of maxillary bone with expansion and shape deformation.

areas representing the tissues should be properly segmented. Choice of appropriate segmentation techniques to extract tissue from MR images has been described, e.g., in [5–9]. In the next phase the degree of correlation between the values of image parameters of healthy/affected tissues and the results of histological examination will be determined. The paper describes the first results obtained by the processing of MR images of bones of healthy patients.

2. PROPOSED METHODOLOGY

In the first phase of the research the process of MR images evaluation was proposed. The methodology consists of the following steps: 1) evaluation of the images of two patients by two different evaluators to assess the quality of the evaluation (correctness of classification of each tissue), 2) evaluation of images of one patient by 10 evaluators to determine the repeatability of image parameters measurement, 3) compilation a database of patients affected by bone diseases (MR images of the jawbone, hip bone, results of blood tests and histology results), 4) evaluation of the entire database of affected patients, 5) determine the correlation between the assessed parameters from MR images, results of blood tests and histological examination, 6) assembly a model for the

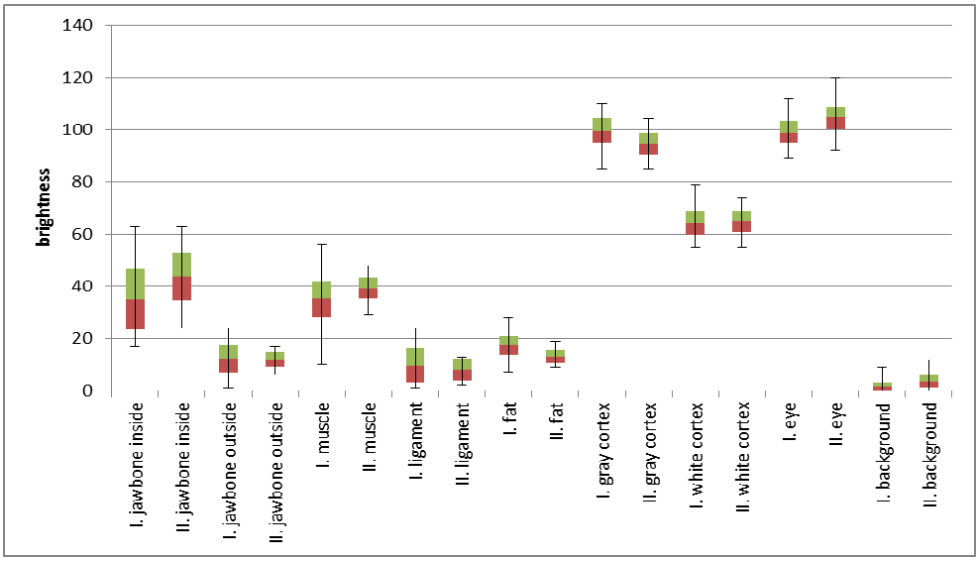

Figure 2: Comparison of brightness distribution in selected areas (tissues) evaluated patient by two evaluators, images were obtained by STIR sequence, I. and II. denotes the firts and second evaluator.

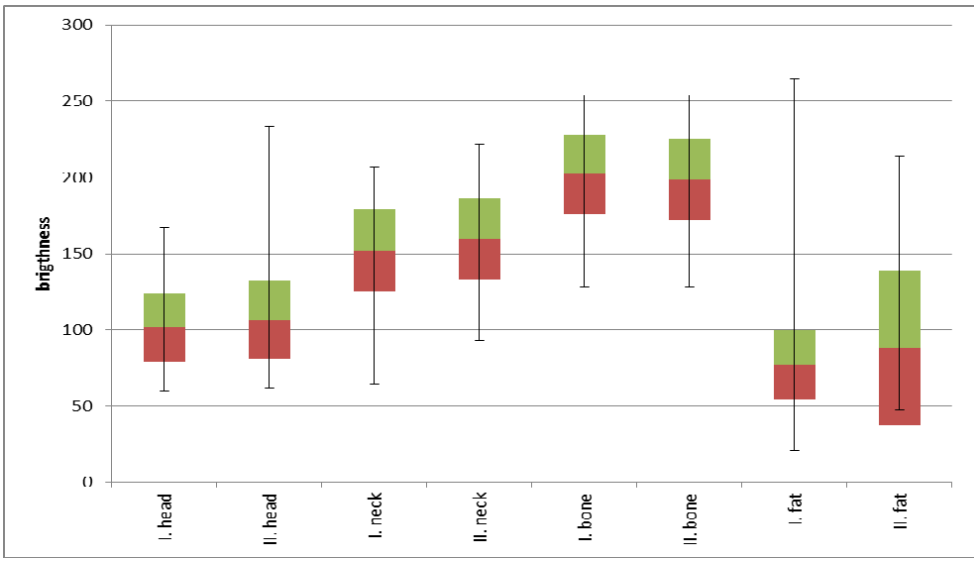

Figure 3: Comparison of brightness distribution in selected areas (tissues) evaluated patient by two evaluators, images were obtained by STIR sequence, I. and II. denotes the firts and second evaluator.

classification of bone diseases.

3. EVALUATION RESULTS

Available MR images showing the area of jawbone and hip bone of the same person/patient were evaluated. The hip bones were displayed for their large size. The values if the parameters identified in MR images of the hip bone can also be used as a reference in evaluation of parameters in jawbone images. Their big advantage is high resolution at which the error caused by incorrect classification of bones and the poor evaluation of the distribution of brightness can be practically suppressed. The article describes the results of evaluation of images obtained by sequences STIR (Short TI Inversion Recovery) and single shot Leber DWI (Diffusion Weighted Images). In selected tissues (see Figs. 2–5) following parameters were evaluated: area, the average brightness value, maximum and minimum brightness value and standard deviation. The boxplots in Figs. 2–5 show the evaluated parameter as follows: upper and lower boundaries of each boxplot represent the maximum and minimum brightness, interface between the green and the red rectangle shows the

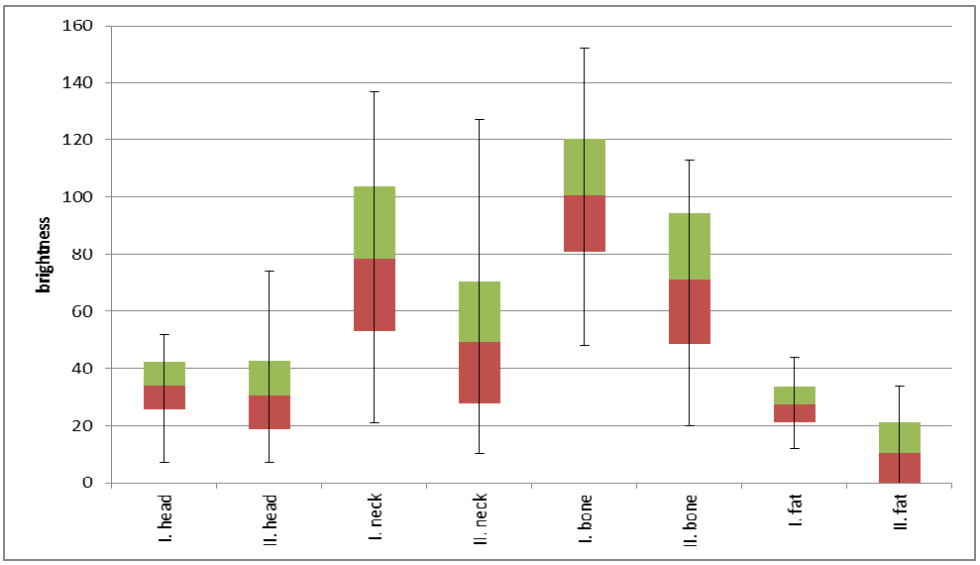

Figure 4: Comparison of brightness distribution in selected areas (tissues) evaluated patient by two evaluators, images were obtained by Leber Single Shot DWI sequence, I. and II. denotes the firts and second evaluator.

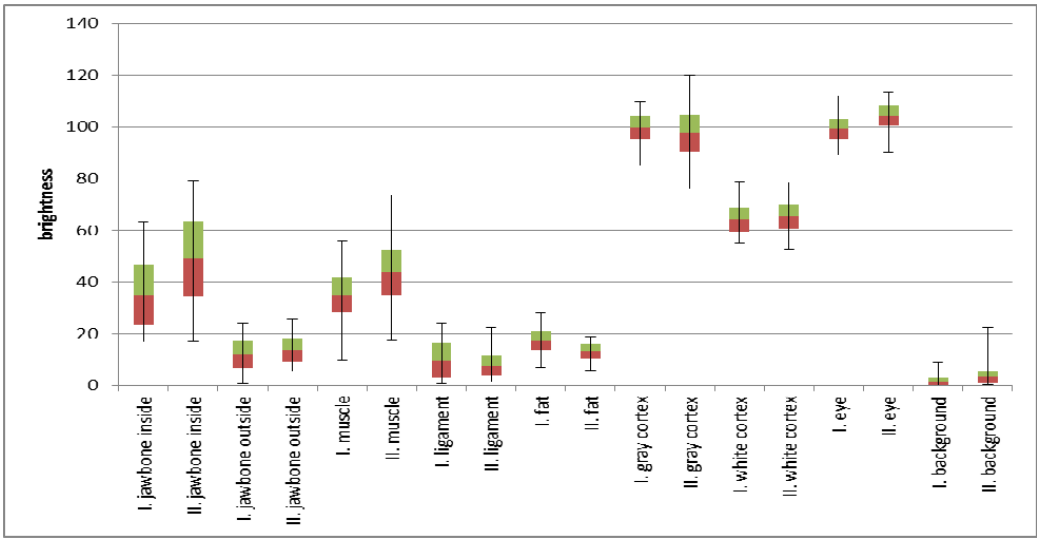

Figure 5: Comparison of brightness distribution in selected areas (tissues) of two patients evaluated by one evaluator, images were obtaines by STIR sequence, I. and II. denotes the firts and the second patient.

mean brightness and height of each rectangle shows the standard deviation of brightness.

Evaluation results presented in Fig. 4 corresponds to problematic evaluation of diffusion images. The position of individual tissues is necessary to search by registration with those tissues in the images weighted by relaxation time T1 or T2, since in the DWI images of tissue distribution of very difficult to distinguish.

4. CONCLUSIONS

The article describes the initial study in the processing of MR images of human tissues (around the jaw and hip bone). This is the first step in the proposed processing methodology, which is to determine the quality of image of two healthy people evaluation by one evaluator and subsequently evaluate a healthy person by two evaluators. The referred boxplots shows the possibility of individual tissues distinctiveness based on the distribution of brightness in MR images. Evaluation results presented in Fig. 4 corresponds to problematic evaluation of diffusion images. The position of individual tissues is necessary to search by registration with those tissues in the images weighted by relaxation time T1 or T2, since in the DWI images of tissue distribution of very difficult to distinguish. The graph in Fig. 5 shows that the repeatability of the evaluation by one evaluator is satisfying.

Our next work in this area will be focused on evaluation of parameter of MR images in patients affected by bone diseases mentioned. Bone disorders area currently diagnosed with invasive histological examination. The possibility of using MR imaging to a reliable determination of parameters of particular diseases and their recognition would spare the patient's painful procedure and it would speed up the diagnosis.

The aim of our future research will be creation of a model for the classification of selected bone diseases by non-invasive method by finding relations between MR image data, the results of histological examination and blood test results.

ACKNOWLEDGMENT

This work was supported in part by the Grant project GAP102/11/0318, 102/12/1104, project FEKT-S-11-5/1012 and CZ.1.07.2.3.00.20.0175.

REFERENCES

1. Haacke, E. M., R. W. Brown, M. R. Thompson, and R. Venkatesan, *Magnetic Resonance Imaging: Physical Principles and Sequence Design*, John Wiley & Sons, 1999.
2. Fukunaga, K., *Introduction to Statistical Pattern Recognition*, Elsevier, 1990, ISBN 0122698517.
3. Kassner, A. and R. E. Thornhill, "Texture analysis: A review of neurologic MR imaging applications," *Neuroradiol Journal*, Vol. 2010, No. 31, 809–816, 2010.
4. Pham, D. L. and J. L. Prince, "Robust unsupervised tissue classification in MR images," *IEEE International Symposium on Biomedical Imaging: Nano to Macro*, Vol. 1, 109–112, 2004.
5. Bartusek, K., E. Gescheidtova, and J. Mikulka, "Data processing in studying biological tissues, using MR imaging techniques," *33rd International Conference on Telecommunication and Signal Processing*, 171–175, 2010.
6. Mikulka, J., E. Gescheidtova, and K. Bartusek, "Perimeter measuerement of spruce needles profile using MRI," *PIERS Proceedings*, 1128–1131, Beijing, China, Mar. 23–27, 2009.
7. Mikulka, J., K. Bartusek, and E. Gescheidtova, "Processing of NMR slices for preparation of multi-dimensional model," *13th International Conference on Biomedical Engineering (ICBME)*, 186–189, 2009.
8. Mikulka, J., "Monitoring of diseases progression by MR," *PIERS Online*, Vol. 6, No. 8, 723–725, 2010.
9. Liberda, O., K. Bartusek, Z. Smekal, and J. Mikulka, "Data processing in studying the temporomandibular joint, using MR imaging and sonographic techniques," *DSP 2009: 16th International Conference on Digital Signal Processing*, 2009.

Why Gamma Photons Induce Cherenkov Effect

Antonio Puccini
Department of Neurophysiology, Order of Malta, Naples, Italy

Abstract— Pavel Alekseyevich Cherenkov was the first one to point out (1934) the effect coming from the impact of γ radiation with the high terrestrial atmosphere layers. Gamma photons (Ps) hit the molecules of the terrestrial atmosphere with such a strong impact to remove electrons with a speed bigger than the solar light in the same mean. Besides, these electrons, so much accelerated, emit ultraviolet (UV) Ps as well as visible Ps, with a violet colour and a brilliant blue: *Cherenkov Light* (CL). CL too travels with a speed higher than the visible light in high atmosphere.

As we know our atmosphere is constantly bombarded by electromagnetic radiations (EMRs). As for γ rays, X or UV radiation too hit atoms of the atmosphere molecules pushing away the electrons but in these circumstances the removed electron is not able to emit the CL, since the emitted Ps are not quicker than the common light in the atmosphere. Why is a γP able to accelerate the electron with a bigger speed than a XP or a less energetic P, that is with a lower frequency, can do? We think that the difference comes from the impact force with which the EMR hit the atmospheric molecules and their electrons. The force can be quantified by the value of the *momentum* (p) coming from the formula $p = h/\lambda$ where h is Planck'constant and λ is the wave length of the considered P.

Our calculations show that a visible P has a $p = 1.325 \cdot 10^{-22}$ [g · cm/s], whereas a XP with $\lambda = 10^{-9}$ [cm] has a $p = 6.625 \cdot 10^{-18}$ [g·cm/s], and a γP with $\lambda = 10^{-12}$ [cm] has a $p = 6.625 \cdot 10^{-15}$ [g·cm/s].

Since, as Fermi reminds us, the p of an EMR *quantum* is transferred entirely to the hit electron (we only detract the value of W_o indicating the energy necessary to extract the electron, about a few eV), we could explain why only electrons removed by γPs manage to acquire such a *kinetic energy* to be able to exceed the light speed, in the same mean, and emit a light, the CL, faster than the common light.

1. INTRODUCTION

In 1934 the Russian scientist Pavel Alekseyvic Cherenkov was the first to point out the effect generated by the impact of γ radiation and the layers of high terrestrial atmosphere [1]. As we know the most energetic γ radiations hitting the Earth are emitted by intense electromagnetic (EM) sources represented mainly by explosions of supernovae or by the collision of two stars of neutrons, creating Gamma Ray Bursts (GRBs). In the first case the emission lasts ≈ 20 seconds (only rarely it lasts a few minutes); in the second case the emission mostly lasts about 5 seconds. GRBs represent the most powerful source of EM emission known, second only to the Big Bang [2]. Cherenkov pointed out that γ radiations, hitting the molecules of the high atmosphere, can make them free electron. What surprised Cherenkov was that electrons hit by γ radiations travelled with a speed higher than the visible light in the air, and that at this speed they could emit EM radiations (EMRs) which wavelength λ) moved from brilliant blue, to violet, and in bigger quantity to ultraviolet (UV). Surprisingly also this radiation, today known as *Cherenkov Radiation*, or *Cherenkov Light* (CL), travels with a speed higher than the visible light in the same mean.

2. DISCUSSION

We may wonder: how is it possible that a particle travels with a higher speed than the light? However it is not surprising since we are referring to the speed of light in a mean different from vacuum. Thus no physical law or theory are violated. This can be explained easily considering that the atmospheric refraction index is bigger than the vacuum refraction index (n_v). If we consider $n_v = 1$, we have that the atmospheric refraction index is: 1.000293, carbon dioxide's is 1.00045, water's is 1.333. Thus, common visible light going through the atmosphere travels with a speed lower than in vacuum (c), as we know c is $299792.458(\pm 0.4)$ km/sec [3]. When the light goes through a mean different from vacuum its speed is given by the ratio c/n. Hence, as the light goes through water its speed is $299792.458/1.333 = 224000$ km/sec, that is it travels $\approx 1/3$ slower than in vacuum. That is why a small particle can travel in the atmosphere with a speed bigger than common visible light. Besides, the particles we are considering are electron and positrons, that is

the lightest elementary particles, thus the impulse they receive by gamma photons (γPs) can make them accelerate till a relativistic speed.

This is the crucial point, we think, when considering the CL. This radiation, indeed, is emitted only if the hit particle is also accelerated sufficiently. *Conditio sine qua non*: within EM Spectrum only γPs manage to give electrons such a speed to be able to emit the CL. Why doesn't it happen with EMRs with lower frequency (f)? It is useful to underline that CL, or *Cherenkov Effect*, seems to us very similar to the photoelectric effect (PEE) or to the Compton Effect. In these cases too the electrons are thrown out from the struck atom by a sufficiently energetic EMR. The only difference is that for PEE it is necessary just the visible light, in the case of Compton Effect it is necessary the force given by XPs to throw out electrons from graphite, whereas in order to have the *Cherenkov Effect* it is necessary exclusively γPs. Why? An explanation can be found in the different EM frequencies used. As we know our atmosphere is constantly bombed by EMRs of several types. Just as γ rays, X radiation too, or the UV radiation hit the atoms of the atmospheric molecules, throwing away electrons from them, however in these cases the electron will not be able to emit the CL. Why? The XP does not manage to give the hit electron a kinetic Energy (E_{kin}), that is a speed similar to the one given by a γP. This is the difference and the explanation. However this explanation seems to us not sufficient. What is the intimate physical mechanism so that, in the atmosphere, an electron hit by a XP does not emit CL? We can say because it has not been sufficiently accelerated, as a γP is able to do instead. We wonder then: why a γP manages to accelerate the electron with a speed bigger than a XP is able to do, or a less energetic P? It hasn't been explained properly, however it is what happens with PEE. As Lenard first pointed out, when some metals are struck by EMRs with different λ electrons are pushed out with different velocities, in a rate inversely proportional to the value of λ and directly proportional to the f of the EM wave (EMW). Lenard, in fact, "had discovered that when the light hit certain metals it caused the emission of electrons from their surface, just as the light had the power to push out the electrons from the atoms. When physicists started to make experiments on this phenomenon (PEE) they realized, with great surprise, that if they raised the light intensity, the energy of the emitted electrons did not increase; what influenced them instead, were the different colours of the λ of the light used: for instance, the blue light gave the electrons a bigger speed than the yellow light. A red light of any intensity did not cause at all the emission of electrons in certain metals. None of these phenomena could be explained by the old theories of light. Why was the blue light able to do something which the red light was not able to do? Einstein found the answer: an electron had to be hit by a *quantum* of energy higher than a minimum value in order to absorb enough energy (E) to abandon the surface of the metal" [4]. That is, higher than the E which keeps the electron linked to the atom: *threshold value* or *shearing value* [5]. This is illustrated in Einstein Equation (1):

$$E_{kin} = h \cdot f - E_{link}, \tag{1}$$

where E_{kin} is the kinetic energy acquired by the hit electron, the speed at which it moves away; $h \cdot f$ is the energy of the incident P (h is Planck constant); E_{link} gives the binding energy of the electron, that is the energy (E) necessary to free it from the metal or, in our case, from the atmospheric molecules (it is also called *extraction work* and corresponds to some eV). Thus, saying that the electron hit by the blue light goes faster than one hit by a red P, is like saying that the E_{kin} that the blue P transfers to the electron is bigger than the one given by the red P. With this concern Asimov says: "Anyway, the higher the energy of the quantum, the higher also the speed of the electron pushed out of the metal" [4]. Thus we can say that it is E, that is f to make the difference, since it has been proved that a more energetic P gives a bigger speed to the hit electron than a P with a lower f, that is less energetic. It seems to us not sufficiently accurate, though not wrong, to attribute only to the E of the P (its f) the physical explanation of the phenomenon. With which physical means can the simple E of the P give the struck electron a bigger or lower speed? We should say: the *energy of the momentum* (p), that is the impact force carried out by the p of the incident P on the electron [6, 7]. With this regards, as Einstein [8] pointed out, we know that all particles, including the P, have a p. In fact Weinberg says: "Each P carries a well definite E and p'' [9]. Similarly Feynman writes: "a P is like a particle, in that it carries an E and a p. The p of a P is a certain constant (h) divided by the wavelength (λ)" [10] (2):

$$p = h/\lambda, \tag{2}$$

where h is $6.625 \cdot 10^{-27}$ [erg·s]. From Equation (2) we have that the more λ decreases the more its p increases. Therefore the p isn't constant for the Ps, but is inversely proportional to λ. Let us

verify it. The p of the Ps belonging to a γ radiation of $\lambda = 10^{-12}$ [cm] corresponds to:

$$p = h/\lambda = 6.625 \cdot 10^{-27} \,[\mathrm{erg} \cdot \mathrm{s}]/10^{-12} \,[\mathrm{cm}]. \tag{3}$$

Since $1\,\mathrm{erg} = \mathrm{g}{\cdot}\mathrm{cm}/\mathrm{s}^2{\cdot}\,\mathrm{cm}$, we can write:

$$p = 6.625 \cdot 10^{-27} \,[\mathrm{g} \cdot \mathrm{cm}^2/\mathrm{s}]/10^{-12} \,[\mathrm{cm}], \tag{4}$$

$$p = 6.625 \cdot 10^{-15} [\,\mathrm{g} \cdot \mathrm{cm}^2/\mathrm{s}]. \tag{5}$$

This is the p value of a γP with a medium E. Let us consider instead XPs with $\lambda = 10^{-9}$ [cm] and let us calculate their p:

$$p = 6.625 \cdot 10^{-27} \,[\mathrm{erg} \cdot \mathrm{s}]/10^{-9} [\mathrm{cm}], \tag{6}$$

$$p = 6.625 \cdot 10^{-18} \,[\mathrm{g} \cdot \mathrm{cm}/\mathrm{s}]. \tag{7}$$

Whereas, with common visible Ps, with a medium λ, we have:

$$p = 6.625 \cdot 10^{-27} \,[\mathrm{erg} \cdot \mathrm{s}]/5 \cdot 10^{-5} [\mathrm{cm}], \tag{8}$$

$$p = 1.325 \cdot 10^{-22} \,[\mathrm{g} \cdot \mathrm{cm}/\mathrm{s}]. \tag{9}$$

What can we infer from these calculations? We learn that common light hits the electron with a really significant *pushed force.* Thus, rather than a general *energetic action*, not described in the physical characteristics of the phenomenon, the ejection of the electron from the atom, by Ps, seems to us a pure *mechanical effect* mediated by the p. It is the impulse given by the P to move away the electron from the metal. The bigger the value of p (as it is possible to infer from our calculations), the bigger the removal speed of the electron (as Lenard has demonstrated with the red and blue lights) [11]. In fact the E_{kin} of the removed electrons is equivalent to the *push force* indicated by the p' value of the incident P [12]. As Fermi reminds us, the P tranfers all its p to the hidden particle [13].

Hence, we have that if the electrons hit by Ps with different λ (and different p) move away with different speed, this means that also different Ps propagate with different motion values, since the impulse carried by the P, through its p, is passed almost completely to the electron [14, 15]. Therefore it should be inferred, for instance, that the blue Ps in order to give a bigger propulsive push to the hit electron, should travel with a higher speed than the red ones! This can explain Lenard's observations. Thus, to be more precise it is the p of the P which needs to have the necessary *force* to remove the electron from the struck metal. We have seen the huge differences existing between the p of a γP and the p of a visible P. It is just this difference which can explain, for instance, why the Compton Effect is not elicited by radio Ps, visible Ps, or UV Ps. It is necessary the *impact force* generated by the p of a X P to start the Compton Effect. This is indisputable.

Let us analyse now why, unlike blue Ps, red Ps do not manage to remove the electron from most metals. As Asimov reminds us "a blue light *quantum* has an E double than a red light *quantum*" [4]. This is confirmed if we calculate the *momenta* values of their Ps. Let's consider a red P, with $\lambda = 780$ nanometres, that is $7.8 \cdot 10^{-5}$ [cm]. Let us calculate its p:

$$p = h/\lambda = 6.625 \cdot 10^{-27} \,[\mathrm{erg} \cdot \mathrm{s}]/7.8 \cdot 10^{-5} \,[\mathrm{cm}], \tag{10}$$

$$p = 6.625 \cdot 10^{-27} \,[\mathrm{g} \cdot \mathrm{cm}^2/\mathrm{s}]/7.8 \cdot 10^{-5} \,[\mathrm{cm}], \tag{11}$$

$$p = 0.8493 \cdot 10^{-22} \,[\mathrm{g} \cdot \mathrm{cm}/\mathrm{s}] = 8.493 \cdot 10^{-23} \,[\mathrm{g} \cdot \mathrm{cm}/\mathrm{s}]. \tag{12}$$

This is the p of a red P. Let us calculate now the p of a blue P, with $\lambda = 390$ nanometres, that is $3.9{\cdot}10^{-5}$ [cm]:

$$p = 6.625 \cdot 10^{-27} \,[\mathrm{erg} \cdot \mathrm{s}]/3.9 \cdot 10^{-5} [\mathrm{cm}] = 6.625 \cdot 10^{-27} \,[\mathrm{g} \cdot \mathrm{cm}^2/\mathrm{s}]/3.9 \cdot 10^{-5} \,[\mathrm{cm}]. \tag{13}$$

We have:

$$p = 1.6987 \cdot 10^{-22} \,[\mathrm{g} \cdot \mathrm{cm}^2/\mathrm{s}]. \tag{14}$$

We can notice that the p, that is the impulse, the *force* with which the blue P hits the electron is exactly double than the force with which the p of the red P impacts on the electron (just as stated by Asimov). This is why, differently from blue P, the red P does not manage to remove the

electron from the metal target. There is one more question, even more important, which physical mechanism has not yet been clearly explained, and not sufficiently pointed out: why electron struck by the blue light move away from the metal with a speed bigger than those struck by the red light?

We should ask the same question about what happens in the atmosphere: why γPs manage to induce the *Cherenkov Effect*? In other words: why the other EMRs do not manage to accelerate the electrons in the same way of γ rays? With this respect in literature we find: "as all other particles the P has a its own p, expressed also by the formula:

$$p = mv, \tag{15}$$

though it is massless" [16]. From Equation (15), thus, we infer that p of a particle, including the P, is strictly correlated to its propagation speed, in a given direction [17]. From (15) with no doubt we can infer that in a particle p and velocity (v) are directly proportional. Hence, a particle with a p bigger than the p of other particles, will have a bigger speed too. This happens also with Ps. As a consequence those Ps having a high p (such as γPs) will propagate more quickly than Ps with a p having a lower speed, such as the Ps of the visible light or radio Ps.

3. CONCLUSIONS

In this way we can understand easily the *Cherenkov effect*: γPs manage to accelerate electron to relativistic speeds (with a consequent emission of CL), just because atmospheric electrons struck by γ Ps travel with a higher speed than electrons struck, for instance, by XPs or by visible Ps, which *momenta* are respectively showed in Equations (5), (7), (9). Thus, according to basic Mechanics laws, the different E_{kin} acquired by the struck electron, can be considered a faithful and irrefutable evidence of the different incident particle's speed. Of course they are very small differences, impossible to detect and without any influence on our daily life, however they may underline how the EM signal comes from long distances, as when it is generated by GRBs. Measuring this signal it has been observed that it comes on Earth through a long *EM Swarm*, which lasts a few days and is known as *Afterglow*. Well, considering that the different EMW bands travel at the same speed, if between the first and the last EM signal emitted by the GRB pass only a few minutes, at the same time when these signal arrive on Earth they should have the same time, that is they should have the same difference in the time of arrival, at the most a few minutes between the first and the last. However it is not so! The *EM Swarm* goes on even for a few days. It is really puzzling. There is no convincing explanation which may explain such a discrepancy [2]. Yet there is an explanation, it is under our eyes, the surprising duration of the *EM Swarms* proves that during the route some EMWs *gain time* respect to the other EMWs which remain behind. Though they leave with at most a few minutes difference, they reach the Earth with an *extended* difference in time which can be even of a few days! It is clear that these EMWs travelled with different velocities. We hope astronomers will be able to detect a GRB with a γ ray satellite so to have the time to direct immediately on the EM source different probes sensitive to the different wave length of the EM spectrum. We expect that Em signals coming from GRB would be detected firstly by γ ray satellites, secondly by X ray satellites, lately by those with a UV length and optical telescopes and eventually by radio and IR ray probes.

In short, from *Cherenkov Effect* we get to the point that Ps do not propagate all at the same velocity, but according to the value of their respective *momenta*.

REFERENCES

1. Cherenkov, P. A., "Visible light from clear liquids under the action of gamma radiation," *Doklady Akademii Nauk SSSR*, Vol. 2, 451, 1934.
2. Puccini, A., "Uncertainty principle and electromagnetic waves," *Journal of Electromagnetic Waves and Applications*, Vol. 19, No. 7, 885–890, 2005.
3. Savyer, K., *National Geographic Italia*, Vol. 4, 13, 1999.
4. Asimov, I., *Asimov's New Guide to Science,* 1984; Mondadori Ed., Milano, 417–418, 2004.
5. Einstein, A., *Annalen der Physik,* Vol. 17, 143, 1905.
6. Puccini, A., "The momentum of photon may explain the measurement's paradox in the subatomic world," *PIERS Proceedings*, 27–30, Suzhou, China, Sept. 12–16, 2011.
7. Puccini, A., "A mechanical effect induced by electromagnetic radiation may explain the wave function collapse of a quantum object," *PIERS Proceedings*, 726–728, Marrakesh, Morocco, Mar. 20–23, 2011.

8. Einstein, A., *Physikalische Zeitschrift,* Vol. 18, 121–128, 1917.
9. Weinberg, S., *The First Three Minutes. A Modern View of the Origin of the Universe*, 1977; Mondadori Ed., Milano, 196, 1980.
10. Feynman, R. P., *The Feynman Lectures on Physics,* California Institute of Technology 1965; Ital. Ed., Zanichelli, Bologna, I, 17–11, 2001.
11. Puccini, A., "The inflationist expansion of the universe was conducted by very high energy photons," *PIERS Proceedings*, 819–822, Cambridge, USA, Jul. 5–8, 2010.
12. Puccini, A., "Quantum mechanics suggests that photons with different energy do not travel at the same speed," *PIERS Proceedings*, Marrakesh, Morocco, 729–733, Mar. 20–23, 2011,
13. Fermi, E., *Atomi Nuclei Particelle,* Boringhieri Ed., 24, Torino, 2009.
14. Puccini, A., "About the zero mass of photon," *Progress In Electromagnetics Research*, Vol. 55, 117–146, 2005.
15. Puccini, A., "About the zero point energy, zero point mass, zero point temperature and zero point motion in the subatomic world and photonics," *Progress In Electromagnetics Research Symposium Abstracts*, 1169, Suzhou, China, Sept. 12–16, 2011.
16. Lesch, H., *Physik fur die Westentasche,* Verlag, P., Munchen, 2003; Ponte alle Grazie Ed., Milano, 39, 2007.
17. Puccini, A., "Light weighs," *Progress In Electromagnetics Research B*, Vol. 8, 161–177, 2008.

Anderson Transition May Be Induced by the Self Collapse of the Electron Wave Function

Antonio Puccini
Department of Neurophysiology, Order of Malta, Naples, Italy

Abstract— When in a crystalline solid, perfectly regular and good conductor, there are *impurities* we have that the solid undergoes a sudden change of state, that is a *transition* from conductor to insulating. In these circumstances the electrical current does not pass freely since electrons meet significant resistances (i.e., the *impurities*), as a consequence they tend to concentrate in a restricted area of the crystal. What happens is that the Wave Function (WF) of the electron previously extensive, *delocalised*, is now *localised*. We wonder how all these take place. What is the physical mechanism which makes the electron become localizable?

What we can clearly notice is that the behaviour of the electron is completely changed. At fist it propagated as a wave, without resistances and dissipation of energy, just as a quantum object (QO), *delocalised* and propagating as a superimposition of quantum states. Whereas, when the electron meets, along its path, a certain number of *impurities* (represented by atoms different from those making the solid crystalline), the electron is *localised* as a corpuscle.

The drastic change of the QO behaviour (from undulating-like to corpuscular-like) normally happens when we try to observe it, when we carry out a measurement. Though in our case no measurement has taken place, the electron behaves as it had been measured. What happens is that electrons, or rather their WFs, reflecting on the *impurities* and other reflected electrons, concentrate in a restricted area of the crystal.

We believe that in these circumstances, as a consequence of the impact, a self collapse of the electron's WF takes place. In this way electron become localizable, behaving as particles rather than waves.

1. INTRODUCTION

In a good conductor, represented by a crystalline solid, electrons propagate as waves, without superimposition of quantum states. In these circumstances, in fact, the wave function(WF) of each electron, indicated with $\Psi_{(x,t)}$, or simply Ψ, is *delocalized*, just as an undisturbed quantum object (QO) [1, 2]. According to de Broglie's intuition, electrons can be represented by waves extending along the solid [3, 4]. Ψ describes both their wave and particle character [5]. As Maiani reminds us "in a perfectly regular solid, electrons are described by waves extending along the whole solid. In these conditions the electric current flows into the crystal without any resistance" [6].

On the contrary, the resistance, and therefore the energy dissipation that allows us to heat our food in an electric cooker, is due to defects of the crystal itself: defects represented by the presence of impurities, i.e., atoms (randomly distributed) different from the atoms of the crystal [6]. In fact, as Anderson pointed out [7], above a certain concentration of such *impurities*, i.e., above a certain level of disorder, an abrupt change of the behavior of electrons occurs. Electrons cease to be waves extended on the whole crystal (i.e., *delocalized*) and *localize* around the centers of impurities. The solid changes abruptly state, from conductor becomes an insulator. In short, "In order to trap a quantum particle we may just need the disorder" [8].

A regular crystal is constituted by a series of atoms arranged at positions forming a Bravais lattice which, as it is known, can be described as follows:

$$R = n_1\mathbf{a}_1 + n_2\mathbf{a}_2 + n_3\mathbf{a}_3, \tag{1}$$

where R is the lattice, $\mathbf{a}_1$, $\mathbf{a}_2$, $\mathbf{a}_3$ are three non-complanar vectors and n_1, n_2, n_3 are integers. The unit cell is then defined as the volume of space that translated by the lattice vectors fills the space without gaps or overlaps. A system of this kind has a condition that is crucial for many of its physical characteristics: the Hamiltonian which describes it has a translational invariance [9].

2. DISCUSSION

The conduction of electricity in a perfect solid crystalline is conveyed by the electrons and described by the mathematical formalism of Bloch [10]. The energy of these electrons is expressed by the

Hamiltonian (H) described by Schrodinger equation [11]:

$$H = p^2/2m + V_{(x,t)}, \tag{2}$$

where m is the mass of the electron, p its *momentum*, V expresses the potential energy of the electron, which *argument* (x, t) reveals its space-time coordinates. The hypothesis of translational invariance of the Hamiltonian, together with the assumption of the *locality* of the potential V present in it, helps ensure the validity of the Bloch theorem, whereby the electronic eigenfunctions are of the following form:

$$\Psi_k(r) = V_k(r)E^{ik\cdot r}, \quad V_k(r+R) = V_k(r). \tag{3}$$

They are composed of a phase and a periodic part in the lattice. That is, they are functions extended throughout the system and have the property:

$$\Psi_k(r+R) = \Psi_k(r)E^{ik\cdot R}. \tag{4}$$

The eigenvalues of the system are distributed according to continuous function, represented by energy bands, $E_n(k)$, relating to the wave vector k that, in the limit of infinite crystal, can be considered (for each direction) a continuous variable; Ψ is the electronic wave function [9]. Then the spectrum of an ordered solid is composed of continuous intervals of energies allowed for the system (bands) whose eigenvectors are *delocalized* over the entire system. Thus Bloch theorem explains suitably the conductive properties of a solid, with the mentioned order characteristics, thanks to the peculiarities of the electronic Ψ. Therefore, in a regular crystal structure an electron is able to move through the crystal with a nearly constant velocity. It is a diffusive motion and the distance traveled by an electron is called *mean free path*. In such conditions, the electric current flows in the crystal without resistance.

In 1958 Anderson, studying the diffusion of electrons in the presence of random potential amplitude, subverted the fundamental assumptions of current theories, according to which the electronic states is still extended also in the presence of high disorder. As Anderson pointed out [7] if the number and the presence of *impurities* increases, the *disorder* within the crystal lattice increases too and the conductivity of the metal itself is affected.

As Anderson described "in this simple model the essential randomness is introduced by requiring the energy to vary randomly from site to site. It is shown that at low enough densities no diffusion at all can take place, and the criteria for transport to occur are given. In this paper, in fact, we attempt only to construct the simplest model we can think of which still has some expectation of representing a real physical situation reasonably well, and to prove a theorem about the model. The theorem is that at sufficiently low densities, transport does not take place; the exact wave functions are *localized* in a small region of space. We assume that we have sites $_j$ distributed in same way, regularly or randomly, in three-dimensional space; the array of sites we call the 'lattice'. We then assume we have entities occupying these sites. They may be spins or electrons or perhaps other particles, but let us call them spins here for brevity. If a spin occupies sites $_j$, it has energy E_j which (and this is vital) is a stochastic variable distributed over a band of energies completely randomly, with a probability distribution *P(E)dE* which can be characterized by a width W. Finally, we assume that between the sites we have an interaction matrix element $V_{jk}(r_{jk})$, which tranfers the spins from one site to the next. V_{jk} may or may not itself be a stochastic variable with a probability distribution." [7]. Anderson adds: "We also obtain a fairly good estimate of the critical density at which the theorem fails. An additional criterion is that the forces be of sufficiently short range — actually, falling off as $r \to \infty$ faster than $1/r^3$- and we derive a rough estimate of the rate of transport in the $V \propto 1/r^3$ case. Our basic technique is to place a single 'spin' on site n at initial time $t = 0$, and to study the behaviour of the wave function thereafter as a function of time. Our fundamental theorem may be restated as: if $V(r_{jk})$ falls off at large distances faster than $1/r^3$, and if the average value of V is less than a certain critical V_c of the order of magnitude of W; then there is actually no transport at all, in the sense that even as $t \to \infty$ the amplitude of the wave function around site n falls off rapidly with distance, the amplitude on site n itself remaining finite. One can understand this as being caused by the failure of the energies of neighboring sites to match sufficiently well for V_{jk} to cause real transport. Instead, it causes virtual transitions which spread the state, initially localized at site n, over a large region of the lattice, without destroying its localized character. More distant sites are not important because the probability of finding one

with the right energy increases much more slowly with distance than the interaction decreases. This theorem leaves two regions of failure (and therefore transport) to be investigated, namely, $V \propto 1/r^3$, as in spin diffusion by dipolar interactions, and $V \sim W$, or the high-concentration limit. In both cases, the methods used to prove the fundamental 'nontrasport' theorem will probably allow us to outline an approach to the transport problem. In the $1/r^3$ case, we show that transport may be much slower than the estimates of Reference [2] would predict. In the case $V \sim W$, we show that transport finally occurs not by single real jumps from one site to another but by the multiplicity of very long paths involving multiple virtual jumps from site to site" [7].

The novelty highlighted by Anderson is that the *localized states* do not contribute any more to the charge transport, so they have a significant influence on the electrical properties of materials, indeed in such circumstances a conductor can become an insulator.

With his mathematical formalism, perfectly reasonable, detailed and elegant, Anderson provides a valid explanation for this peculiar phenomenon. However, what do not appear clear to us are the physical modalities with which this phenomenon is fulfilled; namely the intimate real mechanism, through which, suddenly, in a conductor has ceased the propagation of the electric current, ie the Ψ diffusion of the electrons vanishes.

It seems that the core of the phenomenon is in the changes occurring to de Broglie *associated waves*, related to the electrons. In fact, in our opinion, the most important thing pointed out by Anderson is that as the *disorder* in a conductor increases, the *electron waves* turn from *delocalized* in *localized*: i.e., they stop spreading through the crystalline solid, which therefore from conductor becomes insulator. In short, what remains to be investigated is this: what is the physical mode through which the wave function (Ψ) of the electron is *localized*, and then stops spreading. The energy of these electrons has been fully described by Schrodinger, as shown in Equation (2). As it is well known the quantum-mechanical formalism developed by Schrodinger describes a QO during its linear evolution phase, or Unitary Phase (*U Phase*). During this phase "the QO is *delocalized* and behaves almost as a wave. During this evolution phase of the QO, probably the quantum superimpositions are distributed, spread, throughout the available space" [5].

This is what happens when the crystalline solid behaves as a conductor. This physical condition of the QO lasts until it is disturbed, observed, that is until it interacts, when the *electron waves* meet the obstacles, the *impurities*. It is just what seems to happen when the electron beats against the *impurities* reported by Anderson. What happens exactly? On close reflection, as first pointed out by Anderson, the conductor becomes insulator when the *electronic wave* (Ψ), which was traveling *delocalized* along the crystalline solid, hitting the *impurities is localized*. This is the crux of *Anderson Localization*. But what happens to the wave function (Ψ) of the electrons when they collide with these obstacles? Anderson talks of 'quantum jumps'. In fact, as we learn from Quantum Mechanics, what happens is that the observation, the measurement (M) modifies the physical system (in the microscopic world) we are examining [12, 13]: not only does it deviate immediately the trajectory of the observed QO but, what is even more interesting, very likely it generates also a deep change in its physical states. The M, in fact, induces the *transformation* of the QO, that is the transformation of its quantum state, known as *quantum jump*, represented by the quantum-mechanic formalism by:

$$\langle \Psi | \phi \rangle |^2, \tag{5}$$

which describes the *probability* that the WF of a QO *jumps* in one of the *possible selfstates*, indicated by $|\phi\rangle$, which represents one out of two or more *orthogonal* alternative possibilities: the other can be $|q\rangle$, $|X\rangle$, etc., which depend on the kind of observation, the kind of M carried out. What happens is that with the M *quantum states collapse*, that is *quantum superimpositions* which characterize the WF of the QO observed. The M generates the WF *collapse* (WFC) of the examined QO [14, 15].

We think that this happens both with the M and the *Anderson Localization*. As Penrose reminds us "before the M the QO is potentially detectable in one of the points of its *wave volume*, each point corresponding to a *probability amplitude*. The *square of the modulus* of the, $|\psi|^2$, has to be interpreted as the *density of probability* to find the particle, its *quantum state*, in one of the several possible positions. It is more likely to find the particle where its WF is maximum in absolute value; so the probability to find the particle in the space is 1, that is $\|\psi\| = 1$ (100% of probabilities), where:

$$\|\psi\| = \int_E^3 |\psi(x)|^2 dx^1 \wedge dx^2 \wedge dx^3, \tag{6}$$

that is the integral of $|\psi|^2$ on all the space gives the total probability to find the particle in a place

of the tridimensional physical space, with coordinates x^1, x^2, x^3. During this evolution phase of the QO, probably the quantum superimpositions are distributed, *spread*, throughout the available space. Whereas with the M we have the collapse of the superimpositions of the different quantum states characterizing the QO: they may converge in a circumscribed, *localised*, space. Thus, the M of the position of a QO generates the so called *reduction* of quantum superimpositions which characterize it, also known as *Amplitude Reduction*, or *Reduction of the state vector* (***R*** *Process)*" [16].

3. CONCLUSIONS

Therefore, the *R process* is closely related to the WFC of QO, process in which the *associated wave* (Ψ) of the QO considered is *intercepted and localizes*: that is, becomes detectable in a small space. We believe that the same also occurs when the *electron waves* hit the *impurities* reported by Anderson. The only difference is that in the case of M there is the real intention to observe the phenomenon, as in the *experiment of the two holes* where we want to see which hole the QO goes through. On the contrary, in the crystalline solid the electron waves collide spontaneously against *impurities* and *localize* without the interference of any observer: a *decoherence process* occurs. However, the 2 physical systems represented seem to be entirely superimposable: an undisturbed QO, not measured, is *delocalized* and detectable in potentially one of the points of the *wave volume*. Thus the QO *lives* its linear evolution phase (*U phase*). Similarly, the *electron waves* traveling freely in a regular crystalline solid are *delocalized*, and they are also detectable in one of the points of their *wave volume*. It can be assumed, therefore, that even in these circumstances, the Ψ of the electron traveling in a conductor *lives* its *U Phase*.

Moreover, similarly to what occurs during the M process of a QO, with the immediate WFC of the QO and induction of the *R process*, — in its turn associated to the *localization* of the relative WF (Ψ) — likewise when in a conductor the electronic wave (Ψ) hits the *impurities* its collapse takes place, ie a spontaneous WFC, resulting in the *localization* of the quantum particle in a small area of space.

We therefore conclude that the intimate physical mechanism by which the *Anderson Transition* phenomenon takes place in reality could be a consequence of the *R Process* which undergoes an *electronic wave* within a crystalline solid. A *R Process* in its turn related to a spontaneous WFC of the QO considered, a *self-WFC* induced by the impact of the electrons against the *impurities* present in the conductor.

REFERENCES

1. Puccini, A., "A mechanical effect induced by electromagnetic radiation may explain the wave function collapse of a quantum object," *PIERS Proceedings*, 726–728, Marrakesh, Morocco, Mar. 20–23, 2011.
2. Puccini, A., "About the zero mass of photon," *Progress In Electromagnetics Research*, Vol. 55, 117–146, 2005.
3. De Broglie, L., *Comptes Rendus*, Vol. 177, 507–510, 1923.
4. De Broglie, L., "Recerches sur la theorie des quanta," Thesis, Université Paris IV-Sorbonne, Paris, 1924.
5. Puccini, A., "Quantum mechanics suggests that photons with different energy do not travel at the same speed," *PIERS Proceedings*, 729–733, Marrakesh, Morocco, Mar. 20–23, 2011.
6. Maiani, L., "Fisica oltre le particelle," *Il Sole 24 Ore*, No. 157, 41, 2008.
7. Anderson, P. W., *Phys. Rev.*, Vol. 109, No. 5, 1492–1505, 1958.
8. Inguscio, M., "Fisica condensata," *Il Sole 24 Ore*, No. 166, 38, 2008.
9. Farchionni, R., Seminar held at the Department of Physics, University of Pavia-Italy, Dec. 1, 1992.
10. Bloch, F., *Phys. Rev.*, Vol. 70, 460–473, 1946.
11. Schrodinger, E., *Phys. Rev.*, Vol. 28, No. 6, 1049–1070, 1926.
12. Puccini, A., "About the zero point energy, zero point mass, zero point temperature and zero point motion in the subatomic world and photonics," *PIERS Proceedings*, 1169–1171, Suzhou, China, Sep. 12–16, 2011.
13. Puccini, A., "The "Missing Mass" in the universe may be represented by the dynamic-mass of the photons," *PIERS Proceedings*, 816–818, Cambridge, USA, Jul. 5–8, 2010.
14. Puccini, A., "The momentum of photon may explain the measurement's paradox in the sub-atomic world," *PIERS Proceedings*, 27–30, Suzhou, China, Sep. 12–16, 2011.

15. Puccini, A., "About the interference induced by electrons why does the electron behave like a wave," *Progress In Electromagnetics Research*, Vol. 58, 199–222, 2006.
16. Penrose, R., *The Road to Reality*, 517–518, 2004 Roger Penrose; 2005 RCS Libri, Milano.

The Momentum of Luminous Photon Can Explain the Mystery of the Scission of the Water Molecule, Fundamental Event in the Clorophyllose Photosynthesis

Antonio Puccini
Department of Neurophysiology, Order of Malta, Naples, Italy

Abstract— The complex phenomenon of clorophyllose photosynthesis (CP) has been largely clarified in detail, covering both the Light or Photochemistry Phase (Light Reaction), and the Dark or Chemistry (Dark Reaction) Phase. As it is known, Light Reaction, which works only in the presence of light, occurs within the chloroplast where chlorophyllose Photo Systems, using a system of electronic transport which uses *conjugated double bindings* present in the chlorophyll porphyrin ring, allow the storage of the captured sunlight. It is also the light to make the breakdown of individual water molecules contained in the chloroplasts occur. What happens is that the chlorophyll behaves as a pump which removes electrons from a *provider* (the molecule of water), after the latter has been severed from the sunlight: Water photolysis (WP).

Yet, to date, the performance of the WP has not yet been clarified. In a rather simplistic and non-specific way, it is argued that it is the energy of light to induce the WP, but without going into details, without specifying the physical manners with which the phenomenon is performed. According to our calculations, the *momentum (p)* of common sunlight striking chloroplasts and water molecules contained therein is equal to $1.325 \cdot 10^{-22}$ [g·cm/s]. It is a truly remarkable impact strength, 100.000 times higher than the restmass of the electrons involved in the 2 *covalent bindings* between the oxygen atom and the 2 hydrogen atoms the water molecule is made of. Therefore, we think it is this push effect induced by luminous Ps to cause the WP, as well as being transmitted in full to the hit electrons, giving them a high kinetic energy, such as to make them take the porphyrin ring of chlorophylls, with its consequences (activation of the CP).

1. INTRODUCTION

Photosynthesis is a complex physiochemical phenomenon which presumably dates back to about 3 and a half billion years ago with cyanobacteria, which began to free (as waste) oxygen molecular (O_2) in the atmosphere. In the span of 2 billion years, the O_2 increased progressively, so it was possible and convenient for the cells to *breath*, namely the use of O_2, since it yielded 18 times as much energy. It was so delineated the gradual move from the prekariotic cell to the eukaryotic one or, from anaerobic to aerobic cells. So for about a billion and a half years the mechanism of clorophillose photosynthesis (CP) has been carried out mainly by algae, and even more, by plants. Due to space we will not describe the mechanism of CP in its deepest details. As it is known, the CP consists of transforming the energy (E) of the sunlight in chemical E. There are 2 stages: LUMINOUS STAGE or PHOTOCHEMISTRY (light reaction) and DARK PHASE or CHEMISTRY (Dark Reaction). While the photochemistry phase works only in the presence of light, the chemistry phase can work both in the dark and in the light. In the Luminous Phase there is a production of chemical E from luminous E, whereas in the Dark Reaction there is a production of glucose at the expense of the chemical E previously accumulated. These reactions take place in cellular organelles, chloroplasts, localized in the cytoplasm of cells of the green parts of plants, where they can get to the concentration of 500000 per mm^2.

As it is well known in the chloroplasts there is a system of tylacoidales membranes containing photosynthetic pigments, where it is possible to distinguish primarily the molecules of chlorophyll *a* and chlorophyll *b*, arranged to form respectively the Photo System I and II. The fundamental nature of such pigments is their absorption spectrum, which generally includes the wavelengths (λ) between 400 and 700 nanometers (nm), with absorption peaks at the extremes of the visible spectrum and low levels in the central areas. Thus, with the Light Reaction chlorophylls *b* and other accessory pigments, or *antenna pigments*, collect a portion of the luminous E, convert it into electronic excitation which migrates for *inductive resonance* (so an excited molecule transfers its E to a contiguous molecule, which in turn is energized, and so on...) until it reaches the chlorophyll *a*, since this is the only one which is able to pass to an excited state activating CP. Indeed, there are special molecules of chlorophyll *a* called *trap molecules*, since the E collected by the Photo System II remains trapped in them. This happens because these *trap molecules* are characterized

by energy levels lower than other molecules of chlorophyll, so they can only receive the excitation transmitted by other molecules of the photosynthesis unit, but they cannot forward it. This is the *reaction center* where chemical reactions are activated, including the splitting of water molecules by the solar radiation: *hydrolysis*, or *photolysis* of water (WP). Each individual molecule of water is divided by the sunlight into its components, so the oxygen is released into the atmosphere, whereas hydrogen is used to form a reductant molecule: nicotinamide adenosine diphosphate (NADPH). The flow of excited electrons passes through two transport chains from Photo System II to Photo System I, providing E for the production of adenosine triphosphate (ATP). In the Dark Reaction the carbon of the CO_2 is reduced to glucose in a cycle of reactions (Calvin cycle) in which are also involved the NADPH and the ATP coming from the Light Reaction.

2. DISCUSSION

It is known that the chlorophyll molecules are made up of the polycyclic ring of porphyrins, from which branches off a long hydrocarbon chain. When the chlorophyll is struck and activated by light the following reaction triggers:

$$\mathrm{H_2O + NADP + ADP + P} + hf \rightarrow \mathrm{NADPH + ATP} + 1/2\mathrm{O_2} + \mathrm{H^+} + 2\mathrm{e^-}, \tag{1}$$

where the light (in this case expressed by its energy value: hf) causes the splitting of the water molecule into its components, including the ionization of the 2 hydrogen atoms (H), each of them splitting into a proton (H^+) and an electron (e^-), which transform the electron acceptor NADP into $NADPH^-$, as well as inducing the phosphorylation of the ADP to ATP. Under normal conditions, i.e., without the effect of light, the electrons would not be able to leave the water molecules, since the reaction is energetically unfavorable. The energy stored in the bonds of ATP and NADPH is used to construct organic molecules according to the Calvin cycle, events that take place during the Dark Reaction. Therefore, during the first Light Reaction the chlorophyll, excited by Ps, behaves as a pump removing electrons from a *dator* (the water contained in the chloroplasts) to transfer them to an *acceptor*: in this way the flow of electrons stores E in the ADP-ATP systems and accumulates reducing potential in the NADP-NADPH systems. Besides, it is important to consider that a fundamental stage of CP, which occurs during the Dark Reaction, uses carbon dioxide (which the plant absorbs from the atmosphere), water (sucked from the ground) and light (radiated by the sun) and leads to the synthesis of a molecule of glucose:

$$6\mathrm{CO_2} + 12\mathrm{H_2O} + hf \rightarrow \mathrm{C_6H_{12}O_6} + 6\mathrm{O_2} + 6\mathrm{H_2O}, \tag{2}$$

where hf expresses the E of a photon (P), which along with Planck formula [1]:

$$\mathrm{E} = hf \tag{3}$$

is represented by the product of the frequency (f) of the P for Planck's constant (h), which corresponds to $6.625 \cdot 10^{-27}$ [erg·s]. It is important to underline that in Equation (2) the oxygen released during the CP comes from the splitting of water molecules and it is not the one contained in the molecules of carbon dioxide. Therefore, in order to have the chemical reaction shown in Equation (2), it is necessary that first the WP takes place. It occurs in the following ways:

$$2\mathrm{H_2O} + hf \rightarrow \mathrm{O_2} + 4\mathrm{H^+} + 4\mathrm{e^-}. \tag{4}$$

As we know, in a single water molecule the 2 H atoms and the oxygen atom (O) are held together by a *covalent bond*, that is sharing 2 pairs of electrons. In each of these pairs an electron (e^-) is made available by H and the other by O. From the geometrical point of view the water molecule is a tetrahedron slightly distorted, where the 2 H are on 2 of the 4 vertices of the tetrahedron and form an angle of 105° (the O is the vertex). On the other 2 vertices of the tetrahedron clouds of negative electrical charge are formed caused, obviously, by the electrons. Since O attracts strongly the electrons of 2 H, these electrons tend to keep close to O. It follows that the water molecule is polar, with one pole + and a pole −. However, the 2 charges are perfectly balanced, so that the water molecule is electrically neutral. The peculiar geometric shape of the water molecule favors the creation of *bridge hydrogen bonds* with adjacent water molecules, and due to the tetrahedral shape each water molecule gives rise to *4 H bonds*. It is important to remember that such *H-bridge bonds* are relatively weak, in contrast to the *covalent bond*. Since the O has 6 electrons in the outer orbit, the 2 lacking electrons for its stability, are taken from the 2 H, creating with each of them

a *covalent bond*, characterized precisely by sharing 2 electrons between O and H , which leads to the establishment of a common outer orbital. Therefore, the bond that allows the formation of a water molecule is not created by the action of the electric force between ions of opposite charge (as occurs in *ionic bonds*), but only through the *sharing of electrons*: it is this double pair of electrons in common to keep together the water molecule.

Thus, when we examine the *water photolysis* carried out with the CP, we need to take into consideration the cleavage of these 2 types of chemical bonds: 1) *The H-bridge bond* which links together more water molecules; 2) the *covalent bond* that stabilizes the single molecule of water, considered in the liquid state. As previously mentioned it is not difficult to demolish the *H bridges*, since these bonds are quite weak. In the second case, however, it is necessary a bigger E to break the *covalent bond* between the single atom of O bound to the 2 electrons of the H atoms. To this regard, it has been always maintained that it is the E of the sunlight to determine the WP during the CP. This phenomenon is also illustrated, from the chemical point of view, in Equation (4). Yet we know that the ways in which this phenomenon is expressed by the physical point of view, have not yet been fully clarified. What is the intimate mechanism, real, with which single Ps cause the splitting of water molecules? It has not yet been revealed in details how the WP phenomenon is carried out. As Einstein reminds us each P, besides a its own E, shown in Equation (3), has a its own *momentum* too [2]. As it is known this *momentum* (p) is not a specific characteristic of the Ps, but it belongs to any particle, also material, as shown by the formula of de Broglie [3]:

$$\lambda = h/p \rightarrow p = h/\lambda. \tag{5}$$

As Weinberg [4] reminds us the mean wave lenght (λ) of the solar light corresponds to $5 \cdot 10^{-5}$ [cm] so using Equation (5), we calculate the p of these Ps:

$$p = 6.625 \cdot 10^{-27}\,[\mathrm{erg} \cdot \mathrm{s}]/5 \cdot 10^{-5}\,[\mathrm{cm}]. \tag{6}$$

Since the energetic value of erg is expressed in [g·cm/s^2·cm], that is in [g·cm^2/s^2], we have:

$$p = 6.625 \cdot 10^{-27}\,[\mathrm{g} \cdot \mathrm{cm}^2/\mathrm{s}]/5 \cdot 10^{-5}\,[\mathrm{cm}] = 1.325 \cdot 10^{-22}\,[\mathrm{g} \cdot \mathrm{cm}/\mathrm{s}]. \tag{7}$$

This is the impact force of each P of the mean solar light. It is a remarkable force especially if we consider that it is 100000 times greater than the restmass of an electron ($9.1 \cdot 10^{-28}$ [g]) [5–8]. So, this is the crucial point: it is not a mere energetic action induced by the solar light to break the *H-bridge bonds* (which keep together the contiguous water molecules), and induce the photolysis of water in the course of CP. It is rather an effective mechanical action that solar Ps carry out through their *momenta*, with a really remarkable impact force, which manages easily to break the *H-bridge bonds* between the water molecules, so that the latter are released . It is useful to point out that the power of impact with which the light hits the water contained in the chloroplasts (namely in the *reaction centers*) is so considerable as to be able to break the *covalent bonds* which allow the formation of each individual water molecule. In this way, with the *water photolysis*, the light frees a pair of electrons from each water molecule which has been divided. As Fermi reminds us, when a P hits another particle transmits to it almost its entire p [9] What happens is that electrons liberated from *covalent bonds* are able to acquire a significant Kynetic E [10, 11]. In our opinion, it is this significant *push effect*, induced by the p if incident Ps [12, 13], to allow the struck electrons to quickly cross the steps along the porphyrin ring and make all the electrons in the chain get affected by a similar *impact force*. As we know like many other organic molecules of biological interest, especially those involved in the capture of light radiations in the visible spectrum, in the porphyrin ring too and in its side chain it is possible to find sequences of carbon atoms linked alternately with single bond and double bond. Just these *conjugated double bonds* represent the main common characteristic among the photosynthetic pigments and allow an easier transfer of electrons of the *double bonds.* The longer the side chain of the porphyrin ring, rich in these *conjugated double bonds* the closer the absorbed radiations get to the red color. On the contrary, a chain of single bonds only absorbs ultraviolet radiation.

We can read by Feynman that a structure very similar to porphyrin is represented by the tridimensional morphological composition of the rhodopsin (visual purple), i.e., the photosensitive retinal pigment which permits the vision mechanism in the animal kingdom. Just as chlorophylls are contained in the parallel lamellae present in the chloroplasts, rhodopsin is contained in a number of parallel plane layer arranged in the rod cells present in the retina of the living. "The rhodopsin,

which is the pigment, is a big protein which contains a special group called *retinene*, and which is, undoubteldy, the main cause of the absorption of light. We do not understand the reason for the places, but it is very likely that there is some reason for holding all the rhodopsin molecules parallel. The chemistry of the thing has been worked out to a large extent, but there might be some physics to it. It may be that all of the molecules are arranged in some kind of a row so that when one is excited an electron, which is generated, say, may run all the way down to some place at the end to get the signal out, or something. This subject is very important, and has not been worked out. It is a field in which both biochemistry and solid state physics, or something like it, will ultimately be used. This kind of a structure, with layers, appears in other circumstances where light is important, for example in the chloroplast in plants, where the light causes photosynthesis. If we magnify those, we find the same thing with almost the same kind of layers, but there we have chlorophyll, of course, instead of retinene. It has a series of *alternate double bonds* along the side chain, which is characteristic of nearly all strongly absorbing organic substances, like chlorophyll, blood, and so on. The reason why such a series of *double bonds* absorbs light very strongly is also known. We may just give a hint: The alternating series of double bonds is called a *conjugated double bond*; a *double bond* means that there is an extra electron there, and this extra electron is easily shifted to the right or left. When light strikes this molecule, the electron of each *double bond* is shifted over by one step. All the electrons in the whole chain shift, like a string of dominoes falling over, and though each moves only a little distance (we would expect that, in a single atom, we could move the electron only a little distance), the net effect is the same as though the one at the end was moved over to the other end! It is the same as though one electron went the whole distance back and forth, and so, in this manner, we get a much stronger absorption under the influence of the electric field, than if we could only move the electron a distance which is associated with one atom. So, since it is easy to move the electron back and forth, *retinene* absorbs light very strongly; that is the machinary of the physical-chemical end of it" [14].

3. CONCLUSIONS

Similarly to the vision mechanism, in the case of CP, we think it is the considerable impact force with which the solar Ps affect the water and chlorophylls, so the p of incident Ps can be transmitted to the electrons involved, which in their turn are poured with a significant kinetic E in the porphyrin circuit (rich in *conjugated double bonds*), sufficient to activate all the subsequent stages, just as occurs with *retinene*. So we have that the sunlight (which physical effect is represented mainly by the mechanical action performed through the p of its Ps) is captured by electrons of the porphyrin ring, which pass from their fundamental energetic levels to an excited state, for by the significant *push effect* undergone by luminous incident Ps, are accelerated sufficiently to contribute to the CP. This transport of electrons in the Light Reaction can be represented by the reaction of oxidation-reduction represented by Equation (1). As already mentioned, in normal conditions an electron could not leave the water to reduce the $NADP^+$, since the reaction is energetically unfavorable. Therefore, this electron transfer occurs using specifically and exclusively the E and the impact force transmitted to these electrons from the p of the Ps absorbed by the Photo System II. We reiterate, therefore, that rather than a non-specific energetic action carried out by the light, it appears most appropriate to consider that to trigger the mechanism of the CP, activating the transport of electrons in the porphyrin circuit, is a consequence of the mechanical effect mediated by the p of the solar Ps. Furthermore, as previously described and discussed, this same mechanical action performed by the remarkable mechanical impact force of the common sunlight, is also expressed on the water molecules contained in the chloroplasts, breaking their bonds. Thus, it is possible to explain the physical contents that could help dispel the fog that still surrounds the mechanism of WP in CP: it is the mechanical action exerted by the p of the incident solar Ps (which, as it can be inferred from our calculations shown in Equation (7) is comparable to the *push effect* of 100 proton masses) to determine the breaking of the *H-bridge bonds* between contiguous water molecules and, even more important, to induce the breaking of *covalent bonds* within individual water molecules, inducing their cleavage.

REFERENCES

1. Planck, M., *Annalen der Physik*, Vol. 4, 553–563, 1901.
2. Einstein, A., *Annalen der Physik*, Vol. 17, 132–148, 1905.
3. De Broglie, L., *Comptes Rendus*, Vol. 177, 507–510, 1923.

4. Weinberg, S., *The First Three Minutes. A Modern View of the Origin of the Universe*, Vol. 75, 1977 by Steven Weinberg, Mondadori ed., Milano, 2001.
5. Puccini, A., "The equivalent rest-mass of photon," *PIERS Proceedings*, 723–725, Marrakesh, Morocco, Mar. 20–23, 2011.
6. Puccini, A., "About the zero point energy, zero point mass, zero point temperature and zero point motion in the subatomic world and photonics," *PIERS Proceedings*, 1169–1171, Suzhou, China, Sep. 12–16, 2011.
7. Puccini, A., "Light weighs," *Progress In Electromagnetics Research B*, Vol. 8, 161–177, 2008.
8. Puccini, A., "About the specific heat of black holes," *PIERS Proceedings*, 981–983, Cambridge, USA, Jul. 5–8, 2010.
9. Fermi, E., *Atomi, Nuclei, Particelle*, Boringhieri ed. (To), Vol. 24, 2009.
10. Puccini, A., "About the zero mass of photon," *Progress In Electromagnetics Research*, Vol. 55, 117–146, 2005.
11. Puccini, A., "A mechanical effect induced by electromagnetic radiation may explain the wave function collapse of a quantum object," *PIERS Proceedings*, 726–728, Marrakesh, Morocco, Mar. 20–23, 2011.
12. Puccini, A., "The "Missing Mass" in the universe may be represented by the dynamic-mass of the photons," *PIERS Proceedings*, 816–818, Cambridge, USA, Jul. 5–8, 2010.
13. Puccini, A., "The momentum of photon may explain the measurement's paradox in the sub-atomic world," *PIERS Proceedings*, 27–30, Suzhou, China, Sep. 12–16, 2011.
14. Feynman, R. P., *The Feynman Lectures on Physics*, Vol. 1, 1965; 1989 California Institute of Technology; Zanichelli ed. (Bologna), Vol. I, 36–8, 9, 10, 2001.

Multiparametric Data Collection and Data Processing of Animal Tissues in MRI Images

P. Marcon[1], **K. Bartusek**[2], **and M. Cap**[1]

[1]Department of Theoretical and Experimental Electrical Engineering,
Brno University of Technology, Kolejni 2906/4, Brno 612 00, Czech Republic
[2]Institute of Scientific Instruments, Academy of Sciences of the Czech Republic,
Kralovopolska 147, Brno 612 64, Czech Republic

Abstract— The introduction for MRI revolutionized bone marrow imaging because this technique provides images with excellent soft tissue contrast. To determine the properties of bone and bone marrow and their pathology, we have to know the properties of surrounding tissues. It is also important for the segmentation of individual tissues. The size and shape of tissues can often help to diagnose various pathologies. In this paper, we focused on multiparametric data collection of animals' tissues. As the source images was these weighted images chosen: PD, T_1, T_2, and SWI tissue parameters in terms of a multivariate. As a measured sample chicken wing was used. Several parameters (maximal value, minimal value, mean value and standard deviation) were evaluated in this sample in displayed tissues: skin, fat, muscle, bone and bone marrow. The obtained data could be used with advantage for multi-parametric analysis and for image segmentation.

1. INTRODUCTION

The research of pathology of bone and bone marrow is currently very interesting. The introduction for MRI revolutionized bone marrow imaging because this technique provides images with excellent soft tissue contrast. In adults the bone marrow is in general composed of fatty tissue, which appears hyper intense on T_1 and T_2 weighted images and occurs hypointense on MR-sequences with fat-saturation [1, 2]. In case of trauma, tumor or infection infiltration, replacement and depletion of fatty bone marrow takes place resulting in intermediate to hypointense signals on T_1-weighted images and hyperintense signals on STIR (short-tau inversion recovery) and T_2 weighted images with fat-saturation. These changes obscure the distinct appearance of fatty bone marrow and serve as early indicators of pathology, which makes this imaging technique a very sensitive diagnostic tool [3].

To determine the properties of bone and bone marrow and their pathology, we have to know the properties of surrounding tissues. It is also important for the segmentation of individual tissues. The size and shape of tissues can often help to diagnose various pathologies. The quality o any image segmentation, however, is limited by the quality of the obtained images from MR tomography system. In magnetic resonance imaging (MRI), tissue contrast is based mostly on the T_1 and T_2 (T_2^*) relaxation times, proton spin density (PD) and susceptibility weighted imaging (SWI) and diffusion [4, 5]. Classification of tissues can be improved by optimizing the imaging protocol based on the underlying statistics of these parameters.

In this paper, we focused on multiparametric data collection of animals' tissues. As the source images was these weighted images chosen: PD, T_1, T_2 and SWI tissue parameters in terms of a multivariate. As a measured sample chicken wing was used. Several parameters (maximal value, minimal value, mean value and standard deviation) were evaluated in this sample in displayed tissues: skin, fat, muscle, bone and bone marrow. The obtained data could be used with advantage for multi-parametric analysis and for image segmentation.

2. METHODS OF MRI MEASUREMENT

All clinical diagnostic images must demonstrate contrast between normal anatomical features and any pathology. If there is no contrast difference, it is impossible to detect abnormalities within the body. One of the main advantages of MRI compared with other imaging modalities is the excellent soft tissue discrimination in resulting image [6].

The basic method for measurement theses parameters is the conventional spin echo (see Figure 1). This pulse sequence uses a 90° excitation pulse followed by one or more 180° rephasing pulses to generate a spin echo on time called T_E. If only one echo is generated, a T_1 weighted image can be obtained using a short echo time T_E and short repetition time between individual

spin echo sequences — T_R. For proton density and T_2 weighting a two RF rephrasing pulses generating two spin echoes are applied. The first echo has a short T_E and a long T_R to achieve proton density weighting, and the second has a long T_E and a long T_R to achieve T_2 weighting. For more information about sequences and coding see studies reported in [4] and [6].

For SWI images we used one of the MR measurement methods — the Gradient echo (GE), see Figure 2. This method is very sensitive to inhomogeneities of the static magnetic field and this can be useful for susceptibility measurement [12]. Because the reaction field is generated proportionally to material susceptibility, it is possible to use the GE method for its measurement [13]. The GE sequence depicted in Figure 2 with the parameters: echo time $T_E = 17\,\mathrm{ms}$, repetition time $T_R = 5\,\mathrm{s}$, was used to obtain an MR image of the reaction field in the vicinity of the measured sample.

The MR image obtained using the GE technique is phase-modulated by the magnetic induction change and, on condition of proper experiment arrangement we can obtain the image of magnetic field distribution in the specimen vicinity described in [5]. Evaluation of various tissues such as skin, fat, muscle, bone and bone marrow can help us to diagnose various pathologies. The images were evaluated maximum values, minimum values, mean and standard deviation. Collected parameters we can continue to serve for multiparametric analysis and segmentation of tissues.

3. METHODS OF MRI MEASUREMENT

Experiment was accomplished on a MR tomograph at the Institute of Scientific Instruments, Academy of Sciences of the Czech Republic (ISI ASCR). The MR tomograph dispose of static field flux density $B_0 = 4.7\,\mathrm{T}$, $1\,\mathrm{H}$ nuclei resonance frequency is $200\,\mathrm{MHz}$. Method was tested on the chicken wing, especially bone: ulna and radius. Similar multiparametric data collection could be used also for human tissue.

On the Figure 3 you can see proton density weighted image. For the measurement was used SE

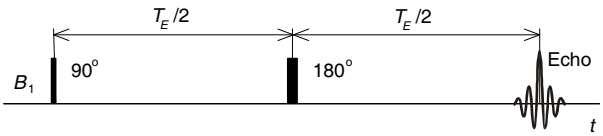

Figure 1: Diagram of the spin echo measurement sequence.

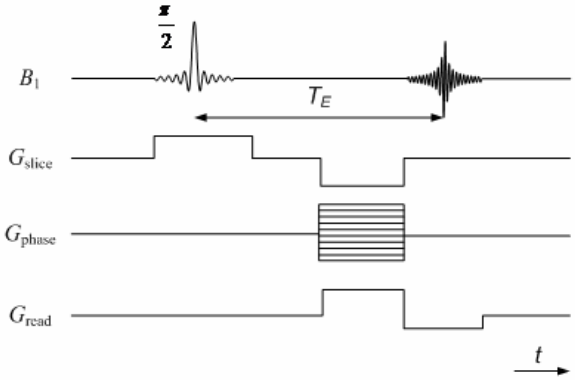

Figure 2: Diagram of the gradient echo measurement sequence.

Figure 3: PD weighted image of chicken wing and ROI.

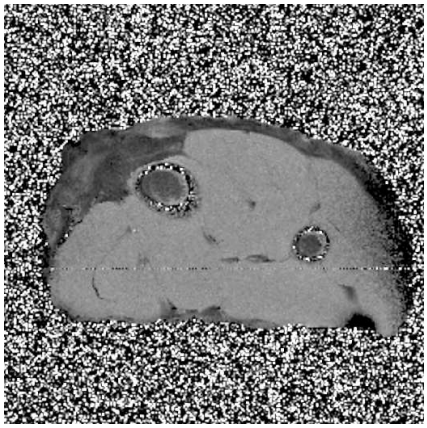

Figure 4: T_1 weighted image of chicken wing.

Table 1: Parameters of the tissues in PD weighted image (SE, $T_E = 16\,\text{ms}$, $T_R = 1\,\text{s}$).

N.	Tissue	Min	Max	Mean	s.d.
1	Skin	51653	153448	102479	28057
2	Fat	42071	161661	112615	22149
3	Muscle	47566	84594	66039	7599
4	Bone	4584	36015	16020	7419
5	Bone marrow	35541	115868	82564	14103

Table 2: Parameters of the tissues in PD weighted image (SE, $T_E = 16\,\text{ms}$, $T_R = 1\,\text{s}$, $T_I = 16 \div 2500\,\text{ms}$).

N.	Tissue	Min [ms]	Max [ms]	Mean [ms]	s.d. [ms]
1	Skin	293	436	353	32
2	Fat	231	471	301	36
3	Muscle	466	843	650	55
4	Bone	0	1297	453	327
5	Bone marrow	252	523	344	48

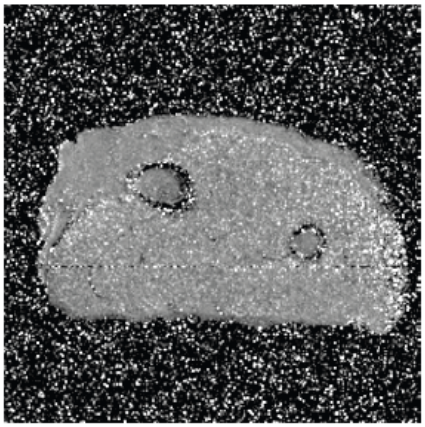

Figure 5: T_2 weighted image of chicken wing.

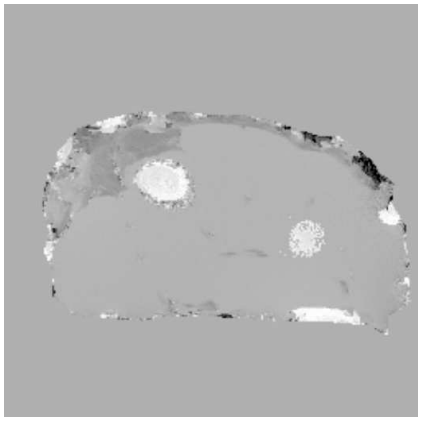

Figure 6: SWI weighted image of chicken wing.

Table 3: Parameters of the tissues in T_2 weighted image (SE, $T_E = 15$, 16, 17 ms and $T_R = 1\,\text{s}$).

N.	Tissue	Min [ms]	Max [ms]	Mean [ms]	s.d. [ms]
1	Skin	32	61	47	8
2	Fat	28	92	47	9
3	Muscle	21	208	50	19
4	Bone	0	331	27	62
5	Bone marrow	15	104	40	11

sequence with these parameters: $T_E = 16\,\text{ms}$, $T_R = 1\,\text{ms}$ and resolution of the image: $128 \times 128\,\text{px}$ and size of the image: $30 \times 30\,\text{mm}$. In this image are shown the areas from which the parameters of tissues were evaluated (Region of interest — ROI). The evaluated parameters are shown in Table 1.

On the Figure 4 you can see T_1 weighted image. For the measurement was used Inversion recovery SE sequence with these parameters: $T_E = 16\,\text{ms}$, $T_R = 1\,\text{ms}$ and time between 180° RF pulse — inversion $T_I = (16,\ 50,\ 200,\ 500,\ 1000,\ \text{and}\ 2500)\,\text{ms}$. The resolution of the image: $128 \times 128\,\text{px}$ and size of the image: $30 \times 30\,\text{mm}$. The evaluated parameters of T_1 weighted image are shown in Table 2.

On the Figure 5 you can see T_2 weighted image. This image is calculated from three images which are measured by SE sequence with these parameters: $T_E = (15,\ 16,\ 17)\,\text{ms}$ and $T_R = 1\,\text{s}$. The resolution of the images: $128 \times 128\,\text{px}$ and the size of the images: $30 \times 30\,\text{mm}$. The evaluated

Table 4: Parameters of the tissues in SWI weighted image (GE, $T_E = 6\,\text{ms}$).

N.	Tissue	Min [$\times 10^{-6}$]	Max [$\times 10^{-6}$]	Mean [$\times 10^{-6}$]	s.d. [$\times 10^{-6}$]
1	Skin	−15.1	−4.09	−9.67	2.96
2	Fat	−11.6	1.37	6.65	2.59
3	Muscle	0.19	4.08	2.05	0.54
4	Bone	16.5	51.26	32.98	5.17
5	Bone marrow	−21.0	28.52	1.83	12.5

parameters of T_2 weighted image are shown in Table 3.

On the Figure 6 you can see SWI weighted image. For the measurement was used GE sequence (see Figure 2) with these parameters: $T_E = 6\,\text{ms}$ and 7 ms. The resolution of the image: $256 \times 256\,\text{px}$ and size of the image: $30 \times 30\,\text{mm}$. The evaluated parameters of SWI weighted image are calculated and shown in Table 4.

4. CONCLUSIONS

The aim of this work was to measure several parameters inside and close to the small bones and to determine acquisition sequence with the best contrast for a specific tissue imaging. To measure three types of MR data spin-echo method was used.

Proton density weighted images shows good contrast and very good signal to noise ratio in all examined tissues. These images are easily measurable and feasible for consequent image processing. This kind of weighting appears to be the best for image segmentation. T_2^* weighted images show worst contrast and small signal to noise ratio. Image segmentation and tissue differentiation will be difficult in this type of image.

We also examined the data achieved by measurement of gradient echo and calculated SWI weighted image. The signal processing is more difficult in this case, but the information obtained about bone marrow is very interesting. In area, where is the edge of the bone the phase jump is measured. This phase jump is feasible especially in image segmentation.

Future work will be focused on analyzing of the multi-parametric data of the tissues, which were mentioned in this paper. Now we know intensity of healthy tissues inside and outside of the small bones. Measured images were segmented with an aim to distinguish healthy and pathological tissue. The values in tables are very important for selection of segmentation methods such as thresholding, edge analysis by Sobel mask, watershed and very interesting method based on region-based level set approach or active contour [7, 8]. The segmentation can play an important role in determining pathology in animal tissues even in human tissues.

ACKNOWLEDGMENT

This work was supported within GACR 102/11/0318 and GA102/12/1104 and GA FEKT-S-11-5/1012.

REFERENCES

1. Moulopoulos, L. A., et al., "MR prediction of benign and malignant vertebral compression fractures," *Journal of Magnetic Resonance Imaging*, Vol. 6, 668–674, 1996.
2. Johnson, G., D. H. Miller, D. MacManus, P. S. Tofts, D. Barnes, E. Boulay, and W. McDonald, "Primary title: STIR sequences in NMR imaging of the optic nerve," *Neuroradiology*, Vol. 29, 238–245, Springer, Berlin, Heidelberg, 2004.
3. Rupp, R. E., N. A. Ebraheim, and R. J. Coombs, "Magnetic resonance imaging differentiation of compression spine fractures or vertebral lesions caused by osteoporosis or tumore," *Spine*, Vol. 20, 2499–2503, 1995.
4. Vladingerbroek, M. T. and J. A. Den Boer, *Magnetic Resonance Imaging*, Springer-Verlag, Heidelberg, Germany, 1999, ISBN 3-540-64877-1.
5. Marcon, P., K. Bartusek, M. Burdkova, and Z. Dokoupil, "Magnetic susceptibility measurement using 2D magnetic resonance imaging," *Measurement Science and Technology*, Vol. 22, 2001.
6. Prince, J. L., Q. Tan, and D. Pham, "Optimization of MR pulse sequences for Bayesian image segmentation," *Medical Physics*, 1995.

7. Mikulka, J., "ImageJ Plugins for microscopic image processing," *34th International Conference on Telecommunications and Signal Processing*, 541–543, 2011.
8. Batrusek, K., E. Gescheidtova, and J. Mikulka, "Data processing in studying biological tissues, using MR imaging techniques," *33 th International Conference on Telecommunications and Signal Processing. Budapest: Asszisztenda Szervezo*, 171–175, 2010.

The Method of Correction the B_1 Errors in Magnetization Transfer Ratio MTR

M. Alkhaddour and R. Kubasek
Department of Theoretical and Experimental Electrical Engineering
Brno University of Technology, Kolejni 4, Brno 612 00, Czech Republic

Abstract— The meaning of MRI is based on the concept of the magnetic sum vectors, M_z and M_{xy}, which related with resonant frequency RF, where the physics idea in MRI is influenced by the external magnetic field B_0 on the nuclear magnetic moment vector of proton in hydrogen, but the radio-frequency RF field B_1 errors is based on magnetization transfer ratio MTR measurements, and radio frequency RF no uniformity, so it is important to correct the B_1 errors in magnetization transfer ratio measurements, so this paper will discuss about the methods of correction at large volumetric radio frequency RF field, and this correction based on the double-angle method DAM.

Two factors are related with B_1 field mapping techniques, the first one is double angle method DAM, and the other one is the fast spin-echo FSE, where the value of magnetization transfer ratio depends on the amplitude of the magnetization transfer MT pulse [1].

The aim from this paper to explain the B_1 errors in the MTR and the method of correction of the errors, by using B_1 field mapping, to obtain a minimum histogram dispersion of MTR, where the RF causes MTR histograms to be wide, thus the non-uniformity of B_1 causes changes in the intensity of across MR images [2].

1. INTRODUCTION

Protons in the tissue has a benefit in the magnetic resonance imageing MRI, where protons in tissue can be founded in two pools, where the free water pools (A) has a high ability of spins, and the other pool is semi-solid pool (B) are move less, MRI technique can not watch the immobile pool, because the immobile spins happen at very short T_2 relaxation times (10–15 µs), MRI methods depends on the relaxation behavior of tissue to obtain contrast using magnetization transfer MT imaging methods. The exchange of magentization between the two pools via dipolar interactions and diffusion is magnetization transfer [3].

2. METHOD

The relation between MTR and B_1 is nonlinear, the difference between tissue types causes the discrepancy between MTR and B_1. Flip angle α is defined between magnetization vectors before and after excitation by RF impulse, where the extension of flip angle depends on the energy. Where the gene amplitude-modulated RF impulse is given as:

$$\alpha = \gamma \int_0^{t_{RF}} B_1 \, dt, \tag{1}$$

where γ is the gyromagnetic ratio of the nuclei, and the case of RF impulse with rectangular envelope we can the flipangle express by simple expression:

$$\alpha = \gamma B_1 t_{RF,} \tag{2}$$

In MR tomography the flip angle $\alpha = 90°$ is preferable, where the value of transversal component of magnetization M_{xy} is maximum, and the size of xy part of flip angle after end of excitation is given by:

$$M_{xy} = M_0 \sin \alpha, \tag{3}$$

The most widelyused measure of the amount of MT is the MT ratio MTR which is given by the following equation:

$$MTR = 100 \left[\frac{M_0 - M_s}{M_0} \right], \tag{4}$$

where radio frequency RF is applied to the immobile pool slightly off resonance for the free pool, where the MT ratio is between MT saturation Ms and without saturation M_0. The MR images

are used by dimension 60×60 mm (256×256 pixels) was measured by the spin echo SE method with the different flip angles. The flip angle vary from $\beta = 135°$ to $\beta = 300$, where the transmitter power has variations from 6 dB to -9 dB. The images were normalized to the images maximum amplitude, corresponding to 90 exciting impulse. The MT effect is produced by immobile protons. The amplitudes of the normalized images were converted into the RF magnetic field induction B_1 by use of the following equation:

$$B_1 = B_1, 90 \arcsin\left(\frac{M}{M_0}\right) \tag{5}$$

The errors in the amplitude of RF pulse directly propagate to errors in the measured MTR. The maps of field B_1 are shown in Fig. 1, where they obtained for RF power attenuation -6 dB, where k is maximal and the noise is minimal. The Fig. 1 shows the $B_{\max} = 13$ mT and $B_{\min} = 5$ mT for orthogonal to axis in the middle of the FR coil. The influence of the eddy current induced in the conducting specimens where the MR image deformation was examined, that means that the flip angle at the ideal configuration rise up to 150°. The MR images have 60×60 mm in dimension (256×256 pixels) by the spin echo (SE) method with 66° flip angles. The specimens is from Au-Pt-Ag alloy, were used for dental implants. Where $\rho = 5.37\,\mathrm{sm/m^2}$, $\chi = -24.1^{-6}$.

The effects the collection of a B_1 map is important to correct B_1 errors, where these errors are the most important things, where the type of tissue are related with MTR, and the B_1 errors related with dielectric resonance which arise the RF field inside an object. Where the fraction of immobile spins has a little value, but the MTR will be reduce, the fraction of fixed spins in the tissue is given as following $f = M_0^B/(M_0^A + M_0^B)$, and the errors of the measured MTR depend on the errors in RF. The FSE sequence is done twice, with the excitation stage of the sequence altered to reduce acquisition. The FSE sequence is done twice, with the excitation stage of the sequence altered to reduce acquisition time. Where the flip angle FA for the first pulse in the sequence is altered from 90 to $a = 60$ at the first acquisition, at the second acquisition, the flip angle is altered to $2a = 120$ to reduce the acquisition time [3].

Non-uniform B_1 transmission B_{1+} produces varying flip angle, causing intensity, MTR histogram is influenced by RF causing the histogram to be broadened, the strength of B_1 field related to magnetization transfer ratio histogram analysis when the data has a large volume of interest are included.

The double angle methods DAM, with fast spin-echo FSE readout, are used in B_1 field mapping technique to quantify B_1 errors and correct MTR maps and histograms. Where the double angle method can be used to measure the field of B_1 by calculating a flip-angle map. Two images are acquired I_1 with prescribed tip angle I_1 and I_2 with prescribed tip angle $\alpha_2 = 2\alpha_1$. All other signal-affecting sequence parameters are constant [1].

To calculated the effective FA distribution by abtain the ratio of the signal intrnsities by using the first and the second acquisitions. To image all tissue type a sequence is sufficient for complete longitudinal relaxation of TR. The effective FA can be calculated using the simple realation. Where the ratio of signals then depends only on the FA of the second acquisitions the transverse magnetization after the first pulse depends on sin α, where $I_2\ /I_1 = \sin(2a)/\sin(a) = 2\cos(a)$, where I_1

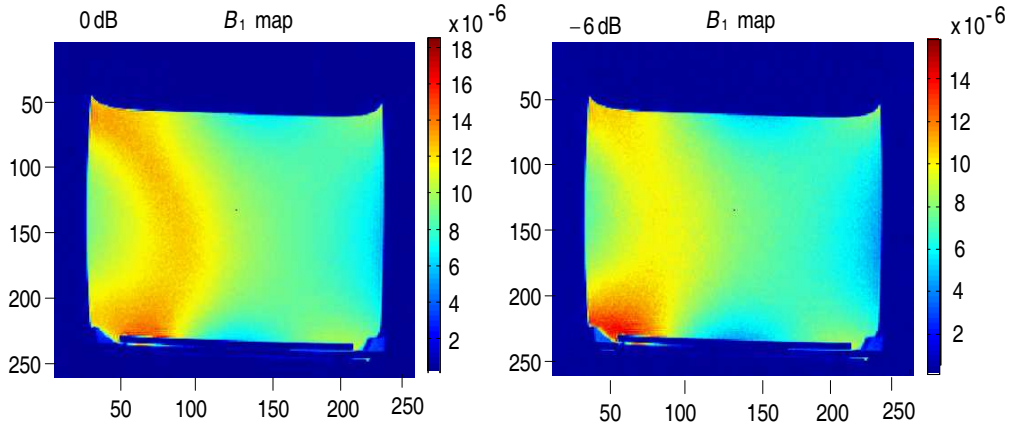

Figure 1: Maps of field B_1.

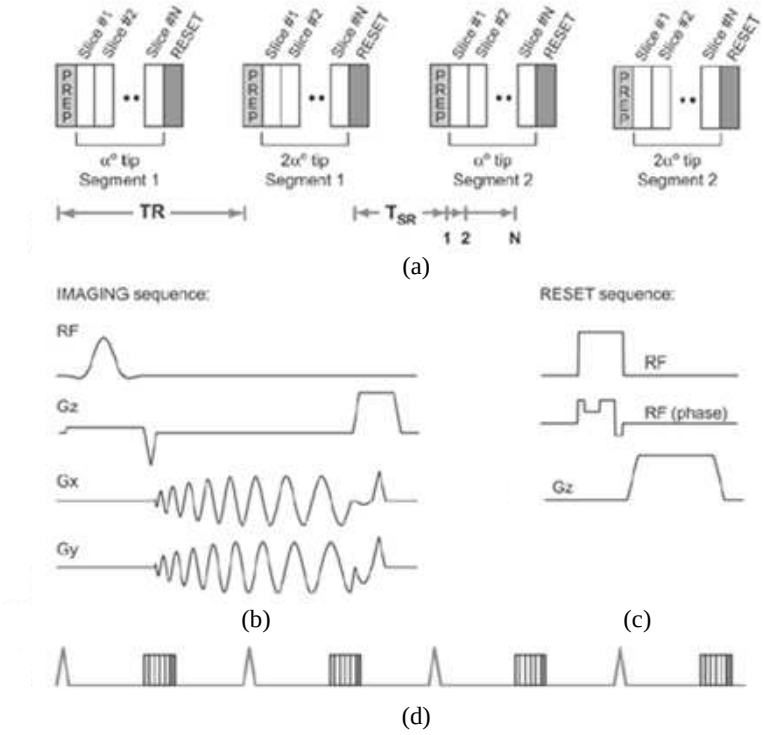

Figure 2: Spiral distribution of B_{1+} mapping pluse sequence.

and I_2 are the signal intensities from the first and the second acquisitions, respectively.

$$\alpha = \cos^{-1}(I_1/2I_2) \tag{6}$$

A now method is used for magnitude mapping of highly rapid B_{1+}, the homogeneity of the active B_1 field (B_{1+}), when the surface coils are applied at RF transmission, where the field is high than 3 T for in-vivo magnetic resonance imaging MRI. To measure the coverage with high spatial resolution in a few seconds a new method from the double angle method with a B_1 insensitive magnetization-reset sequence, where the repetition time (TR) is independent of T_1.

At tow flip at two flip angles a flip angle can be mapped to compute the inverse cosine, in using map of flip angle with modest supposition of the action of the excitation pulse, it is possible to measured the spatial distribution of B_{1+}, where different flip angles a short TR sequence is often used.

Slices and imaging sequence of a simple slice-selective excitation Fig. 2 shows the spiral distribution for B_{1+} mapping pulse sequence, the acquisition of multiple and reset sequence consists of a B_1 insensitive and non-spatially selective saturation pulse followed by a dephaser [1].

Flip angles prescribed are 60 and 120 degrees, the imaging sequence has a tip pulse, readout, and gradient spoiler, while the reset sequence has a composite 90-degree pulse (which is insensitive to both B_1 variations and off-resonance) and a gradient spoiler and short echo time [4]. A linear transmit/receive extremity coil was used to produce a B_{1+} map in the leg of a normal volunteer, both with the new method and the reference double-angle method with a long TR (3 s).

3. CONCLUSIONS

The aim of this paper was to report a modifying method of DAM. This method has the purpose of accelerating 3D imaging speed. The B_1-induced errors in magnetization transfer ratio measurements were presented by means of B_1 field mapping. We also mentioned the principles which are related to B_1 errors, which are MTR measures and RF nonuniformity.

ACKNOWLEDGMENT

This work was supported by/within the project of the Grant Agency of the Czech Republic No. 102/09/0314 and project from Education for Competitiveness Operative Programme CZ.1.07.2. 3.00.20.0175 (Electro-researcher).

REFERENCES

1. Charles, H. C., J. M. Pauly, and K. S. Nayak, "Saturated double-angle method for rapid B_1 mapping," *Magnetic Resonance in Medicine*, Vol. 55, 1326–1333, 2006.
2. Wang, D., S. Zuehlsdorff, and A. C. Larson, "Rapid 3D radiofrequency field mapping using catalyzed double-angle method," *NMR Biomed.*, Vol. 22, 882–890, 2009.
3. Samson, R. S., C. A. M. Wheeler-Kingshott, M. R. Symms, D. J. Tozer, and P. S. Tofts, "A simple correction for B_1 field errors in magnetization transfer ratio measurements," *Magnetic Resonance Imaging*, Vol. 24, 255–263, 2006.
4. Bartusek, K. and E. Gescheidtova, "Measurement of radio frequency magnetic field," *PIERS Online*, Vol. 2, No. 6, 555–558, 2006.

Influence of Material Properties on the Quality of NMR Images

R. Kubásek and M. Alkhaddour
Department of Theoretical and Experimental Electrical Engineering
Brno University of Technology, Kolejni 2906/4, Brno 612 00, Czech Republic

Abstract— The paper describe method for basic and RF field inhomogeneity estimation in NMR based on T_2 and T_2^* measurement. The method combine gradient and spin echo acquisitions techniques to differentiate relaxation T_2 and T_2^*. Computed inhomogeneity of basic and RF field can be done in desired area of interest or can be done in imagine approach pixel by pixel. The exponential approximation of relaxation process has to be solved.

1. INTRODUCTION

The physical phenomenon in which the magnetic field of the nuclei of some atoms of the substance under examination reacts mutually with a rotating magnetic field is called NMR (Nuclear Magnetic Resonance). NMR spectroscopy and tomography require the basic magnetic field B_0 to be generated with a high homogeneity [1]. The homogeneity of basic magnetic field can be distorted by measured object. It is not necessary to be magnetic, just different susceptibility can lead to distortion in images. Figure 1 shows the same specimen filed with water and with bubble at top. The boundary between water ($\chi = -9.5 \times 10^{-6}$) and air ($\chi = 4 \times 10^{-7}$) leads to B_0 distortion. Figure 1(a) shows image obtained by SE (Spin Echo). Figure 1(b) shows image obtained by GE (Gradient Echo). Measurement techniques with SE compensate B_0 inhomogeneity and then the distortion in image is much less then in image obtained by GE. Properties of relaxation measurement techniques using SE and GE methods can be used to inhomogeneity estimation.

High homogeneity of RF field in the working space of MR tomograph depends on construction of a probe and on its adjustment. The mapping of RF magnetic field is commonly based on an MR image measurement of the homogenous testing specimen with optimally determined flip angle for obtaining the maximum contrast in the measured map of RF magnetic filed [2] and [3]. The local B_1 field strength in each examination can be obtained using repeated acquisitions with different RF-impulse amplitudes ('transmit gain', 'flip angle') [4]. The inhomogeneity can be corrected by the use of a map of the spatial distribution of the B_1 field acquired either through computer simulation, or through the measurement of the field. There are two major advantages in actually measuring the B_1 distribution; it makes the registration of the map against MR images easier and, also, a measured B_1 field compensates for imperfections in the coil design. The relaxation measurement using SE and GE is firstly used for B_0 inhomogeneity estimation. Next chapter shows approach of B_1 estimation from relaxations via magnetization transfer ratio.

2. INHOMOGENEITY ESTIMATION FROM RELAXATIONS

The GE and SE method in NMR measurement techniques are well know [4]. We ca measure relaxation process after excitation by changing echo time, see Figure 2(a). Number of measurements performed depends on requirements and time possibility. Own measurement can be perform on

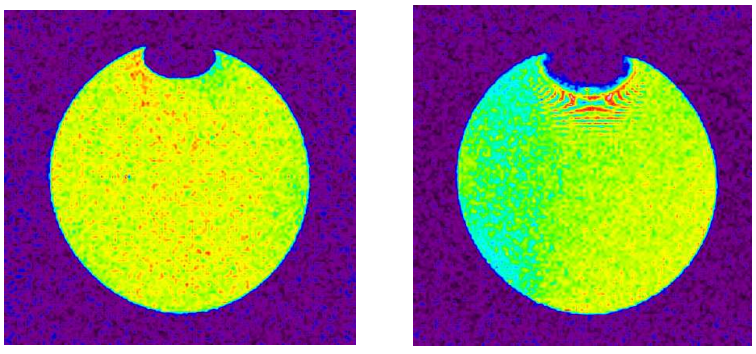

(a) (b)

Figure 1: (a) SE, (b) GE image of sphere vessel filed with water.

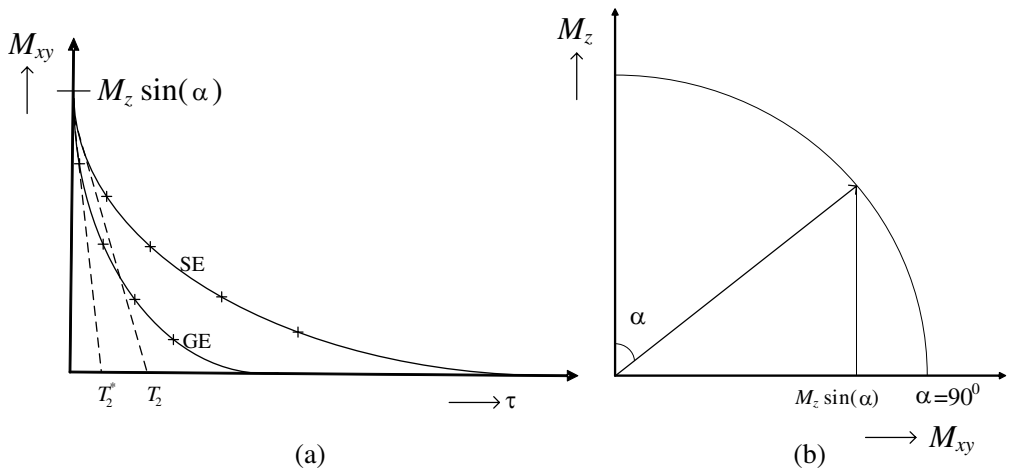

Figure 2: (a) Relaxation process after excitation, (b) flip angle representation.

whole specimen by hard excitation pulse, on selectively chosen layer or area of specimen, and on pixel/voxel in imaging sequence use.

The measured data is necessary to approximate by exponential function. Both constants of exponential course are needed, magnetization after excitation M_{xy} and time constant T_2 or T_2^*. At least three measured magnitude of FID (Free Induction Decay) signal at different echo time τ are necessary for approximation. The echo times τ should be chosen wisely. First echo time at minimal value as possible regarding to tomograph technical parameters. Last one at approximately three times of relaxation T_2. Other echo times distribute linearly between these two points. If we measure whole image, we need make approximation in every pixel/voxel. For images with high resolution is important computational complexity of approximation algorithm. For example genetic algorithm is not suitable one.

Basic field inhomogeneity B_0 has influence on relaxation process. The different frequency oscillation given by different flux density in space deformed in value of B_0 can be seen as dephasing of magnetization. Dephasing leads to faster drop of FID signal and to shorter relaxation T_2^*. The SE method compensate inhomogeneity B_0, therefore we measure true relaxation T_2. We just need to exclude influence of diffusion and movements by chosen of suitable specimen. Basic field inhomogeneity B_0 is given by:

$$\begin{aligned} \frac{1}{T_2^*} &= \frac{1}{T_2} + \frac{1}{T_2'} = \frac{1}{T_2} + \gamma \Delta B_0, \\ \Delta B_0 &= \frac{\frac{1}{T_2^*} - \frac{1}{T_2}}{\gamma}, \end{aligned} \tag{1}$$

where γ is gyromagnetic ratio of H_2. Value ΔB_0 is overall and in some way average value of B_0 inhomogeneity. It is not easy to determine exact value of B_0, like in B_0 inhomogeneity estimation from spectral width of FID signal.

Magnitude of NMR signal immediately after excitation is proportional to basic filed strength represented by M_{xy} and flip angle α by:

$$Mxy = Mz \cdot \sin(\alpha). \tag{2}$$

The flip angle is linear function of B_1 field strength and length of excitation pulse t_e:

$$\alpha = \gamma B_1 t_e. \tag{3}$$

The map of B_1 inhomogeneity can be represented by map of flip angle α. The task is to find M_{xy} in time $\tau = 0$. The M_{xy} ratio is theoretically the same for both GE and SE method. We can use average of GE and SE M_{xy} weighted by exponential approximation quality.

3. CONCLUSION

Estimation of B_0 and B_1 inhomogeneity from relaxations T_2 and T_2^* and initial magnetization after excitation M_{xy} is useful method. Benefit is fact, that one inhomogeneity do not have influence

to other one. Only limitation is in lost FID signal magnitude below noise level in case of high inhomogeneity.

ACKNOWLEDGMENT

This work was supported by/within the project of the Grant Agency of the Czech Republic No. 102/09/0314 and project from Education for Competitiveness Operative Programme CZ.1.07.2.-3.00.20.0175 (Electro-researcher).

REFERENCES

1. Vlaardingerbroek, M., *Magnetic Resonance Imaging*, Springer-Verlag, 2000.
2. Cunningham, H. C., J. M. Pauly, and K. S. Nayak, "Saturated double-angle method for rapid B_1 mapping," *Magnetic Resonance in Medicine*, Vol. 55, 1326–1333, 2006.
3. Zuehlsdorff, D. W. S. and A. C. Larson, "Rapid 3D radiofrequency field mapping using catalyzed double-angle method," *NMR Biomedicine*, Vol. 22, 882–890, 2009.
4. Bartusek, K., E. Gescheidtova, and R. Kubasek, "Mapping of radiofrequency magnetic field in MR tomography," *International Conference on Fundamentals of Electrotechnics and Circuit Theory*, 135–138, Gliwice, 2006.
5. Haacke, E. M., R. W. Brown, M. R. Thompson, and R. Vankatesan, *Magnetic Resonance Imaging Physical Principles and Sequence Design*, Wiley & Sons, 1999.

The Measured of Air Ions Mobility Spectrum

Z. Roubal and R. Kadlec
Department of Theoretical and Experimental Electrical Engineering
Brno University of Technology, Kolejní 2906/4, Brno 612 00, Czech Republic

Abstract— It was confirmed that the concentration of light air ions has positive influence on the human health. For an objective appraisal of the influence of synthetic sources of negative air ions, the comparison with natural environment is a necessary precondition. The concentration of air ions and their mobility spectrum can be determined by means of the gerdien tube. When measured with the gerdien tube, the spectrum mobility can be calculated from the measured saturation characteristics. The determination of air ions mobility spectrum is strongly dependent on the noise in the measure signal. In this paper, the authors describe methods of decreasing the noise, fluctuation and oscillation in the measured signal. The calculated air ions mobility spectrum does not include any incorrect flicker in its course.

1. INTRODUCTION

In industrial zones, where the environment air is often polluted with dust and smog, the concentration of air ions can be regulated or measured only with difficulty. Any thus impaired area shows an inherent deficiency of negative ions and, conversely, an abundance of positive ions complementing the nano- and microscopic dust particles. Significantly, the described aspects have a markedly negative effect on the overal degree of fatigue and professional performance of a human being [1–3]. The impact of the environment on a human organism has been analyzed in studies [1–3]. In the DTEEE laboratories, the methodology supporting the measurement of air ions concentration and mobility spectrum utilizes an aspiration condenser [3]; this method is dependent upon a suitable approximation of the saturation characteristics.

2. ASPIRATION METHOD

A gerdien tube (GT) is instrumental towards the measurement of air ions concentration assuming that the volume of tested air has not been limited and the ions are continuously generated. In the time domain, it is possible to measure only ions of one polarity by means of a gerdien tube; then, following a certain interval, ions of the other polarity can be measured. Ionized air is sucked into the gerdien tube by a fan. A homogeneous electric field is set between the inner and the outer electrode. If an electric ion shows a negative electric charge and the collecting inner electrode has a positive electric potential, the ion is progressively attracted to the inner electrode. Provided that the ion impinges upon the electrode, it will induce an electric current that is measured by the help of a sensitive electrometric picoampermeter [4]. The velocity of the ions motion in the electric field can be described by mobility k [$\mathrm{m^2 \cdot V^{-1}\ s^{-1}}$].

It is possible to determine boundary mobility k_m for every gerdien tube configuration.

All ions showing an index of mobility greater than k_m will impinge upon the inner electrode; however, only a proportionate part of them will impinge in ions whose mobility is smaller than k_m. Based on the aspiration condenser parameters, the air flow volume rate is defined as

$$M = \left(r_2^2 - r_1^2\right) \cdot \pi \cdot v_x, \tag{1}$$

where M, r_2, r_1, v_x ... are the air flow volume rate, the outer electrode radius, the inner electrode radius, and the air flow velocity, respectively.

The main parameter applied for the definition of air ions mobility consists in boundary mobility k_m,

$$k_m = \frac{\varepsilon_0 \cdot \varepsilon_r \cdot M}{C_{AK} \cdot U_{AK}}, \tag{2}$$

where ε_0, ε_r, C_{AK}, U_{AK} ... are the vacuum permittivity, the relative permittivity, the GT capacity, and the GT polarization voltage, respectively. Then, for current I measured by the electrometric picoampermeter, we can define

$$I_{k<k_m} = \frac{k}{k_m} \cdot n \cdot q \cdot M, \quad I_{k \geq k_m} = n \cdot q \cdot M, \tag{3}$$

where n, q ... are the volume concentration of ions and the elementary charge, respectively.

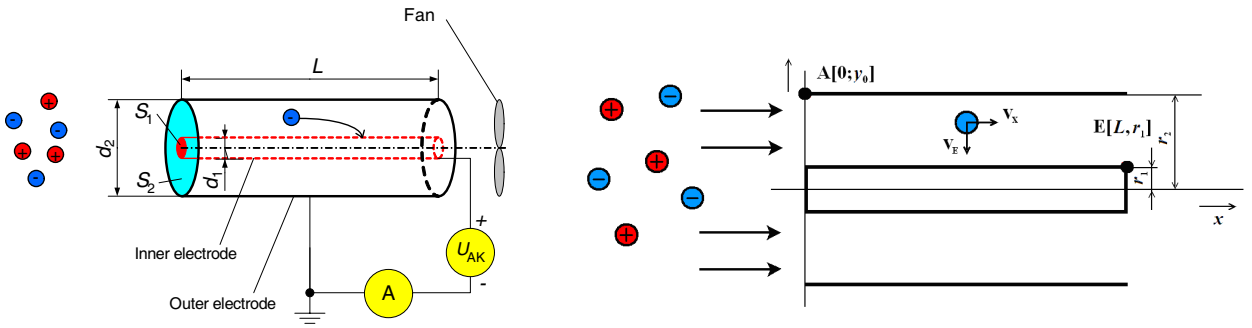

Figure 1: The basic principle of a gerdien tube.

2.1. Concentration of the Volume Density of Ions

The condition of equivalence between an ion charge and an electron elementary charge is satisfied only in light ions, which implies that the condition is not valid in heavy ions that contain several charges of the described type. Then, the relevant situation is referred to as relative number of ions per volume unit. The starting point for the determination of an ion mobility consists in the quantity of charge q and volume concentration of electric charge ρ [3, 4].

$$n_{+-}(k_1, k_2) = \frac{\rho_{+-}(k_1, k_2)}{q}. \tag{4}$$

Now, net electric current in the circuit can be written in the form of

$$I = M \cdot \frac{1}{k_m} \int_0^{k_m} k \cdot \rho(k) \mathrm{d}k + M \cdot \int_{k_m}^{\infty} k \cdot \rho(k) \mathrm{d}k. \tag{5}$$

It is advantageous [4] to express the characteristics of the aspiration condenser by the help of function G. Equation (5) can be modified to the form

$$I = \int_0^{\infty} G(k) \cdot \rho(k) \cdot \mathrm{d}k, \tag{6}$$

for the gerdien tube, function G is given

$$G = \begin{cases} \dfrac{C \cdot U \cdot k}{\varepsilon_0} & k < k_m \\ M & k \geq k_m \end{cases} \tag{7}$$

3. INFLUENCE OF GROUNDING ON THE TIME DEPENDENCE OF AIR ION CONCENTRATION

In the DTEEE laboratories, the concentration of air ions was measured for several variants of the gerdien tube grounding. In the first variant, we did not use any grounding board, and the iontmeter was powered from an isolated source. In Fig. 2, the result of time dependence on the concentration of air ions is shown. The frequency spectrum of air ion concentration obtained by means of the FFT is indicated in Fig. 3. The represented result shows significant parasitic oscillation at the frequency of 0.2 Hz.

In the second variant, the gerdien tube was positioned onto and conductively connected with an aluminium grounding board. The course of time dependence of air ion concentration is in Fig. 4, while Fig. 5 shows the frequency spectrum. The result is significantly better, without any fluctuation and parasitic oscillation.

Another tested variant consisted in an arrangement where only the gerdien tube was grounded; the aluminum board was not applied. The time dependence is indicated in Fig. 6, while the frequency spectrum can be seen in Fig. 7. The results show that the grounding board is necessary only for very accurate calibration measurements. For normal measurements realized in a natural environment it is sufficient to ground only the gerdien tube.

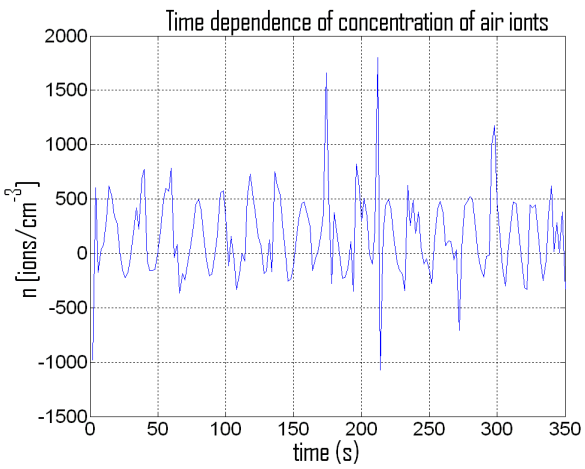

Figure 2: Time dependence of air ion concentration for a non-grounded gerdien tube.

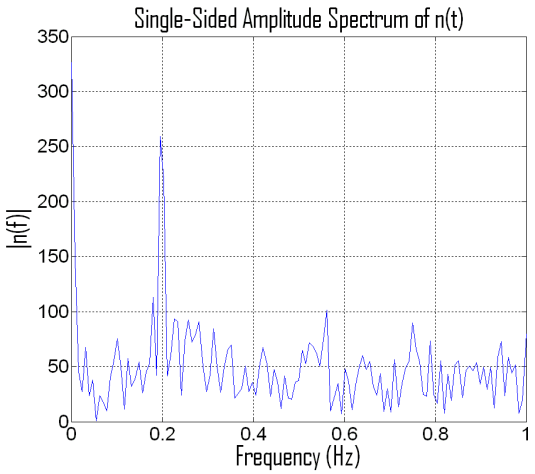

Figure 3: The frequency spectrum of air ion concentration for a non-grounded gerdien tube.

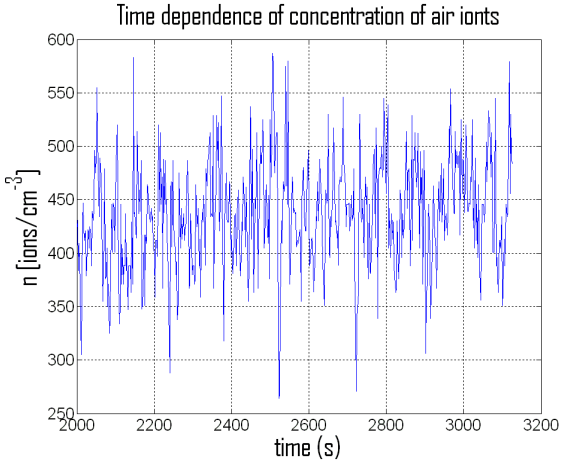

Figure 4: Time dependence of air ion concentration for the grounding aluminum board.

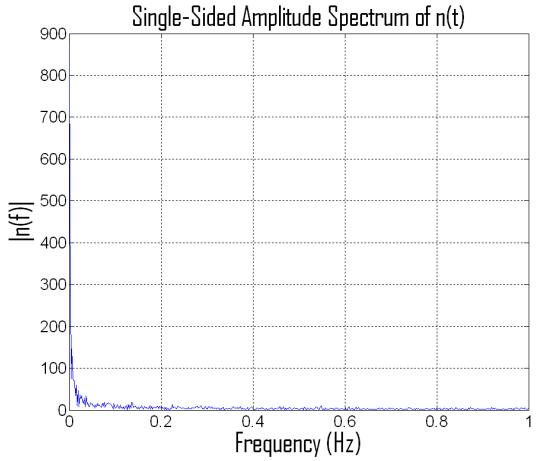

Figure 5: The frequency spectrum of air ions for the grounding aluminum board.

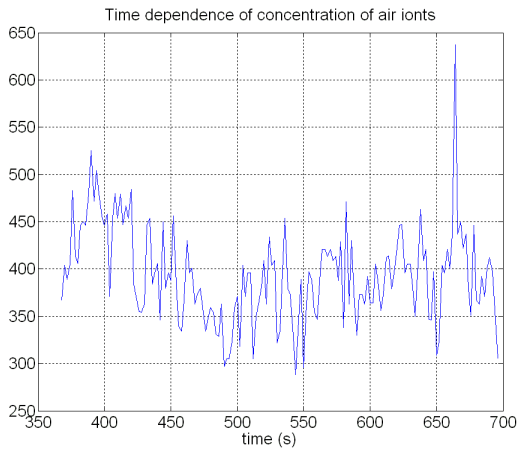

Figure 6: Time dependence of air ion concentration for the grounded gerdien tube.

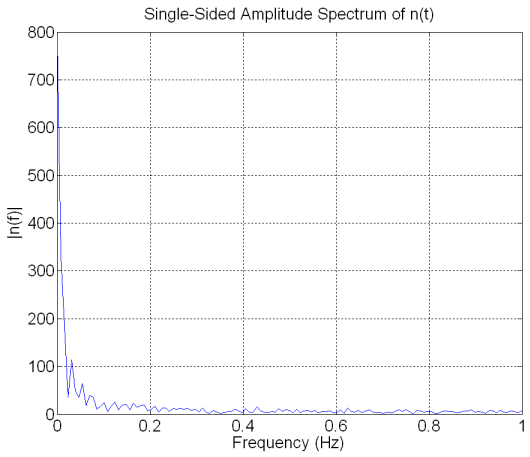

Figure 7: The frequency spectrum of air ions for the grounded gerdien tube.

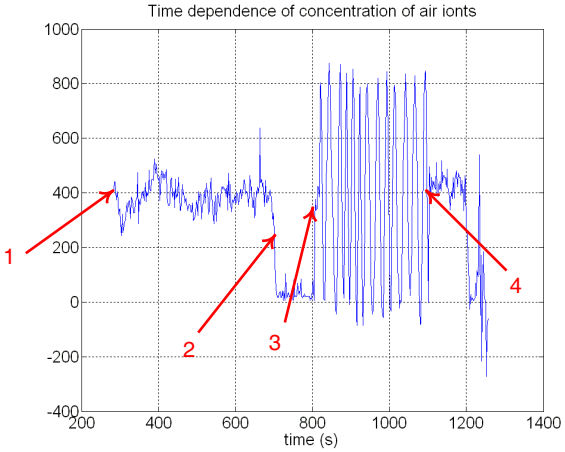

Figure 8: The influence of grounding on the oscillation.

Figure 9: A new configuration of the measurement equipment: gerdien tube provided by the ISI brno

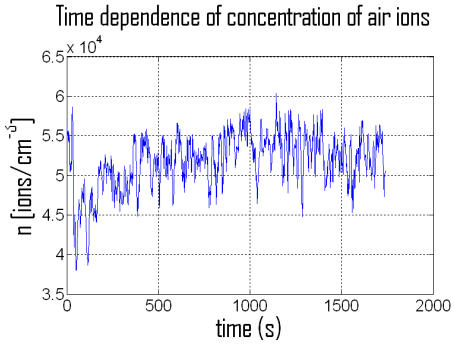

Figure 10: Time dependence of air ion concentration for a fan with the voltage of 12 V.

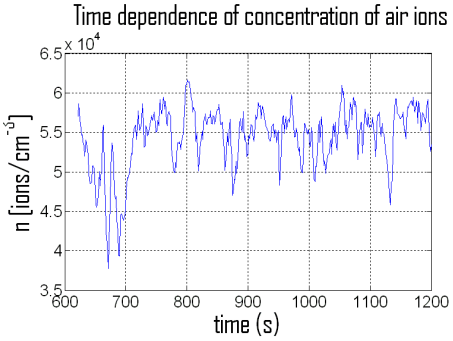

Figure 11: Time dependence of air ions concentration for a fan with the voltage of 15 V.

In order to confirm the influence of grounding on the level of noise and parasitic oscillation within the measured concentration of air ions (Fig. 8), we grounded the gerdien tube (interval 1–2) and disabled the fan. Within intervals 3–4, the fan was turned on again, with the gerdien tube left without grounding. The occurrence of significant oscillation illustrates the necessity of grounding the gerdien tube during measurement. After regrounding (time point 4), the parasitic oscillation stopped.

4. INFLUENCE OF THE AIR FLOW VOLUME RATE ON THE CHARACTER OF THE TIME DEPENDENCE OF AIR ION CONCENTRATION

The gerdien tube of the DTEEE laboratories was optimized to laminar flow and minimal turbulence inside the tube. In the older gerdien tube type provided by the ISI, the influence of changes in the air flow volume rate velocity on the frequency spectrum of air ion concentration was examined. For this purpose, the measuring station of the ISI was modernized to enable a fully automated measurement process similar to that realized with the DTEEE gerdien tube. The new configuration is shown in Fig. 7. In Fig. 8, the time dependence of air ions concentration is measured for a fan with the voltage of 12 V; Fig. 9 indicates the same process for a fan with 15 V of voltage.

5. CONCLUSION

It follows from the measured time dependence that the gerdien tube must be correctly grounded. In the case of a reference measurement, the gerdien tube ought to be positioned onto a metal grounding board. For normal measurement in natural conditions, it is sufficient to ground only the gerdien tube. If the gerdien tube is not duly grounded, the measured signal exhibits oscillation. The frequency of this oscillation is dependent on the gerdien tube dimension; in the gerdien tube

provided by the DTEEE, the frequency was 0.2 Hz. Any additional reduction of noise, fluctuation and oscillation of the measured air ion concentration can be achieved by means of decreasing the air flow volume rate. All the above-mentioned negative factors cause the discontinuity of the saturation characteristic and, thus, make it impossible for us to correctly determine the spectrum of air ion mobility.

ACKNOWLEDGMENT

The work described in the paper was financially supported by the research project GACR 102/09/0314, research plan MSM 0021630513, and project of the BUT Grant Foundation FEKT-S-11-15.

REFERENCES

1. Tammet, H. F., *The Aspiration Method for Determination of Atmospheric-ion Spectra*, IPST, Jerusalem, 1970.
2. Charry, J. M. and R. Kavet, *Air Ions: Physical and Biological Aspects*, Crc Press Inc., Boca Raton, Florida, 1987.
3. Kondrashova, M. N., E. V. Grigigorreko, A. N. Tikhonov, T. V. Sirota, A. V. Temnov, I. G. Stavrovskaya, N. I. Kosyakova, N. V. Lange, and V. P. Tikonov, "The primary physic-ochemical mechanism for the beneficia biological/medical effects of negative air ions," *IEEE Trans. Plasma Scien.*, Vol. 28, No. 1, 230–237, 2000.
4. Roubal, Z. and M. Steinbauer, "Design of electrometric amplifier for aspiration condenser measurement," *PIERS Proceedings*, 1430–1434, Xi'an, China, Mar. 22–26, 2010.

The Study of Cell Growth in Tissue Culture in the Magnetic Field

M. Pokludová and E. Hutová
Department of Theoretical and Experimental Electrical Engineering
Brno University of Technology, Kolejni 4, Brno 61200, Czech Republic

Abstract— Most materials have a property to create their own magnetic field when exposed to an external field. The human body is partly diamagnetic, which means that the effect of the external field can cause the body's own field. Long-term exposure of magnetic fields on blood and nervous system has positive effects, these effects are utilized in the treatment method called magneto therapy. Similar positive effects can be traced in the plant tissue culture. Samples of spruce embryos grown in the plastic Petri's dishes were placed between the permanent magnets (with defined magnetic field gradient) in a dark place with no effect of the external lighting at a constant temperature and humidity. Samples were periodically removed from the magnetic field and moved in isolated box throughout the outdoor environment into the room with NMR tomograph for imaging individual tissue cultures. The aim of this project is to confirm the hypothesis that the samples in a magnetic field of permanent magnets will grow faster than the control samples taken off the effect of magnets while keeping both in a constant temperature and humidity. After the fifteen days the last measurement was carried out and the results of all measurements were evaluated using the programs Marevisi and Matlab. Observed parameters of individual samples were processed into graphs. The graphs can confirm the hypothesis of faster growth in samples of the magnetic field of permanent magnets, although the transfer was not maintained at constant temperature which resulted in fogging of dishes. This had no significant effect on the growth of the samples.

1. INTRODUCTION

The tissue culture, cultivation of the isolated parts of plants grown in an artificial environment, is very useful for the studies of growth because living plant cells retain the functional properties of the tissue from which they were obtained [1]. To determine the internal structure of plant of tissue, samples were scanned using the nuclear magnetic resonance (NMR), which is one of the non-destructive methods that cause no harmful radiation. The great advantage of NMR is the high contrast in the image when displaying soft tissues. Physical principle of nuclear magnetic resonance is based on the fact that protons and neutrons have their specific angular momentum, called spin, which gives the magnetic momentum to the whole atomic nucleus [2].

The basic scanning of method of MR images is the spin echo pulse sequence (SE), which consists of two consecutive RF pulses with the phase 90° and 180°, their duration is in order of several milliseconds. By applying the first pulse the magnetization vector flips to the transverse plan. Due to the T_2^* relaxation occurs the dephasing of nuclei. The application of second pulse, before the total dampening of signal, leads to rephasing nucleus, and the spin echo is detected in the receiving coil [3].

2. EXPERIMENTAL MEASUREMENETS

Samples of tissue cultures of early spruce embryos were prepared at Mendel University in Brno and grown in plastic Petri dishes with the diameter of 50 mm. In each dish there was placed a cluster of plant tissue culture. Dishes with clusters were divided into two groups. The first group (dishes 1–9) was inserted into the scope of permanent magnets with a magnetic field gradient. Properties of magnets are listed in Table 1. The second group (dishes 10–15) was placed outside the scope of permanent magnets, this was the control group. All dishes were placed in a dark place (no influence by the external lighting) while maintaining a constant temperature and humidity. Dishes were periodically withdrawn from the application of magnets and moved in an isolated box through the outside environment into the room with nuclear magnetic resonance tomograph (NMR) to obtain images of clusters. This device is located in the Institute of Scientific Instruments Academy of Sciences of the Czech Republic in Brno. Images from the NMR tomograph were obtained by spin echo method with parameters: $T_E = 16,\ 30$ ms, $T_R = 1$ s. Individual times were chosen to achieve the best image contrast. The size of the resulting images are 128×128 pixels and the size of operating point is 30×30 mm. Individual slices have a width of 2 mm and are spaced 2 mm.

Table 1: The parameters of permanent magnets used in the experiment.

Neodymium magnets			Ferrite magnets		
Dish	**B [T/m]**	**Magnet size [mm]**	**Dish**	**B [T/m]**	**Magnet size [mm]**
1	33.3	50 × 25	**5**	5.1	50 × 50
2	33.1	50 × 25	**6 and 7**	5.2	50 × 50
3	16.6	Diameter 80	**8 and 9**	5.68	50 × 50
4	12.0	Diameter 100	**10 to 15**	-	-

Table 2: The sample evaluation of the first measurement of tissue cultures.

Dish/cut	**3**	**4**	**5**	**6**
1		197	147	21
2		163	173	148
3		102	156	175
4	5	165		
5	189	134		
6	28	125		
7		133	189	57
8		128	121	
9		84	135	
10		75	102	183
11		141	84	
12		132	262	130
13		156	276	211
14		174	191	48
15	149	244	229	

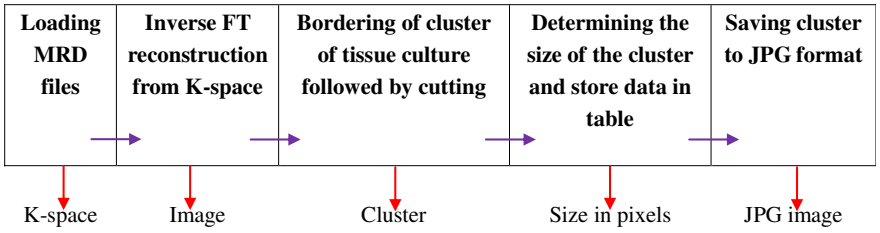

Figure 1: Diagram of evaluation of MR images.

The whole procedure of processing image is shown in block diagram in Figure 1. A more detailed description of the image processing is given in the article [4]. At first the image was loaded in the program Marevisi and converted using the IFT to the final image. Subsequently, individual clusters were bordered and were cut from the surrounding environment. The information about size of cluster in pixels was obtained in the program Marevisi. To obtain the integral of intensity of the image were cut data inserted into the program Matlab [5]. Watched parameters of individual samples were inserted into the table and plotted on graphs. The Table 2 shows the size of the clusters in pixels in the first measurement of tissue culture using NMR methods. The next table (Table 3) shows the total size in pixels with their integrals of intensities of image from all three measurements (which are plotted in Figure 2).

For the assessment of growth of clusters are individual sizes expressed as a percentage and ranked from lowest values to higher (Table 4). From the Table 5 can be seen that the majority of

Table 3: Data from measurements of tissue cultures.

Dish	1st day		8th day		13th day	
	Size [pixel]	Integral [$\times 10^3$]	Size [pixel]	Integral [$\times 10^3$]	Size [pixel]	Integral [$\times 10^3$]
1	365	42.4	1055	107.2	2253	218.9
2	484	55.9	1032	110.5	2381	249.3
3	433	44.1	804	90.6	2029	233.7
4	170	24.1	1011	114.1	2362	231.1
5	323	40.4	1036	109.2	2401	240.5
6	153	19.0	786	90.3	1760	250.1
7	379	41.4	1028	113.9	1908	206.8
8	249	23.1	853	89.3	1866	200.2
9	219	20.9	342	39.6	388	37.8
10	360	44.5	575	61.4	1738	182.4
11	225	29.2	929	100.1	2304	238.7
12	524	56.6	1190	144.8	2357	273.5
13	643	61.3	1238	130.9	2871	300.8
14	413	43.1	1104	120.7	2769	289.2
15	622	69.9	1097	112.4	1542	176.6

Table 4: Cluster sizes sorted by percentage in two.

1st day		8th day	
Dish	Size [%]	Dish	Size [%]
9	15.61644	9	17.71689
10	15.97222	15	24.791
15	17.63666	13	44.65008
3	18.56813	12	44.98092
13	19.2535	3	46.85912
2	21.32231	10	48.27778
12	22.70992	2	49.19421
14	26.73123	7	50.34301
7	27.12401	1	61.72603
1	28.90411	14	67.046
5	32.0743	5	74.33437
8	34.25703	8	74.93976
11	41.28889	11	102.4
6	51.37255	6	115.0327
4	59.47059	4	138.9412

Table 5: Data from measurements of tissue cultures.

Dish	1st day	8th day	13th day
	Integral [%]	Integral [%]	Integral [%]
1	1	1	1
2	1.318	1.03	1.13
3	1.03	0.84	1.06
4	0.56	1.06	1.05
5	0.95	1.01	1.09
6	0.44	0.84	1.14
7	0.97	1.06	0.94
8	0.54	0.83	0.91
9	0.49	0.36	0.17
10	1.04	0.57	0.83
11	0.68	0.93	1.09
12	1.33	1.35	1.24
13	1.44	1.22	1.37
14	1.01	1.12	1.32
15	1.64	1.04	0.80

control clusters occurs in the first part of the table (their size has increased more slowly than other clusters). The fastest growth had cluster in the dish number 4, which grew up in scope neodymium permanent magnet. The second largest increase had the cluster in the dish number 6, this sample has grown in scope of the ferrite magnet. Cluster in the dish number 9 almost did not increase in size, even though it was influenced by scope of permanent magnet. It is possible that when it was transferred through outdoors into the room with NMR tomography, outdoor temperature had some influence. In the Table 5 there are given integrals of intensities of the signals converted to percentages and plotted in the graph shown on Figure 3.

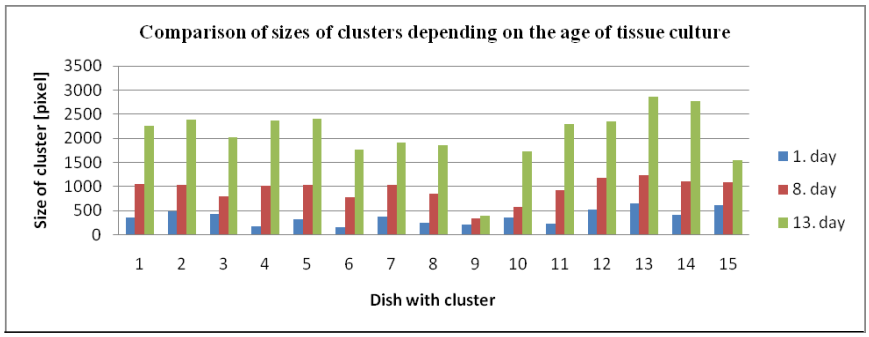

Figure 2: The comparison of the size of growth all tissue cultures from all three measurements.

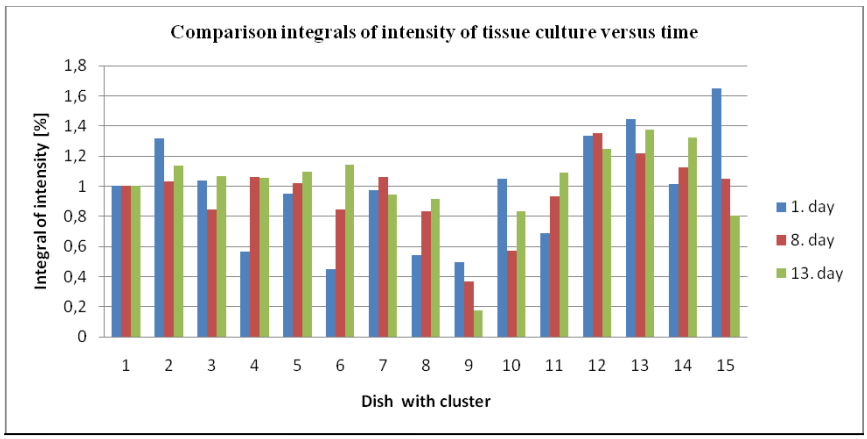

Figure 3: The comparison of the integrals of intensities of tissue samples in all three measurements.

3. CONCLUSIONS

The hypothesis of a faster growth samples in scope the magnetic field of permanent magnets cannot be confirmed, because constant conditions were not observed during the transfer dishes through the outdoor environment into the room with NMR tomograph. This temperature effect was visibly demonstrated on dishes by their internal bedew. Since the dishes were bedewed, we believe that the action of external magnetic field moved their dew point.

ACKNOWLEDGMENT

This work was supported within the framework of the research plan MSM 0021630513 and project GACR 102/11/0318 and project of the BUT Grant Agency FEKT-S-11-5/1012.

REFERENCES

1. Stewart, F. C., M. O. Mapes, and K. Mears, "Growth and organized development of cultured cells. II: Organization in cultures grown from freely suspended cells," *American Journal of Botany*, Vol. 45, No. 10, 705–708, 1958.
2. Liang, P. and P. Lauterbur, *Principles of Magnetic Resonance Imaging,* IEEE Press, New York, 1999.
3. Vlaardingerbroek, M. T. and J. A. Den Boer, *Magnetic Resonance Imaging*, Springer-Verlag, Berlin, 1999, ISBN 3-540-64877-1.
4. Al Khaddour, M. and M. Pokludová, "Vliv magnetického pole na tkáňovou kulturu," *Zborník Workshop of Electrotechnical Research and Practice*, VŠB-TUO, Ostrava, 2012, ISBN 978-80-248-2664-6.
5. Bartušek, K., E. Gesheidtová, R. Křížek, and Z. Dokoupil, "Zpracování dat při studiu růstu raných smrkových embryí zobrazovacími MR technikami," *Elektrorevue*, 2008.

Methodology of Thermal Properties Measurement

J. Hrozek[1], **M. Pokludova**[1], **D. Nespor**[1], **and K. Bartusek**[2]

[1]Deptartment of Theoretical and Experimental Electrical Engineering
Brno University of Technology, Kolejni 2906/4, Brno 612 00, Czech Republic
[2]Institute of Scientific Instruments, Academy of Sciences of the Czech Republic
Kralovopolska 147, Brno 612 64, Czech Republic

Abstract— This paper deals with a methodology of temperature dependencies measurement of thermal properties. Specific heat and thermal conductivity are two thermal properties contained here. Thermal properties of each matter are dependent on their own temperature and are various in whole temperature range. Temperature dependencies of many commercial materials are well known. But temperature dependencies of biological tissues are very bad to find. However knowledge of these parameters is very important for the thermal processes computer simulation. The methodology described here goes out of current methods deficiencies. Thermal conductivity of biological tissues is measured with the needle probe. This method has some deficiencies which are described in this paper. Specific heat is measured with Differential Scanning Calorimetry (DSC). The DSC is conventional method without serious deficiencies. Big disadvantage of current thermal properties measurement is in necessary using of both methods, i.e., two devices are used. Simultaneous measurement of thermal conductivity and specific heat is the main advantage of our methodology. Results of temperature dependencies measurement will be used in computer simulation for hypothermia cancer destroying.

1. INTRODUCTION

The thermal conduction and the specific heat are two most important thermal properties of each matter for computer simulation. However these parameters could be very different in whole temperature range. Knowledge of these temperature dependencies is very important for correct results obtaining. For example see Figures 1(a) and (c) where temperature dependencies of stainless steel AISI 302 are shown.

We need to know temperature dependencies of the bio-material thermal properties. These properties will be used for real experiment of hypothermia optimization. We have to use two physical approaches for obtaining of all important data. The first one is calculation of thermal conductivity from known parameters of system, see Equation (1) and Figure 1(b). It's necessary to have only small temperature gradient $T_1 - T_2$ about 1 K for exact determination of the thermal conductivity by the temperature in 1/2 of Δx.

$$Q = k \cdot A \cdot \frac{T_1 - T_2}{\Delta x} \Rightarrow k = \frac{Q \cdot \Delta x}{A \cdot (T_1 - T_2)}, \tag{1}$$

where Q is heat transfer [W], k is thermal conductivity [W/(m·K)], A is area [m^2], T_1, T_2 are temperatures on both sides of material [K], Δx is thickness [m],

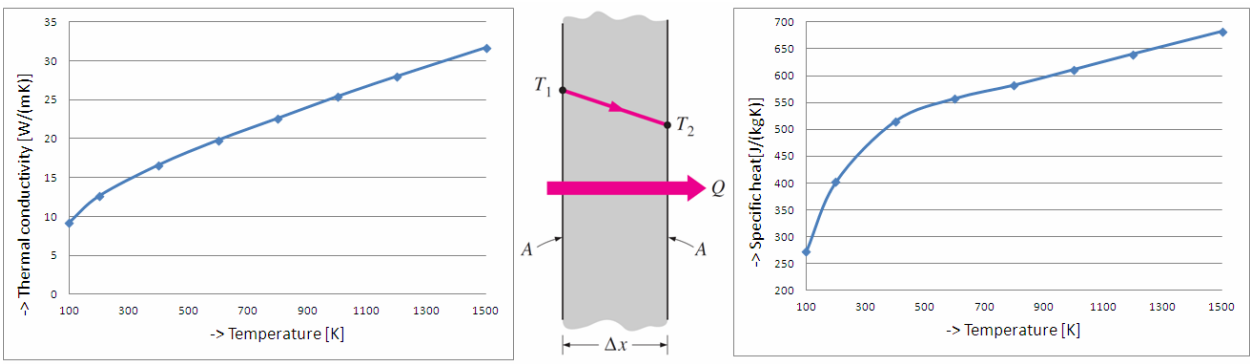

(a) (b) (c)

Figure 1: (a) Thermal conductivity. (b) Heat transfer scheme. (c) Specific heat.

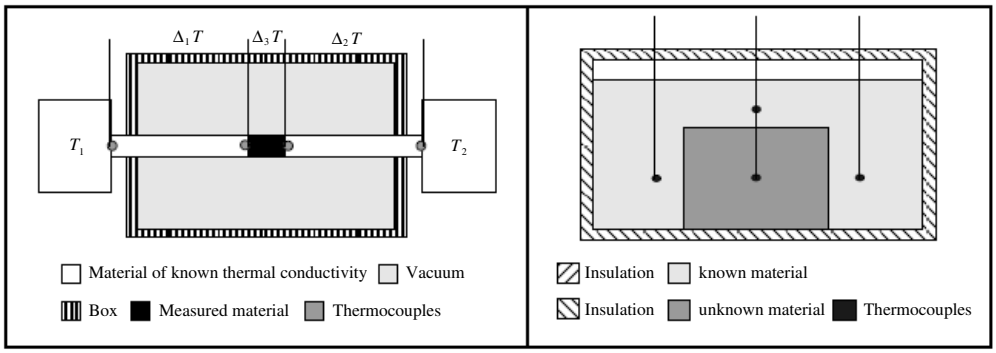

(a) (b)

Figure 2: Principle scheme of (a) thermal conductivity measurement, (b) calorimetry.

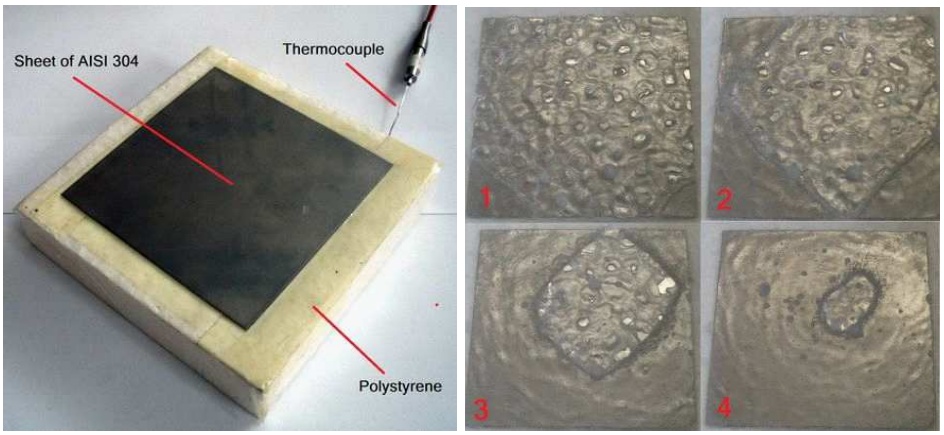

(a) (b)

Figure 3: (a) Measurement with thermocouple. (b) Visual method of measurement.

The second physical approach is the calorimetry. The main principle of the calorimetry is in heat transferring from first matter of known weight to second matter of known weight. We need temperature stable state for reading of specific heat by this temperature. The principle of the calorimetry is obvious from the Equation (2).

$$Q_1 = Q_2 \Rightarrow C_1 \cdot m_1 (T_1 - T) = C_2 \cdot m_2 (T - T_2) \Rightarrow C_2 = \frac{C_1 \cdot m_1 (T_1 - T)}{m_2 (T - T_2)}, \tag{2}$$

where C_1, C_2 are specific heats of both matters [kJ/(kg·K)], m_1, m_2 are weights [kg], T_1, T_2 are initial temperatures [K], T is the final stable temperature [K]. Equation (2) could be expressed like Equation (3) corresponds with our experiment configuration.

$$C_P = \frac{Q}{m \cdot (T_1 - T_2)}, \tag{3}$$

where C_P is specific heat capacity at constant pressure, Q is heat [W], m is weight [Kg].

2. MEASUREMENT OF CONVECTION HEAT TRANSFER COEFFICIENT

The first part of real experiment is focused on finding a convection heat transfer coefficient of immersed surface of stainless steel AISI 304. First experiment is displayed in Figure 3(a). Stainless steel AISI 304 sheet of dimensions $0.08 \times 0.08 \times 0.001$ m was putdown in liquid nitrogen. Top side of sheet was isolated with polystyrene and the thermocouple was in contact with this side. The temperature measurement was started with putting in liquid nitrogen simultaneously. We stopped the measuring time when the temperature on non cooled side of the sheet came stable and very close to the temperature of liquid nitrogen.

Temperature of steel sheet falls from 292 K to the stable temperature of liquid nitrogen 77 K during 40 s. Second experiment is displayed in Figure 3(b). The steel sheet about temperature 292 K was putdown to liquid nitrogen and stopwatch was launched. First quadrant displays boil of liquid nitrogen on whole sheet surface. The boil retreats from corners to the middle during the measure time. The stopwatch was stopped after 42 s when the boil disappeared. These values are very important for next calculation. If we suppose next parameters of the steel sheet AISI 304 like density $\rho = 7900\,\mathrm{kg/m^3}$, immersed surface of steel sheet $S = 0.00672\,\mathrm{m^2}$, weight $m = 0.051\,\mathrm{kg}$ and specific heat described with Equation (4).

$$C_p(T) = 7.01e^{-13} \cdot T^5 - 3.38e^{-9} \cdot T^4 + 6.3e^{-6} \cdot T^3 - 5.66e^{-3} \cdot T^2 + 2.58 \cdot T + 6.49, \qquad (4)$$

It is possible expressed heat required to increase temperature of whole steel sheet about 1 K from Equation (4). Summary of all these heat give us totally heat necessary for temperature change from 77 to 292 K. Totally heat is 4074 J or 101.84 W (J/s), because time of temperature change is 40 s. This heat was applied to surface $0.0064\,\mathrm{m^2}$ therefore heat flow is $15155\,\mathrm{W/m^2}$. Temperature change is 216 K and convection heat transfer coefficient is then $70.16\,\mathrm{W/(m^2{\cdot}K)}$. This convection heat transfer coefficient is then used in computer simulation of laboratory preparation design.

3. LABORATORY PREPARATION DESIGN AND COMPUTER SIMULATION

Laboratory preparation will be realized for measuring of thermal conductivity and specific heat simultaneously. The principal scheme of laboratory preparation is displayed in Figure 2(a).

Two stainless steel AISI 304 rods of 0.006 m in diameter and 0.15 mm length are inserted in vacuum. The measured sample of tissue is situated between these two rods in AL pan. The aluminium pan is hermetic closed and its volume is about little micro litre and it is usually used in DSC (Differential Scanning calorimetry). Heat stable sources are realized like two radiators cooled with liquid nitrogen and heated with electric power heating. Power of cooling is regulated with depth of immerse into container of liquid nitrogen. Electric power heating is realized with heating coil. We need adjust temperatures in range 76 K to body temperature about 310 K. The thermocouples are placed on boundaries of matter. The main idea of realized experiment corresponds with Equations (1) and (2). We know thermal conductivity of stainless steel but we don't know the thermal conductivity of measured material a heat transfer thru it. Therefore we have to set up 10 K temperature gradient with two stable heat sources. Then we can read temperatures on ends of two steel rods and assume the same heat transfer is thru the measured sample. These temperatures may be used in left side of Equation (1). We obtain heat transfer which can be used in right side of Equation (1). The result is then the thermal conductivity of measured material about known temperature. The stainless steel AISI 304 is used because its temperature dependecies of thermal

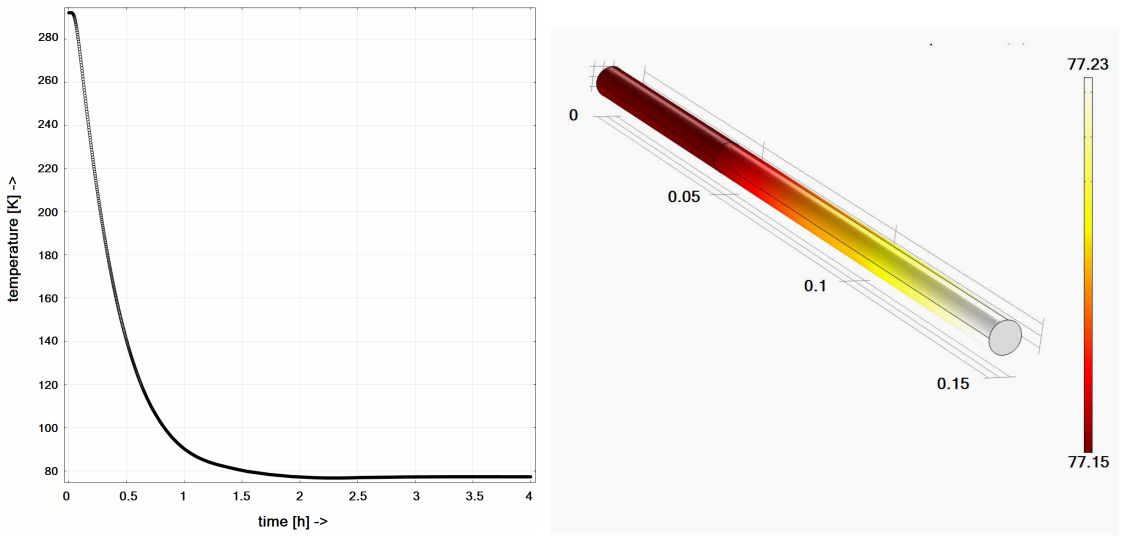

Figure 4: (a) Temperature rate in opposite end of 0.015 m AISI 304 rod. (b) Temper temperature distribution in whole steel prism after 1.5 h.

properties are known and closer to bio-material then other known metal materials. Assumtion of bio-material thermal conductivity is about 0.5 W/m and specific heat is about 3600 J/(kg·K) instead of thermal conductivity of AISI 304 about 12 W/m and specific heat is about 400 J/(kg·K).

4. RESULTS

Real experiment with stainless steel sheet AISI 304 of dimensions $0.08 \times 0.08 \times 0.001$ m and liquid nitrogen gave us convection heat transfer coefficient 70.16 W/(m^2·K). This value was used for computer design and simulation. Results are displayed in Figure 4. Time for stable temperature state in opposite end of 0.15 m steel rod is then estimated over 2 hours.

5. CONCLUSIONS

The main goal of research discrabed in this paper is temperature dependecies meeasurement of bio-material thermal properties. This properties are very important for next computer simulation for optimization of hypothermia. The stainless steel AISI 304 is used because its temperature dependecies of thermal properties are known and closer to bio-material then other known metal materials. Assumtion of bio-material thermal conductivity is about 0.5 W/m and specific heat is about 3600 J/(kg·K) instead of thermal conductivity of AISI 304 about 12 W/m and specific heat is about 400 J/(kg·K). Maybe we can use material with higher thermal conductivity, because time to stable temperature state is relatively long. Suitable are AISI 4130, AISI 1095, AISI 1020 or AISI 1006 for example. Next part of research will be focused on laboratory preparation realizing and on real measurement of temperature dependencies of bio-material thermal properties. Final part of this research will be focused on cryosurgery optimization.

ACKNOWLEDGMENT

The research described in the paper was financially supported by a grant of the Czech Ministry of Industry and Trade No. FR-TI1/001, GACR 102/09/0314, and project of the BUT Grant Foundation No. FEKT-S-11-5/1012. This work was also partially supported by EC and MEYS CR (project No. CZ.1.05/2.1.00/01.0017).

REFERENCES

1. Incropera, F., et al., *Fundamentals of Heat and Mass Transfer*, 6th Edition, 1024, Wiley, 2006, ISBN 978-0-471-45728-2.
2. Cho, Y., *Bioengineering Heat Transfer: Advances in Heat Transfer*, 443, Academis Press Limited, London, 1992, ISBN 0-12-020022-8.
3. Zhmakin, A. I., *Fundamentals of Cryobiology: Physical Phenomena and Mathematical Models*, 280, Springer, Berlin, 2009, ISBN 978-3-540-88784-3.
4. Akay, M., *Biomedical Engineering*, Vol. 1 and 5, John Wiley and Sons, Hoboken, New Jersey, 2006, ISBN-13 978-0-471-24967-2.
5. Hrozek, J., D. Nespor, and K. Bartušek, "Temperature dependencies measurement, proposal and preparing," *PIERS Proceedings*, 357–360, Kuala Lumpur, Malaysia, Mar. 27–30, 2012.

Measurement of Magnetic Flux Density by NMR Using Unsymmetrical Spin Echo

T. Kříž[1], **K. Bartušek**[1, 2], **and R. Kořínek**[1, 2]

[1]Department of Theoretical and Experimental Electrical Engineering
Brno University of Technology, Kolejní 4, Brno 612 00, Czech Republic
[2]Academy of Science of the Czech Republic, Institute of Scientific Instruments
Královopolská 147, Brno 612 64, Czech Republic

Abstract— Post processing of magnetic flux density by measured by nuclear magnetic resonance is described in this article. Unsymmetrical spin echo was used to a magnetic field measurement. Magnetic flux density was measured outside the conductive specimen. The cooper specimen was made on surface of Printed Circuit Board (PCB). Direct current source was connected to the measured specimen.

1. INTRODUCTION

The measurement was assembled to obtain magnetic field values in neighborhood of specimen connected to the current source. The measured values will be used to reconstruction of specimen conductivity. The reconstruction of specimen conductivity from magnetic field values is inverse problem. For this purpose the EIT regularization methods are used. Details can be found in [1]. All magnetic flux density components must be measured in case of conductivity reconstruction task.

There is a lot of different ways for magnetic field measurement. Most of these methods are based on Hall effect. The magnetic field components were measured in three different times but it is very difficult to move the measuring head precisely to measuring points. It is better to use nuclear magnetic resonance (NMR) to measure magnetic field because one component of magnetic flux density $\mathbf{B}$ is measured in whole specimen at the same time.

There is one very important condition — to use low level of direct current. The level of source current has to be established with view to possibility of changes in specimen material properties.

The NMR approach was chosen to measure the magnetic field. It is possible to measure small values of magnetic field by NMR. Gradient echo method (GE) or unsymmetrical spin echo method (SE) can be use for magnetic field measurement. Both methods have advantages and disadvantages. The GE is very sensitive to basic magnetic field $\mathbf{B}_0$ changes but it is necessary to unwrap the image phase. The phase unwrapping is very difficult and it is multivalent in the case of neighboring pixels with phase change higher than 2π. Disadvantage of SE method is smaller sensitivity to changes of basic magnetic field $\mathbf{B}_0$. It isn't necessary to unwrap of phase correction the phase of image obtained by this method. The values of phase are between 2π.

2. MEASUREMENT ASSEMBLY

Several specimens have been prepared for experimental measurement. Two basic shapes of specimens were chosen. The first shape is circle and second shape is ring. Both types of specimens were prepared with and without defects. The specimens diameter is $d = 34\,\mathrm{mm}$. These specimens were created on printed circuit board (PCB) with copper thickness of $35\,\mu\mathrm{m}$. Direct current source was connected to specimens. The current value was adjusted to $I = 27\,\mathrm{mA}$.

To obtain magnetic field map it is necessary to place suitable material over specimen. Distilled water of level 2 mm was used as measured medium. Magnetic field distribution has been measured only in this layer. In order to measure the distribution of magnetic flux components the specimen was placed into the working place of NMR tomography. Specimen arrangement for measure the B_y component of the magnetic field by tomography is shown in Fig. 1(a). In order to measure the B_x component the specimen was rotated in perpendicular position in relation to the previous one.

Frequency encoded image represents the result of NMR measurement. Using inverse Fourier transformation it is obtained a complex image. The phase and module image is necessary to calculate the magnetic field.

The main information about magnetic field distribution is encoded in phase image. The interval of phase is $(\pi; -\pi)$. It is necessary to phase correction of unwrap the phase image. Initial point for

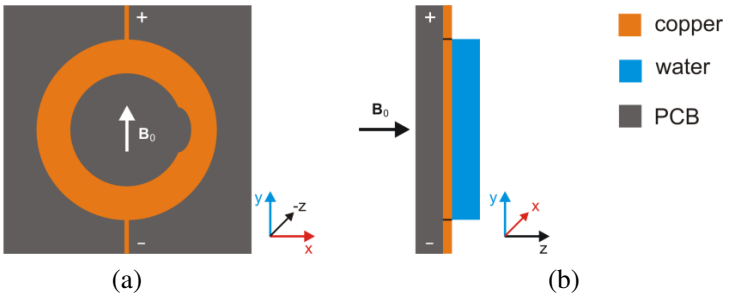

Figure 1: Specimen arrangement, (a) y-component, (b) z-component.

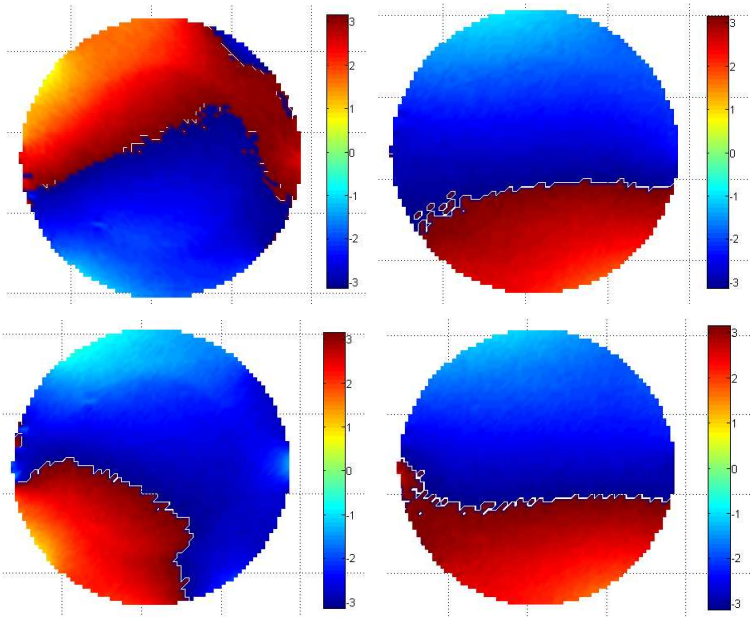

Figure 2: Phase images.

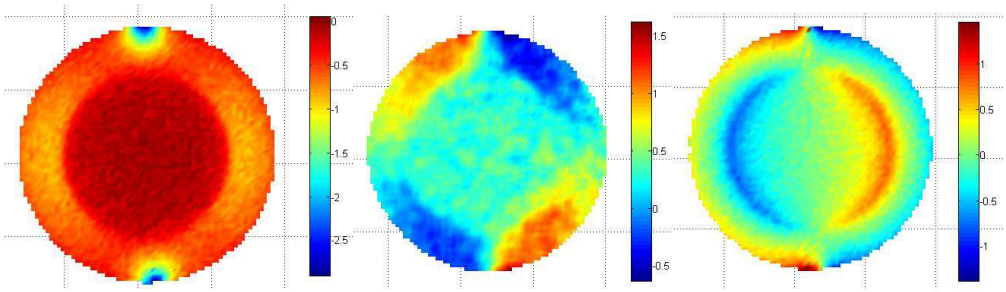

Figure 3: Magnetic flux density component B_x, B_y and B_z — phase correction.

phase unwrapping is identified from module image. A differential measurement has been used for background signals suppression and to obtain a magnetic field map around the specimen. Differential measuring was used to obtain magnetic flux density values. Four measurements were taken for each component of the magnetic field. Two measurements for each time shift of the spin echo value $+T_p$ and $-T_p$ were taken. One of the measurements was taken for a positive current direction and the second fort the negative current direction. Information about magnetic flux density is encoded in phase image if unsymmetrical spin echo is used. Changes of values of magnetic field relatively to static magnetic field $\mathbf{B}_0$ are given by following Equation (1):

$$\Delta B = 0.5 \left(\frac{\Delta\varphi_{+Te} - \Delta\varphi_{-Te}}{\gamma \cdot T_E} \right)^{+} - 0.5 \left(\frac{\Delta\varphi_{+Te} - \Delta\varphi_{-Te}}{\gamma \cdot T_E} \right)^{-}, \tag{1}$$

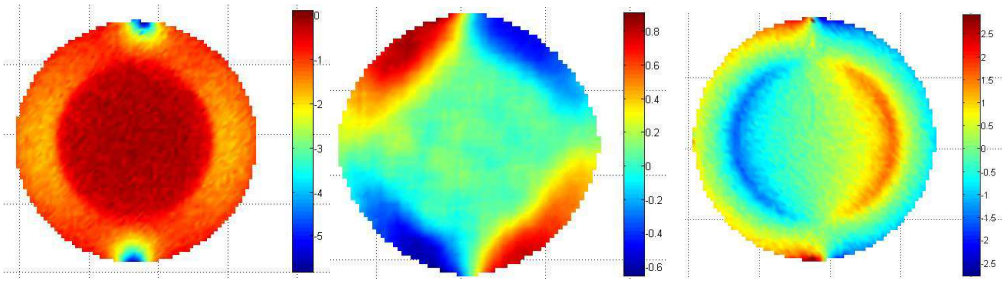

Figure 4: Magnetic flux density component B_x, B_y and B_z — unwrap.

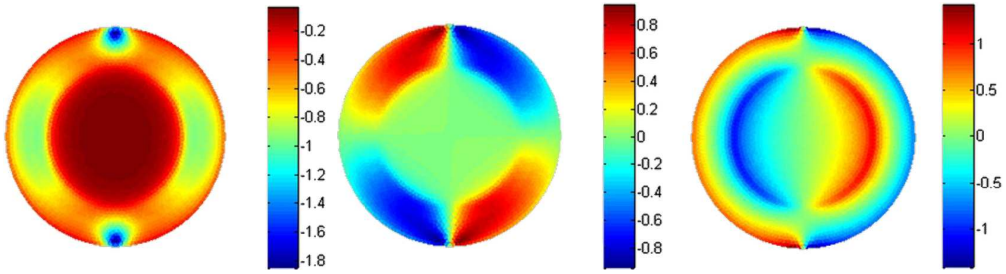

Figure 5: Magnetic flux density component B_x, B_y and B_z — calculated.

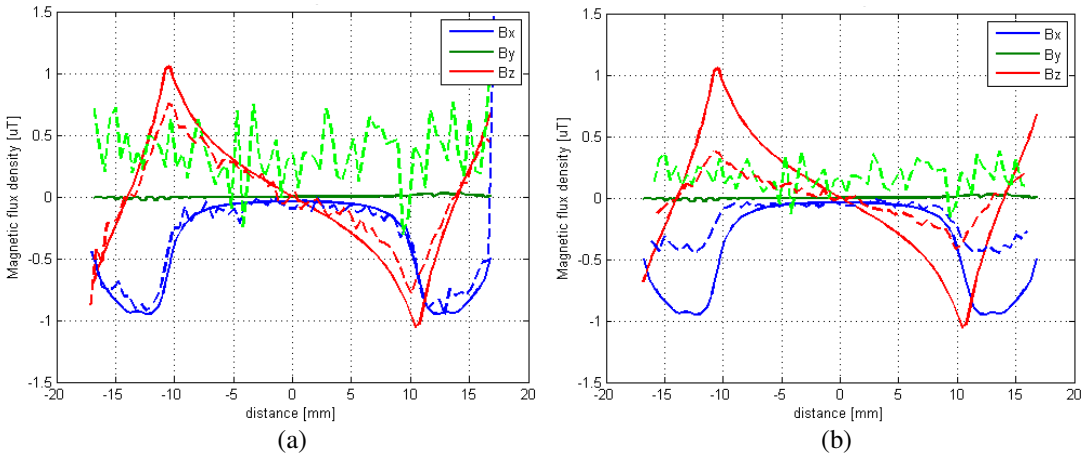

Figure 6: Comparison of results phase (a) correction and (b) unwrap dash line measured data.

where ΔB is change of $\mathbf{B}_0$, T_E is time echo, $\Delta\varphi$ is coded phase and γ is gyro-magnetic spin ratio.

3. NUMERICAL SIMULATION

In order to verify the measured values by NMR tomography numerical models were built for each specimen. Geometrical models were discretized by linear triangles elements. The models consist of approximately 5000 elements and of 2600 nodes. The electrodes were placed on y axis outer elements. The source current was adjusted to 27 mA. The copper conductivity was adjusted to $\sigma = 59.59\,\mathrm{MS/m}$. Direction of current corresponded to negative y ax. Electrical potential was solved by finite element method. The current was calculated on each element. These current values were used for calculation of magnetic field components. For magnetic flux density components evaluation was used Biot-Savart'law [3]. Components of magnetic flux density were calculated by averaging of values measured two millimeters above models. Average value was calculated from forty values for each element. There were used triangle meshes. We suppose that the surface current density $\mathbf{K}$ is constant on each element. The x- and y-component of magnetic flux density in examined point,

which is given by coordinates $[x_i, y_i, z_i]$, can be calculated by means of superposition principle.

$$B_{ix} = \frac{\mu_0}{4\pi} \sum_{j=1}^{NE} R_{ijz} \frac{\Delta S_j}{R_{ij}^3} K_{jy}, \quad B_{iy} = -\frac{\mu_0}{4\pi} \sum_{j=1}^{NE} R_{ijz} \frac{\Delta S_j}{R_{ij}^3} K_{jx}, \quad i = 1, \ldots, NE \tag{2}$$

where ΔS is element area, K is surface current density component, x, y, z are element center coordinates and R is distance between centers of elements.

4. MEASUREMENT AND SIMULATION RESULTS

The x-, y- and z-components are shown in Fig. 4. Comparing measured and simulated magnetic field distribution we can see that distribution of magnetic fields is corresponding. Diversity between measured and simulated values is due to signal phase periodicity in measured layer.

5. CONCLUSIONS

Comparing measured and simulated results it is obvious that the measured data obtained by NMR tomography aren't suitable to use as input data for conductivity reconstruction. Our future work will be focused on improvement of magnetic field measurement by NMR tomography.

ACKNOWLEDGMENT

The research described in the paper was financially supported by project of the BUT Grant Agency FEKT-S-11-5/1012 and projekt CZ.1.07.2.3.00.20.0175, Elektro-výzkumník.

REFERENCES

1. Vladingerbroek, M. T. and J. A. Den Boer, *Magnetic Resonance Imaging*, Springer-Verlag, Heidelberg, Germany, 1999, ISBN 3-540-64877-1.
2. Seo, J. K., O. Kwon, and E. J. Woo, "Magnetic resonance electrical impedance measurement tomography (MREIT): Conductivity and current density imaging," *Journal of Physics: Conference Series*, Vol. 12, 140–155, 2005.
3. Dedek, L. and J. Dedkova, *Elektromagnetismus*, 232s, VITIUM, 2. vyd. Brno, 2000, ISBN 80-214-1548-7.

A Comparison of Characteristics in Parallel and Series Connections of Active Lossy FDNR Blocks

Z. Szabó and J. Sedláček
Department of Theoretical and Experimental Electrical Engineering
Brno University of Technology, Czech Republic

Abstract— At present, modern active elements together with the utilization of the synthesis method based on purposefully lossy RLC prototypes enable us to realize ARC filters (for the frequency range within units of MHz) applying simple and economical selective building FDNR blocks that successfully work with one active element (OZ). This research report contains a complex analysis of attributes characterizing lossy active functional blocks; the authors show that the connection of active blocks with a series substitute model is significantly more advantageous than the commonly used parallel substitute scheme solution. A substantial benefit brought by this type of connection consists in the fact that, at higher frequencies, it does not exhibit the parasitic transmission zero which causes considerable problems in the case of parallel connections. Other related advantages of the described solution can be seen in its lower sensitivity to real parameters of the active elements, lower sensitivity to the variation of impedance level, and significantly higher (up to 20 dB) attainable circuit dynamics.

1. DESIGN AND REALIZATION OF FILTERS HAVING LOSSY PARAMETERS

The process of designing active filters based on RLC prototypes involves the application of several different types of active selective blocks. The design of low-pass filters very often employs the Bruton transformation, in which the structure of an RLC prototype is transformed to the RCD structure. Here, the elementary structural blocks applied are active elements known as dual capacitors (and frequently referred to in literature as FDNRs — frequency dependent negative resistors). In high-pass ARC filters, synthetic inductors (SIs) are often utilized as active blocks simulating the properties of a coil. These active blocks, realized in different circuit configurations and having different numbers of active circuit elements (operational amplifiers or OAs), have been described in sources such as [1, 2, 4].

In order to provide experimental verification of partial conclusions made within previous investigation into the properties of the designed active lossy block filters, several above-specified networks were realized as test samples on printed circuits. The related transmission properties (mainly the modular frequency characteristics and the circuit dynamics) obtained by means of computer modeling were compared with the experimentally measured values.

2. UNIVERSAL MEASURING STATION

A universal measuring station was set up together with the concept of a suitable measurement methodology in order to facilitate the measurement of transmission properties of various two-port networks within a wider frequency range. A block diagram of the measuring station is presented in Fig. 1.

Figure 2 then shows the first-designed model connection of the realized 5th order low-pass sample filter with lossy dual capacitors; the buffer amplifiers are indicated as well.

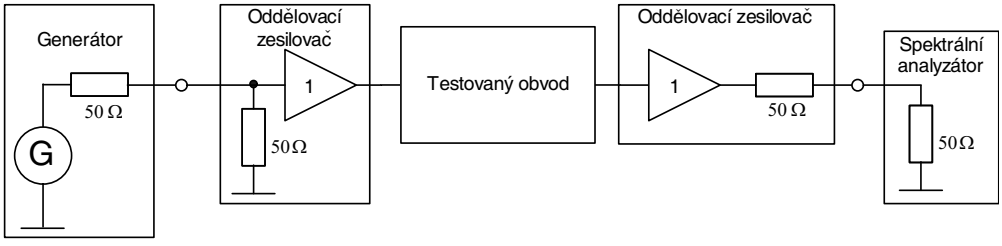

Figure 1: Block diagram of the measurement apparatus testing the designed filtration circuits.

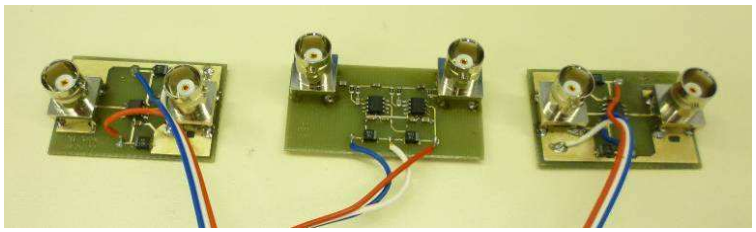

Figure 2: Block amplifiers and the filtration circuit.

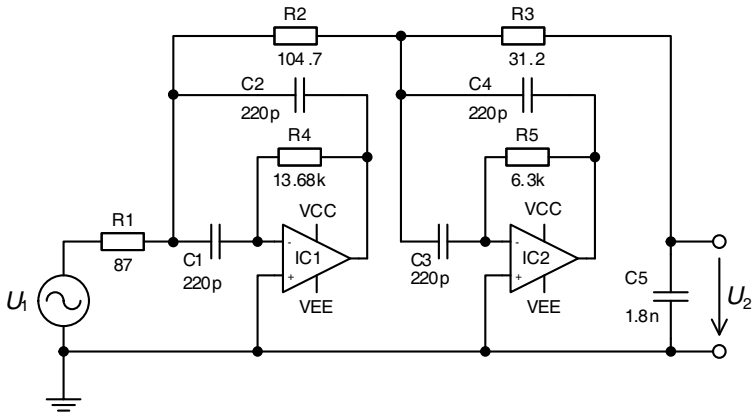

Figure 3: Connection of the 5th order low pass filter with the threshold frequency of 1 MHz — FDNR V — parallel loss.

3. MEASUREMENT RESULTS OBTAINED WITH THE REALIZED FILTERS

In agreement with the objective of this section of our analysis (namely the verification of theoretical assumptions and conclusions resulting from computer-based simulations of circuits), we applied the created program [1, 2] to design and realize low-pass and high-pass filters having the above-discussed lossy active blocks (dual capacitors and synthetic inductors). These filters were realized as samples.

Based on the previously presented subchapters, attention was paid mainly to two elementary types of active blocks with a different substitution diagram; thus, we focused on the connection of active blocks with a series substitution diagram marked as type I and with a parallel substitution diagram marked as type V.

3.1. Measurement Results of the Low-pass FDNR Filter (Parallel Loss)

A connection diagram of the designed filter is shown in Fig. 3. According to the graphs of modular frequency characteristics in Fig. 4, these characteristics approach the theoretically calculated values. The influence of properties of real active elements is evident from the graph: The shift of frequency characteristics in the stopband towards the lower frequencies gains in intensity with increasing narrowness of the active element transmission band.

Measurement of the filter dynamics (Fig. 5) fully confirmed the results established through circuit modeling. This type of circuit provided a comparatively small dynamic range (approximately 300 mV with the supply voltage of 5 V, and about 200 mV with the supply voltage of 3.5 V).

3.2. Measurement Results of the Low-pass FDNR I Filter (Series Loss)

Connection diagram of the designed filter is shown in Fig. 6, and the measured characteristics are presented within the graphs in Fig. 7. These graphs indicate very good agreement between the modular frequency characteristics and its theoretical counterpart within the stopband. In the passband, the measured characteristics show a slight decrease; as indicated by later measurements, this decrease occurred owing to the failure to keep the correct load impedance value. Graphs of the characteristics confirm our previously made conclusions: This circuit exhibits lower sensitivity to real properties of the elements, and the characteristics for both types of the operational amplifiers are virtually identical.

Similarly, the measurement of attainable dynamics (Fig. 8) also confirmed the conclusions made in previous subchapters. The measurement results show markedly higher attainable dynamics in

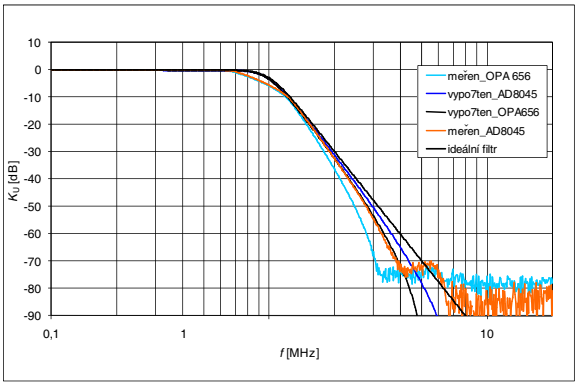

Figure 4: Transmission of the low-pass filter with the threshold frequency of 1 MHz — FDNR V — parallel loss.

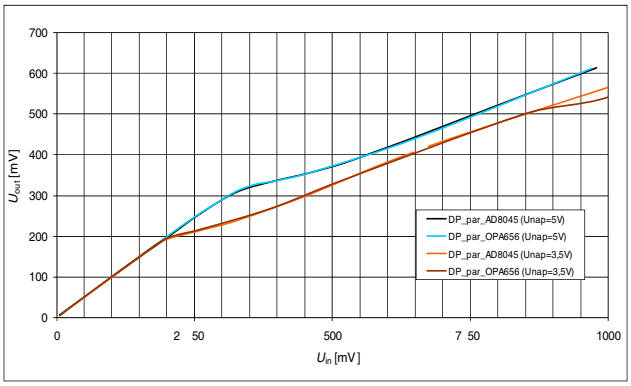

Figure 5: Dependencies of the LP output voltage on the input voltage at the frequency of 500 kHz.

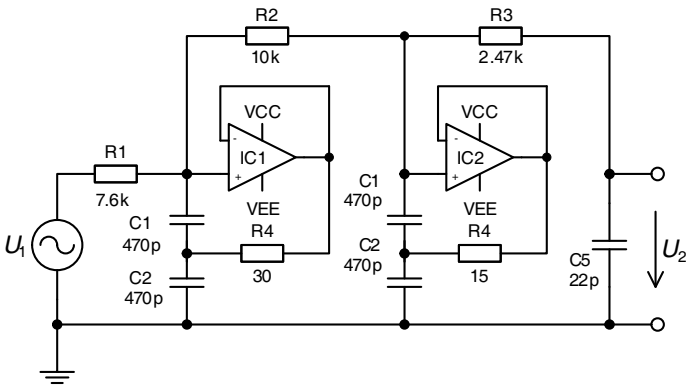

Figure 6: Connection of the 5th order low-pass filter with the threshold frequency of 1 MHz — FDNR I — series loss.

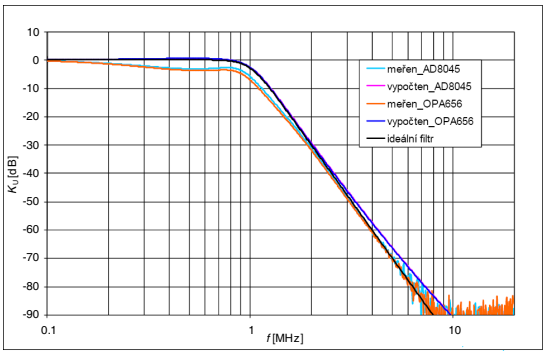

Figure 7: Low-pass transmission with the threshold frequency of 1 MHz — FDNR I — series loss.

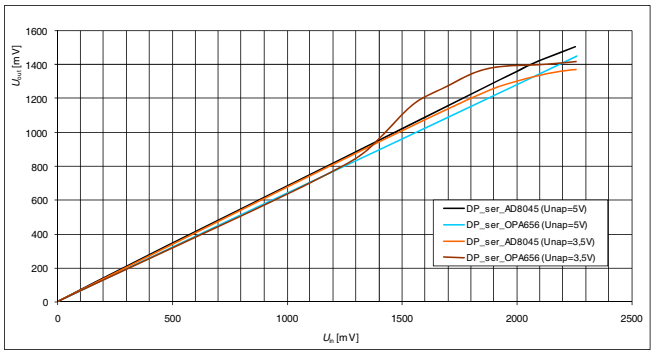

Figure 8: Dependencies of the LP output voltage on the input voltage at the frequency of 500 kHz.

these types of circuit (transmission linearity of up to 2000 mV even with the reduced supply voltage of 3.5 V), which is in full agreement with theoretical conclusions presented within the available research reports [2]. The measured values indicate that, with lower supply voltage values, the AD 8045 operational amplifier shows better results.

3.3. Measurement Results of the High-pass Filter with Synthetic Inductors (Parallel Loss)

Connection diagram of the designed filter is provided in Fig. 9, and the measured modular frequency characteristics are shown in the graphs within Fig. 10.

Modular frequency characteristics of the measured sample filters are almost equal to the ideal characteristics for both types of the operational amplifiers.

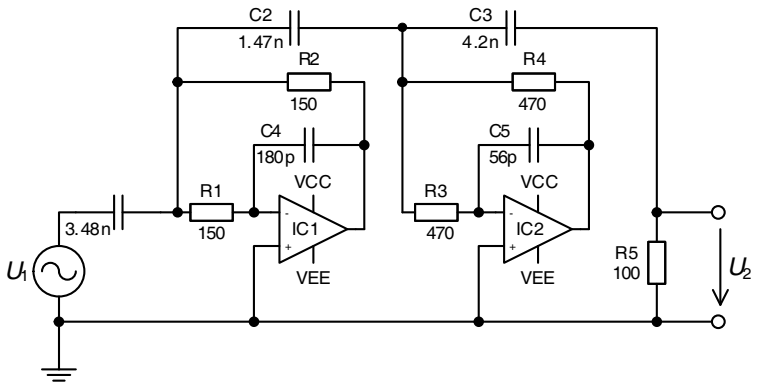

Figure 9: Connection of the 5th order high-pass filter with the threshold frequency of 1 MHz — SI — parallel loss.

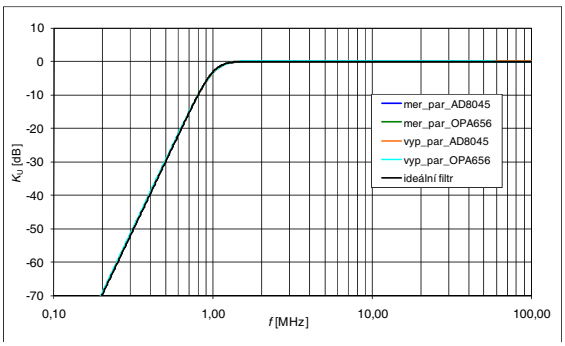

Figure 10: High-pass transmission with the threshold frequency of 1 MHz — SI — parallel loss.

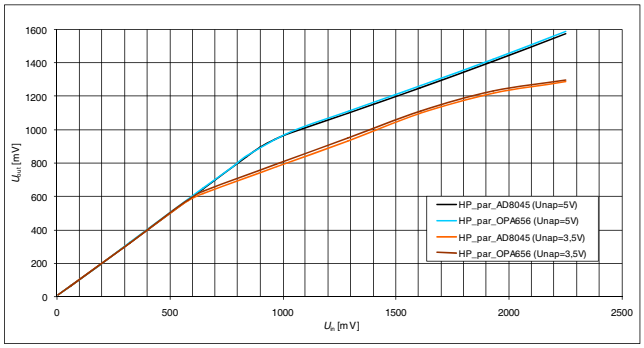

Figure 11: Dependencies of the HP output voltage on the input voltage at the frequency of 2 MHz.

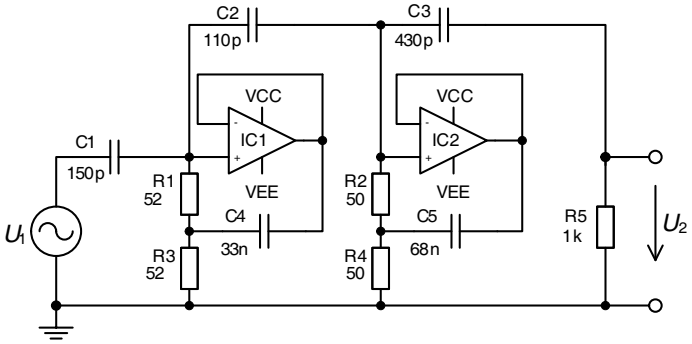

Figure 12: Connection of the 5th order high-pass filter with the threshold frequency of 1 MHz — SI — series loss.

The attainable circuit dynamics are expressed by the curves in Fig. 11; these curves are virtually identical for both types of the operational amplifiers, and the maximum input voltage may reach the approximate values of 900 mV with the supply voltage of 5 V and 550 mV with the supply voltage of 3.5 V.

3.4. Measurement Results of the High-pass Filter with Synthetic Inductors (Series Loss)

Connection diagram of the designed filter is provided in Fig. 12, and the measured modular frequency characteristics shown in the graphs within Fig. 13 indicate very good agreement between the theoretical and the measured values. In the passband frequency area towards higher frequencies, both the measured and the modeled characteristics exhibit small transmission decrease (approximately 1 dB). The measurement of attainable circuit dynamics (Fig. 14) provides results similar to those obtained with low-pass filters.

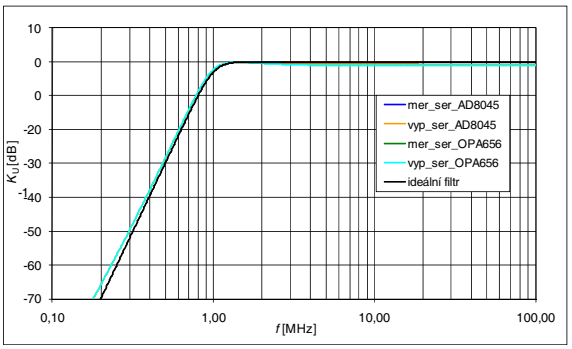

Figure 13: High-pass transmission with the threshold frequency of 1 MHz — SI — series loss.

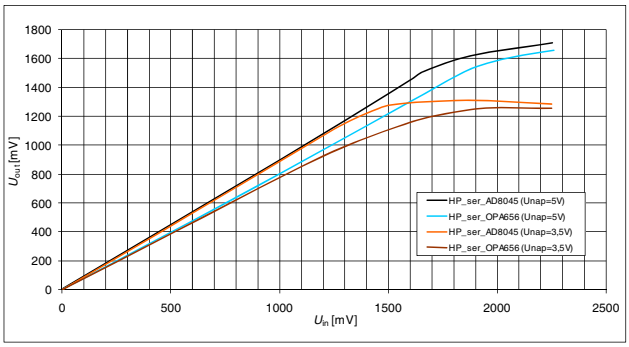

Figure 14: Dependencies of the HP output voltage on the input voltage at the frequency of 500 kHz.

Dynamic range in these types of circuit is substantially wider than in parallel loss circuits (the maximum input voltage of approximately 1700 mV with the supply voltage of 5 V; with the circuit supply voltage of 3.5 V, the corresponding value may attain 1300 mV).

4. CONCLUSION

This research report contains a complex analysis of properties of lossy active functional blocks (lossy dual FDNR capacitors and SI synthetic inductors). In addition to considering the most frequently applied manners of connection, we analyzed and compared the properties of five different methods of connection in active circuits of both types. The related comprehensive analysis of properties of these connections was centered on the frequency characteristics and sensitivity to real parameters of active circuits (operational amplifiers) and passive elements. Importantly, we acquired a large number of novel information.

It was determined that the connection of active blocks with a series substitute model provides several advantages as opposed to the most frequently utilized connection with a parallel substitute scheme. A substantial advantage of these types of connection consists in the fact that, at higher frequencies, they do not exhibit the transmission parasitic zero, which often causes substantial problems within the parallel connection. Other favorable factors can be seen in the lower sensitivity of the connection to real parameters of the active element, lower sensitivity to impedance level changes, and substantially higher (up to 20 dB) attainable circuit dynamics.

The conclusions obtained by means of computer modeling of the above-discussed circuits were fully confirmed by several measurements performed on the realized sample filters. We utilized practical connections of the low-pass and high-pass filters of the second and the higher orders to verify the perspective of using these blocks together with newly introduced operational amplifiers at frequencies reaching units of MHz.

The benefit brought by this section of the report consists also in the measuring station design and in the verification of the measurement methodology that enables us to examine the parameters of active two-port networks within a wide range of frequencies.

Thus, the information provided within the related chapter may not only contribute toward wider practical utilization of the discussed circuits, but also help researchers to improve their designs and optimize active frequency filters using these economical functional blocks.

ACKNOWLEDGMENT

The research described in the paper was financially supported by grant of the Czech Ministry of Industry and Trade No. FR-TI1/368, project of the BUT Grant Foundation FEKT-S-11-5/1012, and project No. CZ.1.07.2.3.00.20.0175, Elektro-výzkumník.

REFERENCES

1. Szabó, Z., "A contribution to optimal synthesis of filters," 118s, Dissertation Thesis, Faculty of Electrical Engineering and Communication, Brno University of Technology, 2012.
2. Szabó, Z. and J. Sedláčk, "A simple economical building FDNR blocks with modern operational amplifiers," *PIERS Proceedings*, 1113–1117, Moscow, Russia, Aug. 18–21, 2009.
3. Sedláčk, J., Z. Szabó, and R. Kadlec, "Optimized ARC filters using goal-lossy GIC," *PIERS Proceedings*, 591–596, Beijing, China, Mar. 23–27, 2009.

4. Sedláčk, J., Z. Szabó, and V. Michal, "A non-cascade synthesis of optimized ARC filters," *TIEF 2007*, 1–7, UTEE, FEKT VUT v Brně, Paris, 2007, ISBN 978-80-214-3476-9.
5. Hájek, K., V. Michal, J. Sedláčk, and M. Steinbauer, "A simple method of goal — Directed lossy synthesis and network optimization," *Advances in Electrical and Electronic Engineering*, 249–253, Žilina, 2006, ISSN 1336-1376.
6. Hájek, K., V. Michal, and J. Sedláčk, "Modern operational amplifiers and their degeneracy effects on active filter performance," *IC — SPETO 2006*, 505–507, Gliwice, Ustroň, 2006.
7. Hájek, K. and J. Sedláčk, "Lossy LC ladder prototypes and their use for ARC filter optimization," *Wseas Transactions on Electronics*, Vol. 2, No. 3, 94–99, Jul. 2005, ISSN 1109-9445.
8. Martinek, P. and T. Daša, "Evolutionary algoritmes by ARC filter synthesis," *ECCTD 05*, 155–159, Cork, 2005.

Compact Metamaterial-based Bias Tee Design for 1.55 μm Waveguide-photodiode Based 71–76 GHz Wireless Transmitter

Merih Palandöken[1], **Vitaly Rymanov**[2], **Andreas Stöhr**[2], **and Tolga Tekin**[1]

[1]Technische Universität Berlin, Gustav-Meyer-Allee 25, Berlin 13355, Germany
[2]Universität Duisburg-Essen, Lotharstr. 55, Duisburg 47057, Germany

Abstract— In this paper, a compact metamaterial-based bias-tee design is proposed for the integration of 1.55 μm photodetectors in E-band wireless transmitter module. The bias-tee is designed in the form of two slotted Split-Ring Resonators (SRR) in DC bias line with a magnetic coupling distance inbetween. The photodiode is isolated from DC bias line with an RF signal suppression level better than 28 dB between 71–76 GHz. The insertion loss is better than 0.3 dB with a minimum return loss of 23 dB at RF port in the whole operation band. Due to sub-wavelength resonance feature of SRRs, the bias tee can be correspondingly miniaturized in length and width. The RF performance of proposed bias tee is compared with that of conventional $\lambda/4$ transmission line based bias-tee. The effects of geometrical parameters are additionally investigated in order to verify the design approach and determine the critical design parameters.

1. INTRODUCTION

The progressive growth in communication technologies has been brought by optical and wireless communications technologies. These two technologies have started to merge to create a new inter-disciplinary area called Microwave and Millimeter-Wave Photonics (MWP) [1]. MWP technology aims at achieving advancement and improved functions in telecommunications systems that cannot be achieved by the individual technologies, but can be achieved mainly through the combination of radio-wave and photonic technology. Therefore, MWP is nowadays an important technology for various commercially available high data-rate applications in millimeter-wave and even THz frequency ranges [2–4]. One optical component in miniaturized MWP systems is the photodiode. In order to generate high power millimeter waves in broad band, the optimum operation of photodiodes in wireless communication networks is very important [5]. Therefore, in addition to the design parameters, DC biasing of photodiodes has to be correspondingly achieved with a sufficiently good RF isolation at DC port.

Metamaterials are artificially structured materials providing electromagnetic properties not encountered in nature. Negative permittivity and permeability materials are quite important consequences of artificial material based design methodology. The material parameters can be modified in terms of frequency band and magnitude in a controlled manner depending on the arrangement and geometrical parameters of metallic inclusions [6–8]. These unit cells are basically electrically small resonators, which could be in the form of electrically small electric and magnetic dipoles [7]. SRR is the first negative permeability unit cell, which was proposed by Pendry [9].

In this paper, a compact metamaterial-based bias-tee design is proposed for the integration of 1.55 μm waveguide photodiodes in E-band wireless transmitter. The bias-tee design is explained first with the geometrical parameters in Section 2. The numerical results are illustrated in Section 3 with the resonant current distribution and parametrical analysis of geometric dimensions on the transmission and isolation parameters. In Section 4, the concluding remarks are conducted with the comparison to the conventional $\lambda/4$ bias-tee design.

2. BIAS-TEE DESIGN

The metamaterial-based bias-tee is shown in Figure 1 along with the geometrical parameters. The signal width and gap between ground and signal line of RF line at ports 1 and 2 are 350 μm and 100 μm, respectively. The length of CPW line from port 1 to the junction point with port 3, L_{RF} is 1.3 mm. The length of DC line, L_{DC} is 1.6 mm. The first SRR is located on DC line with shift distance of $d_{DC} = 170$ μm. The length and width of outer ring resonator are 0.4 mm and 0.28 mm, respectively. The length and width of inner ring resonator are 130 μm and 160 μm, respectively. Two SRRs are separated from each other with a distance of 60 μm. The whole bias-tee is 1.6 mm × 0.49 mm. The via radius is 80 μm. The vias are used in order to suppress the slot line mode excited due to the homogenity along the propagation direction. The geometrical parameters

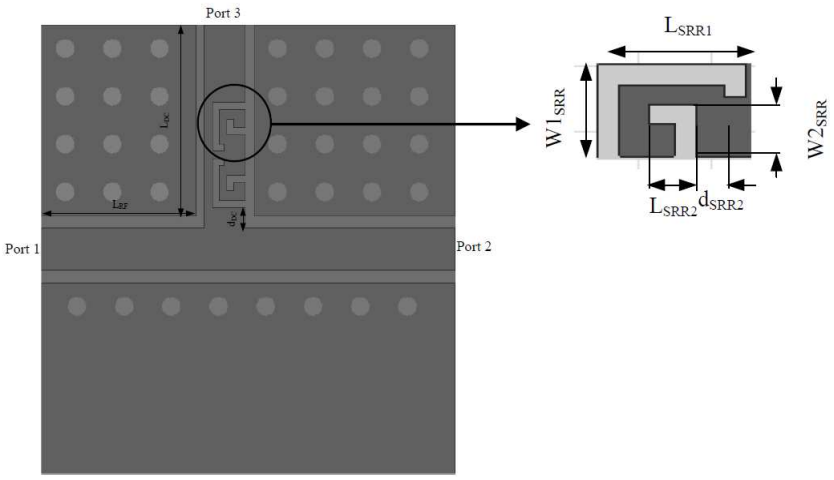

Figure 1: Metamaterial-based bias tee design with the geometric model of half SRR.

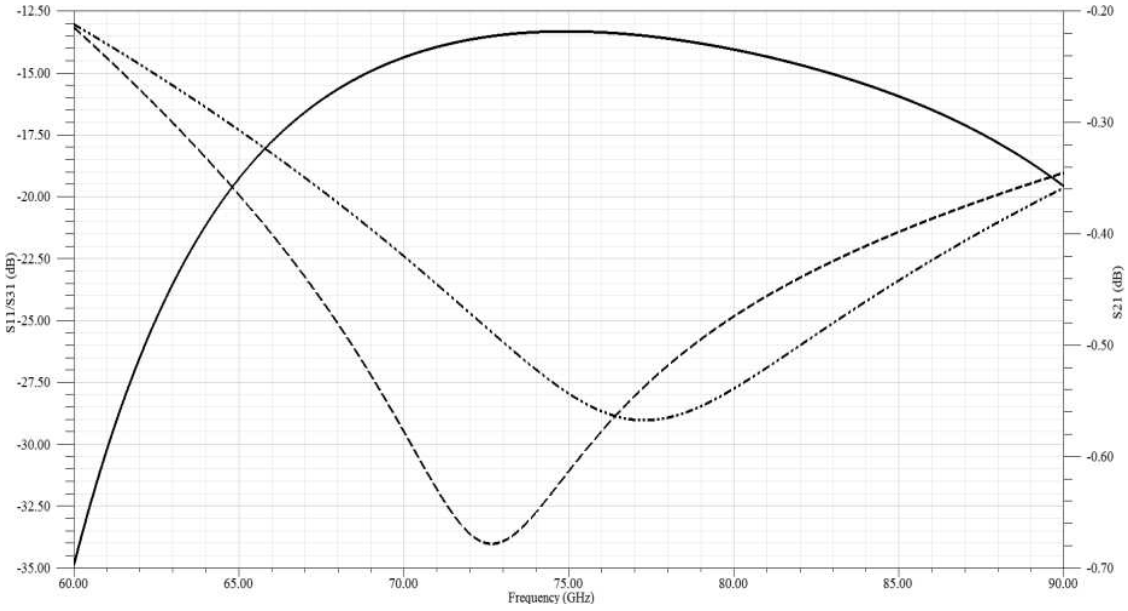

Figure 2: Transmission S_{21} (solid), S_{31} (- - -) and reflection S_{11} (..-..-) parameters of metamaterial-based bias-tee.

are optimized to have high transmission with low RF power into DC port. The substrate is Rogers 5880 with the relative permittivity of 2.2 and loss tangent 0.0009. The substrate thickness is 130 µm with double sided copper metallization.

3. NUMERICAL RESULTS OF METAMATERIAL-BASED BIAS-TEE

The proposed bias-tee is numerically calculated in HFSS. The transmission, reflection and RF isolation in DC port are shown in Figure 2. The RF isolation at DC port is better than 25 dB in the frequency band 68–80 GHz with the maximum isolation of 34 dB at 72.7 GHz. The insertion loss is better than 0.3 dB in the frequency band 66.7–86.7 GHz with the minimum value of 0.2 dB at 75 GHz. The return loss is better than 20 dB in the frequency band 68–90 GHz with the maximum value of 30 dB at 77.3 GHz.

The surface current distribution at the frequency of highest transmission, 75 GHz is shown in Figure 3.

The low RF signal propagation with high wave impedance as a result of electrically small SRRs can be deduced from low current magnitude at DC port. The wave propagation of CPW mode can be clearly observed along RF line. In bias-tee design, there are three critical design parameters to be

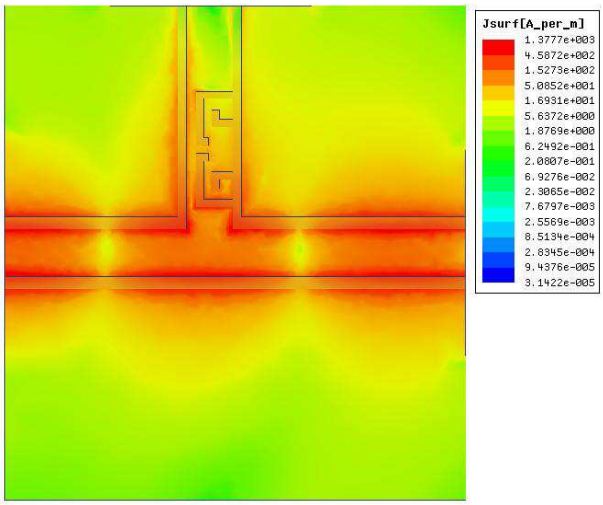

Figure 3: Surface current distribution at 75 GHz.

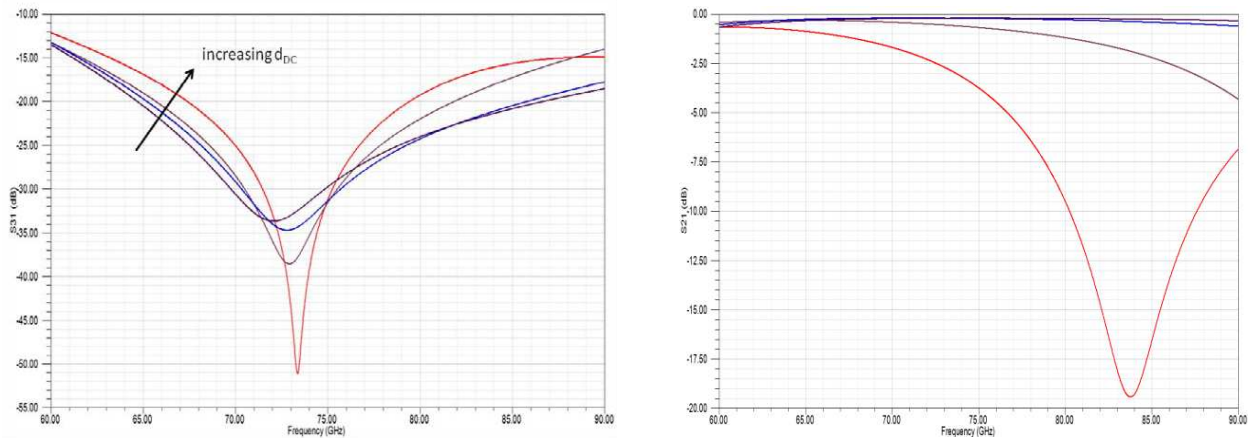

Figure 4: (a) Isolation, S_{31} and (b) transmission, S_{21} parameters of metamaterial-based bias-tee for different d_{DC}.

investigated. The first parameter to be determined is the resonator shape with respective geometric sizes. The length and width of inner and outer rings of one SRR in addition to separation distance of inner and outer rings are optimized to obtain the desired resonance frequency of two coupled $\lambda/4$ resonators. The location of two SRRS in DC line has to be studied as a second parameter to obtain the required phase difference at the junction point for better impedance matching at the input port and isolation at DC port. The effect of this second design parameter is shown in Figure 4 on RF isolation and transmission.

As shown in Figure 4, RF isolation tends to be better for larger d_{DC} due to loading of SRRs with low impedance of DC port, which results low propagating power into DC port. In other words, this is not due to high impedance resulting from two coupled SRRs. It is mainly because of low impedance, which degrades signal transmission correspondingly even high isolation.

The third design parameter is the optimum coupling strength among two SRRs. The isolation and transmission parameters for varying coupling distances are shown in Figure 5.

As shown in Figure 5, RF isolation tends to be worse for larger coupling distance due to ineffective loading of one resonator on DC line. Upper SRR is located with small separation distance to low impedance at DC port for larger coupling distances. This results DC line to be loaded effectively with one rather than two SRRs. The magnetic coupling needed to be obtained at the resonance frequency is therefore degraded, which is the reason of frequency shift to higher frequencies with increasing coupling distances. The proposed bias-tee design has the total size of 1.5 mm $\times$ 0.49 mm,

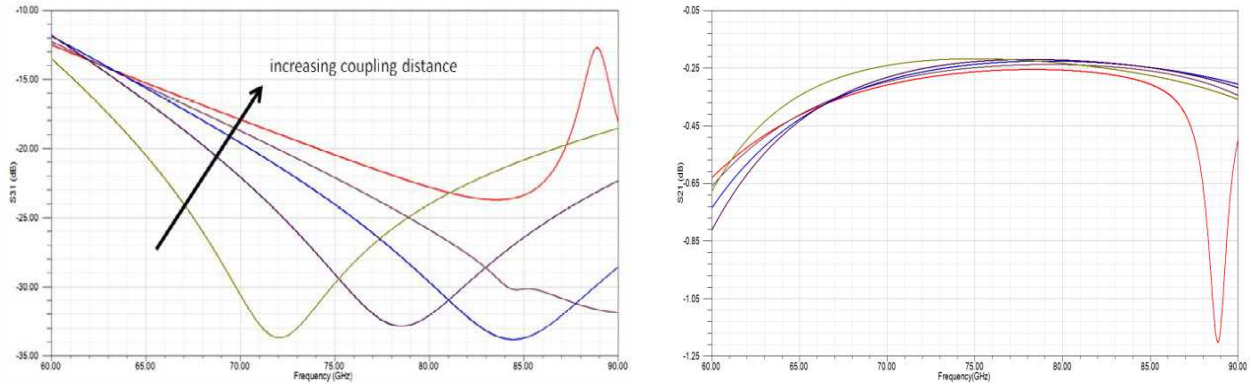

(a) (b)

Figure 5: (a) Isolation, S_{31} and (b) transmission, S_{21} parameters of metamaterial-based bias-tee for different d_{DC}.

which is the dimension of DC bias line. The RF parameters of $\lambda/4$ transmission line based bias-tee is also investigated [10]. The maximum insertion loss of this conventional bias-tee is 0.24 dB at 67.24 GHz with maximum return loss of 52 dB at 65.6 GHz. The maximum RF isolation is 71 dB at 72.2 GHz. The total size is 1.53 mm × 2.06 mm.

4. CONCLUSIONS

In this paper, a metamaterial-based bias-tee design is proposed. It is composed of two slotted half SRRs in the form of $\lambda/4$ resonators on DC bias line, which results the proposed design to be compact. The effects of main design parameters on transmission and isolation parameters are numerically studied to investigate RF properties. RF signal suppression level better than 28 dB between 71–76 GHz and insertion loss better than 0.3 dB are obtained for the optimized bias-tee model. The minimum return loss at RF port is 23 dB in the whole operation band. The insertion loss is better than 0.3 dB in the frequency band 66.7–86.7 GHz with the minimum value of 0.2 dB at 75 GHz. The RF performance of proposed bias tee is compared with that of conventional $\lambda/4$ bias-tee. Due to better insertion loss, and permissible isolation and return loss, the proposed design can be used in 1.55 µm photodetectors based E-band wireless transmitter modules. The important advantage of proposed design is that its length is 25% of that of the conventional design, which yields the matching circuits to be conveniently placed even for highly integrated MWP platforms.

REFERENCES

1. Nagatsuma, T. and Y. Kado, "Microwave and millimeter-wave photonic devices for communications and measurement applications," *Optical Fiber Communication and Optoelectronics Conference*, 63–65, 2007.
2. Wells, J., "Faster than fiber: The future of multi-Gb/s wireless," *IEEE Microw. Mag.*, Vol. 10, No. 3, 104–112, May 2009.
3. Ng'oma, A., D. Fortusini, D. Parekh, W. Yang, M. Sauer, S. Benjamin, W. Hofmann, M. C. Amann, and C. J. Chang-Hasnain, "Performance of a multi-Gb/s 60 GHz radio over fiber system employing a directly modulated optically injection-locked VCSEL," *Journal of Lightwave Technology*, Vol. 28, No. 16, 2436–2444, 2010.
4. Park, C. and T. S. Rappaport, "Short-range wireless communications for next-generation networks: UWB, 60 GHz millimeter-waveWPAN, and ZigBee," *IEEE Wireless Commun.*, Vol. 14, No. 4, 70–78, Aug. 2007.
5. Rymanov, V., S. Babiel, A. Stöhr, S. Lutzmann, M. Palandöken, B. Bouhlal, and T. Tekin, "Integrated E-band photoreceiver module for wideband (71–76 GHz) wireless transmission," *European Microwave Week 2012, European Microwave Conference, EUMC 2012*, Paper No. 1751, Amsterdam, Oct. 29–Nov. 1, 2012.
6. Eleftheriades, G. V. and K. G. Balmain, *Negative Refraction Metamaterials: Fundamental Principles and Applications*, Wiley Interscience, New York, 2005.
7. Caloz, C. and T. Itoh, *Electromagnetic Metamaterials: Transmission Line Theory and Microwave Applications Piscataway*, Wiley/IEEE, NJ, 2005.

8. Engheta, N. and R. W. Ziolkowski, *Metamaterials Physics and Engineering Explorations*, Wiley/IEEE, New York, 2006.
9. Pendry, J. B, A. J. Holden, D. J. Robbins, and W. J. Stewart, "Magnetism from conductors and enhanced nonlinear phenomena," *IEEE Transactions on Microwave Theory and Techniques*, Vol. 47, No. 11, Nov. 1999.
10. Palandöken, M., B. Bouhlal, S. Lutzmann, V. Rymanov, A. Stöhr, and T. Tekin, "Integration platform for 1.55 µm waveguide-photodiode based 71–76 GHz wireless transmitter, international forum on terahertz spectroscopy and imaging," *5th Workshop on Terahertz Technology*, Paper Identity No. 47, Kaiserslautern, Mar. 6–7, 2012.

Ultra-wideband Radio Frequency Beamforming Using Microwave BFNs

F. E. Fakoukakis[1], **T. N. Kaifas**[2], **and G. A. Kyriacou**[1]

[1]Department of Electrical and Computer Engineering
Democritus University of Thrace, Xanthi 67100, Greece
[2]Department of Physics, Aristotle University of Thessaloniki, Thessaloniki 54124, Greece

Abstract— In the present work, a new technique for ultra-wideband radio frequency beamforming, based on the microwave photonics techniques, is introduced. It makes use of high frequency microwave networks to process low radio frequency (RF) wideband signals. The general concept is elaborated, along with its applications to ultra-wideband RF phased arrays. Both transmit and receive modules are designed, concentrating on the beamforming networks, which are based on the well known Butler matrix. Simulation results are presented in detail, whereas comparisons and remarks on future work are given in the end.

1. INTRODUCTION

Radio frequency systems have been used in a large variety of applications, such as communications, military, aviation and atmospheric (ionospheric) research. Throughout the years, the need for wideband operation has become more intense, since systems' requirements demand broadband operation in multiple octaves. Many radio frequency systems use phased arrays (or multibeam antennas) for transmit/receive operation, exploiting beamforming and directional beam-steering. This necessity became inevitable with the current trend towards Software Defined Radio (SDR) and Cognitive Radio (CR). Their concepts ask for digitally (software) controllable and multifunctional radio frequency front-ends. Regarding the antenna this demand is translated to ultra-wideband structures able to precisely control their beam direction and radiation pattern shaping, but should be miniaturized to yield compact structures conformably integrated over the device package (e.g., mobile unit). Thus, a wideband phased array must be integrated in the system. However, nontrivial difficulties arise when trying to design a wideband array, since the operation frequency band of the components is always limited. Despite that, quite enough wideband systems have been operated, presenting an operational frequency range of a few octaves.

In this study, a new technique for ultra-wideband radio frequency beamforming is presented. The technique mimics the principles of "microwave photonics" systems, where a microwave signal is translated into the optical regime, using an electro-optical modulator and an optical signal as a carrier [1, 2]. The modulated signal is processed with optical circuitry. The use of the optical carrier signal allows for the processing of ultra-wideband microwave signals, which occupy a very small fraction (percent) of bandwidth at the high optical frequencies, thus operational bandwidth extends up to many GHz. That means that an ultra-wideband microwave signal can be operated and processed, without the need for wideband techniques. As far as microwave phased arrays are concerned, the microwave signal modulates an optical carrier which is in turn split into a number of channels equal to the number of the antenna elements. The modulated optical signal in each channel undergoes the desired phase shift, which is the same independently of the microwave frequency (within a multiple GHz band), thus introducing the desired true-time delay (TTD). The signal of each channel is then demodulated by a simple diode detector, amplified accordingly and fed to the corresponding antenna element. A similar approach is followed in the receiver. This technique is called photonic beamforming [2, 3]. The same design principle is used herein, to accomplish ultra-wideband operation for radio frequency signals. The carrier signal used now is a microwave one, which exhibits an operational bandwidth of about 5–10%, that is, a few hundreds of MHz. This operational bandwidth constitutes a multiple octave bandwidth for a radio frequency signal with a frequency of several MHz. Thus, the microwave carrier signal offers ultra-wideband operation to the radio frequency signal.

This method is applied to the design of ultra-wideband radio frequency phased arrays and beamforming networks operating in the VHF/UHF bands. Multiple octave bandwidth offers true-time delay (TTD) operation for phased array systems, avoiding beam-squint and pattern degradation with frequency variation. The emphasis is given on the design of the beamforming networks, which

are based on the well known Butler matrix [4]. Moreover, system design ideas will be presented, for both transmit and receive architectures. The possibility of integrating transmit and receive functions into one architecture will be examined, along with extending the whole design technique to millimeter wave bands.

2. SYSTEM DESIGN

The basic design architecture of the proposed transmit system is presented in Fig. 1(a). The RF signal lies in the VHF/UHF bands whereas the microwave signal used has a center frequency of 10 GHz. The RF signal (f_m) modulates the microwave one (f_c), using an amplitude modulator (e.g., balanced mixer). The modulated signal is fed to a Butler matrix network through a digitally controlled MMIC switch. The Butler matrix is designed at the center carrier frequency (10 GHz). Thus, the Butler matrix processes the modulated microwave signal, applying the desired phase and amplitude distributions. The spectral bandwidth occupied by a dual-side band (DSB) amplitude modulated (AM) signal is $2f_{m(\max)}$ (where $f_{m(\max)}$ the maximum modulating frequency), as depicted in Fig. 1(b). The operational bandwidth at the center carrier frequency extends to a few hundreds of MHz, offering a multiple octave bandwidth to the RF signal. The microwave signal is downconverted to the RF band with the use of a crystal Schottky diode and fed to the antenna elements, after proper amplification. On the other side of the link, the receiver upconverts the incoming RF signals, creating again a microwave modulated signal which is fed to a similar Butler matrix and processed accordingly. Finally the signal is demodulated through a crystal diode

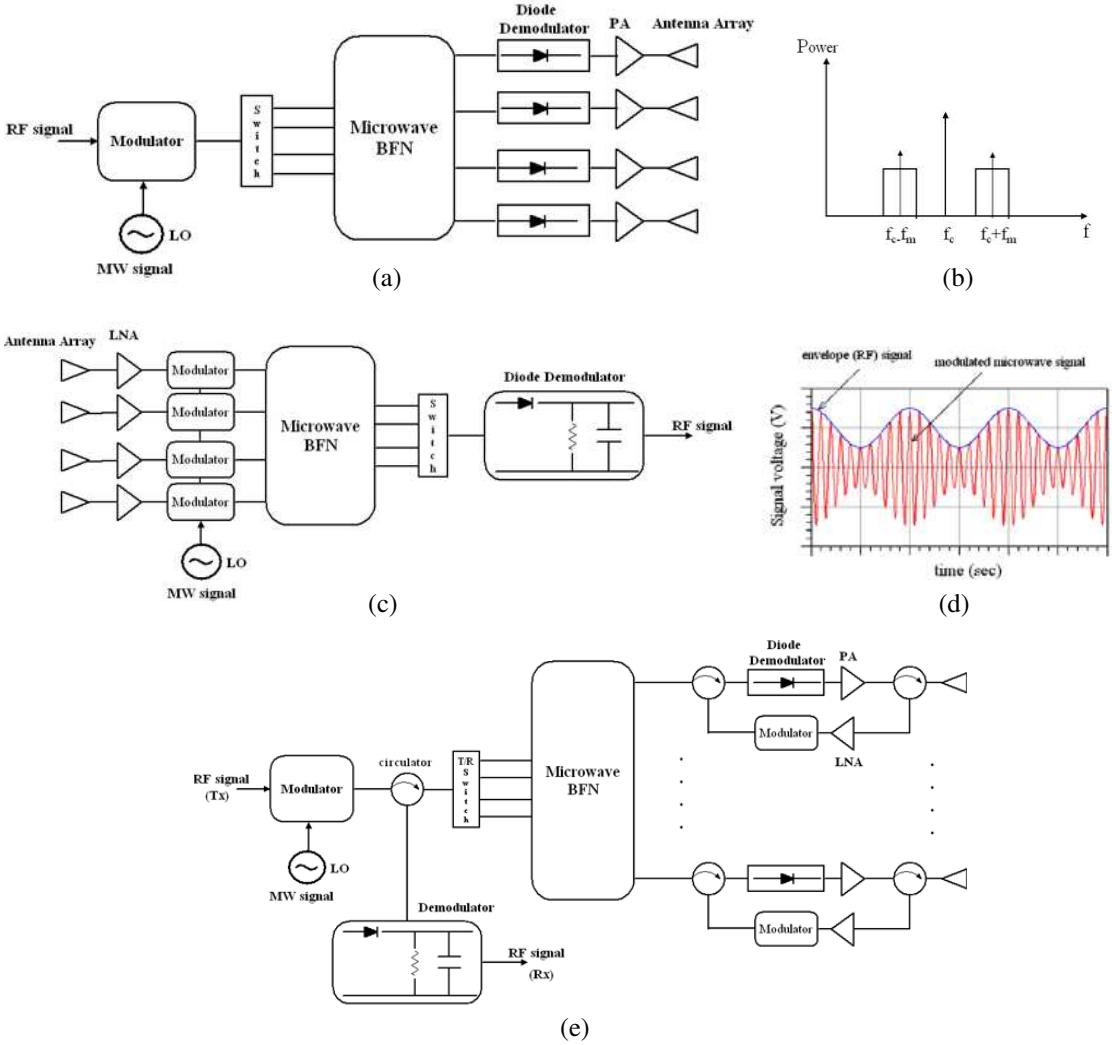

Figure 1: Design architectures of the proposed system. (a) Transmit system. (b) Spectral representation of the modulated signal. (c) Receive system. (d) Time domain representation of the signals. (e) T/R system architecture.

demodulator, as shown in Fig. 1(c). Low-noise amplifiers are used at the antenna array output ports to reduce the signal-to-noise ratio, in order to attain the required low noise figure.

Figure 1(d) depicts a representation of the modulated/demodulated signals. The amplitude modulated microwave signal is generated by the modulator, whereas the RF signal (envelope of the modulated signal) is detected with the use of the crystal diode detector (demodulator).

The above transmit/receive architectures (Figs. 1(a), 1(c)) are most likely to be implemented separately. This would be preferable in respect with the Butler matrix beamforming network since it operates at a high microwave frequency, it will be a compact device. However, the wideband RF antenna elements will be electrically large and it sounds preferable to exploit the same antenna array for the transmit and receive operations. Thus, an alternative architecture is proposed in Fig. 1(e). Since the Butler matrix is completely passive and reciprocal, it could be used for both transmit and receive functions, along with a T/R MMIC switch, as depicted in Fig. 1(e). The modulating/demodulating processes are separated with the use of circulators, connected at the antenna ports and at the input of the T/R switch.

3. BEAMFORMING NETWORK DESIGN

The most critical part of the system is the antenna array beamforming network (BFN), along with the ultra-wideband RF antennas. The BFN is based on the well known Butler matrix. Besides the classical phase sequences provided by the Butler matrix, providing multiple orthogonal beams and amplitude shaping is tried herein, aiming at an improvement of the sidelobe levels from the -13 dB to less than -30 dB. The network presented herein, has been modified to produce a tapered amplitude distribution at its output ports. Fig. 2(a) shows the schematic diagram of the 4 input-4 output Butler matrix that has been used. In order to achieve the tapered amplitude distribution, the second row hybrid couplers (shown in red color) are designed for an unequal power division, using the equivalent circuit presented in Fig. 2(b) [5]. A tapered amplitude distribution offering a -33 dB Chebyshev pattern was chosen. The network is designed in microstrip form, using a Rogers substrate with dielectric constant $\varepsilon_r = 3.38$, thickness $h = 0.508$ mm and loss tangent $\tan\delta = 0.0027$. The demanded line crossings are implemented with the use of microstrip crossovers [6]. The layout of the 4×4 Butler matrix is shown in Fig. 3.

The network was designed and simulated, in order to obtain its S-parameters and verify its behaviour. Fig. 4 presents some characteristic examples of the return and insertion loss curves,

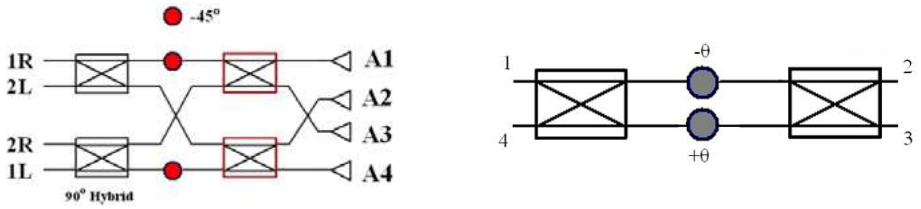

Figure 2: Schematic diagrams of the circuits. (a) 4×4 Butler matrix. (b) Unequal division hybrid coupler.

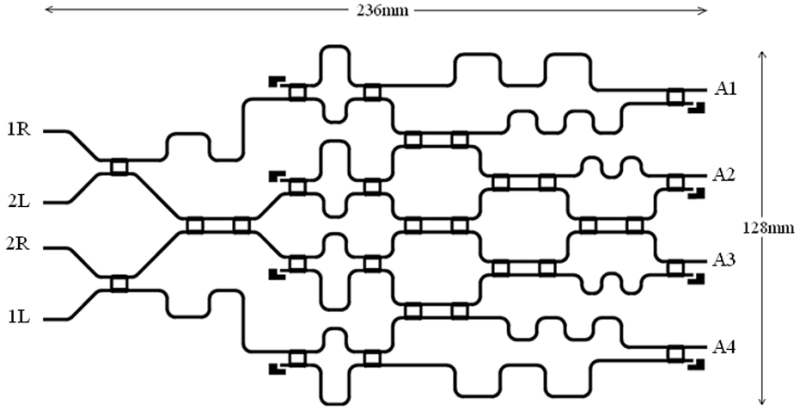

Figure 3: Microstrip layout of the designed 4×4 Butler matrix.

obtained by network simulation. Fig. 4(a) shows the return loss (RL, reflection coefficient) of $2R$ and $2L$ characteristic input ports. Keeping as a rule for the wideband operation that the VSWR should remain below 1.2 ($RL < -20\,\text{dB}$), the observed bandwidth is specified to be about 900 MHz (9%). Fig. 4(b) presents the insertion loss curves (IL, transmission coefficients) obtained by the excitation of $1R$ input port, obtained at the four output ports. The transmission coefficients inside the specified bandwidth remain at an acceptable level. Moreover, the transmission coefficient data, where transformed into amplitude and phase excitations at the matrix output ports. In particular, the target (theoretical) values are $-6.7\,\text{dB}$ and $-14.5\,\text{dB}$, whereas simulation gave an average of $-9.5\,\text{dB}$ and $-16.5\,\text{dB}$ within a 2 dB and 2.5 dB variation, respectively.

According to the simulation results and amplitude modulation spectrum demands, the 900 MHz bandwidth is appropriate for a 450 MHz RF amplitude modulating signal ($f_{m(\max)} = 450\,\text{MHz}$). The lowest modulating frequency is kept at 50 MHz. Thus, the modulating signal that could be used lies in the 50–450 MHz region.

The S_{ij} values were utilized to define the input data to an antenna simulation tool to produce the antenna radiation patterns. Rectangular microstrip antenna elements were chosen for simulation purposes , designed at the center modulating frequency of 250 MHz, on the same dielectric substrate referred above. The inter-element distance was kept to a half free-space wavelength ($\lambda_o/2$). The simulation results for the array radiation patterns are presented in Fig. 5.

As referred above, it is deduced from the simulation results that S-parameters maintain a nominal bandwidth of about 900 MHz. This frequency bandwidth can contain about one decade to 3.5 octaves of the modulating VHF/UHF signal. Thus, the designed 10 GHz Butler matrix behaves as an ultra-wideband network for an RF signal, without the use of any wideband design techniques.

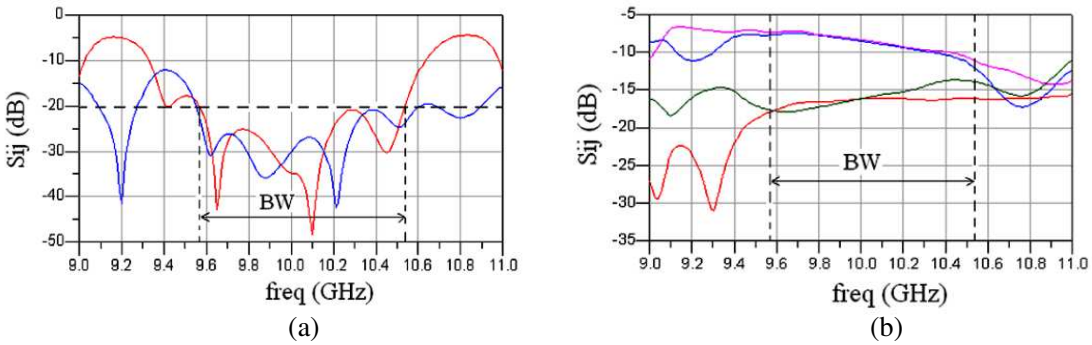

Figure 4: Simulation results of the 4×4 Butler matrix. (a) Return loss of $2R$, $2L$ input ports. (b) Insertion loss between $1R$ input port-outputs.

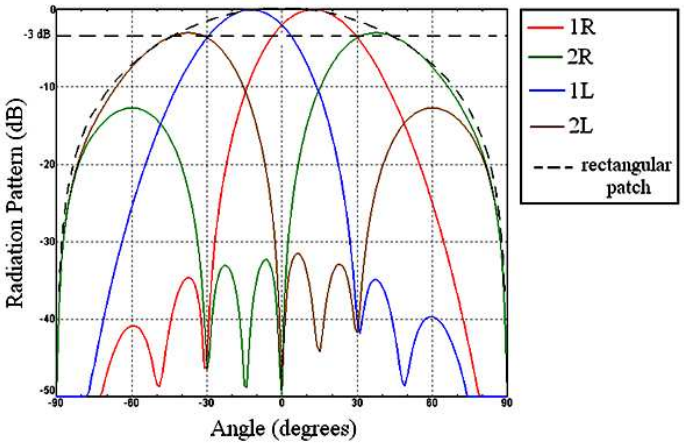

Figure 5: Simulated radiation patterns of the 4 beams at the center RF frequency.

4. THOUGHTS ON POSSIBLE RF ULTRA-WIDEBAND ANTENNAS

Depiction of wideband radiation patterns can be performed by designing and ultra-wideband antenna element, covering the 50–450 MHz region. Such a study is not part of the present work. However, an appropriate solution could be the Vivaldi antenna [7], in printed or slot form. Examples of wideband phased arrays using Vivaldi antenna elements can be found in the literature [8].

5. CONCLUSION

A new design idea for ultra-wideband VHF/UHF phased arrays was introduced. The idea mimics the microwave photonics techniques. In our case, the high frequency signal lies in the microwave region (instead of the optical carrier), whereas the low frequency signal is in the VHF/UHF bands. The system design was presented, along with the design and simulation of the beamforming network. Simulation results show that the network presents a nominal bandwidth extending from one decade to about 3.5 octaves of the RF signal, practically offering a true-time delay operation. Such systems could be used for the ultra-wideband demands of SDR and CR, especially if the highest frequency processing could be performed in the millimeter wave region. Future work includes development and integration of a prototype system, along with the study of extending the technique to millimeter wave frequencies.

REFERENCES

1. Iezekiel, S., ed., *Microwave Photonics: Devices and Applications*, John Wiley & Sons, 2009.
2. Yao, J., "Microwave photonics," *IEEE Journal of Lightwave Technology*, Vol. 27, No. 3, Feb. 2009.
3. Bratchikov, A. N., "Photonic beamforming in ultra-wideband phased antenna arrays: Present day and perspectives," *3rd International Conference on Ultrawideband and Ultrashort Impulse Signals*, Sevastopol, Ukraine, 2006.
4. Butler, J. L. and R. Lowe, "Beamforming matrix simplifies design of electronically scanned antennas," *Electronic Design*, Vol. 9, 170–174, Apr. 1961.
5. Cummings, W. C., "Multiple beam forming networks," Technical Note 1978-9, MIT Lincoln Lab, Apr. 1978.
6. Wight, J. S., W. J. Chudobiak, and V. Makios, "A microstrip and stripline crossover structure," *IEEE Transactions on Microwave Theory and Techniques*, Vol. 24, 270, May 1976.
7. Gibson, P. J., "The Vivaldi aerial," *9th European Microwave Conference*, 101–105, 1979.
8. Schaubert, D. H., "Wide-band phasedarrays of Vivaldi notch antennas," *10th International Conference on Antennas and Propagation*, Vol. 1, 6–12, 1997.